Complexity

Cyber-Enabled Intelligence Control and Security Optimization for Complex Microgrid Networks

Lead Guest Editor: Jingang Lai
Guest Editors: Xiaoqing Lu, Ruoli Tang, and Xin Li

Cyber-Enabled Intelligence Control and Security Optimization for Complex Microgrid Networks

Complexity

Cyber-Enabled Intelligence Control and Security Optimization for Complex Microgrid Networks

Lead Guest Editor: Jingang Lai
Guest Editors: Xiaoqing Lu, Ruoli Tang, and Xin Li

Contents

Hindawi
Complexity
Volume 2021, Article ID 8839595, 16 pages
https://doi.org/10.1155/2021/8839595

Research Article

State Characteristic Clustering for Nonintrusive Load Monitoring with Stochastic Behaviours in Smart Grids

Ruotian Yao,[1] **Hong Zhou**,[1] **Dongguo Zhou**,[1] **and Heng Zhang**[2]

[1]*School of Electrical Engineering and Automation, Wuhan University, Wuhan 430072, China*
[2]*Flight Automatic Control Research Institute, Xi'an 710065, China*

Correspondence should be addressed to Hong Zhou; hzhouwuhee@whu.edu.cn and Dongguo Zhou; dgzhou1985@whu.edu.cn

Received 7 August 2020; Accepted 20 July 2021; Published 31 July 2021

Academic Editor: Francesco Lo Iudice

Integrating the nonintrusive load monitoring (NILM) technology into smart meters poses challenges in demand-side management (DSM) of the smart grid when capturing detailed power information and stochastic consumption behaviours, due to the difficulties in accurately detecting load operation states in real household environments with the limited information available. In this paper, a state characteristic clustering (SCC) approach is presented for promoting the performance of event detection in NILM, which makes full use of multidimensional characteristic information. After identifying different types of state domains in an established multidimensional characteristic space, we design a sliding window difference search method (SWDS) to extract their initial clustering centre. Meanwhile, the mean-shift updating and iterating procedures are conducted to find the potential terminal stable state according to the probability density function. The above control strategy considers the transient events and stable states in a time-series dataset simultaneously, which thus allows the exact state of complex events to be obtained in a fluctuating environment. Moreover, a multisegment computing scheme is applied for fast computing in the state characteristic clustering process. Experiments of three different cases on both our real household dataset and REDD public dataset are provided to reveal the higher performance of the proposed SCC approach over the existing related methods.

1. Introduction

Recent years have witnessed an increasing attention to energy management in the smart grid, which forms a two-directional information flow between the supply side and demand side. Load monitoring is an effective method to obtain users' stochastic consumption behaviours in the demand side [1]. Suffering from the high cost of the intrusive load monitoring (ILM) approach, which needs to install sensors on every appliance, the nonintrusive load monitoring (NILM) technology can provide detailed load consumption information for both customers and utilities through uniform module [2]. Due to the increasing numbers of flexible loads, distributed generators, electric vehicles, etc. in the future smart grids and microgrids [3, 4], most utility companies are prone to encourage users to participate in demand response to maintain the load balance. Therefore, integrating the NILM algorithm into smart meters becomes an inevitable trend, in which utility companies can realize efficient demand-side management (DSM) based on the demand behaviour of energy consumers [5].

Most NILM approaches on the demand side demonstrated that tracking the consumption of main appliances in residential buildings can help consumers to minimize power consumption [6]. On the other hand, for the supply side, obtaining consumers' multidimensional consumption information enables the precise prediction of stochastic energy demand [7], the optimization decision [8], and power-sharing control of microgrids [9]. To this end, an original NILM framework was proposed in [10]. Following this line, a lot of works had contributed to the development of the algorithm for accurate load monitoring. Many different optimization approaches are presented, which mainly relied on pattern recognition, signal processing, cloud computing, and machine learning for processing voltage, current, harmonics, and other behaviour features [11–14]. Among them, related results can be classified into event-based and state-based approaches. The latter case includes the hidden

Markov model (HMM) and its variants [1, 15, 16], whereas the former case generally depends on the transient state and the change signals due to the increasing aggregate power induced by the turning on load [17]. Moreover, the majority of machine learning (including neural network) based methods applied for NILM require a training set for load modelling, which are generally regarded as supervised learning methods. However, the standard dataset for training needs to be collected in advance for every specific appliance in households.

In order to directly obtain the operating state of loads, modified event detection methods are applied for recent event-based approaches [18–22]. For an event detection algorithm, the intuitive idea is to determine transient events by using a trigger threshold in detecting power signals [18]. To obtain the load waveform from the aggregate signal, a two-step iterative shrinkage threshold algorithm in the high-frequency domain was presented in [19]. Shi et al [20] introduced a hybrid similar time window algorithm to perform demand prediction in a lower-resolution dataset. The generality of the algorithm benefited from the improved cross-prediction approach, without knowing historical data. Also, for low sampling NILM systems, two novel event detection algorithms, variance and mean absolute deviation, are proposed [21]. By balancing the optimal window width and optimal performance, the aggregated active power data of real-world dataset can be captured based on a sliding window. Among the existing approaches, the switch signature will be extracted first, and then effective features will be stored into the database for further load identification [23, 24].

However, event-based approaches are dependent on the transient and stable state events; thus, missing any event may lead to the deviation of disaggregation results. The challenge of high precision event acquisition mechanism is how to identify complex event states in a real-world residential environment with fluctuation. Following this line, to tackle the problems of the optimal combination of the extractor and classifier, an intelligent event-driven NILM approach based on the convolutional neural network is proposed. The energy consumption behaviour and working condition of appliances in a residential dataset can be identified effectively [22]. By combining an unsupervised event detection method with an additive factorial HMM, energy disaggregation results are obtained by online cloud computing [14]. As a sequential analysis method, the cumulative sum (CuSum) method can detect small deviations in the process by calculating the deviations between the sample value and the target value.

CuSum is commonly used for change point detection in the non-Bayesian setting when both prechange and post-change probability density functions are known [25]. Furthermore, in order to solve the problem of quickest detection of dynamic events in systems, a Network-CuSum algorithm based on the breadth-first search and a thresholding approach were presented in [26]. However, because of the accumulative property, even small fluctuations can lead to an increase (or decrease) in the cumulative sum. Hence, the approaches, especially those extracting power signal events as features, are susceptible to noises, such as jitter and outlier. Better results can be achieved by using thresholding and filtering algorithms under a fluctuation environment, but the basic idea should be improved further for the accurate NILM system.

Most unsupervised methods can be applied directly to time-series data without training datasets. Therefore, recent studies have attempted to identify load operating states by using clustering algorithms. The graph spectral clustering approach implements the power consumption forecast of a set of houses according to the current and previous appliance states [27]. In order to capture the timestamp of a transient event between two adjacent stable states, a modified density-based spatial clustering of applications with noise (DBSCAN) algorithm is proposed [28]. Moreover, multilayer perceptron classifiers are built for nonlinear loads by using harmonic characteristics. A stable state segmentation detector and a linear discriminant classifier group are used in [29] for load detection by considering the global characteristic similarity. As an iterative and nonparametric algorithm, mean shift and its variants are widely used in data clustering and denoising. By iterating through the probability density space, the clustering centre of the data can be located. Moreover, mean shift can identify clusters with different shapes, sizes, and densities due to its unsupervised property. In [30], an improved semisupervised kernel mean-shift clustering implements an automatic estimation of mean-shift parameters and automatically recovers an unknown number of clusters. In the mean-shift iteration process, a threshold parameter needs to be set as a stopping criterion to terminate the iteration process. Therefore, Aliyari Ghassabeh and Rudzicz [31] proposed a modified mean shift to guarantee the convergence of the data sequence without the stopping criterion.

Applying load detection approaches of NILM to real residential environments is a challenge for many algorithms. A fundamental problem is how to detect complex transient events (such as continuously varying transient states) in fluctuating environments effectively. Obviously, some threshold-based approaches (such as the trigger threshold method) do not have the property of detecting slowly changing events and long slope load transition stages. The approaches as mentioned above mainly employ the active/reactive power as the unique characteristic in the NILM system. To the authors' knowledge, there is very limited work on event detection using the mean-shift clustering iterative method in the multidimensional characteristic space. However, in the multidimensional space, clustering centres of stable states are more centralized than those of some transition states. Also, some state transition processes that cannot be reflected by one-dimensional data series can be clearly demonstrated in the multidimensional space. It is also a challenge to detect small-power devices when multiple loads are operating simultaneously. Motivated by these, we propose a state characteristic clustering (SCC) approach for demand side with stochastic behaviours, in which all data points collected by the NILM module will form several clusters in a multidimensional characteristic space. The proposed state domain definition is different from the often-adopted stable states of load events. A load event indicates

that an appliance is turned on or off, and the process in which the appliance runs normally and smoothly is called a stable state. However, the state domain defined in this paper represents the clustering region in the multidimensional characteristic space. Multidimensional steady-state data can be grouped in a specific domain around the cluster centre, while transient states are presented as a series of discrete points due to differences in time and space during load switching. Therefore, by the sliding window difference search (SWDS) method, initial cluster centres and state domains will be identified, respectively. Moreover, adjacent clusters can be shifted and merged by the mean-shift process as a terminal stable domain. Therefore, stochastic load events can be further captured. The main contributions of this paper are in the following aspects:

(i) Although a hybrid detection approach and a subtractive clustering approach are used in [32] and [33], respectively, only aggregated active/reactive power data are often considered to detect the load event of residential appliances. Therefore, to avoid the false alarm of using a single power characteristic for event detection, multiple characteristics collected by the NILM module are used in this paper to detect load events from multiple perspectives. We then established a state domain in the multidimensional characteristic space, under which the distribution characteristics of data can be highlighted clearly in groups and the clusters can be therefore divided into stable domains and transition domains according to the dataset.

(ii) The calculation burden of the algorithm will increase due to the large amount of high-frequency data [19]. For threshold-based methods [18], continuously varying transient events cannot be detected effectively in high-fluctuation environments. Therefore, the SWDS is proposed to extract the initial cluster centre of each original domain. Different from the threshold-based method and the CuSum method [26], the detection performance on low sampling rate time-series data can be improved by configuring appropriate SWDS parameters. In addition, due to the cumulative characteristics of CuSum, there will be persistent false alarms, resulting in a low detection accuracy. The proposed method can efficiently detect these complex states from 0.5 Hz aggregated power data in real household datasets.

(iii) Inspired by the mean shift, we present the updating and iteration scheme for state domains in the multidimensional space. To be specific, the initial centres will shift to a new cluster centre by updating and iterating according to the data density, and similar cluster centres will be merged into one domain. Accurate load events and states can be therefore determined synchronously once the original state domains are updated. Since it will take a specific time for SWDS and mean-shift procedure, a multisegment computing scheme is utilized for fast computing.

The outline of this paper is as follows: In Section 2, the definition of the state domain and multidimensional characteristic space are presented. Section 3 proposes the SCC approach, where the SWDS and the fundamental of mean-shift clustering procedure are described in detail. Section 4 gives three cases to verify the effectiveness of the proposed SCC approach, and the performance improvements of SCC on two datasets are proved by comparisons with other popular methods. Finally, conclusions are drawn in Section 5.

2. Establishment of State Domain in a Multidimensional Characteristic Space

The characteristic of a load can be defined by the multidimensional power features in a load identification system. Power features play an essential role in determining the type of load. The active power, reactive power, current harmonics, and other features, which are generated by the original voltage and current, are essential electrical signatures since the appliance is turned ON or OFF. Moreover, features such as running time, usage frequency, and operating time distribution also reflect the operating characteristic of a load. Hence, an event of a load can be considered as a signal switching (electrical or nonelectrical signals) in a state domain. An example of the transition of the state domain in a 3-dimensional space is shown in Figure 1.

Consider a d-dimensional nonzero dataset Ω^d with n elements, $\Omega^d = [\omega_1, \omega_2, \omega_3, \ldots, \omega_n]$, where $\omega_i \in R^d$ denotes a multidimensional characteristic vector. The state domain can be represented as a cluster, so a load event can be detected by finding the cluster centre of a data block. Moreover, a stable domain may shift from the current position to a new state when a load event occurs. By identifying the two stable domains, the transient process associated with these two states is represented by their transfer trajectory, which is defined as a transition domain.

When all loads are running normally, we consider the current state is a stable state with an initial cluster centre ω_a. Therefore, we define that the dataset at this time interval is contained within a stable domain Φ_A. Then, when a load is switched from an OFF state to an ON state (or vice versa), all electrical signals will transfer to another state. In the multidimensional characteristic space, we denote this transfer trajectory as a transition domain Φ_{ab}. Furthermore, the final stable state is Φ_B with a cluster centre ω_b. Then, the set of data points can be given by $\Omega_A = \{\omega | \omega \in \Phi_A\}$, $\Omega_B = \{\omega | \omega \in \Phi_B\}$, and $\Omega_{ab} = \{\omega | \omega \in \Phi_{ab}\}$, respectively. Each point in the state domain is distributed in a limited area. On the contrary, Φ_{ba} represents the transition from state Φ_B to state Φ_A.

Generally speaking, a whole operating period of an appliance consists of at least a transition domain and two stable domains. The stable domain represents the regular operation of the appliance, and its power data vary within a specific range of

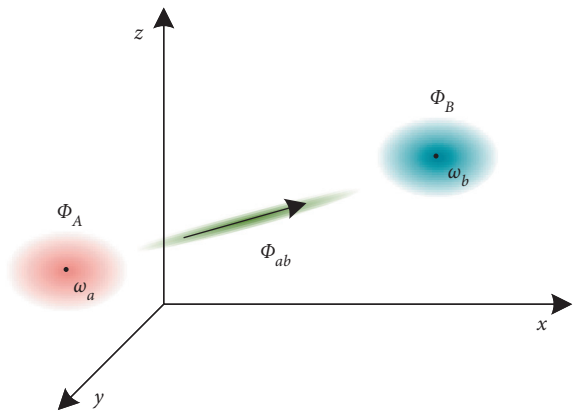

Figure 1: An example of stable domain and its transfer trajectory in a 3-dimensional characteristic space.

fluctuations. Also, the power data change during the state transition process. Notably, the transition state and the stable state usually appear alternately in a time-series dataset.

Figure 2 illustrates the changes of active power P, reactive power Q, and 3rd current harmonic H of an air-conditioner during an operating period. It can be seen that the transient state and the stable state occur alternately ($\Phi_A - \Phi_{ab} - \Phi_B - \Phi_{bc} - \Phi_C$). In the transient state Φ_{ab} (sampling points 27–45), active power and 3rd current harmonics slowly rise when the air-conditioner is started because of the operation of the compressor. At the same time, the reactive power decreases. In the stable state Φ_B (sampling points 45–155), the load reaches a stable running state with small fluctuations. In the last stage, all three characteristic curves show abrupt declines when the load is turned off, and the state returns to its initial state.

Missing or multiple detections in the slow-varying transient process often pose a challenge to accurate load monitoring systems. By mapping the multiple power data into a characteristic space, small fluctuations during the transition process can be effectively captured. As seen in Table 1, active power distribution of the air-conditioner in Figure 2 is analysed in detail. For the active power P, it can be seen that the standard deviation of transition domains is higher than that of stable domains (as shown in bold in Table 1). Therefore, we present an appropriate method to find the number of clusters and their initial centres accurately.

3. Proposed State Characteristic Clustering Approach

This section first describes the SWDS algorithm, which is employed in the determination of the initial cluster centre, and then presents the SCC approach and the iteration process of clustering points. Moreover, in order to make the algorithm more suitable for practical demand-side energy management, the multisegment computing scheme is used to increase the execution time.

3.1. The Sliding Window Difference Search. Finding appropriate initial cluster centres can improve the precision of the SCC approach effectively. If a point that belongs to a transition domain is selected, the shifting process of the clustering algorithm will be affected. Therefore, this paper presents an SWDS algorithm to extract the initial distribution characteristic of stable domain data by detecting the switching signatures of electrical loads.

For a time-series power data, define a sliding window $Y(i)$ with width m:

$$Y_i = \left[\omega_{p,i}, \omega_{p,i+1}, \ldots, \omega_{p,i+m-1}\right]. \tag{1}$$

Then, the mean value Y_i of characteristic p in the sliding window $Y(i)$ is

$$\overline{Y}_i = \frac{\omega_{p,i} + \omega_{p,i+1} + \cdots + \omega_{p,i+m-1}}{m}. \tag{2}$$

Assume that the difference between i and j of characteristic p can be represented as

$$\psi_{i,j} = \left|\omega_{p,i} - \omega_{p,j}\right|, \tag{3}$$

where $i < j \leq m$. Thus, we define a background noise parameter θ according to the dataset; that is, the difference of the data in the sliding window can be limited to an appropriate range.

To initialize the cluster centre, let $\eta_{i,s}$ be the difference between two cluster centres; therefore, we have

$$\eta_{i,s} = \left|\overline{Y}_i - \overline{Y}_s\right|. \tag{4}$$

Let γ represent as the minimum number of load events in the current data series. Thus, if $\eta_{i,s} > \gamma$, then the event in the current sliding window can be detected. Consequently, a stable domain ω_i will be selected while the following two conditions meet simultaneously:

$$\begin{cases} \psi_{i,j} < \theta, \\ \eta_{i,s} > \gamma. \end{cases} \tag{5}$$

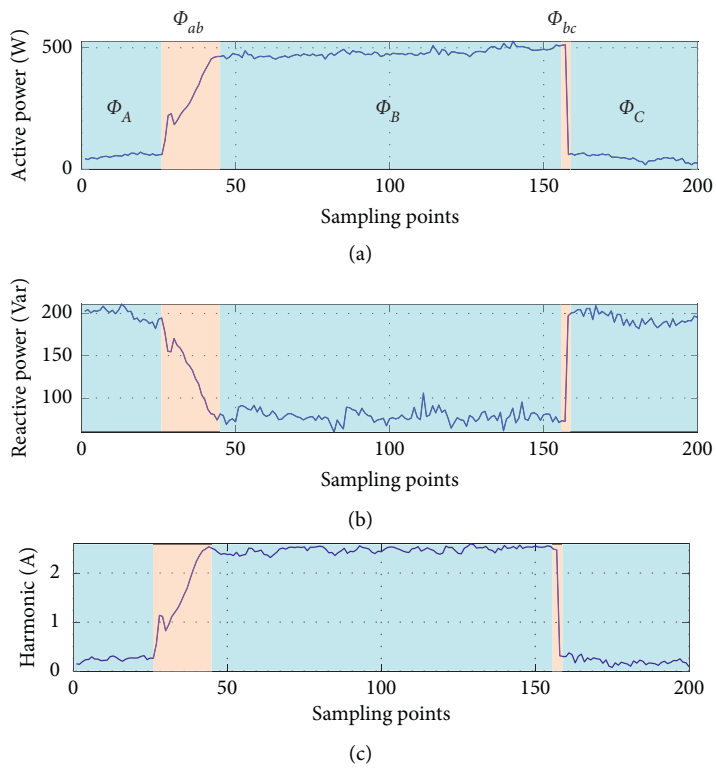

FIGURE 2: An operating period of an air-conditioner, where Φ_A, Φ_B, and Φ_C are stable states and Φ_{ab} and Φ_{bc} are transient states.

Figure 3 shows an example of the SWDS process. As we can see, a window with width m slides over the data series and a load event occurs on $Y(i)$. By calculating $\psi_{i,j}$ and $\eta_{i,s}$, i can be set as the initial cluster centre in this data block.

3.2. Mean-Shift-Based State Clustering. As a density-based clustering approach, the mean-shift clustering algorithm does not need any prior conditions and statistical parameter estimation. The extremum of probability density function can be calculated quickly by the gradient iteration and then converge to a cluster centre with the highest probability density. The main process of state clustering is as follows.

Consider a multidimensional characteristic space B_h with a fixed bandwidth h in a nonzero dataset Ω; thus, the objective function can be written as

$$B_h(x) = \left\{y \middle| \|y - x\|^2 \leqslant h^2\right\}, \tag{6}$$

where x is the centre of the multidimensional space, y represents a data point of the space, and h is the bandwidth that determines the search range for maximum density points. Usually, a smaller bandwidth has higher detecting performance for the loads with small power. However, a bandwidth that is too small will be sensitive to the power fluctuation and easily cause over classification.

For a d-dimensional space with n data points, the sample point density estimator by mean-shift process can be expressed as [30]

$$\widehat{f}_h(x) = \frac{1}{nh^d} \sum_{x_i \in B_h} K\left(\left\|\frac{x - x_i}{h}\right\|^2\right), \tag{7}$$

where x_i represents the i-th data and $K(x)$ represents the radial basis kernel function. For a profile function $k(x)$, $K(x)$ is given as follows:

$$K(x) = c_{k,d} k\left(\|x\|^2\right), \tag{8}$$

where $c_{k,d}$ is the normalized constant. In this paper, the *Epanechnikov* kernel $K_E(x)$ is used by considering to keep the least-mean-square error.

$$K_E(x) = \begin{cases} \frac{1}{2}(d+2)\left(1 - \|x\|^2\right), & \|x\| \leqslant 1, \\ 0, & \text{else}, \end{cases} \tag{9}$$

$$k_E(x) = \begin{matrix} 1 - x, & 0 \leqslant x \leqslant 1, \\ 0, & \text{else}. \end{matrix}$$

Next, the initial centre will shift to a new cluster centre by the mean-shift process according to the data density. To obtain the maximum density point, let

$$\nabla \widehat{f}(x) = 0. \tag{10}$$

Thus, the derivative of the objective function could be described as

Table 1: State characteristic distribution of the air-conditioner during an operating period.

Domain	Section	Number of sampling points	Standard deviation (W)	Average power (W)
Stable	Φ_A	27	8.21	21.8
Transition	Φ_{ab}	18	**117.20**	132.09
Stable	Φ_B	110	15.36	483.77
Transition	Φ_{bc}	2	**319.14**	286.42
Stable	Φ_C	43	12.20	44.05

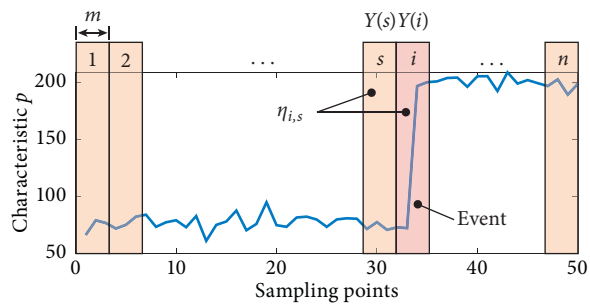

Figure 3: Cluster centre initialization process by SWDS.

$$\nabla \hat{f}_{h,k}(x) = \frac{2c_{k,d}}{nh^{d+2}} \sum_{x_i \in S_h} (x - x_i) k'\left(\left\|\frac{x - x_i}{h}\right\|^2\right). \tag{11}$$

Now, we reduce that

$$\nabla \hat{f}_{h,g}(x) = \frac{2c_{k,d}}{nh^{d+2}} \left[\sum_{x_i \in S_h} g\left(\left\|\frac{x - x_i}{h}\right\|^2\right)\right] m_{h,g}(x), \tag{12}$$

for given $g(x) = -k^0(x)$, where

$$m_{h,g}(x) = \frac{\sum_{i=1}^{n} x_i g\left(\left\|x - x_i/h\right\|^2\right)}{\sum_{i=1}^{n} g\left(\left\|x - x_i/h\right\|^2\right)} - x, \tag{13}$$

is the updated direction of the new cluster centre.

3.3. Update and Iteration Procedure. By repeated iterations, the mean value moves in the direction of the highest density area. The iteration can be expressed as follows:

$$x_{k+1} = x_k + m_{h,g}(x_k). \tag{14}$$

Finally, the peak point x_p of the probability density function and its $B_h(x)$ can be obtained, which represents the current stable domain centre and the current high-dimensional space, respectively. More in detail, the main process of state characteristic clustering is as follows:

(i) Select one or more points in the sampled data domain as an initial cluster centre.

(ii) Set an iteration termination threshold e and the high-dimensional space bandwidth h according to the characteristics of power fluctuation, where e is determined by the allowable error range.

(iii) Calculate the mean-shift vector $m_{h,g}(x)$ of $B_h(x)$ in each high-dimensional space according to equation (13).

(iv) Move $B_h(x)$ along to the mean-shift vector $m_{h,g}(x)$ by equation (14).

(v) If $m_{h,g}(x) > e$, then record the density centre of this new stable domain and continue the iterative process. If $m_{h,g}(x) < e$, then it indicates that this high-dimensional space belongs to the same stable domain as the previous one, so as to merge the two cluster centres and end the iteration.

It should be noted that in order to make use of time-series information and reduce the interference of irrelevant data during the mean-shift process, this paper sets the clustering range of each initial cluster centre by SWDS.

Since the units and dimensions of each characteristic data are different, it is necessary to normalize the data. Let $\omega_{p,i}$ represent the value of characteristic p of point i, then the data can be normalized as follows:

$$x_i^p = \begin{cases} \dfrac{\omega_{p,i} - \omega_{p,\min}}{\omega_{p,\max} - \omega_{p,\min}}, & \omega_{p,i} \in \left[\omega_{p,\min}, \omega_{p,\max}\right], \\ 1, & \omega_{p,i} > \omega_{p,\max}, \\ 0, & \omega_{p,i} < \omega_{p,\min}, \end{cases} \tag{15}$$

where $\omega_{p,\min}$ and $\omega_{p,\max}$ represent the maximum and minimum values of characteristic p in the current dataset, respectively.

The measuring environment of power data will affect the selection of bandwidth h. Therefore, we have prerecorded

the d-dimensional characteristic of each appliance in stable domains. After normalization, h can be further defined as

$$h = \sqrt{\frac{1}{N} \sum_{x_i \in \Omega^d} \left\| x_i - \overline{x} \right\|^2}, \tag{16}$$

where $\overline{x}$ represents the density centre obtained by taking the mean value of points in the space.

3.4. The Multisegment Computing Scheme. In practice, we can usually get at least one data point for each domain by using SWDS. According to the characteristics of these data points, the distribution of state domains can be obtained. For the width m of a sliding window, it determines the amount of data to be detected. Therefore, based on this property, we conclude that for a larger m, the SWDS can reduce error detections by power fluctuations in the detecting process. On the contrary, a smaller window width can improve the detecting performance in the case of load events occurring at a small time interval.

Therefore, in real-case scenario, there exists a trade-off between the optimal window width and the best detecting performance. Furthermore, for a large amount of data, in order to improve the processing efficiency of the proposed method, the multisegment computing scheme is used in this paper. Figure 4 shows a simple demonstration of the proposed SCC approach with the multisegment computing scheme.

We conducted separate clustering for each w sampled data and then obtained the power characteristic of each data block. First, the minimum length of each block should be defined appropriately. It should be noted that w is much larger than m in real-world dataset, and each data block will contain multiple SWDS and mean-shift processes. Therefore, SWDS detection results are not unique. Then, for each detected initial cluster centre, mean shift will be processed separately to determine the final cluster centre. After all the stable/transition is determined, the relative key data point will be recorded and stored in the form of numerical ranges along time series. Note that if the number of stable domains $M > 2$, then it will be regarded as there are events in this block. Then, turn to the next data block and repeat the process. By combining with SWDS and mean-shift clustering, the state characteristic clustering can be calculated faster in blocks along with time series.

4. Experimental Results and Discussion

In this part, experiment results of three different cases are carried out to demonstrate the performance of the proposed SCC approach. Here, household appliance dataset, which includes air-conditioner, rice cooker, microwave oven, induction cooker, electric kettle, TV, refrigerator, electric fan, and desktop computer, is stored in the database. Each appliance was turned ON/OFF for several times to verify the effectiveness of the proposed method. Notably, the NILM data sampling module in our lab, which collects the total active power, reactive power, and harmonics data, uploads data every two seconds. Besides, the proposed SCC is compared with existing algorithms in each case to further verify the proposed method in terms of effectiveness.

The event detection process is taken sequentially with time, and the purpose is to identify the occurrence and termination of load events accurately. The trigger threshold (TT) method is a quick and simple method, especially for high-power resistive appliances [18]. It uses a threshold parameter to capture appliance switch signals. As we mentioned in the previous section, event points in the dataset can be extracted by comparing to the sum of the minimum cumulative sum statistics. Therefore, the bilateral-CuSum (BC) method with known prechange and postchange distributions will be effective for multistate events [26]. For comparison, the TT, BC, and proposed SCC methods are used to verify the performance of event detection in different cases, respectively.

4.1. The Detection of Continuously Varying State. In this case, the work mainly focuses on a load with a continuously varying transient state. For instance, the power curve of an air-conditioner increases slowly since it is turned on. To our knowledge, this is a challenge for many existing event detection algorithms because the power changes slowly rather than a transient signal.

Figure 5 illustrates the starting process of the air-conditioner. It can be seen that there exist three states: the stable state without any load running (Φ_A), transient state, and stable state with the air-conditioner running (Φ_B). Roughly speaking, the active power changes about 450 W between two stable domains Φ_A and Φ_B. The actual transient event occurred at point 105. Then, after undergoing a slow climb about 15 points, the state reaches Φ_B domain.

In order to reduce the influence caused by data fluctuation, here, the threshold parameter for judging the load event is set as $P_{\min} = 70$ W for each algorithm. That is, a power change over $P_{\min}$ is considered as a valid load event. For the BC method, the minimum mutation parameter $\Delta_{\min}$ is set to 200 and the noise parameter θ is set to 20. For the proposed SCC method, the significant parameters mentioned in Section 3.2 are shown in Table 2.

For the proposed SCC, Figure 6 illustrates the state transition process with a continuously varying state in a P-Q-H 3-dimensional space. Note that all power characteristics are normalized before the state clustering process. Figure 6(a) shows an overview of the state transition process. It can be seen that the two domains Φ_A and Φ_B are very far apart in this 3-dimensional space. The data points connecting the two domains belong to a continuously varying event. It is obvious that this long state transition process can only be shown in a multidimensional characteristic space. For stable domain Φ_A in Figure 6(b), SWDS first determines the initial cluster centre (black triangle) and then shifts to the terminal cluster centre (red triangle) by the mean-shift process, where the terminal cluster is the region with highest data density. Moreover, we use the green line to mark the shift trajectory of the cluster centre.

Table 3 shows the event detection results of the TT, BC, and proposed SCC methods. The comparison with ground

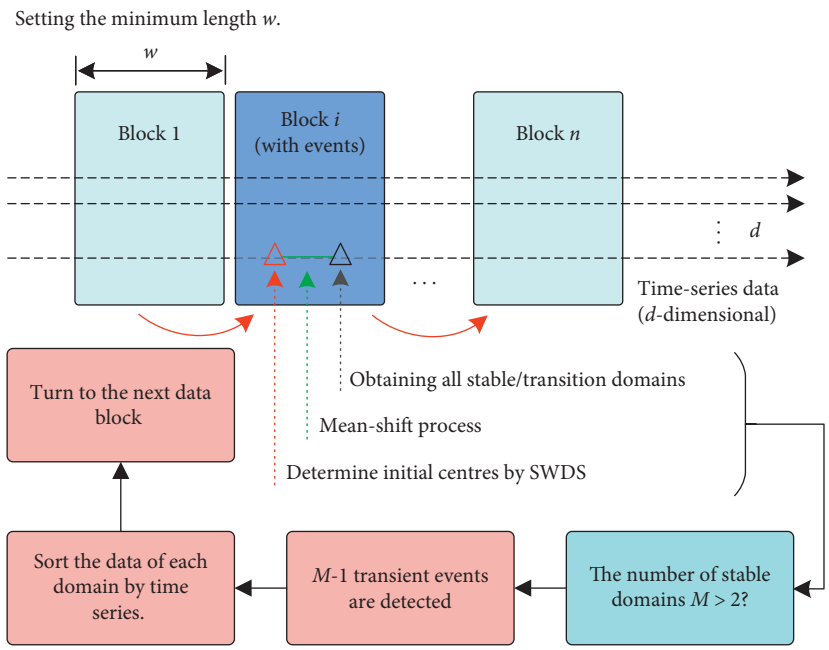

Figure 4: The multisegment computing mechanism of SCC by block calculation.

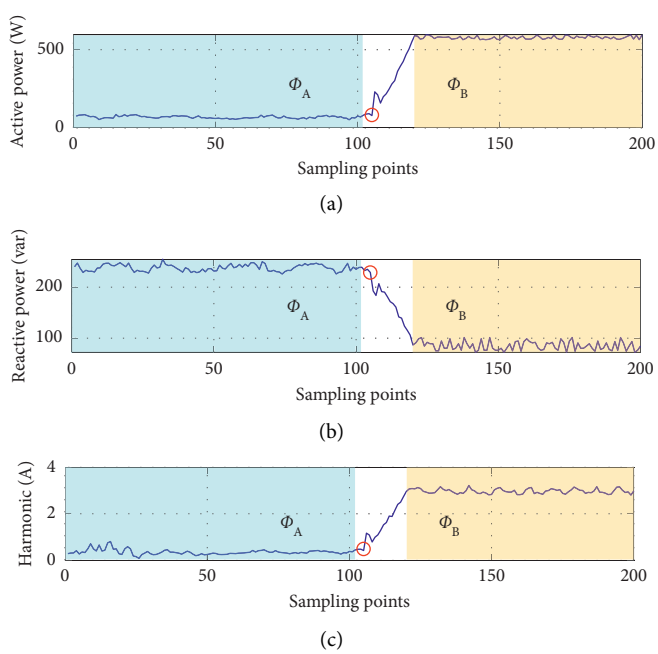

Figure 5: Three states of an air-conditioner during the whole operating process, where the continuously varying transient state between Φ_A and Φ_B lasted 50 seconds.

truth (GT) data shows that the TT method fails to detect the event. This complex state cannot be detected by just thresholds. The BC method captures two load events at 111 and 116 points, respectively, that lead to multidetection. In contrast, the proposed SCC method avoids false detection from the load undergoing the long transient process and gets the almost correct starting point. Therefore, the proposed SCC method in multidimensional space has higher detection accuracy for such continuously varying events.

4.2. Detection Performance of Small Power Loads under a Fluctuating Environment. In this case, it mainly demonstrates the proposed method in separating the load with small power loads from a fluctuating environment with other loads overlapping. Figure 7 illustrates the case that an induction cooker with 2000 W active power is turned to ON state at sampling point 10 and then a computer runs at point 26. From the visual of inspection, the computer almost cannot be found just through the active power curve. It is

Table 2: Some significant parameters in the SCC method.

Parameter	Symbol	Value
Bandwidth	h	0.05
Data block length	ω	200
Iteration termination threshold	e	0.01
Noise parameter	θ	30
Minimum active power	$P_{\min}$	70
Minimum spacing between domains	Γ	70
Window width	m	3

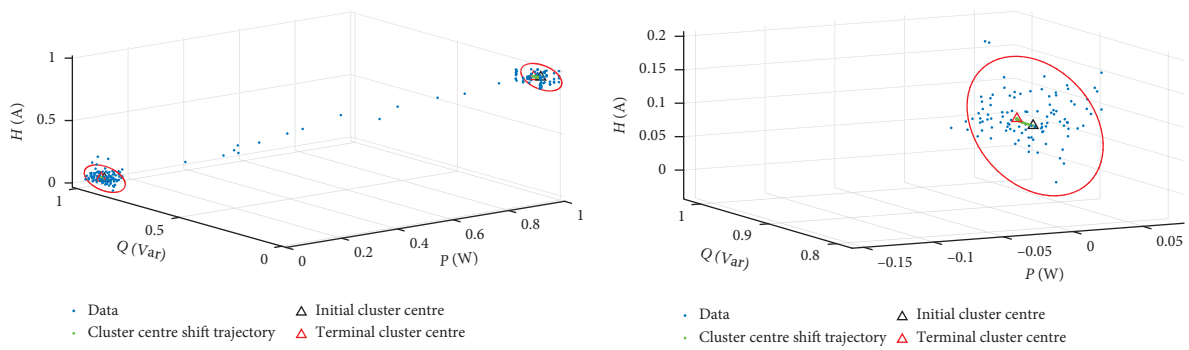

Figure 6: The SCC process of an air-conditioner with a continuously varying state in a (P)-(Q)-(H) 3-dimensional space (after normalization). (a) The overview of state transition process. (b) The cluster centre of stable domain Φ_A and its shift trajectory.

Table 3: Event detection results of three methods for continuously varying state.

Methods	Event points
GT	105
TT	–
BC	111 and 116
SCC (proposed)	105

because that the induction cooker produced a 70 W fluctuation, while the power of the computer is just 70–90 W. At this point, the load events of the computer are easy to overlap with the background fluctuation. Nevertheless, the proposed SCC method can distinguish these two load events by multiple characteristics in the 3-dimensional space. As seen in Figure 7, red circles denote the boundary of the B_h by mean-shift clustering.

For more understanding, Figure 8 illustrates the whole process of state clustering. First, there are five initial stable domains named Φ_A–Φ_E, which are detected by SWDS. In addition, the domain Φ_C has four initial cluster centres and Φ_E contains two initial cluster centres. For domains Φ_A, Φ_B, and Φ_D, they just have a corresponding initial cluster centre. As can be seen in Figure 8, the initial centres of the domain Φ_C are merged into a single cluster centre by using mean-shift clustering, and the same as the initial centres of the domain Φ_E, while other domains retain their original cluster centre. Therefore, the number of cluster centres is $M = 5$, corresponding to 5 stable domains. Therefore, this case has $M - 1$ transient events. Finally, four load events can be detected according to those clusters.

Furthermore, to demonstrate that the proposed SCC method is less sensitive to the parameter setting, here, experiments on different parameter settings are carried out for comparison. In order to measure the efficiency of each event detection algorithm, the accuracy metric F-measure in machine learning is introduced. Generally, the event detection results can be divided into four categories: true positive (TP), which indicates the algorithm detect load events correctly; true negative (TN), which indicates that no events occur and the algorithm gives no alarms; false positive (FP), which indicates that the algorithm detects an event but does not actually occur; and false negative (FN), which indicates that the algorithm did not correctly detect the events that occurred. Moreover, the F-measure (FM) is a metric by combining the multiple-detection rate and missing detection rate. Therefore, a higher FM represents a better performance.

Tables 4–7 show the F-measure results of threshold $P_{\min}$, minimum mutation parameter $\Delta_{\min}$, minimum spacing Γ, and bandwidth h on TT, BC, and SCC methods, respectively.

Table 4 shows the influence of different trigger threshold parameters. The TT method, which is judged by a single

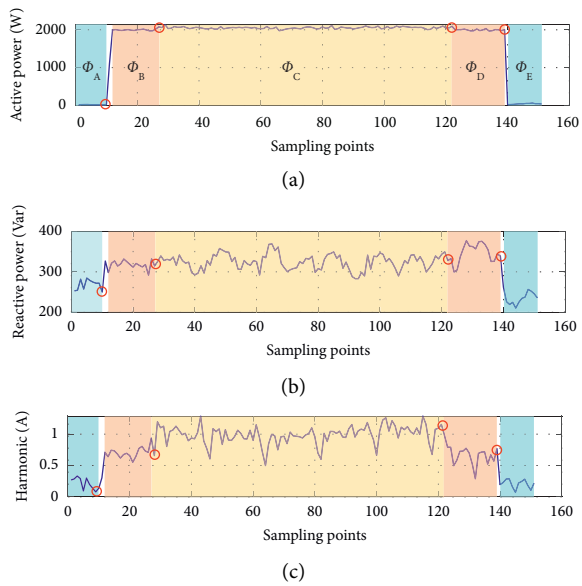

Figure 7: A computer is turned on in a noisy environment with an induction cooker running, where Φ_C represents its stable domain.

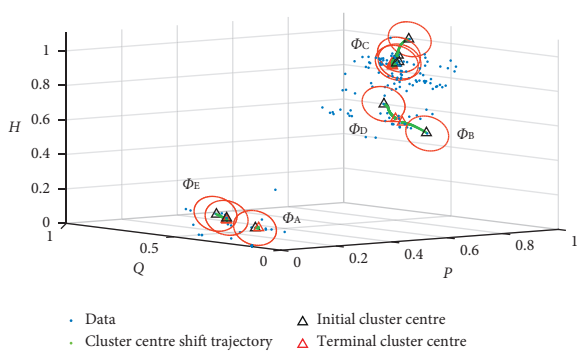

Figure 8: The state transition and cluster centre merging process under a fluctuating environment (after normalization).

point, may make small power loads' power signature confuse with background noises. Table 5 shows that the optimal value of the parameter in bilayer CuSum should be properly set by accurate statistics on the power in the database. Also, the bilateral-CuSum method is sensitive to the power of a single point at the beginning of a transient event, and the accuracy of FM declines quickly after the optimal value. Tables 6 and 7 reflect that the proposed method has a wide range of optimal parameter settings. Therefore, the performance of the SCC method has its advantage in terms of the parameter configuration for load detection.

4.3. Real Household Scenario with Long-Term Stochastic Behaviour. In this case, the user's stochastic behaviours during the actual operation of multiple appliances are considered. Therefore, ten appliances in real household scenario are randomly switched 100 times for a long-term operation test. The aggregate time-series data containing about 4000 sampling points were recorded in MySQL database previously. Similar to the first two cases, in order to show the performance evaluation of the proposed SCC method, the TT and BC methods are used for comparison. Here, the optimal parameters are selected according to the tables in Section 4.2. In the following, the results will be discussed in detail.

Figure 9 shows the distribution of data points in this time-series dataset, where Figure 9(a) shows the aggregate active power curve during this long-term operation. Red points represent the SWDS result of detected stable state. Figure 9(b) shows the overall distribution of data points in a *P-Q-H* 3-dimensional space (without normalization). It can be found that the stable points are almost correctly detected by the proposed method.

Taking the data block (2400–2800) as an example, Figure 10(a) indicates the cluster centre's shift and merging process. The adjacent initial cluster centres are finally converged to one stable domain, corresponding to load events. Finally, each stable domain is determined by a certain cluster centre. As seen in Figure 10(b), the original initial

Table 4: The influence of different thresholds $P_{\min}$ on the performance of the TT method.

$P_{\min}$	TP	FP	FN	FM
60	4	9	0	0.46
70	4	5	0	0.61
80	4	3	0	0.72
90	4	3	0	0.72
100	3	2	1	0.66
110	2	1	2	0.57

Table 5: The influence of different minimum mutation parameters $\Delta_{\min}$ on the performance of the BC method.

$\Delta_{\min}$	TP	FP	FN	FM
60	4	7	0	0.53
70	4	3	0	0.72
80	4	1	0	0.89
90	4	0	0	1.00
100	3	0	1	0.86
110	2	0	2	0.67
120	2	0	2	0.67
130	2	0	2	0.67

Table 6: The influence of different minimum spacings Γ between domains on the performance of the SCC method.

Γ	TP	FP	FN	FM
30	4	4	0	0.67
40	4	2	0	0.80
50	4	2	0	0.80
60	4	0	0	1.00
70	4	0	0	1.00
80	4	0	0	1.00
90	4	0	0	1.00
100	2	0	2	0.67

Table 7: The influence of different bandwidths h on the performance of the SCC method.

h	TP	FP	FN	FM
0.01	3	1	1	0.75
0.02	4	0	0	1.00
0.03	4	0	0	1.00
0.04	4	0	0	1.00
0.05	4	0	0	1.00

cluster centre is replaced by the terminal cluster centre after executing the SCC approach. For ease of presentation, we normalized the original power data into [0, 1].

In this case, there are a total of 16 initial cluster centres after SWDS processing. Furthermore, results show that there are 13 stable domains and 12 transition domains, which means that 12 events are detected. For the ease of description, the statistical results of this environmental scenario are shown in Figure 11, where each block length is $w = 400$. The SCC results are almost consistent with the GT data.

Moreover, the FM performance of the proposed SCC method and the comparison results with other methods are shown in Table 8.

It can be seen from Table 8 that the FN of the TT method is low because the threshold is set according to the actual power information. Events will be recorded when the power value exceeds $P_{\min}$. However, when the power fluctuates greatly, or the power rises slowly, there is a phenomenon that a single event will be judged as a group of events; thus, the FP is higher than other methods. The FP of the bilateral-CuSum algorithm is also high because of the limit of window width m, which will cause false alarms on slowly rise events easily. Because massive noise can be easily confused with small power signatures, its FN is also higher than other methods. For the SCC in this paper, both FP and FN are relatively low, because this method has a good detection performance for long-term transient events. Also, small changes in power signals can be more easily captured in the multidimensional spaces. As an approach with multiple characteristic properties, SCC can accurately detect small switching signatures

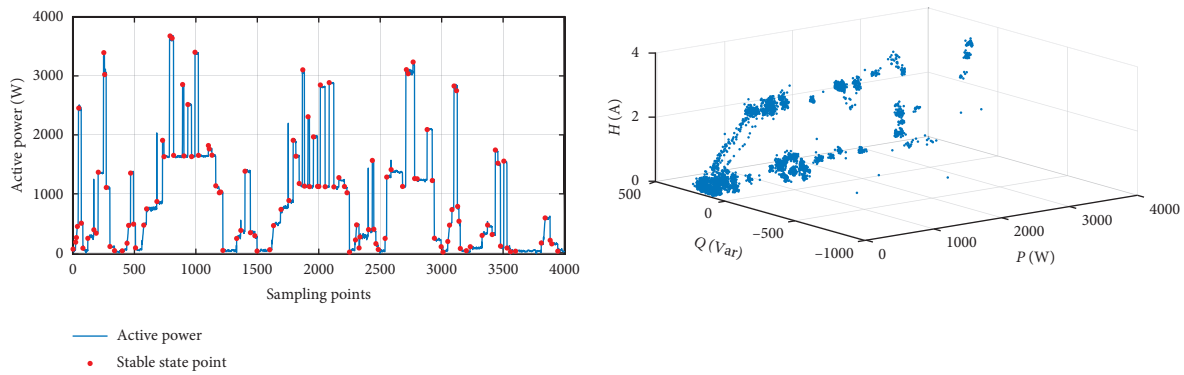

(a) (b)

Figure 9: The distribution of data points generated by 10 appliances with stochastic behaviours. (a) The aggregate active power curve during a long-term operation, where red points represent the stable state. (b) Data points in the (P)-(Q)-(H) 3-dimensional space.

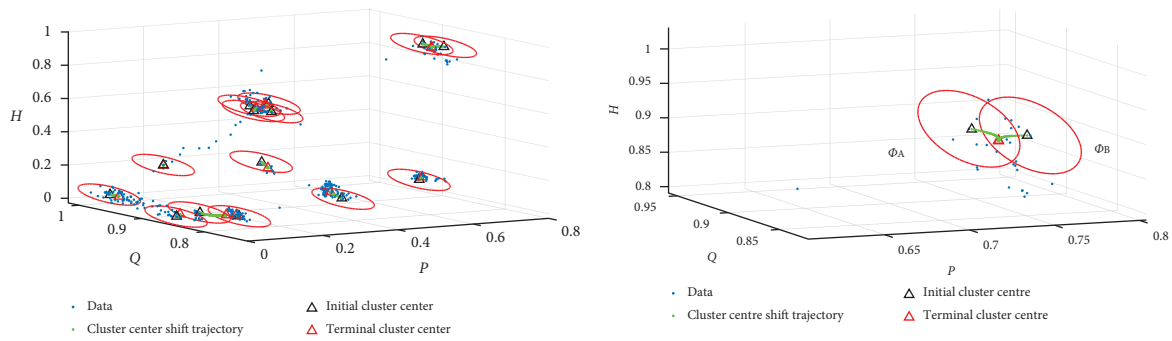

(a) (b)

Figure 10: The SCC process in data block 2400–2800 (after normalization). (a) The detailed state domains in the data block by executing SCC. (b) A merging process of adjacent cluster centres in 2710–2780.

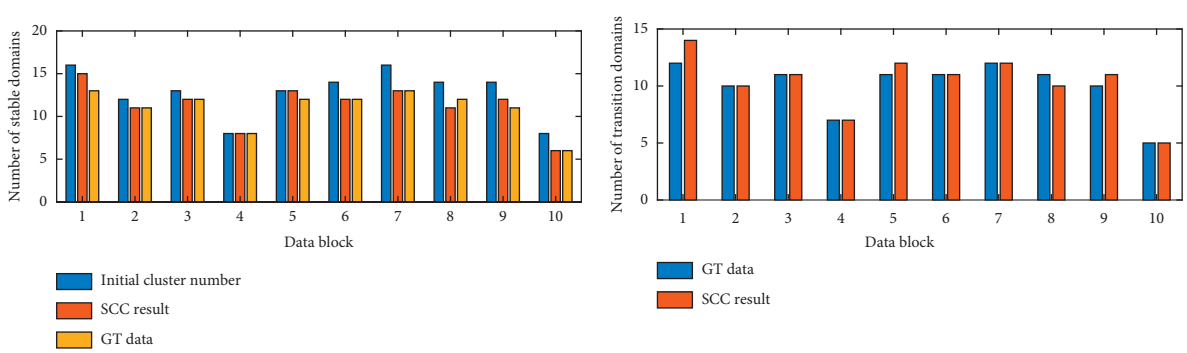

(a) (b)

Figure 11: Comparison of SCC results and ground truth data in this stochastic environmental scenario with 10 data blocks.

in the fluctuation environment. Therefore, the proposed SCC reduces the number of false detection or missing detection in reality. However, it should be noted that when the event occurs at block boundaries, the next stable state may not be detected accurately.

Furthermore, to verify the effectiveness of the proposed method, the precision (P) and recall (R) of all three methods mentioned above are computed. They can be described as

$$P = \frac{\mathrm{TP}}{\mathrm{TP} + \mathrm{FP}}, \tag{17}$$

$$\mathrm{R} = \frac{\mathrm{TP}}{\mathrm{TP} + \mathrm{FN}}. \tag{18}$$

Figure 12 draws the P-R curve of these methods. By calculating the equilibrium point when $P = R$, it can be seen

Table 8: The F-measure (FM) performance of 3 methods in this environmental scenario.

Method	TP	FP	FN	FM
TT	99	28	1	0.87
BC	90	20	10	0.85
SCC (proposed)	98	5	2	0.97

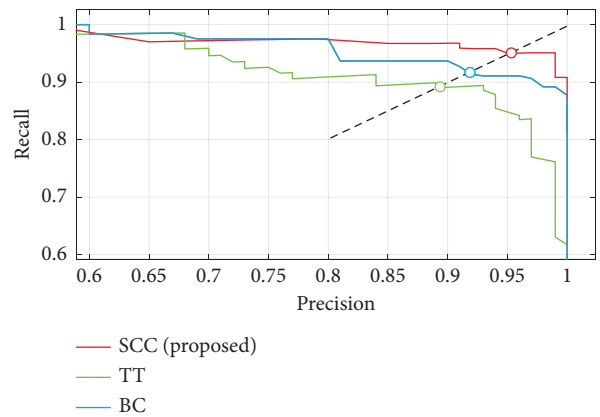

Figure 12: *P-R* performance of each method in the stochastic environmental scenario.

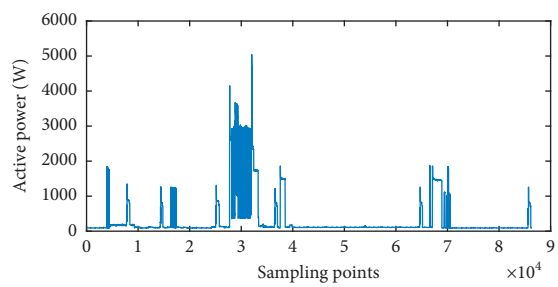

Figure 13: The aggregate power curve of house 3 in REDD.

that the proposed SCC in this paper performs better than others, where the algorithm with larger value has a better performance.

4.4. Validation with Data from REDD Public Dataset. This case aims to validate the effectiveness of the proposed SCC method on a widely used public dataset. Moreover, the experimental results are expanded by comparing the proposed SCC with other existing methods.

The reference energy disaggregation data set (REDD) is one of the most used public datasets for NILM system [34]. It includes the low-frequency data at a 1 Hz sampling rate of all six houses and two sets of high-frequency data at 15 kHz sampling rate. In order to obtain multidimensional power profiles, here, we perform fast Fourier transform (FFT) on high-frequency data to obtain active/reactive power signals every 2 seconds and 1–10 order current harmonics. Figure 13 shows the aggregate power curve of house 3 on April 22, 2011.

The house 3 in REDD, which we used in this section, contains 20 kinds of electric appliances. Therefore, we change the original experimental parameters according to the power characteristic of REDD. Some significant parameters for REDD dataset are shown in Table 9.

Then, we use the above parameters to test the selected data series of house 3, and the results are shown in Table 10.

As can be seen in Table 10, the TT and BC methods have much more false alarms than that of the SCC method, resulting in low overall FM accuracy. Therefore, these test results suggest that our proposed method based on state clustering is insensitive to the dataset difference. The SCC has better detection performance on both REDD and our own dataset than other existing works.

Table 9: Some significant parameters for REDD dataset.

Parameter	Symbol	Value
Bandwidth	h	0.05
Data block length	ω	60
Iteration termination threshold	e	0.01
Noise parameter	θ	10
Minimum active power	$P_{\min}$	70
Minimum spacing between domains	Γ	70
Window width	m	3

Table 10: Experimental results on REDD dataset.

Method	TP	FP	FN	Recall	Precision	FM
TT	147	44	11	0.9304	0.7696	0.8424
BC	154	35	4	0.9747	0.8148	0.8876
SCC (proposed)	131	2	27	0.8291	0.9850	0.9003

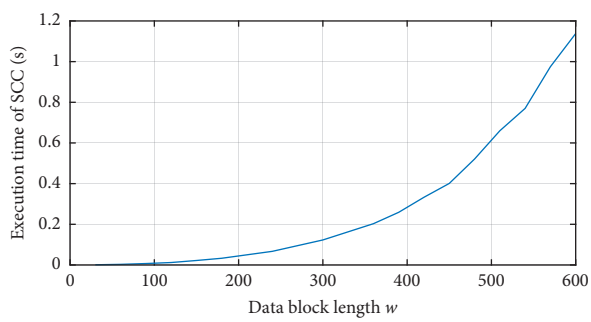

Figure 14: Execution time analysis of different data blocks (w).

4.5. Execution Time Analysis. The NILM system is mostly used for demand-side management in the smart grid. Therefore, these are expected to be real-time methods (i.e., calculations completed before the next data block is collected). Therefore, the execution time of the proposed SCC method is analysed in this section.

The execution time of SCC is mainly determined by the preprocessing time, response delay, and state clustering time. The preprocessing time includes the time needed to calculate power RMS, current harmonics, etc. Response delay time includes data block acquisition time, sliding window width, and sliding frequency. It is worth saying that the SCC runs independently in each data block; therefore, in order to improve the execution speed, the parameter configuration of block length is essential. To further analyse the execution time of SCC, in this paper, we use different data block lengths w to detect a 24 h time-series household data and record the average execution time of each process.

Figure 14 shows the effect of different data blocks w on execution time. The results show that even in a data block with a 600-point length, the SCC execution time is only 1.14 s. Therefore, the proposed SCC method can carry out real-time load monitoring in real residential environments. Overall, for an accurate demand response process, the execution time can be further reduced by changing the data block length and data sampling rate.

5. Conclusions

Based on the sliding window difference search and mean shift, a state characteristic clustering approach for demand-side nonintrusive load monitoring is proposed. The proposed SCC approach can achieve the operating state of several electrical appliances in a household effectively, which utilizes multidimensional aggregated data collected by an NILM module. In this approach, SWDS is used to find the initial cluster centre of each state domain, and then adjacent clusters can be shifted or merged as one stable domain in a multidimensional space. Multidimensional power features can reflect the real operation characteristic of loads and are more reliable than a single power feature, especially in a high-fluctuation environment. Three cases on both our real household dataset and REDD dataset show that the proposed SCC method can improve the detection performance of load events. Also, by comparing with two existing methods, the results demonstrate that the proposed SCC method has a higher F-measure accuracy in a complex real

residential environment and public dataset. Besides, for real-time demand response in the future smart grid, we proposed a multisegment computing scheme to improve the execution time.

In the following work, a more reliable model with complex states and appliances will be further considered and then applied to achieve load identification. Meanwhile, business environments with office equipment are also worth investigating.

Data Availability

The private household data used to support the findings of this study are included within this paper. The encrypted multidimensional power data were not given in full since they belong to a smart meter installed in a customer's premise.

Conflicts of Interest

The authors declare that there are no conflicts of interest regarding the publication of this paper.

Acknowledgments

This work was supported by the National Natural Science Foundation of China under grant no. 61873195.

References

[1] R. Bonfigli, E. Principi, M. Fagiani, M. Severini, S. Squartini, and F. Piazza, "Nonintrusive load monitoring by using active and reactive power in additive factorial hidden markov models," *Applied Energy*, vol. 208, pp. 1590–1607, 2017.

[2] M. S. Piscitelli, S. Brandi, and A. Capozzoli, "Recognition and classification of typical load profiles in buildings with non-intrusive learning approach," *Applied Energy*, vol. 255, Article ID 113727, 2019.

[3] J. Lai, X. Lu, X. Yu, and A. Monti, "Cluster-oriented distributed cooperative control for multiple ac microgrids," *IEEE Transactions on Industrial Informatics*, vol. 15, no. 11, pp. 5906–5918, 2019.

[4] J. Lai, X. Lu, X. Yu, and A. Monti, "Stochastic distributed secondary control for ac microgrids via event-triggered communication," *IEEE Transactions on Industrial Informatics*, vol. 11, no. 4, pp. 2746–2759, Jul. 2020.

[5] F. Luo, G. Ranzi, W. Kong, Z. Y. Dong, S. Wang, and J. Zhao, "Non-intrusive energy saving appliance recommender system for smart grid residential users," *IET Generation, Transmission & Distribution*, vol. 11, no. 7, pp. 1786–1793, 2017.

[6] S. Ghosh, A. Chatterjee, and D. Chatterjee, "Improved non-intrusive identification technique of electrical appliances for a smart residential system," *IET Generation, Transmission & Distribution*, vol. 13, no. 5, pp. 695–702, 2019.

[7] J. A. Mueller and J. W. Kimball, "Accurate energy use estimation for nonintrusive load monitoring in systems of known devices," *IEEE Transactions on Smart Grid*, vol. 9, no. 4, pp. 2797–2808, 2018.

[8] D. García, I. Díaz, D. Pérez, A. A. Cuadrado, M. Domínguez, and A. Morán, "Interactive visualization for nilm in large buildings using non-negative matrix factorization," *Energy and Buildings*, vol. 176, pp. 95–108, 2018.

[9] J. Lai and X. Lu, "Nonlinear mean-square power sharing control for ac microgrids under distributed event detection," *IEEE Transactions on Industrial Informatics*, vol. 17, no. 1, pp. 219–229, 2020.

[10] G. W. Hart, "Prototype nonintrusive appliance load monitor," MIT Energy Laboratory Technical Report, and Electric Power Research Institute Technical Report, Electric Power Research Institute, Washington, DC, 1985.

[11] S. Naderian and A. Salemnia, "Method for classification of *pq* events based on discrete gabor transform with fir window and t2fk-based svm and its experimental verification," *IET Generation, Transmission & Distribution*, vol. 11, no. 1, pp. 133–141, 2017.

[12] M. Aiad and P. H. Lee, "Energy disaggregation of overlapping home appliances consumptions using a cluster splitting approach," *Sustainable Cities and Society*, vol. 43, pp. 487–494, 2018.

[13] B. Buddhahai, W. Wongseree, and P. Rakkwamsuk, "A non-intrusive load monitoring system using multi-label classification approach," *Sustainable Cities and Society*, vol. 39, pp. 621–630, 2018.

[14] M. A. Mengistu, A. A. Girmay, C. Camarda, A. Acquaviva, and E. Patti, "A cloud-based on-line disaggregation algorithm for home appliance loads," *IEEE Transactions on Smart Grid*, vol. 10, no. 3, pp. 3430–3439, 2019.

[15] W. Kong, Z. Y. Dong, D. J. Hill, J. Ma, J. H. Zhao, and F. J. Luo, "A hierarchical hidden markov model framework for home appliance modeling," *IEEE Transactions on Smart Grid*, vol. 9, no. 4, pp. 3079–3090, 2018.

[16] S. Makonin, F. Popowich, I. V. Bajic, B. Gill, and L. Bartram, "Exploiting hmm sparsity to perform online real-time non-intrusive load monitoring," *IEEE Transactions on Smart Grid*, vol. 7, no. 6, pp. 2575–2585, 2016.

[17] M. G. Cominola and A. E. Rizzoli, "A hybrid signature-based iterative disaggregation algorithm for non-intrusive load monitoring," *Applied Energy*, vol. 185, pp. 331–344, 2017.

[18] J. Liang, S. K. K. Ng, G. Kendall, and J. W. M. Cheng, "Load signature study—Part I: basic concept, structure, and methodology," *IEEE Transactions on Power Delivery*, vol. 25, no. 2, pp. 551–560, 2010.

[19] X. Wu, X. Han, and K. X. Liang, "Event-based non-intrusive load identification algorithm for residential loads combined with underdetermined decomposition and characteristic filtering," *IET Generation, Transmission & Distribution*, vol. 13, no. 1, pp. 99–107, 2019.

[20] X. Shi, H. Ming, S. Shakkottai, L. Xie, and J. Yao, "Nonintrusive load monitoring in residential households with low-resolution data," *Applied Energy*, vol. 252, p. 113283, 2019.

[21] U. Rehman, T. T. Lie, B. Valles, and S. R. Tito, "Event-detection algorithms for low sampling nonintrusive load monitoring systems based on low complexity statistical features," *IEEE Transactions on Instrumentation and Measurement*, vol. 69, no. 3, pp. 751–759, 2020.

[22] D. Yang, X. Gao, L. Kong, Y. Pang, and B. Zhou, "An event-driven convolutional neural architecture for non-intrusive load monitoring of residential appliance," *IEEE Transactions on Consumer Electronics*, vol. 66, no. 2, pp. 173–182, 2020.

[23] S. Lin, L. Zhao, F. Li, Q. Liu, D. Li, and Y. Fu, "A nonintrusive load identification method for residential applications based on quadratic programming," *Electric Power Systems Research*, vol. 133, pp. 241–248, 2016.

[24] X. Wu, D. Jiao, K. Liang, and X. Han, "A fast online load identification algorithm based on vi characteristics of high-

frequency data under user operational constraints," *Energy*, vol. 188, Article ID 116012, 2019.

[25] P. S. Jain, S. Bhashyam, and A. P. Kannu, "Algorithms for change detection with sparse signals," *IEEE Transactions on Signal Processing*, vol. 68, pp. 1331–1345, 2020.

[26] S. Zou, G. Fellouris, and V. V. Veeravalli, "Quickest change detection under transient dynamics: theory and asymptotic analysis," *IEEE Transactions on Information Theory*, vol. 3, no. 65, pp. 1397–1412, 2019.

[27] C. Dinesh, S. Makonin, and I. Bajic, "Residential power forecasting using load identification and graph spectral clustering," *IEEE Transactions on Circuits and Systems II: Express Briefs*, vol. 66, no. 11, pp. 1900–1904, 2019.

[28] Z. Zheng, H. Chen, and X. Luo, "A supervised event-based non-intrusive load monitoring for non-linear appliances," *Sustainability*, vol. 10, no. 4, p. 1001, 2018.

[29] J. Yu, Y. Gao, Y. Wu, D. Jiao, C. Su, and X. Wu, "Non-intrusive load disaggregation by linear classifier group considering multi-feature integration," *Applied Sciences*, vol. 9, no. 17, p. 3558, 2019.

[30] S. Anand, S. Mittal, O. Tuzel, and P. Meer, "Semi-supervised kernel mean shift clustering," *IEEE Trans Pattern Anal Mach Intell*, vol. 36, no. 6, pp. 1201–1215, 2014.

[31] Y. Aliyari Ghassabeh and F. Rudzicz, "Modified mean shift algorithm," *IET Image Processing*, vol. 12, no. 12, pp. 2172–2177, 2018.

[32] M. Lu and Z. Li, "A hybrid event detection approach for non-intrusive load monitoring," *IEEE Transactions on Smart Grid*, vol. 11, no. 1, pp. 528–540, 2020.

[33] N. Henao, K. Agbossou, S. Kelouwani, Y. Dube, and M. Fournier, "Approach in nonintrusive type i load monitoring using subtractive clustering," *IEEE Transactions on Smart Grid*, vol. 8, no. 2, pp. 812–821, 2017.

[34] J. Z. Kolter and M. J. Johnson, "REDD.: a public data set for energy disaggregation research," in *Proceedings of the SustKDD Workshop Dataon Data Mining Applications in Sustainability*, vol. 1, pp. 1–6, San Diego, CA, USA, 2011.

Hindawi
Complexity
Volume 2021, Article ID 6659941, 13 pages
https://doi.org/10.1155/2021/6659941

Research Article

Research on Optimal Control Strategy for Unpowered Downslope of High-Voltage Inspection Robot Based on Motor Temperature Rise in Complexity Microgrid Networks

Zhiyong Yang,[1] Qiao Fang,[1] Zihao Zhang,[1] Xing Liu,[1] Xianjin Xu,[1] Yu Yan,[2] and Chen Miao[2]

[1]*College of Mechanical Engineering, Hubei University of Technology, Wuhan 430068, China*
[2]*State Grid of Hunan Electric Power Company Maintenance Company, Changsha 410004, China*

Correspondence should be addressed to Zhiyong Yang; yzy@hbut.edu.cn

Received 16 November 2020; Revised 13 January 2021; Accepted 27 April 2021; Published 12 May 2021

Academic Editor: Xin Li

In order to avoid the motor damage caused by excessive temperature rise of armature winding of the walking motor during braking of high-voltage inspection robot in complexity microgrid networks, an unpowered downhill speed and energy recovery optimization control strategy is proposed based on temperature rise characteristics of the walking motor. Firstly, the thermal equivalent circuit model of the walking motor is established, and the mapping relationship between the armature winding temperature of the walking motor and ambient temperature is solved; secondly, the influence of armature winding temperature on unpowered downhill speed and energy recovery control strategy of robot is analyzed; thirdly, according to the temperature of front and rear wheel walking motors and the temperature difference between them, the optimal control strategy of unpowered downhill speed and energy recovery of robot is put forward; fourthly, by adjusting the duty ratio u of the energy consumption speed control system and the front wheel feedback brake distribution factor λ, the temperature difference between the front and rear wheel walking motors is reduced. Through the experimental analysis on the simulated line, it is verified that the unpowered downhill speed and energy recovery optimization control method based on the temperature rise characteristics of the walking motor can effectively reduce the temperature difference between the front and rear wheels.

1. Introduction

With the development of high-voltage inspection robot technology in complexity microgrid networks, most high-voltage transmission lines are typical catenary structures. The line between two adjacent towers is downhill first and then uphill. The downhill section provides conditions for the robot to realize unpowered downhill speed control and energy recovery. The robot performs inspection tasks along the transmission line. With the inspection tasks, the walking motor temperature gradually increases, especially in the unpowered downhill process. On the one hand, if the traveling motor generates serious heat and the heat cannot be dissipated in time, it will affect the working performance and service life of the motor, and in severe cases, it will damage the motor winding due to the burning of the insulating paint; on the other hand, the encoder is installed at the end of the traveling motor. According to the heat conduction characteristics, when the temperature of the traveling motor rises, it will inevitably cause the encoder temperature to rise, and the encoder will reach the highest working temperature before the traveling motor. When the encoder temperature exceeds the maximum allowable temperature for a certain period of time, it will cause irreparable damage to the encoder and make the speed and direction of the robot uncontrollable. In addition, it often happens that the inspection robot cannot finish the inspection task on time due to lack of power during the inspection. Therefore, the unpowered downhill speed and energy recovery optimization control strategy based on the

temperature rise characteristics of the walking motor is particularly important and imminent.

In the past, many scholars had done extensive research on motor speed control and put forward many advanced control strategies. At present, motor speed control methods include PID, sliding mode, internal model, and adaptive, predictive, and active disturbance suppression control [1–8]. A predictive control strategy combining DC-DC converter with PMDC machine is proposed in [9]; it was proposed to quantitatively adjust the power consumption of the energy consumption resistor by adjusting the on-off duty ratio of the energy consumption circuit, so as to realize speed control in downhill process in [10]. A fuzzy logic controller was proposed to provide accurate steering angle and driving speed to control robot speed in [11]. An optimal control strategy based on active disturbance rejection control (ADRC) was proposed to achieve high-precision control of PMSM in [12]. Although these methods can control motor speed well, the temperature rise characteristics of the motor are not studied. Temperature rise characteristics of permanent magnet synchronous motor were analyzed in [13–15]. According to the special structure and related theories of the motor, the equivalent model of the motor temperature rise was established, and the correctness of the model was verified by experiments in [16–18]. The influence of winding temperature rise on mechanical characteristics, such as copper loss, iron loss, and efficiency, was analyzed by the finite element method in [19]. The characteristics of the eight constants that vary with the motor temperature and the residual flux density are shown in [20].The abovementioned methods have studied and analyzed the influencing factors of motor temperature rise and the mutual influence between motor temperature rise and motor, and established an equivalent model. However, they have not studied the specific control strategy and temperature rise characteristics of patrol robot during speed control, and with the support of literature review, no research has been found on the control strategy and temperature rise characteristics of high-voltage patrol robot during speed control. Therefore, it is particularly important to propose an optimal control method of unpowered downhill speed and energy recovery based on the temperature rise characteristics of the walking motor.

The novelty of this paper lies in the fact that an optimal control method of unpowered downhill speed and energy recovery based on the temperature rise characteristics of the walking motor is proposed for the first time. Firstly, the thermal equivalent circuit model of the walking motor is established, and the mapping relationship between the armature winding temperature and environmental temperature of the walking motor is solved. The influence of armature winding temperature on unpowered downhill speed and energy recovery control strategy of the robot is analyzed. According to the temperature of front and rear wheel walking motors and the temperature difference between them, the optimal control strategy of unpowered downhill speed and energy recovery of the robot is put forward by adjusting the duty ratio of the energy consumption speed control system and the front wheel feedback brake distribution factor, and the temperature difference between the front and rear wheel walking motors is reduced. Through the experimental analysis on the simulated line, it is verified that the unpowered downhill speed and energy recovery optimization control method based on the temperature rise characteristics of the walking motor can effectively reduce the temperature difference between the front and rear wheels.

2. Line Condition and Circuit Model

2.1. Line Inspection Robot Line Conditions. As shown in Figure 1, it is a simplified model of the running environment of the high-voltage inspection robot in complexity microgrid networks. Most of the high-voltage transmission lines are typical catenary structures. Between two adjacent towers, the lines are downhill first and then uphill. The downhill section provides conditions for the robot to realize unpowered downhill speed control and energy recovery. In the downhill process, it is necessary to control the speed of the inspection robot. In order to prevent the motor from being damaged due to the rapid temperature rise in the speed control process, this paper proposes an optimal control strategy of unpowered downhill speed and energy recovery based on the temperature rise characteristics of the walking motor. The configuration diagram of inspection robot is shown in Figure 2, and the walking motor is the MaxonRE40 motor.

2.2. Thermal Equivalent Circuit Model of the Walking Motor. In order to ensure the normal operation of the robot in the process of unpowered downhill, and to avoid the motor damage caused by excessive temperature in the process of braking and speed control, the armature winding temperature of the walking motor needs to be monitored in real time. In the process of patrol inspection, the heat sources of temperature rise of the walking motor include copper loss on winding, air resistance loss, and mechanical loss, among which copper loss on winding accounts for the vast majority. Figure 3 is the curve of resistance R_{T_W} of armature winding changing with temperature in the range of −50°C–200°C.

It can be seen from Figure 3 that the resistance R_{T_W} of the armature winding of motor changes linearly with temperature, and the resistance R_{T_W} of the armature winding at temperature T_W is

$$R_{T_W} = R_{25} \cdot \left(1 + \alpha_{Cu}\left(T_W - 25\right)\right), \tag{1}$$

where R_{25} is the resistance value of the armature winding of the motor at 25°C and α_{Cu} is the temperature coefficient of copper, which is $0.0039\,\mathrm{K}^{-1}$. Accordingly, the resistance value of the armature winding of the motor can also be calculated with reference to the external environment at temperature T_A, and the formula (1) can be expressed as

$$R_{T_w} = R_{T_A} \cdot \left(1 + \alpha_{Cu}\left(T_w - T_A\right)\right), \tag{2}$$

where R_{T_A} is the resistance value of the armature winding of the motor at temperature T_A, and the unit is Ω.

Figure 4 is a heat flow diagram and its equivalent circuit between the armature winding, the shell, and the external environment of the motor, where T_w is the temperature of

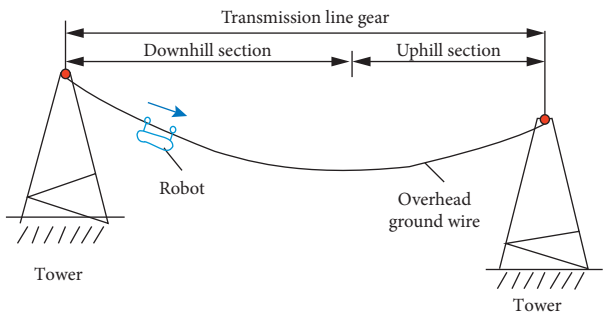

Figure 1: Simplified model of the robot's operating environment.

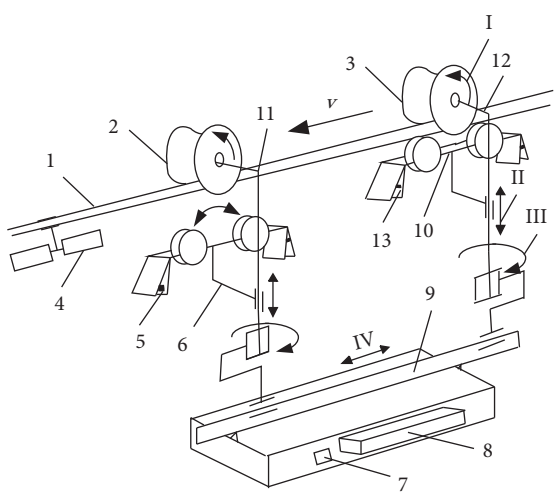

Figure 2: Configuration diagram of the patrol robot for crossing obstacles. (1) Ground wire; (2) front wheel; (3) rear wheel; (4) antivibration hammer; (5) forearm collision detection sensor; (6) forearm pressing mechanism; (7) switching circuit; (8) energy storage battery; (9) body; (10) rear arm pressing wheel; (11) forearm; (12) rear arm; (13) rear arm collision detection sensor.

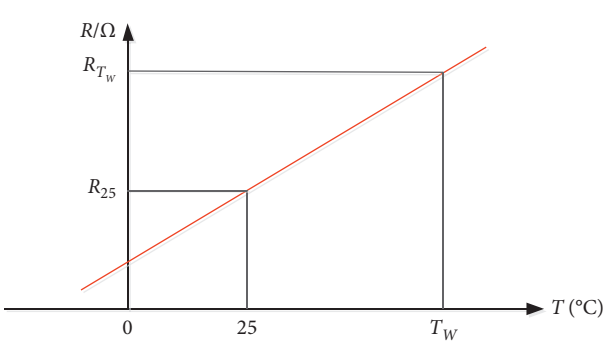

Figure 3: Curve of armature winding resistance changing with temperature.

the armature winding of the motor in K; T_s is the temperature of motor stator and casing, in K; T_A is the ambient temperature in K; the temperature difference between armature winding of the motor and ambient temperature is ΔT_w ($\Delta T_w = T_w - T_A$), which is similar to the voltage difference U_1 in equivalent circuit. The temperature difference

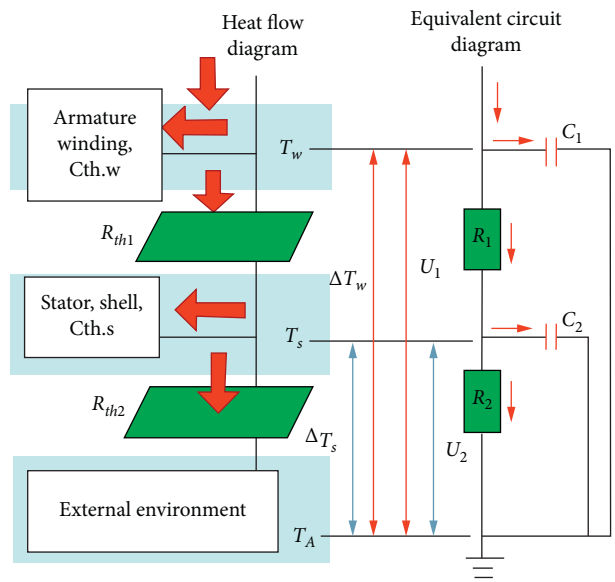

Figure 4: Heat flow diagram and equivalent circuit diagram.

between stator, casing, and ambient temperature of motor is ΔT_s ($\Delta T_s = T_s - T_A$), which is similar to the voltage difference U_2 in an equivalent circuit.

Joule heat P_v is generated when the motor winding flows through current, which changes the temperature of the motor winding by $\Delta T_w'$, resulting in a temperature difference between the motor winding and the motor stator and casing. Heat flows to the motor stator through air in the form of thermal convection. The thermal resistance between the armature winding and the stator and casing is R_{th_1}, which is similar to the resistance R_1 in an equivalent circuit. The absorbed energy Q_w of the motor armature winding is

$$Q_w = C_{Cu} \cdot m_w \cdot \Delta T_w' = C_{th.w} \cdot \Delta T_w', \tag{3}$$

where C_{Cu} is the specific heat capacity of copper, C_{Cu} = 380 (j/kgk); m_w is the mass of armature winding of motor, in kg; and $C_{th.w}$ is the heat capacity of motor armature, and the unit is J/K.

Similarly, when the motor stator and shell absorb the heat generated by motor windings, the temperature of the stator and shell rises. For convenience of analysis, it is assumed that the permanent magnets, shell, and flange of the motor have the same temperature. When there is a temperature difference between the motor stator and shell and the external environment, the heat will flow from the motor shell to the external environment. The thermal resistance between the stator and shell and the external environment is R_{th_2}, which is similar to the resistance R_2 in the equivalent circuit. Heat Q_s absorbed by motor stator and casing is as follows:

$$Q_s = C_{F_e} \cdot m_s \cdot \Delta T_s' = C_{th.w} \cdot \Delta T_s'. \tag{4}$$

In the formula, C_{F_e} is the specific heat capacity of iron in j/(kg·K); m_s is the mass of motor stator and casing, in kg; $C_{th.s}$ is the heat capacity of motor armature, in J/K; and $\Delta T_s'$ is the temperature change of motor stator and casing, in k.

3. The Influence of Temperature Rise on the Motor

According to the motor manual, the rated current I_N corresponds to the maximum allowable continuous current, which has a great relationship with the winding. The rated current of the thin wire winding is smaller than that of the thick wire winding, and the rated torque corresponding to the rated current of different winding series motors of the same model is almost the same. Under the standard environment (ambient temperature 25°C, no radiator on the motor flange, natural convection), the maximum continuous current makes the armature winding reach the maximum allowable temperature $T_{\max}$, and the higher current will cause the winding temperature to be too high.

Figure 5 shows the corresponding relationship between motor winding temperature and running time. It can be seen from the figure that

(1) When the armature working current $I > I_N$, or the output torque $M > M_N$, the final temperature of the motor winding will exceed the maximum allowable temperature $T_{\max}$; therefore, before the final temperature reaches, the motor operation must be stopped, resulting in the limited running time of the motor.

(2) When the armature working current $I = I_N$ or the output torque $M > M_N$, the final temperature of the motor winding will reach the maximum allowable temperature $T_{\max}$.

(3) When the motor armature working current is $I < I_N$, or the output torque is $M < M_N$, the final temperature of the motor winding will be lower than the maximum allowable temperature $T_{\max}$, so the motor running time will not be limited under this condition.

The parameters of the motor manual are obtained under the ambient temperature of 25°C and standard assembly conditions. It can be seen from formula (3) that when the temperature of armature winding changes, the resistance of armature winding will also change. Similarly, the rated current and rated torque of motor will also change for different ambient temperatures. According to the formula of temperature difference between armature winding of motor and external environment:

$$T_{\max} - 25^{\circ}C = \left(R_{th1} + R_{th2}\right) \cdot R_{T_{\max}} \cdot I_N^2\left(25^{\circ}C\right), \tag{5}$$

$$T_{\max} - T_A = \left(R_{th1} + R_{th2}\right) \cdot R_{T_{\max}} \cdot I_N^2\left(T_A\right). \tag{6}$$

In formulas (5) and (6), $I_N(25^{\circ}C)$ is the rated current of the motor when the ambient temperature is 25°C, and the unit is A; $R_{T_{\max}}$ is the resistance value of motor winding at the maximum allowable temperature $T_{\max}$, and the unit is Ω; $I_N(T_A)$ is the rated current of the motor when the ambient temperature is t, and the unit is A. According to formulas (5) and (6),

$$\frac{T_{\max} - 25^{\circ}C}{T_{\max} - T_A} = \frac{\left(R_{th1} + R_{th2}\right) \cdot R_{T_{\max}}}{\left(R_{th1} + R_{th2}\right) \cdot R_{T_{\max}}} \cdot \frac{I_N^2\left(25^{\circ}C\right)}{I_N^2\left(T_A\right)} = \frac{I_N^2\left(25^{\circ}C\right)}{I_N^2\left(T_A\right)},$$

$$I_N\left(T_A\right) = I_N\left(25^{\circ}C\right)\sqrt{\frac{T_{\max} - T_A}{T_{\max} - 25^{\circ}C}}. \tag{7}$$

The values of thermal resistance and maximum continuous current in the motor parameter table are obtained by installing the motor on a vertical plastic plate and after a series of tests. Mounting the motor on a radiator will significantly reduce the thermal resistance R_{th2} between the motor casing and the environment. For the motor of model MaxonRE40, the end face of the motor has a metal flange mounting hole. If it is mounted on a good metal heat conductor, the thermal resistance R_{th2} can be reduced by 50%. Therefore, in specific applications, the change of thermal resistance R_{th2} must be determined by actual installation and environmental conditions, and $R_{th2.\mathrm{mod}}$ is defined as the corrected thermal resistance between the motor casing and the environment under different installation conditions. Figure 6 shows a heat flow diagram between the motor housing and the environment.

It can be seen from the figure that in the practical application process, the real thermal resistance of the motor is expressed by the corrected thermal resistance $R_{th2.\mathrm{mod}}$ between the motor casing and the external environment. If the corrected thermal resistance $R_{th2.\mathrm{mod}}$ between the motor casing and the external environment is known, the rated current $I_N(T_A)$ of the motor corresponding to different environmental temperatures can be calculated in a simple and accurate way. The formula for $R_{th2.\mathrm{mod}}$ is

$$R_{th2.\mathrm{mod}} = \Delta T_S \cdot \frac{1 - \alpha_{Cu} \cdot R_{th1} \cdot R_{T_A} \cdot I^2}{R_{T_A} \cdot I^2 \cdot \left(1 + \alpha_{Cu}\Delta T_S\right)}. \tag{8}$$

According to formulas (5) and (6), the rated current $I_N(T_A)$ and rated output torque $M_N(T_A)$ of the motor at different ambient temperatures T_A are

$$I_N\left(T_A\right) = I_N\left(25^{\circ}C\right) \cdot \sqrt{\frac{T_{\max} - T_A}{T_{\max} - 25^{\circ}C} \cdot \frac{R_{th1} + R_{th2}}{R_{th1} + R_{th2.\mathrm{mod}}}}, \tag{9}$$

$$M_N\left(T_A\right) = M_N\left(25^{\circ}C\right) \cdot \sqrt{\frac{T_{\max} - T_A}{T_{\max} - 25^{\circ}C} \cdot \frac{R_{th1} + R_{th2}}{R_{th1} + R_{th2.\mathrm{mod}}}}, \tag{10}$$

where $M_N(25^{\circ}C)$ is the rated output torque of the motor at 25°C, and the unit is Nm.

Let $k_M = (M_N(T_A)/M_N(25^{\circ}C))$ be the rated torque variation coefficient and $k_A = (I_N(T_A)/I_N(25^{\circ}C))$ be the rated current variation coefficient, as shown in Figure 7, which shows the curves of k_A and k_M under different ambient temperatures. It can be seen from the figure that with the increase of ambient temperature, the rated current and torque of the motor will decrease, and after the temperature exceeds 100°C, the decline rate of the rated current

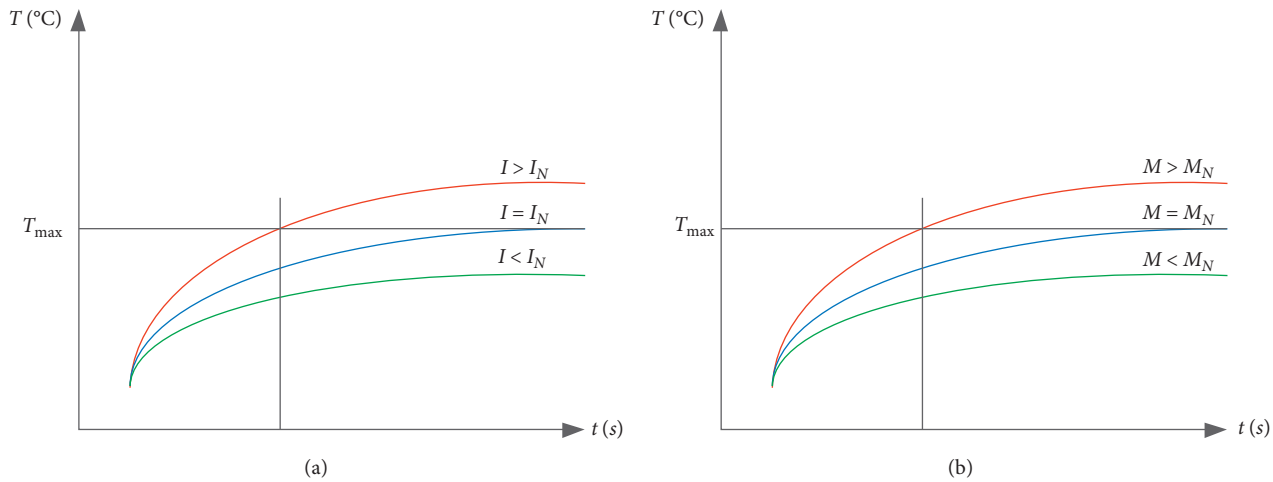

Figure 5: Corresponding relationship between motor winding temperature and running time. (a) Winding temperature variation curves under different working currents. (b) Winding temperature variation curves under different output torques.

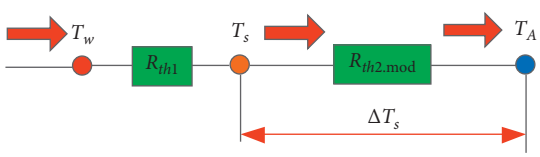

Figure 6: Heat flow diagram between motor casing and environment.

and torque of the motor will increase rapidly; under the same environmental temperature, if the motor is installed on a good heat conductor, the thermal resistance between the motor shell and the external environment will be reduced, thus increasing the rated current and torque of the motor.

4. Analysis of the Influence of Temperature Rise on Control Strategy

Figure 8 shows the force analysis of the front and rear wheels of the robot in the process of unpowered downhill. Figure 8(a) shows the force analysis of the front wheel of the robot. F_{P1} and F_{V1} are the forces of the robot's forearms on the front wheel in the tangential direction of the ground wire and in the direction perpendicular to the ground wire, respectively, and the unit is N; G_{w1} is the gravity on the front wheel, in N. The front wheel mass is m_1 in kg; w_1 is the angular velocity of the front wheel in rad/s; T_1 is the braking torque generated by energy consumption braking of front wheels, and the unit is Nm. Figure 8(b) shows the stress analysis of the rear wheel of the robot, and the meaning of each parameter is the same as that of the Figure 8(a).

From the force analysis in Figure 8, it can be seen that the torque of the front and rear wheels of the robot O_1' and O_2' are

$$\begin{cases} F_{X1}r - T_1 - T_{f1} = J_1\dfrac{d\omega_1}{dt}, \\ F_{X2}r - T_2 - T_{f2} = J_2\dfrac{d\omega_2}{dt}. \end{cases} \tag{11}$$

The total braking torque generated by the front and rear wheels of the robot without power and constant-speed downhill is

$$T_1 + T_2 = \left(\frac{G\tan\theta}{\sqrt{1+\tan^2\theta}} - \frac{Gf}{\sqrt{1+\tan^2\theta}} - \frac{\rho C_D A}{2}v^2\right)r. \tag{12}$$

It can be seen from the above formula that the braking torques T_1 and T_2 of the front and rear wheel traveling motors are

$$T_1 = i\eta_T\eta_m k_t i_{a1} = i\eta_T\eta_m k_t\frac{U}{R_{T_{w1}} + R_s} = \frac{i\eta_T\eta_m k_t k_e n}{R_{T_A}\cdot\left(1+\alpha_{Cu}\left(T_{w1} - T_A\right)\right) + R_s}, \tag{13}$$

$$T_2 = \frac{ui\eta_T\eta_m k_t k_e n}{R_{T_{w2}} + R_Z} = \frac{ui\eta_T\eta_m k_t k_e n}{R_{T_A}\cdot\left(1+\alpha_{Cu}\left(T_{w2} - T_A\right)\right) + R_Z}. \tag{14}$$

In formula (13), η_T is the transmission efficiency of motor reducer; η_m is the working efficiency of the motor. A current sensor is used to detect the charging current ia1 of the front wheel to the battery, where k_e is the electromotive force constant, k_t is the torque constant, n is the motor speed, u is the PWM wave duty ratio, i is the circuit current,

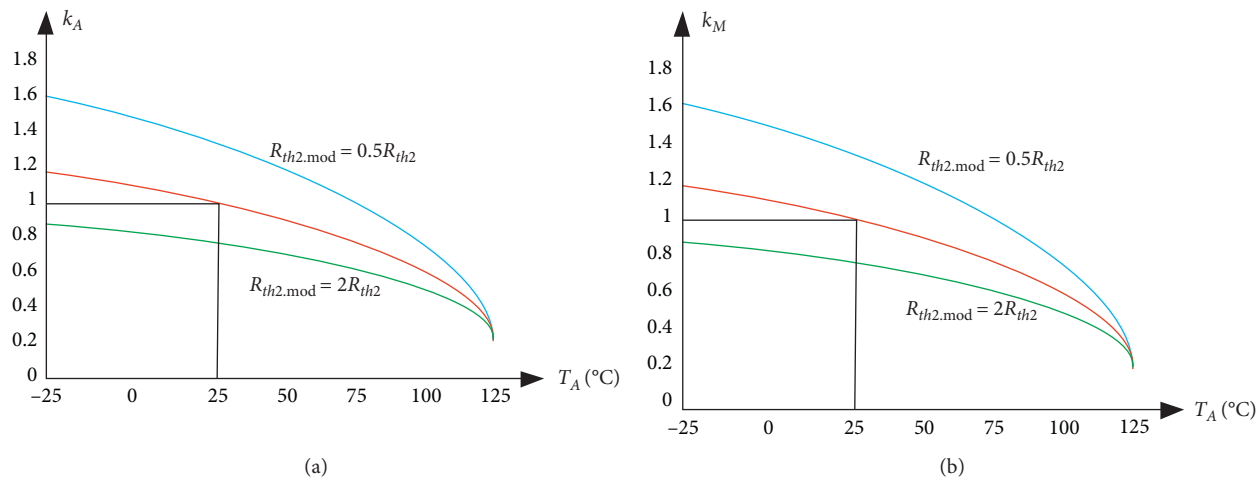

Figure 7: Variation curves of k_A and k_M under different ambient temperatures. (a)k_A change curve at different ambient temperatures. (b)k_M change curve at different ambient temperatures.

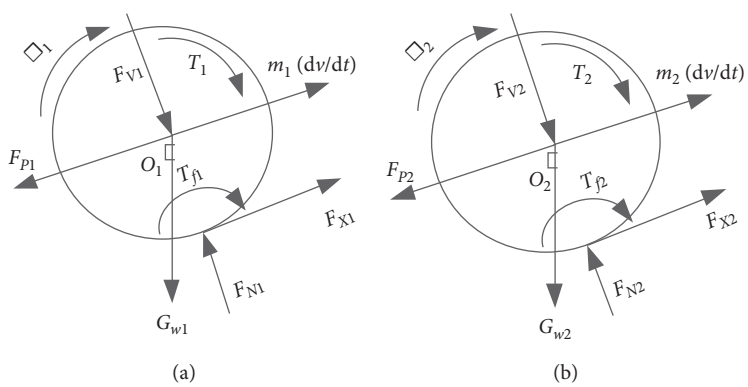

Figure 8: Force analysis of front and rear wheels of robot. (a) Force analysis of robot front wheel. (b) Force analysis of robot rear wheel.

R_Z is the energy consumption resistance, R_s is the internal resistance of the robot compound power supply, and the unit is ω. In order to facilitate the study of the influence of the walking motor temperature on unpowered downhill speed control and energy recovery, the influence of the internal resistance R_s of the compound power supply with temperature and SOC is not considered; T_{w1} is the armature winding temperature of the robot front wheel walking motor, and the unit is k; in formula (14), T_{w2} is the armature winding temperature of the robot rear wheel walking motor, and the unit is k; it can be seen from formulas (13) and (14) that the braking torque provided by the front and rear wheel traveling motors decreases with the increase of temperature during the unpowered constant speed downhill of the robot, and the braking torque required by the energy consumption braking of the rear wheel traveling motors will increase in order to keep the robot going downhill at a constant speed without power.

When the robot goes downhill at a constant speed without power, the duty ratio u_0 of the PWM wave of the rear wheel energy consumption braking circuit is

$$u_0 = \frac{\left(R_{T_{w2}} + R_Z\right)r}{i\eta_T\eta_m k_t k_e n}\left(\frac{G\tan\theta}{\sqrt{1+\tan^2\theta}} - \frac{Gf}{\sqrt{1+\tan^2\theta}} - \frac{\rho C_D A}{2}v^2\right) - \frac{i_{a1}}{k_e n}. \tag{15}$$

According to equation (15), when the slope of ground wire is θ, the robot goes downhill unpowered at a constant speed v, and the armature resistance $R_{T_{w2}}$ will increase linearly as the temperature of the armature winding of the rear wheel traveling motor rises. In order to keep the robot going downhill at a constant speed without power, the duty

ratio u_0 of PWM wave in the energy consumption control system of the rear wheel walking motor will also increase linearly. With the increase of duty ratio u_0 of the PWM wave in energy consumption speed control system, the current flowing through the armature winding of rear wheel walking motor will also increase, the Joule heat generated by armature winding will increase, and the internal heat balance of motor will be destroyed, which will further cause the temperature of rear wheel walking motor to rise.

It can be seen from formula (9) that the rated current $I_N(T_A)$ of the motor decreases gradually with the temperature rise of the motor. To ensure the safety of the robot walking motor and avoid the damage of the walking motor in the process of unpowered downhill, the braking current of the two walking motors should be less than the rated current $I_N(T_A)$.

5. Strategy Optimization

According to the above analysis, it can be seen that the change of armature winding temperature of the walking motor has an impact on its braking torque, rated torque, and rated current. Therefore, with the change of armature winding temperature of the walking motor, the control strategy of unpowered downhill speed and energy recovery needs to be optimized accordingly in order to make the robot run smoothly and safely at a constant speed. In order to recover the feedback braking energy to the maximum extent, the feedback braking distribution factor λ should be made as large as possible without considering the slippage of the front and rear wheels of the robot. In order to make the robot go downhill at a constant speed without power, the PWM duty ratio u_0 of the rear wheel energy consumption braking speed control system and the front wheel feedback braking distribution factor λ are, respectively,

$$u_0(\theta, v, T_{w1}, T_{w2}) = \frac{\left(R_{T_A}(1+\alpha_{Cu}(T_{w2}-T_A)) + R_Z\right)r}{i\eta_T\eta_m k_t k_e n}\left(\frac{G\tan\theta}{\sqrt{1+\tan^2\theta}} - \frac{Gf}{\sqrt{1+\tan^2\theta}} - \frac{\rho C_D A}{2}v^2\right) - \frac{1}{R_s + R_{T_A}(1+\alpha_{Cu}(T_{w1}-T_A))}, \tag{16}$$

$$\lambda(\theta, v, T_{w1}) = \frac{i\eta_T\eta_m k_t k_e n}{r\left(G\sin\theta - Gf\cos\theta - \left(\rho C_D A v^2/2\right)\right)\left(R_{T_{w1}} + R_s\right)} = \frac{i\eta_T\eta_m k_t k_e n}{r\left(G\sin\theta - Gf\cos\theta - \left(\rho C_D A v^2/2\right)\right)\left(R_{T_A}(1+\alpha_{Cu}(T_{w1}-T_A)) + R_s\right)}. \tag{17}$$

It can be seen from formulas (16) and (17) that the PWM wave duty ratio u_0 and the front wheel feedback brake distribution factor λ of the rear wheel energy consumption brake speed control system are related to the slope θ of the line where the robot is located, the downhill speed v, and the armature winding temperatures T_{w1} and T_{w2} of the front and rear wheel traveling motors. Therefore, considering the influence of the walking motor armature winding temperature on PWM duty ratio u_0 and front wheel feedback braking distribution factor λ of energy consumption braking speed control system, it is necessary to monitor the walking motor armature winding temperature T_{w1} and T_{w2} in real time, and optimize unpowered constant speed downhill control strategy and feedback braking distribution factor λ.

The highest working temperature of the armature winding of the walking motor is $T_{\max}$. In order to avoid damage caused by excessive temperature during unpowered downhill, the armature winding temperatures T_{w1} and T_{w2} of front and rear wheels should not be higher than that of the robot front and rear wheels ($T_{w1} \le T_{\max}$, $T_{w2} \le T_{\max}$), In order to avoid service life difference caused by large temperature difference, the temperature difference (ΔT) of the armature winding of front and rear wheels should meet the following requirements:

$$0 \le \Delta T = \left|T_{w1} - T_{w2}\right| \le \Delta T_{\max}. \tag{18}$$

In formula (18), $\Delta T_{\max}$ is the maximum allowable temperature difference between armature windings of front and rear wheel traveling motors, and the unit is k. When the total braking torque provided by the robot front and rear wheel traveling motors meets the condition of unpowered constant speed downhill, the feedback braking distribution factor λ is adjusted to distribute the braking torque required by the robot front and rear wheel traveling motors for unpowered constant speed downhill, so as to achieve the purposes of reducing the braking current flowing through the armature winding of the traveling motor with high temperature and improving the braking current of the armature winding of the traveling motor with low temperature, so that the temperature difference between the armature windings of the front and rear wheels is $\Delta T \le \Delta T_{\max}$. Figure 9 shows a diagram of unpowered downhill optimization control strategy based on the walking motor temperature, and the specific implementation strategy is as follows:

During the unpowered and constant-speed downhill process of the robot, the temperature detection system detects the aluminum flange temperatures T_{A1} and T_{A2} of the front and rear wheel traveling motors in real time, and

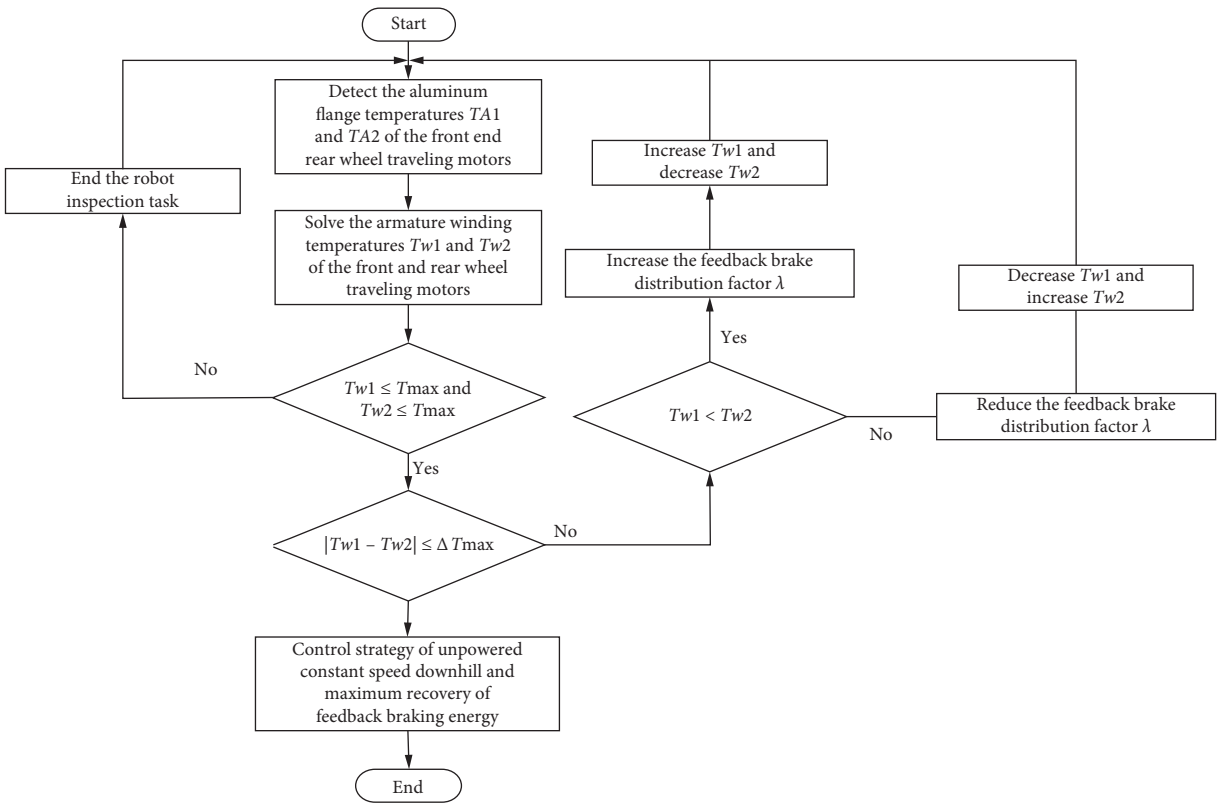

Figure 9: Unpowered downhill optimization control strategy based on walking motor temperature.

solves the armature winding temperatures T_{w1} and T_{w2} of the front and rear wheel traveling motors through the temperature difference between the motor armature windings and the external environment. When $T_{w1} > T_{\max}$ or $T_{w2} \leq T_{\max}$, the armature winding temperature exceeds the highest working temperature of the traveling motors. In order to avoid the damage of the traveling motors caused by excessive temperature and ensure the safe and stable operation of the robot on the transmission line, the robot should immediately finish the inspection task and wait for the armature winding temperatures of the two traveling motors to drop to normal. When $T_{w1} \leq T_{\max}$ and $T_{w2} \leq T_{\max}$, the control strategy of the front wheel feedback brake distribution factor for the temperature difference between the armature windings of the front and rear wheel traveling motors is as follows:

(1) When $\Delta T = |T_{w1} - T_{w2}| > \Delta T_{\max}$ and $T_{w1} < T_{w2}$, on the premise that the total braking torque of the front and rear wheels is unchanged when the robot goes downhill at a constant speed without power, the feedback braking torque of the front wheels is increased by increasing the distribution factor λ, and the energy consumption braking torque of the rear wheels is reduced, so that the temperature difference of armature windings of the front and rear wheels traveling motors satisfies $\Delta T \leq \Delta T_{\max}$.

(2) When $\Delta T = |T_{w1} - T_{w2}| > \Delta T_{\max}$ and $T_{w1} > T_{w2}$, by reducing the front wheel feedback braking distribution factor λ, the front wheel feedback braking torque is reduced, and the rear wheel energy consumption braking torque is increased, so that the temperature difference between the armature windings of the front and rear wheel traveling motors meets $\Delta T \leq \Delta T_{\max}$.

(3) When $\Delta T = |T_{w1} - T_{w2}| \leq \Delta T_{\max}$, the robot implements the unpowered constant speed downhill control strategy, and increases the front wheel feedback braking distribution factor λ, so as to recover the feedback braking energy to the maximum extent.

6. System Preparation and Experimental Results

Figure 10 shows the block diagram of the walking motor temperature detection system of the inspection robot. During the unpowered downhill process of the robot, the front and rear wheel temperature sensors, respectively, detect the aluminum flange temperatures of the front and rear wheel walking motors, obtain the temperature information through the ARM microprocessor, calculate the motor armature winding temperature by the walking motor armature winding temperature analysis system, and optimize the unpowered downhill speed and energy recovery control strategy according to the front and rear wheel walking motor armature winding temperature. Because the robot performs patrol inspection on the high-voltage transmission line, in order to enable the ground operators to

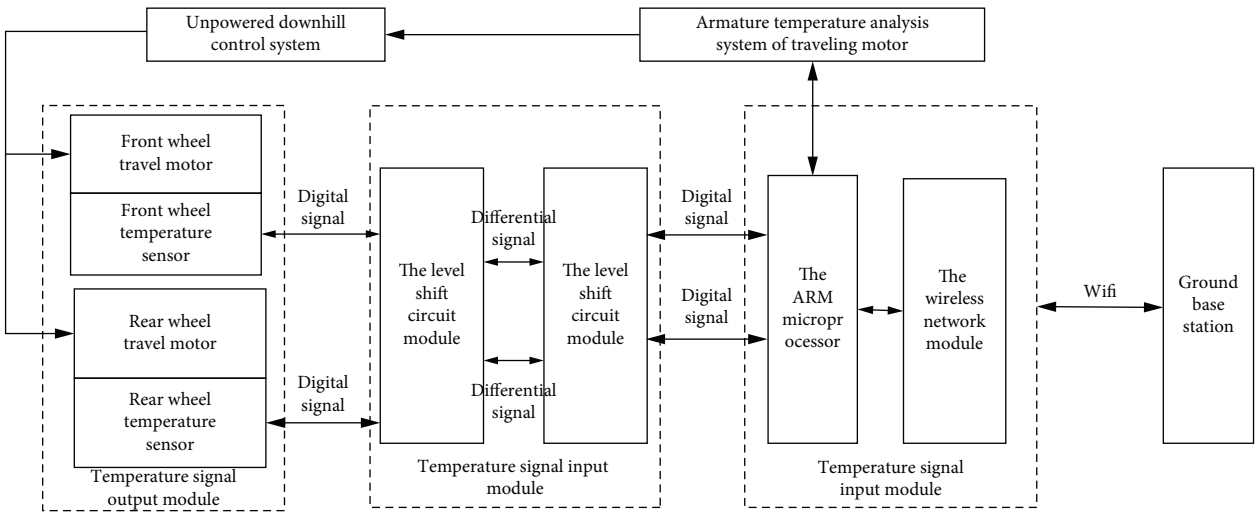

Figure 10: Block diagram of temperature detection system.

monitor the temperature of the front and rear wheel walking motors in real time, the wireless network module is adopted to transmit the temperature information of the front and rear wheel walking motors to the ground base station through wireless WIFI. Figure 11 shows the temperature detection system of the robot walking motor.

Figure 12 is the field experiment running diagram of the robot between #114 and #119 tower sections. Among them, between #114 and #117 towers, the height difference between two adjacent towers is negative, so the distance of the robot in the downhill section between two adjacent towers is higher than that in the uphill section; in #117–#119 towers, if the height difference between two adjacent towers is positive, the distance of the robot in the uphill section is higher than that in the downhill section between adjacent towers, as shown in Figure 13, which is the schematic diagram of robot running between #114 and #119 towers.

Figure 14 is the temperature change curve of the front and rear wheel traveling motors of the robot in the servo drive mode between # 114 and # 119 towers. It can be seen from the figure that the temperature of the front and rear wheel traveling motors of the robot gradually rises as the robot performs the inspection task between the sections, and when the temperature of the walking wheel reaches 80°C (the highest temperature of the encoder working normally is 85°C), the robot stops performing the inspection task, and then starts to perform the inspection task when the temperature of the walking wheel drops to a safe temperature. Taking the robot's patrol task between towers #115 and #116 as an example, the distance of the downhill section of the robot is higher than that of the uphill section, and the height difference between adjacent towers in this section is the largest. It can be seen from the figure that the temperature rise of the rear wheel walking motor is slightly faster than that of the front wheel in the downhill section, and the maximum temperature difference between the front and rear wheel walking motors is 1.2°C. Therefore, when the robot goes downhill in servo drive mode, the downhill resistance provided by the rear wheel walking motor is slightly higher than that of the front wheel. Taking the robot's patrol inspection task between #118 and #119 towers as an example, the uphill section between the sections has the longest distance. It can be seen from the figure that the temperature of the front wheel walking motor is slightly faster than that of the rear wheel in the uphill section, so when the robot climbs between the sections, the servo driving force of the front wheel is higher than that of the rear wheel.

Figure 15 is the temperature change curve of the front and rear wheel walking motors of the robot in the unpowered constant speed downhill mode. It can be seen from the figure that the temperature difference between the front and rear wheel walking motors has a greater increase compared with the whole operation of the robot in the servo drive mode. In the unpowered downhill mode, the temperature rise of the rear wheel traveling motor is faster than that of the front wheel; therefore, in the unpowered downhill mode, the downhill braking force provided by the rear wheel is higher than that of the front wheel, which makes the temperature difference between the front and rear wheel traveling motors gradually increase. In the uphill stage, the robot switches to servo drive mode, and the driving force provided by the front wheel is higher than that of the rear wheel, so that the temperature difference between the front and rear wheels gradually decreases.

Figure 16 shows the temperature change curve of walking wheels optimized by unpowered downhill strategy based on the temperature of walking wheels. It can be seen from the figure that the temperature difference between the front and rear wheels of walking motors is 8.8°C after the robot inspects the #116–#117 gears, and the robot performs unpowered downhill strategy optimization based on the temperature of walking wheels in the downhill section between #117 and #118 gears. After the robot completes unpowered downhill execution, the temperature difference between the front and rear wheels of walking motors drops to 6°C. Therefore, if the temperature difference between the front and rear wheel traveling motors exceeds 8°C, the robot starts the unpowered downhill strategy optimization based

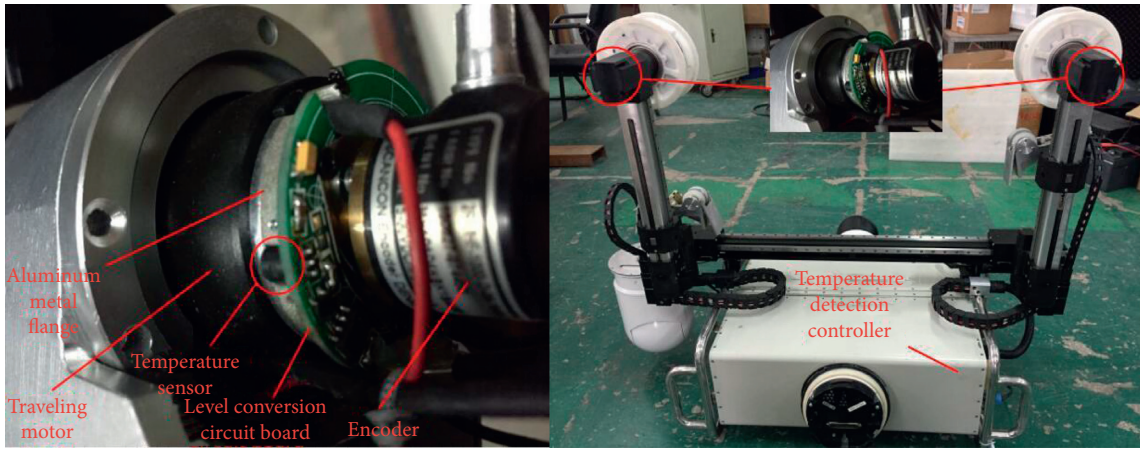

Figure 11: Temperature detection system of the walking motor.

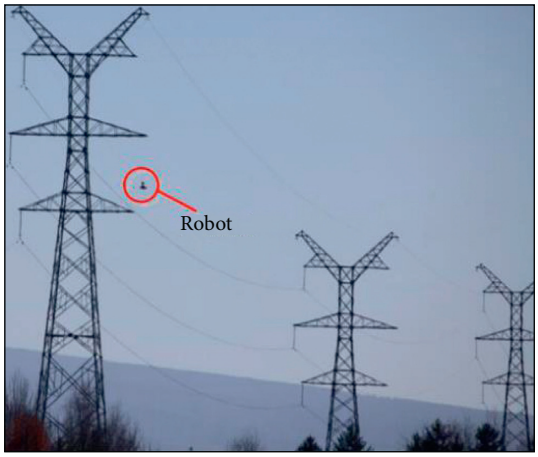

Figure 12: The robot's field experiment operation diagram between #114 and #119 pole towers.

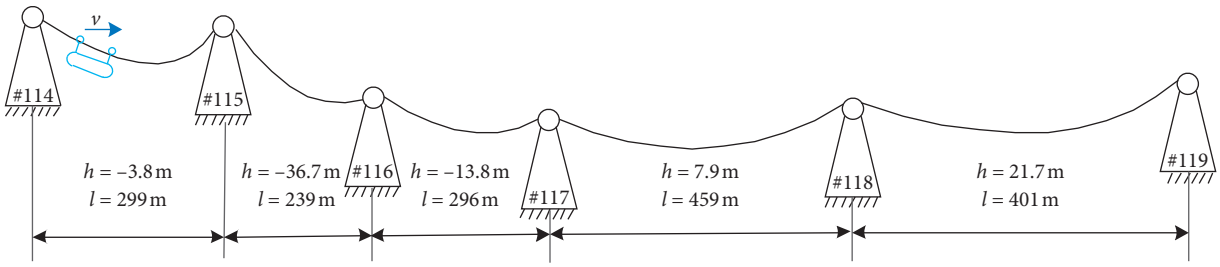

Figure 13: Schematic diagram of robot operation in gear #114–#119.

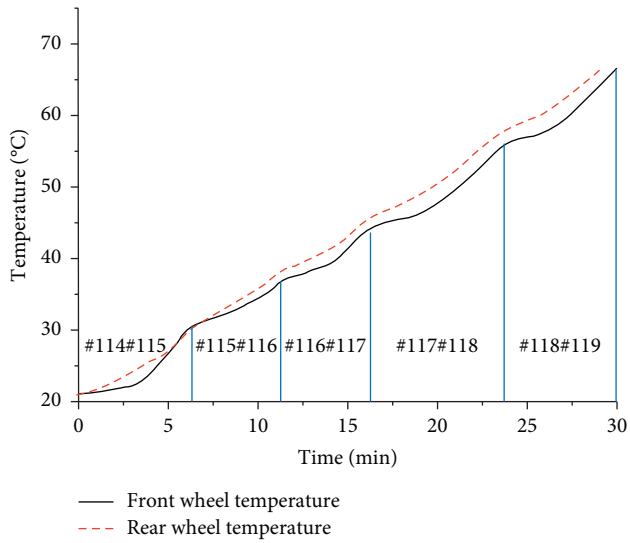

Figure 14: Temperature change curve of traveling wheel in servo drive mode.

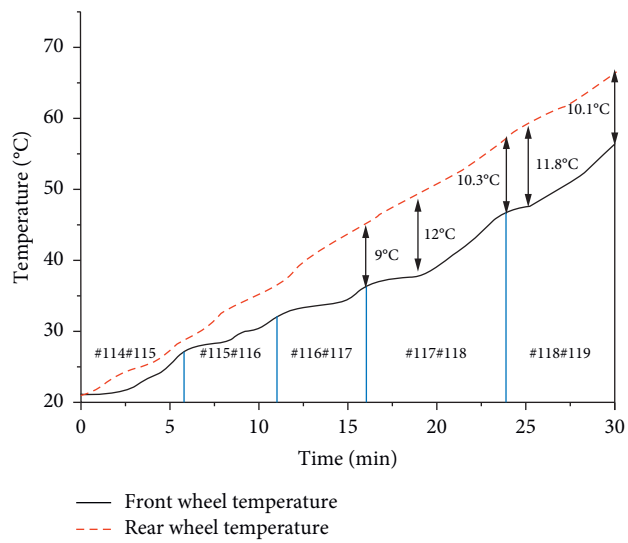

Figure 15: Temperature change curve of walking wheel of unpowered downhill model.

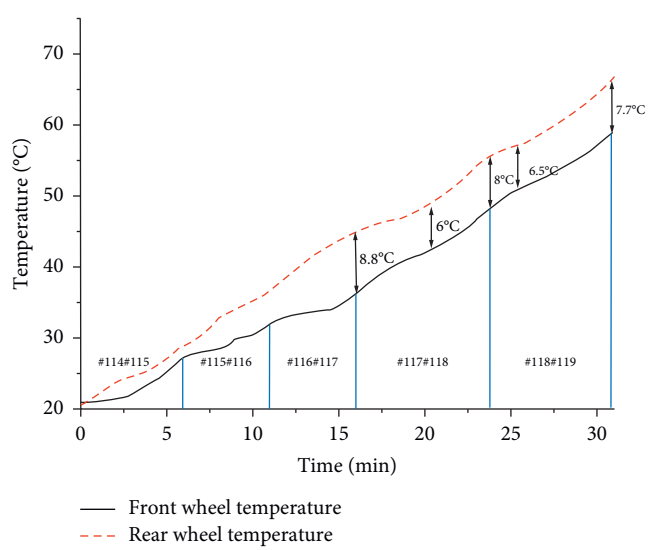

Figure 16: Temperature change curve of walking motor after optimization by unpowered downhill strategy.

on the traveling wheel temperature, which reduces the temperature difference between the front and rear wheel traveling motors.

7. Conclusion

With the rapid development of complexity microgrid network lines, the application of high-voltage inspection robots is more and more extensive. This paper puts forward the optimal control strategy based on unpowered downhill speed and energy recovery of inspection robots in complexity microgrid networks for the first time. By adjusting the duty ratio u of the energy consumption speed control system and the distribution factor λ of the front wheel feedback brake, the temperature difference between the front and rear wheel traveling motors is reduced, thereby preventing the motor and encoder from being damaged due to the rapid temperature rise of the traveling motor. Through the experimental analysis on the simulated line, it is verified that the unpowered downhill speed and energy recovery optimization control method based on the temperature rise characteristics of the walking motor can effectively reduce the temperature difference between the front and rear wheels, thereby preventing the traveling motor from being damaged by the motor and encoder due to the rapid temperature rise.

Data Availability

The data used to support the findings of this study are available from the corresponding author upon request.

Conflicts of Interest

The authors declare that they have no conflicts of interest.

Acknowledgments

This work was supported by a grant from the National Natural Science Foundation of China (no. 51907055) and Education Department Outstanding Young and Middle-aged Science and Technology Innovation Team Project of Hubei Province (no. Q20191404).

References

[1] J.-W. Jung, V. Q. Leu, T. D. Do, E.-K. Kim, and H. H. Choi, "Adaptive PID speed control design for permanent magnet synchronous motor drives," *IEEE Transactions on Power Electronics*, vol. 30, no. 2, pp. 900–908, 2015.

[2] J. Liu, H. Li, and Y. Deng, "Torque ripple minimization of PMSM based on robust ILC via adaptive sliding mode control," *IEEE Transactions on Power Electronics*, vol. 33, no. 4, pp. 3655–3671, 2018.

[3] Y. Xie, X. Tang, B. Song, X. Zhou, and Y. Guo, "Data-driven adaptive fractional order PI control for PMSM servo system with measurement noise and data dropouts," *ISA Transactions*, vol. 75, pp. 172–188, 2018.

[4] H. Guo, J. Xu, and Y.-H. Chen, "Robust control of fault-tolerant permanent-magnet synchronous motor for aerospace application with guaranteed fault switch process," *IEEE Transactions on Industrial Electronics*, vol. 62, no. 12, pp. 7309–7321, 2015.

[5] A. D. O. D. S. Dantas, A. F. O. D. A. Dantas, J. T. L. S. Campos, D. L. De Almeida Neto, C. E. T. Dórea, and D. Huang, "PID control for electric vehicles subject to control and speed signal constraints," *Journal of Control Science and Engineering*, vol. 2018, Article ID 6259049, 11 pages, 2018.

[6] H. Yu, H. R. Karimi, and X. Zhu, "Research of smart car's speed control based on the internal model control," *Abstract and Applied Analysis*, vol. 2014, Article ID 274293, 5 pages, 2014.

[7] W. T. Asfu, "Stator current-based model reference adaptive control for sensorless speed control of the induction motor," *Journal of Control Science and Engineering*, vol. 2020, Article ID 8954704, 17 pages, 2020.

[8] K. L. Luna, E. R. Palacios, and A. Marin, "A fuzzy speed controller for a guide robot using an HRI approach," *IEEE Latin America Transactions*, vol. 16, no. 8, pp. 2102–2107, 2018.

[9] V. Šlapák, K. Kyslan, M. Lacko, V. Fedák, and F. Ďurovský, "Finite control set model predictive speed control of a DC motor," *Mathematical Problems in Engineering*, vol. 2016, Article ID 9571972, 10 pages, 2016.

[10] H. Jian, W. Gongping, W. Wei, Y. Shoudong, L. Ming, and Y. Zhiyong, "Unpowered downhill speed control method of patrol robot," *Journal of Zhejiang University*, vol. 49, no. 10, pp. 1878–1884, 2015.

[11] P. Kannan, S. K. Natarajan, and S. S. Dash, "Labview based autonomous agricultural robot using fuzzy logic controller," *American Journal of Applied Sciences*, vol. 10, no. 11, pp. 1413–1418, 013.

[12] Y. Meng, B. Liu, and L. Wang, "Speed control of PMSM based on an optimized ADRC controller," *Mathematical Problems in Engineering*, vol. 2019, Article ID 1074702, 18 pages, 2019.

[13] G. Lian, H. Li, B. Chen, F. Ban, and J. Zhang, "Characteristic analysis and temperature rise calculation of PMSM under different power supply modes," *IEEE Transactions on Applied Superconductivity*, vol. 29, no. 2, pp. 1–5, 2019.

[14] Q. Lu, X. Zhang, Y. Chen, X. Huang, Y. Ye, and Z. Q. Zhu, "Modeling and investigation of thermal characteristics of a water-cooled permanent-magnet linear motor," *IEEE Transactions on Industry Applications*, vol. 51, no. 3, pp. 2086–2096, 2015.

[15] B. Kim, M. Choi, K. Park, B. Kim, X. Maldague, and T. Takagi, "Analysis of IPMSM characteristics considering the temperature change," *International Journal of Applied Electromagnetics and Mechanics*, vol. 45, no. 1–4, pp. 315–321, 2014.

[16] Q. Lv, Z. Yao, L. Zhou, and L. Pan, "Effect of temperature rise on characteristics of a standing wave ultrasonic motor," *Journal of Intelligent Material Systems and Structures*, vol. 30, no. 6, pp. 855–868, 2019.

[17] Y. Xia, Y. Han, Y. Xu, and M. Ai, "Analyzing temperature rise and fluid flow of high-power-density and high-voltage induction motor in the starting process," *IEEE ACCESS*, vol. 7, pp. 35588–35595, 2019.

[18] Y. Xu, M. Ai, and Y. Yang, "Heat transfer characteristic research based on thermal network method in submersible motor," *International Transactions On Electrical Energy Systems*, vol. 28, no. 3, Article ID e2507, 2018.

[19] H.-J. An, G.-W. Cho, S.-H. Woo, and G.-T. Kim, "The optimal design of single sided PMLSM for considering winding temperature rising according to thickness of teeth," *Journal of Electrical Engineering and Technology*, vol. 8, no. 2, pp. 339–344, 2013.

[20] J. Nakatsugawa, Y. Iwaji, and Y. Enomoto, "Extension of mathematical models taking temperature variation in permanent magnet synchronous motors into consideration," *Electrical Engineering in Japan*, vol. 199, no. 3, pp. 48–56, 2017.

Hindawi
Complexity
Volume 2021, Article ID 6697792, 12 pages
https://doi.org/10.1155/2021/6697792

Research Article

Robust Switching Gain-Based Fractional-Order Sliding Mode Control for Wind-Powered Microgrids

Minghao Zhou,[1] Siwei Cheng,[1] Long Xu,[2] Likun Wang,[1] Qingbo Guo,[1] and William Cai[1]

[1]*School of Electrical and Electronics, Harbin University of Science and Technology, Harbin, China*
[2]*School of Automation, Southeast University, Nanjing, China*

Correspondence should be addressed to Long Xu; long.xu.rmit@gmail.com

Received 22 October 2020; Revised 16 February 2021; Accepted 24 February 2021; Published 24 March 2021

Academic Editor: Ruoli Tang

This study proposes a novel fractional-order sliding-mode control strategy with robust switching gain to achieve reliable and high quality of wind-powered microgrid systems. Three fractional-order sliding mode controllers are designed to generate continuous control signals and regulate the outer DC-link voltage loop and inner current loop in the grid-side inverters. High robustness and stability of the grid-side inverter can be guaranteed even in the presence of parameter variations and external disturbances. Owing to the fractional-order sliding manifold and fractional-order integral control law, the chattering is attenuated. The fractional-order robust adaptive switching gain is designed to avoid overestimating the upper bound of matched/unmatched uncertainties, save the control energy, and guarantee the rapidity and robustness of the convergence. Simulations validate the proposed method.

1. Introduction

Distributed generation (DG) has paid more and more attention because of its advantages, such as low investment, clean environment protection, high reliability of power supply, and flexible power generation [1]. Beside the aforementioned advantages, DG unit may bring some problems to the grid, such as voltage fluctuations, voltage deviations, and bidirectional power flow. To give full play to the efficiency of the distributed generation systems, the most effective way is to combine the distributed generation and loads to form a microgrid connecting to the main grid. The active power and reactive power between the microgrid and the main grid can be flexibly exchanged. If the main power grid fails, the microgrid will be instantly separated from the main grid and run in the isolated island mode to guarantee the power supply of important loads [2].

In the wind-powered microgrid system, the voltage source inverters (VSIs) are widely used as grid-side inverters. However, this type of converter has a characteristic that the high-frequency harmonics exist in the voltage waveform. Therefore, filters must be used to filter the harmonics out. LCL filters, as commonly used filters, have superior performance in harmonic attenuation and lower current ripple if compared with the L filter, another commonly used filter. Due to the structures and resonances of LCL filters, the LCL filters are rather complicated, which means the control schemes for LCL filters are difficult to implement. The traditional control methods cannot have good performance when applied in the control of LCL filters [3, 4], which may have poor reference tracking and stability problems. In [5], a proportional resonant (PR) controller with a PI controller is designed to get a better dynamic response in terms of disturbance compensation. However, the high gain was introduced by PR, which can cause a larger steady-state error [6].

There are many uncertainties existed in the wind powered microgrid system, such as parameter variations of LCL filters, grid voltage sag, and frequency fluctuation. Sliding mode control (SMC) is extensively used to deal with aforementioned problems due to its high robustness, fast dynamics responses, and simplicity in the control algorithm. It is suitable to use SMC for the control of the grid-side inverters (GSI), on account of its attractive advantages [7–12]. In [9], an integral-type terminal sliding mode control is proposed to get a high dynamics response in the wind

energy conversion system with LCL filters. In [13], a sliding mode controller with Kalman filter (KF) is proposed in a three-phase unity power factory rectifier. An SMC method by modifying reaching law for the variable-speed direct-driven wind energy conversion systems is proposed in [14]. In [15, 16], PI-type sliding surfaces are presented to remove the steady-state error. In [17], a super-twisting sliding mode (STSM) for a gearless wind turbine is developed, so that the system has distinguished robustness against disturbances. In [18], a novel direct active and reactive power control of grid-connected DFIG-based wind turbine systems is presented, which employed a novel SMC to calculate the required rotor control voltage. In [19], an advanced SMC scheme is designed for wind energy conversion systems with a non-linear disturbance observer.

The aforementioned SMC strategies are all based on integer order calculus which restricts the development of the control theory [20]. With the development of fractional-order calculus, the fractional-order SMC (FOSMC) has been a topic of intense research. Compared with traditional integral order calculus, fractional calculus increases the variability of differential and integral degrees of freedom, which brings new flexibility to the design of control systems [21, 22], so that it has both advantages of fractional calculus and the SMC. The memorial and genetic traits are the typical characteristics of FOSMC, which can predict the control behavior of the system to a certain extent, reduce the switching probability of the control behavior in the reaching process, and thus improve the continuity of the control [23, 24]. A new time-delay estimation-based fractional-order NTSM controller and an intelligent robust fractional-order LSM controller are proposed in [25, 26], but the boundary layer leads to steady-state errors. An adaptive fractional-order TSM is developed in [27]; however, the singularity exists.

To achieve higher performances of wind-powered microgrid systems, this study proposes a fractional-order SMC method with robust adaptive switching gain for GSI. Fractional-order sliding mode controllers are designed for the outer DC-link voltage loop and inner current loop in GSI. The DC-link voltage and current errors can be controlled to converge to zero and chattering can be avoided. High performances of GSI can be guaranteed even in the presence of external disturbances and parameter variations. The remainder of this study is organized as follows: Section 2 briefly introduces the fractional calculus and the wind-powered microgrid systems with a squirrel cage induction generator (SCIG) and the model of GSI with LCL. Section 3 presents the fractional-order SMC design for GSI. Section 4 shows the simulation results. Finally, Section 5 gives a conclusion.

2. Preliminaries

Composed of a wind turbine, an SCIG, a converter, and an LCL-type filter, a SCIG wind turbine system is shown in Figure 1. Figure 2 shows the detailed circuit of the wind-powered microgrid control system, and the definition of symbols in Figure 2 is given in Table 1. The PWM converter consists of a machine-side rectifier (MSR), a DC-link capacitor C with its voltage u_{DC}, and a grid-side inverter. The wind turbine delivers the energy P_{Ge} to MSR through the SCIG. The MSR and GSI are controlled separately using fractional-order SMC strategies proposed in the study.

Due to the existence of the uncertainties in the GSI system, which may be caused by aging, temperature, saturation effects, and some parameter variations have to be considered as follows when modeling the system:

$$\begin{cases} L_{\mathrm{Ij}} = L'_{\mathrm{Ij}} + \Delta L_{\mathrm{Ij}}, \\ R_{\mathrm{Ij}} = R'_{\mathrm{Ij}} + \Delta R_{\mathrm{Ij}}, \end{cases} \\ \begin{cases} L_{\mathrm{Gj}} = L'_{\mathrm{Gj}} + \Delta L_{\mathrm{Gj}}, \\ R_{\mathrm{Gj}} = R'_{\mathrm{Gj}} + \Delta R_{\mathrm{Gj}}, \end{cases} \\ \begin{cases} C_j = C_j + \Delta C_j, \\ R_{\mathrm{Cj}} = R_{\mathrm{Cj}} + \Delta R_{\mathrm{Cj}}, \end{cases} \\ j = a, b, c, \tag{1}$$

where Δ stands for the parameter variations.

With the harmonic of grid voltages and the loss of switches ignored, the model of the GSI systems can be expressed as follows:

$$\begin{cases} C\dot{u}_{\mathrm{DC}} = i_L - i_I, \\ \dot{i}_j = -\dfrac{R_{\mathrm{Ij}}}{L_{\mathrm{Ij}}} i_j - \dfrac{1}{L_{\mathrm{Ij}}} u_{\mathrm{Cj}} + \dfrac{u_{\mathrm{DC}}}{L_{\mathrm{Ij}}} S_j, \\ \dot{i}_{\mathrm{Gj}} = -\dfrac{R_{\mathrm{Gj}}}{L_{\mathrm{Gj}}} i_{\mathrm{Gj}} + \dfrac{1}{L_{\mathrm{Gj}}} u_{\mathrm{Ck}} - \dfrac{1}{L_{\mathrm{Gj}}} e_j, \\ \dot{u}_{\mathrm{Cj}} = \dfrac{1}{C_{\mathrm{Ij}}} i_j - \dfrac{1}{C_{\mathrm{Ij}}} i_{\mathrm{Gj}} + R_{\mathrm{Cj}}\left(\dot{i}_j - \dot{i}_{\mathrm{Gj}}\right), \\ \qquad j = a, b, c, \end{cases} \tag{2}$$

where S_j, $j = a, b, c$ are the inputs of the PWM modulator, and $i_I = S_a i_a + S_b i_b + S_c i_c$.

In view of the uncertainties of parameters, the model of the GSI systems (2) can be rewritten in the vector form as

$$\begin{cases} C\dot{u}_{\mathrm{DC}} = i_L - i_I, \\ \dot{i}_G = -\mathbf{L}_G^{-1}\mathbf{R}_G\mathbf{i}_G - \mathbf{L}_G^{-1}\mathbf{e} + \mathbf{L}_G^{-1}\mathbf{u}_C + \boldsymbol{\sigma}_G\mathbf{u}_C + \Delta\mathbf{d}_G, \\ \dot{u}_C = \left(\mathbf{C}^{-1} - \mathbf{L}_I^{-1}\mathbf{R}_C\mathbf{R}_I\right)\mathbf{i} - \left(\mathbf{C}^{-1} - \mathbf{L}_G^{-1}\mathbf{R}_C\mathbf{R}_G\right)\mathbf{i}_G + \mathbf{L}_G^{-1}\mathbf{R}_C\mathbf{e} \\ \quad -\left(\mathbf{L}_I^{-1} + \mathbf{L}_G^{-1}\right)\mathbf{R}_C\mathbf{u}_C + \mathbf{L}_G^{-1}\mathbf{R}_C u_{\mathrm{DC}}\mathbf{S} + \boldsymbol{\sigma}_C u_{\mathrm{DC}}\mathbf{S} + \boldsymbol{\rho}_C, \end{cases} \tag{3}$$

where $\mathbf{S} = [S_a, S_b, S_c]^T$, $\mathbf{i}_G = [i_{\mathrm{Ga}}, i_{\mathrm{Gb}}, i_{\mathrm{Gc}}]^T$, $\mathbf{u}_C = [u_{\mathrm{Ca}}, u_{\mathrm{Cb}}, u_{\mathrm{Cc}}]^T$, $\mathbf{i} = [i_a, i_b, i_c]^T$, and $\mathbf{e} = [e_a, e_b, e_c]^T$, and the parameters $\mathbf{L}_I = [L_{\mathrm{Ia}}, L_{\mathrm{Ib}}, L_{\mathrm{Ic}}]^T$, $\mathbf{R}_k = \mathrm{diag}(R'_{\mathrm{ka}}, R'_{\mathrm{kb}}, R'_{\mathrm{kc}})$, $k = I, G, C$; $\mathbf{L}_l = \mathrm{diag}(L'_{la}, L'_{lb}, L'_{lc})$, $l = I, G$; and $\mathbf{C} = \mathrm{diag}(C'_a, C'_b, C'_c)$. It can be assumed that the uncertainties σ_G, $\Delta\mathbf{d}_G$, σ_C, and ρ_C are upper-bounded.

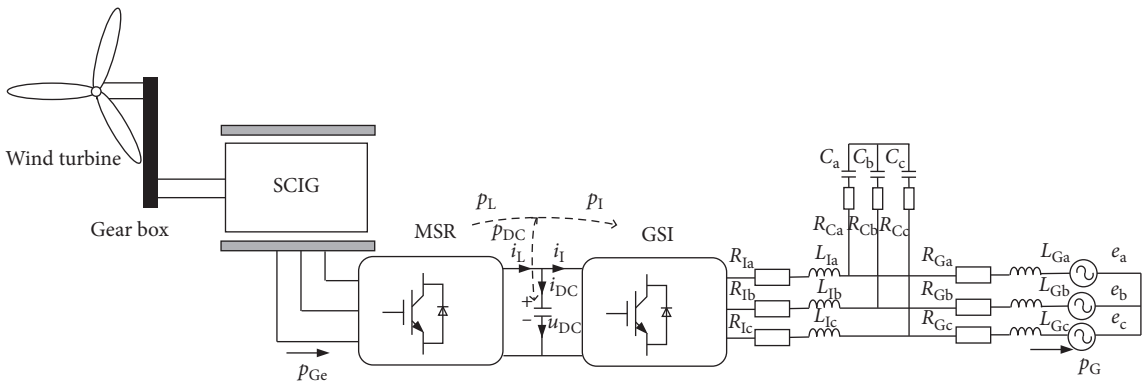

Figure 1: An SCIG wind turbine system.

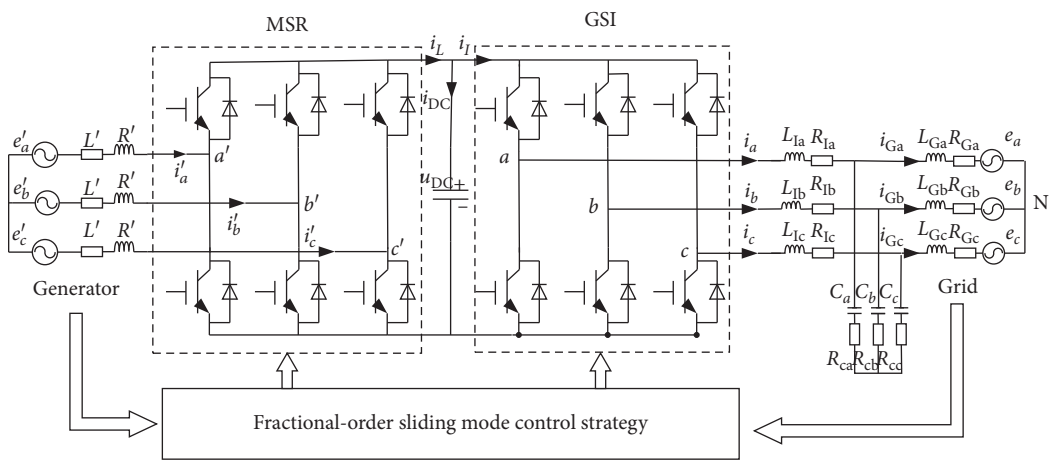

Figure 2: Wind powered microgrid control system.

Table 1: Definition of the symbols in Figure 2 ($j = a, b, c$).

Symbol	Definition
e'_j, i'_j	Generator voltages and currents
L', R	Inductors/resistances of the L-type filter of the generator
i_L	Output current of the MSR
i_I	Input current of GSI
i_{DC}	Current through the capacitor
e_j	Grid voltages
i_j, i_{Gj}	Currents flowing through the LCL filters L_{Ij}, L_{Gj}
u_{Cj}	Voltages in LCL filter capacitors C_j

For the controller design, the model of the GSI system (3) can be transformed to the form in the $\alpha\beta$-stationary coordinate by the Clarke transformation; then, equation (3) can be rearranged as follows:

$$\begin{cases} C\dot{u}_{\mathrm{DC}} = i_L - i_I, \\ \dot{i}_{G2} = -\mathbf{T}_1\mathbf{L}_G^{-1}\mathbf{R}_G\mathbf{T}_2\mathbf{i}_{G2} - \mathbf{T}_1\mathbf{L}_G^{-1}\mathbf{T}_2\mathbf{e}_2 + \mathbf{T}_1\mathbf{L}_G^{-1}\mathbf{T}_2\mathbf{u}_{C2} + \mathbf{T}_1\boldsymbol{\sigma}_G\mathbf{T}_2\mathbf{u}_{C2} + \mathbf{T}_1\Delta\mathbf{d}_G, \\ \dot{u}_{C2} = \mathbf{T}_1\left(\mathbf{C}^{-1} - \mathbf{L}_I^{-1}\mathbf{R}_C\mathbf{R}_I\right)\mathbf{T}_2\mathbf{i}_2 - \mathbf{T}_1\left(\mathbf{C}^{-1} - \mathbf{L}_G^{-1}\mathbf{R}_C\mathbf{R}_G\right)\mathbf{T}_2\mathbf{i}_{G2} + \mathbf{T}_1\mathbf{L}_G^{-1}\mathbf{R}_C\mathbf{T}_2\mathbf{e}_2 \\ -\mathbf{T}_1\left(\mathbf{L}_I^{-1} + \mathbf{L}_G^{-1}\right)\mathbf{R}_C\mathbf{T}_2\mathbf{u}_{C2} + \mathbf{T}_1\mathbf{L}_G^{-1}\mathbf{R}_C u_{\mathrm{DC}}\mathbf{T}_2\mathbf{S}_2 + \mathbf{T}_1\boldsymbol{\sigma}_C u_{\mathrm{DC}}\mathbf{T}_2\mathbf{S}_2 + \mathbf{T}_1\boldsymbol{\rho}_C, \end{cases} \tag{4}$$

where $\mathbf{S}_2 = [S_\alpha, S_\beta]^T$, $\mathbf{i}_{G2} = [i_{G\alpha}, i_{G\beta}]^T$, $\mathbf{i}_2 = [i_\alpha, i_\beta]^T$, $\mathbf{u}_{C2} = [u_{C\alpha}, u_{C\beta}]^T$, and $\mathbf{e}_2 = [e_\alpha, e_\beta]^T$.

3. FOSM Controller Design for GSI

The GSI control system is presented in Figure 3. There are three feedback control loops in the system: the DC-link voltage loop, the current loop, and the LCL filter capacitor voltage loop, where $*$ stands for the reference. To depress the effect of unbalanced gird-voltages and deal with the parameter variations, three FOSM controllers with robust switching gains are designed for the three loops. The fractional-order calculus used in three controllers is defined by α^{th}-order Caputo.

To ensure the stability of the controller, the following are the reasonable assumptions:

$$\left|{}_{t_0}^{C}D_t^{\alpha-1} i_L\right| \le U_{\text{DC}}, \tag{5a}$$

$$\left\|{}_{t_0}^{C}D_t^{\alpha}\left(\mathbf{T}_1\boldsymbol{\sigma}_G\mathbf{T}_2\mathbf{u}_{C2}^{*} + \mathbf{T}_1\Delta\mathbf{d}_G\right)\right\| \le U_G, \tag{5b}$$

$$\left\|{}_{t_0}^{C}D_t^{\alpha}\left(\mathbf{T}_1\boldsymbol{\sigma}_C u_{\text{DC}}\mathbf{T}_2\mathbf{S}_2 + \mathbf{T}_1\boldsymbol{\rho}_C\right)\right\| \le U_C, \tag{5c}$$

where U_{DC}, U_G, and U_C are the unknown upper bounds of the uncertainty vectors.

Figure 4 shows the flow chart of the whole algorithms of the fractional-order controllers for the grid-side converters. These three controllers are designed to guarantee that the errors of the DC voltage, current voltage, and the LCL capacitor voltage can converge to zero.

Lemma 1 (see *[28]). The nonautonomous fractional-order system* ${}_{t_0}^{C}D_t^{\alpha}(\mathbf{x}(t)) = f(t, \mathbf{x}(t))$ *is Mittag–Leffler stable at the equilibrium point* $\boldsymbol{x}(t) = 0$*, if a continuous and differentiable Lyapunov function* $V(t, \boldsymbol{x}(t))$*:* $R^{+} \longrightarrow R$ *and class-K function* ϕ_i $(i = 1, 2, 3)$ *satisfies*

$$\begin{aligned} &\phi_1(\|\mathbf{x}(t)\|) \le V(t, \mathbf{x}(t)) \le \phi_2(\|\mathbf{x}(t)\|), \\ &{}_{t_0}^{C}D_t^{\alpha}V(t, \mathbf{x}(t)) \le -\phi_3(\|\mathbf{x}(t)\|). \end{aligned} \tag{6}$$

3.1. DC-Link Voltage Controller. Define the DC-link voltage error as $\overline{u}_{\text{DC}} = u_{\text{DC}} - u_{\text{DC}}^{*}$. Then, the error dynamics of the DC-link voltage can be obtained from equation (4) as follows:

$$\dot{\overline{u}}_{\text{DC}} = \frac{(i_L - i_I)}{C}. \tag{7}$$

A fractional-order sliding manifold for the DC-link voltage error dynamic (7) is chosen as follows:

$$\mathbf{s}_{\text{DC}} = {}_{t_0}^{C}D_t^{\alpha}\overline{u}_{\text{DC}} + \lambda_{\text{DC}}\overline{u}_{\text{DC}}, \tag{8}$$

where $0 < \alpha < 1$ is the fractional order, and $\lambda_{\text{DC}} > 0$ is a constant.

Theorem 1. *Along the fractional-order sliding manifold (8), the DC-link voltage error dynamic (7) can be guaranteed to converge to its equilibrium point, if a fractional-order integral virtual control law with its robust adaptive switching gain is designed as follows:*

$$i_I^{*} = i_{\text{Ieq}}^{*} + i_{\text{In}}^{*}, \tag{9a}$$

$$i_{\text{Ieq}}^{*} = C\lambda_{\text{DC}}{}_{t_0}^{C}D_t^{1-\alpha}\overline{u}_{\text{DC}}, \tag{9b}$$

$$i_{\text{In}}^{*} = {}_{t_0}^{C}I_t^{\alpha}\left(k_{\text{DC}}\text{sgn}\left(s_{\text{DC}}\right)\right), \tag{9c}$$

$$k_{\text{DC}} = \mu{}_{t_0}^{C}I_t^{\beta}\left|s_{\text{DC}}\right|, \tag{9d}$$

where $k_{DC} > 0$ *is the robust adaptive switching gain,* $0 < \beta < 1$ *is the fractional order of the fractional integrator, and* μ *is a positive constant.*

Proof. Substituting the error dynamics of the DC voltage (7) into the fractional-order sliding manifold (8) yields

$$s_{\text{DC}} = \frac{{}_{t_0}^{C}D_t^{\alpha-1}\left(i_L - i_I^{*}\right)}{C} + \lambda_{\text{DC}}\overline{u}_{\text{DC}}. \tag{10}$$

Considering the fractional-order integral virtual control laws (9a) and (9b) gives

$$s_{\text{DC}} = \frac{{}_{t_0}^{C}D_t^{\alpha-1}\left(i_L - i_{\text{In}}^{*}\right)}{C}. \tag{11}$$

Consider a Lyapunov function$V_{\text{DC}} = 0.5s_{\text{DC}}^2$. Differentiating V_{DC} gives

$$\dot{V}_{\text{DC}} = s_{\text{DC}}\dot{s}_{\text{DC}} = \frac{s_{\text{DC}}\left({}_{t_0}^{C}D_t^{\alpha}i_L - {}_{t_0}^{C}D_t^{\alpha}i_{\text{In}}^{*}\right)}{C}. \tag{12}$$

Substituting the fractional-order integral virtual control law (9c) with its robust adaptive switching gain (9d) into the above yields

$$\begin{aligned} \dot{V}_{\text{DC}} &= \frac{s_{\text{DC}}\left({}_{t_0}^{C}D_t^{\alpha}i_L - k\text{sgn}(s)\right)}{C} \\ &\le -\frac{\left|s_{\text{DC}}\right|\left(k - \left|{}_{t_0}^{C}D_t^{\alpha}i_L\right|\right)}{C} < 0, \end{aligned} \tag{13}$$

which indicates that the DC-link voltage error dynamic (7) will reach to the equilibrium point. On $s_{DC} = 0$, from (8), it can be seen that the system will behave in the identical fashion as

$${}_{t_0}^{C}D_t^{\alpha}\overline{u}_{\text{DC}} + \lambda_{\text{DC}}\overline{u}_{\text{DC}} = 0. \tag{14}$$

Based on Lemma 1, it can be obtained that when $s_{\text{DC}} = 0$, the DC-link voltage error dynamic (7) will converge to its equilibrium points along the fractional-order sliding manifold. This completes the proof. And the block diagram of the control algorithm of DC-link voltage is shown in Figure 5.

Based on equation (4), the following power equation set can be obtained:

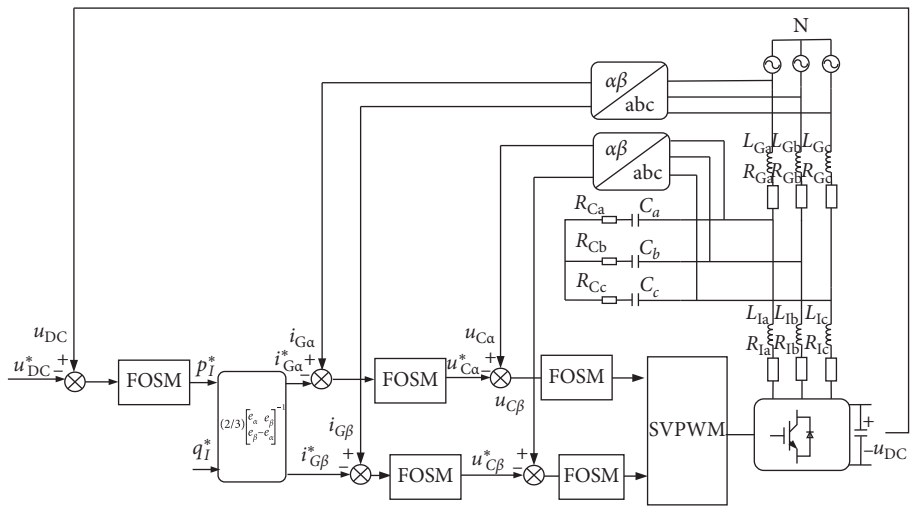

Figure 3: Block diagram of the GSI control system.

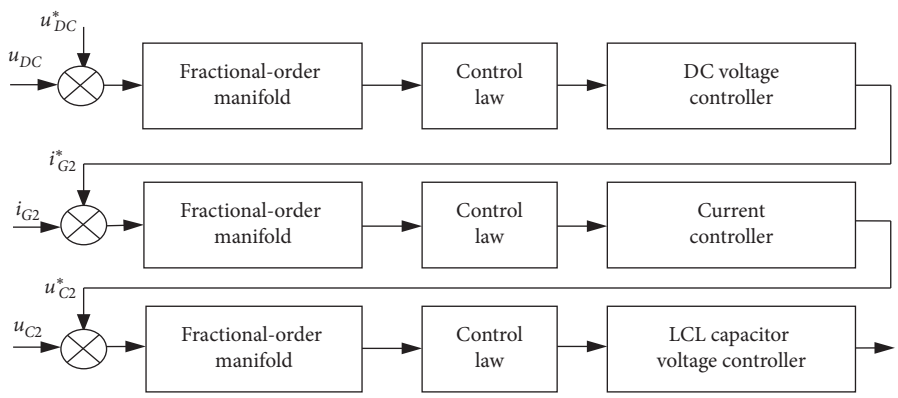

Figure 4: The flow chart of the proposed algorithms.

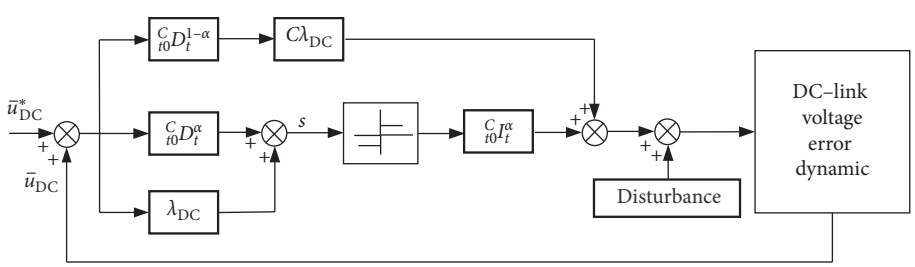

Figure 5: Block diagram of the control algorithm of the DC-link voltage controller.

$$\begin{cases} p_{DC} = p_L - p_I, \\ p_{DC} = C\dot{u}_{DC}u_{DC}, \\ p_L = i_L u_{DC}, \\ p_I = i_I u_{DC}. \end{cases} \tag{15}$$

Due to the complex power $S_I = 1.5(e_\alpha + je_\beta)(i_{G\alpha} - ji_{G\beta}) = p_I - jq_I$, and the references for the instantaneous active and reactive powers satisfy $p^*_I = u_{DC}i^*_I$ and $q^* = 0$, respectively; the references for the output currents can be obtained as follows:

$$\begin{bmatrix} i^*_{G\alpha} \\ i^*_{G\beta} \end{bmatrix} = \frac{2}{3}\begin{bmatrix} e_\alpha & e_\beta \\ -e_\beta & e_\alpha \end{bmatrix}^{-1}\begin{bmatrix} p^*_I \\ q^*_I \end{bmatrix}. \tag{16}$$

3.2. Current Controller. Define the current error as $\bar{i}_{G2} = \mathbf{i}_{G2} - \mathbf{i}^*_{G2}$. Then, current error dynamics can be obtained according to (4) as follows:

$$\dot{\bar{i}}_{G2} = -\mathbf{T}_1\mathbf{L}_G^{-1}\mathbf{R}_G\mathbf{T}_2\mathbf{i}_{G2} - \mathbf{T}_1\mathbf{L}_G^{-1}\mathbf{T}_2\mathbf{e}_2 + \mathbf{T}_1\mathbf{L}_G^{-1}\mathbf{T}_2\mathbf{u}_{C2} + \mathbf{T}_1\boldsymbol{\sigma}_G\mathbf{T}_2\mathbf{u}_{C2} + \mathbf{T}_1\Delta\mathbf{d}_G - \dot{i}_{G2}^{*}. \tag{17}$$

A fractional-order sliding manifold for current error dynamic (17) is chosen as follows:

$$\mathbf{s}_{G2} = {}_{t_0}^{C}D_t^{\alpha}\bar{i}_{G2} + \boldsymbol{\lambda}_{G2}\bar{i}_{G2}, \tag{18}$$

where $0 < \alpha < 1$ is the fractional order, and $\boldsymbol{\lambda}_{G2} = \mathrm{diag}\,(\boldsymbol{\lambda}_{G2\alpha}, \boldsymbol{\lambda}_{G2\beta})$, $\boldsymbol{\lambda}_{G2\alpha}$, $\boldsymbol{\lambda}_{G2\beta} > 0$ are all constants.

Theorem 2. *Along the fractional-order sliding manifold (18), the current error dynamic (17) can be guaranteed to converge to its equilibrium point, if a fractional-order integral virtual control law with its robust adaptive switching gain is designed as follows:*

$$\mathbf{u}_{C2}^{*} = \mathbf{u}_{C2\mathrm{eq}}^{*} + \mathbf{u}_{C2n}^{*}, \tag{19a}$$

$$\mathbf{u}_{C2\mathrm{eq}}^{*} = \left(\mathbf{T}_1\mathbf{L}_G^{-1}\mathbf{T}_2\right)^{-1}\left({}_{t_0}^{C}D_t^{1-\alpha}\left(\boldsymbol{\lambda}_{G2}\bar{i}_{G2}\right) + \mathbf{T}_1\mathbf{L}_G^{-1}\mathbf{R}_G\mathbf{T}_2\mathbf{i}_{G2} + \mathbf{T}_1\mathbf{L}_G^{-1}\mathbf{T}_2\mathbf{e}_2 + \dot{i}_{G2}^{*}\right), \tag{19b}$$

$$\mathbf{u}_{C2n}^{*} = -\left(\mathbf{T}_1\mathbf{L}_G^{-1}\mathbf{T}_2\right)^{-1}{}_{t_0}^{C}I_t^{\alpha}\left(\frac{k_{C2}\mathbf{s}_{G2}}{\|\mathbf{s}_{G2}\|}\right), \tag{19c}$$

$$k_{C2n} = \mu_{C2}\,{}_{t_0}^{C}I_t^{\beta}\|\mathbf{s}_{G2}\|, \tag{19d}$$

where $k_{C2n} > 0$ is the robust adaptive switching gain, $0 < \beta < 1$ is the fractional order of the fractional integrator, and $\mu > 0$ is a constant.

Proof. Substituting the current error dynamic (17) into the fractional-order sliding manifold (18) yields

$$\mathbf{s}_{G2} = {}_{t_0}^{C}D_t^{\alpha-1}\begin{pmatrix} -\mathbf{T}_1\mathbf{L}_G^{-1}\mathbf{R}_G\mathbf{T}_2\mathbf{i}_{G2} - \mathbf{T}_1\mathbf{L}_G^{-1}\mathbf{T}_2\mathbf{e}_2 + \mathbf{T}_1\mathbf{L}_G^{-1}\mathbf{T}_2\mathbf{u}_{C2} \\ +\mathbf{T}_1\boldsymbol{\sigma}_G\mathbf{T}_2\mathbf{u}_{C2} + \mathbf{T}_1\Delta\mathbf{d}_G - \dot{i}_{G2}^{*} \end{pmatrix} + \boldsymbol{\lambda}_{G2}\bar{i}_{G2}. \tag{20}$$

Considering the fractional-order integral virtual control laws (19a) and (19b) gives

$$\mathbf{s}_{G2} = {}_{t_0}^{C}D_t^{\alpha-1}\left(\mathbf{T}_1\mathbf{L}_G^{-1}\mathbf{T}_2\mathbf{u}_{C2n}^{*} + \mathbf{T}_1\boldsymbol{\sigma}_G\mathbf{T}_2\mathbf{u}_{C2}^{*} + \mathbf{T}_1\Delta\mathbf{d}_G\right). \tag{21}$$

Differentiating the above with respect to time t gives

$$\dot{s}_{G2} = {}_{t_0}^{C}D_t^{\alpha}\left(\mathbf{T}_1\mathbf{L}_G^{-1}\mathbf{T}_2\mathbf{u}_{C2n}^{*} + \mathbf{T}_1\boldsymbol{\sigma}_G\mathbf{T}_2\mathbf{u}_{C2}^{*} + \mathbf{T}_1\Delta\mathbf{d}_G\right). \tag{22}$$

Consider a Lyapunov function $V_{G2} = 0.5\mathbf{s}_{G2}^{T}\mathbf{s}_{G2}$. Differentiating V_{G2} gives

$$\dot{V}_{G2} = \mathbf{s}_{G2}^{T}\dot{s}_{G2} = \mathbf{s}_{G2}\,{}_{t_0}^{C}D_t^{\alpha}\left(\mathbf{T}_1\mathbf{L}_G^{-1}\mathbf{T}_2\mathbf{u}_{C2n}^{*} + \mathbf{T}_1\boldsymbol{\sigma}_G\mathbf{T}_2\mathbf{u}_{C2}^{*} + \mathbf{T}_1\Delta\mathbf{d}_G\right). \tag{23}$$

Substituting the fractional-order integral virtual control law (19c) with its robust adaptive switching gain (19d) into the above yields

$$\begin{aligned}\dot{V}_{G2} &\le \mathbf{s}_{G2}\left(-k_{G2}\frac{\mathbf{s}_{G2}}{\|\mathbf{s}_{G2}\|} + {}_{t_0}^{C}D_t^{\alpha}\left(\mathbf{T}_1\boldsymbol{\sigma}_G\mathbf{T}_2\mathbf{u}_{C2}^{*} + \mathbf{T}_1\Delta\mathbf{d}_G\right)\right) \\ &\le -\|\mathbf{s}_{G2}\|\left(k_{G2} - \left\|{}_{t_0}^{C}D_t^{\alpha}\left(\mathbf{T}_1\boldsymbol{\sigma}_G\mathbf{T}_2\mathbf{u}_{C2}^{*} + \mathbf{T}_1\Delta\mathbf{d}_G\right)\right\|\right) < 0,\end{aligned} \tag{24}$$

which means that the error dynamics of the current (17) will reach to zero. On $\mathbf{s}_{G2} = 0$, it can be seen from (18) that the system will behave according to the following equation:

$${}_{t_0}^{C}D_t^{\alpha}\bar{i}_{G2} + \boldsymbol{\lambda}_{G2}\bar{i}_{G2} = 0. \tag{25}$$

Based on Lemma 1, it can be obtained that when $\mathbf{s}_{G2} = 0$, the current error dynamic (26) will converge to its equilibrium points along the fractional-order sliding manifold. This completes the proof.

3.3. Filter Capacitor Voltage Controller. The switching control signal $\mathbf{S}_2$ in the system (4) is designed to force the actual voltage to track its virtual control reference. Define the current error as $\bar{u}_{C2} = \mathbf{u}_{C2} - \mathbf{u}_{C2}^{*}$. Then, filter capacitor voltage error dynamics are as follows:

$$\begin{aligned}\dot{\bar{u}}_{C2} = {} & \mathbf{T}_1\left(\mathbf{C}^{-1} - \mathbf{L}_I^{-1}\mathbf{R}_C\mathbf{R}_I\right)\mathbf{T}_2\mathbf{i}_2 - \mathbf{T}_1\left(\mathbf{C}^{-1} - \mathbf{L}_G^{-1}\mathbf{R}_C\mathbf{R}_G\right)\mathbf{T}_2\mathbf{i}_{G2} \\ & + \mathbf{T}_1\mathbf{L}_G^{-1}\mathbf{R}_C\mathbf{T}_2\mathbf{e}_2 - \mathbf{T}_1\left(\mathbf{L}_I^{-1} + \mathbf{L}_G^{-1}\right)\mathbf{R}_C\mathbf{T}_2\mathbf{u}_{C2} + \mathbf{T}_1\mathbf{L}_G^{-1}\mathbf{R}_C u_{\mathrm{DC}}\mathbf{T}_2\mathbf{S}_2 \\ & + \mathbf{T}_1\boldsymbol{\sigma}_C u_{\mathrm{DC}}\mathbf{T}_2\mathbf{S}_2 + \mathbf{T}_1\boldsymbol{\rho}_C - \dot{u}_{C2}^{*}.\end{aligned} \tag{26}$$

A fractional-order sliding manifold for filter capacitor voltage error dynamic (17) is chosen as

$$\mathbf{s}_{C2} = {}_{t_0}^{C}D_t^{\alpha}\overline{u}_{C2} + \boldsymbol{\lambda}_{C2}\overline{u}_{C2}, \tag{27}$$

where $0 < \alpha < 1$ is the fractional order, and $\boldsymbol{\lambda}_{C2} = \text{diag}\ (\boldsymbol{\lambda}_{C2\alpha}, \boldsymbol{\lambda}_{C2\beta})$, $\boldsymbol{\lambda}_{C2\alpha}$, $\boldsymbol{\lambda}_{C2\beta} > 0$ are all constants.

Theorem 3. *Along the fractional-order sliding manifold (27), the LCL capacitor voltage error dynamics (26) can be guaranteed to converge to its equilibrium point, if a fractional-order integral actual control law with its robust adaptive switching gain is designed as follows:*

$$\mathbf{S}_2 = \mathbf{S}_{2\text{eq}} + \mathbf{S}_{2n}, \tag{28a}$$

$$\begin{aligned}\mathbf{S}_{2\text{eq}} = &\left(u_{\text{DC}}\mathbf{T}_1\mathbf{L}_G^{-1}\mathbf{R}_C\mathbf{T}_2\right)^{-1}\left[-\mathbf{T}_1\left(\mathbf{C}^{-1} - \mathbf{L}_I^{-1}\mathbf{R}_C\mathbf{R}_I\right)\mathbf{T}_2\mathbf{i}_2 - \mathbf{T}_1\mathbf{L}_G^{-1}\mathbf{R}_C\mathbf{T}_2\mathbf{e}_2 + \dot{u}_{C2}^{*}\right.\\ &\left.+\mathbf{T}_1\left(\mathbf{C}^{-1} - \mathbf{L}_G^{-1}\mathbf{R}_C\mathbf{R}_G\right)\mathbf{T}_2\mathbf{i}_{G2} + \mathbf{T}_1\left(\mathbf{L}_I^{-1} + \mathbf{L}_G^{-1}\right)\mathbf{R}_C\mathbf{T}_2\mathbf{u}_{C2} - {}_{t_0}^{C}D_t^{1-\alpha}\boldsymbol{\lambda}_{C2}\overline{u}_{C2}\right],\end{aligned} \tag{28b}$$

$$\mathbf{S}_{2n} = -\left(u_{\text{DC}}\mathbf{T}_1\mathbf{L}_G^{-1}\mathbf{R}_C\mathbf{T}\right)^{-1}{}_{t_0}^{C}I_t^{\alpha}\left(\frac{k_2\mathbf{s}_{C2}}{\|\mathbf{s}_{C2}\|}\right), \tag{28c}$$

$$k_2 = \mu_{2n}{}_{t_0}^{C}I_t^{\beta}\|\mathbf{s}_{C2}\|. \tag{28d}$$

Proof. Substituting the LCL capacitor voltage error dynamic (26) into the fractional-order sliding manifold (27) yields

$$\mathbf{s}_{C2} = {}_{t_0}^{C}D_t^{\alpha-1}\begin{pmatrix}\mathbf{T}_1\left(\mathbf{C}^{-1} - \mathbf{L}_I^{-1}\mathbf{R}_C\mathbf{R}_I\right)\mathbf{T}_2\mathbf{i}_2 - \mathbf{T}_1\left(\mathbf{C}^{-1} - \mathbf{L}_G^{-1}\mathbf{R}_C\mathbf{R}_G\right)\mathbf{T}_2\mathbf{i}_{G2}\\ +\mathbf{T}_1\mathbf{L}_G^{-1}\mathbf{R}_C\mathbf{T}_2\mathbf{e}_2 - \mathbf{T}_1\left(\mathbf{L}_I^{-1} + \mathbf{L}_G^{-1}\right)\mathbf{R}_C\mathbf{T}_2\mathbf{u}_{C2} + \mathbf{T}_1\mathbf{L}_G^{-1}\mathbf{R}_C u_{\text{DC}}\mathbf{T}_2\mathbf{S}_2\,\boldsymbol{\lambda}_{C2}\overline{u}_{C2}\\ +\mathbf{T}_1\boldsymbol{\sigma}_C u_{\text{DC}}\mathbf{T}_2\mathbf{S}_2 + \mathbf{T}_1\boldsymbol{\rho}_C - \dot{u}_{C2}^{*} + {}_{t_0}^{C}D_t^{1-\alpha}\end{pmatrix}. \tag{29}$$

Considering the fractional-order integral virtual control laws (28a) and (28b) gives

$$\mathbf{s}_{C2} = {}_{t_0}^{C}D_t^{\alpha-1}\left(\mathbf{T}_1\mathbf{L}_G^{-1}\mathbf{R}_C u_{\text{DC}}\mathbf{T}_2\mathbf{S}_{2n} + \mathbf{T}_1\boldsymbol{\sigma}_C u_{\text{DC}}\mathbf{T}_2\mathbf{S}_2 + \mathbf{T}_1\boldsymbol{\rho}_C\right). \tag{30}$$

Differentiating the above with respect to time t gives

$$\dot{s}_{C2} = {}_{t_0}^{C}D_t^{\alpha}\left(\mathbf{T}_1\mathbf{L}_G^{-1}\mathbf{R}_C u_{\text{DC}}\mathbf{T}_2\mathbf{S}_{2n} + \mathbf{T}_1\boldsymbol{\sigma}_C u_{\text{DC}}\mathbf{T}_2\mathbf{S}_2 + \mathbf{T}_1\boldsymbol{\rho}_C\right). \tag{31}$$

Consider Lyapunov function $V_{C2} = 0.5\mathbf{s}_{C2}^T\mathbf{s}_{C2}$. According to the fractional-order integral virtual control law (24c) with its robust adaptive switching gain (24d) into the above yields

$$\dot{V}_{C2} = \mathbf{s}_{C2}\dot{s}_{C2} = -\|\mathbf{s}_{C2}\|\left(k_2 - \left\|{}_{t_0}^{C}D_t^{\alpha}\left(\mathbf{T}_1\boldsymbol{\sigma}_C u_{DC}\mathbf{T}_2\mathbf{S}_2 + \mathbf{T}_1\boldsymbol{\rho}_C\right)\right\|\right) < 0, \tag{32}$$

which indicates that the error dynamics of filter capacitor (26) will reach to zero. On $\boldsymbol{s}_{C2} = 0$, it can be seen from (27) that the system will behave in the following identical fashion:

$${}_{t_0}^{C}D_t^{\alpha}\overline{u}_{C2} + \boldsymbol{\lambda}_{C2}\overline{u}_{C2} = 0. \tag{33}$$

Based on Lemma 1, it can be obtained that when $\boldsymbol{s}_{C2} = 0$, the current error dynamics (25) will converge to its equilibrium points along the fractional-order sliding manifold. This completes the proof.

4. Simulations

In order to verify the effectiveness of the proposed method, some simulations are carried out using Matlab. Table 2 provides the parameters of GSI. The parameters of the controllers are as follows: $k = 60$, $k_d = 100$, $\eta = 100$, $\mathbf{C} = \text{diag}\ (80, 80)$, $\mu = \text{diag}\ (3/5, 3/5)$, and $\mathbf{T} = \text{diag}\ (100, 100)$.

The simulations of PI and FOSMC are shown in Figure 6. It can be seen that the DC-link voltage is quickly converged to 700 V and stays around at 700 V under both control strategies. Compared with PI, the proposed FOSMC method can effectively improve the dynamic response of DC-link voltage and reduce the peak value and settling time of DC-link voltage, which enhance the disturbance rejection. From Figures 6(b) and 6(c), the instantaneous active power and reactive power are controlled to converge to their reference value. Therefore, it can be concluded that the control objective has been achieved.

The simulations of the current controller are shown in Figure 7. In Figure 7(a), it can be seen that the current can track the reference quickly and precisely. In Figure 7(b), $u_{c\alpha}^{*}$ and $u_{c\beta}^{*}$ have a high degree of sinusoidal, which means the harmonics barely exist in the voltage. Meanwhile, total harmonic distortion (THD) of the output currents of GSI are shown in Figure 7(c) which is a measurement of the harmonic distortion present. It can be known from Figure 7(c) that THD is extremely closed to zero, which means that the

Table 2: Parameters of GSI.

Parameter	Value (kW)
Rated power	2
DC-link voltage	700
DC-link capacitor	6800
Filter inductor	1.5
Phase resistor	0.4
Phase voltage of the grid	311

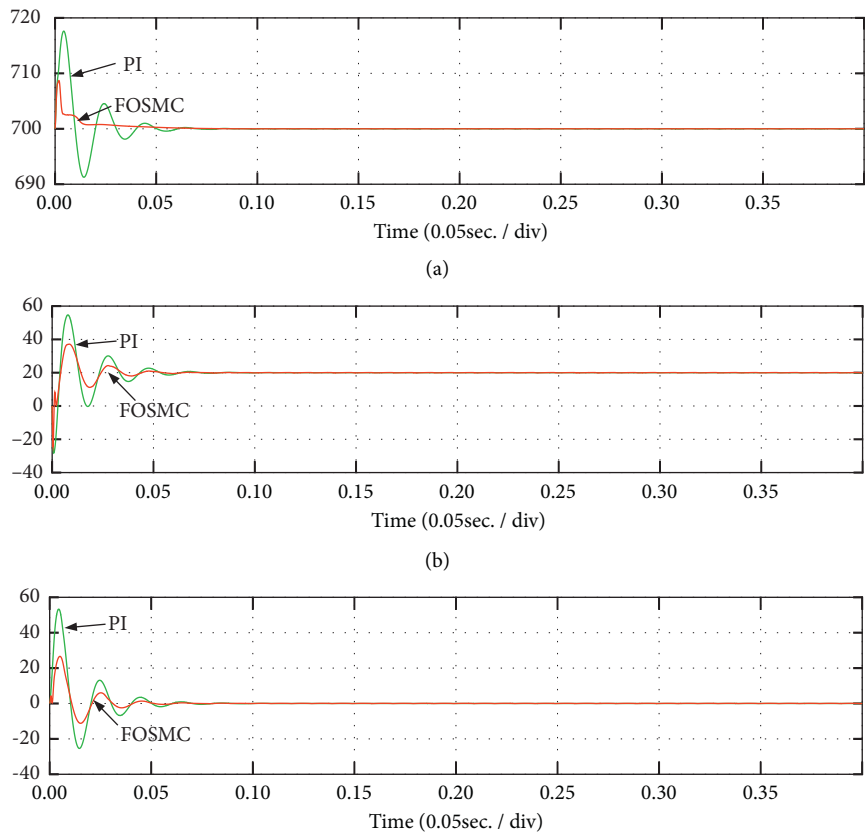

Figure 6: The simulation results of the grid-side converter. (a) u_{DC} (SMC)(V)/u_{DC} (PI)(V), (b) P (SMC)(KW)/P (PI)(KW), and (c) Q (SMC)(KW)/Q (PI)(KW).

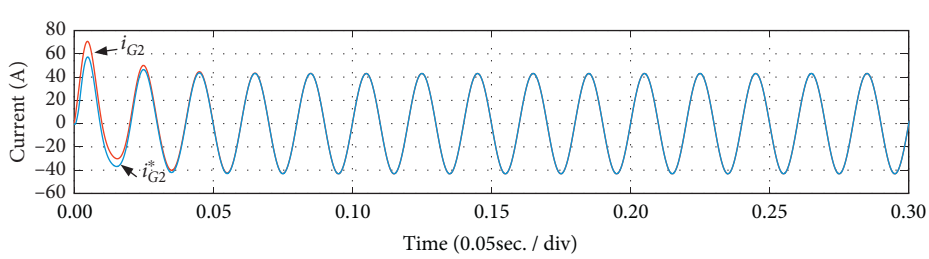

(a)

Figure 7: Continued.

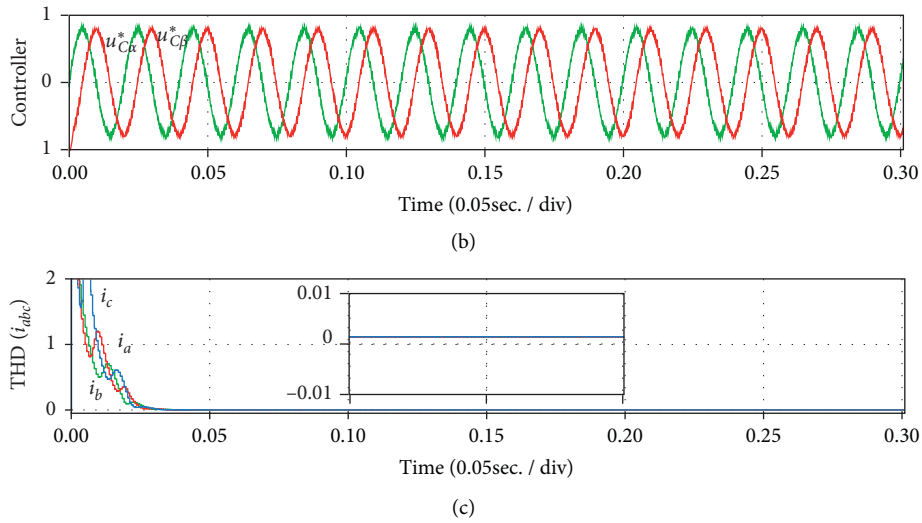

Figure 7: The simulation results of current controller. (a) Current (A), (b) controller, and (c) THD (i_{abc}).

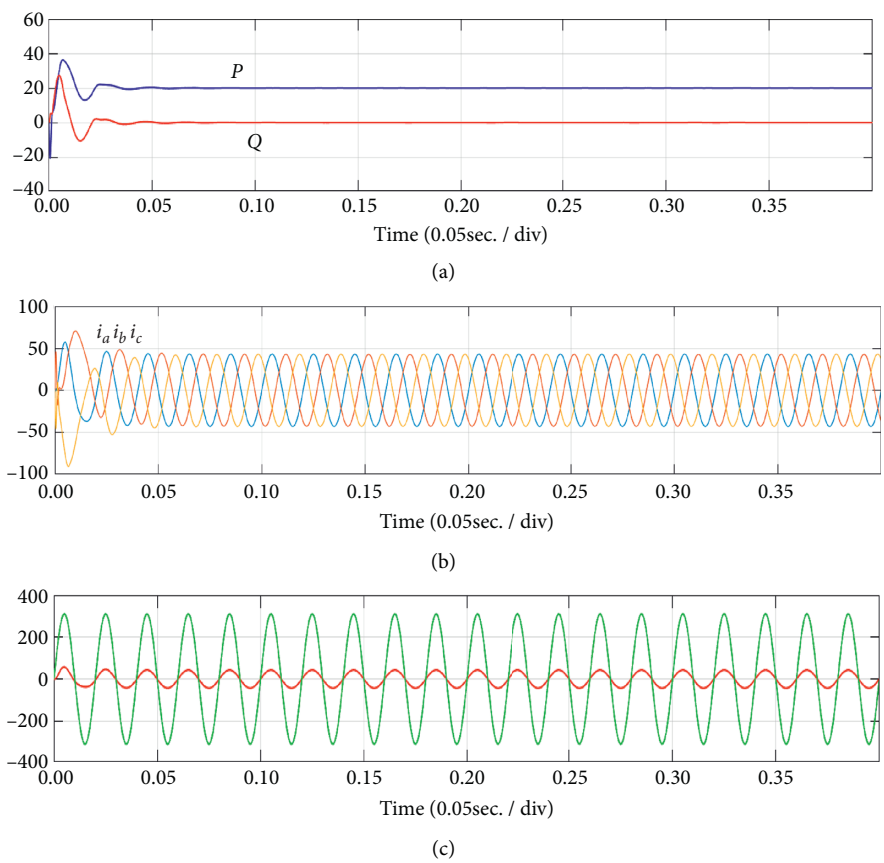

Figure 8: The simulation results for the case where the three filter inductances change their values precisely and quickly. Compared with the traditional SMC, the proposed FOSMC method can eliminate chattering, and the adaptive gain can avoid overestimating the upper boundary of the parameter variations and external disturbance to obtain a better control performance. The simulation results validate the proposed method. (a) P(KW)/Q(KVar), (b) i_{abc} (A), and (c) e_a(A)/i_{abc} (A).

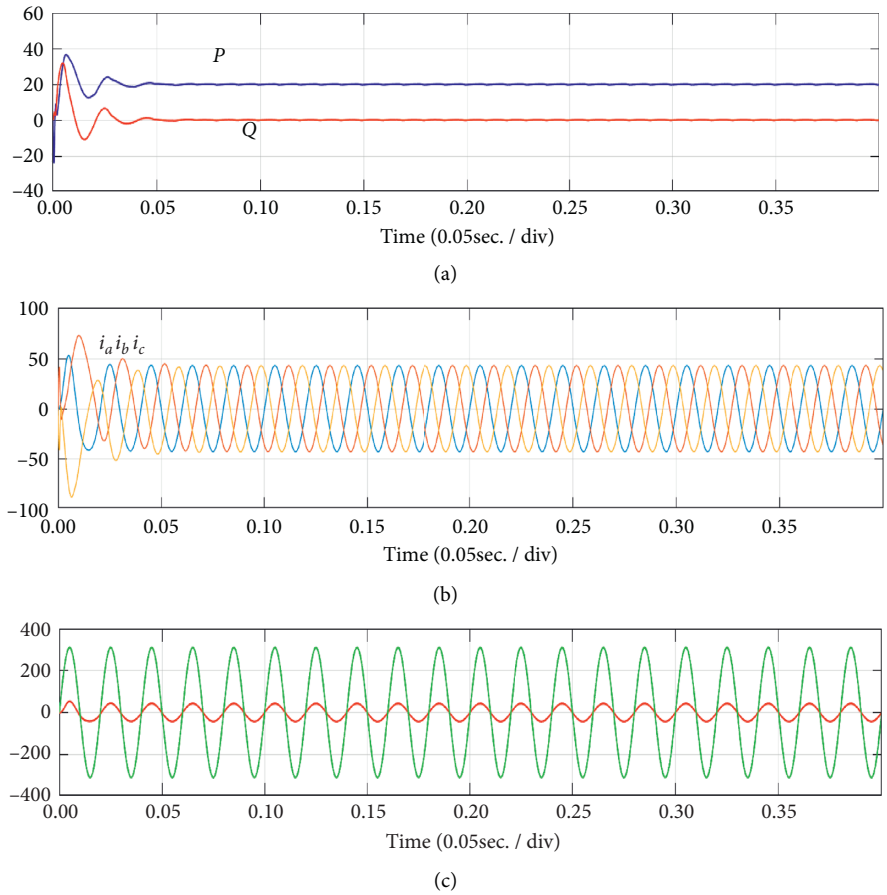

Figure 9: The simulation results for the case where the three resistors change their values. (a) P(KW)/Q(KVar), (b) i_{abc} (A), and (c) e_a(A)/i_{abc} (A).

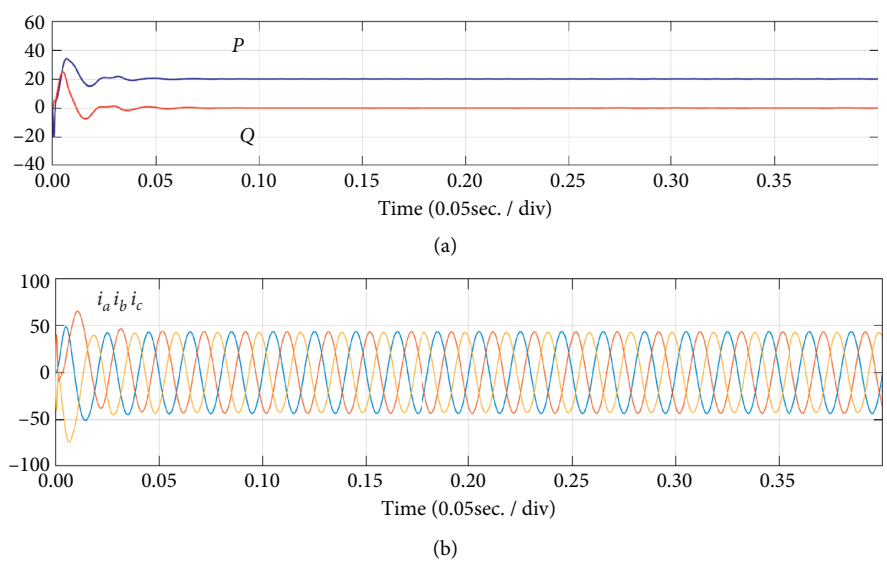

Figure 10: Continued.

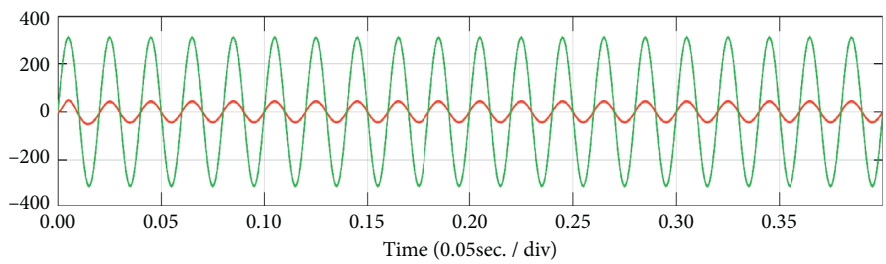

(c)

Figure 10: The simulation results when resistors and inductance are all different. (a) P(KW)/Q(KVar), (b) i_{abc} (A), and (c) e_a(A)/i_{abc} (A).

harmonic in the current is eliminated and the quality of grid energy can be guaranteed.

Figures 8–10 show the simulation results when the filter inductances and resistors are changed. Figure 8 depicts the case that values of filter inductances are changed and the resistors keep unchanged. The filter inductances are changed from 1.5 mH to 2 mH. Figure 9 depicts the case that values of the resistors are changed from 0.4 Ω to 0.6 Ω, and three filter inductances keep unchanged. Figure 10 depicts the case for varying resistors and varying filter inductances. The values of resistors and the filter inductances are changed to 1.5 Ω and 2 mH. It can be seen that the changes are not obvious under FOSMC in the view of parameter change, which means that the proposed method has a strong robustness against the parameter variation. From the simulation results in Figures 8(c)–10(c), it can be concluded that the voltage and current have the same phase angle, which means that the unit power factor can be guaranteed. The basics of fractional calculus are shown in appendix.

5. Conclusions

In this study, a novel fractional-order sliding mode control strategy with robust switching gain is proposed to achieve reliable and high quality of wind-powered microgrid systems. Fractional-order sliding mode controllers generate continuous control signals and regulate the outer DC-link voltage loop and current loop in GSI. Considering the parameters variation and external disturbance, the outer DC-link voltage and inner current can track their references.

Appendix

A. Basics of Fractional Calculus

The theory of fractional-order calculus is closely related to the traditional integral order calculus. Grünwald–Letnikov (GL), Riemann–Liouville (RL), and Caputo definitions, shown as follows, are three most definitions of the fractional-order differentiation used in literature and practical applications.

Definition 1 (see [29]). The αth-order GL fractional derivative for a function $f(t)$: $R^+ \longrightarrow R$ is defined as

$$ {}_{t_0}^{GL}D_t^{\alpha} f(t) = \lim_{h \longrightarrow 0} h^{-\alpha} \sum_{m=0}^{[(t-t_0)/h]} (-1)^m \binom{\alpha}{m} f(t - mh), \tag{A.1} $$

where $\alpha \in R$ is the fractional order, t_0 and t are the limits of the operation, $[\cdot]$ denotes the integer value function, and h is the time increment, and

$$ \binom{\alpha}{m} = \frac{\Gamma(\alpha+1)}{\Gamma(m+1)\Gamma(\alpha-m+1)} = \frac{\alpha!}{m!(\alpha-m)!}, \tag{A.2} $$

where $\Gamma(\cdot)$ is the well-known Euler gamma function.

Definition 2 (see [29]). The αth-order RL fractional derivative for a function $f(t)$: $R^+ \longrightarrow R$ is defined as

$$ {}_{t_0}^{RL}D_t^{-\alpha} f(t) = \frac{1}{\Gamma(u-\alpha)} \frac{\mathrm{d}^u}{\mathrm{d}t^u} \int_{t_0}^{t} \frac{f(\tau)}{(t-\tau)^{\alpha-u+1}} \mathrm{d}\tau, \tag{A.3} $$

where $u - 1 < \alpha \leq u$, $u \in N$.

Definition 3 (see [29]). The αth-order Caputo fractional derivative for a continuous function $f(t)$: $R^+ \longrightarrow R$ is defined as

$$ {}_{t_0}^{C}D_t^{\alpha} f(t) = \frac{1}{\Gamma(u-\alpha)} \int_{t_0}^{t} \frac{f^{(u)}(\tau)}{(t-\tau)^{\alpha-u+1}} d\tau, \tag{A.4} $$

where u is defined in (2). Meanwhile, the αth-order Caputo fractional integration for a function $f(t)$: $R^+ \longrightarrow R$ is defined as

$$ {}_{t_0}^{C}I_t^{\alpha} f(t) = {}_{t_0}^{C}D_t^{-\alpha} f(t) = \frac{1}{\Gamma(\alpha)} \int_{t_0}^{t} \frac{f(\tau)}{(t-\tau)^{1-\alpha}} \mathrm{d}\tau. \tag{A.5} $$

Data Availability

The data used in the simulations are carried out using Matlab-Simulink and are available from the corresponding author upon request.

Conflicts of Interest

The authors declare that they have no conflicts of interest.

Acknowledgments

This work was supported in part by the Postdoctoral Science Foundation of Heilongjiang Province of China (2901051432), the National Natural Science Foundation of China under Grant (51907042 and 62003086), the Fundamental Research Funds for the Central Universities (2242020R20015), and in part by China Postdoctoral Science Foundation funded project (2020M671294).

References

[1] X. Lu, J. Lai, and G. P. Liu, "Master-slave cooperation for multi-DC-MGs via variable cyber networks," *IEEE Transactions on Cybernetics, Early Access*, 2020.

[2] J. Lai, X. Lu, Z. Dong, and S. Cheng, "Resilient distributed multiagent control for AC microgrid networks subject to disturbances," *IEEE Transactions on Systems, Man, and Cybernetics: Systems*, pp. 1–11, 2021.

[3] J. Dannehl, C. Wessels, and F. W. Fuchs, "Limitations of voltage-oriented PI current control of grid-connected PWM rectifiers with LCL filters," *IEEE Transactions on Industrial Electronics*, vol. 56, no. 2, pp. 380–388, 2009.

[4] F. Blaabjerg, R. Teodorescu, M. Liserre, and A. V. Timbus, "Overview of control and grid synchronization for distributed power generation systems," *IEEE Transactions on Industrial Electronics*, vol. 53, no. 5, pp. 1398–1409, 2006.

[5] M. Liserre, R. Teodorescu, and F. Blaabjerg, "Multiple harmonics control for three-phase grid converter systems with the use of PI-RES current controller in a rotating frame," *IEEE Transactions on Power Electronics*, vol. 21, no. 3, pp. 836–841, 2006.

[6] G. Shen, X. Zhu, J. Zhang, and D. Xu, "A new feedback method for PR current control of LCL-filter-based grid-connected inverter," *IEEE Transactions on Industrial Electronics*, vol. 57, no. 6, pp. 2033–2041, 2010.

[7] Y. Feng, F. Han, and X. Yu, "Chattering free full-order sliding-mode control," *Automatica*, vol. 50, no. 4, pp. 1310–1314, 2014.

[8] Y. Feng, X. Yu, and Z. Man, "Non-singular terminal sliding mode control of rigid manipulators," *Automatica*, vol. 38, no. 12, pp. 2159–2167, 2002.

[9] X. Zheng, Y. Feng, F. Han, and X. Yu, "Integral-type terminal sliding-mode control for grid-side converter in wind energy conversion systems," *IEEE Transactions on Industrial Electronics*, vol. 66, no. 5, pp. 3702–3711, 2019.

[10] M. Zhou, Y. Feng, and C. Xue, "Deep convolutional neural network based fractional-order terminal sliding-mode control for robotic manipulators," *Neurocomputing*, vol. 416, pp. 143–151, 2020.

[11] B. Sun, Y. Cao, Z. Guo et al., "Sliding-mode stabilization of memristive neural networks with leakage delays and control disturbance," *IEEE Transactions on Neural Networks and Learning Systems*, 2019.

[12] Y. Wang, Y. Cao, Z. Guo, T. Huang, and S. Wen, "Event-based sliding-mode synchronization of delayed memristive neural networks via continuous/periodic sampling algorithm," *Applied Mathematics and Computation*, vol. 383, Article ID 125379, 2020.

[13] R. Guzman, L. G. de Vicuna, J. Morales, M. Castilla, and J. Matas, "Sliding-mode control for a three-phase unity power factor rectifier operating at fixed switching frequency," *IEEE Transactions on Power Electronics*, vol. 31, no. 1, pp. 758–769, 2016.

[14] S. M. Mozayan, M. Saad, H. Vahedi, H. Fortin-Blanchette, and M. Soltani, "Sliding mode control of PMSG wind turbine based on enhanced exponential reaching law," *IEEE Transactions on Industrial Electronics*, vol. 63, no. 10, pp. 6148–6159, 2016.

[15] J. Liu, F. Zhou, and C. Zhao, "A PI-type sliding mode controller design for PMSG-based wind turbine," *Complexity*, vol. 2019, Article ID 2538206, 12 pages, 2019.

[16] R. Errouissi and A. Al-Durra, "A novel PI-type sliding surface for PMSG-based wind turbine with improved transient performance," *IEEE Transactions on Energy Conversion*, vol. 33, no. 2, pp. 834–844, 2018.

[17] M. Nasiri, S. Mobayen, and Q. Zhu, "Super-twisting sliding mode control for gearless PMSG-based wind turbine," *Complexity*, vol. 2019, Article ID 6141607, 15 pages, 2019.

[18] J. Hu, H. Nian, B. Hu, Y. He, and Z. Q. Zhu, "Direct active and reactive power regulation of DFIG using sliding-mode control approach," *IEEE Transactions on Energy Conversion*, vol. 25, no. 4, pp. 1028–1039, 2010.

[19] T. D. Do, "Disturbance observer-based fuzzy SMC of WECSs without wind speed measurement," *IEEE Access*, vol. 5, pp. 147–155, 2017.

[20] Y. Wang, L. Gu, Y. Xu, and X. Cao, "Practical tracking control of robot manipulators with continuous fractional-order nonsingular terminal sliding mode," *IEEE Transactions on Industrial Electronics*, vol. 63, no. 10, pp. 6194–6204, 2016.

[21] Y. Tang, X. Zhang, D. Zhang, G. Zhao, and X. Guan, "Fractional order sliding mode controller design for antilock braking systems," *Neurocomputing*, vol. 111, pp. 122–130, 2013.

[22] H. Delavari, P. Lanusse, and J. Sabatier, "Fractional order controller design for a flexible link manipulator robot," *Asian Journal of Control*, vol. 15, no. 3, pp. 783–795, 2013.

[23] L. Gao, Z. Wang, K. Zhou, W. Zhu, Z. Wu, and T. Ma, "Modified sliding mode synchronization of typical three-dimensional fractional-order chaotic systems," *Neurocomputing*, vol. 166, pp. 53–58, 2015.

[24] M. P. Aghababa, "Design of a chatter-free terminal sliding mode controller for nonlinear fractional-order dynamical systems," *International Journal of Control*, vol. 86, no. 10, pp. 1744–1756, 2013.

[25] Y. Wang, G. Luo, L. Gu, and X. Li, "Fractional-order non-singular terminal sliding mode control of hydraulic manipulators using time delay estimation," *Journal of Vibration and Control*, vol. 22, no. 19, pp. 3998–4011, 2016.

[26] H. Delavari, R. Ghaderi, A. Ranjbar, and S. Momani, "Fuzzy fractional order sliding mode controller for nonlinear systems," *Communications in Nonlinear Science and Numerical Simulation*, vol. 15, no. 4, pp. 963–978, 2010.

[27] D. Nojavanzadeh and M. Badamchizadeh, "Adaptive fractional-order non-singular fast terminal sliding mode control for robot manipulators," *IET Control Theory & Applications*, vol. 10, no. 13, pp. 1565–1572, 2016.

[28] Y. Li, Y. Chen, and I. Podlubny, "Mittag-Leffler stability of fractional order nonlinear dynamic systems," *Automatica*, vol. 45, no. 8, pp. 1965–1969, 2009.

[29] I. Podlubny, *Fractional Differential Equations*, Academic Press, Cambridge, MA, USA, 1999.

Hindawi
Complexity
Volume 2021, Article ID 6695688, 11 pages
https://doi.org/10.1155/2021/6695688

Research Article

Design and Collaborative Operation of Multimobile Inspection Robots in Smart Microgrids

Nankai Chen and Yaonan Wang

College of Electrical and Information Engineering, Hunan University, Changsha 410082, China

Correspondence should be addressed to Nankai Chen; chennk@hnu.edu.cn

Received 19 November 2020; Revised 21 February 2021; Accepted 8 March 2021; Published 17 March 2021

Academic Editor: Xin Li

This paper investigates the substation inspection problems of multimobile robots for large power stations in smart microgrids. Most multirobot inspection robots generally face the challenge of path planning, while the current widely used biological excitation neural network (BENN) methods often have the defect of the neuronal active field near boundaries and obstacles. To end this, we propose an improved biological excitation neural network (IBENN) method for path planning based on a detailed architecture and ontology framework, through which the single-point inspection, multipoint inspection, and full-area inspection tasks of substations in smart microgrids can be well completed. Simulation results show that the designed IBENN-based multirobot collaboration inspection (MRCI) system can effectively shorten the path as well as the number of turns and then show better performance than most existing results when implementing various substation inspection tasks.

1. Introduction

Safe and stable supply of electricity is of great significance to ensure the sound and rapid development of the economy and society, whereas the grid and substation generally suffer from long-term exposure to the wild during the transmission and transformation process. It is necessary to detect and maintain transmission lines and substations regularly to prevent large-scale grid accidents, among which substation equipment maintenance is an important mean to ensure safe operation of smart microgrids, improve the economy of power grid operation, and provide good services [1–4].

Most of the current maintenance work still relies on manual operation, which has the disadvantage of dangerous working environment and high maintenance cost. Moreover, the factors of high intensity, low efficiency, and cannot work around the clock are also the main difficulties that manual inspection must face. In view of this, intelligent automation technology has gradually replaced manpower to become a new trend of inspection work due to the rapid technology development. By simulating operation behavior, robots have been used in the detection process of smart grids, which cannot only reduce work risks and human consumption but also provide accurate data detection and data collection. However, most inspection robots used in power stations are manually remote-controlled rather than autonomously operated and are used alone, lacking cooperation between multiple robots.

Inspection robots often carry out comprehensive and detailed inspection regularly for the equipment in the substation of smart microgrids to achieve all-weather, nodead, and efficient inspection work. Therefore, the multirobot intelligent inspection system should possess the functions of (i) autonomic path planning (planning a safe and optimal path traverses all task points with known information and information shared by other robots); (ii) environmental perception (sensing task points, obstacles, etc.); (iii) fault detection (it should be able to collect data through visible-light camera, infrared thermal imager, ultrasonic device, and other devices and transmit the acquired information to the background through the communication module for observation and analysis); (iv) remote operation

(the staff can realize the continuous monitoring of the specific fault after the abnormal situation is found by the remote operation robot).

Inspection robots have been researched for more than thirty years. The substation inspection robot was first developed by Mitsubishi Corporation of Japan, Quek North Hydro Corporation of Canada, and University of São Paulo of Brazil [5–7]. A teleoperated robotic platform called LineScout Technology was introduced in [8], which has the capability to clear most obstacles that were found on the grid; however, the main functions and application modules were limited to the specified platform. Following this line, a method of detecting power grid lines by using the unmanned aerial vehicle (UAV) in the complex environment was presented in [9–11]. Furthermore, the inspection operations of flying robots and climbing robots for power stations have also been made preliminary attempts [12], although mobile robots were more widely used in the field of intelligent inspection of power stations of smart microgrids, no matter wheel-type or crawler-type robots.The above methods were based on single robots, which have become increasingly unable to meet the demand requirement of operation with the increase of the number of tasks and operation difficulty. Multirobot collaboration inspection (MRCI) has become an important research direction in robot research because of the natural coordination advantages; however, it is more complex and difficult than single robots in terms of scheduling and control, especially for the challenging path planning issues, which is the focus of this article. Some research achievements have been made in path planning of multiple robots. Yu and LaValle [13] investigated on optimal multirobot path planning over four minimization objectives by combining the ILP model algorithm with the heuristic algorithm. Their approach could achieve good levels of efficiency. Kelin and Pratihar [14] integrated the genetic algorithm with the A^* algorithm to design an approach used to plan the paths of multiple robots. Pradhan et al. [15] researched the problem of multiple robots moving towards individual goals within a common workspace, whereas the motion of every individual robot is deduced by a novel Particle Swarm Optimization-tuned Feed-Forward Neural Network. Luo et al. [16] proposed a neural dynamics approach for complete area coverage navigation by multiple robots and achieved high computational efficiency. Woosley and Dasgupta [17] proposed an abstraction that models the uncertainty in the paths and a Markov decision process-based algorithm that selects paths for the multirobots to find the task ordering that could reduce the overall distance. In the study by Rogers et al. [18], they also developed an approach, where the multiple robots were guided in their decision to select a location by a utility function that combines Gaussian process-based distributions for information entropy and communication signal strength. In a study performed by Imeson and Smith [19], a framework for solving multirobot motion planning problems with complex constraints had been introduced. They also proposed an algorithm that leverages recent advances in Satisfiability Modulo Theory to combine state-of-the-art SAT and TSP solvers. Ayari and Bouamama [20] proposed a new dynamic distributed particle swarm optimization algorithm for trajectory path planning of multiple robots in order to find the collision-free optimal path for each robot in the environment. More recently, some heuristic intelligent algorithms were adopted for path planning of the MRCI system, including the path conflict-based search algorithm [21] and the probability window-based multiobjective particle swarm optimization algorithm [22], to name just a few. Nevertheless, autonomous navigation is still one of the most challenging abilities for mobile robots.

Robot navigation consists of four parts: perception, positioning, decision-making, and execution, i.e., all robots must have the ability to sense the surrounding environment through sensors and determine its own position, then work out the motion strategy, and finally control the motor output to achieve the desired trajectory [23]. Several typical robot navigation methods include railway track, magnetic navigation, and pattern recognition. Since the railway track navigation method lacks of flexibility and needs hard work for the orbit construction [24], the magnetic navigation was introduced in [25, 26] considering the substation environment adaptability and cost, where the RFID tag information (detected by the RFID reader) is uploaded to the control system via the communication port to achieve the positioning of the inspection robot parking or turning movements. The pattern recognition-based navigation method employs noncontact sensors such as cameras and lidars to identify the road and, in turn, determines the robot's forehead posture, the current road, and the next location to be inspected. However, it requires a large amount of calculation and has high uncertainty [27].

As the substation environment is relatively fixed, the static map of the whole substation can be planned offline. In addition, since the substation studied in this paper is an outdoor environment, GPS navigation which has the advantages of high positioning accuracy, and a simple structure is adopted after comprehensive consideration of the mobile robot's path flexibility and comprehensive cost. Based on this, this paper mainly studies the multirobot autonomous navigation problem in power stations of smart microgrids, and multimobile robots are used to complete the collaborative inspection operation in the outdoor large-scale substation. In the following, the inspection tasks are divided into three categories: single-point inspection, multipoint inspection, and all-area inspection. We will design different MRCI algorithms to complete different inspection tasks efficiently.

The rest of the parts are organized as follows. Section 2 formulates the multirobot collaborative inspection problem, and the main IBENN-based navigation method is proposed in Section 3. Section 4 shows the implementation process and verifies the effectiveness of the established IBENN-based MRCI system in three different inspection tasks, and the paper is concluded in Section 5.

2. Problem Formulation and Modeling

We first establish the intelligent inspection robot system modeling in Subsection A and introduce three important inspection tasks and the commonly used BENN method, respectively, in Subsections B and C.

2.1. Intelligent Inspection Robot System Modeling. The system is divided into two parts: remote control platform and robot body, as shown in Figure 1. The remote console is composed of a host PC and a database, which realizes the functions of information storage, status display, overall planning, and centralized control. The remote control platform controls the inspection robot through a 2.4 G wireless communication module, and the inspection robot sends the videos and images of the inspection operation to the remote control platform through wireless Ethernet. The video capture card is connected to the on-board PC through the PCIE bus, which is used to collect the images of visible-light camera, infrared thermal imager, and the front camera of the mechanical arm. The motor driver is connected to the on-board PC via the USB-CAN transfer card. Auxiliary light source system, ultrasonic ranging module, differential GPS receiving module, and speed measurement block are connected to the industrial control computer through the RS485 bus. The robot is powered by the lithium battery, and each robot realizes data sharing through the wireless communication module.

The substation inspection robot carries a visible-light camera and an infrared thermograph which is used to detect invaders and equipments' fault point, respectively. The host PC plays a supervisory role, such as reading the status from each subsystem, recognizing the equipments from the thermal image, planning the inspection path, and displaying the 3D map. The on-board PC controls the behaviors of the robots, such as movement, obstacle avoidance, and positioning. The associated multirobot collaborative system adopts a hybrid layout, as shown in Figure 2. The host PC is responsible for computing, planning, and scheduling tasks. Information could be shared between the mobile robots over a wireless network.

2.2. Task Classification. We introduce three important inspection tasks here, which will be realized in Section 4 based on the proposed control methods designed in Section 3.

2.2.1. Single-Point Inspection. There are some important areas or fault-prone areas that need to be monitored in large substations of smart microgrids. For these areas, the inspection robot sometimes needs to carry out a single-point inspection. In this situation, the multirobot system assigns the task to a single robot according to the location of the inspection point, the location of each robot, and its ability value and then converts the problem into the path planning problem of the single robot in the known environment.

2.2.2. Multipoint Inspection. In real applications, there are generally more than one important or fault-prone areas that need to be inspected simultaneously. In this situation, the inspection task can be assigned to several robots according to the position of the task points; then, the reasonable paths are designed for each robot to complete the inspection task.

2.2.3. All-Area Inspection. If the entire equipment needs to be inspected, then the robot should move in the whole substation. In this situation, the basic process of multirobot inspection in a known environment includes the following: (a) grouping of multimobile robots in pairs; (b) design the opposite heuristic algorithm for each group of robots; (c) start the inspection, and when it falls into the dead zone, choose the IBENN method to jump out; and, (d) determine whether the entire area has been inspected.

In practical applications, no matter what kind of inspection task, the multimobile robot system needs to decompose and allocate tasks first; then, each robot separately formulates a reasonable inspection path. The commonly used path planning methods mainly include artificial potential field method, A-star algorithm, and fuzzy logic, which, however, have certain defects for different practical problems [28]. In order to accomplish various kinds of inspection tasks, the widely used BENN method will be introduced in the next part, and the IBENN algorithm will be proposed in Section 3.

2.3. Biological Excitation Neural Network (BENN) Method. In the bioexcitation neural network method, the motion space of a mobile robot can be represented by a topological state space composed of a neural network, and the activity value of neurons represents environmental information. The activity values of all neurons are generally initialized to 0, while the changes in the activity values of each neuron are described by the following shunting equation [29, 30]:

$$\frac{\mathrm{d}x_i}{\mathrm{d}t} = -Ax_i + (B - x_i)\left([I_i]^+ + \sum_{j=1}^{k} w_{ij}[x_j]^+ \right) - (D + x_i)[I_i]^-, \tag{1}$$

where x_i is the neural activity of the ith neural, parameters A, B, and D are nonnegative constants representing the passive decay rate, the upper and lower bounds of the neural activity, respectively, k is the number of neurons in the neighborhood, w_{ij} and x_j represent the connection weight and activity of neurons in the neighborhood, respectively, E is a normal number much larger than B, and I_i is the ith external input with the following form:

$$I_i = \begin{cases} E, & \text{target;} \\ -E, & \text{obstacle;} \\ 0, & \text{other.} \end{cases} \tag{2}$$

Excitation signal $S_i^e = [I_i]^+ + \sum_{j=1}^{k} w_{ij}[x_j]^+$, and input inhibition $S_i^i = [I_i]^-$. The nonlinear threshold function $[a]^+$ is defined as $[a]^+ = \max(a, 0)$ and $[a]^- = \max(-a, 0)$. Let d_{ij} is the Euclidean distance between neurons, $w_{ij} = f(d_{ij})$, and $f(a) = (u_0/a)$, u_0 is a positive constant. The robot starts from the starting point to the next position q_n determined by the following formula [31, 32]:

$$q_n \Leftarrow x_{q_n} = \max\left(x_j, j = 1, 2, 3, \ldots, k\right). \tag{3}$$

This method ensures that the positive neuronal activity value can spread outwards and affect the whole state space,

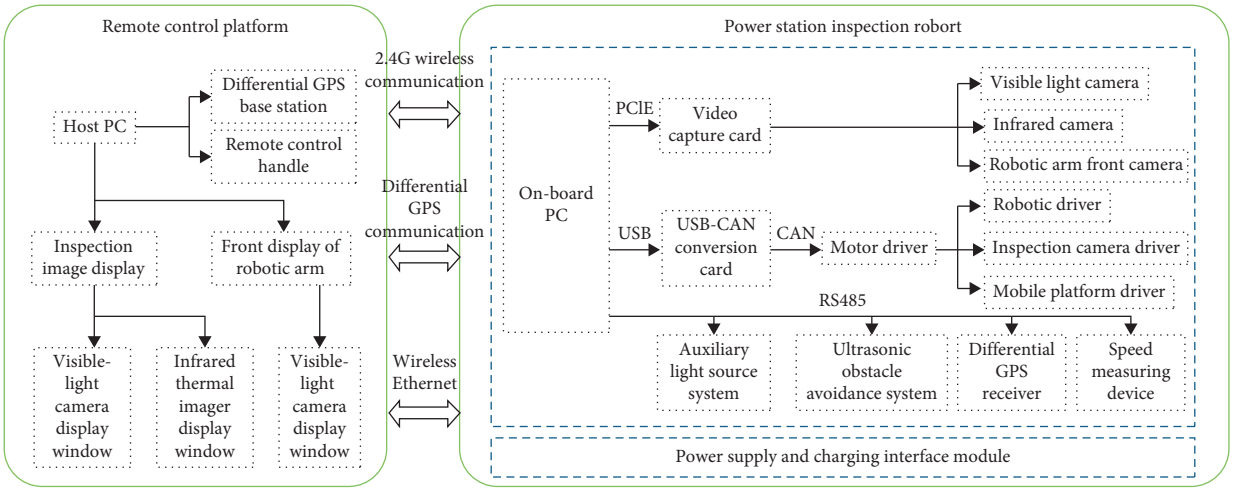

Figure 1: Single robot system architecture in power stations of smart microgrids.

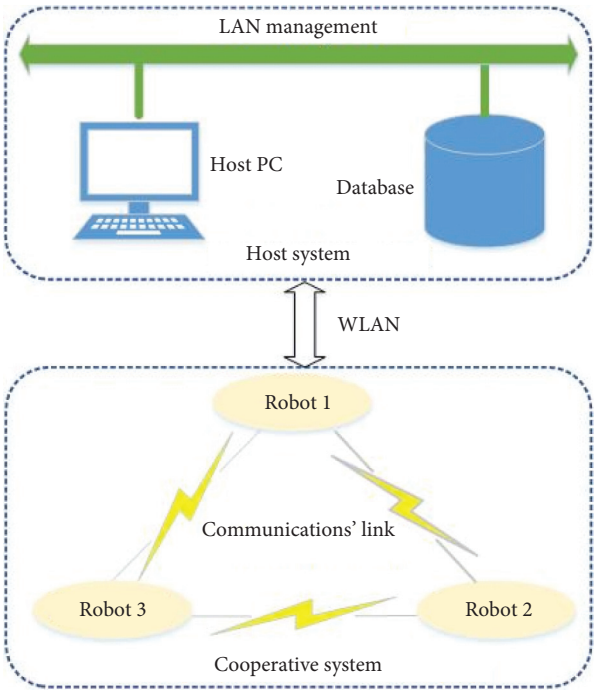

Figure 2: Multirobot system architecture in power stations of smart microgrids.

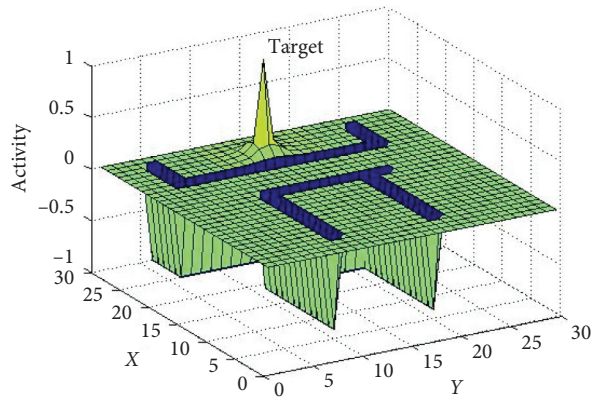

Figure 3: Biological excitation neuronal active field of the BENN method.

while the negative neuronal activity value can only act locally. The neuronal activity values of the target point and the obstacle are, respectively, at the crest and trough of the wave, as shown in Figure 3, so the target point can attract the robot to move towards it, while the obstacle can only repel the robot locally. After the robot reaches the next location from the present location, the next location becomes a new present location unless the present point is the target point. If the found next location is the same as the present location, the robot stays there without any movement.

Although this method can solve the problem of robot path planning, it still has some problems such as nonoptimal path, wrong path judgment, and easy to fall into the dead zone. To end this, an improved bioexcitation neural network algorithm is designed next, which will be applied for the multirobot to complete various types of smart grid inspection tasks.

3. Improved Biological Excitation Neural Network (IBENN) Method

When calculating the neuron activity value near the boundary, the traditional BENN method regards the boundary as an obstacle, making it relatively low relative to the surrounding nonboundary neuron activity value. As a result, the best paths are often overlooked, as shown in Figure 4. As seen, it is better to choose the path along the left boundary in Figure 4(a), and the optimal path is between the two obstacles in Figure 4(b). Moreover, the original method only considers the activity value of surrounding neurons when choosing the next path point, which ignores the robot's steering in the form process. However, robot steering requires deceleration, steering, and acceleration, which greatly increase the power consumption and travel time of the robot.

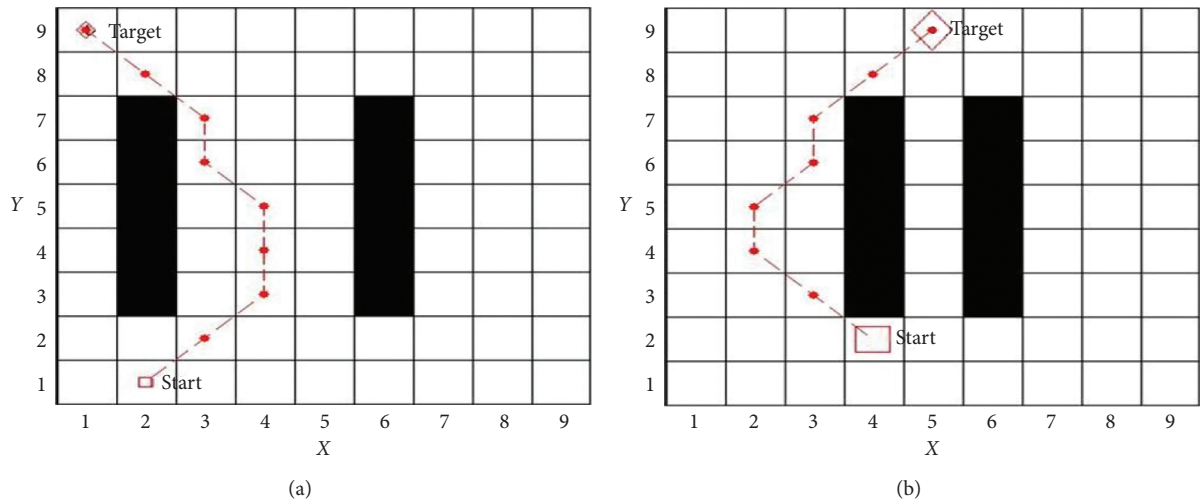

Figure 4: Unreasonable path planning under traditional methods. (a) Path along the boundary. (b) Obstacle intermediate path.

In order to reduce the power consumption of the robot and to smooth the path of the robot, the following path decision method is adopted:

$$q_n \Leftarrow x_{q_n} = \max\left(x_j + c y_j, j = 1, 2, 3, \ldots, k\right), \tag{4}$$

where x_i is the active value at the current position, c is a positive constant, $y_j = 1 - \Delta\theta_j \pi$ is a monotonically increasing function of the moving direction difference between the current to the next robot, and $\Delta\theta_j$ is the absolute angle at which the robot moves from the current position to the next position, e.g., $\Delta\theta_j = 0$ (or $\Delta\theta_j = \pi$) when the robot moves in a straight line (or turns around). Denote the coordinates of the current position $q_c = (x_{q_c}, y_{q_c})$ and the previous position $q_p = (x_{q_p}, y_{q_p})$, then

$$\begin{aligned}\Delta\theta_j = \left|\theta_j - \theta_c\right| &= \arctan\left(y_{q_j} - y_{q_c}, x_{q_j} - x_{q_c}\right) \\ &\quad - \arctan\left(y_{q_c} - y_{q_p}, x_{q_c} - x_{q_p}\right).\end{aligned} \tag{5}$$

The path decision method takes into account the factors of steering and selection of appropriate c, which represents the weight of steering in the path decision, only then a smooth path can be planned. In order to overcome the drawbacks of ignoring the boundary optimal path as well as unreasonable path selection, we propose the following improvement strategies:

Strategy (i). Map extension, i.e., extend the activity range of robot virtual neurons

Strategy (ii). Activity increasing, i.e., increase the activity of neurons near the obstacle and boundary

Strategy (iii). Node deletion, i.e., delete the redundant nodes that do not hinder the passage of robots

The boundary neurons of the original map are extended outward of one circle, respectively. These areas are assumed to be virtual reachable (not treated as obstacles) with the positive activity value and can also spread activity around during the initialization process, but are ignored when choosing the actual path. The main purpose of Strategies (i) and (ii) is to improve the activity value of the original map boundary neurons, which can be considered as a boundary protection for these neurons. In addition, if the robot can bypass the next adjacent node from a certain node without colliding with an obstacle in a path, the deletion of this node can effectively shorten the total length of the path, thus Strategy (iii) can reduce the robot's power consumption and improve work efficiency. To realize these improvements, the following Assumption and Definition are given.

Assumption 1. Neurons outside the boundaries of the original map are virtual nonobstacles, which also have the function of spreading activity values, and their activity values are the average activity values of nonobstacle points in the neighborhood.

Definition 1. If a robot is on a nine-square grid map-centered, the top and bottom, left and right, front left and back right, and front right and back left are, respectively, considered as four sets of symmetrical coordinates. If any pair of symmetrical coordinates are obstacles, the robot is said to be between the obstacles.

If the robot is between the obstacles, the excitation input of the neuron can be calculated by

$$S_i^e = \left[I_i\right]^+ + \frac{n \sum_{j=1}^{k} w_{ij} \left[x_j\right]^+}{n_{\text{pos}}}. \tag{6}$$

When the neuron is not located between the obstacles, the excitation input of the neuron can be calculated by

$$S_i^e = \left[I_i\right]^+ + \frac{\left(n - n_{\text{neg}}\right) \sum_{j=1}^{k} w_{ij} \left[x_j\right]^+}{n_{\text{pos}}}, \tag{7}$$

where n, n_{pos}, and n_{neg} represent the numbers of neighborhood neurons, nonobstacles, and obstacles, respectively. Let $S_i^i = \left[I_i\right]^-$, then system (1) can be rewritten as

$$\frac{dx_i}{dt} = -Ax_i + (B - x_i)S_i^e - (D + x_i)S_i^i. \quad (8)$$

Hence, Strategies (i) and (ii) are used to increase the activity value of neurons near the boundaries or obstacles. In practical application, one of these two strategies can be selected and used together with Strategy (iii) to achieve better path planning.

Figure 5 shows the comparison experiment using Strategies (i) and (iii) with model parameters $A = 10$, $B = D = 1$, $E = 100$, $k = 8$, and $c = 1$. The relevant data comparison is shown in Table 1. It can be seen from Figure 5 and Table 1 that the path length has been reduced from 10.07 to 8.41, and the times of turns have been changed from 4 to 1. Thus, the proposed strategies have obvious improvement effects.

In order to verify the superiority of Strategies (ii) and (iii), the simulation environment is set as a complex maze, and model parameters are also set as $A = 10$, $B = D = 1$, $E = 100$, $k = 8$, and $c = 1$. The initial position of the robot is $(6, 3)$, and the target position is $(1, 30)$. The traditional BENN method, A-star algorithm, and the proposed IBENN method are compared, as shown in Figures 6 and 7. As seen, the proposed IBENN method cannot only solve the problem of path misjudgment but also reduce the path transition, smooth the path, and improve the path quality. Three index comparisons of path length, turn times, and total rotation angle are concluded in Table 2. It can be seen that, compared with the original BENN method, the path length, path turns, and total rotation angle of the proposed IBENN method are reduced by 6.12%, 41.2%, and 64.3%, respectively. Compared with the A-star algorithm, the number of turns and the total rotation angle can be reduced by 16.7% and 16.8%, respectively, under the condition that the path length is unchanged. It concludes that the improved IBENN method shows better performance in terms of path quality and path smoothness than the other methods.

4. Multirobot Cooperative Inspection (MRCI) System

In this section, we will implement the proposed IBENN method to the MRCI system and complete the previously established three inspection tasks.

4.1. Single-Point Inspection. Assume that there are n isomorphic inspection robots with different initial positions and m areas that need to be monitored in a substation of smart microgrids, and one of the areas needs to be continuously monitored at a certain moment. In this situation, the system needs to schedule a robot to complete the task following the principle of minimum cost or maximum benefit. We establish the following mathematical model:

$$f_i(L, D) = \min\left(\varepsilon L_{ij} + \eta D_{ij}, j = 1, 2, 3, \ldots, g_i\right), \quad (9)$$

$$T_i \Leftarrow \cos t_i = \min\left(f_i, i = 1, 2, 3, \ldots, n\right), \quad (10)$$

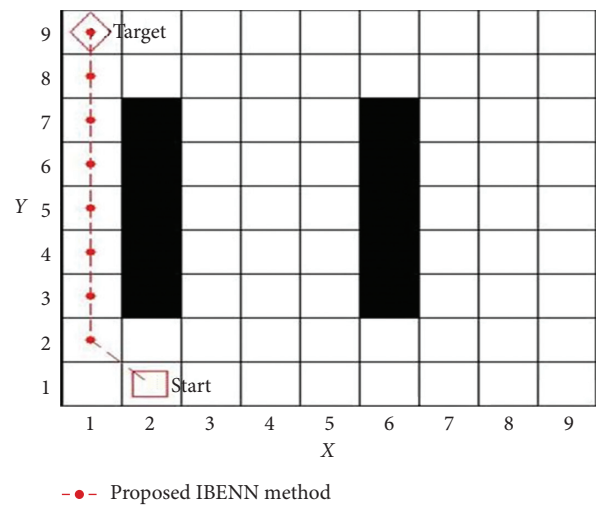

Figure 5: Single-robot path generated by the proposed IBENN method with Strategies (i) and (iii) in the situation of single-point inspection.

Table 1: Comparison results of BENN and IBENN methods.

Evaluation index	BENN	IBENN with strategies (i) and (iii)
Path length	10.07	8.41
Turn times	4	1

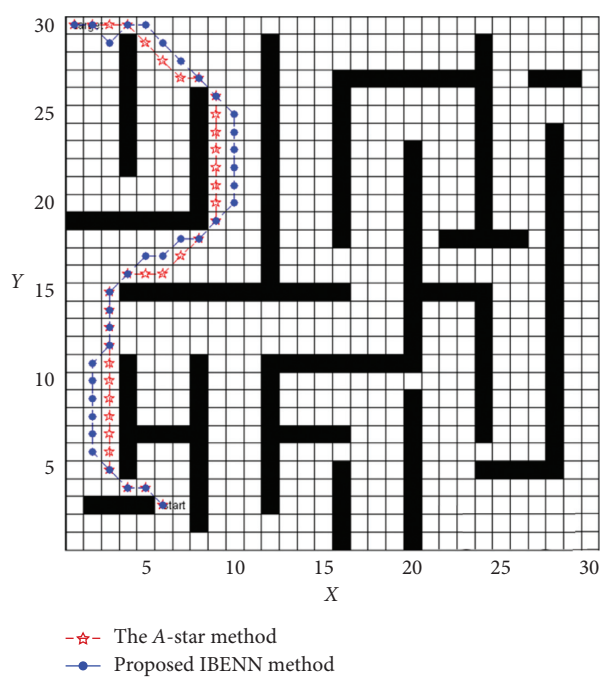

Figure 6: Single-robot path generated by the traditional BENN method and A-star algorithm in the situation of single-point inspection.

where L_{ij} and D_{ij} represent the length and the turning number of the jth path for the ith robot, respectively, ε and η represent the associated weights of L_{ij} and D_{ij}, respectively,

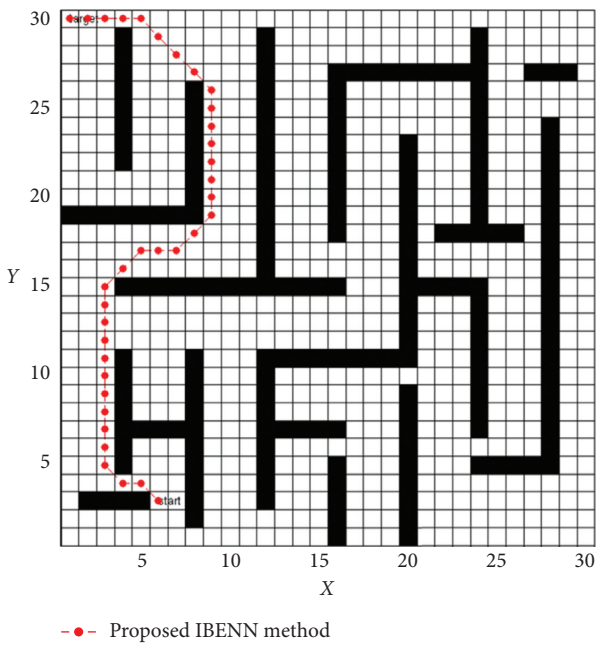

Figure 7: Single-robot path generated by the proposed IBENN method with Strategies (ii) and (iii) in the situation of single-point inspection.

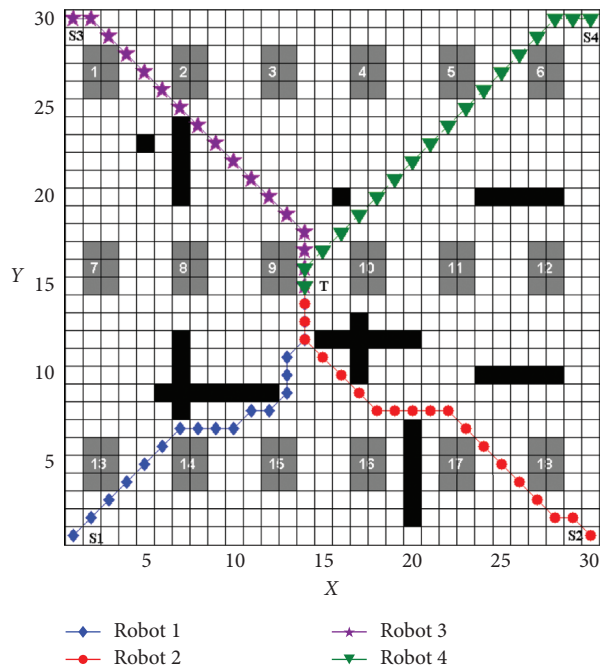

Figure 8: Four-robot path generated by the proposed IBENN-based MRCI system in the situation of single-point inspection.

Table 2: Comparison of the three methods.

Index	BENN	A-star	IBENN with strategies (ii) and (iii)
Path length	40.63	38.14	38.14
Turn times	17	12	10
Rotation angle	21.99	9.43	7.85

Table 3: Comparison of the four-robot path planning.

Index	Robot_1	Robot_2	Robot_3	Robot_4
Path length	21.73	23.56	20.97	22.80
Turn times	18	19	16	17
Rotation angle	6.28	4.71	3.14	7.85

all robots' weights are the same by default in the path decision, g_i represents the number of paths available for the ith robot to complete the task T, and f_i can be considered as the minimum cost of robot i to achieve task T. The objective here is to find the robot i and the optimal path g_i.

To solve this problem, the proposed IBENN method is used to calculate the minimum cost of each robot to complete the task and then compare the optimal cost of each robot. It is necessary that the robot with the lowest cost obtains the task and completes the task according to the optimal path planned. For example, in the 30×30 map shown in Figure 8, gray areas represent parallel devices and black ones represent obstacles in the site, and there are four robots, Robot_1, Robot_2, Robot_3, and Robot_4, with initial positions, $R_1(1,1)$, $R_2(30,1)$, $R_3(1,30)$, and $R_4(30,30)$, respectively. When inspection tasks are needed near equipment $R_{\text{target}}(14,15)$ (i.e., area no. 9), according to the IBENN method, the cost of each robot to complete the task is calculated, as shown in Table 3, and then, each robot offers a quotation according to the above method with $f_1 = 14$, $f_2 = 14.14$, $f_3 = 12.06$, and $f_4 = 15.33$, which can be calculated according to (9) when the parameter is set as $\varepsilon = \eta = 0.5$. According to the calculation, we can choose Robot_3 as the best scheme to execute the task, and other robots determine their priority as a backup according to the cost.

4.2. Multipoint Inspection. In the substation working area, there is occasionally a need to inspect multiple areas, and the advantages of the multirobot cooperation system can be well reflected in this situation. The cost equation of the system can be described as

$$F = \min \cos t = \min \sum_{i=1}^{n} f_i(L_i, D_i) = \min \sum_{i}^{n} \left(\min\left(\varepsilon L_{ij} + \eta D_{ij}, j = 1, 2, 3, \ldots, g_i\right)\right), \tag{11}$$

where g_i represents the total number of paths that robot i can choose to reach the target point. Assume that there are n robots with m areas that need to be inspected ($n > 1$ and $m > 1$) simultaneously, and the collaborative work of robots needs to be determined according to the relationship between the areas m and the robots n.

Case 1. $n \geq m$: assume that a robot can only complete one task, and it can ensure that each uninspected area can be assigned to a robot to perform tasks at the same time. The allocation method is the same as the task allocation method of the single-point robot mentioned above, i.e., each robot puts forward an optimal quotation for each task, and the master robot determines the optimal decision-making scheme based on the quotation of each robot combined with the corresponding bidding algorithm and assigns subtasks to each robot according to the scheme. Then, the problem is first transformed into an assignment problem, which can be solved by the classical Hungarian algorithm [33]. For example, let $n = 6$ and $m = 4$, their positions are shown in Table 4, and the minimum cost of each robot at each task point is solved according to the above method. According to the above allocation method, the following allocation scheme can be obtained: $A_1 \longrightarrow R_1$, $A_2 \longrightarrow R_2$, $A_3 \longrightarrow R_3$, and $A_4 \longrightarrow R_5$, and the total cost $F = 9.94 + 9.69 + 6.81 + 5.71 = 32.15$.

Case 2. $n < m$: it means that a robot needs to complete multiple tasks, and there can also be a situation where one or more robots are idle. For multiple robots at different initial positions, the host computer needs to plan a reasonable path so that all inspection areas can be visited by the robots and the total cost is minimal. We have designed a genetic algorithm to solve this problem. The genetic algorithm adopts the following single-chain coding form, as shown in Figure 8; when decoding, the Robot_2 completes the inspection tasks of Areas 1 and 3 in sequence, and similarly, Robot_1 and Robot_3 complete the tasks of Areas 4 and 6 and Areas 2 and 5 in sequence. This coding method has the advantage of strong readability; however, it is easy to produce infeasible solutions during crossover and mutation. Therefore, different repair algorithms are used to repair the infeasible solutions.

Crossover. Use Partial-Mapped Crossover (PMX) operator when generating a new gene chain. If it is not a feasible solution, then fix it. The specific repair method is to find the repetitive genes in gene chain A that cause infeasible solutions (there may be multiple groups), one of which must be in the cross-replacement gene sequence, then find the gene that maps to the gene in gene chain B, and use it to replace the repetitive genes in chain A that are not in the cross-replacement sequence.

Mutation. Randomly select two genes in the gene chain, and determine whether one of their positions is at the end of the gene chain. If not, exchange their positions in the gene chain.

Selection. The tournament selection method is used, that is, a certain number of individuals are removed from the population each time; then, the best one is selected to enter the offspring population. Repeat this operation until the new population size reaches the original population size.

For example, in a 30×30 map, the initial positions of the Robots $1-3$ are $R_1^{\text{start}}(1,10)$, $R_2^{\text{start}}(15,30)$, and $R_3^{\text{start}}(30,10)$, and the positions of the 6 inspection points are $A_1(11,27)$, $A_2(29,28)$, $A_3(3,18)$, $A_4(16,15)$, $A_5(13,3)$, and $A_6(26,6)$. The initial azimuth of the robot is $(0, -\pi/2, -\pi)$. Using the proposed IBENN method above, the optimal path and the minimum cost between each point can be calculated. The genetic algorithm can draw the following distribution plan:

$$R_1 \longrightarrow A_3 \longrightarrow A_1 \longrightarrow A_4 \longrightarrow A_5; R_2 \longrightarrow A_2; R_3 \longrightarrow A_6. \tag{12}$$

The total cost is 45.28, and the multirobot multipoint inspection path is shown in Figure 9, where the red star indicates the inspection point and the blue star indicates the initial position of each robot.

Table 4: Comparison of the four-robot path planning.

Position	Area_1(9,16)	Area_2(16,16)	Area_3(22,7)	Area_4(22,25)
R_1(1,1)	9.94	14.92	14.88	18.01
R_2(15,1)	10.31	9.69	7.88	16.88
R_3(30,1)	15.96	14.42	6.81	15.23
R_4(1,30)	11.01	11.58	19.87	12.71
R_5(15,30)	10.60	9.56	16.09	5.71
R_6(30,30)	25.18	14.41	15.51	11.32

4.3. All-Area Inspection. Since the substation of smart microgrids is exposed to the outdoors for a long time, it is easy to break into foreign objects or other dangerous goods. It is necessary to conduct regular inspections of the entire power station of smart microgrids for all-area coverage. However, performing this task by a single robot may take a long time and is inefficient. Therefore, a multirobot collaborative whole-area inspection program is designed.

Divide every two robots into a group, and design a heuristic algorithm for each robot. The priority of the heuristic algorithm of the robots in each group is opposite, which ensures that each group of robots can start inspections from different directions. When the robot enters the dead zone position, according to the proposed IBENN method above, the optimal path from the dead zone position to the uninspected area can be planned. The robot moves to this area and continues to inspect according to the original heuristic algorithm. For example, in a 30×30 map, there are parallel devices and various obstacle points, as shown in Figure 10. Two robots in the area are used to coordinate to complete the all-area inspection task. The steering priority of the heuristic algorithm of Robot_1: $W - S - SW - NW - N - E - SE - NE$ and Robot_2: $E - N - NE - SE - S - W - NW - SW$, and the initial positions are $(1,1)$ and $(30,1)$, respectively.

Simulation experiments were carried out in the obstacle-free and obstacle environments, and the results are shown in Figures 11 and 12 and Table 5, where the red and blue represent Robots 1 and 2, respectively, pink dots express repeated path points, dots mean the final position of the robot when the task is completed, and stars represent the initial position. It can be seen from Table 5 that, in a simple map, when there are no other obstacles in the inspection area and only parallel substation equipment,

A_1	A_3	R_2	A_4	A_6	R_1	A_2	A_5	R_3

Figure 9: Gene chain coding of the genetic algorithm.

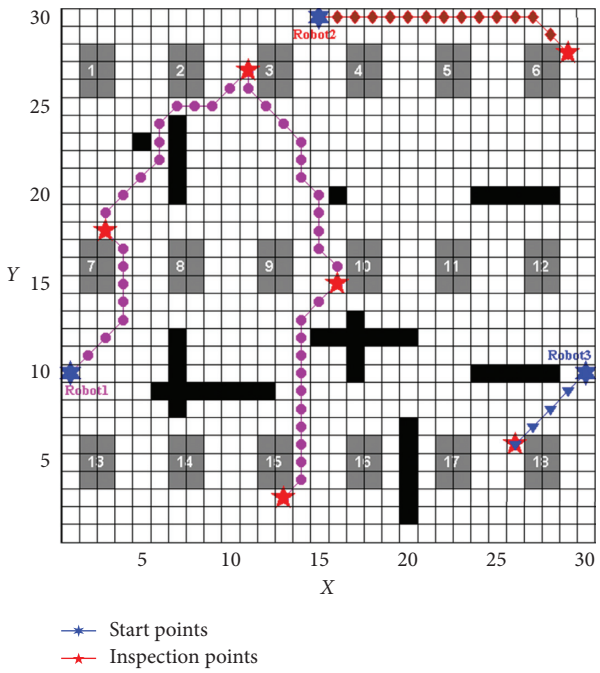

Figure 10: Three-robot path generated by the proposed IBENN based MRCI system in the situation of six-point inspection.

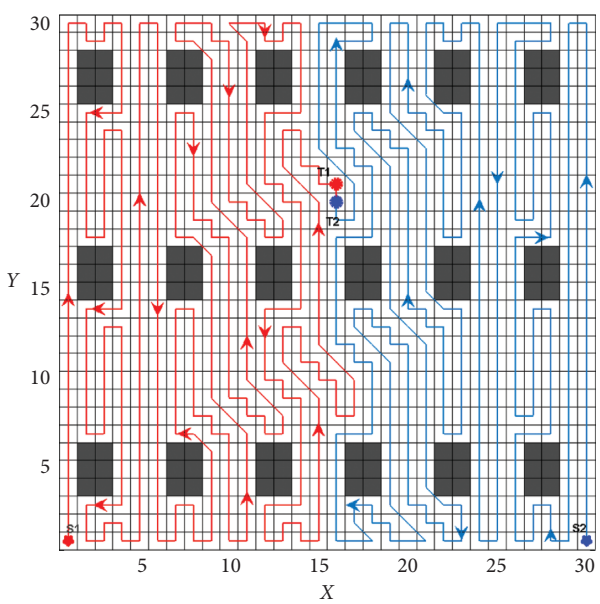

Figure 11: Two-robot path generated by the proposed IBENN-based MRCI system in the situation of all-area inspection without obstacle.

this method can achieve 100% coverage without overlapping areas. When there are various obstacles in the inspection area, this method can also achieve 100% full-coverage inspection, but there is a repetition rate of 2.3%. Hence, compared with other inspection methods, the proposed IBENN method does not need to set a template operator and has strong versatility. Multirobot collaboration can complete the entire area and full-coverage inspection task.

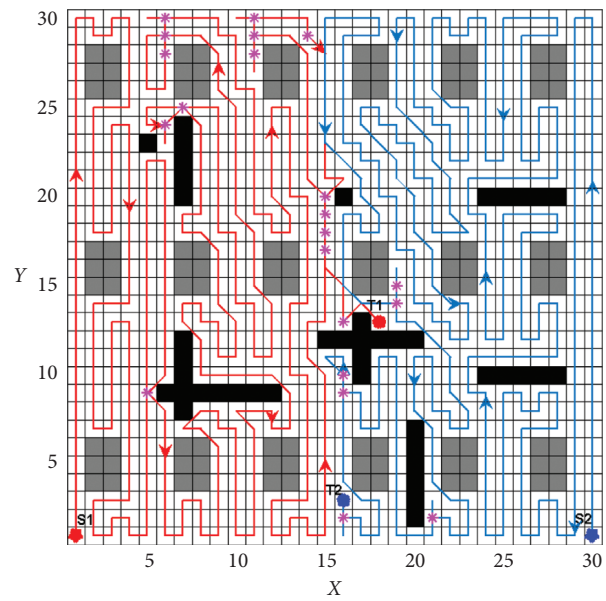

Figure 12: Two-robot path generated by the proposed IBENN-based MRCI system in the situation of all-area inspection complex obstacle.

Table 5: Results in obstacle-free and obstacle environments.

Evaluation index	Obstacle-free environment (%)	Obstacle environment (%)
Coverage rate	100	100
Repetition rate	0	2.3

To further verify the effectiveness of the proposed control schemes, we carry out the simulation experiment with Coppelia Sim Software in the space of 30 m × 30 m. The two inspection robots are in the initial position as $t = 0$, as shown in Figure 13(a), in which the gray cube and dark blue cube represent the equipment area and the obstacle area, respectively. The robot is supposed to inspect at a speed of 1 m/s disregarding the inspection time. Using the above inspection strategy, the experimental results are shown in Figure 13. As seen, the left robot and right robot fall into dead zones, respectively, as $t = 138$ or $t = 365$ in Figures 13(a) and 13(e) and $t = 357$ or $t = 306$ in Figures 13(c) and 13(d). However, in these cases, the inspection machine can jump out of the dead zone by calling the IBENN algorithm, respectively. Furthermore, both robots fall into the dead zone state when $t = 395$, as shown in Figure 13(f). Since there is no undetected area in this situation, it follows that the inspection task has been completed. Therefore, the experiment verifies the feasibility of the cooperation scheme.

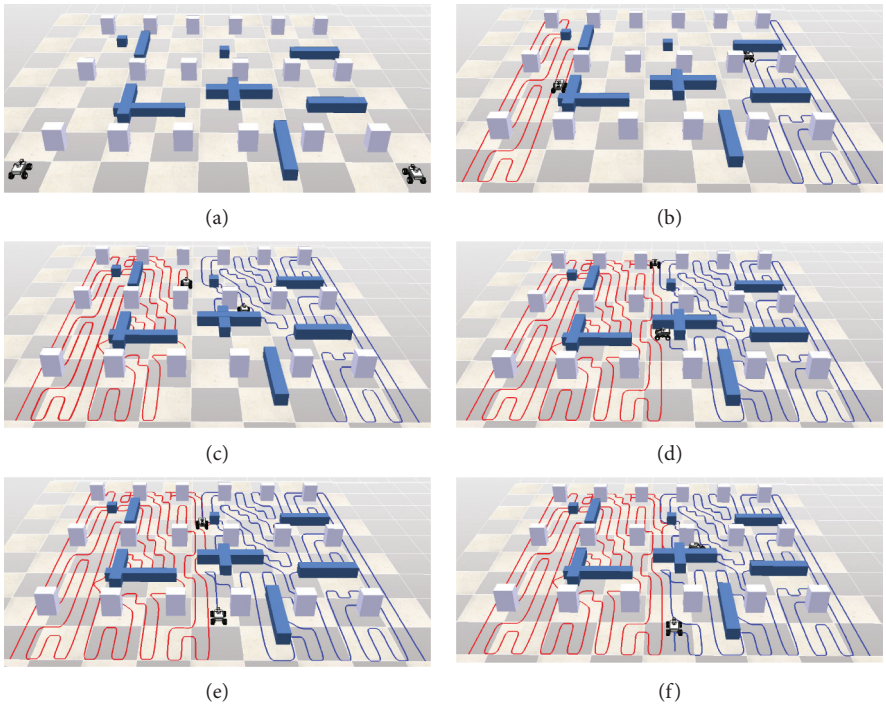

Figure 13: Sequence diagram of cooperative operation of two inspection robots. (a) T = 0. (b) T = 138. (c) T = 306. (d) T = 357. (e) T = 365. (f) T = 395.

5. Conclusion

In this paper, a multimobile robot collaborative operating system for power stations of the smart microgrids is designed, and an improved IBENN method is proposed. Compared with the traditional BENN method and *A*-star algorithm, the improved IBENN algorithm has an obvious optimization effect in path length and turning times. Based on this method, the multirobot cooperative operation strategy is designed to realize the three classic tasks of single-point inspection, multipoint inspection, and full-coverage inspection in the substation of smart microgrids, which verifies the effectiveness of the main results.

Data Availability

All of the data used to support the findings of this study are included within this article.

Conflicts of Interest

The authors declare that they have no conflicts of interest.

Acknowledgments

This work was supported by the National Natural Science Foundation of China under Grant nos. 61733004 and 61773158.

References

[1] A. Peyman and F. Keynia, "Lifetime efficiency index model for optimal maintenance of power substation equipment based on cuckoo optimisation algorithm," *IET Generation Transmission & Distribution*, vol. 11, no. 11, pp. 2787–2795, 2017.

[2] I. Ullah, Y. Fang, and R. Khan, "Predictive maintenance of power substation equipment by infrared thermography using a machine-learning approach," *Energies*, vol. 10, no. 12, pp. 1–13, 1987.

[3] X. Lu, J. Lai, X. Yu, Y. Wang, and J. M. Guerrero, "Distributed coordination of islanded microgrid clusters using a two-layer intermittent communication network," *IEEE Transactions on Industrial Informatics*, vol. 14, no. 9, pp. 3956–3969, 2018.

[4] X. Lu, J. Lai, X. Yu, Y. Wang, and J. M. Guerrero, "A novel secondary power management strategy for multiple AC microgrids with cluster-oriented two-layer cooperative framework," *IEEE Transactions on Industrial Informatics*, vol. 17, no. 2, pp. 1483–1495, 2021.

[5] H. Takahashi, *Development of Patrolling Robot for Substation*, pp. 10–19, Japan IERE Council,Special Document R8903, Japan, 1989.

[6] J. Beaudry and S. Poirier, Véhicule téléopéré pour inspection visuelle etthermographique dans les postes de ransformation, 2012.

[7] J. K. C. Pinto, M. Masuda, L. C. Magrini, J. A. Jardini, and M. V. Garbelloti, "Mobile robot for hot spot monitoring in electric power substation," in *Proceedings of the IEEE/PES Transmission and Distribution Conference and Exposition*, pp. 1–5, Chicago, Illinois, April 2008.

[8] N. Pouliot, P.-L. Richard, and S. Montambault, "LineScout technology opens the way to robotic inspection and maintenance of high-voltage power lines," *IEEE Power and Energy Technology Systems Journal*, vol. 2, no. 1, pp. 1–11, 2015.

[9] A. Cantieri, M. Ferraz, and G. Szekir, "Cooperative UAV-UGV autonomous power pylon inspection: an investigation of cooperative outdoor vehicle positioning architecture," *Sensors*, vol. 20, no. 6384, pp. 1–22, 2020.

[10] Y. Guang and P. Yutian, "Intelligent inspection of marine disasters based on UAV intelligent vision," *Journal of Coastal Research*, vol. 93, pp. 410–416, 2019.

[11] S. Jordan, J. Moore, and S. Hovet, "State-of-the-art technologies for UAV inspections," *IET Radar, Sonar & Navigation*, vol. 12, no. 2, pp. 151–164, 2018.

[12] J. Katranik, F. Pernus, and B. Likar, "A survey of mobile robots for distribution power line inspection," *IEEE Transactions on Power Delivery*, vol. 25, no. 1, pp. 485–493, 2010.

[13] J. Yu and S. M. LaValle, "Optimal multirobot path planning on graphs: complete algorithms and effective heuristics," *IEEE Transactions on Robotics*, vol. 32, no. 5, pp. 1163–1177, 2016.

[14] K. Jose and D. K. Pratihar, "Task allocation and collision-free path planning of centralized multi-robots system for industrial plant inspection using heuristic methods," *Robotics and Autonomous Systems*, vol. 80, pp. 34–42, 2016.

[15] B. Pradhan, A. Nandi, N. B. Hui, and D. S. Roy, "A novel hybrid neural network-based multirobot path planning with motion coordination," *IEEE Transactions on Vehicular Technology*, vol. 69, no. 2, pp. 1319–1327, 2020.

[16] C. Luo, S. X. Yang, and X. Li, "Neural-dynamics-driven complete area coverage navigation through cooperation of multiple mobile robots," *IEEE Transactions on Industrial Electronics*, vol. 64, no. 1, pp. 750–760, 2017.

[17] B. Woosley and P. Dasgupta, "Integrated real-time task and motion planning for multiple robots under path and communication uncertainties," *Robotica*, vol. 36, no. 3, pp. 353–373, 2018.

[18] B. Woosley, P. Dasgupta, J. G. Rogers, and J. Twigg, "Multi-robot information driven path planning under communication constraints," *Autonomous Robots*, vol. 44, no. 5, pp. 721–737, 2020.

[19] F. Imeson and S. L. Smith, "An SMT-based approach to motion planning for multiple robots with complex constraints," *IEEE Transactions on Robotics*, vol. 35, no. 3, pp. 669–684, 2019.

[20] A. Ayari and S. Bouamama, "A new multiple robot path planning algorithm: dynamic distributed particle swarm optimization," *Robotics and Biomimetics*, vol. 4, no. 1, p. 8, 2017.

[21] B. Banerjee and CE. Davis, "Multiagent path finding with persistence conflicts," *IEEE Transactions on Computational Intelligence and AI in Games*, vol. 9, no. 4, pp. 402–409, 2016.

[22] S. Thabit and A. Mohades, "Multi-robot path planning based on multi-objective particle swarm optimization," *IEEE Access*, vol. 7, pp. 2138–2147, 2018.

[23] R. Siegwart, "IR nourbakhsh, and D scaramuzza. "Introduction to autonomous mobile robots," *Industrial Robot*, vol. 2, no. 6, pp. 645–649, 2004.

[24] K. Jiang, Z. Sun, Y. Liu, and J. Sui, "Development and Application of the Rail-type Inspection Robot used in Substation Rooms," *MATEC Web of Conferences*, vol. 139, no. 5, Article ID 00210, 2017.

[25] H. B. Xu, J. H. Liu, and X. Jia, "Substation inspection system based on RFID technology," *Advanced Materials Research*, vol. 734-737, pp. 2846–2850, 2013.

[26] S. Z. Wang, D. Han, and Q. Dong, "The application of RFID in substation inspection system," *Applied Mechanics and Materials*, vol. 295-298, pp. 2433–2436, 2013.

[27] J. Zhu, Y. Sun, and D. Sun, "Design of a laser navigation system for the inspection robot used in substation," *Proceedings of the Spie*, vol. 322, 2017.

[28] C.-J. Huang, Y.-W. Wang, H.-M. Chen et al., "Application of cellular automata and type-2 fuzzy logic to dynamic vehicle path planning," *Applied Soft Computing*, vol. 19, pp. 333–342, 2014.

[29] S. X. Yang and M. Meng, "An efficient neural network approach to dynamic robot motion planning," *Neural Networks*, vol. 13, no. 2, pp. 143–148, 2000.

[30] S. X. Yang and M. Q.-H. Meng, "Real-time collision-free motion planning of a mobile robot using a Neural Dynamics-based approach," *IEEE Transactions on Neural Networks*, vol. 14, no. 6, pp. 1541–1552, 2003.

[31] S. Yang and C. Luo, *A Neural Network Approach to Complete Coverage Path Planning*, pp. 718–724, Systems Man and Cybernetics, 2004.

[32] C. Luo and S. X. Yang, "A bioinspired neural network for real-time concurrent map building and complete coverage robot navigation in unknown environments," *IEEE Transactions on Neural Networks*, vol. 19, no. 7, pp. 1279–1298, 2008.

[33] S. Chopra, G. Notarstefano, M. Rice, and M. Egerstedt, "A distributed version of the Hungarian method for multirobot assignment," *IEEE Transactions on Robotics*, vol. 33, no. 4, pp. 932–947, 2017.

Hindawi
Complexity
Volume 2021, Article ID 6691905, 12 pages
https://doi.org/10.1155/2021/6691905

Research Article

System Optimization and Robustness Stability Control for GIS Inspection Robot in Complex Microgrid Networks

Yu Yan,[1] Wei Jiang,[2,3] Zhiping Luo,[1] Jianjun Zhang,[1] and Weidong Liu[1]

[1]*State Grid Hunan Maintenance Company, Changsha 410004, China*
[2]*Wuhan Textile University, Hubei Key Laboratory of Digital Textile Equipment, Wuhan 430200, China*
[3]*Wuhan Textile University, Hubei Engineering Research Center of Industrial Detonator Intelligent Assembly, Wuhan 430073, China*

Correspondence should be addressed to Wei Jiang; jiangwei2013@whu.edu.cn

Received 27 October 2020; Revised 21 November 2020; Accepted 27 January 2021; Published 27 February 2021

Academic Editor: Ruoli Tang

GIS (gas-insulated switchgear) is important equipment in the substation system in a complex microgrid network. Due to the long-term service in harsh operation environments, the electrical performance of GIS equipment will be seriously affected. Therefore, the regular maintenance of GIS equipment in the substation system is a routine task so as to ensure the normal operation of the microgrid networks. The traditional method relies on manual labor, where not only with the low operation efficiency but also regarding some maintenance, labors cannot reach the inside of the GIS equipment, which seriously restricted the completion of GIS equipment maintenance operation. Based on the above analysis, a basic configuration of a GIS equipment maintenance robot with smart structure, convenient control, and stable motion characteristic has been proposed in this paper. Through the optimization design of the chassis adsorption system, the GIS inspection robot can achieve hanging and vertical adsorption inside the GIS equipment and some special motion status. In this way, the entire GIS equipment can be inspected without blind spots. Through establishing the mechanical model of the GIS inspection robot under the hanging and vertical motion state, the robustness and stability of the GIS inspection robot in the special status have been analyzed, and the corresponding GIS inspection robot robust stability motion control method has also been proposed. Finally, through the integrated design of mechanical system and hardware and software control system, the GIS inspection robot physical prototype system has been developed and the maintenance operation experiment has been carried out in Hunan Electric Power Company Maintenance Company through simulating the internal GIS equipment. The physical prototype can realize the basic movement and special movement in internal GIS equipment without any blind spots and complete the inspection task of GIS equipment operation; the movement of GIS robot is dexterous and stable in the whole operation process, which has strong robust stability. The research of GIS inspection robot in the complex microgrid networks has important theoretical significance and practical application value for the intelligent operation and maintenance management of substation system in complex microgrid networks.

1. Introduction

There are a large number of GIS (gas-insulated switchgear) types of equipment [1–4] built in the power system substation networks, GIS is a metal-enclosed equipment, and once there is an internal fault, the gas chamber needs to be opened for searching and processing, which not only is very inconvenient but also leads to poor safety and economy. In most cases, GIS equipment maintenance cannot directly dismantle the faulty spot. It needs to be dismantled layer by layer, which needs the recovery time, and a small problem may cost so much and take half a month. From the current internal defects, more than 80% of the internal defects are mainly small problems, such as fixing fitting loose, poor cleanliness, and some other small problems. In order to ensure the safety and reliable and stable operation of the substation network, using GIS inspection robots to assist or even replace manual maintenance of GIS equipment can not only improve working efficiency but also liberate the labors from the dangerous power maintenance environment. In

order to achieve GIS equipment maintenance without blind spots, the GIS inspection robots should be able to climb along the inside of GIS equipment pipelines. Therefore, the robot climbing ability is the key to GIS equipment maintenance operations. In recent decades, wall-climbing robots [5–8] have been widely used in different fields; it is a special type mobile robot, because its main feature is that it can overcome its own gravity on the surface of the three-dimensional environment and then move to complete the GIS inspection operation. Therefore, the wall-climbing robot not only needs to have the same motion mechanism as the traditional mobile robot but also needs a special adsorption mechanism for the robot to absorb the three-dimensional wall surface. Due to the particularity of the wall-climbing robot motion and the influence of the surface environment, the robot motion control becomes very complicated. Therefore, the research on wall-climbing robots will be more challenging than mobile robots; at the same time, the GIS inspection robots with wall-climbing functions are used to replace humans to complete these high-altitude, high-risk inspection tasks, which can improve working efficiency and protect personnel safety; thus, the research has important theoretical significance and practical application value for the GIS equipment wall-climbing robot in the complex microgrid networks.

GIS inspection robot mainly relies on its climbing ability on the GIS equipment surface; in foreign countries, the research on wall-climbing robots can be divided into three categories [9–11]. The first category is the negative pressure-based wall-climbing robot developed by Miyazaki University in Japan in 1966; the robot is very huge and heavy; after 1990, the wall-climbing robot based on the negative pressure adsorption mechanism was developed rapidly. Although the adsorption method can be adapted to the wall surface of many different materials, it has higher requirements on the wall surface, and the wall surface condition affects the robot motion stability, which limits the development of negative pressure adsorption wall-climbing robots. The second category is the foot-type bionic wall-climbing mode, such as *Rise* series robot based on bionic adsorption, which was developed by Boston Dynamics, *Rise* V_2 is a hexapod bionic wall-climbing robot, the soles of *Rise's* feet have hairy claws which are similar to those of wall-climbing animals, and it relies on multijoint motion to crawl. *Rise* has a bionic spine and tail, which can improve the motion balance of the robot on different walls by changing the state of the spine and tail. *Rise* V_3 is a four-leg bionic wall-climbing robot based on *Rise* V_2, its size is 250 mm in length, its weight is 2 kg, and the speed is 0.3 m/s. It is mainly used in search and rescue operations and can be used for reconnaissance and surveillance. The biggest feature of the *Rise series* [12] robot is that its sole has a special microhair structure adsorption mechanism; through virtue of this mechanism, *Rise* can realize vertical movement without external force, which greatly reduces the overall power consumption of the robot, and as the structure is very complicated, it crawls very slowly. The third category is *Magnebike* wall-climbing robot developed by the Federal Institute of Technology Zurich, Switzerland, with a total weight of 3.3 kg and a volume of $170 \times 130 \times 220\,\text{mm}^3$, with a maximum walking speed of 2.7 m/min and a magnetic adsorption force of 250 N, which is mainly used in pipe inspection and other scenarios; the research has important reference value for GIS equipment maintenance operations. Domestically, the first research on wall-climbing robots in China was in Harbin University of Technology, which successfully developed a wall-climbing robot [13, 14] called *CLR-I* in 1994, *CLR-I's* adsorption method is negative pressure adsorption, with all-directional mobility, and it is able to walk flexibly on the wall surface, but *CLR-I* uses wired and console connection mode, which is extremely inconvenient to control and operate. Four years later, Harbin University of Technology successfully developed the *CLR-II* wall-climbing robot on the basis of *CLR-I*, which aims at the inconvenience of *CLR-I* cable operation, removing wired control, increasing wireless communication technology, and improving the control convenience. The University of the Chinese Academy of Sciences has also made important contributions to wall-climbing robots and its magnetic adsorption track-type wall-climbing robots [15, 16] have optimized the size and structure of the magnetic array, so that the adsorption force reached by the robot is as high as 503 N, which can be well adsorbed to the surface of the conductive magnet and provide a reliable guarantee for the robot motion on the wall surface. However, the track-type structure causes it to move less flexibly and it cannot adapt to the surface appropriately.

Through the above analysis, it can be concluded that the key for the research of GIS inspection robot is its climbing ability in GIS equipment and the key of its climbing ability is mainly dependent on magnetic adsorption mechanism [17, 18] which is to use magnetic force generated between the magnetic source and the conductor magnet, and so as adsorption on the object surface, magnetic sources can be divided into permanent magnet and electromagnetic. Magnetic adsorption form can produce great adsorption force; therefore, magnetic adsorption wall-climbing robot can ignore the impact of surface roughness, which enhances the operational stability [19, 20] of the robot system; the main contribution of this paper is to propose a robot climbing mechanism with adsorption function and its stable climbing inspection and application in power GIS equipment. Therefore, in view of the current power GIS maintenance task in the complex microgrid networks, this paper puts forward a kind of GIS equipment maintenance operation by using the wall-climbing robot with adsorption ability, so as to optimize the design of the streamlined mechanical configuration; then the corresponding control system and physical prototype models have been developed through the simulation and analysis of the GIS inspection robot motion robust stability in the process of operation and walking; this research puts forward the corresponding robust control method. Finally, in GIS equipment, the physical prototype has been used to carry out GIS equipment maintenance operation experiments and robot mechanism streamlined and flexible motion, which can achieve GIS equipment maintenance without blind spots; in the operation process, robot moves stably in the complex microgrid networks environment and can resist electromagnetic interference and other external environment

impacts on the GIS inspection robot; the robot showed a strong robustness. The research of this paper is a new application and exploration for the maintenance of power intelligent microgrid networks; its research and implementation are of great theoretical significance and practical application value to improve the energy efficiency of complex microgrid networks system, promoting the automation and intelligence of power system.

2. GIS Inspection Robot Mechanical System Design and Optimization

2.1. The Overall Design of the GIS Inspection Robot System. When GIS inspection robot replaces manual GIS equipment inspection operation, there are three requirements, which are the stable wall adsorption ability, flexible mobility on three-dimensional walls, and adaptive ability to different wall surfaces. In order to meet the three above requirements, this paper designs a wheel mobile robot that can achieve all-directional climbing inside GIS equipment as shown in Figure 1, where Figure 1(a) is the robot physical prototype operation environment, Figure 1(b) is robot three-dimensional structure, and Figures 1(c)–1(f) are the motion planning of robot inspection operations. The robot is highly modular in design and it consists mainly of all-directional mobile chassis module, magnetic adsorption module, sensors, and electrical control system with mass of 2 kg. The robot can be used as a mobile platform, equipped with small detection equipment and manipulator to complete dust removal maintenance function.

The GIS climbing robot designed in this paper needs to move on the wall and carry manipulator equipment to complete the inspection and maintenance work; considering that the tracking scheme is slow and not flexible enough, the control is difficult, and the adsorption method is relatively single, so all-directional wheat wheel can be selected in the mobile scheme, which has both speed and flexibility, and also the control difficulty is relatively low. Climbing robot in the three-dimensional environment needs to have adsorption capacity, and the robot working environment is mostly ferromagnetic material wall surface, so the use of permanent magnet adsorption scheme has been adopted in order to reduce the volume and mass of the magnets, and the use of Halbach magnetic adsorption array as adsorption scheme can enhance adsorption side magnetism.

2.2. GIS Inspection Robot Mobile Chassis Design and Optimization. The current mobile robot moves in three main ways, which are foot mode, track mode, and wheel mode; wall-climbing robots serve as a branch of mobile robots, and these three methods are also suitable for wall-climbing robots. The wall-climbing robot with track-type mobile scheme is the most commonly used, its advantages are stability, high adaptability to the wall, and strong ability to cross the barrier; GIS wall-climbing robot with wheel scheme is also widely used, and the advantages of wheel robot are simple structure, high efficiency, fast speed, and easy control; the disadvantage is that the wall adaptability is lower than those of track-type mode robot and foot mode robot. Foot mode climbing robot usually uses bionic adsorption scheme; the advantage is that the wall-climbing adaptability is very sound, whether it is flat, surface, irregular surface, all can adapted, the ability to cross the barrier is the strongest. The disadvantage is that it is slow and difficult to control, as the robot requires flexible all-directional mobility; from the above discussion, the GIS robot mobile scheme selects a wheel mobile scheme. Therefore, the robot chassis uses a 3 mm thick carbon fiber plate as a support plate and four McNamee wheels to form an O-shaped all-way chassis, which is shown in Figure 2.

2.3. GIS Inspection Robot Magnetic Adsorption Array Design and Optimization. Three-dimensional wall-climbing ability of GIS robot is on the premise of stable adsorption on the wall surface; the current mainstream adsorption methods include bionic adsorption, negative pressure adsorption, and magnetic adsorption; most industrial productions of pipelines, tanks, and other equipment with curved wall surfaces are made of ferromagnetic materials; this paper adapts magnetic adsorption as a robot adsorption scheme. In order to achieve miniaturization and light weight, magnetic adsorption arrays must be optimized so as to produce large adsorption forces at very small volume and mass. Halbach magnetic arrays are a special form of magnet scheduling which enhances the single magnetic field. The principle is shown in Figure 3, where the longitudinal magnetized magnetic field is shown in Figure 3(a) and the transverse magnetized magnetic field is shown in Figure 3(b), which can theoretically completely cancel out the magnetic field on one side and enhance the magnetic field on the other side; ideally, a complete one-way magnetic field can be obtained.

In the practical applications, the continuous change of magnetic field direction cannot be achieved, usually the magnetic induction direction changes for discrete processing, discrete magnetic blocks at a certain angle of change stitched together to approximate the magnetic induction strength ideal sine changes, the magnetic adsorption array arrangement rules designed in this paper are shown in Figure 4, the super magnetic force of rare Earth NdFeB magnet has been used, with size of $20 \times 10 \times 10$ mm, and the design interval is 1 mm.

Based on the above analysis results, the determined structure of the magnetic array module and its distribution on the platform of GIS inspection robot system is shown in Figure 5; the magnetic array has been constructed according to the pattern of the Halbach array; the whole machine is installed with two adsorption arrays, which distributed on both sides of the chassis and support the carbon plate; in the magnetic body, the wall gap is 5 mm, which can provide nearly 200 N adsorption force.

3. GIS Inspection Robot Control System Design and Optimization

The design of GIS inspection robot control system is the core of the stable operation for the robot whole system, and its hardware configuration level is directly related to the system

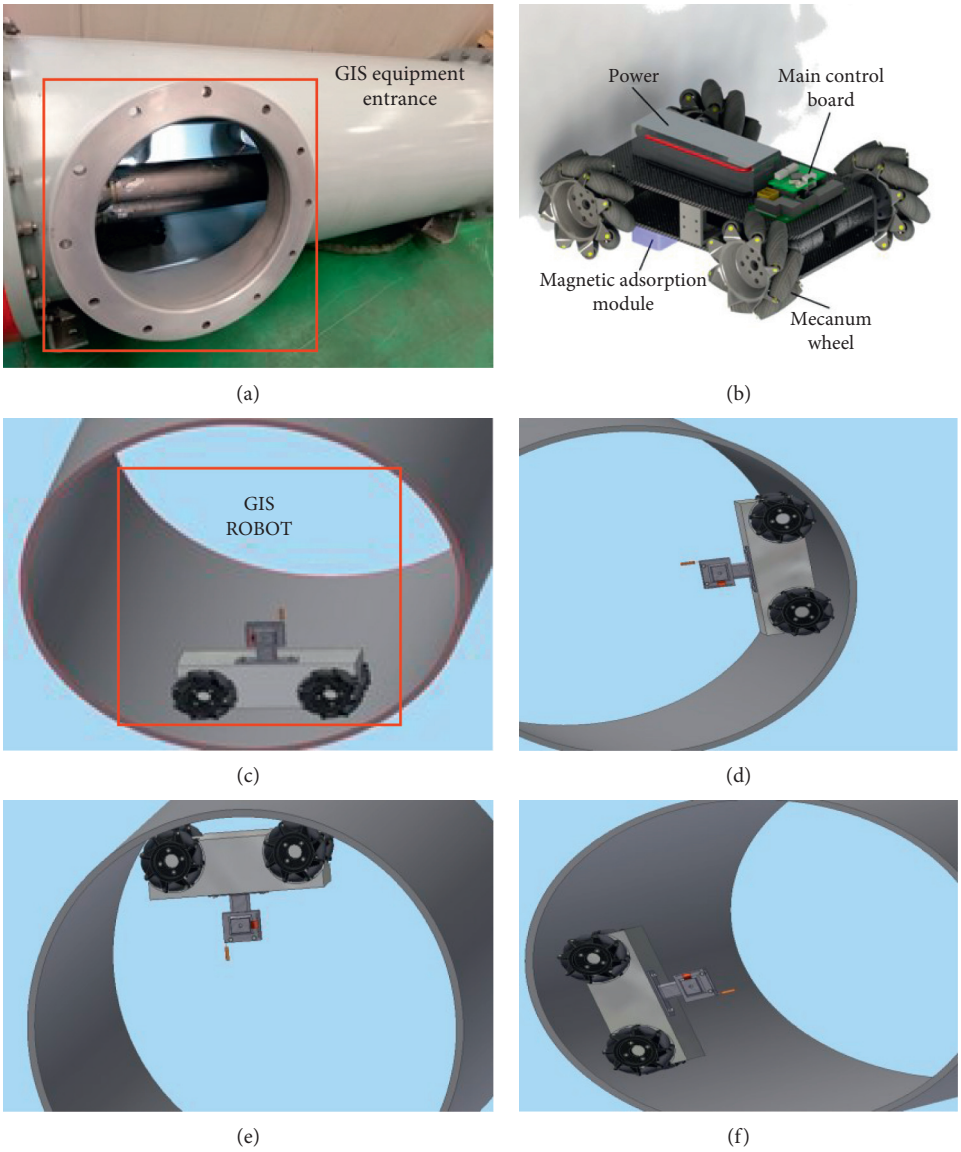

Figure 1: GIS equipment inspection robot with adsorption climbing function. (a) GIS operation environment, (b) robot three-dimensional structure, (c) robot inspection status-1 (initial state), (d) robot inspection status-2 (uphill slope), (e) robot inspection status-3 (apical adsorption), and (f) robot inspection status-4 (downhill slope).

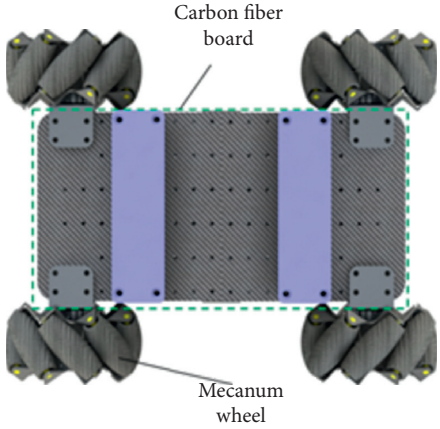

Figure 2: GIS equipment inspection robot chassis structure diagram.

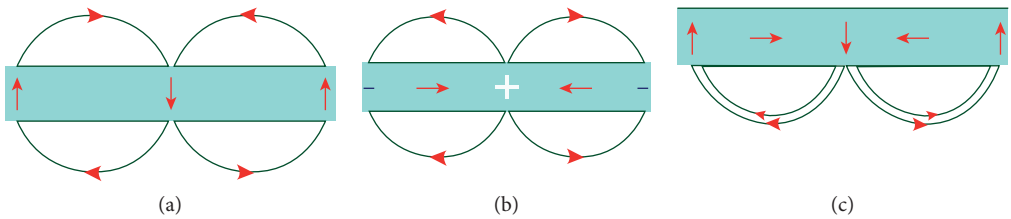

Figure 3: A schematic principle of the Halbach magnetic adsorption array. (a) $m_x = \sin kx$; (b) $m_y = \cos kx$; (c) $m = m_x + m_y$.

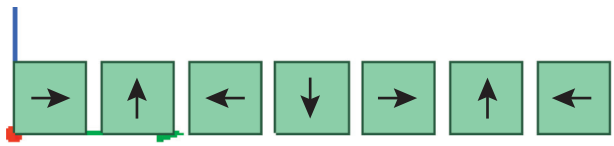

Figure 4: Halbach magnet arrangement rule diagram.

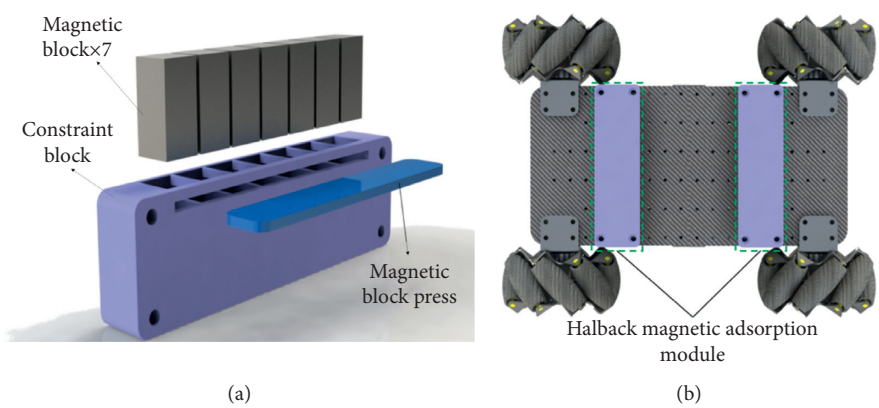

Figure 5: Magnetic array module. (a) Magnet installation structure illustration; (b) distribution of magnetic array on the chassis.

robustness and intelligence, and the design strategy of the control system also determines the functional characteristics, using scope and scalability of the system. According to the functional requirements and design purposes of the GIS inspection robot, the overall block diagram of the robot control system is shown in Figure 6. MPU is the main core of the robot; communication between the different motors and the CAN bus repeater can be achieved by connecting a CAN bus through which the CAN repeater can drive the four motors. CAN repeaters, environment-aware modules, and IMU modules communicate through a CAN bus and MPU so as to complete the overall control of the robot by the MPU.

The motor drive control algorithm used by the GIS (gas-insulated switchgear) inspection robot is a three-ring nested PID (*Proportional Integral Derivative*) algorithm, and the corner data read by the angle encoder that the robot drives the motor can be used as input to the position ring. The input value and the robot chassis motion of the MPU wheel corner data in the position ring PID operation, after the position ring have been solved, the output value can be obtained, the corner data collected by the angle encoder that drives the motor can be used as the input value of the speed ring together with the value after the time difference, and an output value can be obtained after the speed ring with PID operation. This output value is then used as an input to the current ring together with the current status generated by the motor driver, and then the PID operation of the current ring can be performed; the final output value is used as the input value of the motor driver. Through the three-ring nested PID algorithm, the purpose of the robot motor accurate motion control can be finally achieved, the main control objects are three typical motion states of GIS inspection robot, and the structure of the control system is shown in Figure 7.

GIS inspection robot uses STM32F405RGT6 chip as a robot MPU module and completes the speed ring and position ring control on the basis of brushless motor regulator; the robot control board operation frequency can reach up to 85 MHz; its computing power can fully meet the real-time control needs of the robot according to the robot motion and active adaptation functions, as well as the need for volume and quality control, combined with the position of the robot. The D_{ji} *M2006* brushless motor as the driving motor of the chassis and active adaptation body has been selected, which is used in combination with the *C610* brushless motor

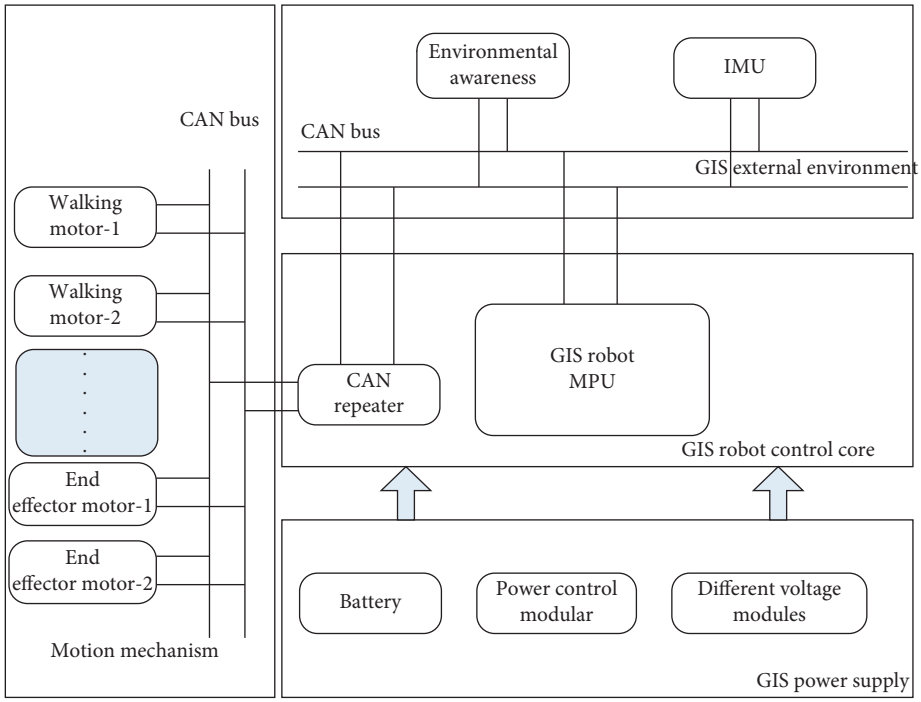

Figure 6: GIS inspection robot controller structure diagram.

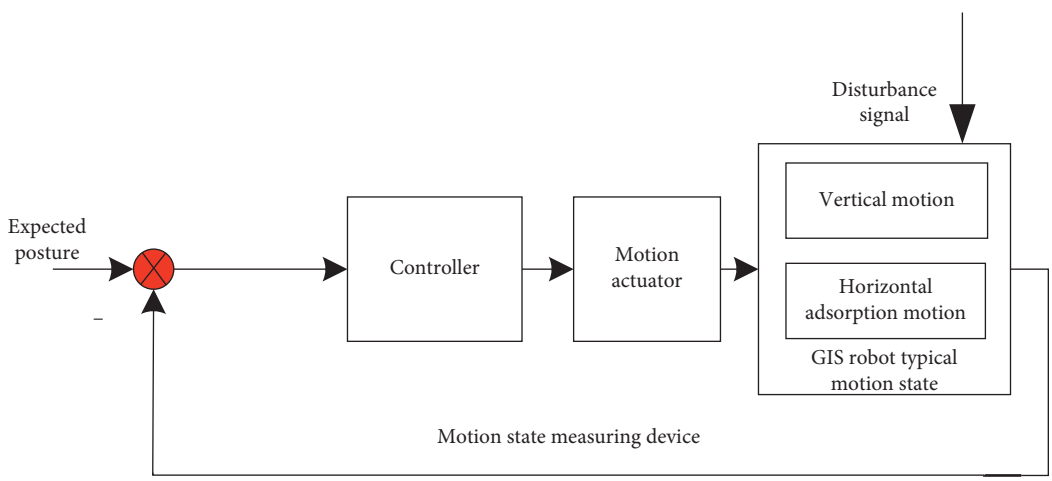

Figure 7: GIS inspection robot control system structure diagram.

regulator, and the whole motion control process can be divided into three parts. First of all, the environment-aware module, the *IMU* module, and the *CAN* repeater module can get the actual attitude information of the robot and take the information of the robot planning path stored in the MPU as the input value of the robot path planning. The MPU then obtains the coordinate values required by the robot so as to reach the destination according to the input value and the preset program and then obtains the corner information of the wheel under each coordinate value according to the motion inverse solution. Finally, the MPU transmits this information to the CAN repeater which completes the drive of the motor according to this information and finally realizes the motion control of the GIS robot. In addition, motion control needs to consider the influence of error as external information to participate in the closed-loop control of robot motion.

4. GIS Inspection Robot Motion Modeling and Robust Stability Control

4.1. Chassis Surface Motion Realization and Stability Analysis. Robot kinematics is an important theory that analyzes the relationship between the motion posture and joint variables of the robot manipulator in the space coordinate system. It is the theoretical basis of the GIS robot inspection control of the operation manipulator; equation (1) is homogeneous transformation matrix; the space posture of the manipulator

can be obtained through the stacking calculation of the homogeneous transformation matrix as shown in equation (2); the posture of the manipulator in the base coordinate system is given as equation (3); equations (2) and (3) can be used to establish an equation relationship to solve the kinematics forward and inverse solutions of the robot manipulator and end effector.

$$ {}^{i-1}_{i}T = \begin{bmatrix} \cos\theta_i & -\sin\theta_i\cos\alpha_i & \sin\theta_i\sin\alpha_i & a_i\cos\theta_i \\ \sin\theta_i & \cos\theta_i\cos\alpha_i & -\cos\theta_i\sin\alpha_i & a_i\sin\theta_i \\ 0 & \sin\alpha_i & \cos\alpha_i & d_i \\ 0 & 0 & 0 & 1 \end{bmatrix}, \tag{1} $$

$$ {}^{0}_{n}T = {}^{0}_{1}T \cdot {}^{1}_{2}T \cdots {}^{n-1}_{n}T = \prod_{i=1}^{n} {}^{i-1}_{i}T, \tag{2} $$

$$ {}^{0}_{n}T = \begin{bmatrix} R_n^0 & P \\ 0 & 1 \end{bmatrix} = \begin{bmatrix} n_x & o_x & a_x & P_x \\ n_y & o_y & a_y & P_y \\ n_z & o_z & a_z & P_z \\ 0 & 0 & 0 & 1 \end{bmatrix}. \tag{3} $$

Chassis walking is the basis for the robot to complete GIS equipment inspection functions, the right chassis motion system designed in this paper needs to achieve way motion on the surface; Figure 8 is the calculation diagram of the chassis in the plane movement, and its motion inverse solution in plane motion is given in the following equation:

$$ \begin{bmatrix} v_1 \\ v_2 \\ v_3 \\ v_4 \end{bmatrix} = \begin{bmatrix} -\cos\alpha - \sin\alpha & -\cos\alpha + \sin\alpha & m+n \\ -\cos\alpha + \sin\alpha & -\cos\alpha - \sin\alpha & m+n \\ \cos\alpha + \sin\alpha & \cos\alpha - \sin\alpha & m+n \\ \cos\alpha - \sin\alpha & \cos\alpha + \sin\alpha & m+n \end{bmatrix} \begin{bmatrix} v_x \\ v_y \\ \omega \end{bmatrix}. \tag{4} $$

In equation (4), v_1, v_2, v_3, v_4 is the speed of three wheels, ω is the rotation angle speed, and v_x, v_y is the speed in the body coordinate system, that is, the relative speed, because the chassis speed performance is independent of the attitude in the world coordinate system, so here is a simplified operation: take the body coordinate system and the world coordinate system X, Y direction rematch; m, n is the x and y distance from the center of rotation to the axis of the wheel which is half the length and width of the chassis; $\theta = 45^\circ$ is the angle between the axle and the x-axis. When moving on a surface, considering that the robot only needs to maintain a definite attitude when moving on the surface, the forward- and cross-shifting in the pipe can be achieved by the characteristics of the wheel chassis, so the angle velocity ω is constantly 0, which brings convenience to the solution of surface motion. Since the deformation of the chassis does not affect the change of the attitude angle α and it is expressed in equation (1) and only changes the wheel base, the motion model of the GIS inspection robot when climbing on the surface is consistent with the plane motion model.

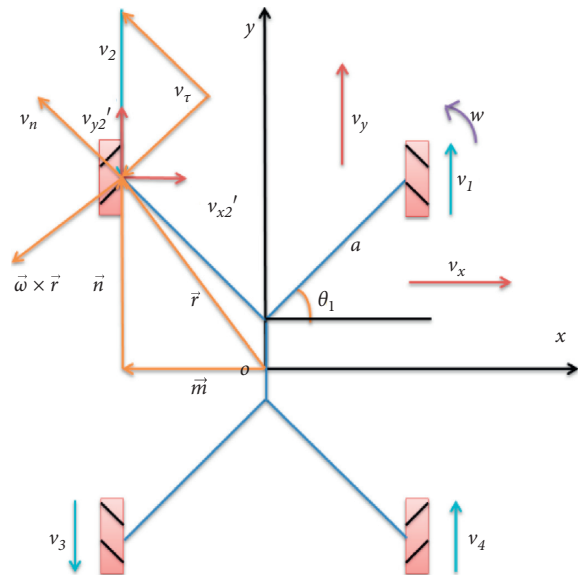

Figure 8: Map of the wheel chassis plane.

4.2. Analysis and Simulation of the Characteristics of Robot Climbing. GIS inspection robot in the three-dimensional wall climbing will affect the stability and flexibility of motion due to changes in the direction of gravity; in this section, through the up and down analysis on vertical wall and cantilever surface in three situations, their own acceleration curve is obtained and the GIS inspection robot start-up momentary acceleration changes and motion stability are analyzed. GIS inspection robot climbing schematic is shown in Figure 9.

In the analysis of the robot motion process, three typical motion processes have been analyzed, which are moving up the wall, moving down the wall, and moving cantilever on the wall. In order to facilitate the analysis, the physical amount involved in the motion process can be simplified, the GIS robot adsorption force in the condition of the three attitudes can be provided by the Halbach magnetic array, and the adsorption force is uniform and the motor drive force is continuous. Based on the above hypothesis, it can be obtained that when the GIS inspection robot moves up the vertical wall, its motion equation is equation (5), when the robot moves down the vertical wall, its motion equation is equation (6), when the robot moves along the horizontal suspension wall, its motion equation is equation (7), and the GIS robot friction force when moving on the wall is equation (8):

$$ M \cdot \ddot{y} = F_{\text{drive}\,1} - c \cdot F_f - G, \tag{5} $$

$$ M \cdot \ddot{y} = F_{\text{drive}\,2} - c \cdot \dot{y} - F_f + G, \tag{6} $$

$$ M \cdot \ddot{x} = F_{\text{drive}\,3} - c \cdot \dot{x} - F_f, \tag{7} $$

$$ F_f = \mu \sum N_i. \tag{8} $$

In the above equations, M represents the total mass of the robot (kg), F_{drive1} represents the total driving force of the wheel motor when the robot moves upward, x represents the

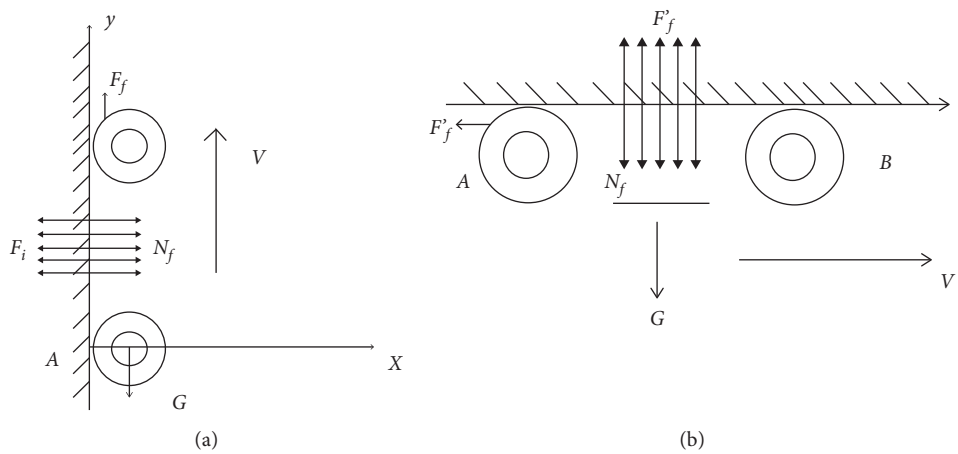

Figure 9: Analysis schematic of climbing characteristics. (a) Vertical schematic; (b) cantilever schematic.

acceleration of the robot, x indicates the speed of the robot, G represents the gravity of the robot system, F_f represents the total sliding friction of the robot, C represents the damping coefficient obtained by a combination of various factors when the robot moves, unit is N/ms, μ represents the coefficient of friction between the McNem wheel and the wall, F_{drive2} represents the total motor-to-wheel drive when the robot moves down, and F_{drive3} represents the total motor-to-wheel drive when the robot moves downwards, which represents the acceleration of the robot when moving horizontally and the speed of the robot when moving horizontally.

5. Simulation and Field Operation Experiment

5.1. Simulation Experiments and Analysis. In this paper, *ANSYS Maxwell* electromagnetic simulation software has been used to simulate the magnet adsorption unit; the magnetic force size of the magnet and the adsorption wall surface can be obtained under different gaps. The simulation parameters are selected as follows: steel-1010 sheet with a 5 mm thickness is placed on each side of the double magnetic adsorption arrays, and the magnetic magnetization direction is specified in accordance with the above rules and the distance between the magnetic adsorption module and the wall surface is used as a sweep parameter, with a range of 3 mm to 8 mm. Finally, the adsorption force of the magnetic adsorption module on the wall surface can be concluded, and the simulation data in Figure 10 can be obtained in Table 1; it can be seen that the magnetic force generated by the ordinary array on both sides of its adsorption unit is exactly the same in the simulation environment; the Halbach array almost eliminates the magnetic field on one side and the magnetic force generated on the other side has greatly increased, about twice that of the ordinary array.

Through the above analysis, we can get the mathematical relationship model between the adsorption force, friction force, robot total mass, and motor total driving moment of Halbach magnetic array in three cases. The robot motion instantaneous acceleration and stability analysis can be carried out by solving the above system and can be simulated using MATLAB/Simulink software; the structure of the Simulink block is shown in Figure 11.

Through running the Simulink simulation, we can obtain the acceleration curve of the robot in three cases, as shown in Figure 12, where the robot starts with a momentary impact, and when the robot moves up the vertical wall, the instantaneous acceleration can reach 7 m/s^2, at which point the robot is subjected to the greatest instantaneous impact, and, again, the momentary acceleration of the downward movement can reach 6 m/s^2, and the instantaneous acceleration along the horizontal cantilever surface is 4 m/s^2. With the increase of start-up time, the robot is subject to self-vibration caused by the discontinuous design of the outer roller of the Mecanum wheel; the robot motion acceleration has rapidly reduced and eventually became zero, at which point the robot will begin to move at a constant speed; that is, the robot will soon reach a stable state, which indicates that the GIS climbing robot system designed in this paper has a certain degree of motion stability.

5.2. GIS Robot Climbing Performance Experiments and Analysis. In this section, the adsorption experiments have been conducted in different environments for the GIS robot prototype, which have been tested in different thicknesses and different wall environments; the gap between the wall surface and the magnetic array was 2 mm during the experiment. Figure 13 is the field operation experiment, with the four typical motion states, respectively, in Figures 13(a)–13(d); in GIS equipment steel pipe suspension surface and vertical wall surface walking experiments, the experimental plane is relatively flat and barrier-free; the robot runs smoothly; overall, GIS inspection robot on different wall surface adaptability and adsorption force meets the climbing requirements of GIS equipment maintenance process; in this simulated working environment, its wall thickness is much

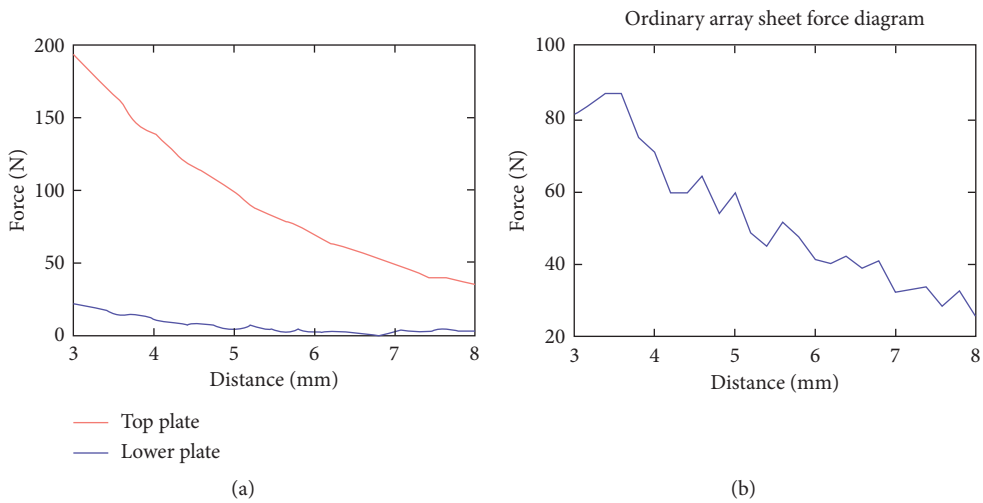

Figure 10: The force contrast of two magnetic arrays on wall surfaces. (a) Force diagram of Halbach array sheets; (b) force diagram of ordinary array sheets.

Table 1: Force data of Halbach array and ordinary array sheets.

Force	Halbach array sheets		Ordinary array sheets (N)
	Top plane (N)	Lower plane (N)	
Max	192	22	86
Min	38	2	12

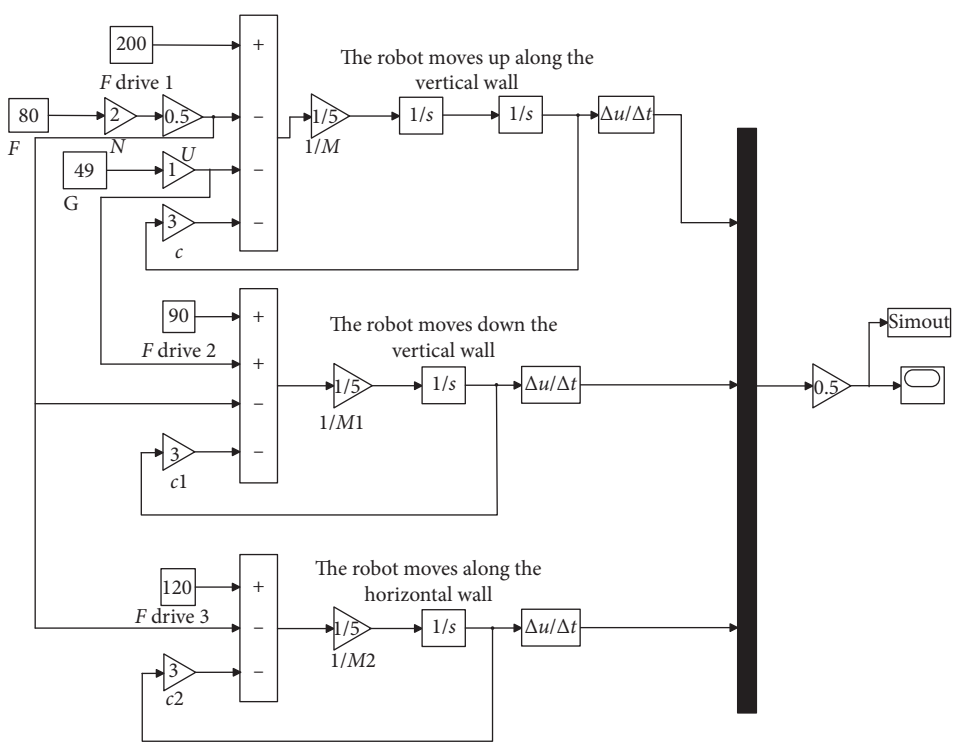

Figure 11: GIS robot control system based on MATLAB/Simulink simulation.

larger than the tin cabinet wall; therefore, the GIS inspection robot can also meet the actual GIS equipment inspection and maintenance needs.

5.3. GIS Robot Field Operation Experiments and Analysis. Selection of the typical GIS equipment was under the jurisdiction of the live working operation center, State Grid

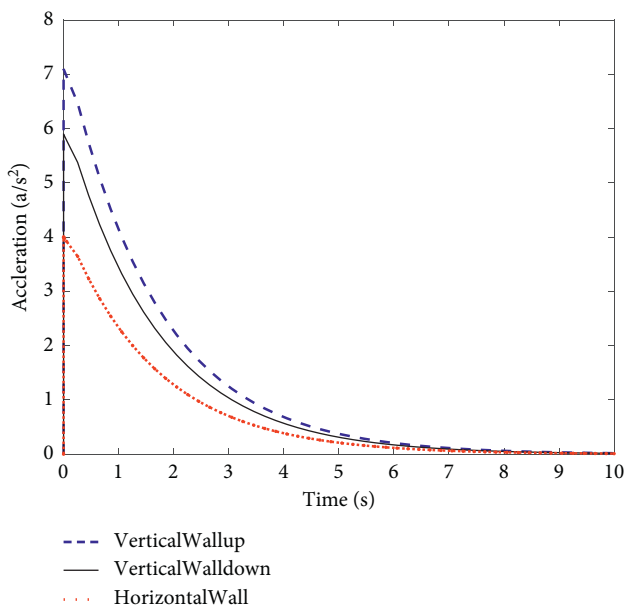

Figure 12: MATLAB/Simulink simulation results.

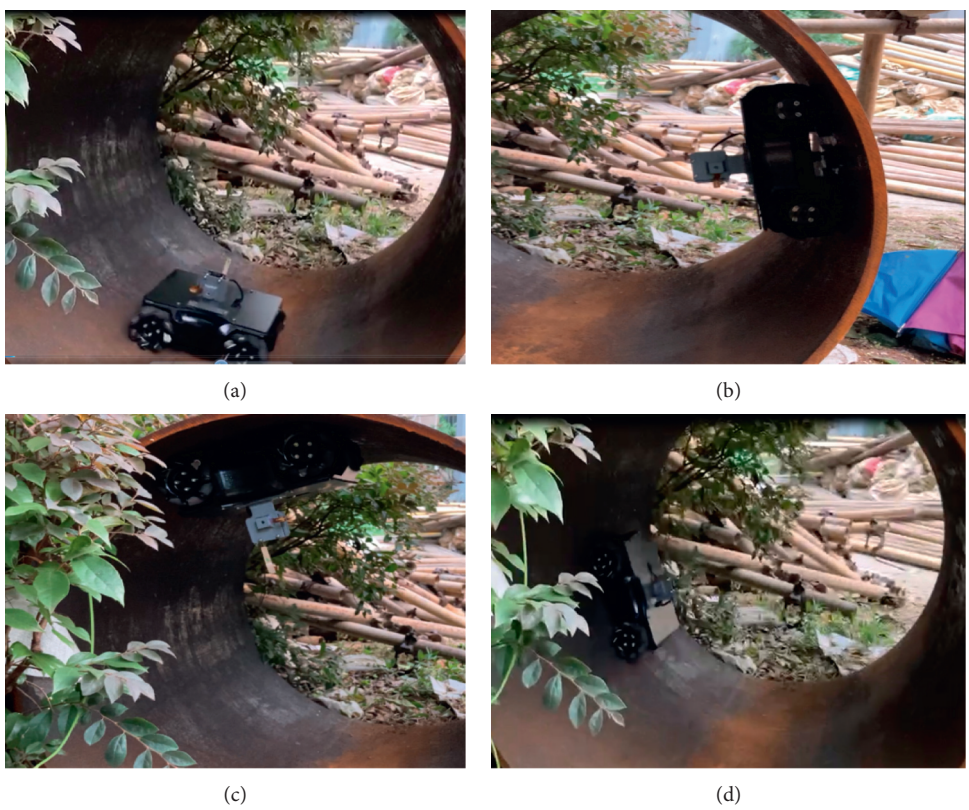

Figure 13: GIS inspection robot climbing performance experiment in simulated environment. (a) Horizontal (initial state), (b) right vertical wall, (c) left vertical wall, and (d) return to initial state.

Hunan Electric Power Co., Ltd.; the inspection operation field experiment has been carried out; Figure 14 shows the movement and inspection status of the GIS inspection robot inside the GIS equipment. It can be seen from the experimental results that the robot can move freely inside the GIS equipment and can realize maintenance operations at any position. Through the operation experiment, the main performance indexes of GIS inspection robot can be obtained and are shown in Table 2; regarding the structure, the robot is small in size and light in weight, which is suitable for

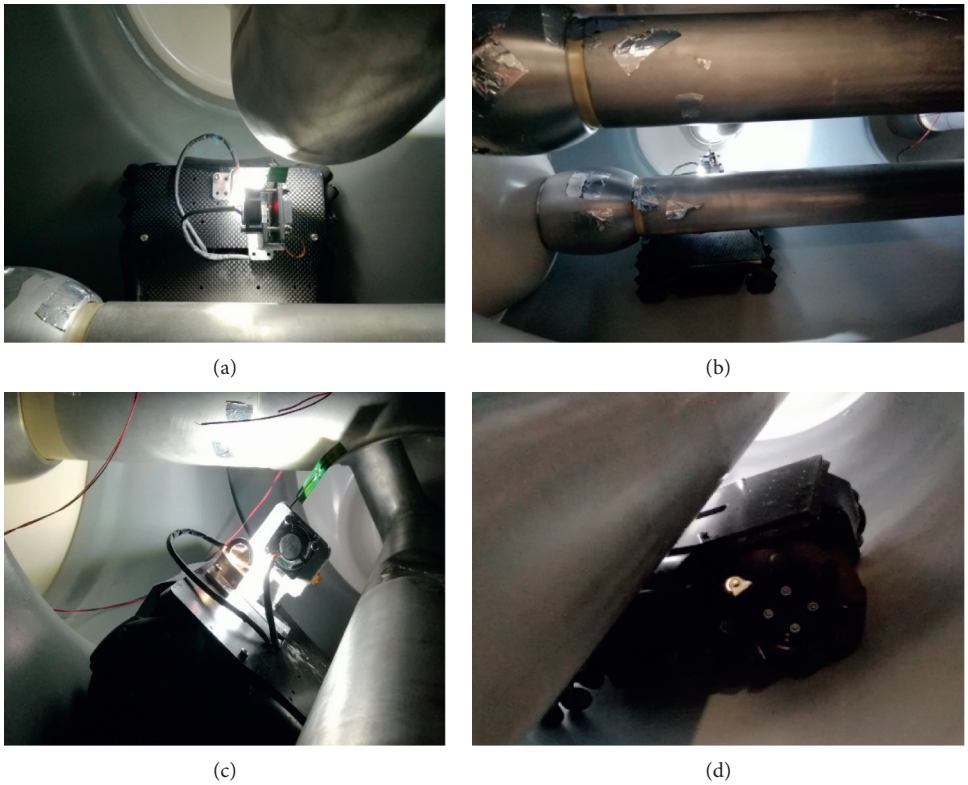

Figure 14: GIS inspection robot field operation experiment. (a) GIS robot field operation state 1, (b) GIS robot field operation state 2, (c) GIS robot field operation state 3, and (d) GIS robot field operation state 4.

Table 2: The main performance indexes of GIS inspection robot.

Main performance indexes	Performance indexes values	Operation process status (whether meeting the operation requirements)
Robot operational efficiency (inspection speed)	3 m/2 min	OK
Main operation objects positioning accuracy	1 mm	OK
Man-machine interaction communication distance	50 m	OK
Overall size of GIS robot	221 × 188 × 154 mm	OK
Total mass of GIS robot	3.3 kg	OK

maintenance in GIS equipment; regarding the other aspects, compared with manual operation, GIS robot inspection efficiency is high, obstacle fault location is more accurate, and remote wireless communication control can be achieved; therefore, the GIS inspection robot developed in this paper has strong engineering practicability in the power system.

6. Conclusions and Future Work

6.1. Conclusions

(1) A basic configuration of GIS inspection robot based on adsorption capability has been proposed, which can climb along the GIS equipment suspension surface and vertical surface, as well as a method for motion planning of maintenance and inspection operations without blind spots within GIS equipment

(2) The typical state force model of GIS inspection robot has been established in the process of internal inspection of GIS equipment, the force model of vertical and overhang surface has been established, the characteristics of its magic have been analyzed, and the robust stability control method of GIS inspection robot has been proposed

(3) An embedded integrated control system architecture and physical implementation method of GIS inspection robot have been proposed, a physical prototype system of GIS inspection robot has been developed, and the feasibility and effectiveness of GIS inspection robot operation have been verified by simulation and field experiments in complex microgrid networks

6.2. Future Work. GIS inspection robot replaces manual operation to complete the task in the narrow working space

of GIS equipment; the main research directions in the future include two parts: one is how to locate the obstacles and work objects independently in the narrow working space of GIS equipment, and the other is how to locate the obstacles and work objects without collision in the narrow working space of GIS equipment; therefore, in the complex operation environment, especially in the disturbance motivation, how to stabilize the robot's operation, that is, the robustness of the robot's operation, will be the focus of the follow-up research.

Data Availability

The data used to support the findings of this study are included within the article.

Conflicts of Interest

The authors declare that they have no conflicts of interest.

Acknowledgments

This work was supported by the Science and Technology Project of Hunan Electric Power Company (B116A320001D-16-16) and 2020 Opening Fund for Hubei Key Laboratory of Digital Textile Equipment (DTL2020010).

References

[1] K.-H. Seok and Y. S. Kim, "A state of the art of power transmission line maintenance robots," *Journal of Electrical Engineering and Technology*, vol. 11, no. 5, pp. 1412–1422, 2016.

[2] X. Yue, H. Wang, and Y. Jiang, "A novel 110 kV power line inspection robot and its climbing ability analysis," *International Journal of Advanced Robotic Systems*, vol. 14, no. 3, pp. 1–10, 2017.

[3] C. M. Shruthi, A. P. Sudheer, and M. L. Joy, "Optimal crossing and control of mobile dual-arm robot through tension towers by using fuzzy and Newton barrier method," *Journal of the Brazilian Society of Mechanical Sciences and Engineering*, vol. 41, no. 6, pp. 245–270, 2019.

[4] C. Antonini, M. Innocenti, T. Horn, M. Marengo, and A. Amirfazli, "Understanding the effect of superhydrophobic coatings on energy reduction in anti-icing systems," *Cold Regions Science and Technology*, vol. 67, no. 1-2, pp. 58–67, 2011.

[5] S. Farhadi, M. Farzaneh, and S. A. Kulinich, "Anti-icing performance of superhydrophobic surfaces," *Applied Surface Science*, vol. 257, no. 14, pp. 6264–6269, 2011.

[6] S. A. Kulinich and M. Farzaneh, "On ice-releasing properties of rough hydrophobic coatings," *Cold Regions Science and Technology*, vol. 65, no. 1, pp. 60–64, 2011.

[7] Y. Wang, J. Yan, Q. Sun, J. Li, and Z. Yang, "A MobileNets convolutional neural network for GIS partial discharge pattern recognition in the ubiquitous power internet of things context: optimization, comparison, and application," *IEEE Access*, vol. 7, pp. 150226–150236, 2019.

[8] X. Fu, H. Feng, and X. Gao, "UAV mobile ground target pursuit algorithm," *Journal of Intelligent & Robotic Systems*, vol. 68, no. 3-4, pp. 359–371, 2012.

[9] W. Wang, G.-P. Wu, Y.-C. Bai et al., "Hand-eye-vision based control for an inspection robot's autonomous line grasping," *Journal of Central South University*, vol. 21, no. 6, pp. 2216–2227, 2014.

[10] E. Peri and A. Tal, "A sustainable way forward for wind power: assessing turbines' environmental impacts using a holistic GIS analysis," *Applied Energy*, vol. 279, Article ID 115829, 2020.

[11] J.-Y. Park, J.-K. Lee, B.-H. Cho, and K.-Y. Oh, "An inspection robot for live-line suspension insulator strings in 345 kV power lines," *IEEE Transactions on Power Delivery*, vol. 27, no. 2, pp. 632–639, 2012.

[12] J. Lai, X. Lu, X. Yu, and A. Monti, "Cluster-oriented distributed cooperative control for multiple ac microgrids," *IEEE Transactions on Industrial Informatics*, vol. 15, no. 11, pp. 5906–5918, 2019.

[13] J. Lai, X. Lu, X. Yu, and A. Monti, "Stochastic distributed secondary control for ac microgrids via event-triggered communication," *IEEE Transactions on Smart Grid*, vol. 11, no. 4, pp. 2746–2759, 2020.

[14] T. Q. Ngo, Y. N. Wang, and T. L. Mai, "Robust adaptive neural-fuzzy network tracking control for robot manipulator," *International Journal of Computers Communications & Control*, vol. 7, no. 2, pp. 341–352, 2016.

[15] R. Miller, F. Abbasi, and J. Mohammadpour, "Power line robotic device for overhead line inspection and maintenance," *Industrial Robot: An International Journal*, vol. 44, no. 1, pp. 75–84, 2017.

[16] V. Alakshendra and S. S. Chiddarwar, "Simultaneous balancing and trajectory tracking control for an omnidirectional mobile robot with a cylinder using switching between two robust controllers," *International Journal of Advanced Robotic Systems*, vol. 14, no. 6, pp. 1–12, 2017.

[17] G. Mamani, J. Becedas, and V. Feliu, "Sliding mode tracking control of a very lightweight single-link flexible robot robust to payload changes and motor friction," *Journal of Vibration and Control*, vol. 18, no. 8, pp. 1141–1155, 2012.

[18] N. Xu and T. Ishihara, "Analytical formulae for wind turbine tower loading in the parked condition by using quasi-steady analysis," *Wind Engineering*, vol. 38, no. 3, pp. 291–309, 2014.

[19] Y. Luo, H. Liu, H. Xue, and K. Lin, "Large-eddy simulation evaluation of wind loads on a high-rise building based on the multiscale synthetic eddy method," *Advances in Structural Engineering*, vol. 22, no. 4, pp. 997–1006, 2019.

[20] J. Lai and X. Lu, "Nonlinear mean-square power sharing control for ac microgrids under distributed event detection," *IEEE Transactions on Industrial Informatics*, vol. 17, no. 1, p. 219, 2021.

Hindawi
Complexity
Volume 2021, Article ID 6659879, 12 pages
https://doi.org/10.1155/2021/6659879

Research Article

Security Risk Analysis of Active Distribution Networks with Large-Scale Controllable Loads under Malicious Attacks

Jiaqi Liang,[1] Yibei Wu,[2] Jun'e Li,[1] Xiong Chen,[3,4,5] Heqin Tong,[3,4,5] and Ming Ni[3,4,5]

[1]*Key Laboratory of Aerospace Information Security and Trusted Computing, Ministry of Education, School of Cyber Science and Engineering, Wuhan University, Wuhan 430072, China*
[2]*Electric Power Research Institute of State Grid Jiangsu Electric Power Co., Ltd., Nanjing 211106, China*
[3]*NARI Group Corporation (State Grid Electric Power Research Institute), Nanjing 211106, China*
[4]*NARI Technology Co., Ltd., Nanjing 211106, China*
[5]*State Key Laboratory of Smart Grid Protection and Control, Nanjing 211106, China*

Correspondence should be addressed to Jun'e Li; jeli@whu.edu.cn

Received 23 November 2020; Revised 20 January 2021; Accepted 9 February 2021; Published 20 February 2021

Academic Editor: Xin Li

With the development of distributed networks, the remote controllability of the distributed energy objects and the vulnerability of user-side information security protection measures make distributed energy objects extremely vulnerable to malicious control by attackers. Hence, the large-scale loads may produce abnormal operation performance, such as load casting/dropping synchronously or frequent and synchronous casting and dropping, and hence, it can threaten the security and stable operation of the distribution networks. First, we analyze the security threats faced by industrial controllable load, civil controllable load, and the gains and losses of attacks on the distribution networks. Considering the factors of cyber attacks, we propose a control model and cyber attack model in active distribution networks (ADNs). And, three types of attacks that the target suffered are defined on the basis of "on" and "off" modes for control. Then, the controllable load was maliciously controlled as the research object, and a suitable scenario is selected. The impact of malicious control of the controllable load on the power supply reliability and power quality of the distribution networks are simulated and analyzed, and risk consequences for different types of attacks are provided.

1. Introduction

With the development of power grid, distributed generation (DG) provided to the distribution networks and suppling the power for surrounding users is an inevitable trend [1, 2]. Hence, the development of distributed energy storage (DES) and controllable load (CL) has greatly promoted the consumption of DG in the distribution networks. The DG, DES, and CL constitute the distributed energy objects in the ADNs. The coordinated control of distributed energy objects through the communication method greatly increases the flexibility and initiative of the distribution networks [3, 4]. However, it also introduces new security risks in the stable operation of the distribution networks. In the meantime, the development of the Internet of things (IoT) enables more and more distributed energy objects to be controlled by the users [5]. For example, DG can be owned by users or third-party companies. Smart homes are moving towards remote control via the Internet. Electric vehicle charging and discharging stations and the terminals of controllable industrial load may be physically touched by users [6]. Therefore, the vulnerability or deficiency of security measures on the user side may make distributed energy objects easier to be controlled by the attackers, which affects the security and stable operation of the distribution networks. If the DG is abnormally started or stopped due to malicious intrusion, the large-scale CLs are synchronously casted/dropped, there is frequent and synchronous casting/dropping caused by malicious controlling, or the DES has abnormal behavior because of cyber attacks, which will break the balance between the electricity supply and demand in the distribution networks. It also disrupts the security and stable operation of

the distribution networks, even causing power-grid cascading failures, collapses, and large-scale outages [7]. This impact may be amplified in ADNs with deep penetration of distributed energy objects.

With the increasing number of incidents of hostile forces attack on critical infrastructure through cyber space, it shows that the cyber attack through the intrusion of cyber space may have a serious impact on the physical system, such as the Iranian nuclear power plant uranium centrifuge damage in 2010 and the Ukrainian power grid outage in 2015 [8]. Therefore, when distributed energy objects suffer from attacks, how to ensure the security and stable operation of ADNs is an urgent problem.

The impact of cyber security risk on power grid operation has been paid more attention. Langner et al. [9] reviewed the process of malware intrusion from cyber technology layer and finally have studied the destructive effects on the physical layer. The Iranian nuclear power plant STUXNET incident is taken as an example, which illustrates the "cyber physical warfare" and related technology mechanism. The studies in [8, 10, 11] analyze the process of large-scale power-grid paralysis caused by hacker attack in Ukraine and put forward some thoughts on power-grid cyber security protection. Sun et al. [12] take the Ukrainian outage as an example and define a cyber-coordinated attack on the power system, which is characterized by devices launched from the cyber space and acting on the physical space. Dán et al. [13] pointed out that, with the development of control and communication technology, the primary power system and the secondary power system deeply interact with the cyber physical power system. When certain (some) equipment of the primary power system or the secondary power system is out of order (due to network attacks, natural disasters, etc.), the impacts caused by it are very likely to spread to the other party's network, causing cascading failure that can seriously impact the safe and stable operation of the power system and causing significant economic losses. Sridhar et al. [2] emphasize the importance of studying the potential impact of cyber attacks, and in order to ensure cyber security, it is necessary to study the cyber-physical relationship of smart grid and the possible attack paths. Rasim et al. [14] illustrate the transmission mechanism of cyber security risks in ECPS and explain the cyber security risks in ECPS and the role of cyber space in physical space with the characteristics of cross-space transmission. Dong et al. [15] analyze the attack modes on ECPS from the perspective of attackers, including attack modes and their harms selected to achieve different goals. However, this kind of research is still relatively preliminary and focuses on general issues. The specific modes of cyber security attacks and their effects on the stable operation of the power grid have not been excavated, and hence, targeted security defense strategies cannot be established. Komninos et al. [16] investigated a number of attacks on smart grid from direct load shifting to smart meter data manipulation. Specifically, in single, small-scale attacks, adversaries can control certain IoT devices, such as smart homes in the smart grid. Using their control, an adversary can induce an abnormal working state in the device, increasing the power usage of the household. In certain cases, aggressive adversaries can cause damage to the devices and their surroundings and even threaten the personal safety of users [17–20]. In terms of large-scale cyber attacks, adversaries can compromise many high-wattage IoT devices to manipulate the power demand in a larger smart grid. For example, Saleh et al. [21] demonstrated a large-scale attack model on real-world grids, using a botnet to turn on and off a large number of IoT devices synchronously, resulting in massive power fluctuations with the potential to cause a large-scale blackout.

At present, there are few studies on the risk of distributed energy objects being maliciously controlled by the attackers. In the research of distributed energy objects in distribution networks, most of the research is on DG, but little about cyber security and cyber attacks [22, 23]. Murty et al. [24] study the impact of DG connection to the distribution networks, which is mainly due to the random fluctuation of DG and has nothing to do with malicious control. Nikolaidis et al. [25] design the protection schemes of the distribution networks with DG, and these schemes are mainly based on the conventional failure of power grid, without considering cyber attacks from the cyber space. Clement-Nyns et al. [26] study the impacts of a large scale of electric vehicle power-charging connection to the distribution networks and propose intelligent charging strategies to optimize the distribution networks' operation, but the study does not consider the situation of charging stations under the cyber attacks. Munkhammar et al. [27] propose the residential electricity-consumption probability model based on residents' habits and formulate a load demand response plan so that residential loads can become participants in optimizing the operation of the distribution networks. Although this behavior may have an impact on the distribution network, unlike the load being maliciously controlled, such impact can be reduced through the policy guidance of the power company [28, 29].

It can be seen that the current research is mainly focused on the active application of communication control methods in the distribution networks, such as demand-side management (DSM), "source" and "load" optimization control, and microgrid control strategies. The security risk introduced to the distribution networks by the popularization of communication technology is seldom considered from the perspective of the attackers. The diversity of access components for the distribution networks increases the difficulty of unified management. Generally, the operating status of the distribution networks is determined by the regulation of the power grid side and the load usage of the user side. Mohsenian-Rad et al. [17] pointed out that the attacker would break the normal order of power grid load management, but this research only considered the attacks on the load management system by penetrating the cyber network and did not consider the security risk of the load being maliciously controlled. Adrian et al. [30] analyzed the risk of large-scale controllable loads in the malicious attack scenario, but they did not analyze the response characteristics of controllable loads. Zhang et al. [31] used ultrasound to activate the voice recognition system of the smart homes and

remotely manipulate voice assistants such as Siri and Hivoice in order to disrupt the distribution network operation. The studies in [30, 31] show that if the attackers can maliciously control cell phones and send turn "on"/"off" commands to smart homes successfully, it can result in a serious imbalance of the power flow in the 10 kV feeder line and bring serious security risks to the safety and stable operation of the distribution network. To sum up, there are few literature works on the impacts of cyber attacks from the user side on distribution networks.

Through the analysis of the above research status, it can be seen that there are few literature works considering the cyber security on the ADNs [32]. The large-scale access of CLs and high-permeability access of DGs are inevitable trends in the development of the distribution networks. Therefore, this paper analyzes the security threats faced by distributed energy objects in ADNs and establishes control models and attack models within ADNs. Then, we focus on this problem through analyzing the impact of large-scale CLs being maliciously controlled on the ADNs and explore abnormal operating characteristics of the ADNs caused by the CLs being maliciously controlled. Hence, this paper discovers the risks of ADNs and provides a basis for the research of ADNs' security control methods in order to help the further development of smart grids.

The rest of this paper is organized as follows: In Section 2, the security threat analysis is introduced. Section 3 considers cyber attacks with the control model, and the cyber attack model in ADNs are proposed. In Section 4, the impact of large-scale CL attacks on ADNs is analyzed. Finally, some conclusions are drawn in Section 5.

2. Security Threat Analysis

According to types of load application, CLs are divided into industrial controllable load and civil controllable load. Specifically, the industrial load is mainly controlled by the industrial control system of the load side, and the civil load is mainly controlled and used by residential users according to demand behavior.

2.1. Safety Threats to Industrial Controllable Load. Industry is of great significance in China's national economy. It is mainly engaged in large-scale production activities, and its electricity consumption accounts for about 70% of the total social electricity consumption. The scale of industrial load is very large, and the concentration ratio is very high. In fact, there is a corresponding control system, which is the industrial control system.

A typical industrial control system is shown in Figure 1, which consists of an enterprise information network, process control network, and field control network. The enterprise information network has traditional IT network attributes, such as mail sending and receiving feature, web browsing feature, enterprise resource planning (ERP), and manufacturing execution system (MES). The middle process control network is the bridge and link connecting the upper and lower layers of the network. On the one hand, it controls and dispatches the field control equipment at the bottom according to the upper-level production instructions, and on the other hand, it conducts real-time monitoring and data statistics on the production situation of the industrial site and provides information feedback for upper-level regulation. The field control network is located at the bottom of the industrial control system, which includes PLC (programmable logic controller), PAC (programmable automation controller), RTU (remote terminal unit), IED (intelligent electronic device), actuator, and other control equipment.

In the past, industrial control systems were physically isolated from external networks. The development and popularization of information communication technology (ICT) has made the field of industrial control increasingly open, and its degree of interaction with the information field has also increased. However, the internal network of the industrial control system does not perform encryption control on the data flow. Usually, as long as the user enters the internal network, any of the network equipment can be accessed, which also leads to a drop in network security [33]. In addition, because industrial control mainly considers functionality, the system behavior characteristics based on this principle and the role characteristics of behavior control personnel are more likely to become the entry point for attackers to intrude into the control system.

The requirement of industrial intelligence has promoted the development of open control systems with modular, reconfigurable, and expandable characteristics. The control network of the open control system has the opening characters. For example, the core components of the open control system are the industrial PC, which are based on the Windows-Intel platform. And, the industrial ethernet is widely used for communication between the components. At the same time, the BUS technology applies embedded systems to field control instruments [34]. In the abovementioned cases, there are loopholes in many systems, such as PC operation system, communication protocol with TCP/IP, and the embedded operation system. Meanwhile, the security protection measure of the industrial control system is mainly based on isolation from other systems, but the underlying security is more vulnerable than other information systems, and it is not subject to the information security policy of the grid management department. Therefore, the industrial controllable load is extremely vulnerable to be attacked by internal workers or external attackers [35] and this, in turn, makes the stable operation of the distribution network affected.

2.2. Security Threats to Civil Controllable Load. The civil controllable load is represented by smart homes. Smart home takes residential buildings as the platform, uses the IoT technology (including integrated wiring technology, network communication technology, and automatic control technology) to realize the interconnection of control terminals and smart homes, and realizes information exchange through the control platform. The control core of the smart home is the control platform, which is implemented by an

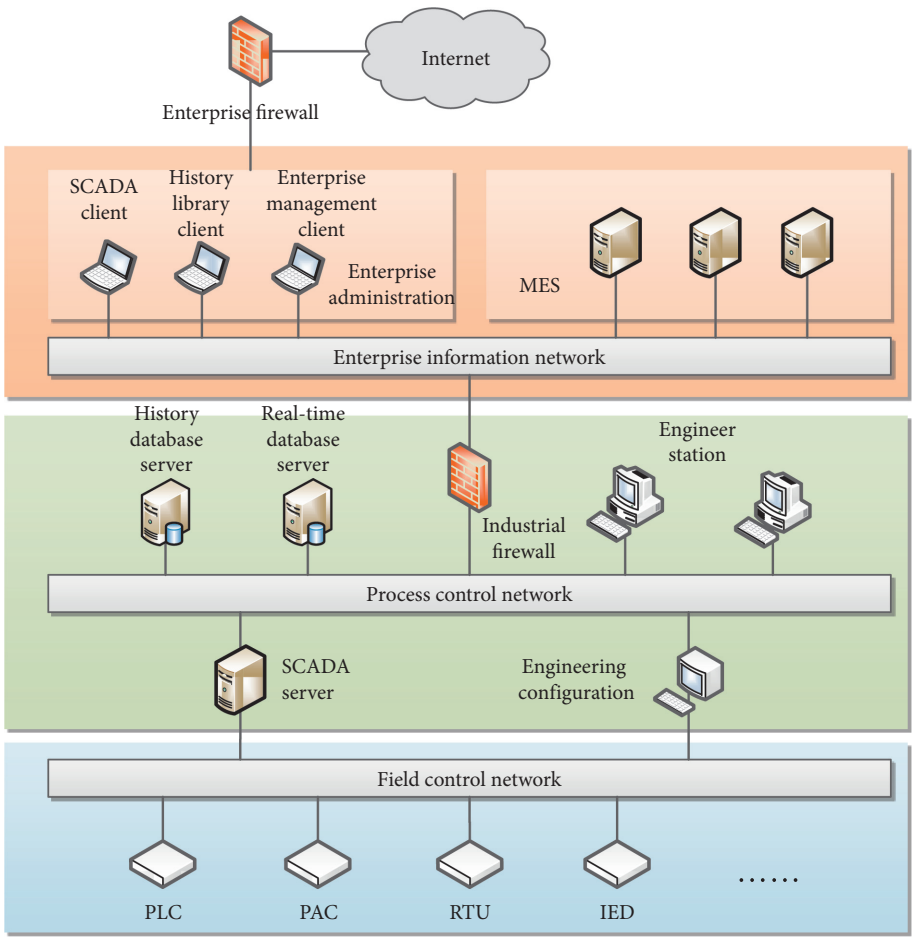

Figure 1: Industrial control system.

embedded microprocessor and can be connected to a control terminal (mobile phone or PC) via the Internet to achieve remote control. The control system of the smart home adopts a three-layer structure design [36]. As shown in Figure 2, the core is the control platform, which is implemented by an embedded microprocessor. It can be connected to the control terminal (mobile phone or PC) via the Internet for remote controlling [37]. However, the smart home control system has almost few security protection measures. According to the characteristics of network composition, the attacker has two attack paths. The first path is to use the loopholes of the embedded system, implant malicious codes into the control platform through the public network, and directly attack the internal network of the control system, to make the smart home work in an abnormal condition. The second path is to intrude the user's control terminal. At this point, the attackers implant malicious codes into smart terminals, such as mobile phones and PCs, and the terminal issues abnormal control commands to the control platform, which eventually leads to abnormal behavior of the smart homes. When the number of the maliciously controlled smart homes is large enough, it leads to the change in load of the distribution networks suddenly and it may affect the reliability of power supply and power quality.

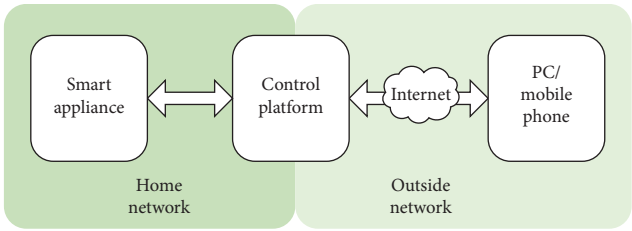

Figure 2: Smart home control system.

In summary, because the industry plays an important role in the national economy, the information security protection requirements of industrial control systems are relatively high, which leads to the cost of attacks become high accordingly. Most of the civil CLs represented by smart homes are not embedded with security mechanisms, and they can be connected to the public network with a long online time. Hence, the cost of the attack becomes extremely low, and the purpose of the attack is easy to realize. Compared with industry load, the security risk of CLs is very low. If a large-scale CL is subjected to malicious control and changes, due to the objective and unpredictable capacity, it will inevitably impact the normal operation of the distribution networks and may even cause cascading failures and

expand the scope of influence. Therefore, this paper selects CLs as the object of cyber attack for subsequent research and analysis.

3. Considering Cyber Attack with the Control Model and the Cyber Attack Model in ADNs

3.1. Control Model. The evaluation index of the distribution network includes power supply reliability, economy, security, and power quality, which are called the controlled variable and are represented by $\boldsymbol{S}$. In general, these controlled variables are determined by the electric power company, such as protection action, dispatching control, and user behavior. The connection of distributed energy objects has increased the initiative of the distribution network and promoted the development of control method diversity. Once large-scale distributed energy objects are controlled by the attackers, the dynamic balance of the distribution network may be disrupted, which can affect the normal operation of the distribution network. Attack behavior is different from normal dispatching, protection, and user behavior because it is unpredictable. Therefore, the distribution network control model with CL is shown in Figure 3, and the controlled variable is as follows:

$$S = f(g, d, u, A). \tag{1}$$

Here, g is the protection action, d isthe dispatching control, u is the normal user behavior, and A is an attack behavior.

Equation (1) is a nonlinear equation. The solution of the equation is related to the input (g, d, u, A) and the initial state of the distribution network. In the traditional distribution network, there is no attack behavior against load, and user behavior is reflected in daily life and production activities. It is a random variable that conforms to a certain law. In the meantime, the distribution network is mainly controlled by dispatching and protection action. According to the state-detection variable, the dispatching system and protection device control the distribution network, which ensures that the controlled variable S meets the requirements of the stable operation of the distribution network. In the distribution network with CLs, the added attack behavior is issued by the attackers and the distributed energy object is used as the attack object. Therefore, the DG and load dynamic balance are broken, and it is also not regulated by the power company. Finally, it may cause the controlled quantity S to deviate from the requirements of security and stable operation of the distribution network, causing safe and stable accidents.

3.2. Attack Model. The cyber attack model contains cyber element $\{M, T\}$ and physical element $P(t)$ and is defined as a double set A_u, which represents the impact mechanism of the attack from the cyber space and acts on the physical space. The attack model in which the CLs are maliciously controlled can be expressed as follows:

$$A_u = \{M, T\} \longrightarrow P(t). \tag{2}$$

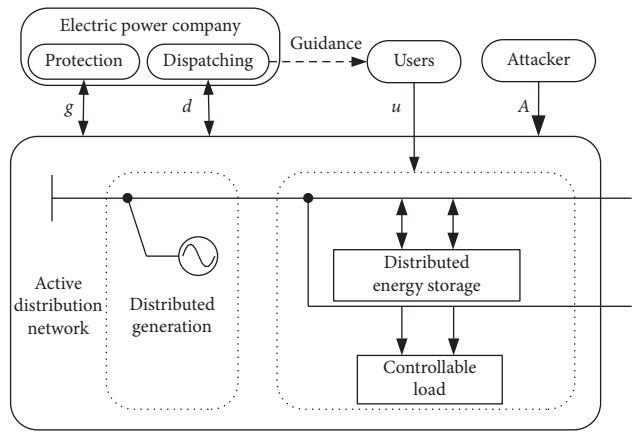

Figure 3: Distribution network control model with CLs.

Here, M is the control command, which is sent by the attackers, such as "on"/"off" represented as command M_{on}/M_{off}, namely, $M = \{M_{\text{on}}, M_{\text{off}}, \ldots\}$. Next, T is the sending time of the control command because the sending time of the cyber command has discrete characteristics, so let $T = t[n]$, where $n = 0, 1, 2, \ldots, n$, and $t[n]$ could be the sequence of time, which is sent from the control command. When large-scale CLs are maliciously controlled by cyber attacks, they are directly manifested as changes in the distribution network load. $P(t)$ is used to represent the load of the distribution network, and the symbol "$\longrightarrow$" represents the mapping relationship between the cyber attack of the information system and the load change of the power system.

Consider that after the malicious control commands are issued, some loads do not change the operating state. So the effective load control rate α is introduced; consider that the network delay and other factors may cause some control commands to be invalid and an effective attack rate β is introduced. So, $P(t)$ is composed of the normal operating load $P_0(t)$ and abnormal operating load $\Delta P(t)$. Hence, the abnormal operating load $\Delta P(t)$ can be expressed as follows:

$$\Delta P(t) = \alpha\beta P_0(t). \tag{3}$$

In this paper, we consider the abnormal operation performance of CLs, such as loads casting/dropping synchronously or frequent and synchronous casting and dropping, and based on these performances, we classify the attacks into three categories accordingly. The details are as follows.

3.2.1. Attack of Loads Casting Synchronously. At a certain point, attackers send M_{on} (synchronously "on," $M = \mathrm{M}_{\text{on}}$) commands to massive CLs. And, attack behavior can be expressed as A_u^{I}. In the meantime, $P(t)$ increases immediately, which can be expressed as follows:

$$P(t) = P_0(t) + \Delta P(t) = P_0(t) + \alpha\beta P_0(t). \tag{4}$$

In the sequence $t[n]$ of control command-sending time, $n = 0$ is the simplest form of attack of loads casting synchronously; when $n \neq 0$, the attack is to keep sending the M_{on}

command and the ADN is kept in a high-load state for a long time.

3.2.2. Attack of Loads Dropping Synchronously. At a certain point, attackers send M_{off} (synchronously "off," $M = M_{\text{off}}$) commands to massive CLs. And, attack behavior can be expressed as A_u^{II}. In the meantime, $P(t)$ reduces immediately, which can be expressed as follows:

$$P(t) = P_0(t) - \Delta P(t) = P_0(t) - \alpha\beta P_0(t). \tag{5}$$

In the sequence $t[n]$ of control command-sending time, $n = 0$ is the simplest form of attack of loads dropping synchronously; when $n \neq 0$, the attack is to keep sending the "M_{off}" command and the ADN is kept in a low-load state for a long time.

3.2.3. Attack of Loads of Frequent and Synchronous Casting and Dropping. Attackers send M_{on} and M_{off} (frequently and synchronously "on and off," $M = M_{\text{on}}$ and M_{off}) commands periodically to massiv CLs, which leads to frequent and synchronous casting and dropping of loads. And, attack behavior can be expressed as A_u^{III}. In the meantime, $P(t)$ increases and drops frequently and synchronously. If we define M_{on} command at $t = [2i]$ and send M_{off} command, while $t = [2i + 1]$, the control command M can be expressed as follows:

$$M = \begin{cases} M_{\text{on}}, & T = [2i], \\ M_{\text{off}}, & T = t[2i+1], \end{cases} \quad i = 0, 1, 2, \ldots, \tag{6}$$

At first, attackers send M_{on} command at $t = [2i]$ and the $P(t)$ will be increased $\alpha\beta P_0(t)$. Then, attackers send M_{off} command while $t = [2i+1]$ and $P(t)$ will be increased $\alpha\beta P_0(t)$, because CLs can be controlled by attackers. At M_{off} command, $\alpha = 1$ and $P(t)$ will be reduced to $\beta P_0(t)$.Therefore, $P(t)$ can be expressed as follows:

$$P(t) = \begin{cases} P_0(t) + \alpha\beta P_0(t), & t \in (t[2i]), \\ P_0(t) + \alpha\beta P_0(t) - \beta P_0(t), & t \in (t[2i+1]), \end{cases} \quad i = 0, 1, 2, \ldots, \tag{7}$$

The attackers, through setting the time interval τ ($\tau = t[n] - t[n-1]$, $n = 1, 2, 3, \ldots$) in the attack command M, can change the casting and dropping frequency of CLs and lead to abnormal performance of those CLs. It may also cause problems such as resonance in serious cases.

4. Analysis on the Impact of Large-Scale CL Attacks on ADNs

The risk of the ADNs was greatly increased when the large-scale CLs were controlled by attackers, and the power quality may also be affected. The attack also resulted in abnormal power consumption of the users and damaged the power supply equipment in severe cases. Therefore, we take the impact of attacks on power quality as an example, and the 10 KV IEEE 33-bus standard distribution system was used as the study case, as shown in Figure 4. Finally, we consider a single DG connected at the end of the line and analyze the impact of the malicious attacks.

4.1. Impact of Load-Casting Attack on Power Quality. Scenario 1: node 18 of the IEEE 33-bus standard distribution system is connected to the DG, and the penetration rate is 100%. Nodes 18, 20, 25, and 30 suffered A_u^{I} attacks ($n = 0$ and $\Delta P/P_0 = 1$).

The node branch model in the ADN is shown in Figure 5. The power flow of branch b_{ij} is from node i to node j. Based on power flow calculation, the voltage of node j can be expressed as follows:

$$V_j = V_i - \Delta V = V_i - \frac{P_j R_{ij} + Q_j X_{ij}}{V_N}. \tag{8}$$

Here, ΔV is the branch voltage drop and $V_N$is the nominal voltage. P_j and Q_j are the active and reactive power of node j, respectively; R_{ij} and X_{ij} are the resistance and reactance of the branch (i, j), respectively. According to the structural parameters of the ADN and the voltage of the power supply terminal, the voltage of each node can be calculated. When the ADN suffered A_u^{I} attacks and lead to increase of the node load, the line voltage dropped very fast and the receiving terminal voltage would also be decreasing, and so low-voltage overruns may occur. According to power quality specifications, the allowable deviation of 10 kV user voltage is ±7% of the system nominal voltage.

We assume that the load is twice the normal operating state after the attacks, and $P/P_N = 0.65$ at this moment. As shown in Figure 6, we obtain the node voltage situation curves, which represent the suffered distribution network before and after the attacks. According to the analysis of the node voltage situation curves, due to the increase of the load caused by the malicious attacks, the voltage of each node has dropped and caused addition of four new low-voltage overlimit nodes, and the power quality had been dropped as well. After further calculation, when $P/P_N > 0.52$ after the attacks, which led to the increase in the low-voltage out-of-limit node number, the power quality of these nodes does not meet the standard power quality.

Compared with the attack scenario of DG connected to the standard distribution system, the attackers need to attack a large-scale CL to make the voltage deviation go beyond the standard range. In addition, the newly added low-voltage overlimit nodes are on branches that do not include DG. Because the voltage is increased by the DG, after the cyber attacks, the voltage of the nodes with DG supply branches is at the allowable range of deviation.

We compare the node voltage distribution of the suffered branch before and after the attacks with the traditional distribution network under the same type of the attack. As shown in Figure 7, the conclusions can be drawn as follows:

(1) If the power line already contains DG and not considering the off-grid status, when it is subjected to A_u^{I} attack against CLs, the DG can be leveraged to improve the power quality of the distribution network and the line is not prone to low-voltage phenomenon.

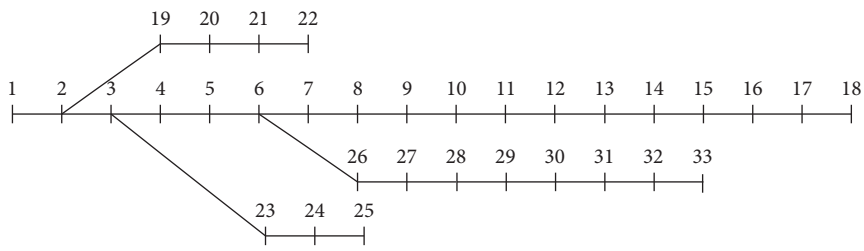

Figure 4: Diagram of IEEE 33-node standard distribution system.

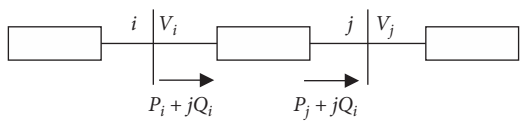

Figure 5: The node branch model.

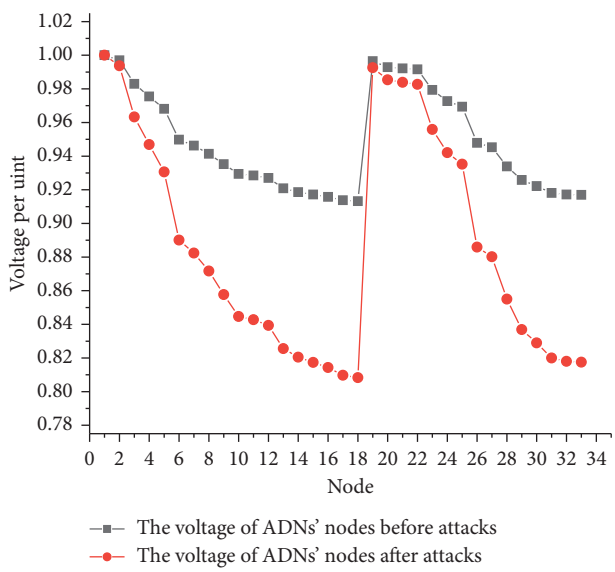

Figure 6: The voltage unit value of ADN nodes before and after A_u^{I} attack.

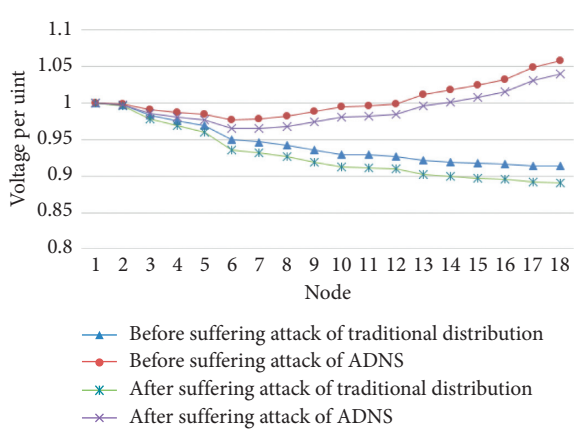

Figure 7: The voltage unit value of traditional ADN nodes before and after A_u^{I} attack.

(2) If the line contains DG and considering the off-line status, when it is subjected to A_u^{I} attack against CLs, DG may be out of operation after the attacks because of poor operation environment, and it can exacerbate voltage dropping and reduce power quality.

(3) If a DG is not connected to the power line, when it is subjected to A_u^{I} attack against CLs, the operation of the DG can be used as an adjustment strategy to improve power quality.

4.2. Impact of Load Dropping Attack on Power Quality. In the traditional distribution network, the voltage rise is caused by load dropping. However, there is only one power supply node on the power side, and it is also limited by the reference voltage. In the ADNs, DG can also provide electrical energy, if the voltage rise caused by the load dropping, it may cause high voltage to exceed the limit and reduce power quality.

Scenario 2: node 18 of the IEEE 33-bus standard distribution system is connected to the DG, and the penetration rate is 100%. Nodes 18, 20, 25, and 30 have suffered A_u^{II} attacks ($n = 0$, $\Delta P/P_0 = 1$).

In order to ensure the normal operation of the ADN, the load balance of each phase should be considered when we set up distribution lines for users. If there is load suffer due to A_u^{II} attack in this area and it is not evenly distributed on each phase line, it will cause unhomogeneous load distribution on each phase line and increases the degree of the three-phase imbalance, and while those disruptions are serious, it will also reduce the power quality.

The calculation of the three-term imbalance can be expressed as follows:

$$\varepsilon = \frac{I_2}{I_1} \times 100\%. \tag{9}$$

Here, I_1 is the effective value of the positive sequence component of the three-phase current and I_2 is the effective value of the negative sequence component of the three-phase

current. In the low-voltage power distribution system, the imbalance of the three-phase load current at the outlet of the distribution transformer should be less than 10%. For the convenience of quantification, assume that the attacked load is concentrated in one phase, that is, single phase.

In scenario 2, three-phase current on the secondary side of the transformer before and after the A_u^{II}attack is obtained through simulation, as shown in Figure 8. Before the attack, the effective value of the three-phase current $I_a = I_b = I_c = 850$ A and the degree of three-phase imbalance is 0; after the attack, the three-phase load is unbalanced, $I_a = I_b = 850$ A, and $I_c = 525$ A, and the three-phase imbalance is 14.8%. It can be seen that the three-phase balance before and after the attack exceeds the standard and the power quality does not meet the standard. Further calculation can be obtained, when single-phase $\Delta P/P_0 = 0.1$ and $\varepsilon = 10\%$. It can be obtained that when single-phase $\Delta P/P_0 > 0.1$, the three-phase imbalance degree exceeds the standard.

If the imbalance degree of three-phase voltage becomes very serious, it will increase line and transformer loss simultaneously and affect the safe operation of electrical equipment. Supplying power under unbalanced voltage conditions may easily cause the user's electrical equipment with a high-voltage one-phase connection to burn out, while the user's electrical equipment with a low-voltage one-phase connection may show abnormal work.

The suffered attack nodes dropped on a large scale in the distribution network. The voltage distribution of each node is shown in Figure 9. It can be seen that, after the A_u^{II} attacks, the voltage of each node is increasing, and the voltage per unit value of node 18 increases from 1.057 to 1.074, which has exceeded the allowable range of power quality voltage deviation and results in reduced power quality.

For the distribution network transformer, the excessive voltage not only reduced service life of transformers, but it may also cause resonance phenomena and harmonic pollution and disrupt other normally operating equipment. For electrical equipment, the excessive voltage can affect the normal operation, while the electrical equipment operated with high voltage for a long time would show reduction in service life and increase in power consumption.

To change the attack intensity, the voltage of each node is shown in Figure 10, where the corresponding attack modes from decentralized attacks to no attacks of the curve are described as follows:

(1) The decentralized attacks: all the nodes with half of the load suffered the A_u^{II} attacks

(2) The centralized large-scale attacks: nodes 18, 20, 25, and 30 of the IEEE 33-bus standard distribution system suffered A_u^{II} attacks, and it resulted in large-scale load of attacked nodes tripping from the line $P/P_N = 0$

(3) The centralized small-scale attacks: nodes 18, 20, 25, and 30 of the IEEE 33-bus standard distribution system suffered A_u^{II} attacks, and it resulted in 50% load of attacked nodes tripping from the line

(4) No attacks

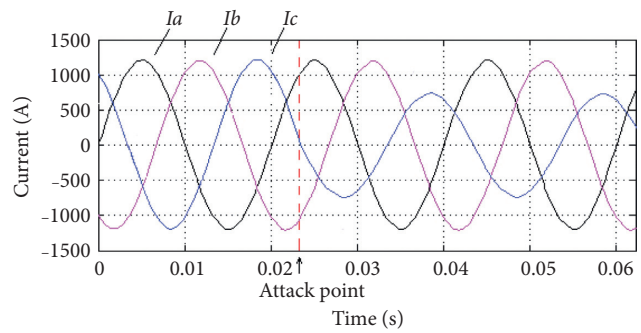

Figure 8: Three-phase current on the secondary side of the transformer before and after the A_u^{II} attack.

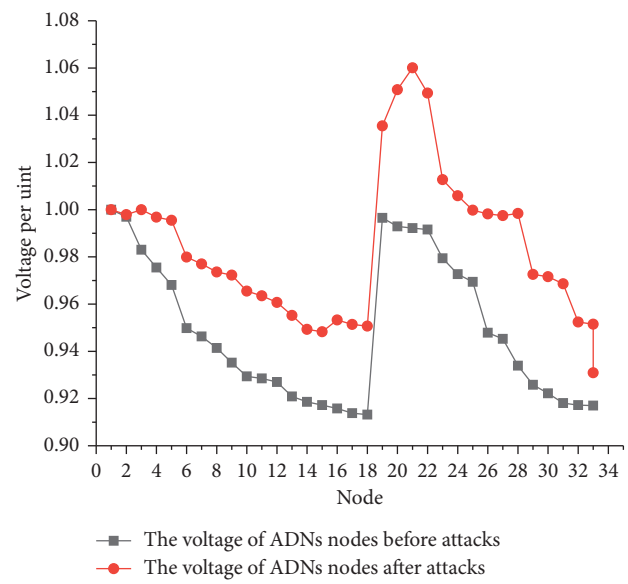

Figure 9: The voltage value of ADNs' nodes before and after A_u^{II} attack.

Among them, attack modes (1) and (2) caused the voltage to exceed the limits and reduced the power quality. Although attack mode (3) raised the node voltage, the voltage deviation index of the power quality still satisfied the specified range.

If the ADNs within a certain attack scenario, where the node 22 is connected to the DG, take this branch line as the analysis object, the voltage distribution of those nodes are shown in Figure 11. Although the node voltage increases are caused by the synchronous dropping attacks, the deviation index of the voltage still satisfied the specified range.

It can be seen that the deviation impact of A_u^{II} attacks on the load voltage of the distribution network is not only related to the attack intensity but also related to the topology of the distribution network.

4.3. Impact of Frequent Casting and Dropping of Load Attacks on Power Quality. Due to the DGs, the power system may be subjected to periodic disturbance of the load and it would cause power oscillation, that is, compelled resonance

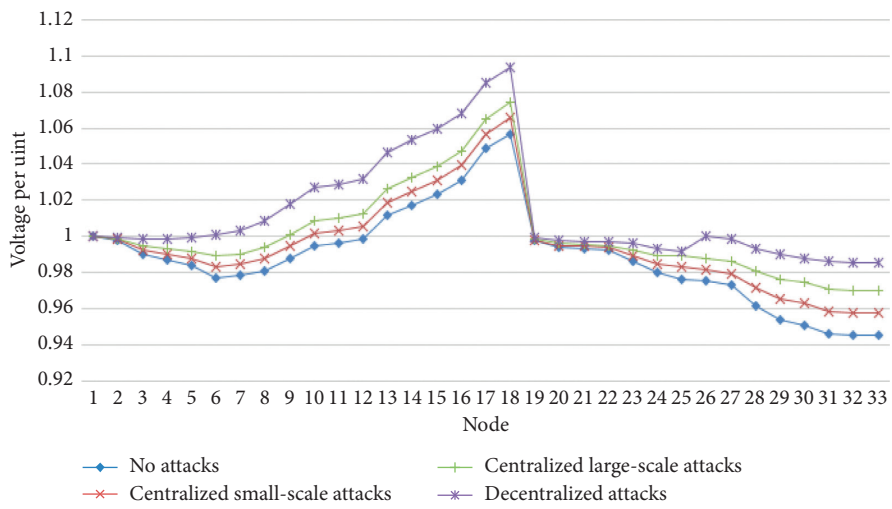

Figure 10: The voltage value of nodes before and after A_u^{II} attack under different attack modes.

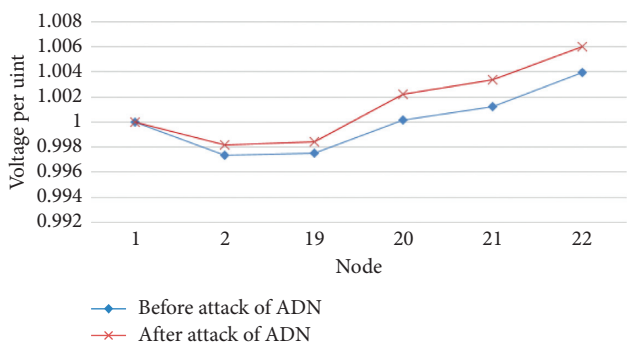

Figure 11: The partial node voltage before and after A_u^{II} attack.

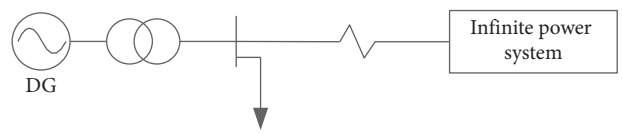

Figure 12: Single-machine (DG) infinite power system.

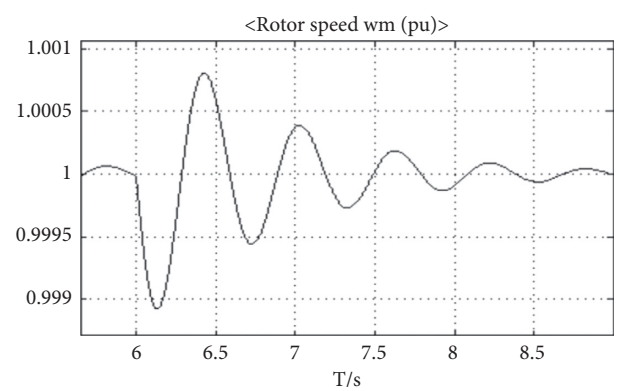

Figure 13: Rotation speed fluctuation after small disturbance.

low-frequency oscillation. The theory of compelled resonance low-frequency oscillation points out that regular small periodic disturbance in the system will cause the power oscillation. If the frequency of the disturbance is consistent with the natural frequency of the system, it will cause resonance, and the compelled oscillation amplitude of the system is the largest at this period.

Assume that the DG is directly connected to the power grid through the generator and select the connection node as a malicious attack object to construct a single-machine infinite system. As shown in Figure 12, the DG is connected into the distribution system through a 0.4 kV/10 kV booster transformer.

To cast small-scale load, while the system is running stably with light load, we can get the generator speed curve, as shown in Figure 13, and the natural oscillation frequency of the system is 1.67 Hz.

Scenario 3: the connection point of the DG suffered the A_u^{III} attack ($t[0] = 6$ s and $\Delta P/P_0 = 1$).

To change the frequency of "casting"/"dropping" of the load, while the same-scale load is attacked, we can obtain the line power curve as shown in Figure 14. When the command "on"/"off" is sent at $\tau = 0.3$ s intervals, as shown in Figure 14(a), the disturbance frequency is 1.67 Hz. When the command "on"/"off" is sent at $\tau = 0.26$ s intervals, as shown in Figure 14(b), the disturbance frequency is 1.87 Hz. When the command "on"/"off" is sent at $\tau = 0.34$ s intervals, as shown in Figure 14(c), the disturbance frequency is 1.47 Hz.

Due to the disturbance frequency being equal to the natural frequency of the system, it results in the largest amplitude of the power fluctuation; when the deviation between the disturbance frequency and the natural frequency of the system increases, the power oscillation curves can also be obtained, but the amplitude of this one is relatively small. And, the amplitude of power oscillations is also related to the scales of the attack load. Compared with Figure 14(a). While the scale of the attack load becomes 50%, the frequency of periodic disturbance is still 1.67 Hz and the oscillation amplitude becomes relatively small, as shown in Figure 15.

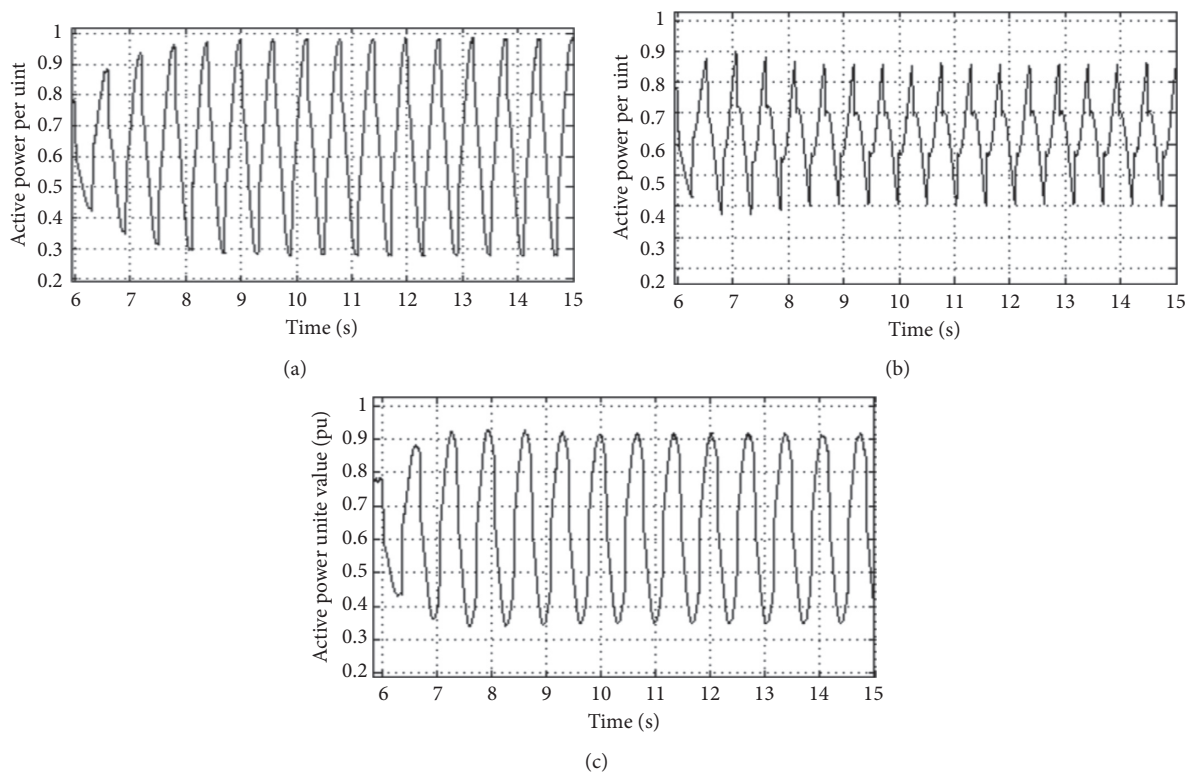

Figure 14: The active power oscillation curve of the line under different disturbance frequencies of (a) 1.67 Hz, (b) 1.87 Hz, and (c) 1.47 Hz.

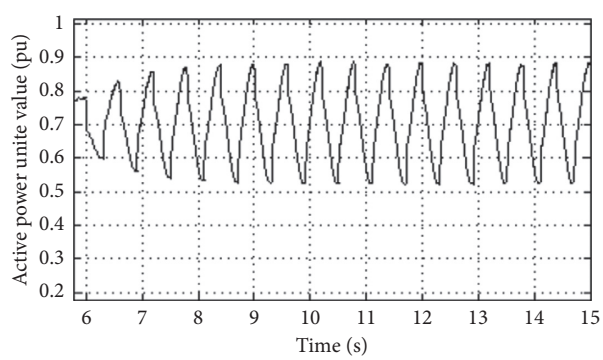

Figure 15: The active power oscillation curve of line under small-scale load attack with a disturbance frequency of 1.67 Hz.

In the traditional distribution network, the load mainly consumes electrical energy passively, and it is usually far away from the generator, with relatively scattered distribution, and it is not easy to have large-scale synchronous "casting"/"dropping". However, with the development of DG connected to the power grid and CLs, it makes the distance between the load and the generator become closer and the load would be maliciously controlled by the attackers. If the large-scale CLs are maliciously controlled and the frequency of periodic "casting" and "dropping" is close to the natural frequency of the system, it may amplify the impact of power fluctuation and affect the power quality of the distribution network.

4.4. Summary on the Influence of CLs by Malicious Control on ADNs. The power quality impact of CLs maliciously controlled by attackers on ADNs can be summarized in Table 1. Compared with the power quality of the distribution network without DG, the DG connected to the power grid can be leveraged to improve the power quality of the distribution networks, such as improving the condition of low-voltage cross-limits. However, while the CLs suffered unpredictable cyber attacks, it can result in dropping or casting of the large-scale CLs frequently and synchronously and the reliability of the distribution network is also reduced. In summary, those impacts can cause power quality problems, such as voltage deviation and voltage fluctuation, and even introduce new

Table 1: Distribution network control model with CLs.

Scenarios	Attack behaviors (A)			Risk
	Attack object	Type of attack	Scale	
IEEE 33-bus standard distribution system	Node 18/20/25/30	A_U^{I}	$1.2 > P/P_N > 0.42$	Low-voltage exceeding limits
IEEE 33-bus standard distribution system	Node 18/20/25/30	A_U^{II}	Single-phase $\Delta P/P_0 > 0.1$	High-voltage exceeding limits
Single-machine (DG) infinite power system	DG access node	A_U^{III}	$1.2 > P/P_N > 0.5$	Power fluctuation and resonance

power quality issues (such as forced resonance at low frequencies). In addition, the impact of cyber attacks on the power supply quality of ADNs is not only related to the attack modes but also related to the topology of the distribution network (such as the connection points of DG). In order to ensure the normal operation of the ADNs, the risks introduced by cyber attacks must be considered.

5. Conclusions

The introduction of distributed energy objects and the full application of communication technologies make distribution networks face new security risks. In this paper, we analyze the security risks of industrial CLs and civil CLs in the distribution networks and compare the revenue and cost of attacks from the perspective of attackers. It can be seen that the cyber attack against civil CLs can obtain a large attack revenues with a small attack cost. Then, an ADN control model considering cyber attacks is established, and at the same time, the attack behavior model is also established. In these models, it provides a clear representation of the attack object, the attack method, and the across-space impact mechanism. Taking power quality as an example, the impacts of A_U^{I}, A_U^{II}, and A_U^{III} attacks on ADNs are analyzed. In summary, the result shows that DG connected to the power grid can improve power quality, but once large-scale CLs are suffered by cyber attacks, it may also cause power quality problems and may introduce new problems, such as low-frequency compelled oscillation.

In the future, there is still a lot of work to be done against the potential security risks of the ADNs introduced by distributed energy objects. Based on the existing research results, we can continue to study the impacts of cyber attacks against civil CL on the security and stable operation of the ADNs such as refining attack models, enriching attack scenarios, and exploring the ADN operation characteristics after the attacks. In order to provide a reference for the power grid to improve its operation control strategy and formulate user-side cyber security standards, we should fully grasp the risks introduced by the CL to the ADNs. In other words, we can refer to the ADN security risk analysis of the scenario where the CLs have suffered malicious control and carry out research on other energy objects in the ADNs as the attack object. In addition, further research on the power grid cascading failures caused by cyber attacks on distributed energy objects can provide a reference for the security and stable operation of the entire power grid.

Data Availability

The data used to support the findings of this study are currently under embargo, while the research findings are commercialized. Requests for data after publication of this article will be considered by the corresponding author.

Conflicts of Interest

The authors declare that there are no conflicts of interest regarding the publication of this manuscript.

Acknowledgments

This work was supported by the Science and Technology Project of State Grid Corporation of China (Research on Cooperative Situation Awareness and Active Defense Method of Cyber-Physical Power System for Cyber Attack; no. SGJSDK00KJJS1800315).

References

[1] Q. Wang, W. Tai, Y. Tang, and M. Ni, "Review of the false data injection attack against the cyber-physical power system," *IET Cyber-Physical Systems: Theory & Applications*, vol. 4, no. 2, pp. 101–107, 2019.

[2] S. Sridhar, A. Hahn, and M. Govindarasu, "Cyber-physical system security for the electric power grid," *Proceedings of the IEEE*, vol. 100, no. 1, pp. 210–224, 2012.

[3] M. S. Mahmoud, M. M. Hamdan, and U. A. Baroudi, "Modeling and control of cyber-physical systems subject to cyber attacks: a survey of recent advances and challenges," *Neurocomputing*, vol. 338, no. 2, pp. 101–115, 2019.

[4] R. Liu, C. Vellaithurai, S. S. Biswas, T. T. Gamage, and A. K. Srivastava, "Analyzing the cyber-physical impact of cyber events on the power grid," *IEEE Transactions on Smart Grid*, vol. 6, no. 5, pp. 2444–2453, 2015.

[5] Y. Cai, Y. Cao, Y. Li, T. Huang, and B. Zhou, "Cascading failure analysis considering interaction between power grids and communication networks," *IEEE Transactions on Smart Grid*, vol. 7, no. 1, pp. 530–538, 2016.

[6] F. Liang, W. Yu, X. Liu, D. Griffith, and N. Golmie, "Toward edge-based deep learning in industrial Internet of things," *IEEE Internet of Things Journal*, vol. 7, no. 5, pp. 4329–4341, 2020.

[7] Z. Wang, M. Rahnamay-Naeini, J. M. Abreu et al., "Impacts of operators' behavior on reliability of power grids during cascading failures," *IEEE Transactions on Power Systems*, vol. 33, no. 6, pp. 6013–6024, 2018.

[8] D. E. Whitehead, K. Owens, D. Gammel, and J. Smith, "Ukraine cyber-induced power outage: analysis and practical

mitigation strategies," in *Proceedings of the 2017 70th Annual Conference for Protective Relay Engineers (CPRE)*, pp. 1–8, College Station, TX, USA, April 2017.

[9] R. Langner, "To kill a centrifuge: a technical analysis of what Stuxnet's creators tried to achieve," Technical Report, Langner Communications, Norderstedt, Germany, 2013.

[10] J. E. Sullivan and D. Kamensky, "How cyber-attacks in Ukraine show the vulnerability of the U.S. power grid," *The Electricity Journal*, vol. 30, no. 3, pp. 30–35, 2017.

[11] R. M. Lee, M. J. Assante, and T. Conway, *Analysis of the Cyber Attack on the Ukrainian Power Grid*, SANS Industrial Control Systems, Bethesda, MD, USA, 2016.

[12] C.-C. Sun, A. Hahn, and C.-C. Liu, "Cyber security of a power grid: state-of-the-art," *International Journal of Electrical Power & Energy Systems*, vol. 99, no. 4, pp. 45–56, 2018.

[13] G. Dan, H. Sandberg, M. Ekstedt, and G. Bjorkman, "Challenges in power system information security," *IEEE Security Privacy*, vol. 10, no. 4, pp. 62–70, 2012.

[14] A. Rasim, I. Yadigar, and S. Lyudmila, "Cyber-physical systems and their security issues," *Computers in Industry*, vol. 100, no. 4, pp. 212–223, 2018.

[15] P. Dong, Y. Han, X. Guo, and F. Xie, "A systematic review of studies on cyber physical system security," *International Journal of Security and Its Applications*, vol. 9, no. 1, pp. 155–164, 2015.

[16] N. Komninos, E. Philippou, and A. Pitsillides, "Survey in smart grid and smart home security: issues, challenges and countermeasures," *IEEE Communications Surveys & Tutorials*, vol. 16, no. 4, pp. 1933–1954, 2014.

[17] A.-H. Mohsenian-Rad and A. Leon-Garcia, "Distributed internet-based load altering attacks against smart power grids," *IEEE Transactions on Smart Grid*, vol. 2, no. 4, pp. 667–674, 2011.

[18] R. Chen, X. Li, and H. Zhong, "novel online detection method of data injection attack against dynamic state estimation in smart grid," *Neurocomputing*, vol. 344, no. 7, pp. 73–81, 2019.

[19] C. Fei, C. Patsios, P. C. Taylor, and Z. Pourmirza, "Using self-organizing architectures to mitigate the impacts of denial-of-service attacks on voltage control schemes," *IEEE Transactions on Smart Grid*, vol. 10, no. 3, pp. 3010–3019, 2019.

[20] S. Khan, R. Khan, and A. H. Al-Bayatti, "Secure communication architecture for dynamic energy management in smart grid," *IEEE Power and Energy Technology Systems Journal*, vol. 6, no. 1, pp. 47–58, 2019.

[21] S. Saleh, M. Prateek, and P. H. Vincent, "BlackIoT: IoT botnet of high wattage devices can disrupt the power grid," in *Proceedings of the 27th {USENIX} Security Symposium ({USENIX} Security 18)*, pp. 15–32, Baltimore, MD, USA, May 2018.

[22] Z. Dong, M. Tian, and L. Ding, "A framework for modeling and structural vulnerability analysis of spatial cyber-physical power systems from an attack-defense perspective," *IEEE Systems Journal*, pp. 1–12, 2020.

[23] T. N. Boutsika and S. A. Papathanassiou, "Short-circuit calculations in networks with distributed generation," *Electric Power Systems Research*, vol. 78, no. 7, pp. 1181–1191, 2008.

[24] V. V. S. N. Murty and A. Kumar, "Optimal placement of DG in radial distribution systems based on new voltage stability index under load growth," *International Journal of Electrical Power & Energy Systems*, vol. 69, no. 3, pp. 246–256, 2015.

[25] V. C. Nikolaidis, E. Papanikolaou, and A. S. Safigianni, "A communication-assisted overcurrent protection scheme for radial distribution systems with distributed generation," *IEEE Transactions on Smart Grid*, vol. 7, no. 1, pp. 114–123, 2016.

[26] K. Clement-Nyns, E. Haesen, and J. Driesen, "The impact of charging plug-in hybrid electric vehicles on a residential distribution grid," *IEEE Transactions on Power Systems*, vol. 25, no. 1, pp. 371–380, 2010.

[27] J. Munkhammar, P. Grahn, and J. Widén, "Quantifying self-consumption of on-site photovoltaic power generation in households with electric vehicle home charging," *Solar Energy*, vol. 97, no. 6, pp. 208–216, 2013.

[28] M. Singh, P. Kumar, and I. Kar, "A multi charging station for electric vehicles and its utilization for load management and the grid support," *IEEE Transactions on Smart Grid*, vol. 4, no. 2, pp. 1026–1037, 2013.

[29] M. P. Moghaddam, A. Abdollahi, and M. Rashidinejad, "Flexible demand response programs modeling in competitive electricity markets," *Applied Energy*, vol. 88, no. 9, pp. 3257–3269, 2011.

[30] D. Adrian, J. Ullrich, and E. R. Weippl, "Grid shock: coordinated load-changing attacks on power grids: the non-smart power grid is vulnerable to cyber attacks as well," in *Proceedings of the 33rd Annual Computer Security Applications Conference*, pp. 303–314, Orlando, FL, USA, September 2017.

[31] G. M. Zhang et al., "Dolphinattack: inaudible voice commands," in *Proceedings of the 2017 ACM SIGSAC Conference on Computer and Communications Security*, pp. 103–117, Dallas, TX, USA, November 2017.

[32] E. Bou-Harb, C. Fachkha, M. Pourzandi, M. Debbabi, and C. Assi, "Communication security for smart grid distribution networks," *IEEE Communications Magazine*, vol. 51, no. 1, pp. 42–49, 2013.

[33] X. Chen, "Industrial control network information security threats and vulnerability analysis and research," *Computer Science*, vol. 39, no. 10, pp. 4188–4190, 2012.

[34] W. Knowles, D. Prince, D. Hutchison, and K. Jones, "A survey of cyber security management in industrial control systems," *International Journal of Critical Infrastructure Protection*, vol. 9, no. 1, pp. 52–80, 2015.

[35] C.-W. Disso, C.-C. Liu, and G. Manimaran, "Vulnerability assessment of cybersecurity for SCADA systems," *IEEE Transactions on Power Systems*, vol. 23, no. 4, pp. 1836–1846, 2008.

[36] L. Sankar, S. R. Rajagopalan, S. Mohajer, and H. V. Poor, "Smart meter privacy: a theoretical framework," *IEEE Transactions on Smart Grid*, vol. 4, no. 2, pp. 837–846, 2013.

[37] M. Li and H.-J. Lin, "Design and implementation of smart home control systems based on wireless sensor networks and power line communications," *IEEE Transactions on Industrial Electronics*, vol. 62, no. 7, pp. 4430–4442, 2015.

Hindawi
Complexity
Volume 2021, Article ID 6635588, 16 pages
https://doi.org/10.1155/2021/6635588

Research Article

Networking of Smart Meters Based on Time-Varying Feature of Low-Voltage Power Line Channel in Microgrid

Ya-Xin Huang,[1] Xiao-Di Zhang,[2] Fei Yu,[1] Yong-Qing Wei,[1] and Hai-Long Zhang[3]

[1]*College of Electrical Engineering, Naval University of Engineering, Wuhan 430072, China*
[2]*State Grid Beijing Electric Maintenance Company, Beijing 100080, China*
[3]*General Construction Company of CCTEB Group Co., Ltd., Wuhan 430064, China*

Correspondence should be addressed to Ya-Xin Huang; haizhixina@126.com

Received 21 November 2020; Revised 29 December 2020; Accepted 15 January 2021; Published 29 January 2021

Academic Editor: Xin Li

In order to manage the electricity consumption information of microgrid users, the reliability of electricity information collection is studied in this paper. The normal communication between the acquisition terminal and the smart meter is a key factor affecting the accurate collection of power information; it is the basis for ensuring the operation of the microgrid as well. In order to improve the reliability of the low power line communication between the acquisition terminal and smart meters, this article first uses the static networking method to layer the smart meters and select relays from them and then select the optimal communication path based on integrating communication quality and relay forwarding number dynamically, which could avoid the signal conflict problem caused by simultaneous communication. Finally, by analyzing the influence of the time-varying power line channel on the smart meter communication, a method based on the integrated communication quality and the relay number to consider the time variability of low power line communication is proposed. Choosing the optimal path of the smart meters when the communication path is abnormal can not only establish a new communication path for communication in time, but also avoid communication failures caused by the time-varying channel. Through MATLAB simulation, the time-varying dynamic network of the power line channel is introduced in this paper, which improves the reliability of the smart meter communication and has certain guiding significance for the actual smart meter network construction in microgrid.

1. Introduction

1.1. Background. In recent years, with the widespread application of renewable energy and the continuous reduction of the energy storage equipment costs, various forms of DC microgrid have emerged. Driven by power electronics technology and energy storage technology including solar, wind, microturbines, and batteries [1, 2], DC microgrid has been developed rapidly. Figure 1 is a schematic diagram of microgrid structure, which includes wind power, solar power, diesel generator, microturbines, and other power sources [3]. With its advantages of easy control, high reliability, and low energy consumption, DC microgrid will become the main power supply structure in remote mountain village and future households [4, 5]. Therefore, how to manage the power consumption of these distributed DC microgrids has become a problem that needs to be solved in the power industry. Smart meter is one of the basic devices for data acquisition of smart grid. It undertakes the tasks of data acquisition, measurement, and transmission of original electric power [6], and it is the basis of information integration, analysis, and optimization, as well as information presentation. According to the country's 13th Five-Year Plan, China will fully enter the "power grid 2.0" in 2020, achieving 100% coverage of smart meters. Therefore, accurate data information collection of smart meters is of great significance to the construction of microgrid.

1.2. Motivation. Traditionally, compared to AC microgrid via event-triggered communication [7], power line communication (PLC) has been widely employed in several microgrid application areas, e.g., for the automation of the power grid [8], for the connection of smart meters [9] (as an

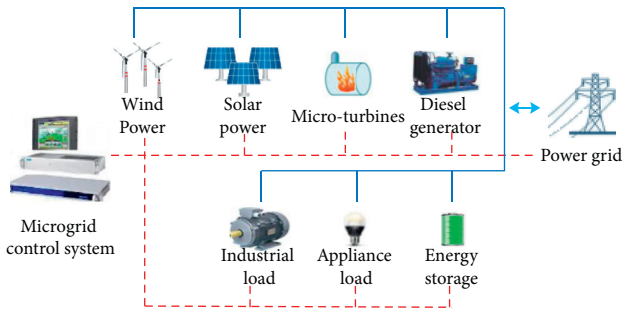

Figure 1: The schematic diagram of microgrid structure.

alternative to wireless connection [10]), and for home automation connected with smart appliances [11].

In practical applications, because the power line has the advantages of wide coverage, low cost, and high transmission speed, it is often used for information acquisition and transmission of smart meters [12]. However, since the power line communication has the characteristics of large signal attenuation, uneven signal distribution, and multipath effects [13, 14], as the communication distance increases, communication failures or anomalies will lead to information collection failures or abnormalities [15, 16]. According to statistics, only 96% of smart meters can accurately collect information [17]. Once the communication between the acquisition terminal (the concentrator) and the smart meter is abnormal, it will not only affect the accuracy and timeliness of the collection data, but also pose a certain threat to the stable operation of the microgrid. Therefore, improving the reliability of smart meter power line communication is of great significance to the intelligent construction of microgrid power supplies.

1.3. Literature Survey. At present, there are two methods to improve the reliability of power line communication. The first method is to increase the probability of correct point-to-point communication. Second, some scholars and manufacturers have begun to focus on the use of network routing (relay) to improve the reliability of power line communication networks.

In order to improve the accuracy of the point-to-point communication, literatures [18–23] mainly studied the PLC performance evaluations based on attenuation and noise models (e.g., additive white Gaussian noise (AWGN), impulse noise, and narrowband interference). The previous low-voltage power line networking technology in [24, 25] is based on artificial spider algorithm, [26, 27] are based on clustering method, [28, 29] are based on ant colony algorithm, and [30–32] are based on genetic algorithm, just for increasing the communication distance between the acquisition terminal and the smart meters. In experiments, the time-varying characteristics of low-voltage power lines have an important influence on the transmission distance of data signals. These networking technologies do not take the time-varying characteristics into account.

1.4. Contribution. A static and dynamic networking method is proposed to avoid the problem of signal conflict when smart meters are used as relay.

The communication distance, relay number, and the time-varying characteristics of low-voltage power line channel are regarded as the main factors of the network, making the network more stable and reliable.

Based on the actual situation, the key parameters in the dynamic networking process are established, and the invulnerability is verified by simulation.

After simulation, when the communication caused by sudden access load on the original communication path is abnormal, a more reliable communication branch can be searched dynamically.

2. The Power User Electric Energy Data Acquisition System

2.1. Network Topology of Smart Meters. Under normal circumstances, the current power user electric energy data acquisition system in the low-voltage platform area consists of an acquisition terminal (concentrator as the acquisition terminal), a communication channel, and a master station system. Within the same transformer control area, the smart meter is connected to a concentrator via a power line, and the concentrator collects power consumption information on the smart meter through the power line; the concentrator transmits the collected power consumption information to the server through the metering system private network, as is shown in Figure 2. The client of power user electric energy data acquisition system can view the power consumption information of each smart meter at any time.

2.2. Preconditions for Communication between the Concentrator and Smart Meters. Ideally, the concentrator could directly communicate with all smart meters in the same transformer distribution network, but due to noise interference, signal attenuation, multipath effects, and other factors in the low-voltage power line channel, the communication distance between the concentrator and the smart meters is limited. In fact, according to experiments, the communication distance between the concentrator and the smart meter is 200 meters to 400 meters. According to [33], the communication distance between smart meters is about 30 meters. When the communication distance between the concentrator and the smart meter exceeds this range, direct communication cannot be established between them. Therefore, in order to realize normal communication between the concentrator and the long-distance smart meters, the smart meters need to be networked; that is, suitable relays are selected between the concentrator and the remote smart meters. The relay has the function of forwarding concentrator instructions and could forward messages from the concentrator to remote smart meters that cannot directly communicate with the concentrator.

2.3. The Function of Concentrator and Smart Meters. The concentrator not only has a function of collecting smart

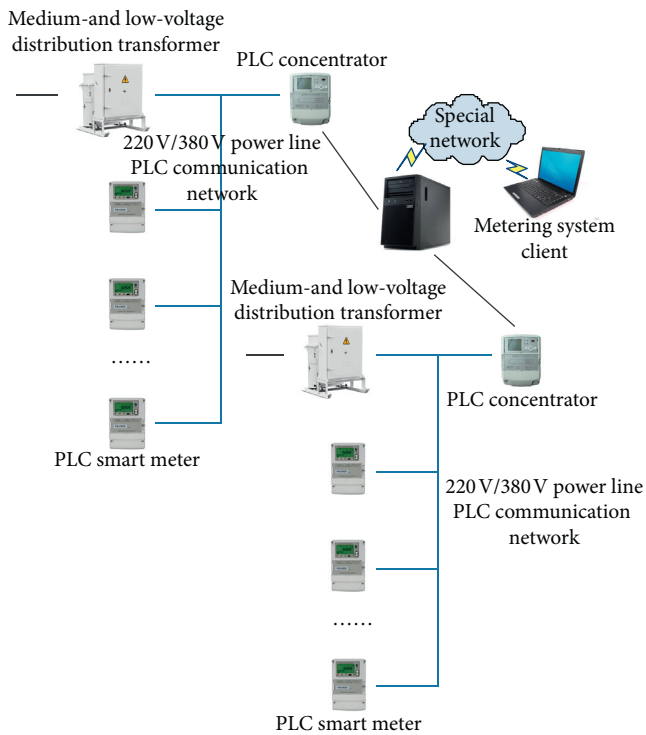

Figure 2: The schematic diagram of user information acquisition system.

meter information, but also has many other functions. Its specific function configuration is shown in Table 1.

In addition to the traditional power metering function, the smart meters also have a two-way data communication function, with multiple data transmission modes [34] and the relay function. In order to establish the communication between the concentrator and the remote smart meter, it is necessary to select the appropriate smart meter as the relay, and the smart meter selected as the relay can forward the message to the remote smart meter. The communication schematic diagram is shown in Figure 3.

3. Static Relay Selection

3.1. Static Relay Selection Method. In this paper, the smart meter that could be used as a relay is firstly selected by a static method referring to [35]. The schematic diagram of selecting the relay for each layer is shown in Figure 4. Search for hierarchy selection from the first layer sequentially, for example, as the first-level relay that can directly communicate with the concentrator, and the smart meters that communicate with the first-level relay are placed in the first layer. In order to avoid communication failures caused by signal conflicts, there is no communication between smart meters of the same level. When smart meters belonging to the first level can communicate with a non-first-level smart meter, the smart meter belonging to the first level is placed in the second-level subnet and serves as a second-level relay. The selection of the relays for other layer subnet is performed in this order; that is, when the upper-level smart meter can communicate with the lower-level smart meter, the upper-level smart meter is used as the lower-level relay.

According to the static relay selection method described above, static relay selection is performed on the logical topology of the smart meter in the experimental area. Figure 5 is a logical topology after the static relay is selected, wherein smart meters of the same color belong to the same-level subnet.

3.2. Problems after Static Relay Selection. The problem with the static relay selection method is that the same common smart meter belongs to the communication range of multiple superior relays at the same time. If multiple relays forward messages to the same smart meter at the same time, signal conflicts will occur, resulting in communication failure, as is shown in Figure 6; the blue nodes are smart meters belonging to multiple superior relays. With reference to the logic topology after static relay selection in Figure 5, each smart meter could establish communication with the concentrator, but since some smart meters belong to multiple relay communication ranges at the same time, if multiple relays forward the packets of the concentrator to the same smart meter at the same time, there will be a signal conflict that causes communication failure.

For example, refer to Figure 4, the no. 11 relay within the communication ranges of no. 7 and no. 15 relays. When the two relays communicate with the no. 11 relay at the same time, the no. 11 relay will not be able to transmit information to the concentrator at time. In actual network communication, with the increase of smart meters, the communication network will become more complex, and the channel capacity and signal conflict will become more and more obvious, which cannot be ignored. Therefore, when a smart

Table 1: Concentrator function configuration.

Sequence number	Project	
1	Data acquisition	Data acquisition of smart meter
2	Data management and storage	Real-time data and current data Historical date data Historical month data Key user acquisition
3	Parameter setting and query	Clock call and timing Terminal parameters Meter reading parameters Other (limit, prepaid, etc.) parameters
4	Event log	Record of important events General event record
5	Data transmission	Communication with main station Data forwarding
6	Local function	Run indication Local maintenance interface
7	Terminal maintenance	Self-checking and self-recovery Terminal initialization Software remote download Resume from break point

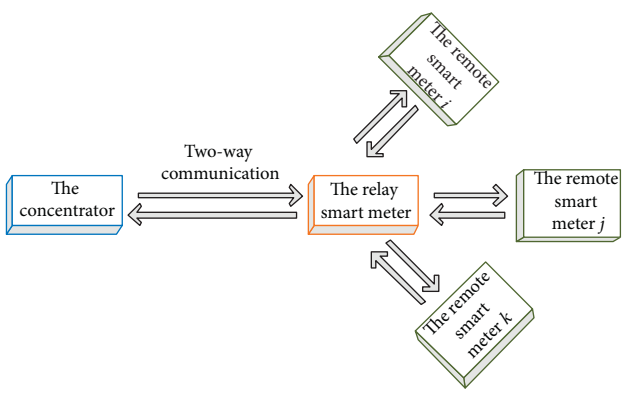

Figure 3: The communication diagram of the remote smart meters.

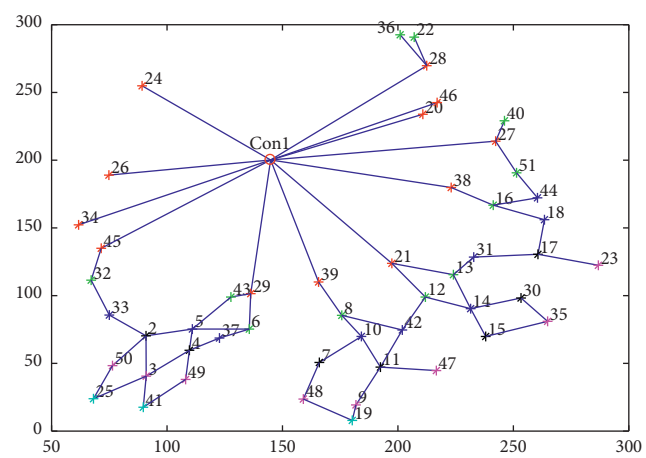

Figure 5: Logical topology after static relay selection.

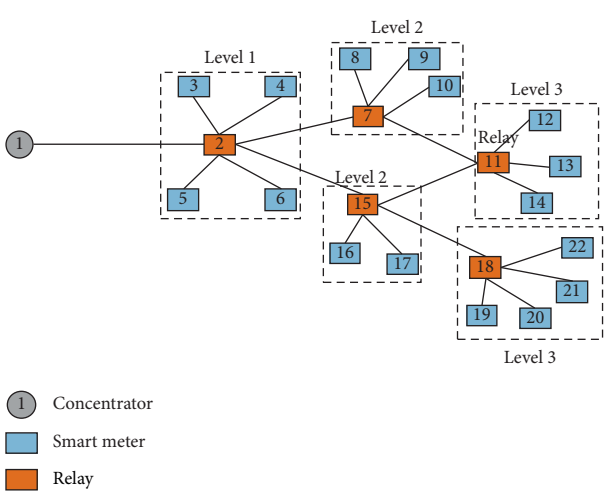

Figure 4: The schematic diagram of static relay selection.

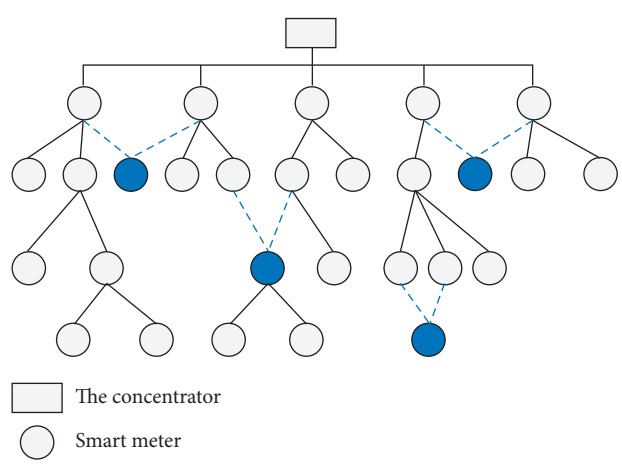

Figure 6: Schematic diagram of logical topology for signal collisions.

meter belongs to multiple superior relays at the same time, finding the optimal relay and communication with it is the key to microgrid network networking.

4. Time-Varying Analysis of Power Line Channels

In microgrid, in order to improve the communication between smart meters and the concentrators, after static relay selection, dynamic relay is also required. There are two main functions of the dynamic relay: the first is to select the best communication path according to the objective function when the remote smart meter to be collected is within the communication range of two or more relays, and the second is to select the other path to communicate dynamically when the data information collected by the concentrator is abnormal. At present, although the cobweb algorithm in the literature proposes a solution when the original communication branch communicates abnormally, it just randomly selects another path without considering the time-variation of the power line channel. In practice, the concentrator collects the data information every 15 minutes from each smart meter. According to the time-varying analysis of the power line channel, it was found that the original communication path has abnormal information at the previous moment, but after 15 minutes, the communication may be restored to normal. Therefore, the time-varying power line channel is one of the key factors affecting the reliability of low-voltage power line communications. When dynamic relay selection is performed, time-varying power line channel needs to be considered.

4.1. Time-Varying Property of Power Line Channel. When a smart meter acts as a relay for forward packets, the random access of the user's load will affect the normal communication of the power line channel. Therefore, referring to the impedance characteristics of 36 low-voltage power systems at the frequency of 0.2–30 MHz, the attenuation characteristics of the typical low-voltage distribution network at frequencies of 0–500 kHz [36], the frequency response of the indoor low-voltage power line channel characteristics [37], and the measurement of channel impedances in [38], this paper mainly analyzes the impact of impedance time-varying on power line channels. In order to facilitate the analysis of channel transmission characteristics when accessing different loads, the transmission line system is regarded as a two-port network according to Galli and Banwell [39], and power line channels are modeled for different network structures and loads.

4.2. Transmission Line Model. According to transmission line theory [40], signals are transmitted in the form of transverse electromagnetic waves (TEM) in the power line. When current is transmitted through two wires, a constantly changing magnetic field appears around the wire. Due to the continuous change of the magnetic field, the induced voltage will cause the voltage change between the wires, and the leakage current between the wires will increase with the increase of voltage and frequency [37]. Therefore, the uniform transmission line model is used as a distributed circuit model composed of a series of components. The circuit diagram of the model is shown in Figure 7.

The characteristic impedance Z_0 and propagation coefficient $r$of the transmission line are calculated according to the following formula:

$$\begin{cases} Z_0 = \sqrt{\dfrac{R_0 + j2\pi f \cdot L_0}{G_0 + j2\pi f \cdot C_0}}, \\ r = \sqrt{(R_0 + j2\pi f \cdot L_0)(G_0 + j2\pi f \cdot C_0)} = \alpha + j\beta, \end{cases} \tag{1}$$

where α is the attenuation coefficient, which indicates the attenuation of the signal; β is the phase shift coefficient, which indicates the phase change of the signal [41].

For ideal uniform power line, R_0, L_0, G_0, andC_0can be calculated based on the following formula:

$$\begin{cases} R_0 = \dfrac{2}{a}\sqrt{\dfrac{f u_c}{\pi \sigma_c}}, \\ L_0 = \dfrac{u}{\pi}\ln\left(\dfrac{d + \sqrt{d^2 + (2a)^2}}{2a}\right), \\ G_0 = \dfrac{\pi\sigma}{\ln\left(\left(d + \sqrt{d^2 + (2a)^2}\right)/2a\right)}, \\ C_0 = \dfrac{\pi\varepsilon}{\ln\left(\left(d + \sqrt{d^2 + (2a)^2}\right)/2a\right)}, \end{cases} \tag{2}$$

where a is the radius of the wire; f is the frequency; u_c is the magnetic permeability of the conductor; σ_c is the conductivity of the conductor; u is the permeability between the two wires; σ is the conductivity between the two wires; d is the distance between the two wires; and ε is the dielectric constant between the wires.

Since the actual line resistance $R$and the conductance Gvary with frequency, they are corrected by the following equation:

$$\begin{cases} R = R_0 \cdot 10^{-5} \cdot \sqrt{f}\left(\dfrac{\Omega}{m}\right), \\ G = G_0 \cdot 10^{-14} \cdot 2\pi f\left(\dfrac{\Omega}{m}\right). \end{cases} \tag{3}$$

Assuming that the transmission line is ideal, any uniform transmission line can be expressed in two-port network. According to the schematic diagram of the two-port model of Figure 8, the voltage and current relation of the two port is

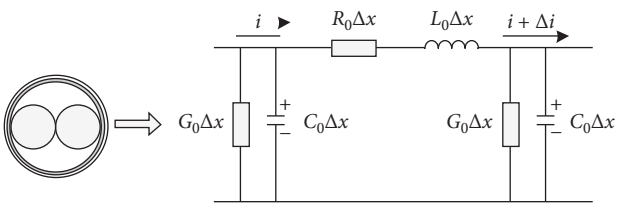

Figure 7: Equivalent circuit of uniform transmission line.

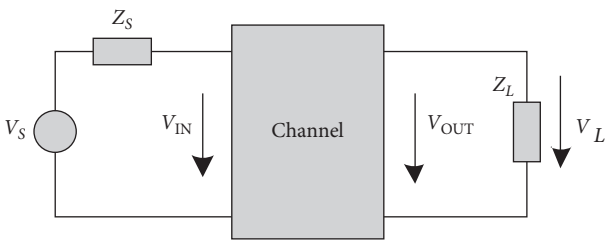

Figure 8: Two-port network schematic diagram.

$$\begin{vmatrix} V_1 \\ I_1 \end{vmatrix} = \begin{vmatrix} A & B \\ C & D \end{vmatrix} \begin{vmatrix} V_2 \\ I_2 \end{vmatrix} = T_f \begin{vmatrix} V_2 \\ I_2 \end{vmatrix}, \tag{4}$$

$$\begin{vmatrix} V_2 \\ I_2 \end{vmatrix} = \begin{vmatrix} A & B \\ C & D \end{vmatrix}^{-1} \begin{vmatrix} V_1 \\ I_1 \end{vmatrix} = \frac{1}{AD - BC} \begin{vmatrix} D & B \\ C & A \end{vmatrix} \begin{vmatrix} V_1 \\ V_2 \end{vmatrix} = T_b \begin{vmatrix} V_1 \\ I_1 \end{vmatrix}, \tag{5}$$

where T_f is forward transmission matrix and T_b is backward transmission matrix.

In Figure 8, the supply voltage is

$$V_s = V_1 + I_1 Z_s. \tag{6}$$

Load voltage is

$$V_2 = I_1 Z_s. \tag{7}$$

Input impedance is

$$Z_{\text{in}}(f) = Z_0 \frac{Z_L \cosh rl + Z_0 \sinh rl}{Z_0 \cosh rl + Z_L \sinh rl} = \frac{AZ_L + B}{CZ_L + D}. \tag{8}$$

The legendary function of the two-port network is

$$H(f) = \frac{V_2}{V_S} = \frac{Z_L}{AZ_L + B + CZ_S Z_L + DZ_S}, \tag{9}$$

$$\begin{cases} A = D = \cosh rl \\ B = Z_0 \sinh rl \\ C = \dfrac{1}{Z_0} \sinh rl \end{cases} \rightarrow T_f = \begin{vmatrix} \cosh rl & Z_0 \sinh rl \\ \dfrac{1}{Z_0} \sinh rl & \cosh rl \end{vmatrix}, \tag{10}$$

where l, r, and Z_0 are the length of conductor, transmission constant, and characteristic impedance of cable, respectively, and the parameter of T_f satisfies $A = D$, $B \neq C$, and $AD - BC = 1$ at any frequency.

4.3. Network Model. In order to establish the communication channel model more accurately, this paper analyzes the network structure of smart meters. In a typical low-voltage distribution network, the lines connected to the trunk and branches are called distribution cabinets, and where the smart meter is generally installed. The branch line is directly connected to each branch plug. In the room, the branch plug is connected to the various sockets through the inner line, and the socket is directly connected to the load with different impedance characteristics. As shown in Figure 9, the trunk line is relatively thick, while the branch line is thinner.

In Figure 9, it can be seen that there is a star-type connection between the distribution cabinet and the branch plug, and there are star-type and bus-type connections between the branching plug and the outlets. In the star structure, the branch plug and the socket are directly connected, while the bus-type connection refers to the socket connected in parallel to one line. If the connection mode is a star connection, it is equivalent to the parallel connection of multiple loads at the node. For the bus connection mode, it is equivalent to the cascading mode of the load, and the specific size is the input impedance of the branch line.

The forward transmission matrix of the branch plug is

$$T_{\text{BT}} = \begin{vmatrix} 1 & 0 \\ \dfrac{1}{Z_{\text{in}}} & 1 \end{vmatrix}. \tag{11}$$

Calculate the input impedance Z_{in} of the branch plug using equation (8).

For a given network, this paper uses a transmission matrix to build a channel model. The total transmission matrix of a star connection can be obtained by cascading, as shown in the following equation:

$$T_f = T_f^{(1)} \cdot T_f^{(2)} \cdot \cdots \cdot T_f^{(N)}, \tag{12}$$

where T_f is a forward transmission matrix of a network composed of N parts and $T_f^{(N)}$ is a forward transmission matrix of part N. The total backward matrix T_b is

$$\begin{aligned} T_b = \left(T_f\right)^{-1} &= T_f^{(N)} \cdot T_f^{(N-1)} \cdot \cdots \cdot T_f^{(1)} \\ &= \prod_{i=1}^{N} \begin{bmatrix} A_i & B_i \\ C_i & D_i \end{bmatrix} = \begin{bmatrix} A & B \\ C & D \end{bmatrix}. \end{aligned} \tag{13}$$

4.4. Load Model. According to the characteristics of the load over time, it is divided into three categories: constant impedance, time-invariant frequency selective impedance, and time-varying frequency selective impedance. This paper sets the low impedance of the load to 5 Ω, the RF standard impedance to 50 Ω, the equivalent transmission line characteristic impedance to 150 Ω, and the high impedance to 1000 Ω. Since the access terminals of most electrical devices have interference capacitances, the impedance of the power line is resistive and inductive. Therefore, when the load connected to the power line is frequency-selective

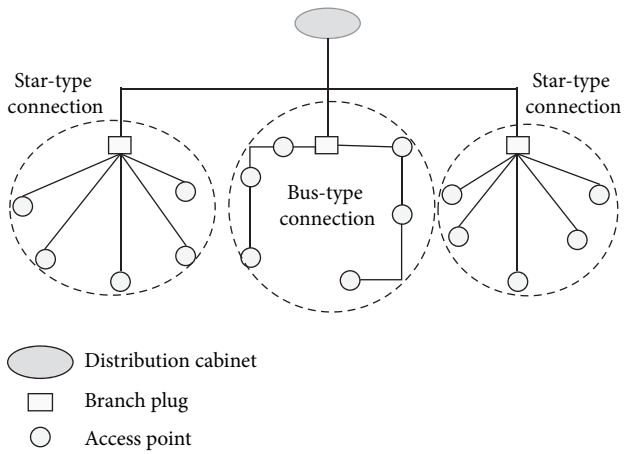

Figure 9: Network structure between smart meters.

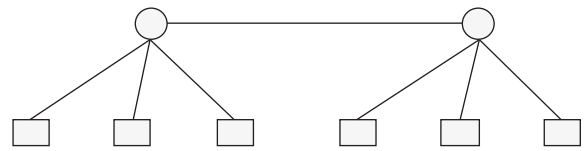

Figure 10: The star network structure.

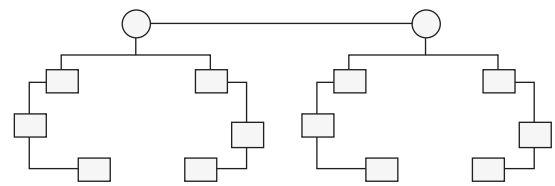

Figure 11: The bus network structure.

impedance, it can be equivalent to an RLC series or parallel connection. Its impedance expression is shown in the following equation:

$$Z_w = \frac{R}{1 + jQ\left(\omega/\omega_0 - \omega_0/\omega\right)},$$
$$Z_s(w) = R + jRQ\left(\frac{\omega}{\omega_0} - \frac{\omega_0}{\omega}\right), \tag{14}$$

where R is the resonant impedance, ω_0 is the resonant frequency, and Q is the quality factor. The setting range of load model parameters in this article is as follows: $R \in \{200, 1800\}\Omega$, $Q \in \{5, 25\}$, $\omega_0/2\pi \in \{1, 30\}$MHz.

According to the measurement results of the channel impedance [40], there are two main types of time-varying load impedances. One is to switch the load impedance value between two values. The other is that the load impedance changes synchronously with the power frequency cycle, and the impedance changes continuously over time. Its expression is shown in the following equation:

$$Z(\omega, t) = Z_A(\omega) + Z_B(\omega)\left|\sin\left(\frac{2\pi}{T_0}t + \phi\right)\right|, \quad 0 \le t \le T_0, \tag{15}$$

where Z_A is the minimum value of the load impedance, Z_B is the increment of the change of the impedance, and ϕ represents the relationship with the power frequency period, which could be considered to be evenly distributed during modeling.

4.5. Time-Varying Channel Modeling Verification and Analysis. According to the measurement data in [37], the distance between the power line of the plug and the socket is set to 20~50 m, and the distance of the communicable power line between the smart meter and the smart meter is 1~30 m.

According to the different connection modes of the load, the network structure between the two smart meters is equivalent to two forms: one is the star network structure in Figure 10, and the other is the bus-type network structure in Figure 11.

For the star network structure in microgrid, when they are connected to a constant load and a frequency-selective load, the change of the power line channel between the two smart meters is shown in Figure 12, where the green line is the change of channel model with a low impedance, the yellow line is the channel model with constant load, the red line is the change of the channel model with constant load and frequency selective load, and the blue line is the change of the channel model with constant load, frequency-selective load, and time-varying frequency-selective load.

For the bus network structure, when they are connected to a constant load and a frequency-selective load, the change of the power line channel between the two smart meters is shown in Figure 13, where the green line is the change of the channel model under constant load, the red line is the change of the channel model under constant load and frequency-selective load, and the blue line is the change of the channel model under constant load, frequency-selective load, and time-varying frequency-selective load.

It can be seen that from Figures 12 and 13, as the frequency of the carrier signal gradually increases, the attenuation in the channel gradually increases, and the more the parallel load is at the same carrier frequency, the more severe the attenuation of the main power line channel between the two smart meters' communication. When the power line carrier frequency is 30 MHz, with the random access of the load, the attenuation of the channel is very large, which has a great impact on communication quality. Besides, the more the load of the random access is, the greater the attenuation of the signal is. Therefore, in order to more effectively network the smart meter, it is necessary to consider the time variation of the channel when accessing the load for the star network structure and bus network structure.

Through the statistical analysis of the electricity consumption information of a certain community, it is found that when the electricity consumption of users increases, communication abnormalities are likely to occur, resulting in abnormal electricity consumption information collected, as shown in Figure 14. This is consistent with the simulation results in Figures 12 and 13. In Figure 14, (a) is the daily electricity consumption collected at different times at a certain collection point, (b) is the data of total electricity

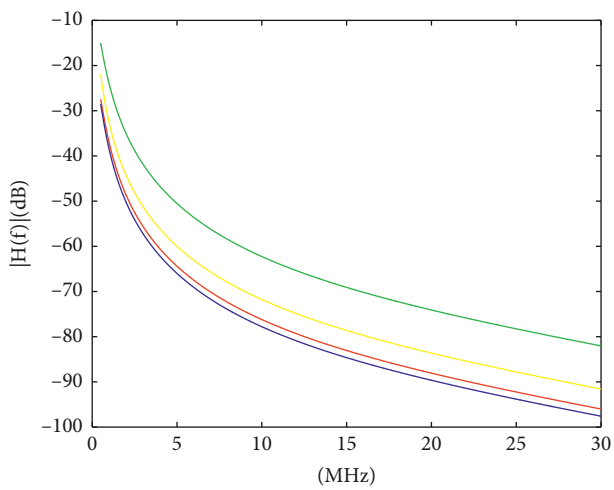

Figure 12: Channel changes in a star network structure.

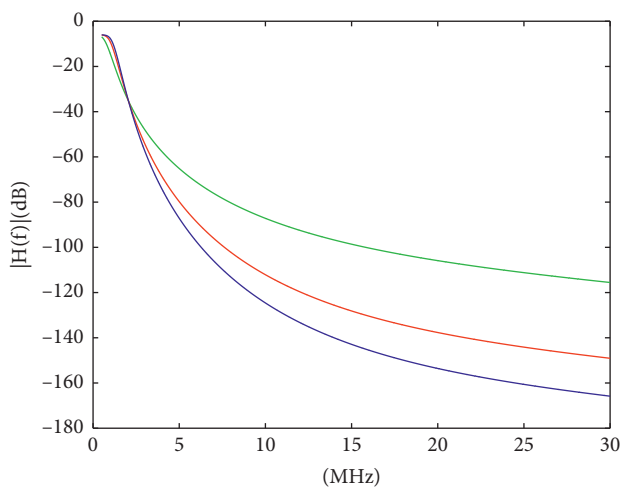

Figure 13: Channel changes in a bus-type network structure.

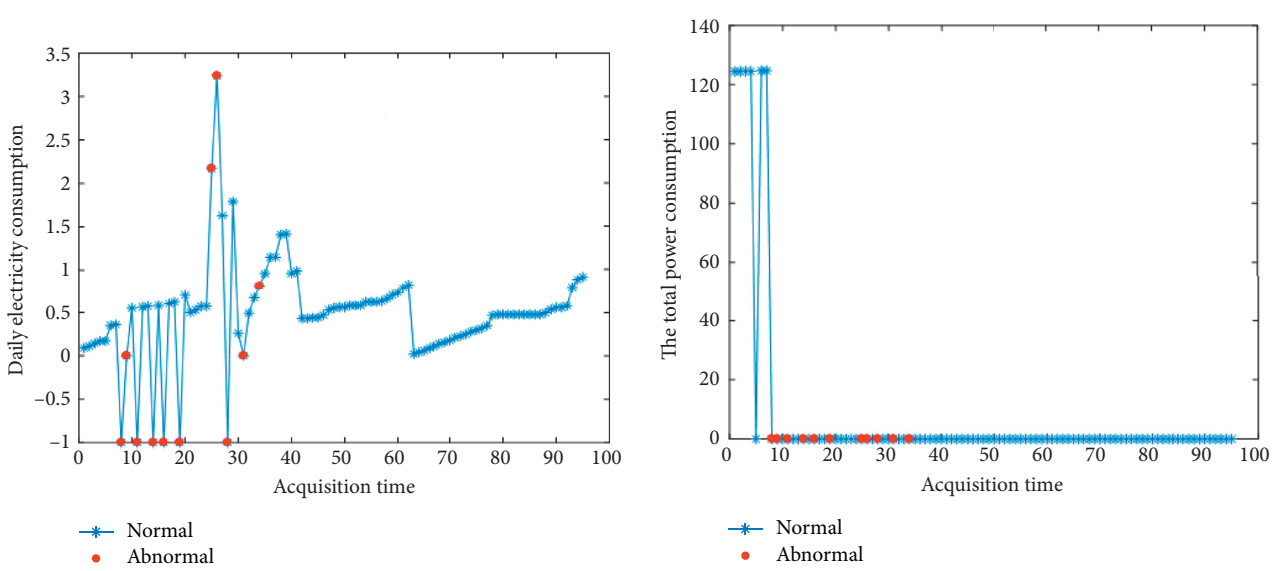

Figure 14: Continued.

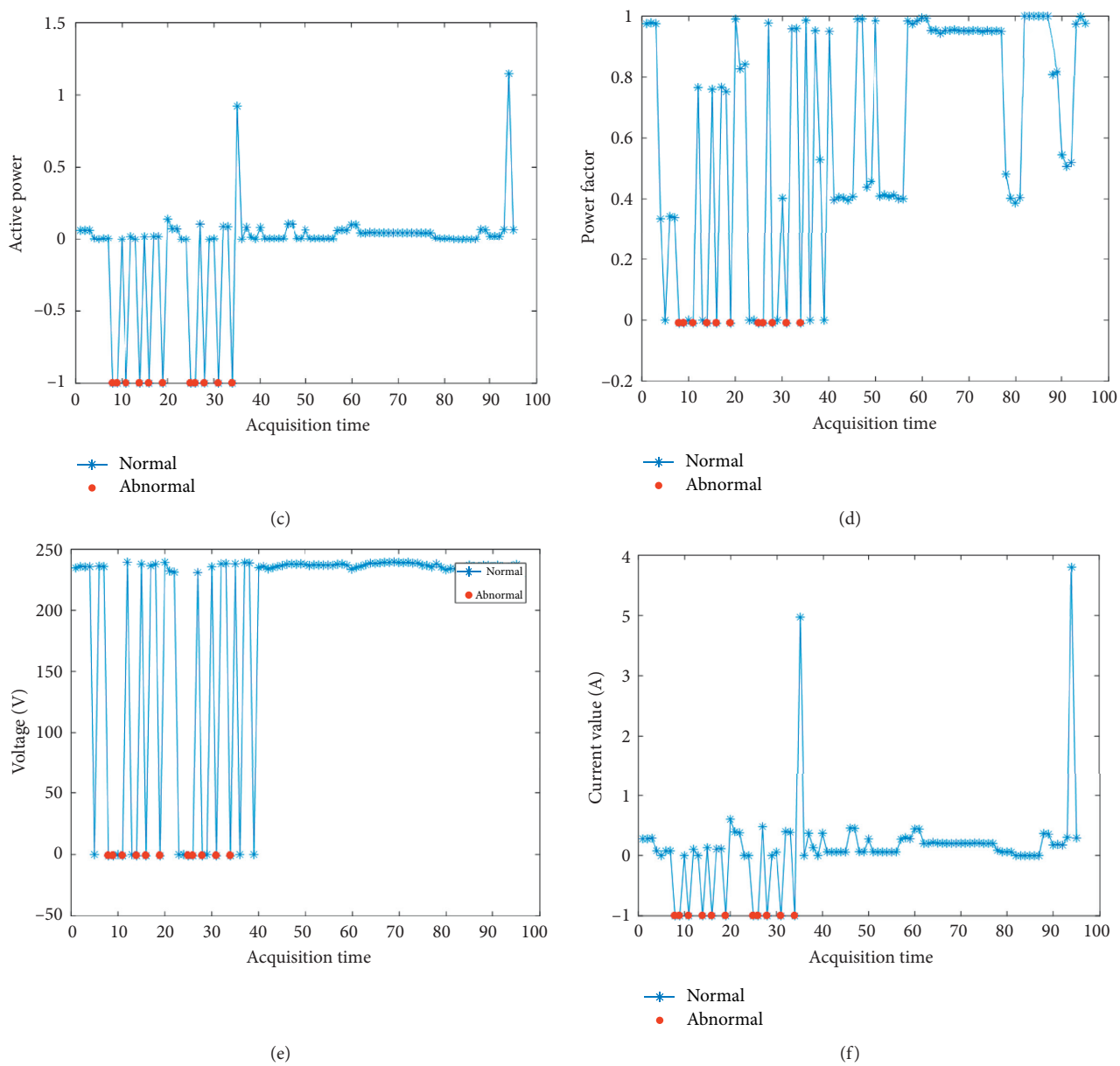

Figure 14: The normal state and abnormal state distribution of the data in the collection point.

consumption at different times, (c) is the active power value collected at different times, (d) is the power factor collected at different times, (e) is the voltage value collected at different times, and (f) is the current value collected at different times. The blue point is normal data; red dots mean anomaly data in the six diagrams of Figure 14.

5. Analysis of Users' Electricity Usage Behavior

According to the statistical characteristics of the users' electricity consumption behavior, this paper will use a relatively large electricity consumption period of time to characterize the time of the load access channel. That is, when the relay is dynamically selected, the power-increasing time is taken as a key factor. In the experimental area, the concentrator collects the information of the smart meter from 0 o'clock and collects it every 15 minutes, so the power consumption information of 96 moments is collected for each smart meter every day. To better mark the time point of collection, this paper uses the number to mark the collection time of the day, starting from 0 o'clock and adding 1 every fifteen minutes, the specific mark is shown in Table 2. According to the statistics of the users' electricity consumption in the test area, it is found that the users' electricity consumption is random, and the change of electricity consumption information varies from month to month. In order to analyze the change rule of the users' electricity consumption behavior, this paper takes August as an example to analyze the users' electricity consumption behavior. Figure 15

Table 2: Digital markup for collecting time points.

00 : 00 1	00 : 15 2	00 : 30 3	00 : 45 4
01 : 00 5	01 : 15 6	01 : 30 7	01 : 45 8
...	...	...	...
23 : 00	23 : 15	23 : 30	23 : 45
93	94	95	96

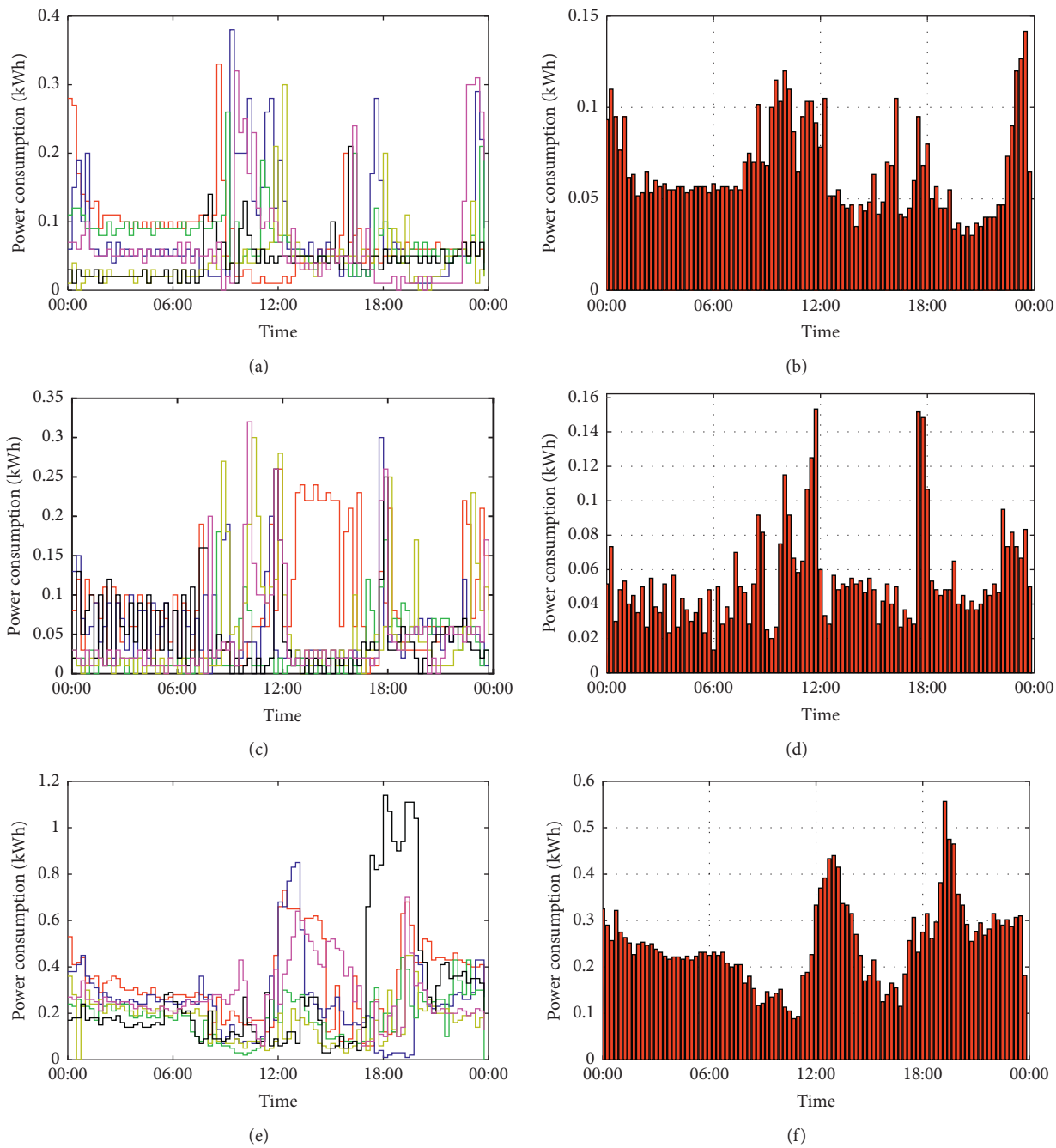

Figure 15: Continued.

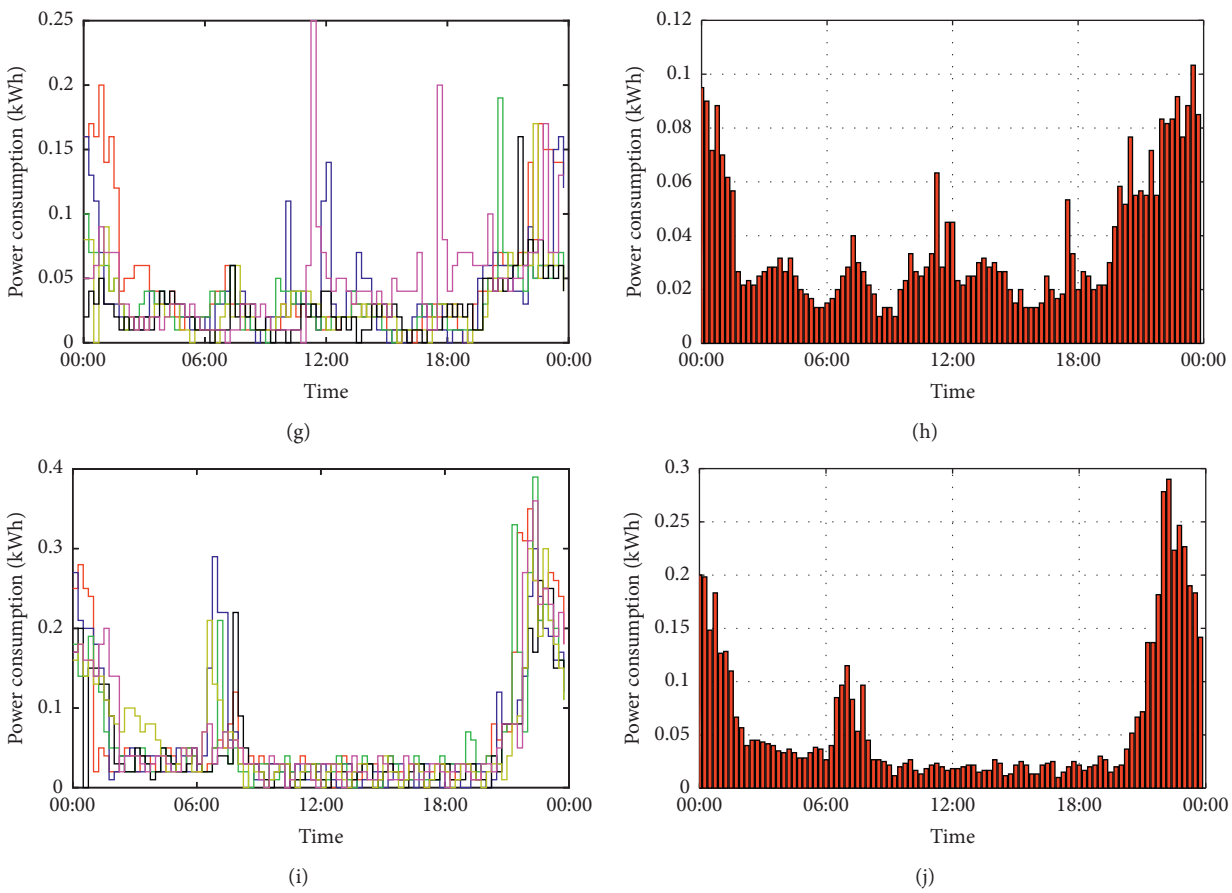

Figure 15: Change of electricity consumption for users in the test area.

shows the changes in the electricity consumption of some users randomly selected in August for 6 days and the average power consumption without considering vacant houses. Figure 15(a) is the change of electricity consumption of five representative users (excluding vacant rooms) in the experimental area for 6 days in August, and Figure 15(b) shows the changes in the average electricity consumption of these representative users at each collection time of the day in August. In Figure 15, each user's power consumption increase time is basically concentrated in one time period; for example, most users' power consumption will increase significantly at 12 o'clock.

In order to analyze the overall power consumption of users in the experimental area, this paper weighs the power consumption of all users in the cell, as shown in Figure 16. In Figure 16, households in the experimental area will have a significant increase in electricity consumption during certain time periods of the day, such as 00 : 30–01 : 30 (marked by the numbers 3–7); 11 : 00–14 : 30 (marked by the numbers 5–59); 18 : 30–20 : 00 (marked by the numbers 75–81); and 21 : 00–23 : 30 (marked by the numbers 85–95), and the time when the power consumption is increased is marked as shown in Table 2. Therefore, in the smart meter networking,

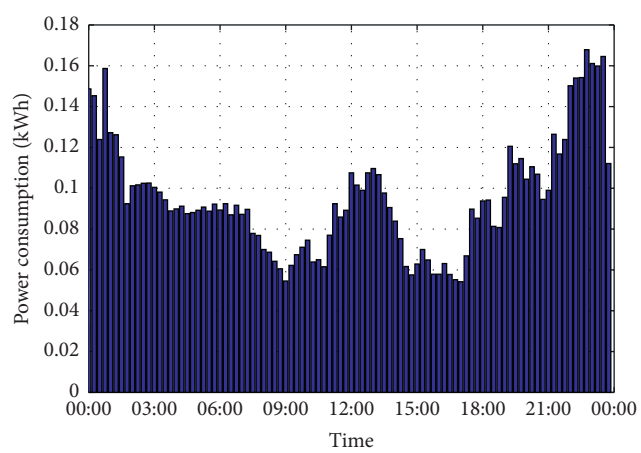

Figure 16: The average electricity consumption of a household in one day.

taking into account the time variability of the power line channel, when the collected information is abnormal, if the time point of collecting abnormal information is within a significantly increased time period, refer to the formula (17) below to dynamically select other communication paths.

6. Dynamic Relay

According to the logical topology between the concentrator and the smart meters after the static relay selection, when the same smart meter communicates with multiple relays at the same time, a dynamic relay method is used to select the communication path. In the dynamic relay, the communication quality Q_d is introduced. Taking the distance between two points in the experiment as the communication quality Q_d, the smaller the value, the better the communication quality.

The number of smart meters relayed by the i relay to the upper relay is

$$F_{i,j} = N_a + N_b, \tag{16}$$

where N_a is the number of smart meters in the j-level subnetwork relayed by the i-number smart meter and N_b is the lower subnet number of the j-level subnetwork relayed by the i-number smart meter.

When the same smart meter belongs to multiple relay communication ranges at the same time, the smart meter performs the optimal path selection according to the link optimization index, for example, the i-number smart meter relay to the k-number smart meter link optimization index:

$$Y_{i,j-k} = \alpha Q_{d_{i,j-k}} + \beta F_{i,j} + \gamma \Delta_k, \tag{17}$$

where $Y_{i,j-k}$ is the link optimization index between the i-number relay and the k-number smart meter in the j-level subnetwork. α is the link optimization weighting coefficient; β is the weighting factor of the number of smart meters that must be forwarded to the upper relay. Δ_k is the difference between the link optimization index of the optimal communication branch and the suboptimal communication link optimization index of the k-number smart meter. γ is the weighting coefficient of data acquisition time when the k-number smart meter communicates with the i-number relay. Let $\alpha + \beta + \gamma = 1$, α, β, and γ can be changed according to the actual situation; in the experiment, the $Y_{i,j-k}$ value is as small as possible. This paper chooses the smallest value of $Y_{i,j-k}$ as the optimal communication path, while closing the suboptimal communication path.

7. Simulation Experiment

7.1. The Establishment of the Initial Optimal Communication Link. When the smart meter belongs to multiple relay communication ranges at the same time, according to the idea of dynamic relay, the optimal communication link is calculated from the lowest level subnet in turn. In the simulation experiment, when the link optimization index is calculated for the first time, set the $\gamma = 0$, α, and β values according to Table 3.

Starting from the lowest-level subnetwork, the link optimization index is mainly determined by the communication quality. With the increase of the subnet level, the number of smart meters required by the superior relay and forwarding communication gradually increases, and its weight gradually increases. When the smart meter belongs to multiple relay communications at the same time, the calculation is performed according to the above parameter settings so as to establish an optimal communication path.

7.2. Dynamic Selection of Communication Branches. The smart meter communicates with the concentrator according to the initial communication branch. In the process of information acquisition, if the information collected at a certain time is empty or abnormal, the link optimization index is dynamically adjusted. According to the user's electricity information in the experimental area, the power consumption will increase obviously in time periods 00 : 30–01 : 30; 11 : 00–14 : 30; 18 : 00–20 : 00; and 21 : 00–23 : 00. The effect of the time-varying load on the power line channel needs to be considered. This paper will set the dynamic relay link optimization parameters as is shown in Table 4. Among them, I refers to subnetwork parameters at each level of the original optimal communication branch during the power increase period; II to subnetwork parameters at all levels of the original suboptimal communication branch during the power increase period; III to subnetwork parameters of all levels of the original optimal communication branch in the nonelectricity increase period; and IV to subnetwork parameters of the original suboptimal communication branch in the nonelectricity increase period.

In the communication process between the concentrator and the smart meters, if the information collected at a certain moment suddenly becomes empty or abnormal, the link optimization index is recalculated for the smart meter according to Table 4, and the link with the smallest link optimization index is still selected as the optimal communication path. Figure 17 shows the optimal communication path after the dynamic relay at the start time, as shown by the yellow line in the figure. For example, when the collection of No. 25, No. 41, and No. 19 smart meters in the figure is empty, and the collection time is in 00 : 30–01 : 30; 11 : 00–14 : 30; 18 : 00–20 : 00; and 21 : 00–23 : 00, the No. 25 smart meter will communicate with No. 3 relay, the No. 41 smart meter will communicate with No. 49 relay, and the No. 19 smart meter will communicate with No. 48 relay, as shown by the red line in Figure 18. At the same time, the blue-dotted line indicates that the communication path is closed.

7.3. Results. When the smart meter was unable to communicate according to the original communication path due to the load, simulation experiments were performed on smart meters 25, 41, and 19, and they were found that they can dynamically select other communication paths for communication as Figure 18 shows. For instance, the original communication path of smart meter 25 is 25-50-2-5-43-29-Con1; the communication path after redynamically selected is 25-3-4-37-6-29-Con1; the original communication path of smart meter 41 is 41-3-4-37-6-29-Con1; the communication path after redynamically selected is 41-49-4-37-6-29-Con1; the original communication path of smart meter 19 is 19-9-11-10-8-39-Con1; and the communication path after redynamically selected is 19-48-7-10-8-39-Con1, thereby improving the communication reliability

Table 3: α and β values of subnets at all levels.

First-level subnet	α	0.70
	β	0.30
Second-level subnet	α	0.75
	β	0.25
Third-level subnet	α	0.80
	β	0.20
Fourth-level subnet	α	0.90
	β	0.10
Fifth-level subnet	α	0.90
	β	0.01

Table 4: α, β, and γ values of subnets at all levels.

Communication branch		I	II	III	IV
First-level subnet	α	0.25	0.15	0.65	0.55
	β	0.25	0.25	0.25	0.25
	γ	0.5	0.6	0.1	0.2
Second-level subnet	α	0.3	0.2	0.4	0.6
	β	0.2	0.2	0.2	0.2
	γ	0.5	0.6	0.1	0.2
Third-level subnet	α	0.35	0.25	0.75	0.65
	β	0.15	0.15	0.15	0.15
	γ	0.5	0.6	0.1	0.2
Fourth-level subnet	α	0.4	0.3	0.8	0.7
	β	0.1	0.1	0.1	0.1
	γ	0.5	0.6	0.1	0.2
Fifth-level subnet	α	0.49	0.39	0.89	0.79
	β	0.01	0.01	0.01	0.01
	γ	0.5	0.6	0.1	0.2

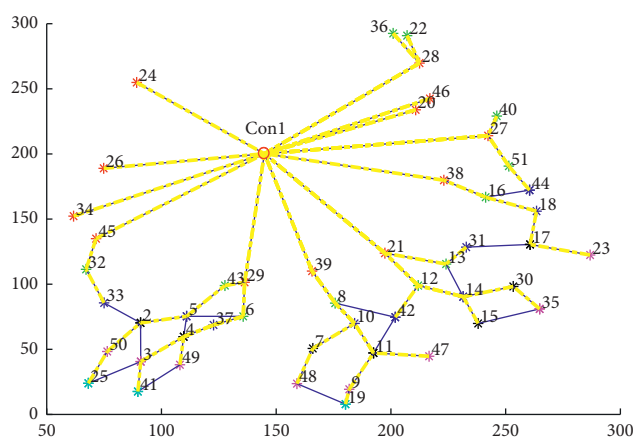

Figure 17: Smart meter communication path after dynamic selection of relay.

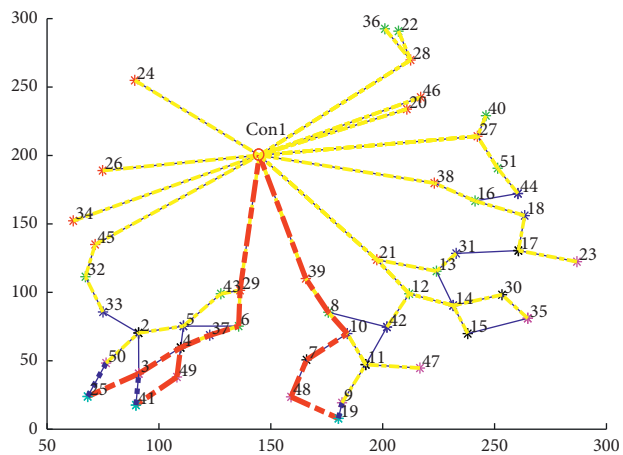

Figure 18: Smart meter communication path after redynamic selection.

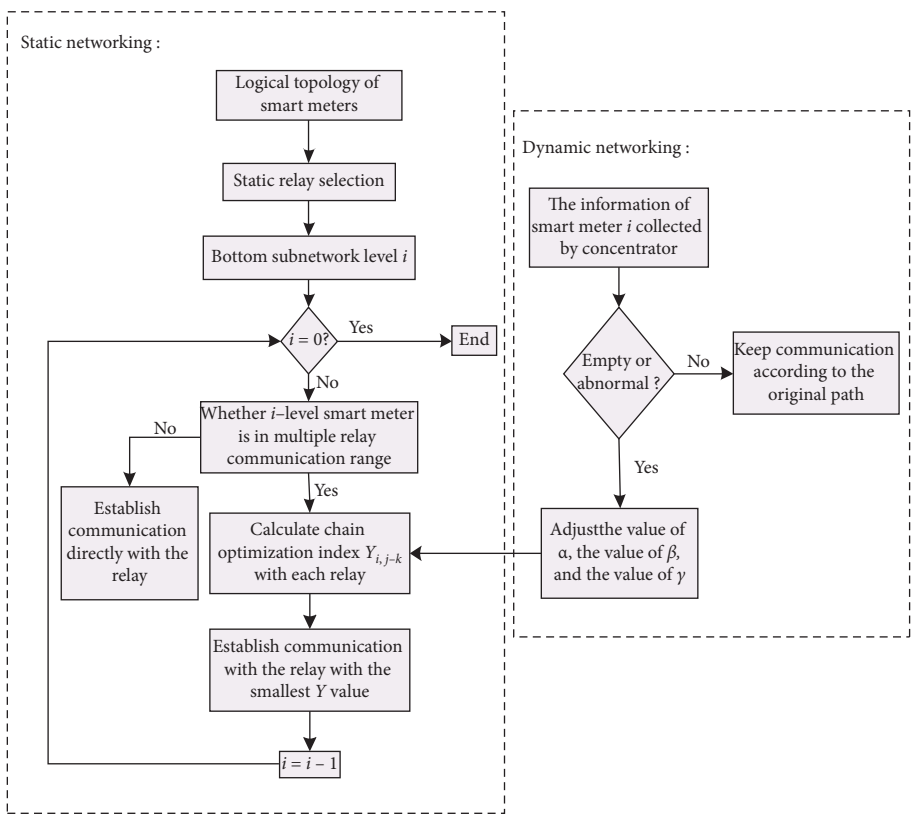

Figure 19: The overall static and dynamic networking flowchart.

performance of smart meters and concentrators. The reliability of intercommunication can ensure accurate collection of electricity information.

7.4. The Static and Dynamic Networking Flowchart. The overall flowchart of static and dynamic networking simulation experiment is shown in Figure 19, where the left panel is the static networking process, and the right panel is the dynamic networking process.

8. Conclusion

In order to improve the reliability of information acquisition in microgrid and the reliability of communication between the concentrator and the smart meters within the same low-voltage platform area, this paper adopts the idea of combining static and dynamic networking, effectively avoiding the communication failure caused by signal conflicts, and analyzes the changes of the power line channel when it suddenly added to the load. It is found that as the load increases, the attenuation of

the high-frequency carrier signals in the power line channel cannot be ignored. Therefore, according to the influence of time-varying load on the power line, this paper analyzes the power consumption behavior of users. When the smart meter and the concentrator fail to communicate during the period when the user's power consumption increases, the optimal link optimization index of the smart meter will be recalculated with reference to the subnetwork parameter values in Table 4 and simulated by MATLAB. Through simulation, the smart meter can reselect the new branch to establish communication with the concentrator. Therefore, considering the communication distance and the number of relays forwarding, this paper considers the power line time-varying as the main factor in the smart meter networking process, which not only makes the selected communication path more reliable, but also puts forward a new idea for power line networking. However, there are still some problems in this paper that need to be further studied. Firstly, this paper only takes August as an example to carry out analysis and simulation experiments; the law of electricity consumption in other months will be studied in the future. Secondly, in terms of dynamic networking, some intelligent algorithms will be considered for networking research in the future. Finally, in order to realize the wide application of dynamic and static networking in practice, related hardware technologies will be studied in the future.

Data Availability

The data used in this paper come from the statistics of electricity consumption information, which has not been published publicly. This paper only takes these data as an example to illustrate the time-varying electricity consumption information.

Conflicts of Interest

The authors declare that they have no conflicts of interest regarding the publication of this paper.

References

[1] J. Lai, X. Yu, and A. Monti, "Stochastic distributed secondary control for ac microgrids via event triggered communication," *IEEE Transactions on Smart Grid*, vol. 11, no. 4, 2020.

[2] J. Lai and X. Lu, "Nonlinear mean-square power sharing control for ac microgrids under distributed event detection," *IEEE Transactions on Industrial Informatics*, vol. 17, no. 1, 2020.

[3] J. Lai, X. Lu, X. Yu, and A. Monti, "Cluster-oriented distributed cooperative control for multiple ac microgrids," *IEEE Transactions on Industrial Informatics*, vol. 15, no. 11, pp. 5906–5918, 2019.

[4] X. Jin, Y. Mu, H. Jia, J. Wu, T. Jiang, and X. Yu, "Dynamic economic dispatch of a hybrid energy microgrid considering building based virtual energy storage system," *Applied Energy*, vol. 194, pp. 386–398, 2017.

[5] J. Lai, H. Zhou, W. Hu, X. Lu, and L. Zhong, "Synchronization of hybrid microgrids with communication latency," *Mathematical Problems in Engineering*, vol. 2015, Article ID 586260, 10 pages, 2015.

[6] S. Tian and W. Luan, "Technical forms and key technologies on energy internet," *Proceedings of the CSEE*, vol. 35, no. 14, pp. 3482–3494, 2015.

[7] J. Lai, X. Lu, X. Yu, and A. Monti, "Stochastic distributed secondary control for ac microgrids via event-triggered communication," *IEEE Transactions on Smart Grid*, vol. 11, no. 4, pp. 2746–2759, 2020.

[8] D. D. Giustina, P. Ferrari, A. Flammini, S. Rinaldi, and E. Sisinni, "Automation of distribution grids with IEC 61850: a first approach using broadband power line communication," *IEEE Transactions on Instrumentation and Measurement*, vol. 62, no. 9, pp. 2372–2383, 2013.

[9] D. Mrozinski, "New approaches to automatic consumption meter reading in Germany," *Computer Standards & Interfaces*, vol. 12, no. 1, pp. 43–52, 1991.

[10] A. Flammini, S. Rinaldi, and A. Vezzoli, "The sense of time in open metering system," in *Proceedings of the 2011 IEEE International Conference on Smart Measurements for Future Grids (SMFG)*, pp. 22–27, Bologna, Italy, November 2011.

[11] J. M. Alonso, J. Ribas, J. J. D. Coz, A. J. Calleja, E. L. Corominas, and M. Rico-Secades, "Development of a distributive control scheme for fluorescent lighting based on LonWorks technology," *IEEE Transactions on Industrial Electronics*, vol. 47, no. 6, pp. 1253–1262, 2000.

[12] Y. Kan, Y. Jing, S. Liang et al., "An improved power line signaling technique based anti-islanding protection approach for distributed generation system," *Proceedings of the CSEE*, vol. 35, no. 13, pp. 3283–3291, 2015.

[13] S. Rinaldi, P. Ferrari, A. Flammini, M. Rizzi, E. Sisinni, and A. Vezzoli, "Performance analysis of power line communication in industrial power distribution network," *Computer Standards & Interfaces*, vol. 42, pp. 9–16, 2015.

[14] J. LiZ. Jia et al., "Network construction method of cable anti-theft network based on improved ant colony algorithm," *Journal of Chongqing University of Technology (Natural Science)*, vol. 31, no. 12, pp. 160–165, 2017.

[15] M. Mishra and M. van Riet, "A channel model for power line communication using 4PSK technology for diagnosis: some lessons learned," *International Journal of Electrical Power & Energy Systems*, vol. 95, no. 12, pp. 617–634, 2018.

[16] W. Cao and C. Yin, "Research on broadband MIMO power line communications model," *Proceedings of the CSEE*, vol. 37, no. 4, pp. 1136–1141, 2017.

[17] Q. Gao, Y. Wang, H. Yang, and N. Liu, "Low-voltage power line meter reading technology research based on multi-band spread spectrum," *Power System Protection and Control*, vol. 42, no. 5, pp. 136–141, 2014.

[18] M. Korki, C. Zhang, and H. Vu, "Performance evaluation of PRIME in smart grid," in *Proceedings of the IEEE International Conference on Smart Grid Communications*, pp. 294–299, Vancouver, Canada, October 2013.

[19] M. Hoch, "Comparison of PLC G3 and PRIME," in *Proceedigns of the 2013 IEEE International Symposium on Power Line Communications and its Applications*, pp. 165–169, Udine, Italy, October 2011.

[20] J. Matanza, S. Alexandres, and C. Rodriguez-Morcillo, "Performance evaluation of two narrowband PLC systems: PRIME and G3," *Computer Standards & Interfaces*, vol. 36, no. 1, pp. 198–208, 2013.

[21] A. Atayero, A. Alatishe, and Y. Ivanov, "Power line communication technologies: modeling and simulation of PRIME physical layer," in *Proceedings of the World Congress on Engineering and Computer Science*, pp. 931–936, San Francisco, CA, USA, October 2012.

[22] M. Korki, N. Hosseinzadeh, and T. Moazzeni, "Performance evaluation of a narrowband power line communication for smart grid with noise reduction technique," *IEEE Transactions on Consumer Electronics*, vol. 57, no. 4, pp. 1598–1606, 2011.

[23] J. Domingo, S. Alexandres, and C. Rodriguez-Morcillo, "PRIME performance in power line communication channel," in *Proceedings of the IEEE International Symposium on Power Line Communications and its Applications*, pp. 159–164, Udine, Italy, July 2011.

[24] X. Liu and L. Zhang, "Performance analysis of power line communication network model based on spider web," in *Proceedings of the ICPE 2011-ECCE Asia*, pp. 953–959, Jeju, Korea, May 2011.

[25] X. Liu, Y. Cui, and D. Xu, "Performance optimization for low voltage power line communication," *Electric Power Automation Equipment*, vol. 37, no. 12, pp. 16–21, 2017.

[26] X. Liu, Y. Li, J. Wang, H. Zhu, and D. Xu, "Clustering-cobweb hybrid multipath blind Routing algorithm and communication protocol design for low-voltage power line communication," *Transactions of China Electrotechnical Society*, vol. 30, no. 1, pp. 337–345, 2015.

[27] Q. Gao, J. Y. Yu, P. H. J. Chong, P. L. So, and E. Gunawan, "Solutions for the "silent node" problem in an automatic meter reading system using power-line communications," *IEEE Transactions on Power Delivery*, vol. 23, no. 1, pp. 150–156, 2008.

[28] H. Su, J. Shi, Z. Liang et al., "Automatic transmission line path selection based on GIS and improved CA," *Electric Power Automation Equipment*, vol. 36, no. 12, pp. 109–114, 2016.

[29] Q. Ran, Y. Wu, and M. Qi, "Research on automatic routing method of low-voltage power line carrier network," *Power System Protection and Control*, vol. 39, no. 10, pp. 53–58, 2011.

[30] K. Chen and X. Hu, "Method of relay routing based on genetic adaptive ant colony system algorithm," *Journal of Central South University (Science and Technology)*, vol. 44, no. 2, pp. 571–579, 2013.

[31] N. Xing, S. Zhang, Y. Shi, and S. Guo, "PLC-oriented access point location planning algorithm in smart-grid communication networks," *China Communications*, vol. 13, no. 9, pp. 91–102, 2016.

[32] L. Zhang, X. Liu, J. Qi et al., "Study of improved hierarchical ant colony routing algorithm for low-voltage power line communication," *Transactions of China Electrotechnical Society*, vol. 29, no. 2, pp. 318–324, 2014.

[33] J.-j. QI, X. U. Dian-guo, Y. Zhou, and L. I. U. Xiao-sheng, "Characteristics model and routing algorithm of power-line communications over low-voltage distributions," *Transactions of China Electrotechnical Society*, vol. 29, no. 16, pp. 56–62, 2009.

[34] F. Ni, P. H. Nguyen, J. F. G. Cobben, H. E. Van den Brom, and D. Zhao, "Three-phase state estimation in the medium-voltage network with aggregated smart meter data," *International Journal of Electrical Power & Energy Systems*, vol. 98, pp. 463–473, 2018.

[35] Y. Wang, X. U. E. Chen, and Y. Jiao, "Hierarchical classification PLC routing algorithm combinating static relay with dynamic relay in medium voltage distribution network," *Electric Power Automation Equipment*, vol. 37, no. 12, pp. 8–15, 2017.

[36] S. Martin, W. Liu, and K. Dostert, "On the impedance of low-voltage distribution at frequencies up to 500 kHz," in *Proceedings of the 2012 IEEE International Symposium on Power Line Communications and Its Applications*, pp. 30–34, Beijing, China, March 2012.

[37] J. Zhang, "Research on characteristics of low voltage power line communication channel," *School of Aeronautics and Astronautics*, vol. 40, no. 20, pp. 4–6, 2013.

[38] T. Zheng, X. Yang, and B. Zhang, "Measurement and research of impedance characteristics of low power networks within frequency band from 1 MHz to 30 MHz," *Power System Technology*, vol. 29, no. 19, pp. 80–84, 2005.

[39] S. Galli and T. Banwell, "A novel approach to the modeling of the indoor power line channel-part II: transfer function and its properties," *IEEE Transactions on Power Delivery*, vol. 20, no. 3, pp. 1869–1878, 2005.

[40] W. Huang, J. Qi, N. Huang, and L. I. Yan, "Experiment and analysis of transmission line parameter for carrier wave communication over low-voltage power line," *Electric Power Automation Equipment*, vol. 28, no. 4, pp. 41–44, 2008.

[41] S. Galli and T. C. Banwell, "A deterministic frequency-domain model for the indoor power line transfer function," *IEEE Journal on Selected Areas in Communications*, vol. 24, no. 7, pp. 1304–1316, 2006.

Hindawi
Complexity
Volume 2021, Article ID 6618708, 10 pages
https://doi.org/10.1155/2021/6618708

Research Article

Quality Classification of Lithium Battery in Microgrid Networks Based on Smooth Localized Complex Exponential Model

Zhelin Huang [1] **and Fangfang Yang** [2]

[1] *Department of Statistics, College of Economics, Shenzhen University, Shenzhen, China*
[2] *School of Data Science, City University of Hong Kong, Tat Chee Avenue, Kowloon, Hong Kong, China*

Correspondence should be addressed to Fangfang Yang; fangfyang2-c@cityu.edu.hk

Received 26 October 2020; Revised 23 December 2020; Accepted 11 January 2021; Published 27 January 2021

Academic Editor: Xin Li

Accurate prediction of battery quality using early-cycle data is critical for battery, especially lithium battery in microgrid networks. To effectively predict the lifetime of lithium-ion batteries, a time series classification method is proposed that classifies batteries into high-lifetime and low-lifetime groups using features extracted from early-cycle charge-discharge data. The proposed method is based on a smooth localized complex exponential model that can extract battery features from time-frequency maps and self-adaptively select the time-frequency resolution to maximize the discrepancy of data from the two groups. A smooth localized complex exponential periodogram is then calculated to obtain the time-frequency decomposition of the whole time series data for further classification. The experimental results show that, by using battery features extracted from the first 128 charge-discharge processes, the proposed method can accurately classify batteries into high-lifetime and low-lifetime groups, with classification accuracy and specificity as high as 95.12% and 92.5%, respectively.

1. Introduction

Energy storage technology is regarded as the last kilometer of new energy development. Energy storage lithium battery in microgrid is a small power generation and distribution system composed of distributed generation, energy storage device, energy conversion device, load, and monitoring and protection device. In order to ensure the safety of power consumption load within the power supply scope of microgrid, the iron lithium battery energy storage system as an important backup of microgrid is essential. At present, the application process of power grid system mainly includes acid battery, flow battery, and iron lithium battery. Lithium-ion batteries have become the most promising solutions for applications in microgrid networks due to their high energy density and high power density.

To ensure safety, battery quality must be assessed and guaranteed within a limited time during production. Assessment of battery quality, which usually uses cycle life as an indicator, requires observation of the actual failure of sample batteries during the evaluation period, which is time-consuming. It is thus important to develop effective methods that can identify the quality of sample batteries and better monitor their health.

Several studies have examined unit-quality monitoring. For examples, Ribeiro [1] and Omitaomu et al. [2] applied SVM for machine fault detection and battery quality control, respectively. Park et al. [3] proposed a dual-feature functional SVM for fault detection of lithium-ion batteries. Peng et al. [4] designed example selection criteria and an active learning algorithm and selected a representative time series instance for battery event detection. However, traditional machine learning methods generally use the capacity degradation curve to evaluate battery quality, which is limited. The limitation of existing methods is as below. First, KNN, SVM, and other machine learning methods are often used in discrete sample classification, but less used in time series classification. Second, the classification results obtained by machine learning method are difficult to be explained by the physical state of batteries. Third, the capacity degradation

curve cannot reflect all the characteristics of the battery. It is abundantly clear that other features, such as voltage and temperature, are highly sensitive to the health of the cells. More specifically, the degree of fluctuation of those extracted features increases with cell aging. When battery cells are fresh, the degree of variation is small; however, this variation increases as battery age increases. Also, low-lifetime batteries tend to show large fluctuations and large variances at an early stage [5, 6]. Therefore, in this work, we explore the use of more features for classifying battery quality and propose a new classification method to explore the change of the degree of variation.

In this paper, a set of battery features extracted from temperature, voltage, and current information are adopted as degradation indicators. These indicators are obtained by applying signal processing methods, such as differential voltage analysis (DV) and incremental capacity analysis (IC), which are thought to be useful for evaluating battery health. For instance, Zhou et al. [7] proposed an average voltage attenuation to estimate remaining useful battery life. Weng et al. [8] used the peak position in the IC curve as a conditional indicator to track the state of health (SOH) of lithium-ion batteries in electric vehicles. Wang et al. [9] adopted two inflection points from the location interval of the DV curve as the SOH indicator. These extracted features are time series data from a series of discharging cycles. The time series data is time-correlated or time-dependent, and their vibration frequency and variance usually differ at various time periods, which make the time series classification problem challenging.

Time domain approaches and frequency domain approaches have been proposed for time series classification. The abovementioned features can be transformed in a time domain and a frequency domain, respectively. Fu et al. [10] combined traditional dynamic time wrapping with uniform scaling. However, when calculating the distance between two time series, the method assigns the same weight to each pair of observations, which may cause errors. The disadvantage of considering only the time domain information is that such information ignores the phase difference between the reference value and the test value, which may cause misclassification when shape similarity is compared. Various methods extract information from the frequency domain. Lines et al. [11] proposed a shapelet transform and constructed a decision tree to carry out the classification. Pulli [12] investigated seismic and explosion discrimination problems using the ratio of spectra. Frequency domain information can only reflect the characteristics if such characteristics remain constant throughout the time period. However, if such characteristic changes in different time periods of the whole time series, then frequency domain information cannot detect these changes.

These works have certain limitations because battery systems usually display nonstationary and nonlinear properties, which means that the degree of fluctuation of the characteristics of the battery will change at different time periods. It is abundantly clear that some features, such as temperature, voltage, and capacity, are highly sensitive to the health of the cell. Their variance is visible between cells.

In this paper, we proposed a smoothed localized complex exponential (SLEX) model, which is based on the SLEX transform for adaptive signal decomposition. The reasons why we use the SLEX transform are as follows. First, the SLEX transform corresponds to a time-frequency decomposition, which enables us to calculate the SLEX periodogram for a specific time-frequency region; thus, it can well capture the differences of the variance in different time period and as a basis for classification. Second, the SLEX transform has been successful in various data analyses [13]. However, in battery life analysis, it remains unexplored. Third, in the proposed method, we use a best tree method (see Section 2.2) to self-adaptively select the best SLEX-basis functions so that our method can maximize the discrepancy between two different groups of the time series, leading to higher prediction accuracies.

The rest of this paper is organized as follows. Some technical details of the SLEX model and the classification method based on the SLEX model are introduced in Section 2. The data and preprocessing methods are introduced in Section 3. The experimental results are reported and discussed in Section 4, and our conclusions are drawn in Section 5.

2. Battery Classification Based on SLEX Transformation

2.1. The SLEX Transform. In this section, we briefly introduce the SLEX transform and some properties of this model.

The SLEX library is a set of bases. Each base has orthogonal vectors with time support which are obtained by dividing the time series of length T in a binary manner (Figure 1). An SLEX basis vector $\psi_{S,\omega}(t)$ that has support on the discrete time block $S = [a_0 + 1, \ldots, a_1]$ and oscillates at frequency ω has the form

$$\psi_{S,\omega}(t) = \Psi_{S,+}(t)\exp\left(i2\pi\omega\frac{t}{|S|}\right) + \Psi_{S,-}(t)\exp\left(-i2\pi\omega\frac{t}{|S|}\right), \tag{1}$$

where a_0 and a_1 are start and end points of the time block S. The windows $\Psi_{S,+}(t)$ and $\Psi_{S,-}(t)$ are two particular smooth windows, with the following forms:

$$\begin{aligned}\Psi_{S,+}(t) &= r^2\left(\frac{t-a_0}{\epsilon}\right)r^2\left(\frac{a_1-t}{\epsilon}\right),\\ \Psi_{S,-}(t) &= r^2\left(\frac{t-a_0}{\epsilon}\right)r^2\left(\frac{a_1-t}{\epsilon}\right),\end{aligned} \tag{2}$$

where $r(\cdot)$ is the sine rising cut-off function:

$$r(u) = \sin\left(\frac{\pi}{4}(1+u)\right). \tag{3}$$

The SLEX library is a collection of bases, each having orthogonal vectors with time support that is obtained by segmenting the time series of length T, in a dyadic manner. The library is constructed by first specifying the finest resolution level J (smallest time block has length $T/2^J$). At resolution level j (where $j = 0, \ldots, J$), the time series is

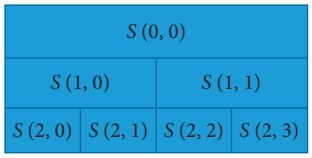

Figure 1: The SLEX library.

divided into 2^j blocks. We denote the block b on level j to be $S(j,b)$ and $M_j = T/2^j$. The SLEX vectors on block $S(j,b)$ are allowed to oscillate at different frequencies $\omega_k = k/M_j$, where $k = -(M_j/2)+1,\ldots,(M_j/2)$.

The SLEX transform consists of the set of coefficients that corresponds to all SLEX vectors defined in the library. The SLEX coefficients on block $S = S(j,b)$ are defined to be

$$\widehat{\theta}_{S,k} = \frac{1}{\sqrt{M_j}} \sum_t X(t)\overline{\psi_{S,\omega_k}(t)}, \tag{4}$$

where M_j is the number of points on block S_j and the frequency is $\omega_k = k/M_j$ and $k = -(M_j/2)+1,\ldots,(M_j/2)$.

The SLEX periodogram is defined as

$$\widehat{\alpha}_{S,k} = \left|\widehat{\theta}_{S,k}\right|^2. \tag{5}$$

For more details about the SLEX model, see [14].

In the following section, we first introduce a best-base selection method that can self-adaptively select the best SLEX base. This method will then be applied to battery data classification.

2.2. Best Base Selection. Because the SLEX transform corresponds to a multilevel decomposition, we denote $S(j,b)$ as the block index. These blocks are of dyadic lengths (Figure 1). For example, if we rescale the entire time series into (0, 1), the blocks of dyadic length will consist of (0, 1/2), (1/2, 1), (0, 1/4), (1/4, 1/2), (1/2, 3/4), (3/4, 1), and so on. The division of $\cup_{S(j,b)}$ determines the time domain resolution and the frequency resolution. For example, if the length of a time series is 1024 and we have a depth of three decompositions, the corresponding division of the time axis is (0, 1/4), (1/4, 1/2), and (1/2, 1) ($\cup_{S(j,b)} = S(2,0), S(2,1), S(1,1)$) and the frequency resolutions are 256, 256, and 512, respectively.

We show how to choose the best base $\cup_{S(j,b)}$ that best reflects the time-frequency decomposition characteristics of the process. Suppose we have two time series, x^1 and x^2.

For a given decomposition depth J, $2^{2^{J-1}}$ different SLEX bases exist. The selection algorithm outlined here is based on the idea of optimal pruning trees, which was first introduced by [15] in the signal-processing literature. This algorithm can automatically find the best base among the possible bases.

(1) Set the maximum depth J to which the tree is grown, which depends on the length T of the time series.

(2) For $j = 0,\ldots,J$, divide the time series into 2^j blocks: block(j,b), $b = 0,\ldots,2^j-1$, block (j,b) corresponding to node (j,b) of the tree.

(3) For $j = 0,\ldots,J$ and $b = 0,\ldots,(2^j-1)$, compute $\widehat{\alpha}_{1,j,b,k}$ and $\widehat{\alpha}_{2,j,b,k}$ of the spectrum in block (j,b) for two time series x^1 and x^2, respectively.

(4) Compute $R_{j,b} = \text{disparity}(\alpha_{1,j,b,k}, \alpha_{2,j,b,k})$, where

$$\text{disparity}\left(\alpha_{1,j,b,k}, \alpha_{2,j,b,k}\right) = \sum_{k=1}^{M_j/2} \frac{\alpha_{1,j,b}}{\left\|x^1\right\|^2} \log \frac{\left(\alpha_{1,j,b}/\left\|x^1\right\|^2\right)}{\left(\alpha_{2,j,b}/\left\|x^2\right\|^2\right)}. \tag{6}$$

(5) For $j = J$ to $j = 0$, $b = 0$ to 2^j-1. If $j = J$, label block (j,b) as terminal. If $j < J$ and if $R(j,b) \geq R(j+1,2b) + R(j+1,2b+1)$, then label the block (j,b) as terminal; otherwise, leave block (j,b) unlabeled and set $R(j,b) = R(j+1,2b) + R(j+1,2b+1)$.

Final segmentation = set of highest labeled blocks = {block (j,b): block (j,b) is labeled and its ancestors are unlabeled}.

2.3. Classification Rules. Given two groups of battery data with high lifetime and low lifetime, respectively, each group has $m = 1,\ldots,N_{\text{low}}$ and $n = 1,\ldots,N_{\text{high}}$ samples of time series with known group labels (low lifetime or high lifetime), respectively. Suppose we have a new sample with unknown group label, and this sample has a periodogram $\widehat{\alpha}_{\text{unknown},i,k}$. We compute the SLEX periodograms from the blocks in $\bigcup S(j,b) = \cup_i S_i$ selected in the last section ($\cup_i S_i$ is a particular dyadic segmentation of the time series) and derive our criteria based on a time-frequency domain approach using the log-likelihood ratio. We introduce the following method to classify the battery with unknown group labels: for each selected time block S_i and frequency k, we denote $\alpha_{\text{low},m,i,k}$ as periodogram of the mth sample in the low quality group and $\alpha_{\text{high},n,i,k}$ as periodogram of the nth sample in the high quality group; then,

$$\alpha_{\text{low},i,k} = \frac{1}{N_{\text{low}}} \sum_{m=1}^{N_{\text{low}}} \alpha_{\text{low},m,i,k}, \tag{7}$$

$$\alpha_{\text{high},i,k} = \frac{1}{N_{\text{high}}} \sum_{n=1}^{N_{\text{high}}} \alpha_{\text{high},n,i,k}. \tag{8}$$

Denote $\alpha = \left\{\alpha_{i,k}\right\}$. Let $p_1(\alpha)$ and $p_2(\alpha)$ be the density under processes π_1 and π_2, respectively, and let $\alpha_{\text{low}} = \alpha_1$ and $\alpha_{\text{high}} = \alpha_2$ be the periodogram under these two processes. The log-likelihoods under these two densities are then, respectively,

$$l\left(\alpha_{\text{low}} \mid \widehat{\alpha}_{\text{unknown}}\right) = -\sum_{\cup S_i} \sum_{k=0}^{M_i/2} \left[\log \alpha_{\text{low},i,k} + \frac{\widehat{\alpha}_{\text{unknown},i,k}}{\alpha_{\text{low},i,k}}\right],$$

$$l\left(\alpha_{\text{high}} \mid \widehat{\alpha}_{\text{unknown}}\right) = -\sum_{\cup S_i} \sum_{k=0}^{M_i/2} \left[\log \alpha_{\text{high},i,k} + \frac{\widehat{\alpha}_{\text{unknown},i,k}}{\alpha_{\text{high},i,k}}\right]. \tag{9}$$

The classification criterion is based on the likelihood ratio, that is, we classify the time series x with unknown type into π_1 if $l(\alpha_{\text{low}}|\widehat{\alpha}_{\text{unknown}}) > l(\alpha_{\text{high}}|\widehat{\alpha}_{\text{unknown}})$; otherwise, it is classified into π_2. Let the classification statistic be

$$\begin{aligned} D_T\left(\alpha_{\text{low}}, \alpha_{\text{high}}, \widehat{\alpha}_{\text{unknown}}\right) &= l\left(\alpha_{\text{low}} \mid \widehat{\alpha}_{\text{unknown}}\right) - l\left(\alpha_{\text{high}} \mid \widehat{\alpha}_{\text{unknown}}\right) \\ &= \sum_{\cup S_i} \sum_k \left[\log \frac{\alpha_{\text{high},i,k}}{\alpha_{\text{low},i,k}} + \left(\widehat{\alpha}_{\text{unknown},i,k}\right)\left(\frac{1}{\alpha_{\text{high},i,k}} - \frac{1}{\alpha_{\text{low},i,k}}\right)\right]. \end{aligned} \tag{10}$$

A flowchart of the proposed classification method to determine the quality of batteries is given in Figure 2.

2.4. Battery Classification Based on SLEX Transformation. We propose that the SLEX model is used to solve the battery classification problem for the following reasons. First, the SLEX model handles nonstationary time series, where the capacity degradation curves and other features such as temperature and voltage curves are nonstationary and nonlinear. Therefore, the model is suitable for processing battery data. Second, the classification method based on the SLEX model is consistent, which means that the more data used for the classification test, the greater the classification accuracy so that the accuracy of classification is guaranteed theoretically [13]. Third, the capacity variance is minimal, when battery cells are fresh, but it increases with increasing battery age [5]. It is abundantly clear that other features, such as voltage and temperature, are highly sensitive to the health of the cells. More specifically, the degree of fluctuation of those extracted features increases with cell aging. Therefore, low-quality batteries tend to show large fluctuations and large variances at an early stage. The SLEX transform corresponds to a time-frequency decomposition, so it can well capture these differences and carry out the classification.

3. Li-Ion Battery Data and Data Preprocessing

3.1. Data. The capacity of a rechargeable battery is usually defined as the available power in ampere-hours (Ah). It is a measure of the battery's basic performance. Cycle life refers to the number of times a charge and discharge cycle is completed before a battery's nominal capacity falls below a predetermined fraction of its initial capacity. Although it is desirable to maintain the initial capacity as much as possible during battery use, the capacity may be reduced by repeated cycles. Figure 3 shows the remaining capacities of 123 samples of commercial graphite cells as the charge and discharge cycle progressed. The data came from [16], who randomly selected the battery cells and cycled them in a temperature-controlled chamber (30°C) under various fast-charging but identical discharging conditions (4°C to 2.0 V). Internal resistance, cell temperature, current, and voltage were continuously measured during the cycle. In the cycle life test, each sample was checked for a specific threshold over a specified number of cycles. The threshold level and number of cycles are usually predetermined based on industry standards (e.g., the threshold value is usually defined as 80% of its initial capacity over 500 cycles; if the capacity is greater than 80% of its initial capacity over 500 cycles, then we define the battery as a high-lifetime battery; otherwise, it is defined as a low-lifetime battery). According to the requirements of the battery, the battery is then assigned to the high-lifetime or low-lifetime group (Figure 3).

3.2. Feature Extraction. In this work, the following features, with reference to [17, 18], were extracted for battery quality classification:

(1) $F1$: capacity
(2) $F2$: $(\mathrm{d}Q/\mathrm{d}V)_{\max}$ which records the y-axis of maximum values on the IC curve
(3) $F3$: $(\mathrm{d}Q/\mathrm{d}V)_{\max}(V)$ which records the x-axis of maximum values on the IC curve
(4) $F4$: mean (ΔQ) which records the mean of difference of Q in adjacent cycles
(5) $F5$: var (ΔQ) which records the variance of difference of Q in adjacent cycles
(6) $F6$: IR is internal resistance
(7) $F7$: $T_{\max}$ is maximum temperature of the cell in each cycle
(8) $F8$: min (ΔQ) which records the minimum value of the difference of Q in adjacent cycles
(9) $F9$: $T_{\min}$ is minimum temperature of the cell in each cycle

$F2$ and $F3$ were extracted from the incremental capacity (IC) curve (peak and voltage shift, respectively). The IC describes the relationship between a capacity change and a voltage change $(\Delta Q/\Delta V)$ during a discharge process (Figures 4(e) and 4(f)). An IC curve is obtained by charging or discharging a battery under a very low current (e.g., 1/30°C) to ensure that the battery operates in a "near equilibrium" condition [19]. Although the battery has a large charge and discharge current when used in a vehicle, as shown in [20, 21], the peak on the IC curve can still be recognized, which reveals important features about battery health for normal charging and discharging data. A study of the relationship between coulombic efficiency and capacity degradation of commercial lithium-ion batteries is shown in [22]. By observing the gradual development of the peak of the IC curve throughout the life cycle, we can understand the battery's aging mechanism.

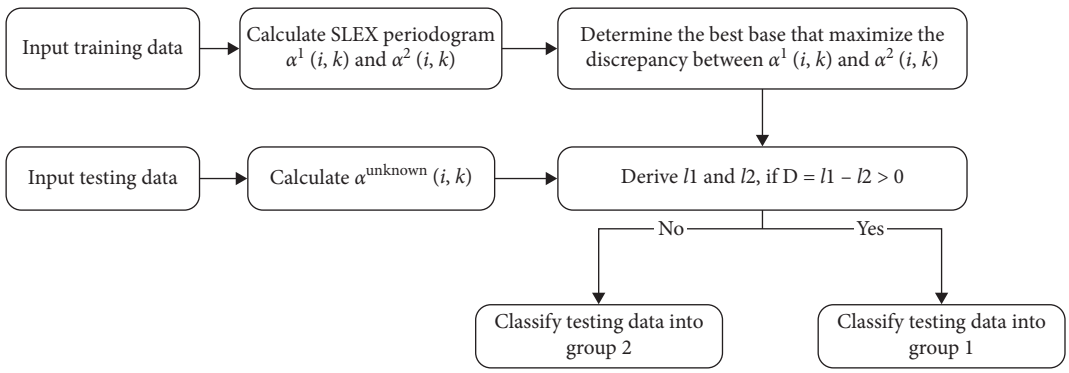

Figure 2: Flowchart of classification process, where training data with low lifetime are in group 1 and training data with high lifetime are in group 2.

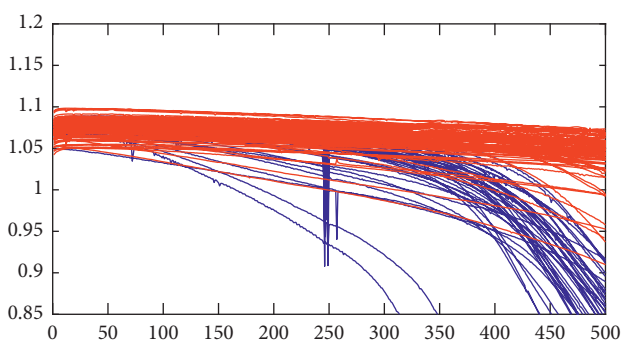

Figure 3: Capacities in different cycles. x-axis: cycle number and y-axis: capacity. Red lines: batteries with high lifetime. Blue lines: batteries with low lifetime.

A loss of active material, loss of lithium inventory, and an increase of IR (Figures 4(g) and 4(h)) are three main processes that cause battery degradation [23]. These factors can be easily identified by an unbalanced drop in peak intensity (y-axis of the IC curve), a decrease in the ratio of peak intensities, and a shift in peak voltage position (x-axis of the IC curve), respectively [6].

We also propose characteristics from the field of lithium-ion batteries, such as cell temperature, initial discharge capacity, and charge time (Figures 4(a) and 4(b)). To capture the electrochemical evolution of a single cell during cycling, several features were calculated from the discharge voltage curve [24]. Specifically, we considered the cycle-to-cycle evolution of $Q(V)$ and the discharge voltage curve as a function of voltage for a given cycle (Figures 4(c) and 4(d)), respectively. Because the voltage range is the same for each cycle, we consider capacity as a function of voltage as the basis for the comparison period.

3.3. Training and Testing Data. There were a total of 83 batteries with high lifetimes and 40 batteries with low lifetimes. We randomly divided these batteries into five folds. The first four folds had 16 batteries with high lifetimes and 8 batteries with low lifetimes, whereas the fifth fold had 19 batteries with high lifetimes and 8 batteries with low lifetimes. Each time, we retained one fold of the time series for classification and used the remaining time series for training a classifier. For each holdout time series, we first selected a basis; we then calculated the SLEX periodograms at the blocks in this basis; finally, we constructed the classifier and assigned the holdout time series. This procedure can be repeated for each fold of the holdout time series. For each feature we proposed, the classification process can be carried out by the following three steps:

1. Divide the data into roughly five equal parts.
(2) For each $i = 1, 2, 3, 4, 5$, train the classifier with other 4 parts and compute the number of TP, FP, FN, and TN (see Table 1) of the ith part.
(3) Sum the number of TP and TN in 5 parts. Calculate the accuracy, sensitivity, and specificity.

The proposed classification method based on the SLEX transform requires that the length of the input data to be a power of 2. Therefore, the experiments were conducted using battery data from the first 128 cycles and the first 256 cycles. The accuracy, sensitivity, and specificity were the three metrics used to evaluate the classification results. See Table 1, for more details.

1. Accuracy = $(TP + TN)/(TP + TN + FP + FN)$
(2) Sensitivity = $TP/(TP + FN)$
(3) Specificity = $TN/(TN + FP)$

"Accuracy" refers to the accuracy of the entire classification. "Sensitivity" refers to the proportion of samples that are actually positive and judged to be positive, whereas "specificity" refers to the proportion of samples that are actually negative and are classified to be negative. In this paper, we mainly focus on specificity and accuracy because these two indicators reflect the recognition accuracy of low-lifetime batteries and the overall recognition accuracy.

4. Experimental Results

We applied the proposed SLEX method to classify a battery time series as either high lifetime or low lifetime.

4.1. Univariate Case. Table 2 shows the classification result using data from the first 128 cycles. Using training data from

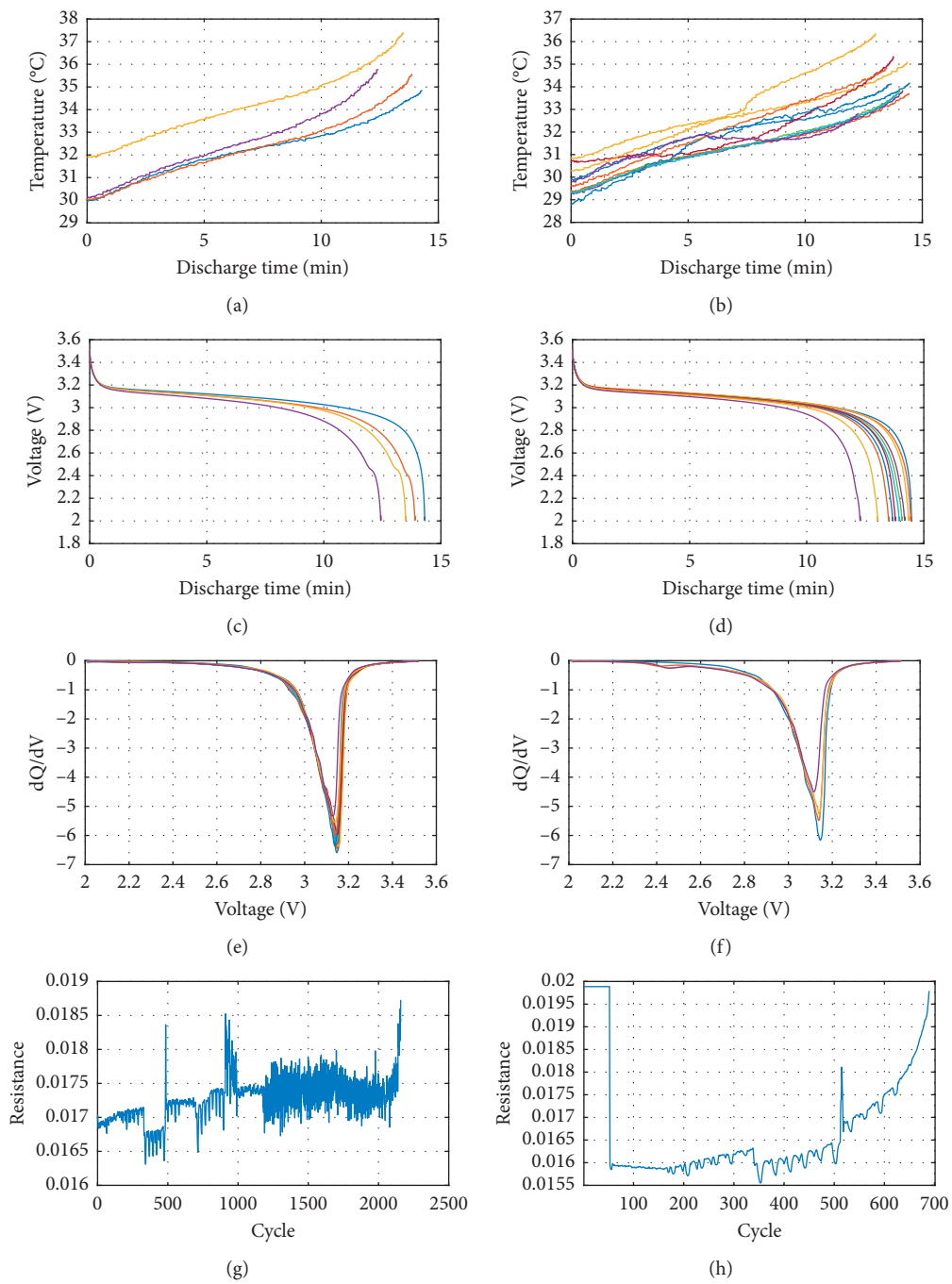

Figure 4: (a) Discharge temperature for cell with low lifetime, every 200 cycles; (b) discharge temperature for cell with high lifetime, every 200 cycles; (c) discharge voltage curves for cell with low lifetime, every 200 cycles; (d) discharge voltage curves for cell with high lifetime, every 200 cycles; (e) IC curve for cell with low lifetime, every 200 cycles; (f) IC curve for cell with high lifetime, every 200 cycles; (g) IR curve for cell with low lifetime; (h) IR curve for cell with high lifetime.

Table 1: Metrics to evaluate classification results.

	Actual positive	Actual negative
Predicted positive	True positive (TP)	False positive (FP)
Predicted negative	False negative (FN)	True negative (TN)

the first 128 cycles, the accuracy of $F1$ is 50.41%. The sensitivity and specificity of $F1$ are 53.01% and 45%, respectively. Here, it is not easy to distinguish the battery quality from the capacity because capacity differs little during the early cycles. Other features we extracted, such as $F4$, $F5$, $F7$, and $F8$, performed much better than the capacity, with classification accuracies exceeding 90%.

We also considered the classification effect using data from the first 256 cycles (Table 3). Using training data from the first 256 cycles, the specificity was much higher, but still insufficient. The classification sensitivity was 96.39% and the

Table 2: Classification results using data from first 128 cycles.

Features	Sensitivity (%)	Specificity (%)	Accuracy (%)
*F*1	53.01	45.00	50.41
*F*2	79.52	70.00	76.42
*F*3	65.06	65.00	65.04
*F*4	96.39	85.00	92.68
*F*5	98.80	85.00	94.31
*F*6	80.72	77.50	79.67
*F*7	93.98	92.50	93.50
*F*8	96.39	87.50	93.50
*F*9	93.98	92.50	93.50

Table 3: Classification results using data from first 256 cycles.

Features	Sensitivity (%)	Specificity (%)	Accuracy (%)
*F*1	96.39	25.00	73.17
*F*2	84.34	50.00	73.17
*F*3	86.75	80.00	84.55
*F*4	87.95	95.00	90.24
*F*5	78.31	90.00	82.11
*F*6	73.49	80.00	75.61
*F*7	97.59	92.50	95.93
*F*8	89.16	90.00	89.43
*F*9	97.59	92.50	95.93

specificity is 25%, which means that high-lifetime batteries could be accurately distinguished, but low-lifetime batteries could not be distinguished correctly. We therefore considered using other features for the classification. The experimental results using data from the first 128 cycles and the first 256 cycles, plotted in Figures 5 and 6, respectively, showed that increasing the amount of data improved the classification specificity of *F*3–*F*8 to a certain extent, but the sensitivity of *F*4, *F*5, *F*6, and *F*8 decreased. Because our experimental data had more high-quality batteries, the overall accuracy rate decreased slightly. Overall, increasing the amount of data only improved the classification accuracy (specificity) of low-quality batteries, whereas the classification of high-quality batteries did not improve. Also, the cost due to longer test times often includes not only production delay costs but also opportunity costs. If we can judge the quality of a battery in fewer cycles, the maintenance and replacement of the battery will be timely. If we use the first 256 cycles of data to make predictions, although the accuracy rate is improved, the overall improvement is limited, and the life expectancy of low-life batteries is less than half at this time. Therefore, it is preferable to use the first 128 cycles of data to make predictions.As shown in Figure 4, the *F*3, *F*4, *F*6, and *F*8 features achieved higher classification accuracy when using the first 128 cycles' data. Features derived from early cycles (such as discharge voltage and temperature) had great predictive performance, even before capacity decay began. We therefore studied the degenerative patterns that did not immediately cause capacity decay, but still showed up in other characteristic curves. Of all the features, the highest classification accuracy was obtained by using the maximum temperature (*F*8) during discharging in the first 128 or 256 cycles, as shown in Figures 5 and 6, respectively. The reason is that, for high-lifetime batteries, the oscillation frequency of the average temperature is lower when discharging, whereas for low-lifetime batteries, the frequency is much higher. Figure 7 shows the values of the different features of the battery in the first 256 cycles. For batteries with low lifetimes, features 4, 6, and 8 tended to fluctuate greatly, and these differences were captured by the proposed method because we compared the time-frequency decomposition maps. For batteries with low lifetimes, feature 3 showed a downward trend, whereas batteries with high lifetimes were relatively stable. This difference was also captured by the proposed model because the SLEX transform was carried out with a window Fourier transform.

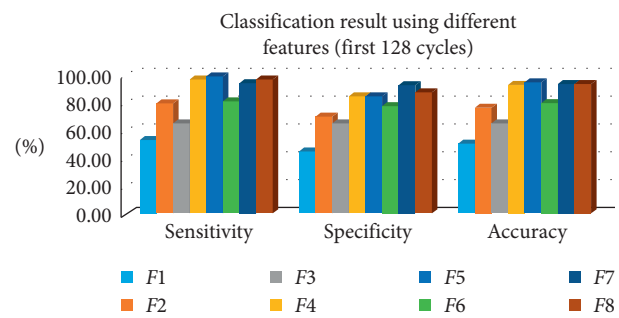

Figure 5: Classification result with data from first 128 cycles.

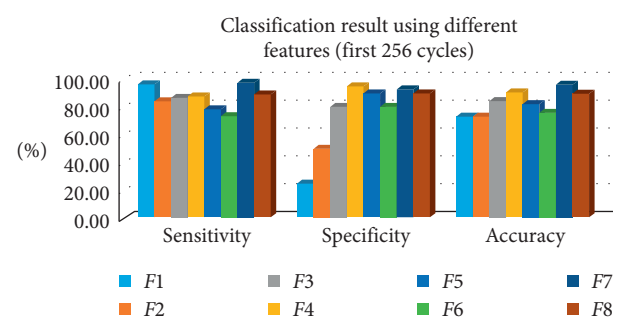

Figure 6: Classification result with data from first 256 cycles.

Therefore, these four indicators performed well in the proposed classification method. These properties were displayed early in the cycle, before the onset of capacity fade, as shown in Figure 7. Therefore, these features presented much greater classification accuracies than the capacity.

4.2. Comparative Study. In this section, the classification accuracy of the proposed method is compared with that of methods such as KNN and SVM because these methods are classic methods for dealing with classification problems, and these two methods have been widely used in the battery field, as described in Section 1. The training and testing procedures (five folds crossvalidation) were the same as those used in the SLEX method, described in Section 3.3.

Considering the diversity of features, classifications based on *F*1, *F*4, and *F*8 were compared and the results are presented in Table 4. For *F*1 (capacity), the classification

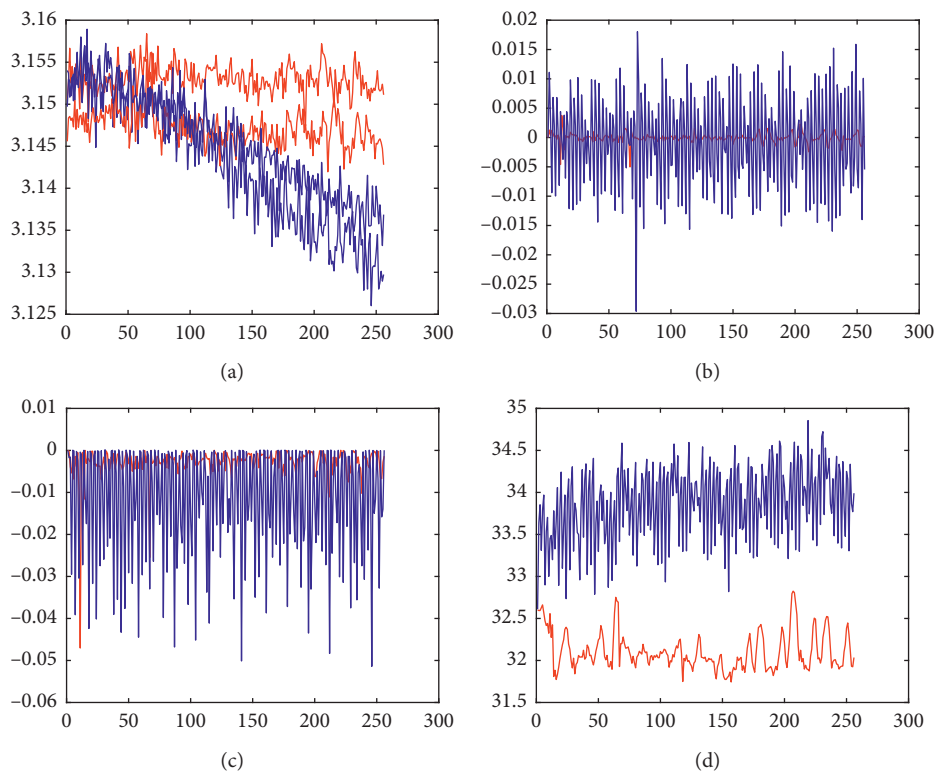

Figure 7: (a) $F3$; (b) $F4$; (c) $F6$; (d) $F8$. High lifetime (red line) and low lifetime (blue line).

accuracy using SLEX was 50.41%, which was not as good as the classification accuracies of KNN and SVM. However, the specificity was 45%, which was greater than that of KNN and SVM. Overall, none of these methods performed well on this feature. For F4 and F8, the SLEX methods achieved a classification accuracy above 90%, which was better than the classification accuracies of KNN and SVM. For low-lifetime batteries, the accuracy of the SLEX method was much higher than that of the other two methods, which is reflected in the value of specificity. Because the high-lifetime batteries samples in datasets are about twice as high as low-lifetime batteries (83 vs. 40), KNN and SVM were more likely to classify unknown batteries as high-lifetime batteries, resulting in lower specificity values for both methods. With the SLEX method, we took the average of the calculated periodograms from both groups according to equations (7) and (8). Therefore, the influence of sample size on the classification problem is avoided.

From the comparative analysis, we reached the following conclusions. First, we learned from the results that little difference in capacity was seen during the early cycle of a battery, so it was difficult to distinguish battery quality from this function, as shown in Table 4. Second, from Table 4, the specificities of KNN and SVM were low because, during the experiment, many low-lifetime batteries were misclassified as high-lifetime types, whereas the SLEX method achieved much better results. Third, because the SLEX method could discern the variations of the nonstationary time series in the variance by spectrum analysis, better classification effect was achieved.

Table 4: Classification performance compared with KNN and SVM.

Feature	Metrics	KNN (%)	SVM (%)	SLEX (%)
$F1$	Sensitivity	90.36	87.95	53.01
	Specificity	22.5	12.5	45
	Accuracy	68.29	63.41	50.41
$F4$	Sensitivity	93.98	84.34	98.80
	Specificity	77.5	75	85
	Accuracy	88.62	81.30	94.31
$F8$	Sensitivity	85.54	98.80	96.39
	Specificity	65	22.5	87.5
	Accuracy	78.86	73.98	93.5

4.3. Multivariate Case. The SLEX method can only be applied to univariate time series. To take multiple features into consideration at the same time, we proposed the following rules to further improve the classification accuracy. As discussed in Section 4.1, we only considered using data from the first 128 cycles. First, we imposed the univariate classification method on each feature, including features 2, 4, 5, 6, 7, 8, and 9 in Table 2, because the classification accuracy using these features is the highest among all features (taking into account the diversity of features, we selected seven dissimilar features). Then, if four or more features classify the battery as high lifetime, the final decision was made to classify the battery into the high-lifetime class; otherwise, the battery was considered to be in the low-lifetime class. The classification results using all seven features together were shown in Table 5 and Figure 8. By using features such as

Table 5: Classification results using data from first 128 cycles.

Features	Sensitivity (%)	Specificity (%)	Accuracy (%)
*F*2, *F*4, *F*5, *F*6, *F*7, *F*8, and *F*9	96.39	92.50	95.12

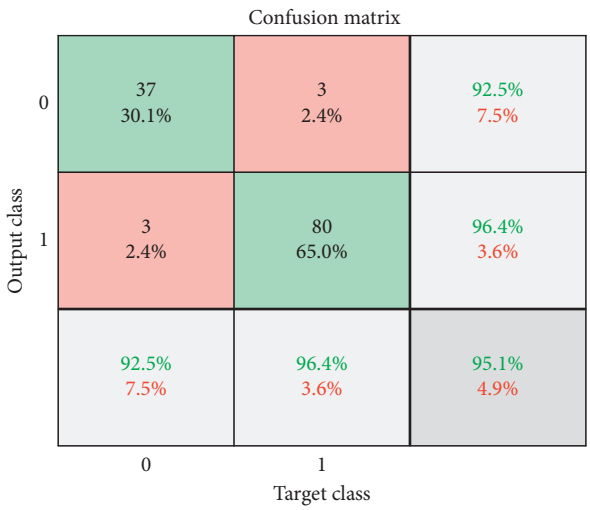

Figure 8: Classification results using data from first 128 cycles.

features that we extracted from each cycle, the sensitivity was 96.39%, which was higher than other features except for F5. In this study, we mainly focused on the values of specificity and accuracy because, in actual application, the accurate identification of low-lifetime batteries is more practical. The classification accuracy improved to 95.12% and the specificity was 92.5%, values that were the best among all results obtained from the first 128 cycles. Therefore, by combining these features, we obtain better classification results overall.

5. Conclusions

In this paper, a classification method based on the SLEX model is proposed to process battery capacity data and monitor battery quality at early stage. Our proposed model aims to classify batteries with high lifetimes and with low lifetimes using only data from the first 128 charge-discharge cycles. The proposed method constructs a classifier that can self-adaptively maximize the discrepancy between two groups of data, which makes it easier to classify data with unknown labels. In Section 4.2, the experimental results showed that the proposed method achieved higher classification accuracy than commonly used method such as KNN and SVM. In addition, the experimental results show that a classification accuracy larger than 90% is achieved by using some features. Moreover, the proposed method performed much better on features extracted from temperature, voltage, and IC curves than on capacity. Among these features, batteries with high lifetime and low lifetime can exhibit different properties early in the charge-discharge cycle, which can be captured by our proposed classification model, as discussed in Section 4.1. Therefore, our proposed features and classification model can match perfectly and get accurate classification results. Because the classification model is only applicable to one-dimensional time series, a voting model based on each factor is proposed in practical application to extend the classification model to the case of multidimensional time series problems. The experimental results show a classification accuracy and specificity of 95.12% and 92.5%, respectively, by using effective features we extracted from the battery discharging process. In practice, assessments using early-cycle battery data (the first 128 cycles) will bring new opportunities for battery optimization and production.

Data Availability

The data used to support the findings of the study are given in [16] for a reference. Supplementary information is available for the previously reported studies at https://doi.org/10.1038/s41560-019-0356-8.

Conflicts of Interest

The authors declare that they have no conflicts of interest.

References

[1] B. Ribeiro, "Support vector machines for quality monitoring in a plastic injection molding process," *IEEE Transactions on Systems, Man and Cybernetics, Part C (Applications and Reviews)*, vol. 35, no. 3, pp. 401–410, 2005.

[2] O. A. Omitaomu, M. K. Jeong, A. B. Badiru, and J. W. Hines, "Online support vector regression approach for the monitoring of motor shaft misalignment and feedwater flow rate," *IEEE Transactions on Systems, Man and Cybernetics, Part C (Applications and Reviews)*, vol. 37, no. 5, pp. 962–970, 2007.

[3] J. I. Park, S. H. Baek, M. K. Jeong, and S. J. Bae, "Dual features functional support vector machines for fault detection of rechargeable batteries," *IEEE Transactions on Systems, Man, and Cybernetics, Part C (Applications and Reviews)*, vol. 39, no. 4, pp. 480–485, 2009.

[4] F. Peng, X. Zhou, H. Liu, H. Tan, Q. Luo, and J. Hu, "A time series classification method for battery event detection," in *Proceedings of the 2017 IEEE 23rd International Conference on Parallel and Distributed Systems (ICPADS)*, pp. 17–24, IEEE, Shenzhen, China, December 2017.

[5] X. Hu, J. Jiang, D. Cao, and B. Egardt, "Battery health prognosis for electric vehicles using sample entropy and sparse Bayesian predictive modeling," *IEEE Transactions on Industrial Electronics*, vol. 63, no. 4, pp. 2645–2656, 2015.

[6] M. Dubarry and B. Y. Liaw, "Identify capacity fading mechanism in a commercial $LiFePO_4$ cell," *Journal of Power Sources*, vol. 194, no. 1, pp. 541–549, 2009.

[7] Y. Zhou, M. Huang, Y. Chen, and Y. Tao, "A novel health indicator for on-line lithium-ion batteries remaining useful life prediction," *Journal of Power Sources*, vol. 321, pp. 1–10, 2016.

[8] C. Weng, X. Feng, J. Sun, and H. Peng, "State-of-health monitoring of lithium-ion battery modules and packs via incremental capacity peak tracking," *Applied Energy*, vol. 180, pp. 360–368, 2016.

[9] L. Wang, C. Pan, L. Liu, Y. Cheng, and X. Zhao, "On-board state of health estimation of lifepo4 battery pack through

differential voltage analysis," *Applied Energy*, vol. 168, pp. 465–472, 2016.

[10] A. W.-C. Fu, E. Keogh, L. Y. H. Lau, C. A. Ratanamahatana, and R. C.-W. Wong, "Scaling and time warping in time series querying," *The VLDB Journal*, vol. 17, no. 4, pp. 899–921, 2008.

[11] J. Lines, L. M. Davis, J. Hills, and A. Bagnall, "A shapelet transform for time series classification," in *Proceedings of the 18th ACM SIGKDD International Conference on Knowledge Discovery and Data Mining*, pp. 289–297, ACM, Beijing, China, August 2012.

[12] J. J. Pulli, "Extracting and processing signal parameters for regional seismic event identification," in *Monitoring a Comprehensive Test Ban Treaty*, pp. 743–754, Springer, Berlin, Germany, 1996.

[13] H.-Y. Huang, H. Ombao, and D. S. Stoffer, "Discrimination and classification of nonstationary time series using the SLEX model," *Journal of the American Statistical Association*, vol. 99, no. 467, pp. 763–774, 2004.

[14] H. Ombao, J. Raz, R. Von Sachs, and W. Guo, "The SLEX model of a non-stationary random process," *Annals of the Institute of Statistical Mathematics*, vol. 54, no. 1, pp. 171–200, 2002.

[15] R. R. Coifman and M. V. Wickerhauser, "Entropy-based algorithms for best basis selection," *IEEE Transactions on Information Theory*, vol. 38, no. 2, pp. 713–718, 1992.

[16] K. A. Severson, P. M. Attia, N. Jin et al., "Data-driven prediction of battery cycle life before capacity degradation," *Nature Energy*, vol. 4, no. 5, p. 383, 2019.

[17] F. Yang, D. Wang, F. Xu, Z. Huang, and K.-L. Tsui, "Lifespan prediction of lithium-ion batteries based on various extracted features and gradient boosting regression tree model," *Journal of Power Sources*, vol. 476, p. 228654, 2020.

[18] F. Xu, F. Yang, Z. Fei, Z. Huang, and K.-L. Tsui, "Life prediction of lithium-ion batteries based on stacked denoising autoencoders," *Reliability Engineering & System Safety*, vol. 208, Article ID 107396, 2020.

[19] M. Dubarry, C. Truchot, and B. Y. Liaw, "Synthesize battery degradation modes via a diagnostic and prognostic model," *Journal of Power Sources*, vol. 219, pp. 204–216, 2012.

[20] X. Han, M. Ouyang, L. Lu, J. Li, Y. Zheng, and Z. Li, "A comparative study of commercial lithium ion battery cycle life in electrical vehicle: aging mechanism identification," *Journal of Power Sources*, vol. 251, pp. 38–54, 2014.

[21] C. Weng, J. Sun, and H. Peng, "A unified open-circuit-voltage model of lithium-ion batteries for state-of-charge estimation and state-of-health monitoring," *Journal of Power Sources*, vol. 258, pp. 228–237, 2014.

[22] F. Yang, D. Wang, Y. Zhao, K.-L. Tsui, and S. J. Bae, "A study of the relationship between coulombic efficiency and capacity degradation of commercial lithium-ion batteries," *Energy*, vol. 145, pp. 486–495, 2018.

[23] M. Kassem, J. Bernard, R. Revel, S. Pélissier, F. Duclaud, and C. Delacourt, "Calendar aging of a graphite/lifepo4 cell," *Journal of Power Sources*, vol. 208, pp. 296–305, 2012.

[24] Z. Huang, F. Yang, F. Xu, X. Song, and K. L. Tsui, "Convolutional gated recurrent unit-recurrent neural network for state-of-charge estimation of lithium-ion batteries," *IEEE Access*, vol. 7, pp. 93139–93149, 2019.

Hindawi
Complexity
Volume 2021, Article ID 6688889, 11 pages
https://doi.org/10.1155/2021/6688889

Research Article

A Nonintrusive Load Monitoring Method for Microgrid EMS Using Bi-LSTM Algorithm

Dongguo Zhou, Yangjie Wu, and Hong Zhou

School of Electrical Engineering and Automation, Wuhan University, Wuhan 430072, China

Correspondence should be addressed to Yangjie Wu; 1035845768@qq.com

Received 21 November 2020; Revised 27 December 2020; Accepted 15 January 2021; Published 23 January 2021

Academic Editor: Ruoli Tang

Nonintrusive load monitoring in smart microgrids aims to obtain the energy consumption of individual appliances from the aggregated energy data, which is generally confronted with the error identification of the load type for energy disaggregation in microgrid energy management system (EMS). This paper proposes a classification strategy for the nonintrusive load identification scheme based on the bilateral long-term and short-term memory network (Bi-LSTM) algorithm. The sliding window algorithm is used to extract the detected load event features and obtain the load features of data samples. In order to accurately identify these load features, the steady state information is combined as the input of the Bi-LSTM model during training. Comprising long-term and short-term memory (LSTM) network and recurrent neural network (RNN), Bi-LSTM has the advantages of stronger recognition ability. Finally, precision (P), recall (R), accuracy (A), and F_1 values are used as the evaluation method for nonintrusive load identification. The experimental results show the accuracy of the Bi-LSTM identification method for load start and stop state feature matching; moreover, the method can identify relatively low-power and multistate appliances.

1. Introduction

The advancement of nonintrusive load monitoring (NILM) is hastened by the ever-increasing requirements for smart microgrid power utilization and demand side management [1]. The long-term and short-term memory NILM has disaggregated real-time energy consumption information with the load detection module installed at the microgrid EMS power input, which is one approach of demand-side management strategies in the smart grid [2]. Compared with traditional intrusive load monitoring, it has several significant advantages such as low cost, excellent data integrity, easy installation, and good practicability [3, 4]. This has become a significant direction for researchers in the microgrid energy management system (EMS).

The NILM process mainly includes data acquisition and processing, event detection, features extraction, and load identification. There are various methods for feature extraction [5] and load identification [6], including supervised classification methods [7], unsupervised clustering methods [8], and optimization methods [9]. Among them, the deep learning algorithms are widely used in the field of load identification [10, 11]. In particular, a low complexity unsupervised NILM algorithm was presented in [12], which has outperformance for event detection compared with recent existing work for unsupervised NILM considering common metrics. A practical solution for nonintrusive type II load monitoring based on deep convolutional neural networks was provided in [13]. Further, three new graph-based semisupervised multilevel load monitoring algorithms were studied in [14, 15], which only needs a small sample of observed power signals annotated with active appliances. They tackled the NILM by applying a novel graph signal processing (GSP) into both the physical signal level and data level. Additionally, a deep learning framework based on a combination of a convolutional neural network (CNN) and LSTM was proposed in [16], in which the proposed hybrid CNN-LSTM model used CNN layers for feature extraction from the input data with LSTM layers for sequence learning. Although the current identification algorithms for multistate

load and low-power load identification have achieved certain recognition performants, their identification of load power and performance improvement still needs further research.

Alternatively, feature construction is also considered as the key step to achieve load monitoring technique. For example, a method based on the dynamic time warping (DTW) algorithm and template library waveform was proposed [17] to cope with the existing problems with the steady load characteristic value method and the superposition of the steady-state waveform of domestic load. In references [18, 19], researchers employed short-time Fourier transform feature extraction and LSTM auto encoder neural networks-based classification and fault detection on DC pulsed load monitoring to demonstrate the effectiveness of nonintrusive load monitoring. In ref. [20], the neural network model was developed to recognize steady-state parameters extracted from low-frequency sampling data, such as real power, current, impedance, and admittance variables. In reference [21], a new algorithm is proposed to classify events of appliance states based on modification of the cross entropy (CE) method, which relies on low-rate sampling of the active power. Nevertheless, this method cannot cope with the identification of low-power appliances.

In this paper, a nonintrusive load monitoring scheme based on Bi-LSTM algorithm is proposed to improve the performance of the nonintrusive load identification. The steady state features are constructed by the active power, reactive power, and the current harmonics features. It is applied to the load identification by combining the steady state information at the beginning and the end of the load state to construct the features data. Then, the nonlinear mapping is carried out to the output layer for the load identification. Besides, in order to address the problem of multiload feature identification, a load start state feature matching method based on the Bi-LSTM model is adopted, and the output of the optimal matching item in the Bi-LSTM model is taken as the final identification result.

The rest of the paper is organized as follows. Section 2 introduces load features construction, which contains both load power signatures and time domain features, followed by an extraction method of load features based on the sliding window algorithm. Then, an overview of the Bi-LSTM algorithm model and load identification scheme based on the Bi-LSTM model is described in Section 3. In Section 4, load feature of the microgrid EMS is trained and tested by recurrent neural network including (RNN), LSTM, and Bi-LSTM for comparison, as well as the verification experiment of identification method of load start and stop state features matching is carried out. The conclusions are drawn in Section 5.

2. Load Features Construction

In load feature construction, the power features and time domain features are mainly considered, which will be discussed in detail.

2.1. Power Feature Construction. Among the existing load features, the active power P is considered as the widely used load features since it undergoes an obvious change when the load turns on/off status switch [22]. Similarly, the reactive power Q also plays an important role in determining the type of appliances, that is, inductivity, capacitance, or resistance of electrical devices. In order to obtain these features from the electrical entrance, the P and Q are calculated by using the transient voltage and current.

Let $v(t)$ and $i(t)$ be the transient voltage and current at time t, and P and Q can be then defined as follows:

$$P = \frac{1}{T}\sum_{t=0}^{T-1} v(t)i(t),$$
$$Q = \frac{1}{T}\sum_{t=0}^{T-1} v\left(t+\frac{1}{4}T\right)i(t), \tag{1}$$

where T represents a period of the voltage wave.

To get more performants for identification, it is necessary to find another type of features. In this paper, the series of the obtained active power and reactive power are listed as follows:

$$P = \{P_1, P_2, \ldots, P_{n1}\},$$
$$Q = \{Q_1, Q_2, \ldots, Q_{n2}\}, \tag{2}$$

where n_1 and n_2 are the ranks belonging to active power and reactive power, respectively. These data are ranked in a plain sequence. Furthermore, to distinguish different loads effectively, especially for the loads with small active power (usually smaller than 100 W), unequal interval segmentation is adopted. The power variation of these loads is subtle that makes difficulty for load identification. Thus, a statistic of load signatures in load database is adopted to get a more accurate interval of power [23]. The P and Q distribution coming from the dataset is illustrated as rectangles with different colors in Figure 1, where load 1 to load 11, respectively, represent bedroom appliances, basement plugs, cloth dryer, cloth washer, dining room plugs, dish washer, network equipment, fridge, heat pump, TV/PVR/AMP, and wall oven. As seen, several loads are concentrated when P belongs to 0–100 and Q belongs to 0–20. This indicates that loads in this range need to be segmented more intensively. Hence, the segmentation point p_i is set as follows:

$$p_i = \left\{ r(p_i) \le \varepsilon \& r\left(p_{(i\pm1)}\right) > \varepsilon | r(p_i) = \frac{1}{\mathrm{nq}}\sum_{i=1}^{n} K\left(\frac{(p-p_i)}{q}\right)\right\}, \tag{3}$$

where $r(p_i)$ is the kernel density of p_i, $\{p_i\}$ $(i = 1\sim n)$ is a set of power points, q is the window width of the kernel density estimation function $K(\cdot)$, and ε is the threshold. According to equation (3), the point where the power signatures can be divided into two groups by the kernel density is the segmentation point.

However, for the complicated situation consisting of various loads, the features P and Q and their variation are not sufficient to identify load with similar electrical features. Therefore, the following subsection selects time domain

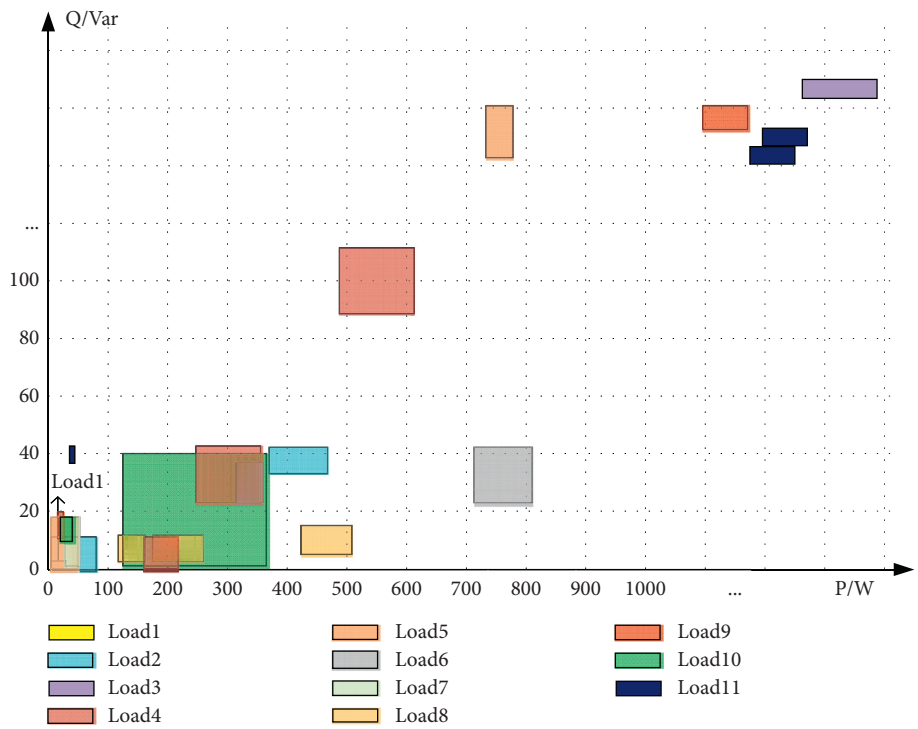

Figure 1: Statistic diagram of load power features.

features as dependable nonelectrical features for load identification.

2.2. Time Domain Feature Construction. Time domain features are often treated as the potential load features [24]. To get all-round information about load features in time domain, this paper introduces the features of working time length and interval, working period, and holiday character.

(i) Working time length: For common microgrid loads, the working time length has almost regularity; i.e., it is an inner character to distinguish different loads [25]. Figure 2 illustrates the working time length counted for eleven loads as shown in Figure 1. It can be seen that most of the microgrid loads work for no more than 100 minutes in a day. A few loads work for over 1400 minutes. In addition, some loads have different working time lengths. Therefore, to construct this type feature, the segmentation method is used as follows:

$$L = \{L_1, L_2, \ldots, L_{m3}\}, \tag{4}$$

where L denotes the length of working time, and m_3 are the amounts of ranks.

(ii) Working time interval: Working time interval of loads can often reflect the users' energy behavior. Similarly, Figure 3 illustrates time interval of the same loads counted. Different color in Figure 3 shows the different load. It can be seen that most of loads are used in the daytime from 6 : 30 to 21 : 30, while, in the night during 21 : 30–6:30, some other loads work. Thus, the time interval in this situation can be generally divided into 9 segments for quantization. The divided segments are shown in Table 1. During 6 : 30–21 : 30, every two hours belongs to one part, and from 21 : 30 to 06 : 30 on the next day, it is divided only into 2 segments, including the late-night period (21 : 30–24 : 00) and the period before dawn (0 : 00–6 : 30).

(iii) Working periodicity: Generally speaking, some of loads often work with periodicity, such as a refrigerator. On the contrary, the working time of loads without periodicity is almost uncertain. Thus, to easily distinguish the two types of loads, the mark here is just used as $T = \{T_1, T_2\}$ with nonperiodicity T_1 and periodicity T_2.

(iv) Holiday character: Different behaviors of the users' routines lead to different frequencies of load usages. For example, the probability of using traditional household electronic will increase when it is on holiday, while the usage of loads for entertainment will decline when it is a weekday since the users go to work. Thus, it is a nonnegligible character in time domain. For convenience, this feature is defined as $F = \{F_1, F_2, F_3\}$, where F_1, F_2, and F_3 denote loads that work every day, every weekday, and sometimes, respectively.

On these bases, load features can be detected and extracted to build the load features database, which will provide training samples. To this end, the load events detection and feature extraction method will be presented as follows.

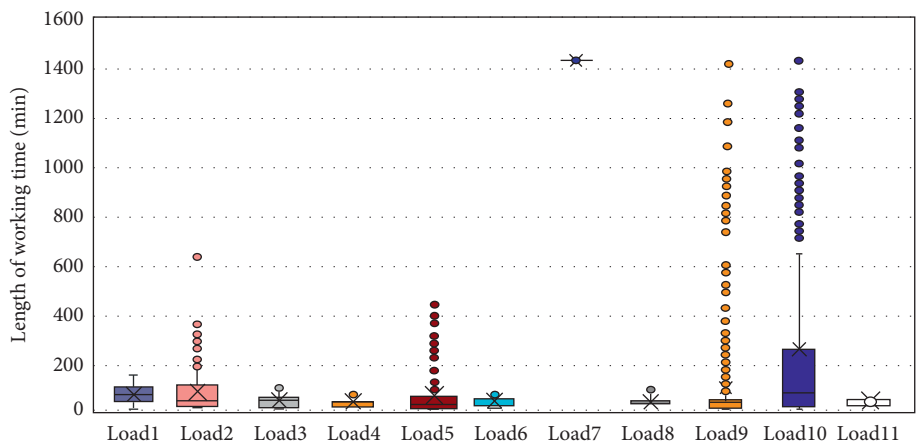

Figure 2: Statistic diagram of load working time length.

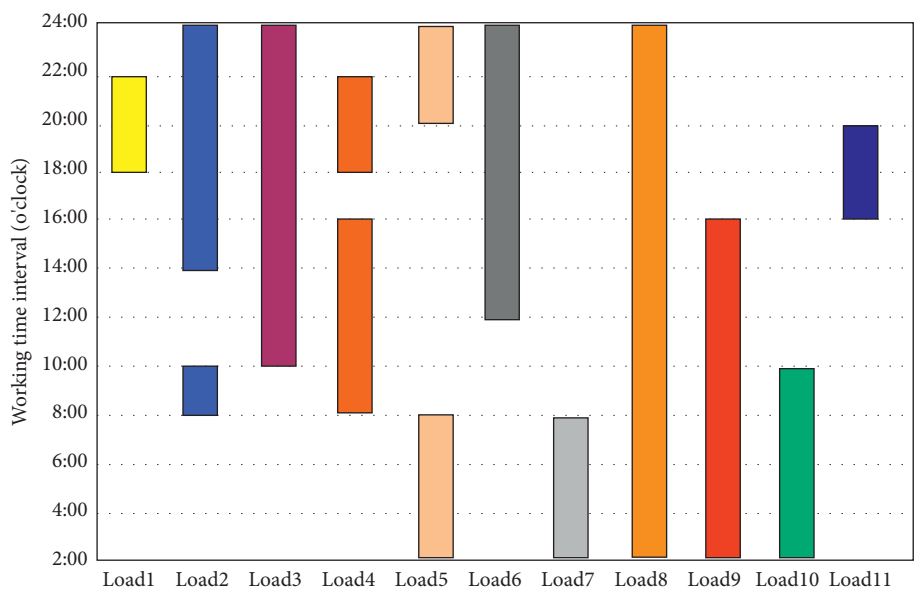

Figure 3: Statistical diagram of working time interval.

Table 1: Segments of working time interval.

t_1	t_2	t_3	t_4	t_5	t_6	t_7	t_8	t_9
0 : 00–6:30	6 : 30–8:30	8 : 30–11 : 30	11 : 30–13 : 30	13 : 30–15 : 30	15 : 30–17 : 30	17 : 30–18 : 30	18 : 30–21 : 300	21 : 30–24 : 00

2.3. Load Event Detection and Feature Extraction. Load events often occurred by turning on or off the load, thus making electrical feature change. Generally, active power is the most significant since the load events happened [26]. The associated evolution curve seems like a step jump, indicating that the load event occurs. In order to obtain the feature, the sliding window algorithm is used to detect these changes and extract the feature through a different method.

For time domain features, the load features are defined as follows:

$$X = \{x(k)\}, \quad k = 1, 2, \ldots, \tag{5}$$

When a load event occurs, the distribution of observation changes. The following hypothesis test is made to see whether there exists a change:

$$H_0\colon X \sim N\left(\mu_0, \sigma_0^2\right), \quad i \geq 1 \leftrightarrow H_1\colon,$$
$$X \sim \begin{cases} N\left(\mu_0, \sigma_0^2\right), & 1 \leq i \leq \tau, \\ N\left(\mu_1, \sigma_1^2\right), & i > \tau, \end{cases} \tag{6}$$

where μ_0 and μ_1 are divided into the average value of the observed quantities; σ_0 and σ_1 are the standard deviation of the observed quantities; τ is a positive integer to record the time of the load event. To be specific, the variation of the mean and variance increases as the sliding window algorithm contains the event occurrence point. Thus, it would be regarded as a load event if the variation of mean and standard deviation exceeds a certain threshold.

The load steady state features have the advantages of easy acquisition and excellent repeatability [27]. However, the features of load running to steady state generally show volatility due to the fluctuation of voltage and current, which lead to different load steady state feature extractions [28]. In order to fully reflect the load operation process, this paper selects the steady state feature near the occurrence point of the load event. When the load event is detected, two steady states of the load event input and output are differentiated. Let a certain length of time series as load input events and cut events be feature vector V_o and V_c, and it can form a set of feature data samples $V_{oc} = [V_o, V_c]$.

The sliding window algorithm is then used to determine the changes in the active power of the load event detection, and the load event is then used to extract load steady state features, enabling the performance improvement of load identification.

3. Load Identification Model

3.1. Bi-LSTM Algorithm Model. The load data collected by noninvasive equipment can be regarded as time series signals. Recurrent neural network (RNN) is an artificial neural network with nodes connected and memory function, which can recognize serialized information effectively [29]. The state is transmitted one-way after going in chronological order, which can only guarantee the forward transmission of information. The improved Bi-RNN scheme adds a hidden layer to the existing RNN model. By comparison, it separates each training sequence forward and reverse as two RNNs and connects the same output layer.

To avoid the problem of gradient disappearance and long-term dependence, we further improve the Bi-RNN model as Bi-LSTM model. In this model, multiple activated neurons are used as hidden layers to selectively save or forget long-term data to satisfy the long-term data dependence requirements. The fundamental of Bi-LSTM consists of two RNN models, where one RNN model trains the data from the forward direction and the other trains the data from the backward direction. The two models then connect the output layer in the Bi-LSTM. Figure 4 shows the structure of Bi-LSTM model, which is a combination of two unidirectional LSTM.

As seen in Figure 4, Bi-LSTM model hidden layer output vectors are marked as A and A', respectively, participating in forward and reverse calculation. In forward calculation, the output A_t of the hidden layer is affected by A_{t-1}. When it calculates in reverse, the value A'_t of the hidden layer is affected by A_{t+1}'. Additionally, the activation function of Bi-LSTM model in Figure 4 is illustrated as follows:

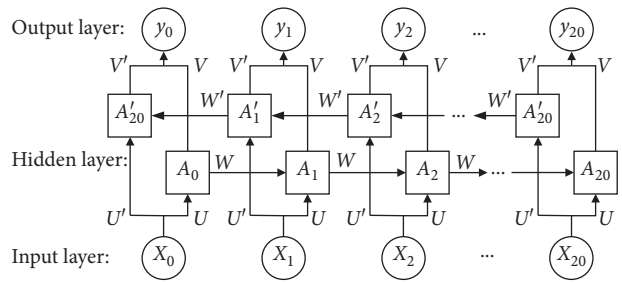

Figure 4: Bi-LSTM algorithm model.

$$\begin{aligned} y_t &= g\left(VA_t + V\prime A_t\right), \\ A_t &= f\left(WA_{t-1} + UX_t\right), \\ A'_t &= f\left(WA'_{t+1} + U'X_t\right), \end{aligned} \tag{7}$$

where $g(\cdot)$ and $f(\cdot)$ represent the output layer neuron activation function and the hidden layer neuron activation function, respectively. V is the weight matrix from the hidden layer to the output layer in forward calculation, whereas W is the weight matrix from the input layer to the hidden layer in forward calculation. Besides, U is the weight matrix from the input layer to the hidden layer calculation, whereas V' is the weight matrix from hidden layer to output layer for reverse calculation. Moreover, W' is the weight matrix of the hidden layer at the first moment in reverse calculation, whereas U' is the weight matrix of the input layer to the hidden layer calculation in reverse.

3.2. Load Identification Scheme Based on Bi-LSTM Model. The load identification scheme of Bi-LSTM neural network consists of training and identification stages. The significant step is to use the SoftMax function to map the data into the range [0, 1], which can be regarded as the probability that the sample data belongs to a certain class [30]. In the classification, cross entropy can represent the degree of proximity between the actual output and the expected output, which is used to calculate losses. In the training step, the neural network realizes the nonlinear fitting from input to output by adjusting the parameters of the weight matrix. Back-propagation through time (BPTT) method adjusts the weight matrix parameters along the gradient direction of error and makes the output results of the neural network approach to the actual results continuously [31]. Here, SoftMax function and cross entropy function [32] are used as the activation function and the loss function of neural network, respectively, in this paper. BPTT method is taken as a training algorithm to establish an identification algorithm model.

The flowchart of load identification scheme is to detect load events, extract input, and cut out load features according to the time of load events, as shown in Figure 5.

In microgrid EMS, there is much electric equipment operating at the same time, and the collected steady-state data will contain the feature vectors of multiple electrical appliances, which is not conducive to identification. In this

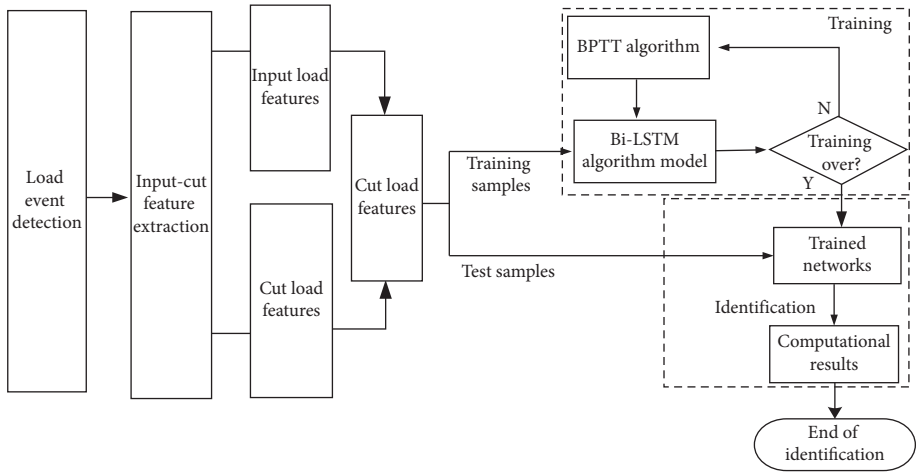

Figure 5: Flowchart of identification scheme flow based on Bi-LSTM model.

paper, a load start state feature matching method based on the Bi-LSTM model is adopted, as shown in Figure 6.

As seen in Figure 6, the time of load event is first determined by load event detection, and the load characteristics of all input and cut out events are extracted. Then, the input and cut-out features of the same appliance are matched as the input of the neural network model. A cut-out (input) feature and all other input (cut-out) features are fed into the Bi-LSTM model according to the combination for identification, and a combination with the highest output probability is taken as the best match.

4. Test Results and Discussion

This work selects eleven representative loads for the test from the microgrid EMS, including the traditional household loads and modern commonly used electronic loads. Without loss of generality, all loads with small power consumption and those with multistatus are selected for demonstrating the performance of our method. Then, based on the above eleven representative loads, five typical loads are randomly selected to verify the experimental verification load start and stop feature matching principle.

4.1. Load Features Extraction of the Microgrid EMS. The sliding window algorithm is used to extract the detected load event features and obtain the load features data samples from the microgrid EMS. The features in the method are constructed by the active power, reactive power, and the fifteen odd-even current harmonics features, which were selected as the input for neural networks. The harmonic component of current can be obtained by fast Fourier transform.

In the load identification scheme for eleven different operating states in microgrid EMS, outputs can be considered as matching a load to the trained sets such that the neural network has outputs as listed in Table 2.

it is specified that each output is a probability value representing the probability that the input data belongs to a certain state. The value range is between 0 and 1, where 0 and 1, respectively, mean that the input data cannot and must belong to the state. The corresponding output state with the highest probability is regarded as the identification result of the input data.

4.2. Training Scenario I. In this test, five-day load features data of the microgrid EMS are picked up for training. In each case, the loads used in the microgrid EMS are not directly illustrated. For example, one day of the active and reactive power curve of one day is drawn in Figure 7.

The labeled data are trained to obtain the probability of each load event by sliding window algorithm. The extracting results are shown in Figure 8. It can be seen that there are 3 loads with powers in the interval 0–30 W in Figure 8(a), 5 loads in 30–100 W in Figure 8(b), 2 loads in 100–1000 W in Figure 8(c), and only 1 load in 1000–2000 W in Figure 8(d).

For verification of the proposed scheme, there are two neural networks for comparison by using the 5-day data for the test. The precision (P), recall (R), accuracy (A), and F_1 values are used as the evaluation indexes to train and test the RNN, LSTM, and Bi-LSTM neural network. The results of the average precision (P), average accuracy (A), average recall (R), and average F_1 of the three neural networks are listed in Table 3.

It can be seen from the four evaluation indexes of identification average precision (P), average accuracy (A), the average recall (R), and average F_1 given in Table 3 that the Bi-LSTM is better than RNN and LSTM. Moreover, Bi-LSTM shows higher computational efficiency and better performance in load identification. Besides, the errors in training and testing of the three neural networks are calculated, as shown in Figures 9 and 10. As seen, the error drop speed is the fastest training in Bi-LSTM scheme than others. At the end of the training period, the three kinds of neural networks finally tend to stabilize, but the Bi-LSTM does not fluctuate since the error drops smoothly, and the stability is reached faster.

Additionally, the error range of test samples for RNN, LSTM, and Bi-LSTM is, respectively, 0.02–0.08, 0.01–0.06,

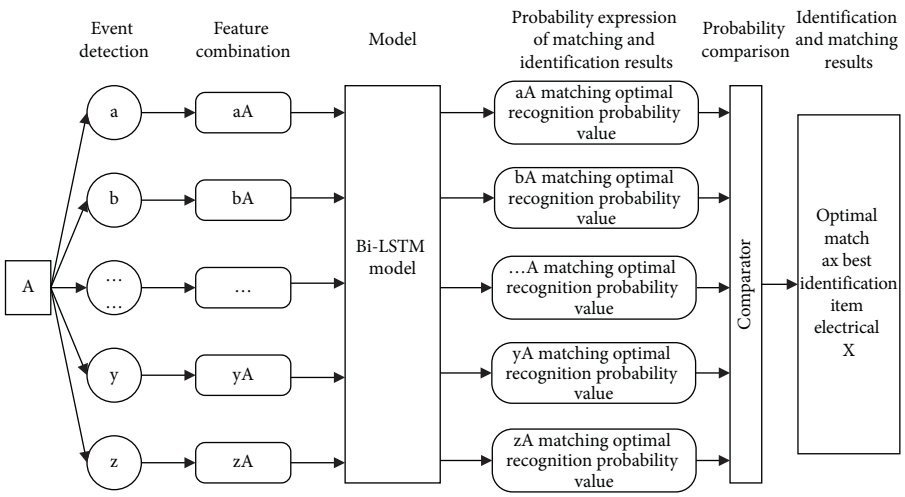

Figure 6: Load start and stop feature matching principle.

Table 2: Neural network model outputs.

Output vector	Power consumption equipment				
	Load1	Load2	.....	Load10	Load11
V_1	1	0	.....	0	0
V_2	0	1	.....	0	0
.....	.....	.....	.....	.....	.....
.....	.....	.....	.....	.....	.....
V_{10}	0	0	.....	1	0
V_{11}	0	0	.....	0	1

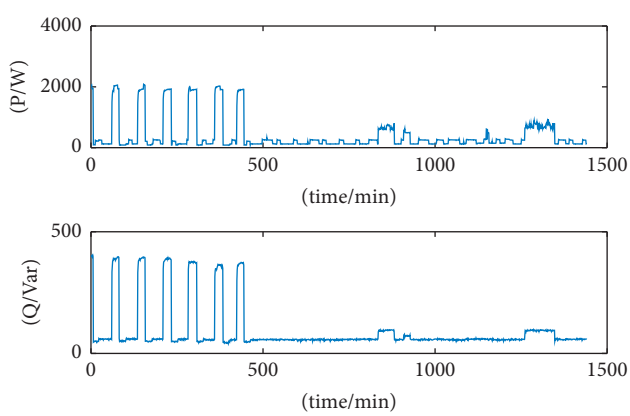

Figure 7: Load power event curves of an example.

and 0.01–0.03 according to Figure 10. It can be seen that the error Bi-LSTM in the test is smaller and more concentrated.

Figure 11 shows the result of load identification. As time increases, the accuracy of the Bi-LSTM and LSTM neural network algorithm identification models increases rapidly, while the accuracy of the RNN neural network algorithm identification model fluctuates greatly. By comparison, the accuracy of the Bi-LSTM neural network algorithm identification model is about 10% larger than that of the LSTM. Therefore, the Bi-LSTM training error converges faster, and the identification error is smaller at the same training times. Additionally, the proposed scheme combining sliding window algorithm and Bi-LSTM shows the satisfactory performance for load identification in these cases.

4.3. Training Scenario II. In this test, based on the above eleven representative loads, five typical loads are randomly selected to train. Turn on and off each load in turn, considering the interval between two starts and stops greater than 50 sampling points. Each sampling point has a time interval of 0.02 seconds. Figure 12 shows the power curve of

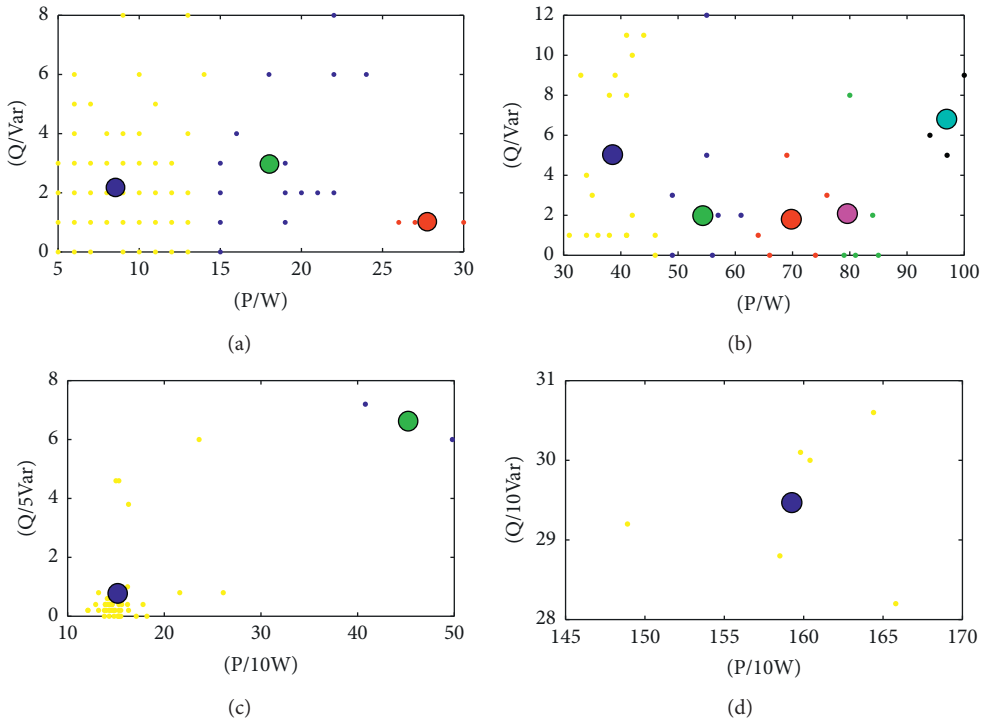

Figure 8: Load extracting result.

Table 3: Average accuracy, precision, recall, and f1 of the neural network.

Neural network	Average accuracy (A) (%)	Average precision (P) (%)	Average recall (R) (%)	Average F_1
RNN	98.70	94.11	91.28	0.93
LSTM	99.29	96.65	95.38	0.96
Bi-LSTM	99.61	97.81	97.44	0.98

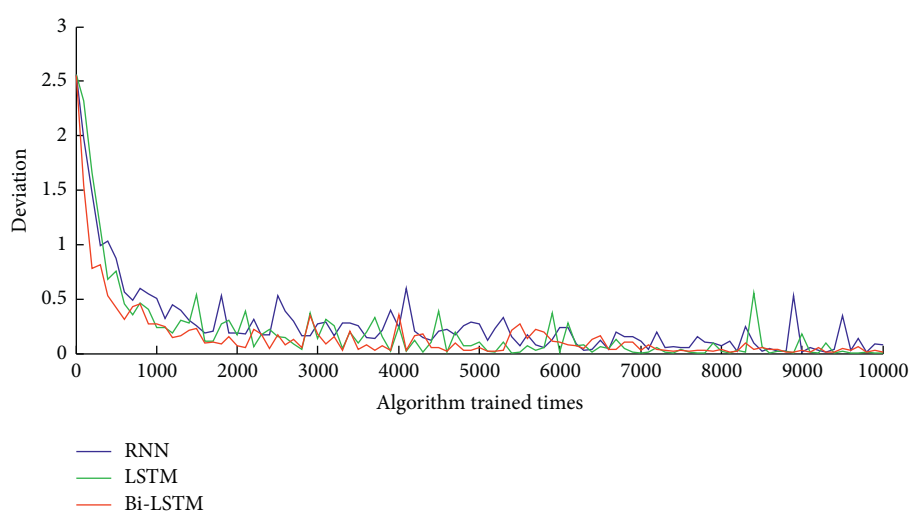

Figure 9: Training error results of the loads.

five typical loads. As seen, the proposed load identification scheme can detect the load starting and ending state, and it has a good adaptability to small disturbances. The results of the on and off event detection are shown in Tables 4 and 5.

Five groups of load samples were obtained by combining load features, which are fed into the Bi-LSTM model according to the combination for identification, and a combination with the highest output probability is

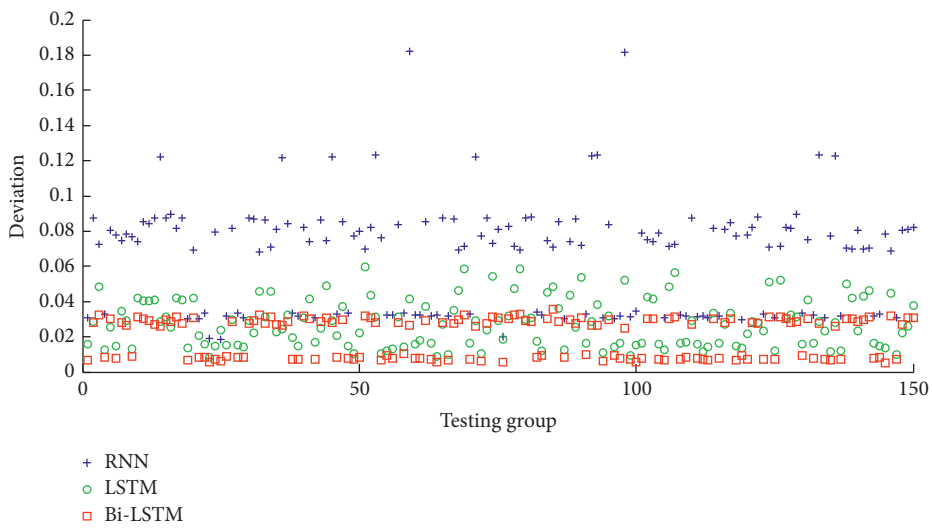

Figure 10: Testing error results of the loads.

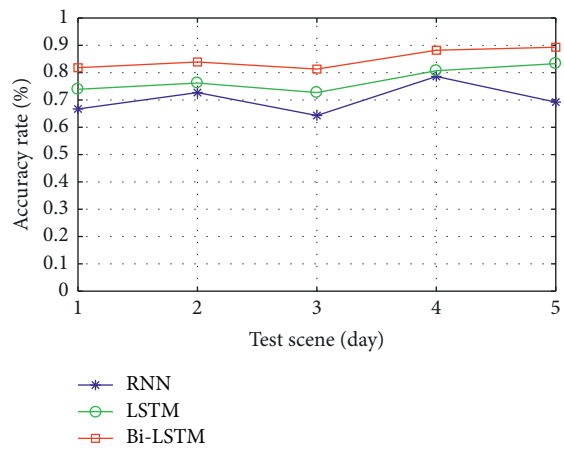

Figure 11: Test results of load identification.

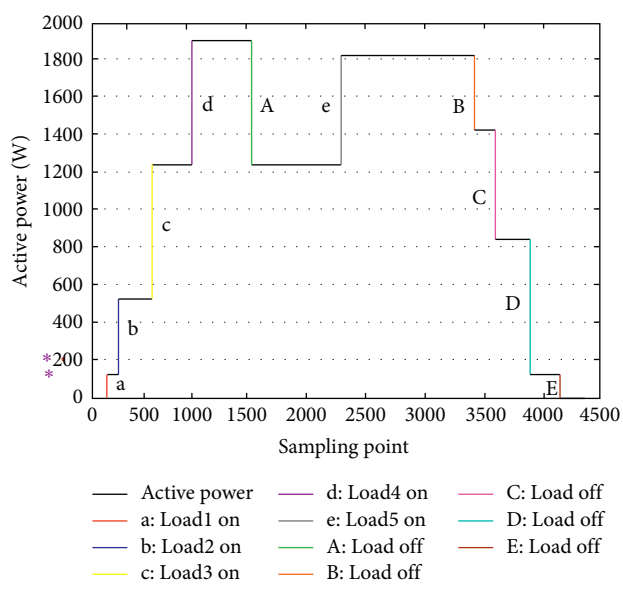

Figure 12: Results of event detection.

Table 4: Test results of input events.

On event	Transition point	Partial extraction of characteristic
A : Load1 on	(180–183)	(63.7532, 63.4903, 62.2736, ...)
b : Load2 on	(325–327)	(449.4157, 449.4989, 449.5203, . . .)
c : Load3 on	(598–600)	(725.9656, 725.9343, 726.2512, . . .)
d : Load4 on	(998–1000)	(673.6530, 673.8846, 674.1954, . . .)
e : Load5 on	(2283–2287)	(602.8433, 603.1875, 601.6605, . . .)

Table 5: Test results of cut out events.

Off event	Transition point	Partial extraction of characteristic
A : Load4 off	(1527–1568)	(642.3375, 647.3315, 647.4980, ...)
B : Load2 off	(3430–3432)	(447.7275, 448.5026, 442.4409, ...)
C : Load5 off	(3532–3534)	(591.7536, 591.6710, 591.6920, ...)
D : Load3 off	(3742–3744)	(720.0392, 720.0419, 720.1326, ...)
E : Load1 off	(4135–4137)	(74.0710, 74.0809, 74.0907, ...)

Table 6: Load matching results.

Off event	Optimal matching items	Standard identification items	Best identification	Probability
A	d	Load4	Load4	0.9999604
B	b	Load2	Load2	0.9999851
C	e	Load5	Load5	0.9999831
D	c	Load3	Load3	0.9999558
E	a	Load1	Load1	0.9999988

taken as the best match. The test results of load matching are shown in Table 6. As seen, the identification results are almost right, and the probability is greater than 99%. To a certain extent, the proposed experimental verification load start and stop feature matching scheme can effectively match and identify load events.

5. Conclusions

On account of cost-effectiveness, nonintrusive load monitoring provides intelligent demand side management and power utilization for microgrid EMS. This paper proposes a Bi-LSTM based nonintrusive load monitoring method, which considers both the power features and time features. To obtain load features from the load events, the sliding window algorithm is adopted in our method. The load features, constructed by the active power, reactive power, and the features of 15 odd-even current harmonics, are selected as input variables of neural network. Besides, the precision (P), recall (R), accuracy (A), and F_1 values are used as the evaluation indexes to train and test the RNN, LSTM, and Bi-LSTM neural network algorithm. And then, experiments on dataset of the five-day microgrid EMS load features verify the proposed load identification performance. Five typical loads are randomly selected in the experiments to verify the proposed main results.

Data Availability

The training data results used to support the findings of this study are included within the article. The raw single-device load data and training data used to support the findings of this study are included within the supplementary information files. All data types used to support the findings of this study are available from the corresponding author upon request.

Conflicts of Interest

The authors declare that they have no conflicts of interest.

Supplementary Materials

The raw single-device load data and training data used to support the findings of this study. (*Supplementary Materials*)

References

[1] Y. Lin and M. Tsai, "An advanced home energy management system facilitated by nonintrusive load monitoring with automated multiobjective power scheduling," *IEEE Transactions on Smart Grid*, vol. 6, no. 4, pp. 1839–1851, 2015.

[2] J.-X. Chin, T. Tinoco De Rubira, and G. Hug, "Privacy-protecting energy management unit through model-distribution predictive control," *Institute of Electrical and Electronics Engineers Transactions on Smart Grid*, vol. 8, no. 6, pp. 3084–3093, 2017.

[3] X. Lu, J. Lai, X. Yu, Y. Wang, and J. M. Guerrero, "Distributed coordination of islanded microgrid clusters using a two-layer intermittent communication network," *Institute of Electrical and Electronics Engineers Transactions on Industrial Informatics*, vol. 14, no. 9, pp. 3956–3969, 2018.

[4] X. Lu, J. Lai, X. Yu, Y. Wang, and J. M. Guerrero, "A novel secondary power management strategy for multiple AC microgrids with cluster-oriented two-layer cooperative framework," *Institute of Electrical and Electronics Engineers Transactions on Industrial Informatics*, vol. 17, no. 2, pp. 1483–1495, 2021.

[5] F. Luo, G. Ranzi, W. Kong, Z. Y. Dong, S. Wang, and J. Zhao, "Non-intrusive energy saving appliance recommender system

for smart grid residential users," *IET Generation, Transmission & Distribution*, vol. 11, no. 7, pp. 1786–1793, 2017.

[6] Y. Xiao, Y. Hu, H. He, D. Zhou, Y. Zhao, and W. Hu, "Non-intrusive load identification method based on improved KM algorithm," *Institute of Electrical and Electronics Engineers Access*, vol. 7, pp. 151368–151377, 2019.

[7] H. Liu, Q. Zou, and Z. Zhang, "Energy disaggregation of appliances consumptions using HAM approach," *Institute of Electrical and Electronics Engineers Access*, vol. 7, pp. 185977–185990, 2019.

[8] D. Saha, A. Bhattacharjee, D. Chowdhury, E. Hossain, and M. M. Islam, "Comprehensive NILM framework: device type classification and device activity status monitoring using capsule network," *Institute of Electrical and Electronics Engineers Access*, vol. 8, pp. 179995–180009, 2020.

[9] C. E. Kement, H. Gultekin, B. Tavli, T. Girici, and S. Uludag, "Comparative analysis of load-shaping-based privacy preservation strategies in a smart grid," *Institute of Electrical and Electronics Engineers Transactions on Industrial Informatics*, vol. 13, no. 6, pp. 3226–3235, 2017.

[10] Y.-H. Lin and M.-S. Tsai, "Non-intrusive load monitoring by novel neuro-fuzzy classification considering uncertainties," *Institute of Electrical and Electronics Engineers Transactions on Smart Grid*, vol. 5, no. 5, pp. 2376–2384, 2014.

[11] P. R. Z. Taveira, C. H. V. De Moraes, and G. Lambert-Torres, "Non-intrusive identification of loads by random forest and fireworks optimization," *Institute of Electrical and Electronics Engineers Access*, vol. 8, pp. 75060–75072, 2020.

[12] Q. Liu, K. M. Kamoto, X. Liu, M. Sun, and N. Linge, "Low-complexity non-intrusive load monitoring using unsupervised learning and generalized appliance models," *Institute of Electrical and Electronics Engineers Transactions on Consumer Electronics*, vol. 65, no. 1, pp. 28–37, 2019.

[13] W. Kong, Z. Y. Dong, B. Wang, J. Zhao, and J. Huang, "A practical solution for non-intrusive type II load monitoring based on deep learning and post-processing," *Institute of Electrical and Electronics Engineers Transactions on Smart Grid*, vol. 11, no. 1, pp. 148–160, 2020.

[14] D. Li and S. Dick, "Residential household non-intrusive load monitoring via graph-based multi-label semi-supervised learning," *Institute of Electrical and Electronics Engineers Transactions on Smart Grid*, vol. 10, no. 4, pp. 4615–4627, 2019.

[15] B. Zhao, K. He, L. Stankovic, and V. Stankovic, "Improving event-based non-intrusive load monitoring using graph signal processing," *Institute of Electrical and Electronics Engineers Access*, vol. 6, pp. 53944–53959, 2018.

[16] M. Alhussein, K. Aurangzeb, and S. I. Haider, "Hybrid CNN-LSTM model for short-term individual household load forecasting," *Institute of Electrical and Electronics Engineers Access*, vol. 8, pp. 180544–180557, 2020.

[17] J. M. Gillis and W. G. Morsi, "Non-intrusive load monitoring using semi-supervised machine learning and wavelet design," *Institute of Electrical and Electronics Engineers Transactions on Smart Grid*, vol. 8, no. 6, pp. 2648–2655, 2017.

[18] Y. Ma, A. Maqsood, K. Corzine, and D. Oslebo, "Long short-term memory autoencoder neural networks based dc pulsed load monitoring using short-time fourier transform feature extraction," in *Proceedings of the 2020 IEEE 29th International Symposium on Industrial Electronics (ISIE)*, pp. 912–917, Delft, Netherlands, June 2020.

[19] D. Oslebo, K. Corzine, T. Weatherford, A. Maqsood, and M. Norton, "Dc pulsed load transient classification using long short-term memory recurrent neural networks," in *Proceedings of the 2019 13th International Conference on Signal Processing and Communication Systems (ICSPCS)*, pp. 1–6, Gold Coast, Australia, December 2019.

[20] K. Basu, V. Debusschere, A. Douzal-Chouakria, and S. Bacha, "Time series distance-based methods for non-intrusive load monitoring in residential buildings," *Energy and Buildings*, vol. 96, pp. 109–117, 2015.

[21] R. Machlev, Y. Levron, and Y. Beck, "Modified cross-entropy method for classification of events in NILM systems," *Institute of Electrical and Electronics Engineers Transactions on Smart Grid*, vol. 10, no. 5, pp. 4962–4973, 2019.

[22] X. Wu, X. Han, L. Liu, and B. Qi, "A load identification algorithm of frequency domain filtering under current underdetermined separation," *Institute of Electrical and Electronics Engineers Access*, vol. 6, pp. 37094–37107, 2018.

[23] R. Bonfigli, E. Principi, M. Fagiani, M. Severini, S. Squartini, and F. Piazza, "Non-intrusive load monitoring by using active and reactive power in additive Factorial Hidden Markov Models," *Applied Energy*, vol. 208, pp. 1590–1607, 2017.

[24] D. F. Teshome, T. D. Huang, and K. Lian, "Distinctive load feature extraction based on fryze's time-domain power theory," *Institute of Electrical and Electronics Engineers Power and Energy Technology Systems Journal*, vol. 3, no. 2, pp. 60–70, 2016.

[25] K. Basu, V. Debusschere, S. Bacha, U. Maulik, and S. Bondyopadhyay, "Nonintrusive load monitoring: a temporal multilabel classification approach," *Institute of Electrical and Electronics Engineers Transactions on Industrial Informatics*, vol. 11, no. 1, pp. 262–270, 2015.

[26] X. Wu, X. Han, and K. X. Liang, "Event-based non-intrusive load identification algorithm for residential loads combined with underdetermined decomposition and characteristic filtering," *IET Generation, Transmission & Distribution*, vol. 13, no. 1, pp. 99–107, 2019.

[27] S. Ghosh, A. Chatterjee, and D. Chatterjee, ""Improved non-intrusive identification technique of electrical appliances for a smart residential system," *IET Generation, Transmission & Distribution*, vol. 13, no. 5, pp. 695–702, 2019.

[28] F. Farokhi and H. Sandberg, "Fisher information as a measure of privacy: preserving privacy of households with smart meters using batteries," *Institute of Electrical and Electronics Engineers Transactions on Smart Grid*, vol. 9, no. 5, pp. 4726–4734, 2018.

[29] J. Fei and C. Lu, "Adaptive sliding mode control of dynamic systems using double loop recurrent neural network structure," *Institute of Electrical and Electronics Engineers Transactions on Neural Networks and Learning Systems*, vol. 29, no. 4, pp. 1275–1286, 2018.

[30] Y. Luo, Y. Wong, M. Kankanhalli, and Q. Zhao, "$\mathcal {G}$ -softmax: improving intraclass compactness and interclass separability of features," *Institute of Electrical and Electronics Engineers Transactions on Neural Networks and Learning Systems*, vol. 31, no. 2, pp. 685–699, 2020.

[31] K. Chen and Q. Huo, "Training deep bidirectional LSTM acoustic model for LVCSR by a context-sensitive-chunk BPTT approach," *Institute of Electrical and Electronics Engineers/ACM Transactions on Audio, Speech, and Language Processing*, vol. 24, no. 7, pp. 1185–1193, 2016.

[32] G. Cui, B. Liu, W. Luan, and Y. Yu, "Estimation of target appliance electricity consumption using background filtering," *Institute of Electrical and Electronics Engineers Transactions on Smart Grid*, vol. 10, no. 6, pp. 5920–5929, 2019.

Hindawi
Complexity
Volume 2020, Article ID 8820332, 13 pages
https://doi.org/10.1155/2020/8820332

Research Article

Study on Multiobjective Modeling and Optimization of Offshore Micro Integrated Energy System considering Uncertainty of Load and Wind Power

Jun Wu,[1] **Baolin Li**,[1] **Jun Chen**,[2] **Qinghui Lou**,[2] **Xiangyu Xing**,[1] **and Xuedong Zhu**[1]

[1]*School of Electrical Engineering & Automation, Wuhan University, Wuhan, China*
[2]*Research Institute Nanjing NARI-Relays Engineering Technology Co., Ltd., Nanjing, China*

Correspondence should be addressed to Baolin Li; baolin-li@whu.edu.cn

Received 21 August 2020; Revised 23 November 2020; Accepted 8 December 2020; Published 24 December 2020

Academic Editor: Xin Li

Offshore micro integrated energy systems (OMIESs) are the basis of offshore oil and gas engineering and play an important role in developing and utilizing marine resources. By introducing offshore wind power generation, the carbon emissions of offshore micro integrated energy systems can be effectively reduced; however, greater challenges have been posted to the reliable operation due to the uncertainty. To reduce the influence brought by the uncertainty, a multiobjective optimization model was proposed based on the chance-constrained programming (CCP); the operating cost and penalty cost of natural gas emission were selected as objectives. Then, the improved hybrid constraints handling strategy based on nondominated sorting genetic algorithm II (IHCHS-NSGAII) was introduced to solve the model efficiently. Finally, the numerical studies verified the efficiency of the proposed algorithm, as well as the validity and feasibility of the proposed model in improving the economy of OMIES under uncertainty.

1. Introduction

Currently, there are 6500 offshore oil and gas platforms worldwide [1], which is expected to become an important way to solve energy and environmental problems worldwide by developing and utilizing marine oil and gas resources [2–4]. These offshore oil and gas platforms are far away from the land and can be categorized as an offshore micro integrated energy system [5]. It contains a variety of energy, such as electricity, gas, and heat, and coordinates and optimizes the economy and energy utilization efficiency through energy coupling equipment (such as the power to gas (*P*2*G*) and direct-fired boilers (GB)). Traditionally, that power is provided by gas turbines (GTs) coupled to electric generators, installed on the platforms, and operating by combustion of natural gas; however, for safety considerations, redundant GTs generally run with lower operating efficiency and higher pollution emissions [6, 7]. By introducing offshore wind power, the carbon emissions of offshore micro integrated energy systems (OMIESs) can be effectively reduced. However, affected by the complex offshore environment, greater challenges have been posted to the reliable operation due to the uncertainty of load and offshore wind power [8]. Therefore, it is of great significance to carry out economic optimization dispatch considering the uncertain factors in the OMIES.

At present, scholars have conducted many studies on the optimal operation model of the IES (integrated energy system) [9–12]. In [9], the photovoltaic uncertainty was described by a series of scenarios; then, the model was proposed based on demand response to realizing coordinated optimization for the multiple energy systems. In [10], the modeling of all equipment in the IES was presented to specify the physical operational constraints, and an optimization model was set up to minimize the total cost, considering the heat energy with different grades. Reference [11] studied the influence on the operational costs and the stability of the regional IES when the controllable loads

including electric vehicles and air conditioning loads were considered a virtual energy storage system (ESS). Reference [12] proposed a two-stage stochastic scheduling scheme of an integrated multienergy system, which considers the wind power uncertainty to achieve the optimal economic operation with the minimum curtailment of wind power. The literature listed above proposed different models of IES optimization scheduling, taking into consideration the intermittency of renewable energy, the different grades of heat energy, and the flexibility brought by ESS. However, few of them focus on the optimization of offshore oil and gas platforms and combine the OMIES with offshore wind power as well as considering the effect of uncertainty.

Generally, there are mainly three different ways to handle the uncertainty of offshore wind power, namely, robust optimization [13, 14], interval optimization [15], and stochastic optimization [16, 17]. Among them, stochastic optimal scheduling uses more accurate probability distribution information of uncertain variables to participate in the modeling and solving of scheduling models. The chance-constrained programming (CCP) model allows some constraints containing uncertain variables to fail in the optimization process, but the probability level of its establishment must meet the confidence level requirements. Reference [18] explored the low-carbon and economic planning of OMIES considering the effect of the production process or the uncertainty of the external environment. With the development of offshore wind power, it is necessary to study the economic operation of the system under uncertainty.

In this paper, the improved hybrid constraints handling strategy based on nondominated sorting genetic algorithm II (IHCHS-NSGAII) was introduced to solve the biobjective optimization model based on CCP to minimize the operating cost and natural gas emission. The paper mainly has the following contributions:

(i) A biobjective optimization model based on CCP was proposed to handle the uncertainty of load and wind power. To maximize wind power penetration, the wind curtailment penalty item was added to the cost objective function. Besides, the natural gas emission was selected as the other objective considering the current situation that there exists a large amount of natural gas emission in actual OMIES

(ii) Based on NSGAII, the hybrid constraints handling strategy was introduced and modified through three aspects, namely, dimensionality reduction, individual repair, and normalization to improve the performance of NSGAII when dealing with complex constraints

(iii) The relationship between natural gas emission and wind power utilization was analyzed by implementing an OMIES example in the Bohai Sea to provide schemes or suggestions for offshore oil and gas platforms

The rest of this paper is organized as follows. Section 2 introduces the OMIES. Section 3 formulates the CCP biobjective optimization problem. Section 4 presents IHCHS-NSGAII. Section 5 shows the numerical results and analysis and the conclusion is drawn in Section 6.

2. Introduction of OMIES

The energy flow of OMIES is shown in Figure 1, which mainly includes electricity, gas, and thermal. Also, different energy is coupled with conversion equipment; for instance, the GTs burn the exploited natural gas to supply electricity to the entire system and simultaneously utilize the high-temperature flue gas generated by the combustion to heat the system [19]. OMIES is formed by multiple offshore oil and gas center platforms interconnected by submarine cables and transmission pipelines.

Generally, the OMIES is different from a general IES. First of all, for the limitation of the capacity of the offshore platform, energy equipment is placed relatively concentrated on the offshore platforms; the physical distance between "source" and "load" is relatively short. Also, the transmission network is not as complicated as that of a land-based power system. Secondly, ensuring steady and safe production is the most thing for offshore oil and gas engineering, thus leading to the redundant configuration of GTs. Besides, the exploited natural gas that cannot be transmitted will be burned by the torch on the platform due to the limitation of the pipelines' transmission capacity, which is known as natural gas emission. So, it is necessary to do some research based on the characteristics of OMIES.

3. CCP Optimization Model

Challenges have been posted to the operation of OMIES due to the uncertainty of load and offshore wind power: on the one hand, in order to reduce pollution emissions and energy waste, the staff hope to reduce the output of GTs and utilize as much wind power as possible; on the other hand, to tackle uncertainty and ensure the safe and stable operation of the system, the power system needs to reserve a certain amount of spare capacity to try to avoid production shutdown due to load shedding, but it will also increase the operating cost of the system. Therefore, it is necessary to establish a multi-objective operation optimization model that takes into account system operating costs and the consumption of wind power.

3.1. Objective Functions

3.1.1. Objective Function 1. Five parts are included in the operating cost, namely, the pollution cost of GTs and GBs, the cost of gas well production, the penalty cost of natural gas emission, and wind curtailment.

$$\min F_1 = \sum_{t=1}^{T} \left[\begin{array}{l} \sum_{i\in\Omega_{gt}} \left[\alpha_{1,i}^{gt} + \alpha_{2,i}^{gt} P_{i,t}^{gt} + \alpha_{3,i}^{gt} \left(P_{i,t}^{gt} \right)^2 \right] + \sum_{j\in\Omega_{gb}} \alpha_j^{gb} G_{j,t}^{gb} \\ + \sum_{k\in\Omega_{cp}} \alpha_k^{\text{well}} G_{k,t}^{\text{well}} + \sum_{k\in\Omega_{cp}} \alpha_k^{\text{gas}} \Delta G_{k,t}^{\text{gas}} + \sum \alpha_i^{\text{wind}} \Delta P_{i,t}^{W} \end{array} \right]. \tag{1}$$

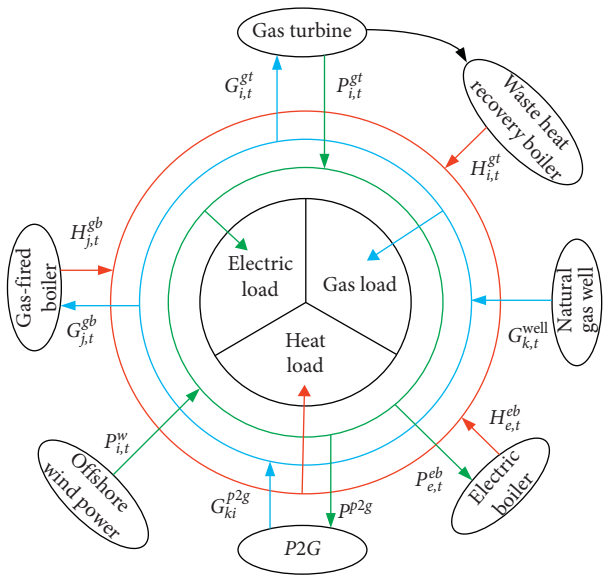

Figure 1: Energy flow of OMIES.

3.1.2. Objective Function 2. The natural gas emission not only causes energy waste but also pollutes the environment, so objective function 2 aims to minimize the natural gas emission.

$$\min F_2 = \sum_{t=1}^{T} \sum \Delta G_{k,i}^{\text{gas}}. \tag{2}$$

3.2. Operation Constraints. The OMIESs contain various kinds of energy and equipment, and the following four types of constraints shall be met for safe operation.

3.2.1. Decision Variable Constraints. Generally, the solution for a practical optimal scheduling problem includes the outputs of all kinds of devices in the whole system, so that the operators can make adjustments at appropriate times to achieve goals. In the OMIES scheduling problem proposed in this paper, the decision variable constraints can be expressed as follows:

$$P_i^{gt,\min} \le P_{i,t}^{gt} \le P_i^{gt,\max}, \tag{3}$$

$$0 \le P_{i,t}^{W} \le P_{i,t}^{W,\text{pre}}, \tag{4}$$

$$G_k^{\text{well, min}} \le G_{k,t}^{\text{well}} \le G_k^{\text{well, max}}, \tag{5}$$

$$0 \le H_{j,t}^{gb} \le H_j^{gb,\max}, \tag{6}$$

$$0 \le H_{e,t}^{eb} \le H_e^{eb,\max}, \tag{7}$$

$$0 \le G_{P2G}^{t} \le G_{P2G}^{t,\max}, \tag{8}$$

$$-\frac{\pi}{2} \le \theta_{h,t} \le \frac{\pi}{2}, \tag{9}$$

$$p_n^{\min} \le p_{n,t} \le p_n^{\max}, \tag{10}$$

$$-R_i^{\text{down}} \le P_{i,t}^{gt} - P_{i,t-1}^{gt} \le R_i^{\text{up}}. \tag{11}$$

Equations (3)–(8) describe the upper and lower bounds of GTs, offshore wind power, gas well, GBs, EBs, and *P2G*, respectively. Equations (9) and (10) are the node angel and node pressure limits. Equation (11) describes the ramp limits of GTs.

3.2.2. System Balance Constraints. For each system, the energy flow in and out at each bus shall be equal.

$$\sum_{i\in h} P_{i,t}^{gt} + \sum_{i\in WG} P_{i,t}^{w} - \sum_{g\in h} P_{gh,t} - E_{h,t}^{\text{load}} - \sum_{e\in h} P_{e,t}^{eb} - P^{p2g} = 0, \tag{12}$$

$$\sum_{k\in n} G_{k,t}^{\text{well}} + G_{k,t}^{p2g} + \sum_{m\in n} G_{mn,t} - \sum_{i\in n} G_{i,t}^{gt} - G_{n,t}^{\text{load}} - \sum_{j\in n} G_{j,t}^{gb} - \sum_{k\in n} \Delta G_{k,t}^{\text{gas}} = 0, \tag{13}$$

$$\sum_{i\in\Omega_{gt}} H_{i,t}^{gt} + \sum_{j\in\Omega_{gb}} H_{j,t}^{gb} + \sum_{e\in\Omega_{eb}} H_{e,t}^{eb} - H_t^{\text{load}} = 0. \tag{14}$$

3.2.3. Equipment Operation Constraints. Equipment in the OMIES is constrained by energy conservation constraints.

$$P_{i,t}^{W,\text{pre}} - P_{i,t}^{W} = \Delta P_{i,t}^{W}, \tag{15}$$

$$G_{i,t}^{gt} = \frac{P_{i,t}^{gt}}{\eta \cdot HV_{\text{gas}}}, \tag{16}$$

$$H_{i,t}^{gt} = \frac{P_{i,t}^{gt} \cdot \left(1 - \eta_{gt} - \eta_{l}\right) \cdot \eta_{whb}}{\eta_{gt}}, \tag{17}$$

$$H_{j,t}^{gb} = \eta_{gb} \cdot HV_{\text{gas}} \cdot G_{j,t}^{gb}, \tag{18}$$

$$H_{e,t}^{eb} = \eta_{eb} \cdot P_{e,t}^{eb}, \tag{19}$$

$$G_{P2G}^{t} = \frac{\eta_{P2G} P_{P2G}^{t}}{H_{g}}. \tag{20}$$

Equation (15) describes the relationship between actual wind power and forecasted value. Equations (16)–(20) are the relationships between the input and output of each equipment. The power flow constraints of OMIES can be found in [20]. The relationship between the flow of natural gas flowing through a pipeline and the pressure at both ends of the pipeline can be found in [21].

3.2.4. Chance Constraints. Offshore oil and gas platforms face a complex and changeable environment. In this paper, the uncertainty of power load and offshore wind power is modeled by stochastic variables. The forecast error of offshore wind power and power load can be expressed by normal distribution as follows:

$$\begin{aligned} \varepsilon_{wt,t} &\sim N\left(0, \sigma_{wt}\right), \\ \sigma_{wt} &= \rho_{wt,t} P_{wt,t} + \rho_{wt,\text{ins}} P_{wt,\text{ins}}, \\ \varepsilon_{\text{load},t} &\sim N\left(0, \sigma_{\text{load}}\right), \\ \sigma_{\text{load}} &= \rho_{\text{load},t} E_{\text{load},t}. \end{aligned} \tag{21}$$

Therefore, the power balance constraint shall be converted as (22) considering the uncertainty.

$$P_{r}\left\{\sum_{i\in h} P_{i,t}^{gt} + \sum_{i\in WG} P_{i,t}^{w} - \sum_{g\in h} P_{gh,t} - \sum_{e\in h} P_{e,t}^{eb} - P^{p2g} - E_{h,t}^{\text{load}}\right\} \geq \eta_{1}. \tag{22}$$

Equation (22) indicates that the power flow shall be met under a certain confidence coefficient.

To ensure the safe operation of the system and prevent the uncertainty of wind power and load from affecting the power balance, the reserve capacity should meet the up- and down-reserve capacity constraints.

$$P_{r}\left\{\sum_{i=1}^{N}\left(P_{i\max} - P_{i}\right) \geq U_{SR} + w_{u} P_{W}\right\} \geq \eta_{2}, \tag{23}$$

$$P_{r}\left\{\sum_{i=1}^{N}\left(P_{i} - P_{i\min}\right) \geq w_{d}\left(P_{W\max} - P_{W}\right)\right\} \geq \eta_{3}. \tag{24}$$

3.3. Transformation of Chance Constraints. Chance constraints in equations (22)–(24) are difficult to handle. And it can be solved by converting into their equivalence type [22].

$$\begin{aligned} &\sum_{i\in h} P_{i,t}^{gt} + \sum_{i\in WG} P_{i,t}^{w} - \sum_{g\in h} P_{gh,t} - \sum_{e\in h} P_{e,t}^{eb} - P^{p2g} \\ &\quad - E_{h,t}^{\text{load}} \geq \inf\left\{K | K = \phi_{1}^{-1}\left(\eta_{1}\right)\right\}, \\ &\frac{1}{w_{u}}\left(\sum_{i=1}^{N}\left(P_{i\max} - P_{i}\right) - U_{SR}\right) - P_{i,t}^{w} \geq \inf\left\{K | K = \phi_{2}^{-1}\left(\eta_{2}\right)\right\}, \\ &\frac{1}{w_{d}}\left(\sum_{i=1}^{N}\left(P_{i} - P_{i\min}\right)\right) - P_{wt,\text{ins}} + P_{i,t}^{w} \geq \inf\left\{K | K = \phi_{3}^{-1}\left(\eta_{3}\right)\right\}. \end{aligned} \tag{25}$$

4. IHCHS-NSGAII

Although NSGAII [23] is recognized as one of the most effective ways to deal with such multiconstrained problems, the proposed model in Section 3 is still difficult to solve due to the complexity of the variable vectors and different kinds of constraints, especially when there might be coupling and nonlinearity. Therefore, a high efficient optimization method was needed to handle the complex multiconstrained multiobjective optimization problem. In this section, a hybrid constraint processing strategy (HCHS) [24] is introduced and modified to improve the performance of NSGAII when dealing with complex constraints.

4.1. Dimensionality Reduction Method. Generally, the equality constraints, such as electric power and gas balance constraints, are not easy to handle for NSGAII, so it is necessary to transfer equality constraints into inequality ones with their own limitations; in the meantime, the vector dimension can be reduced and the solving efficiency of the algorithm would be improved. Taking the power balance constraint as an example, the specific conversion process is as follows.

Equation (12) can be equivalently converted as

$$P_{i,t}^{gt} = P_{gh,t} + E_{h,t}^{\text{load}} + P_{e,t}^{eb} + P^{p2g} - P_{i,t}^{w}. \tag{26}$$

On the other hand, equation (26) shall be met by constraints described in equation (3). Thereby, the equality constraint is equivalently transformed into an inequality one. And the other equality constraints can be converted in the same way.

4.2. Repair Process after Generation of a New Individual. Violation of some constraints that are related to the variables generation process, such as the ramp rate constraints, cannot always be reduced for the individuals. Since the individuals are generated using some heuristic-based stochastic methods in NSGAII, the constraint handling method in [23] cannot reduce the violation of some constraints, such as the

ramp rate constraints and the rated power constraints, related to the variables generation process. Thus, a repair process is needed to convert the infeasible individuals into feasible ones. In this paper, the repair process is utilized to repair the variables corresponding to the active power output of GT, which violates the ramp rate constraints. Since the ramp rate constraint violations appear between the variables with close time intervals, which have strong coupling, it is difficult for the optimization algorithm to reduce them during the evolutionary process. Therefore, it is necessary to "repair" the variables when the population is generated. When a ramp rate constraint is violated, all of the variables $P_{i,t}^{gt}$ in a scheduling period should be repaired from the beginning time interval for the related GT, so that the ramp rate limit and the rated power requirement can be met, simultaneously. It is obvious that the repair process may need much computing resources and time. Besides, considering the proportion of infeasible individuals is dynamic during the whole computation period; the repair probability on the infeasible potential solutions is designed to be updated based on the current stage of the algorithm, as shown as follows:

$$P_{\mathrm{re}}(G_c) = \begin{cases} \left(\dfrac{G_c}{G_s}\right)^2, & G_c \le G_s, \\ 1, & G_c > G_s. \end{cases} \tag{27}$$

It can be seen from equation (27) that the value of P_{re} is small at the beginning of optimization to accept more potential infeasible individuals so that the diversity of the population can be ensured. And when G_c is large enough, all of the individuals which violate the ramp rate constraint should be repaired. But comparing with the microgrid dispatch problem in [24], the OMIES scheduling problem is more complex and the main target is to find feasible solutions. Therefore, to solve the constrained multiobjective problem of OMIES scheduling in this paper, equation (27) is modified as follows:

$$P_{\mathrm{re}}(G_c) = \begin{cases} \dfrac{G_c}{G_s}, & G_c \le G_s, \\ 1, & G_c > G_s, \end{cases} \tag{28}$$

where $G_s = 0.25G_{\max}$. In this way, the average value of P_{re} is increased compared with that in equation (27), and most of the individuals in the population can be repaired during the optimization process.

4.3. Normalization Process in Selection. Considering the types and amounts of constraints in the proposed model, it is efficient to normalize each of the constraint violation before adding up, and the specific details could be found in [24]. It can be seen from Section 2 that in the proposed OMIES scheduling problem, there are various types of constraints, and different types of constraint violations cannot be compared or added directly. Thus, in this paper, the number of violated constraints of different types is also considered as a factor to evaluate the infeasible level of the individuals. The normalization method is modified in this paper as

$$v_{l,k,\mathrm{norm}} = \frac{1}{n_k}\sum_{i=1}^{n_k}\frac{v_{l,k,i} - v_{k,\min}}{v_{k,\max} - v_{k,\min}}. \tag{29}$$

It can be seen from equation (29) that by introducing n_k the normalization process can be more reasonable and the number of violated constraints can be taken into account in the constraints' handling process. Hence, the algorithm would find potential solutions with a lower sum of normalized violations, and the ones with a lower number of violated constraints are preferred during the evolutionary process. Therefore, the average number of violated constraints in the population would drop rapidly, and the feasible regions can be found efficiently.

5. Simulation

In this section, the results of the numerical studies are presented and analyzed, which are conducted based on a modified OMIES located in the Bohai Sea of China in [25] as shown in Figure 2. The optimization models are solved under the MATLAB environment. In addition, a computer with Intel i5-8700 CPU@3.20 GHz and 8 GB memory is used to run the optimization models.

5.1. Parameters of the OMIES. This case is composed of a 6-node power system, a 6-node natural gas system, and a thermal system. EBs are located in nodes 1, 4, and 5 in the power system with capacities of 1.2 MW, 0.95 MW, and 1.1 MW, respectively. Parameters related to GTs are listed in Table 1. The natural gas system consists of 3 gas well nodes and 3 gas load nodes. GBs are located in nodes 1 and 2 with maximum thermal powers of 3 MW and 4 MW, respectively. Parameters related to the gas well are listed in Table 2. And the natural gas caloricity is 9.7 kWh/m^3. The offshore wind turbine is located in node 5 in the power system with a capacity of 9 MW. And the penalty cost coefficient of offshore wind power is 50 \$/MW. Node 2 in the natural gas system and node 4 in the power system are connected by a *P2G* with a capacity of 0.6 MW. The confidence coefficients are all set to 0.95 in this paper. The other parameters could be found in Table 3. By the way, the data used in this paper are collected from an actual offshore oil and gas engineering, and the parameters mentioned above are obtained by fitting or calculating these data.

The forecast curve of electricity, gas, and heat load was shown in Figure 3.

5.2. Results and Discussions. The parameters such as the number of population individuals, mutation rate, and calculation accuracy used in IHCHS-NSGAII are selected referring to [24]. The maximum generation number is set to 20000 generations and the population size is 50.

Besides, in this section, the penalty function method (PFM), constraint domination principle (CDP), and the

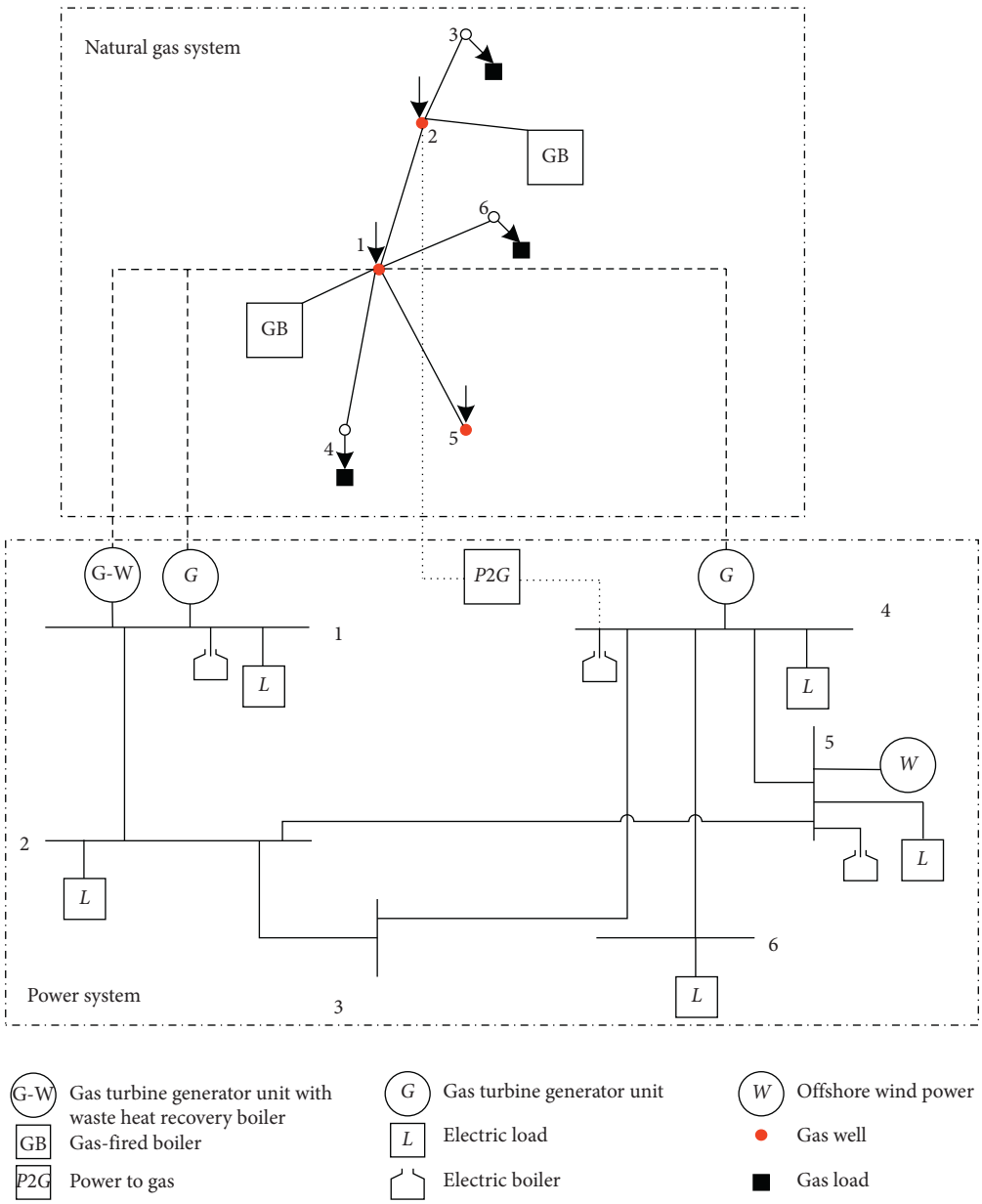

Figure 2: A case of OMIES.

original HCHS are introduced to compare the performance with the improved HCHS. The parameter settings of PFM and HCHS can be found in [24]. Each algorithm is combined with NSGAII and run 10 times. The average feasible solutions using different constraint handling methods are recorded during the evolutionary process.

It can be seen from Table 4 that before 1000 generations, the numbers of feasible solutions obtained are low by all the constraint handling methods, which indicates that the OMIES scheduling problem is very complex with various types of constraints. With the increase of the generations, the feasible solutions become more by CDP, HCHS, and improved HCHS. However, by using PFM, NSGAII cannot find enough feasible solutions. Even after 20000 iterations, NSGAII only finds 15 feasible solutions. As for CDP, the situation is better with 27 solutions, which means that CDP is more effective in dealing with multiconstrained multiobjective optimization problems than PFM. However, nearly half of the obtained solutions are still infeasible. HCHS is based on CDP, but by the hybrid constraints handling methods, it can find more feasible solutions. When HCHS is modified by the method proposed in this paper, it can be seen that it can find a similar amount of feasible solutions with 10000 generations with those by original HCHS after 20000 generations. Moreover, within 18000 iterations, all the solutions in the population are feasible by the proposed improved HCHS. The results indicate that comparing with the existing constraints handling methods, the proposed improved HCHS is more adaptable to the complexity of the multiconstrained OMIES scheduling problem, which can make NSGAII reduce the overall violations considering different constraint types and converge to the feasible

Table 1: Parameters related to GTs [25].

Number of units	1	2	3
Location of units	1	1	4
Maximum output (MW)	0	0	0
Minimum output (MW)	12	9	12
Maximum ramp up rate (MW/h)	3	2	3
Maximum ramp down rate (MW/h)	3	2	3
Whether equipped with WHRB	Yes	No	No
Quadratic pollution coefficient	0.0047	0.0052	0.0074
Linear pollution coefficient	0.0940	0.0730	0.1180
Constant coefficient	0.4900	0.2855	0.5320

Table 2: Parameters related to the gas well.

Number of gas well	1	2	3
Location of gas well	1	2	5
Minimum output of gas well/10^6 m^3	0.1000	0.0113	0.0050
Maximum output of gas well/10^6 m^3	0.1313	0.0158	0.0071
Minimum gas emission/10^6 m^3	0	0	0
Maximum gas emission/10^6 m^3	0.1000	0.0113	0.0050
Cost coefficients of gas production \$/10^6 m^3	20	15	25
Penalty cost coefficients of gas emission \$/10^6 m^3	200	150	250

Table 3: Other parameters.

Parameters	Value
Efficiency of GT	0.4
Heat loss coefficient of GT	0.3
Heat recovery efficiency of WHRB	0.47
Combustion efficiency of GB	0.85
Pollution coefficient of GB	0.24\$/MW
Electrothermal conversion efficiency of EB	0.99
Reserve capacity factor	0.12
Error coefficient of offshore wind power capacity	0.02
Error coefficient of offshore wind power output	0.2
Error coefficient of power load	0.2

regions faster. Therefore, more computational resources can be applied to find better Pareto solutions.

The optimal solution set is shown in Figure 4.

From the perspective of the distribution of the Pareto set, the operating cost and the natural gas emission cannot be perfectly optimized at the same time. The staff need to weigh environmental protection, economy, and stability according to actual needs. And the final Pareto optimal solution is not continuous. For solutions at discontinuities, one objective function may have a small difference, but the other objective function can be greatly optimized. Therefore, particular attention should be paid to the choice of solutions at discontinuities.

What is more, the optimal solutions in the Pareto set of the two objective functions are selected as the two schemes.

Scheme One. The optimal solution for operating cost (operating cost 809.4448 \$ and natural gas emission 400.00 m^3).

Scheme Two. The *optimal* solution for natural gas emission (operating cost 877.844 \$ and natural gas emission 21.00 m^3).

The operating cost comparison of the two schemes is shown in Figure 5, and the specific operating cost values are shown in Table 4.

It can be seen from Figure 5 and Table 5 that the pollution cost of GBs in the two schemes is basically the same. The pollution cost of GTs and GBs, cost of the gas well, and the penalty cost of wind curtailment in scheme one are lower than those in scheme two, while the penalty cost of gas

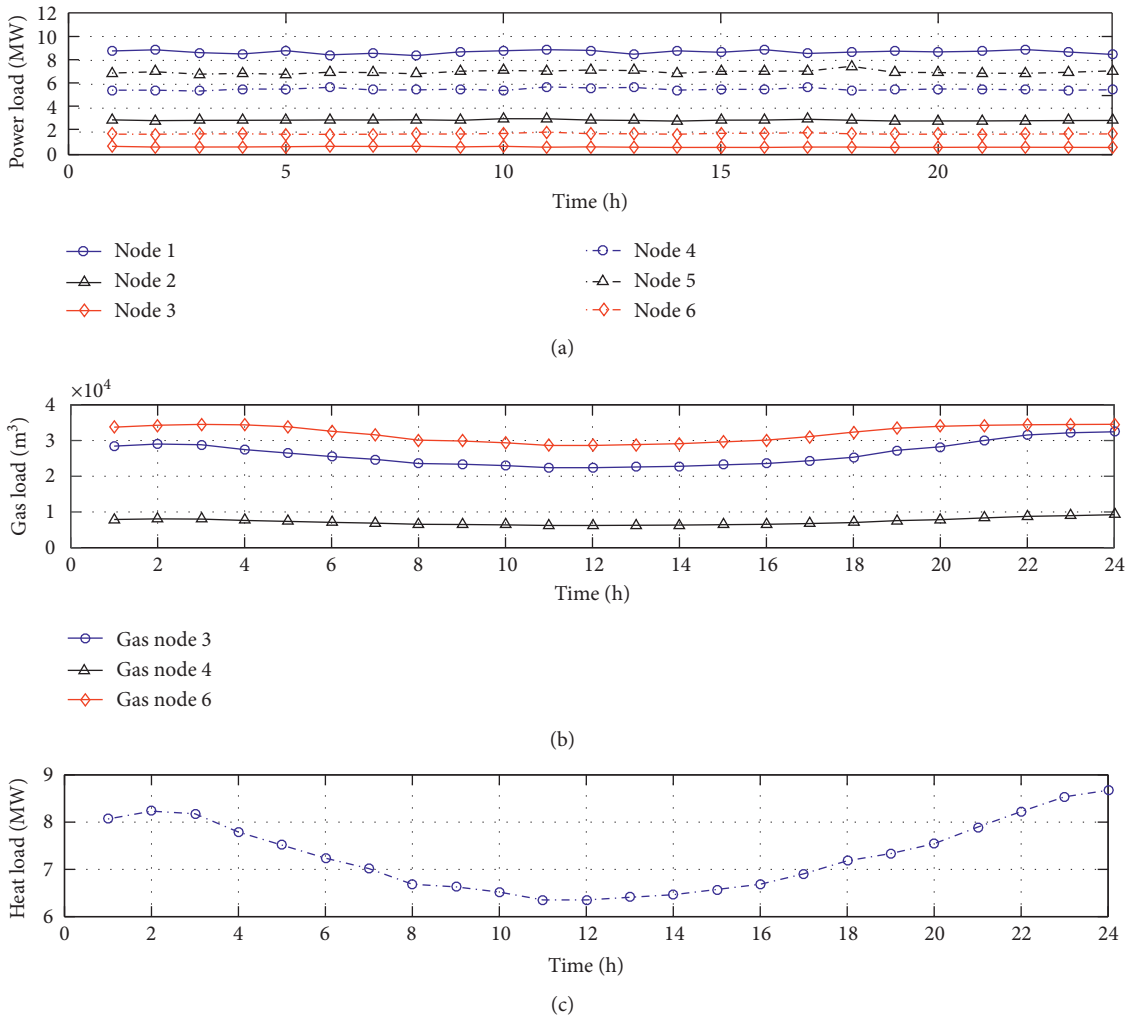

Figure 3: Different load forecast curves.

Table 4: Average feasible solutions using different constraint handling methods during the evolutionary process.

Generations	100	500	1000	3000	5000	10000	15000	18000	20000
PFM	0	2	6	5	8	7	11	13	15
CDP	0	4	9	13	18	24	27	25	27
HCHS	1	5	11	20	22	29	35	39	38
Improved HCHS	3	7	12	22	27	36	47	50	50

emission is opposite since the objective functions of the two schemes are different. The operating cost in scheme one is lower than that in scheme two, about 10.5% lower. It can be seen that when more offshore wind power is consumed, operating costs can be effectively reduced in terms of pollution cost and gas production cost; however, this will also increase natural gas emission.

It can be seen from Figures 6 and 7 that in the actual utilization of offshore wind power, scheme one is slightly better than scheme two. Both schemes show that the optimization strategy used in this paper keeps the curtailed offshore wind power at a very low level for most of the scheduling cycle, and the peak of the curtailed power occurs only around 12–15 hours.

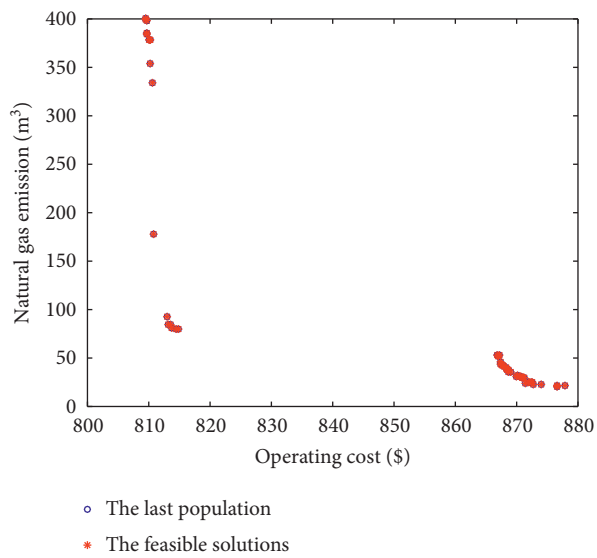

Figure 4: The Pareto set obtained by IHCHS-NSGAII.

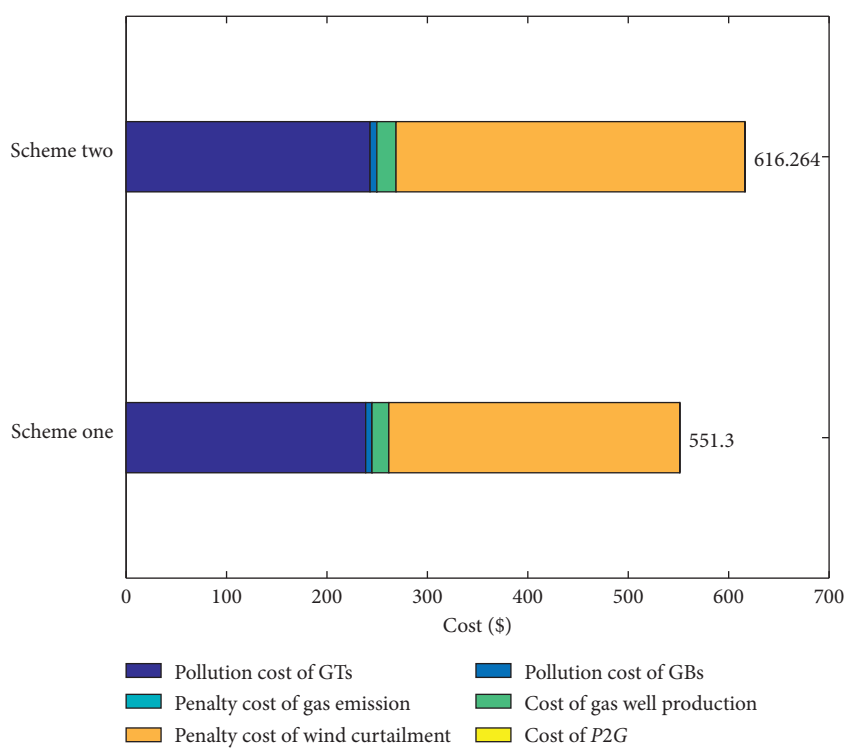

Figure 5: Operating cost structure under different schemes.

Table 5: Specific operating cost values.

Schemes	Pollution cost of GTs/$	Pollution cost of GBs/$	Penalty cost of gas emission/$	Cost of gas well/$	Penalty cost of wind curtailment/$
One	238.5283	6.3072	0.0142	16.7387	289.7100
Two	242.9183	6.7028	0.0008	19.1436	347.4900

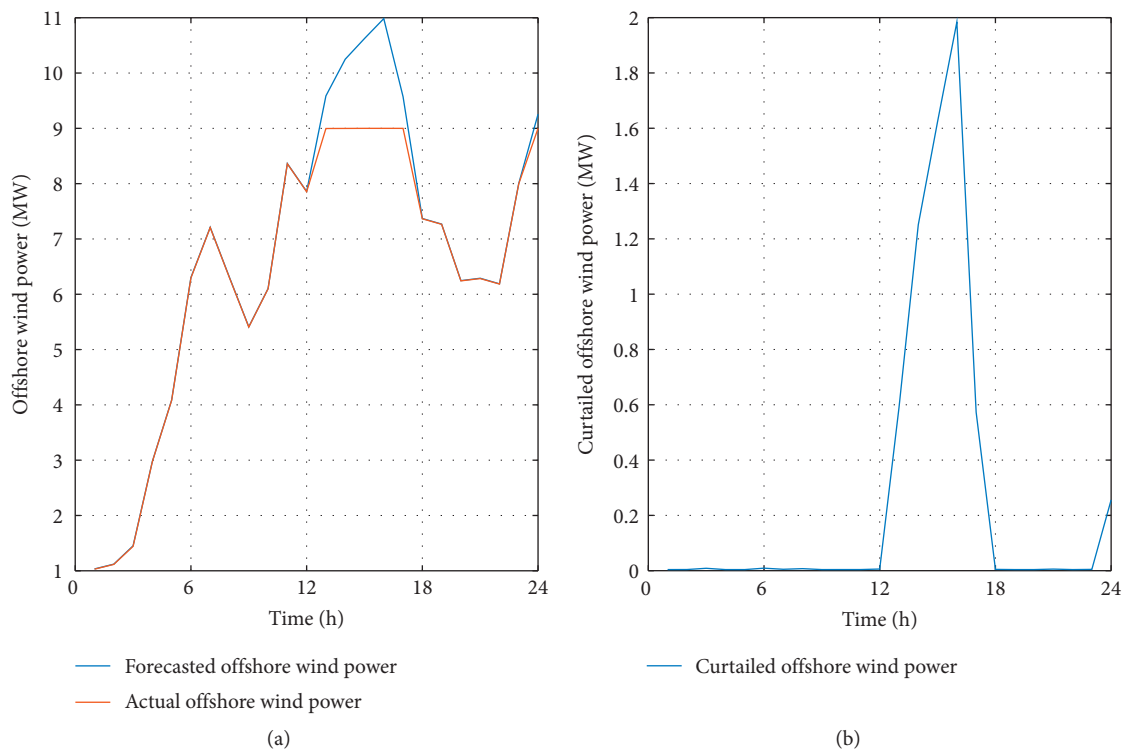

Figure 6: Forecasted and actual offshore wind power in scheme one.

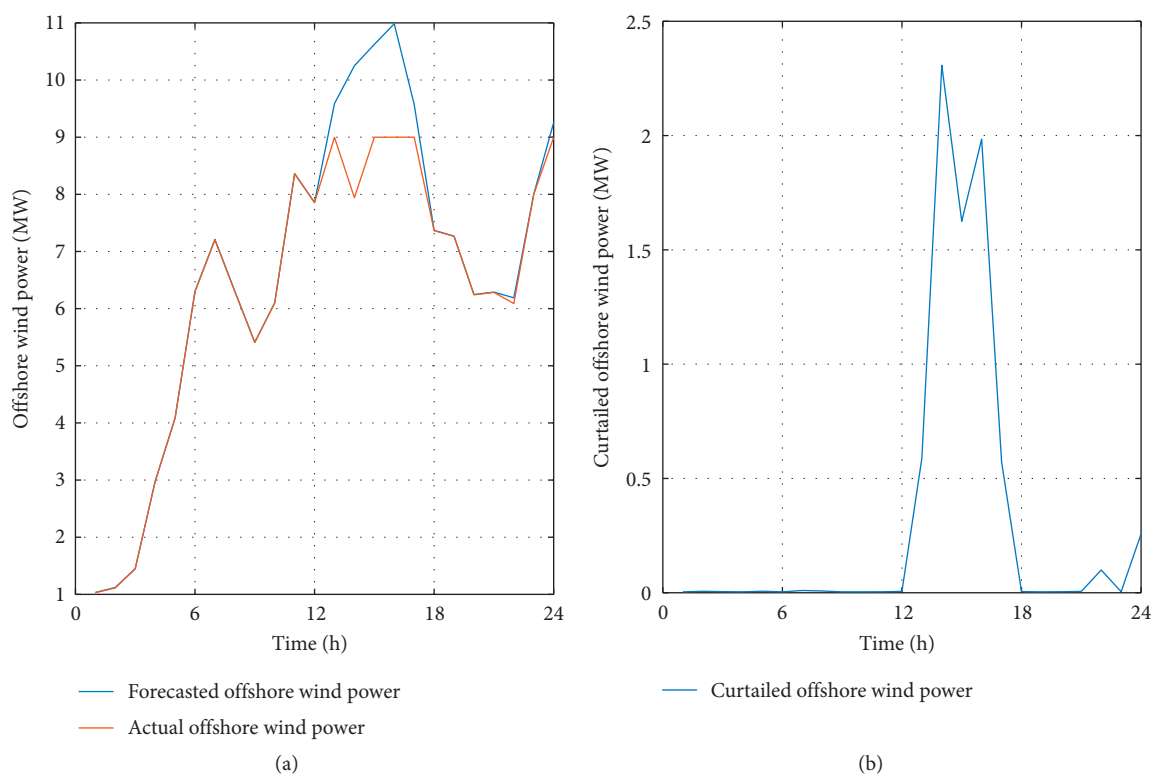

Figure 7: Forecasted and actual offshore wind power in scheme two.

6. Conclusion

While offshore wind power reduces environmental pollution, it also has an impact on the safe and stable operation of OMIES. In this paper, a biobjective optimization model based on the CCP was proposed to improve the economy of OMIES and reduce the natural gas emission; therefore, the natural gas emission and the operating cost containing the pollution cost and wind curtailment penalty cost are selected, respectively, as objective functions. Besides, the IHCHS-NSGAII was proposed to solve the multiconstrained biobjective model fast and efficiently from three aspects, namely, dimensionality reduction, individual repair process, and normalization and weighted sum process in selection. Then, it was applied to an OMIES problem, and the results show that the proposed method can make NSGAII converge to the feasible regions faster; thus, more computational resources can be applied to find better Pareto solutions. Besides, the operating cost and the natural gas emission cannot be perfectly optimized at the same time since the Pareto set is discontinuous. Also, the utilization of offshore wind power improves the economy of OMIES but increases natural gas emissions. Further studies are needed on the influence of the energy storage systems such as battery and gas/heat storage facilities.

Abbreviations

OMIES:	Offshore micro integrated energy system
IES:	Integrated energy system
CCP:	Chance-constrained programming
GT:	Gas turbine
GB:	Gas-fired boiler
EB:	Electric boiler
ESS:	Energy storage system
NSGA II:	Nondominated sorting genetic algorithm II
PFM:	Penalty function method
CDP:	Constraint domination principle
HCHS-NSGAII:	Hybrid constraints handling strategy NSGAII
IHCHS-NSGAII:	The improved hybrid constraints handling strategy based on nondominated sorting genetic algorithm II.

Mathematical Symbols

t:	Index for hours
i:	Index for GTs
j:	Index for GBs
k:	Index for central platforms
(g, h):	Index for power system nodes
(m, n):	Index for gas system nodes
e:	Index for EBs.

Sets

Ω_{gt}:	Set of GTs
Ω_{cp}:	Set of central platforms
Ω_{gb}:	Set of GBs
Ω_{eb}:	Set of EBs.

Variables

$P_{i,t}^{gt}$:	Active power output of GT i in period t
$G_{j,t}^{gb}$:	Gas consumed by GB j in period t
$\Delta G_{k,t}^{\text{gas}}$:	Gas emission of central platform k in period t
$\theta_{g,t}$:	Voltage angel of the power system at node g in period t
$P_{e,t}^{eb}$:	Power consumed by EB e in period t
$p_{n,t}$:	Pressure of gas system at node n in period t
$G_{k,t}^{\text{well}}$:	Gas generated by gas well k in period t
$G_{i,t}^{gt}$:	Gas consumed by GT i in period t
$\Delta P_{i,t}^{W}$:	Curtailed offshore wind power in period t
$P_{i,t}^{W}$:	Actual offshore wind power in period t
$P_{i,t}^{W,\text{pre}}$:	Forecasted offshore wind power in period t
α_i^{wind}:	Penalty cost of curtailed offshore wind power
$P_i^{gt,\max}, P_i^{gt,\min}$:	Maximum and minimum output of GT i
$\alpha_{1,i}^{gt}, \alpha_{2,i}^{gt}, \alpha_{3,i}^{gt}$:	Pollution coefficients of GT i
α_j^{gb}:	Emission coefficient of GB j
α_k^{well}:	Gas production coefficient of central platform k
α_k^{gas}:	Gas emission coefficient of central platform k
x_{gh}:	Reactance of transmission line (g, h)
$P_{gh}^{\max}$:	Capacity of transmission line (g, h)
$R_i^{\text{up}}, R_i^{\text{down}}$:	Ramp up and ramp down limit of GT i
$E_{h,t}^{\text{load}}$:	Power load at node h in period t
C_{mn}:	Constants related to temperature, length, diameter, friction, etc. of pipe (m, n)
$G_k^{\text{well},\max}, G_k^{\text{well},\min}$:	Maximum and minimum production of gas well k
$p_n^{\max}, p_n^{\min}$:	Maximum and minimum pressure of node n
$G_{n,t}^{\text{load}}$:	Gas load at node n in period t
H_t^{load}:	Heat load in period t
$H_j^{gb,\max}$:	Maximum output thermal power of GB j
η_{gt}:	Efficiency of GT
η_l:	Thermal loss coefficient of GT
η_{whb}:	Heat recovery efficiency of WHRB
HV_{gas}:	Natural gas caloricity
η_{eb}:	Efficiency of EB
$P_{gh,t}$:	Power transmitted between line $g$and h in period t
$G_{mn,t}$:	Gas transmitted between pipe m and n in period t
$H_{i,t}^{gt}$:	Heat power provided by WHRB connected with GT i in period t
$H_{j,t}^{gb}$:	Heat power provided by GB j in period t
$H_{e,t}^{eb}$:	Heat power provided by EB k in period t

G_{P2G}^{t}:	Gas converted by $P2G$ in period t
$G_{P2G}^{t,\max}$:	Maximum output of $P2G$
η_{P2G}:	Conversion efficiency of $P2G$
$\varepsilon_{wt,t}$, $\varepsilon_{\text{load},t}$:	Stochastic variables that describe the forecast error of offshore wind power and power load
σ_{wt}, σ_{load}:	Variance of forecast error of offshore wind power and power load
$\rho_{wt,t}$, $\rho_{wt,\text{ins}}$:	Error coefficient of offshore wind power output and capacity
$\rho_{\text{load},t}$:	Error coefficient of power load
η_1, η_2, η_3:	Confidence coefficient of power balance constraint, up-reserve capacity constraint, and down-reserve capacity constraint
U_{SR}:	Coefficient of the reserve requirement
w_u, w_d:	Offshore wind power output demand coefficient for up- and down-reserve
$\phi_1^{-1}(\eta_1)$, $\phi_2^{-1}(\eta_1)$, $\phi_3^{-1}(\eta_1)$:	Inverse function of the normal distribution function
G_c, G_s:	Current and switch generation
P_{re}:	Repair probability
$v_{k,\min}$, $v_{k,\max}$:	Minimum and maximum violation
$v_{l,k,i}$:	i-th constraint violation of the l-th individual
n_k:	Number of violated k-th type of constraints.

Data Availability

The table data and modeling data used to support the finding of this study are included within the article.

Conflicts of Interest

The authors declare that they have no known competing financial interests or personal relationships that could have appeared to influence the work reported in this paper.

Acknowledgments

This work was supported by the National Key Research and Development Program of China, China (No. 2018YFB0904800).

References

[1] M. Leporini, B. Marchetti, F. Corvaro, and F. Polonara, "Reconversion of offshore oil and gas platforms into renewable energy sites production: assessment of different scenarios," *Renewable Energy*, vol. 135, pp. 1121–1132, 2019.

[2] S. D. Musa, T. Zhonghua, A. O. Ibrahim, and M. Habib, "China's energy status: a critical look at fossils and renewable options," *Renewable and Sustainable Energy Reviews*, vol. 81, pp. 2281–2290, 2018.

[3] Maribus gGmbH, *The World Ocean Review-Marine Resources Opportunities and Risks*, Maribus Gemeinnützige GmbH, Hamburg, Germany, https://worldoceanreview.com/wp-content/downloads/wor3/WOR3_en.pdf.

[4] S. Van Elden, J. Meeuwig, J. M. Hemmi, and R. Hobbs, "Offshore oil and gas platforms as novel ecosystems: a global perspective," *Frontiers in Marine Science*, vol. 6, p. 548, 2019.

[5] A. Zhang, G. Peng, W. Yang, G. Qu, and H. Huang, "Risk assessment of offshore micro integrated energy system based on fluid mosaic model," *IEEE Access*, vol. 8, pp. 76715–76725, 2020.

[6] W. He, K. Uhlen, M. Hadiya, Z. Chen, G. Shi, and E. del Rio, "Case study of integrating an offshore wind farm with offshore oil and gas platforms and with an onshore electrical grid," *Journal of Renewable Energy*, vol. 2013, Article ID 607165, 10 pages, 2013.

[7] S. Oliveira-Pinto, P. Rosa-Santos, and F. Taveira-Pinto, "Electricity supply to offshore oil and gas platforms from renewable ocean wave energy: overview and case study analysis," *Energy Conversion and Management*, vol. 186, pp. 556–569, 2019.

[8] M. L. Kolstad, A. R. Årdal, K. Sharifabadi, and T. M. Undeland, "Integrating offshore wind power and multiple oil and gas platforms to the onshore power grid using VSC-HVDC technology," *Marine Technology Society Journal*, vol. 48, no. 2, pp. 31–44, 2014.

[9] J. Zhai, X. Wu, S. Zhu, B. Yang, and H. Liu, "Optimization of integrated energy system considering photovoltaic uncertainty and multi-energy network," *IEEE Access*, vol. 8, pp. 141558–141568, 2020.

[10] J. Zheng, Y. Kou, M. Li, and Q. Wu, "Stochastic optimization of cost-risk for integrated energy system considering wind and solar power correlated," *Journal of Modern Power Systems and Clean Energy*, vol. 7, no. 6, pp. 1472–1483, 2019.

[11] L. Bigarelli, A. Lidozzi, M. Di Benedetto, L. Solero, and S. Bifaretti, "Model predictive energy management for sustainable off-shore oil and gas platforms," in *Proceedings of the 2019 21st European Conference on Power Electronics and Applications (EPE'19 ECCE Europe)*, Genova, Italy, September 2019.

[12] A. Turk, Q. Wu, M. Zhang, and J. Østergaard, "Day-ahead stochastic scheduling of integrated multi-energy system for flexibility synergy and uncertainty balancing," *Energy*, vol. 196, pp. 117–130, 2020.

[13] C. Zhao, J. Wang, J.-P. Watson, and Y. Guan, "Multi-stage robust unit commitment considering wind and demand response uncertainties," *IEEE Transactions on Power Systems*, vol. 28, no. 3, pp. 2708–2717, 2013.

[14] R. Jiang, J. Wang, and Y. Guan, "Robust unit commitment with wind power and pumped storage hydro," *IEEE Transactions on Power Systems*, vol. 27, no. 2, pp. 800–810, 2011.

[15] H. Pandžić, Y. Dvorkin, T. Qiu, Y. Wang, and D. S. Kirschen, "Toward cost-efficient and reliable unit commitment under uncertainty," *IEEE Transactions on Power Systems*, vol. 31, no. 2, pp. 970–982, 2015.

[16] H. Wu, M. Shahidehpour, Z. Li, and W. Tian, "Chance-constrained day-ahead scheduling in stochastic power system operation," *IEEE Transactions on Power Systems*, vol. 29, no. 4, pp. 1583–1591, 2014.

[17] Q. Wang, Y. Guan, and J. Wang, "A chance-constrained two-stage stochastic program for unit commitment with uncertain wind power output," *IEEE Transactions on Power Systems*, vol. 27, no. 1, pp. 206–215, 2011.

[18] A. Zhang, H. Zhang, J. Wu, M. Qadrdan, and Q. Li, "Multi-objective stochastic planning for offshore micro integrated energy systems," *Automation of Electric Power Systems*, vol. 43, no. 7, pp. 129–135, 2019.

[19] D. V. Singh and E. Pedersen, "A review of waste heat recovery technologies for maritime applications," *Energy Conversion and Management*, vol. 111, pp. 315–328, 2016.

[20] D. Sun, X. Xie, J. Wang, Q. Li, and C. Wei, "Integrated generation-transmission expansion planning for offshore oilfield power systems based on genetic Tabu hybrid algorithm," *Journal of Modern Power Systems and Clean Energy*, vol. 5, no. 1, pp. 117–125, 2017.

[21] C. M. Correa-Posada and P. Sánchez-Martín, "Integrated power and natural gas model for energy adequacy in short-term operation," *IEEE Transactions on Power Systems*, vol. 30, no. 6, pp. 3347–3355, 2014.

[22] J. Wu, B. Zhang, Y. Jiang, P. Bie, and H. Li, "Chance-constrained stochastic congestion management of power systems considering uncertainty of wind power and demand side response," *International Journal of Electrical Power & Energy Systems*, vol. 107, pp. 703–714, 2019.

[23] K. Deb, A. Pratap, S. Agarwal, and T. Meyarivan, "A fast and elitist multiobjective genetic algorithm: NSGA-II," *IEEE Transactions on Evolutionary Computation*, vol. 6, no. 2, pp. 182–197, 2002.

[24] X. Li, J. Lai, and R. Tang, "A hybrid constraints handling strategy for multiconstrained multiobjective optimization problem of microgrid economical/environmental dispatch," *Complexity*, vol. 2017, Article ID 6249432, 12 pages, 2017.

[25] J. Wu, B. Li, J. Chen et al., "Multi-objective optimal scheduling of offshore micro integrated energy system considering natural gas emission," *International Journal of Electrical Power & Energy Systems*, vol. 125, Article ID 106535, 2021.

Hindawi
Complexity
Volume 2020, Article ID 8843178, 17 pages
https://doi.org/10.1155/2020/8843178

Research Article

Autonomous Behavior Intelligence Control of Self-Evolution Mobile Robot for High-Voltage Transmission Line in Complex Smart Grid

Wei Jiang,[1,2] **Gan Zuo**,[1] **De Hua Zou**,[3] **Hongjun Li**,[1,4] **Jiu Jiang Yan**,[1] **and Gao Cheng Ye**[1]

[1]*School of Mechanical Engineering and Automation, Wuhan Textile University, Wuhan 430073, China*
[2]*Wuhan Textile University, Hubei Key Laboratory of Digital Textile Equipment, Wuhan 430200, China*
[3]*State Grid Hunan Transmission Maintenance Company, Changsha 410100, China*
[4]*College of Engineering, Huazhong Agricultural University, Wuhan 430070, China*

Correspondence should be addressed to Wei Jiang; jiangwei2013@whu.edu.cn and Hongjun Li; lihongjun@wtu.edu.cn

Received 6 August 2020; Revised 11 September 2020; Accepted 9 October 2020; Published 5 November 2020

Academic Editor: Ruoli Tang

In complex smart grid, the power maintenance robot is important equipment to ensure the reliable operation of high-voltage lines and it is a useful exploration to realize high-quality power transmission. In view of the increasingly prominent contradiction between the robot single operation function and the diversification of power grid maintenance operations, additional with the robot weak autonomous operation and intelligent behavior ability, this paper proposes a new configuration of a reconfigurable power robot with terminal functions and its autonomous operation behavior control method for the three typical tasks which are the high-voltage transmission line insulators, drainage plates, and dampers maintenance. Through the analysis and planning of the robot operation behavior, the robot finite state machine (FSM) model in the three operation states has been established. Through the introduction of the state transfer function in the FSM, the automatic switching control between the robot key operation states can be realized, and the robot motion planning can be optimized. The movement and working flow of the robot improve the robot operation intelligence and operation efficiency. Based on this, the robot autonomous operation control system has been designed and the robot physical prototype has been developed for three maintenance tasks of insulators, drainage plates, and dampers. Finally, simulation experiments and field operation tests verify the effectiveness and engineering practicability of the proposed method. Compared with traditional manual control, the autonomous behavior control method can significantly improve the robot operational efficiency and operational intelligence. At the same time, the robot multitask function and autonomous behavior control under different tasks can be realized and the method has strong versatility for different task objects and different line environments. The research and its promotion have important theoretical significance and practical application value for the power system operation and maintenance integration management.

1. Introduction

Electricity is the lifeblood of the national economy and high-voltage cables are an important channel for power transmission. Their special geographical environment and harsh natural environment will cause various faults on line, in order to ensure the safe, normal, and stable operation of high-voltage transmission lines, thereby, effectively reducing economic losses. It is necessary to regularly and irregularly perform maintenance and construction operations on line fittings and their operation environment [1–4]. At present, such special operations in dangerous and harsh environments are all performed manually, which not only is labor-intensive and low-efficient but also poses great personal safety risks. Regarding the maintenance operations far away from the poles and towers, the live working can be performed only in the condition of power outages. As the assessment indicators of power transmission quality and operation safety are getting higher and higher, as well as the urgent needs of modern power system operation and management automation, the

contradiction between this manual operation method and modern high-quality power transmission has become more and more prominent. Therefore, it is an effective measure to replace the live line operation performed by the live line maintenance robot [5–8], which has important practical application value for improving operation efficiency, operation reliability, and worker safety. The robots currently studied are mostly only oriented to double operations [9, 10], and most of them are only oriented to a single operation. Due to the wide variety and dispersion of line maintenance operations, power grid companies will inevitably need to configure robots of different types of operations, which result in high purchase and maintenance costs. Namely, the contradiction between the robot single operation function and the diversification of the power grid maintenance operation objects in the existing research has become more and more prominent [11, 12]. Therefore, the study of multitask-oriented power maintenance robots and their autonomous operation behavior control so as to realize the multipurpose function of the robot mobile platform has important theoretical significance and practical value for building a resource-saving and environment-friendly integrated operation of the power transmission grid. In order to improve the robot autonomous behavior ability and operation efficiency, the robot is required to have a strong autonomous behavior control ability. In terms of autonomous behavioral control, there are mainly autonomous behavior control methods based on expert systems [13, 14], fuzzy logic [15, 16], neural network [17, 18], swarm intelligence algorithm [19, 20] and, additionally, the hierarchical planning method [21, 22] which have already been adopted to the power line inspection robot through using generative reasoner to create behavior sequences online at the behavior planning layer, it combined with the behavior interpretation knowledge base generated offline at the action layer, and to achieve automatic robot obstacle crossing on power line. A finite state machine model [23, 24] has been proposed and used in inspection robot obstacle crossing on HVTL; however, this method can only realize the robot's local obstacle crossing and semiautomatic obstacle crossing. In [25–28], a multisensor-based transmission line identification and robot spatial posture positioning method has been proposed; however, it did not perform multisensor information fusion processing, thereby affecting the improvement of the overall robot operation efficiency. Through the above analysis, we can know, there is currently no universal robot autonomous behavior control method since the complicated robot operation can be abstracted into a series of state combinations from the operation beginning to the task completion; in this way, the complex operation process of the robot has been simplified and the key to the improvement of the robot autonomous behavior ability is the free switching between different joint states. Therefore, the goal of robot behavior planning for multitask tasks in the ultrahigh-voltage multisplit environment is to formalize model descriptions of different types of tasks and robot motion control behaviors in all layers. This facilitates the completion of automatic reason and decision control and achieves the purpose of the electric power line robot autonomous operation.

Based on the above analysis, this article is aimed at the multisplit multitask power transmission maintenance robot. Based on the analysis of the robot completion insulator replacement, drainage plate tightening, and damper replacement of three typical operations' motion planation, the design method of hierarchical control has been adopted and the robot motion behavior during the operation can be divided into a combination of multiple basic behaviors by defining the basic behavior of the robot arm joint motion. The finite state machine (FSM) model is used to realize the management and control of the combined behavior and the robot operation motion behavior has been decomposed. By selecting and setting a reasonable operation state transfer function, the robot three different operations have been planned and optimized for motion control, compared with the traditional manual control, and the operation status reduces the operation intensity of the operator and improves the operation efficiency. At the same time, for some special states that the robot may appear in the operation process, a mechanism for handling robot abnormal behavior of the robot is designed. Finally, the experimental verification of the feasibility and engineering practicability of the robot behavior control algorithm designed in this paper through simulation and field operation experiments are of great significance for accelerating the robot practical process.

2. The Function Realization of Multitask Reconfigurable Robot System

2.1. Mechanical Configuration Analysis and Synthesis of Multitask Robots. Through the analysis of the three operation tasks and operation principles of insulator (auxiliary) replacement [29], drainage plate bolt tightening [30], and damper replacement [31], the three operation tasks can be completed, respectively. The degrees of freedom required by the robot manipulator and their corresponding functions are shown in Tables 1–3.

It can be concluded from Tables 1–3 that in order to complete the three tasks, the number of DOF and the functions required by the robot dual operation arms are completely the same. The only difference is the DOF and functions of the manipulator. Therefore, the live maintenance robot can be designed using the configuration mode of the robot mobile platform and the manipulator reorganization. The mobile robot platform can be shared by the three operations. The mobile robot is equipped with different manipulators to complete different tasks. The configuration of the mobile robot and entity model is shown in Figure 1. It is mainly composed of a control box, a double walking arm, a double operation arm, a double walking wheel and its clamping mechanism, and several main parts. The operation arm 1 is fixed on the machine body and it has three DOF which are rotation, stretch, and vertical movement. In addition to the three DOF of the operation arm 1, the operation arm 2 also has a horizontal joint, which can move laterally along the body to realize the pushing out and loading of the insulator string. The dual operation arms have a total of seven three. The double operation arms end effector can be reorganized and installed with different manipulators,

Table 1: Configuration analysis of insulator (auxiliary) replacement robot.

Insulator (auxiliary) replacement operation				
	Robot mobile platform		Robot operation manipulator	
	Operation arm 1	Operation arm 2	Manipulator 1	Manipulator 2
Number of DOF>	Vertical/stretch/rotation (3 units)	Horizontal/vertical/stretch/ rotation (4 units)	Clamping/pushing block mechanism (3 units)	Clamping mechanism (1 unit)
Function	Reach operation space through coordinated joint movement	Reach operation space through coordinated joint movement	The bowl head hanging plate clamps the W pin and pushes in	The insulator is clamped and pushed out/loaded by the stretch mechanism

Table 2: Configuration analysis of the operation robot for drainage plate bolt tightening.

Drainage plate bolt tightening operation				
	Robot mobile platform		Robot operation manipulator	
	Operation arm 1	Operation arm 2	Manipulator 1	Manipulator 2
Number f DOF	Vertical/stretch/rotation (3 units)	Horizontal/vertical/stretch/ rotation (4 units)	Bolt fixing mechanism (0 units)	Bolt tightening mechanism (1 unit)
Function	Reach operation space through coordinated joint movement	Reach operation space through coordinated joint movement	Realize the fixation of the bolt head	Realize nut tightening operation

Table 3: The configuration analysis of the damper maintenance robot.

Damper replacement operation				
	Robot mobile platform		Robot mobile platform	
	Operation arm 1	Operation arm 2	Manipulator 1	Manipulator 2
Number of DOF	Vertical/stretch/rotation (3 units)	Horizontal/vertical/stretch/ rotation (4 units)	Clamping mechanism (1 unit)	Pitch/bolt tightening mechanism (2 units)
Function	Reach operation space through coordinated joint movement	Reach operation space through coordinated joint movement	Clamping damper	Realize different angle nut tightening operations

respectively, to complete the three functions of insulator replacement, drainage plate bolt tightening, and damper replacement.

2.2. The Key Postures of the Robot Operation Process. After the insulator maintenance robot is online, the dual operation arms can be adjusted from the initial posture to the working posture, and they travel along the wire and detect and locate the suspension clamps to achieve rough positioning to the insulator string. By fine-tuning each joint of the operation arm, the positioning of the bowl head hanging plate, W pin, and insulator steel cap can be completed and the bowl head hanging plate can be clamped, the W pin can be pushed out, the insulator steel cap can be clamped, and the insulator ball head is pushed out so that the insulator string can be changed from a fixed state to a free state, so as to facilitate manual replacement. The motion simulation of the operation planning entity is shown in Figure 2.

After the drainage board maintenance robot is online, the dual operation arms can be adjusted from the initial posture to the working posture and travel along the wire, detecting and positioning the press-connection-pipe to determine the initial position of the robot to tighten the bolts. The adjustment can be completed by adjusting the joints of the operation arm. The positioning of the bolt head, nut, and the connection with the operation manipulator can be realized. The entity motion simulation of the operation planning is shown in Figure 3.

After the damper robot is online, the dual operation arms can be adjusted from the initial posture to the working posture, travel along the wire, and roughly be positioned to the replacement workspace of the damper, which can be completed by adjusting the joints of the operation arm, especially the movement of the pitch mechanism, the bolt head, nut positioning and the realization of the docking with the operation manipulator and the bolt head and nut, the tightening of the nut, and the clamping of the damper; the

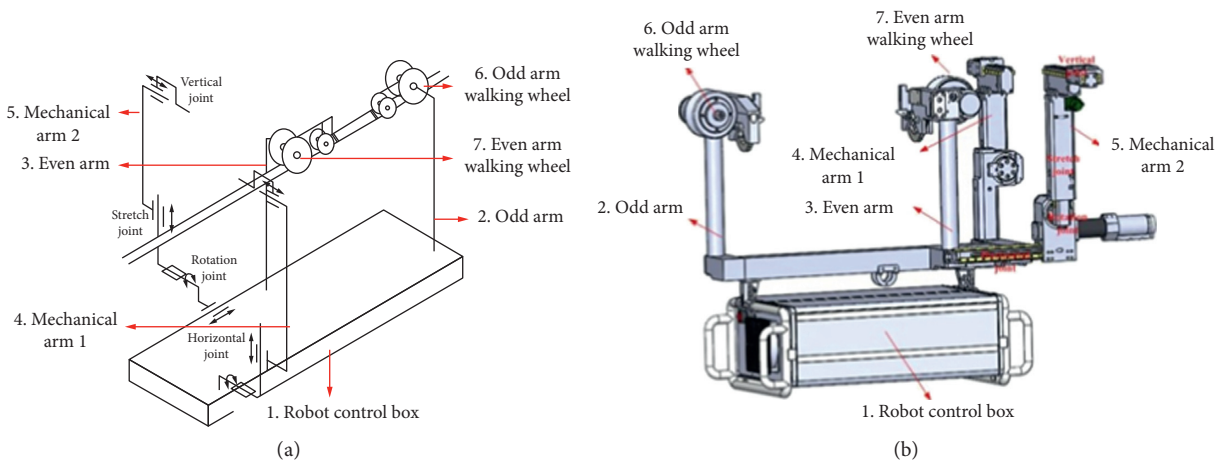

Figure 1: Configuration and entity model of live maintenance robot mobile platform. (a) Configuration. (b) Entity model.

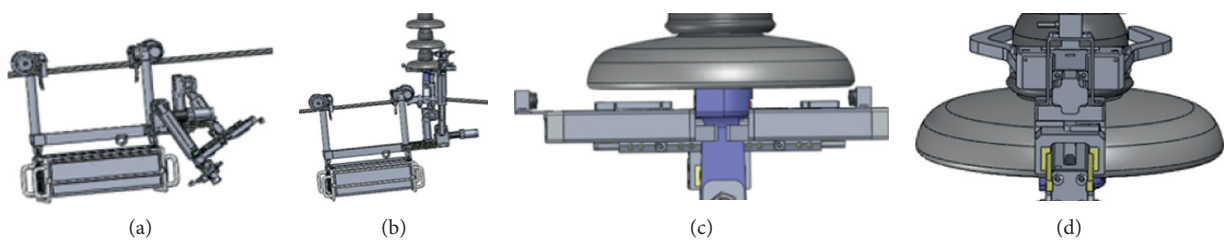

Figure 2: Insulator replacement operation planning entity motion simulation. (a) Initial posture. (b) Working posture. (c) Bowl head plate clamping. (d) Insulator steel cap clamping.

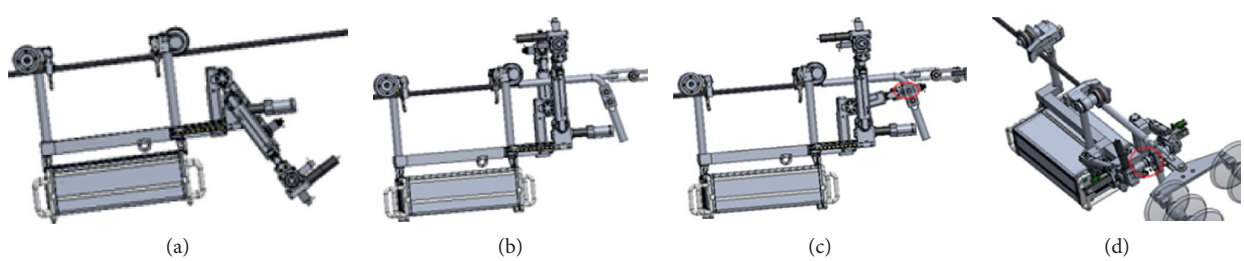

Figure 3: Entity motion simulation of bolt tightening plan for drainage plate. (a) Initial posture. (b) Working posture. (c) Fixing of bolt head. (d) Bolt tightening operation.

physical motion simulation of the operation planning is shown in Figure 4.

2.3. The Design Principle of Robot Terminal Reconfiguration for Multitasks. The reconfiguration of the robot operation terminal can be divided into two categories which are static reconfiguration and dynamic reconfiguration. The static reconfiguration is the assembly and reorganization of the terminal by the operator. Dynamically reconfigurable is the movement of the robot's own modules to replace the operation end. Combining with the actual application requirements of special power operation robots, this article adopts the realization method of terminal static reconfiguration. According to the operation task of the live maintenance robot, the corresponding operation end reconstruction principle has been proposed. For different operation tasks, corresponding actuators are required and the structure of the robot is modularized. According to different tasks, the corresponding actuators are selected to reorganize the robot operation ends. According to the functions of each part of the robot, the robot can be divided into two categories. The first category is the operation manipulator, including the bowl head hanging plate clamping and W pin-pushing end, insulator string pushing end, bolt fixing and bolt tightening end, damper clamping and supporting mechanism, and damper bolt tightening and loosening mechanism. The operation end directly acts on the operation object, making small-scale movements and fine-tuning the posture as needed. The second category is the

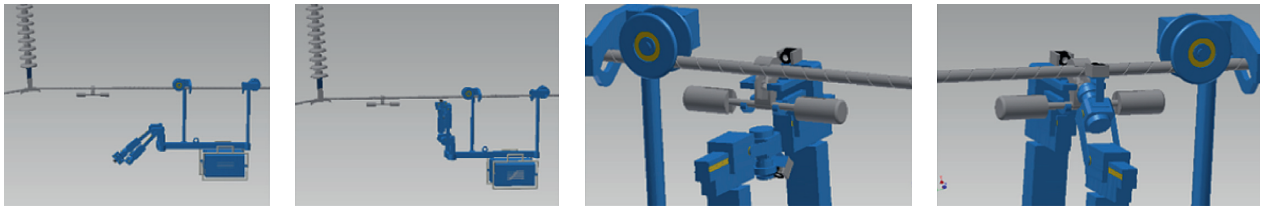

(a) (b) (c) (d)

Figure 4: Entity motion simulation of the damper replacement robot. (a) Initial posture. (b) Working posture. (c) Fixing bolt head. (d) Bolt tightening operation.

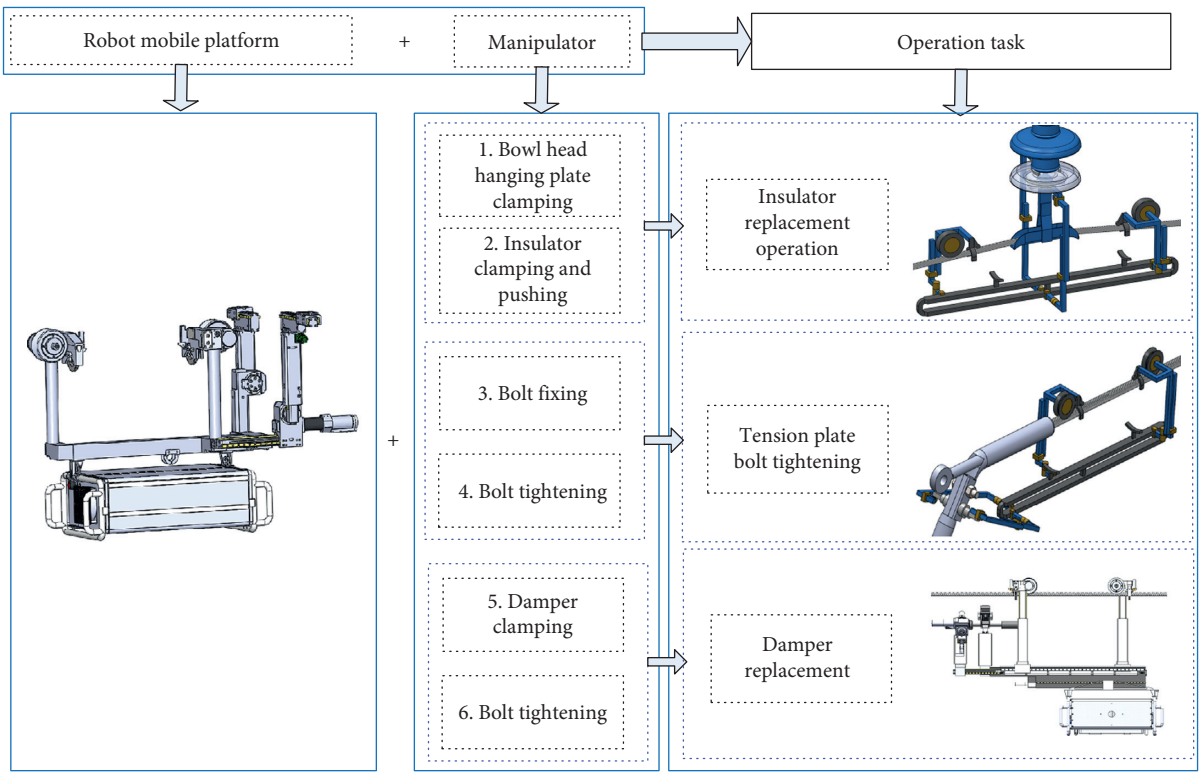

Figure 5: The principle of reconfigurable modular design for multiple tasks.

mobile robot platform for live maintenance, which includes dual manipulators, dual operation arms, and mobile platforms. Each manipulator is composed of multiple joints in series, and each joint moves in coordination to perform terminal positioning or coordinate with the corresponding terminal. The dual mobile arms and dual manipulators coordinate and cooperate to complete different tasks of walking. The mobile platform is the carrier of the entire robot. The mobile platform of the live maintenance robot completes the corresponding operation tasks by carrying different operation ends. The principle of reconfigurable end functions is shown in Figure 5. According to the principle of module division and terminal reconstruction, insulator (auxiliary) replacement, bolt tightening, and damper replacement live working robots are all composed of double operation arms and the mobile robot equipped with double operation manipulators and the mobile robot is used as refactoring the platform. For other multitask robots terminal reconstruction methods can be designed and implemented based on this principle.

3. Robot Operation Behavior Analysis and Planning Control

3.1. Analysis of Robot Operation Behavior. In order to clearly describe the robot operation process, the state vector is used to describe the robot key posture. The robot operation can be regarded as the change process of the robot key posture caused by the robot execution. Table 4 shows the definition of the robot state vector.

Using the above representation method, the robot has a total of 2 [12] possible states. Because robots face different tasks and different tasks of robots have specific processes, many postures are not allowed to appear when robots are working. Therefore, through analyzing the robot posture, effective postures can be screened out. As shown in Table 5,

Table 4: Robot state vector.

Digit	Status meaning		Parameter
0	Vertical mechanism state		0: move forward; 1: move backward
1	Horizontal mechanism state		0: move in; 1: move out
2	Stretch mechanism state	Robot mobile platform	0: extend; 1: shorten
3	Rotation mechanism state		0: rotate clockwise; 1: rotate counterclockwise
4	Walking mechanism		0: walking; 1: stop
5	Insulator clamping mechanism state		0: clamping; 1: release
6	Bowl head hanging plate clamping mechanism state	Insulator maintenance	0: clamping; 1: release
7	W pin push mechanism status		0: push out; 1: push in
8	Drainage plate bolt tightening mechanism state	Drainage plate maintenance	0: tightening; 1: loosen
9	Damper clamping mechanism state		0: clamping; 1: release
10	Damper bolt tightening mechanism	Damper maintenance	0: clamping; 1: release
11	Damper bolt tightening pitch mechanism		0: up; 1: down

Table 5: The robot's effective state vector value.

State vector	Meaning	Vector value
S_0	Initial state	0×0000
S_1	Insulator steel cap clamping state	0×0001
S_2	Clamping state of bowl head hanging plate	0×0010
S_3	W pin rolling out status	0×0011
S_4	Alignment of drainage plate bolts	0×0100
S_5	Alignment of drainage plate nut	0×0101
S_6	Damper clamping state	0×0110
S_7	Damper bolt alignment state	0×0111
S_8	Damper clamping mechanism state	0×1000
S_9	Damper screw bolt mechanism	0×1001
S_{10}	Damper bolt tightening pitch mechanism	0×1010
S_{11}	Standby state-1	0×1011
S_{12}	Standby state-2	0×1100
S_{13}	Standby state-3	0×1101
S_{14}	Standby state-4	0×1110
S_{15}	Standby state-5	0×1111

effective state screening can greatly optimize the robot operation flow.

3.2. Robot Autonomous Operation Behavior Planning

3.2.1. Definition of Robot Behavior. The robot motion behavior in the operation process from part to the whole mainly includes joint motion behavior, arm motion behavior, robot motion behavior, and robot abnormal behavior processing. Among them, the basic behavior of the robot joint motion behavior (JMB) is defined as a module that is directly connected to the drive mechanism and sensors and has specific motion functions. Manipulator action behavior AMB (arm motion behavior) is a robot arm behavior that can achieve specific functions, which is composed of several basic joint behaviors and a joint behavior inference device as shown in the following equation, where AMBi is the combination behavior and $\boldsymbol{F}$ is the joint state transition function:

$$AMP = \left(\mathrm{JMP}_1, \mathrm{JMP}_2\mathrm{JMP}_3, \ldots, \mathrm{JMP}_n, F\right). \quad (1)$$

Robot motion behavior (RMB) is composed of several operation arm behaviors, as well as the robot walking mechanism and behavior inference device. Its activation and execution are consistent with the operation arm motion behavior. The robot motion behavior is defined as equation (2), wherein AMB is defined in the above and F is the state transition function. The C++ thread pseudocode is used and can be formally expressed as Algorithm 1:

$$RMP = \left(\mathrm{AMP}_1, \mathrm{AMP}_2\mathrm{AMP}_3, \ldots, \mathrm{AMP}_n, \text{Walking Action}, F\right), \quad (2)$$

Due to the complex working environment of electric power robots, there are many steps in the operation process and strict sequence of steps. In addition, the robot will inevitably encounter some special situations, such as interruption of information transmission, sensor, and industrial computer crash. Therefore, it is necessary to introduce an exception handling mechanism to ensure personnel safety, line safety, equipment safety, and normal operation tasks.

3.2.2. Robot Operation Behavior Planning Based on Task Decomposition. Regarding the specific electric maintenance robot, the whole robot operation process can be divided into four basic behaviors, namely, the behavior of the robot arm 1, the behavior of the robot arm 2, the behavior of the work

```
Set Joint Motion Behavior;
Struct s_inputParas (MotionBehaviorName, InputList, Status Transfer);
Struct s_outParas (OutputLit);
Procedure Join Motion Behavior StatusCtrl ()
{
   BOOL bOver = FALSE
   BeginThread (s_inputParas);
      switch (s_inputParas)
{
         case 1: Joint Motion Behavior1 (...); break;
         case 2: Joint Motion Behavior2 (...); break;
         case 3: Joint Motion Behavior3 (...); break;
         (...)
         case n: Joint Motion Behaviorn (...); break;
         default: break;
   EndThread();
}
}
```

Algorithm 1: Autonomous planning algorithm for robot motion behavior.

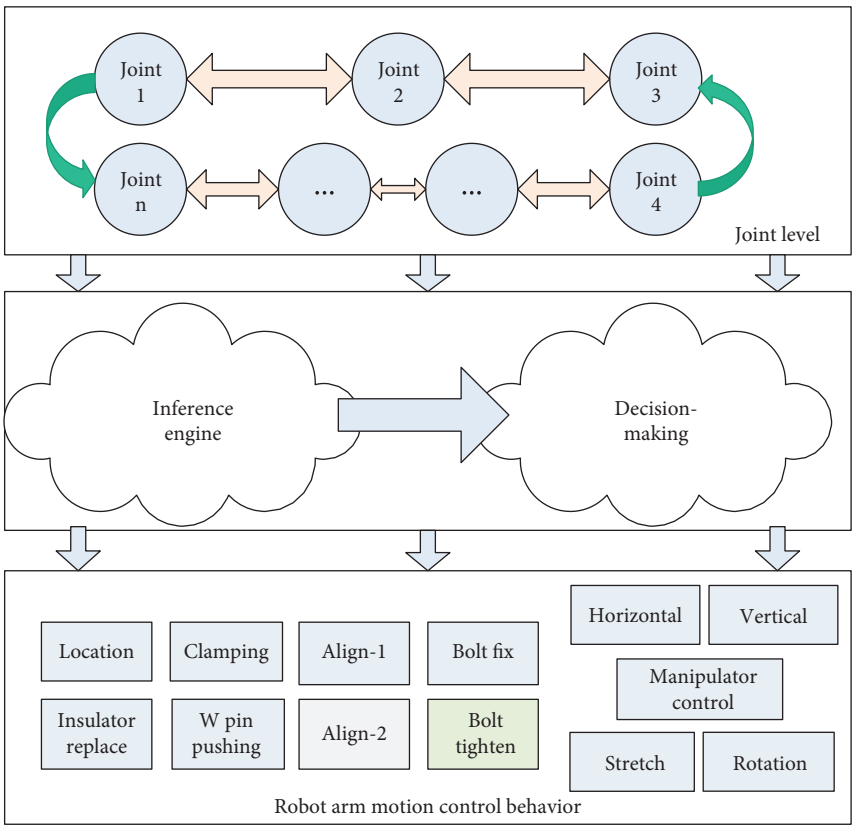

Figure 6: Robot task decomposition and behavior planning.

end 1, and the behavior of the work end 2. Each behavior can be completed by several robot posture adjustments and also includes multiple robot state transitions. For each behavior of the robot, the corresponding state transfer function can be set separately, by inputting the initial state and target state of the robot and behavior parameters to complete the robot state transition. Therefore, the whole process of completing different tasks on the power transmission line by the robot represented by the basic behavior and combined behavior of the robot can be obtained as shown in Figure 6.

3.2.3. Robot Operation Behavior Control. The architecture of robot autonomous behavior control can be divided into four

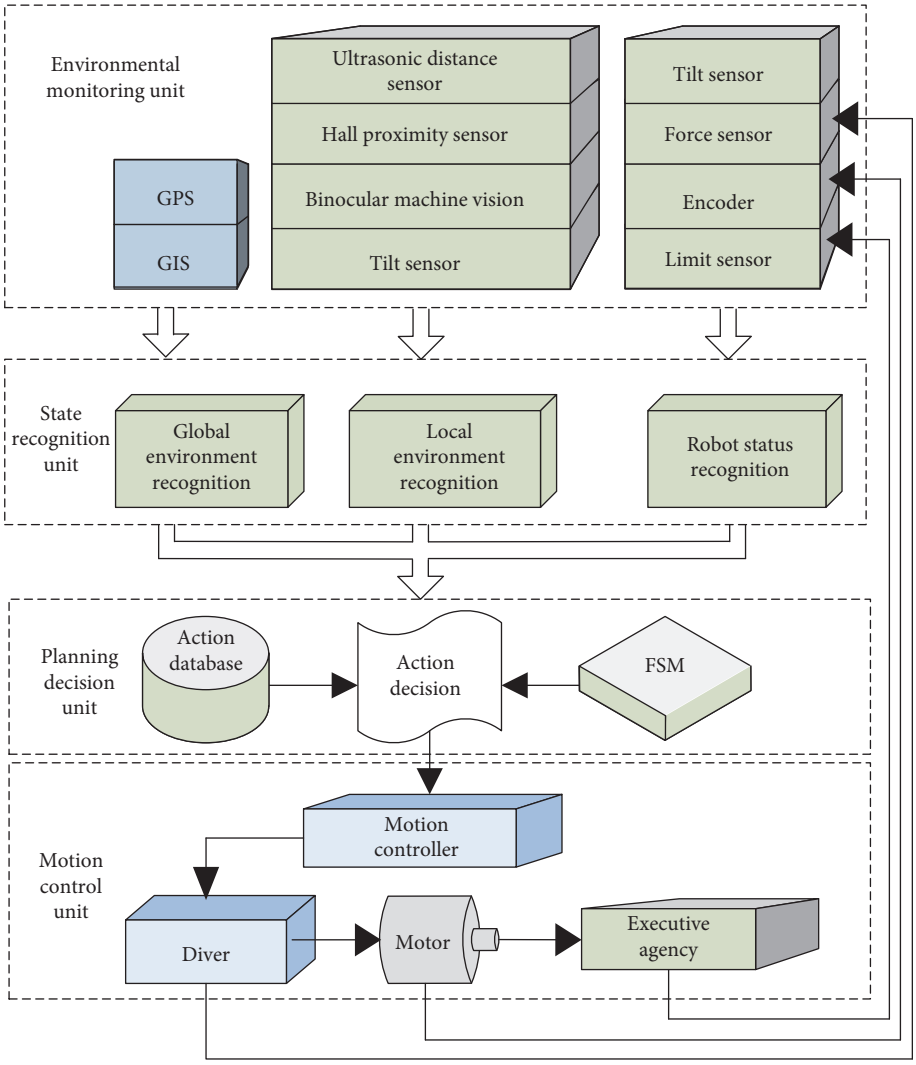

Figure 7: Robot schematic diagram of autonomous behavior control.

units as shown in Figure 7, namely, environmental monitoring unit, state recognition unit, planning decision unit, and motion control unit. Among them, the environment monitoring unit is mainly used by the robot to detect and perceive the robot operation environment with various sensors carried by itself, which is also the basis for the robot intelligent decision-making. Based on the monitoring of the robot's local and global environment, the robot can recognize and detect its own operation status. Then, the robot motion planning decision can be made through the behavior database and FSM model, and finally, the motion control unit drives the robot joint motors to realize intelligent autonomous operation control.

4. Robot Operation FSM and Autonomous Control System Design

4.1. FSM Design for Insulator Replacement Operation. Finite state machine is a mathematical model that represents a finite number of states and behaviors such as transitions and actions between these states. A finite state machine M is a five-tuple, $M = (K, E, T, S, Z)$ wherein K is a finite set and each element in it is called a state. E is a finite alphabet and each element of it is called an input character. T is a conversion function which is a mapping on $K \times E \longrightarrow K$. S is an element in K, which is the only initial state. Z is a subset of K, a final state set. When the online maintenance robot is performing insulator replacement operations, the robot dual operation arms and their ends need to take a series action, including multiple states and state transition rules. These actions have been proved to be the most feasible way through many experiments. They are set according to the operation object task and the robot's own mechanism. It is also based on experience planning. The robot FSM design for insulator replacement is shown in Figure 8. The operation can be divided into nineteen states, which are triggered by nineteen events. The event can be described as follows: (1) operation arm 1 turns forward; (2) operation arm 2 turns forward; (3) robot goes online; (4) operation arm 1 turns backward; (5) operation arm 2 turns backward; (6) operation arm 2 extends; (7) the robot moves forward at a low speed; (8) the robot walking wheel touches the suspension clamp;

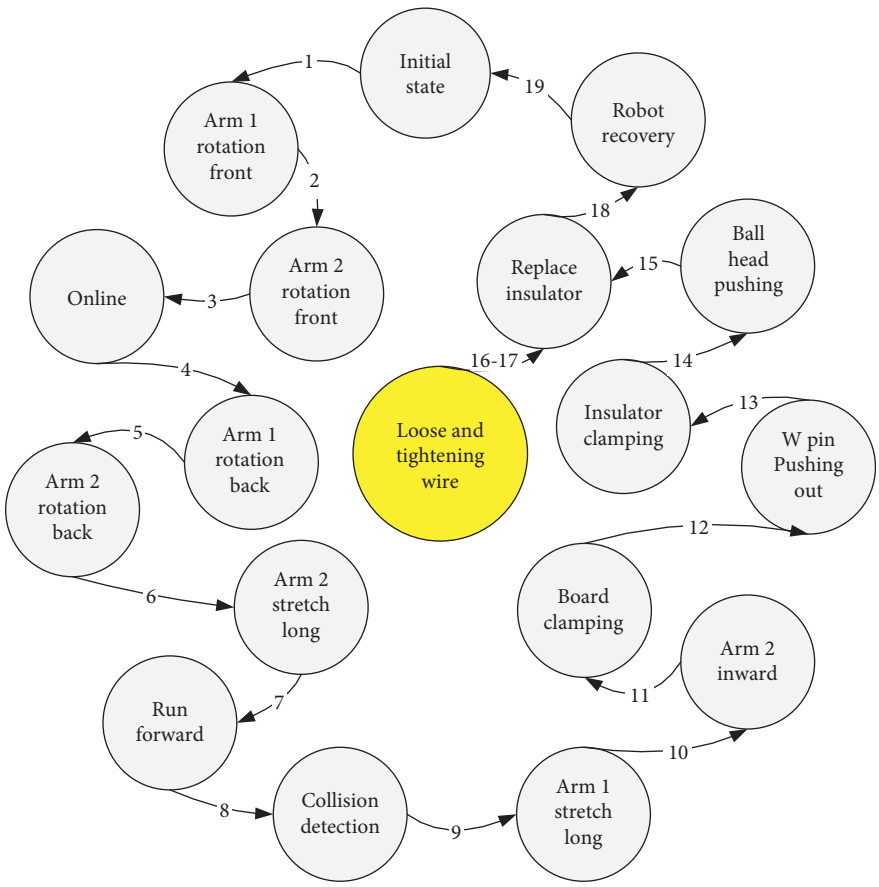

Figure 8: FSM design for insulator replacement operation.

(9) the operation arm 1 extends; (10) the operation arm 1 moves inward; (11) the operation hand 1 clamps the bowl head hanging plate; (12) push out W pin; (13) clamping of the insulator; (14) push out the ball head; (15) replace the insulator; (16) loose the wire; (17) tightening the wire; (18) restore the robot posture; and (19) return the robot to the initial state.

4.2. FSM Design for Drainage Plate Bolt Tightening Operation. According to the abovementioned bolt tightening operation motion planning and manual experience operation, the FSM design when the robot performs the drainage plate tightening operation can be obtained as shown in Figure 9. The operation can be divided into eighteen states, which are triggered by eighteen events. The event description is as follows: (1) operation arm 1 turns forward; (2) operation arm 2 turns forward; (3) robot goes online; (4) operation arm 1 turns backward; (5) operation arm 2 turns backward; (6) operation arm 2 extends; (7) the robot moves forward at a low speed; (8) the robot walking wheels collide with the press-connection-pipe; (9) operation arm 2 moves forward; (10) operation arm 1 turns forward; (11) operation manipulator 2 moves forward; (12) both arms move inward; (13) operation manipulator 1 fixes the bolt head; (14) operation manipulator 2 tightens the nut; (15) the nut has been tightened and the operation is completed; (16) the operation end exited; (17) and the robot returns to the initial state.

4.3. FSM Design for Damper Replacement Operation. According to the motion planning of the damper operation and manual experience operation, the FSM design of the robot during the replacement of the damper can be obtained as shown in Figure 10. The operation can be divided into nineteen states, which are triggered by nineteen events. The event description is as follows: (1) operation arm 1 turns forward; (2) operation arm 2 turns forward; (3) robot goes online; (3) operation arm 2 turns backward; (4) robot coarse positioning damper; (5) operation arm 1 extends; (6) operation arm 1 moves inward; (7) operation arm 2 extends; (8) operation arm 2 pitch; (9) bolt align; (10) align success; (11) align fail; (12) fix bolt head success; (13) fix bolt head fail; (14) arm 1 stretch; (15) arm 1 stretch inward; (16) manipulator 2 tightens the nut; (17) operation is completed; (18) operation end exited; and (19) the robot returns to the initial state.

4.4. Design of Object-Oriented Autonomous Operation Control System. Generally speaking, the robot operation process can be divided into two behaviors which are arm motion and

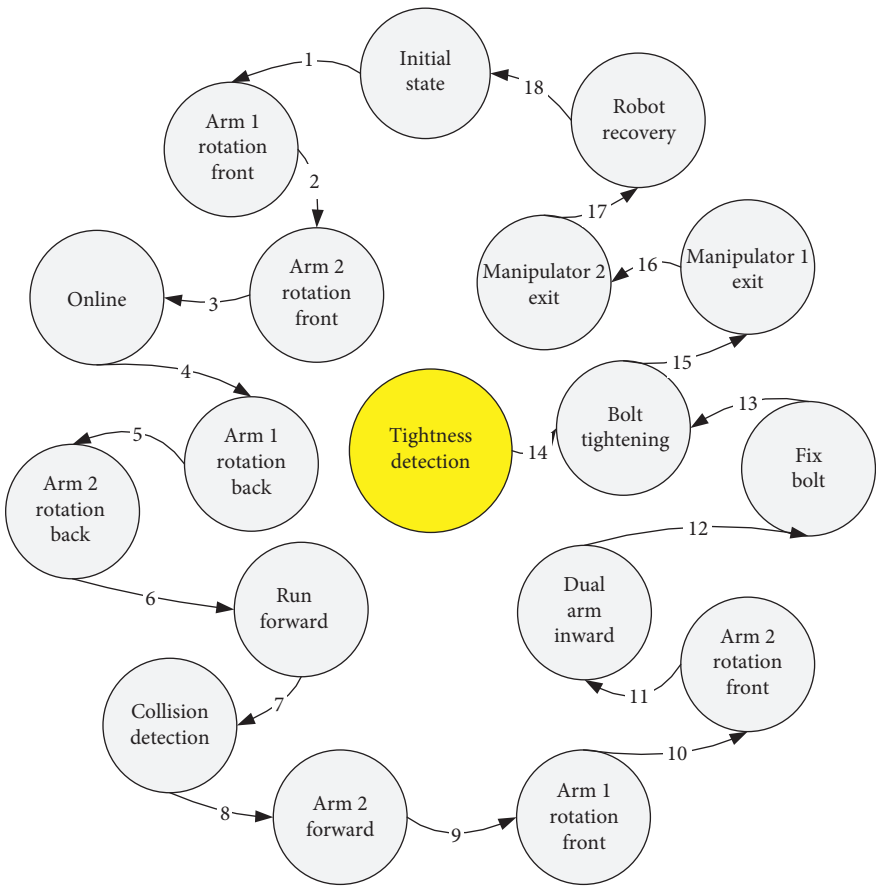

Figure 9: FSM design of drainage plate tightening operation.

end-effector motion. Each behavior includes detailed steps for executing each motor. The robot compiles the robot operation behavior plan according to the task type and stores it in the robot database. The robot autonomously selects the behavior plan to execute the action after detecting the operation object; that is, the robot behavior planning sequence is established as shown in Figure 11. The sequence includes the motor steps and parameters from the robot detection of the operation object to the end effector. The robot behavior planning sequence is the optimal motion plan set by the designer based on the robot experience value. During the robot autonomous operation, the behavior will be interrupted due to some uncontrollable factors such as the PC restart. Therefore, the robot is required to have the ability to self-recover behavior after the system restarts. The premise is that the robot can "memorize" the motor running value and the corresponding key sensor information in the motion sequence step executed before the failure after the industrial computer restarts; then the robot can use this to continue the motion plan at the breakpoint. Therefore, the state parameter sequence is added on the basis of the robot behavior motion planning sequence and stored in the robot database system to store the robot real-time status information, including the number of steps in the running action sequence, the execution status of this step, the hall sensor light potential information, count value of the motor executed in this step, and tilt sensor information. The step in the state parameter sequence corresponds to the steps in the robot action sequence. The status contains three states "not started," "end," and "in progress." The hall sensor records information about each actuator's collision or in position. The motor count value can record the motor's running mileage in the current step in real time. The inclination sensor information reflects the robot's posture state at this time, and its autonomous operation control can be realized through the interaction of sensor information carried by the robot itself.

After the robot restarts from the breakpoint, it first recognizes the step and status in the state parameter sequence and then combines the motor count value and sensor information value to complete the continuation of the action planning sequence. In the process of robot adaptive operation, the state information sequence can save the movement and environment information under the current behavior of the robot in real time and provide detection and decision-making functions for the robot's autonomous operation behavior. The flowchart of the robot autonomous operation principle is shown in Figure 12. The object-oriented design

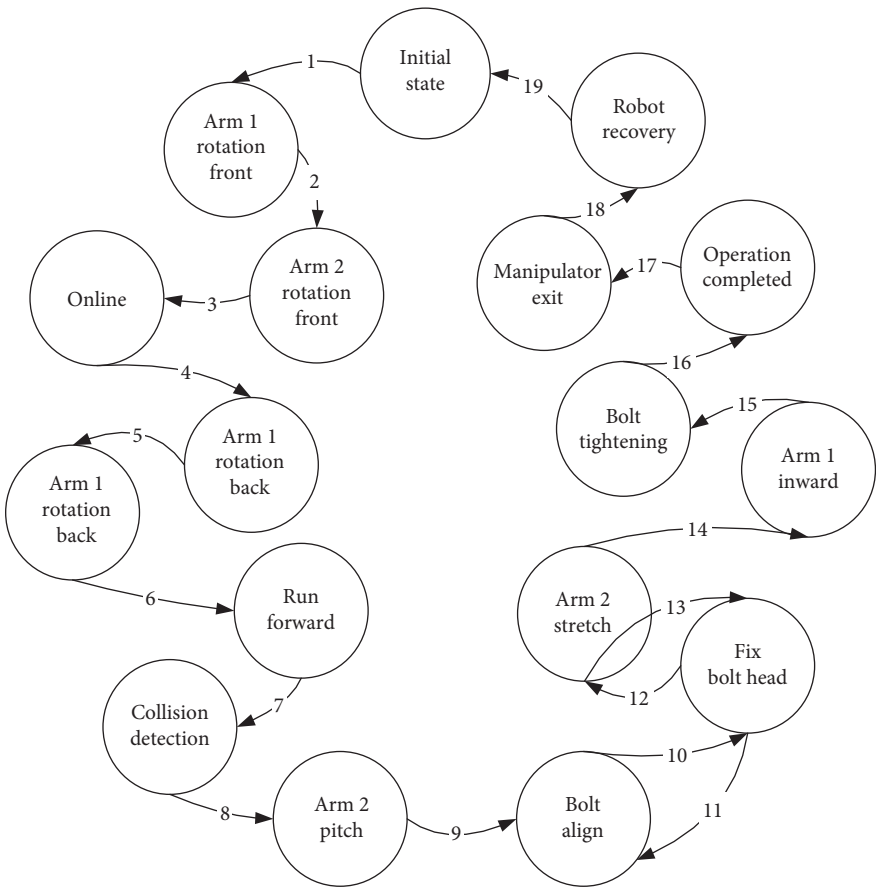

Figure 10: FSM design for damper replacement robot.

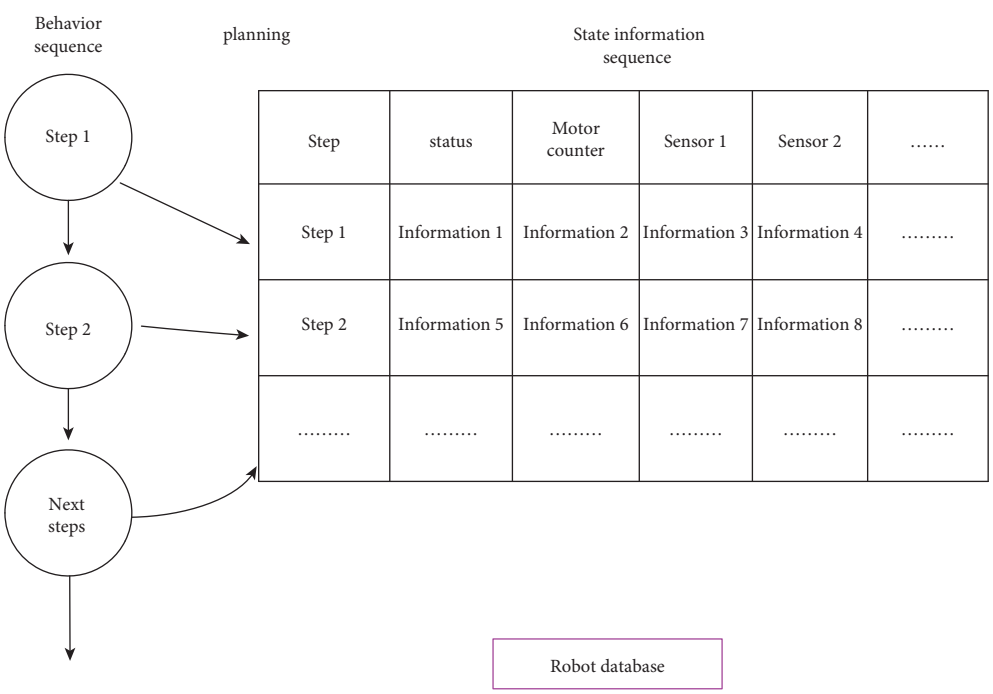

Figure 11: Robot status information sequence.

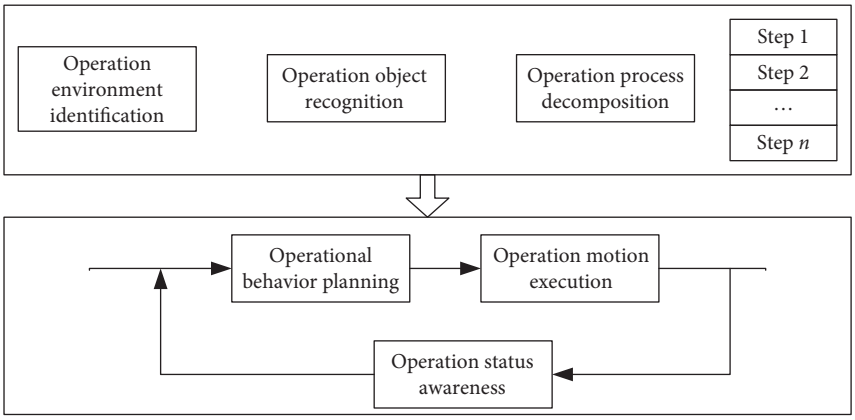

Figure 12: Schematic diagram of robot autonomous operation.

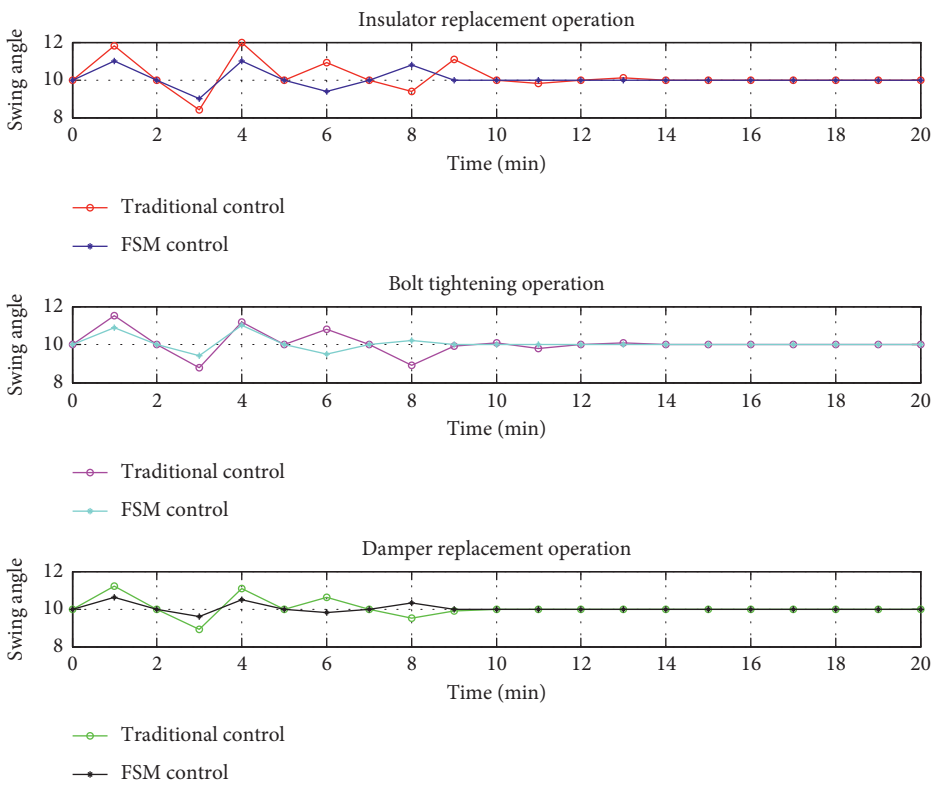

Figure 13: Robot performance under different methods.

method is used when designing the autonomous operation control system. Compared with the original process-oriented fixed program, the object-oriented design method converts the robot motor control into a natural language description of the robot motion. The realization process of the program is brief and clear. The robot operation steps can be described as the movement of each mechanism, so as to get rid of the attention of the underlying motor movement and the sensor configuration, avoiding the complicated and tedious process of process-oriented design methods. At the same time, the robot operation program design is clear, and the human-machine interaction is simple, which is conducive to the promotion and use of robots subsequent maintenance.

5. Experimental Research

5.1. Simulation Experiment. In order to verify the effectiveness of the robot FSM behavior control method, three different tasks have been used as the research objects. For each task, traditional manual tasks and the FSM autonomous behavior tasks proposed in this paper are used to control the robots. The sensor signal carried by itself monitors the working status of the robot in real time to evaluate the robot

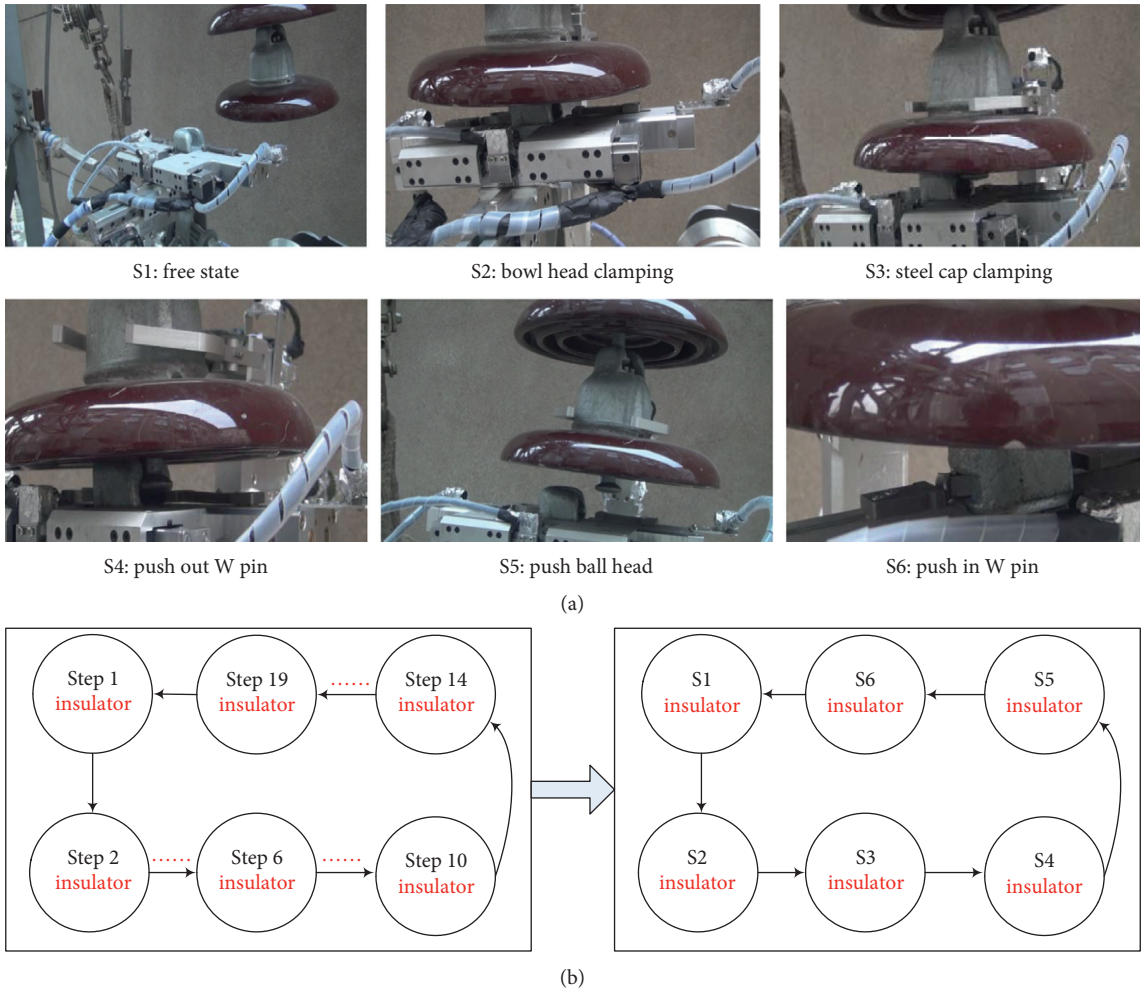

Figure 14: Field experiment of autonomous behavior control for insulator maintenance robot. (a) Insulator operation main process. (b) Insulator operation FSM optimization.

performance under different control methods. The obtained simulation results are shown in Figure 13. The horizontal axis of the three sets of graphs is time and the vertical axis is the robot swing angle. The inclination angle of the robot operation line is 10 degrees and three different operating experiments are performed twice.

Through the three sets of simulation results for insulator replacement, bolt tightening, and damper replacement, it can be seen that, based on the robot operation motion control under the FSM autonomous behavior control method, the system swing angle is smaller than the manual control method and the time for the robot to reach the equilibrium state is less than the manual method, especially in the process of damper replacement being more obvious. The main reason is that under the FSM autonomous behavior control method, robot motion planning has been further optimized. Some redundant motions in the operation process are eliminated. At the same time, the robot multijoint linkage control is integrated in some time periods. Therefore, the robot robustness motion and the robot operation efficiency have been significantly improved. Therefore, the simulation experiment verifies the effectiveness of the FSM-based robot autonomous behavior control method.

5.2. Field Operation Experiment. In order to verify the effectiveness of the robot autonomous behavior control method under different tasks, this paper developed a robot physical prototype system for insulators, drainage plates, and damper maintenance operations, under the jurisdiction of the State Grid Hunan Electric Power Transmission Maintenance Co., Ltd.; three types of operations tests were carried out on the live line. It can be seen from Figure 14 that in the process of insulator replacement using the autonomous behavior control method, the free state insulator-bowl head hanging plate, clamping-steel cap, W pin-pushing, ball head-pushing, a series of smooth states and behavior transition, and the robot insulator replacement operation can be successfully completed. Due to the intelligent behavior control, the actual operation steps of insulator replacement have reduced from nineteen steps of FSM theoretical model to six; according to the average value of the statistical experiment data, the robot operation

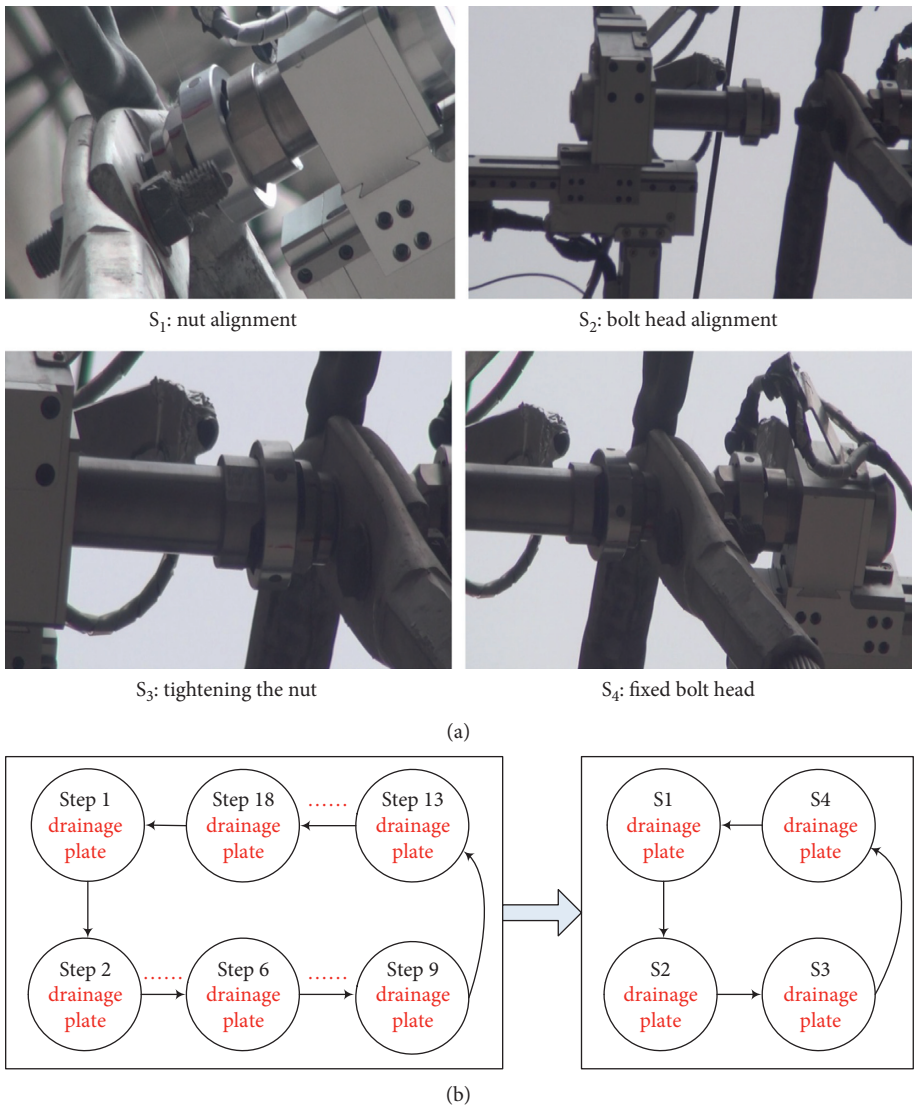

Figure 15: Field autonomous behavior control of drainage plate maintenance robot. (a) Drainage plate operation main process. (b) Drainage plate operation FSM optimization.

efficiency increased and the robot autonomous behavior ability and intelligence were significantly improved.

It can be seen from Figure 15 that, during the maintenance operation of the drainage plate, a series of state and behavior transitions smoothly from the robot nut alignment-bolt head alignment-nut-fixing bolt head, and the robot drainage plate fastening operation is successfully completed. Due to the intelligent behavior control, the actual operation steps of drainage plate tightening have reduced from eighteen steps of FSM theoretical model to four; taking the average statistical data, the robot operation efficiency has increased and the robot autonomous behavior especially the bolts autonomous capture and positioning on the drainage plate by the end sleeve of the manipulator is much more accurate.

It can be seen from Figure 16 that, in the process of replacement of the damper, a series of state and behavior transitions smoothly by bolt alignment-tightening the bolt-line clamp alignment-line clamp clamping, and the robot damper replacement operation is successfully completed. Due to the intelligent behavior control, the actual operation steps of damper replacement have reduced from nineteen steps of FSM theoretical model to four. Taking the average statistical data, according to the average of the statistical data, the robot operation efficiency has increased and the robot autonomous behavior, especially the holding mechanism of the old damper and the alignment and positioning control of the damper bolts, has been significantly improved.

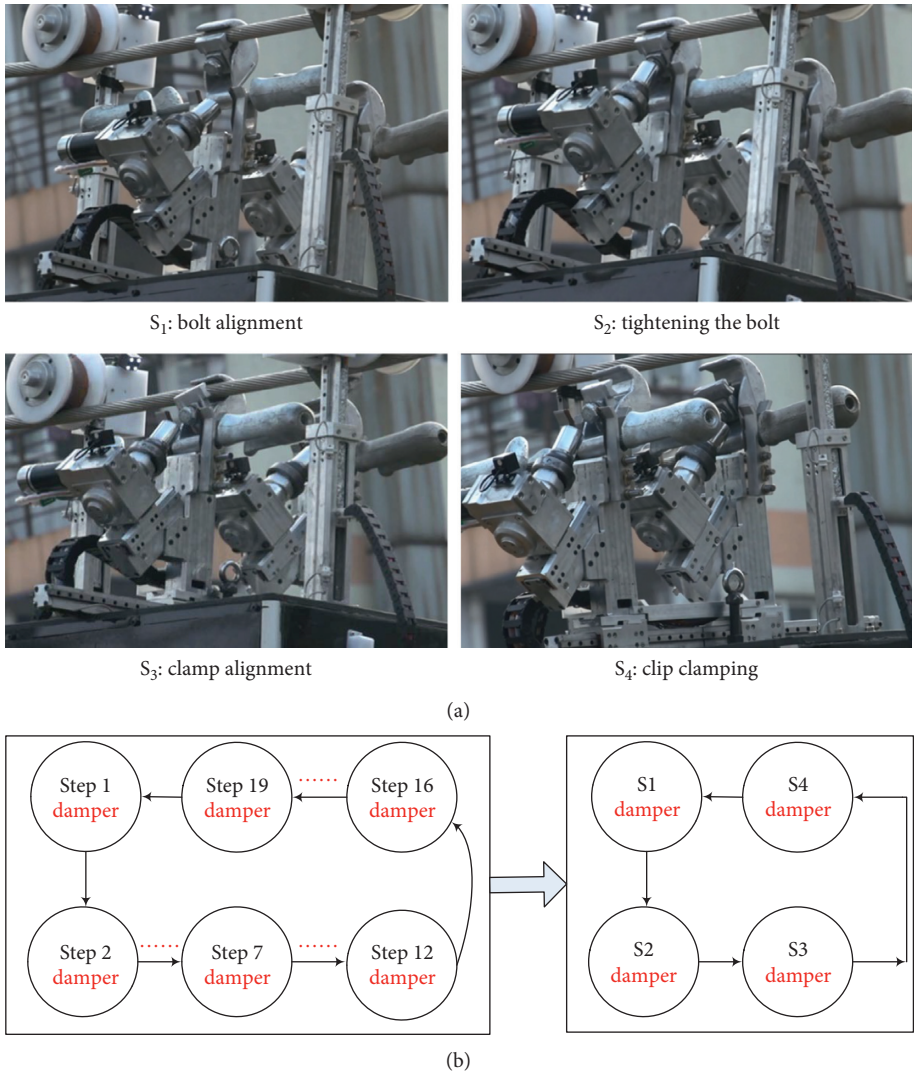

Figure 16: Field experiment of autonomous behavior control for damper replacement robot. (a) Damper operation main process. (b) Damper operation FSM optimization.

6. Conclusion and Future Work

6.1. Conclusion

(1) According to the maintenance requirements of transmission line insulators, drainage plates, and dampers, the basic configuration of the reconfigurable mobile robot at the end of the wheel-arm compound that travels along the transmission line has been designed, and the corresponding operation motion planation has been proposed and developed; it is suitable for the physical prototype of the robot of 220 kV live line.

(2) The robot operation motion behavior can be divided into three categories which are joint behavior, operation arm behavior, and robot behavior. The robot finite state machine model for three different tasks has been designed and a hierarchical architecture, finite state machine model of the robot autonomous behavior control method, has been proposed.

(3) Using the designed FSM model and the robot autonomous behavior control method, three operations have been performed on the 220 kV line with insulators, drainage plate tightening, and damper maintenance. The experimental results show that the autonomous behavior control method can effectively improve robot performance intelligence and operation efficiency.

6.2. Future Work. The live working robot and its high-voltage transmission line operation environment constitute a complex rigid-flexible coupling; in order to meet the basic needs of complex, changeable line environment and practical application, there are still much research that needs to be carried out, such as autonomous behavior control methods. The robustness of the line environment, structural parameters, internal and external disturbances, and uncertain factors still needs further research, the quantified processing method of disturbances and uncertain factors in

autonomous behavior motion control, the dynamic modeling of robots in a flexible operation environment, and its parameter identification methods. The breakthrough in these key technologies is the key to further improve the robot operation intelligence.

Data Availability

The experiment data used to support the findings of this study are included within the article.

Conflicts of Interest

The authors declare that there are no conflicts of interest regarding publishing this manuscript.

Acknowledgments

This work was supported by the 2020 Opening Fund for Hubei Key Laboratory of Digital Textile Equipment (DTL2020010) and 2020 Intelligent Live Working Technology and Equipment (Robot) Hunan Province Key Laboratory Opening Fund (2020KZD1001).

References

[1] X. Zheng, G. Wu, W. Jiang, F. Fan, and J. Zhu, "Rigid-flexible coupling dynamics with contact estimator for robot/PTL system," *Proceedings of the Institution of Mechanical Engineers, Part K: Journal of Multi-Body Dynamics*, vol. 234, no. 4, p. 635, 2020.

[2] N. Pouliot, P.-L. Richard, and S. Montambault, "LineScout technology opens the way to robotic inspection and maintenance of high-voltage power lines," *IEEE Power and Energy Technology Systems Journal*, vol. 2, no. 1, pp. 1–11, 2015.

[3] M. Wang, G. Wu, F. Fan, Q. Ji, W. He, and Q. Cao, "Dynamic network topology control of branch-trimming robot for transmission lines," *Electronics*, vol. 8, no. 5, p. 549, 2019.

[4] N. Pouliot, D. Mussard, and S. Montambault, "Localization and archiving of inspection data collected on power lines using LineScout technology," in *Proceedings of the Applied Robotics for the Power Industry (CARPI)*, pp. 197–202, Zurich, Switzerland, September 2012.

[5] K.-H. Seok and Y. S. Kim, "A state of the art of power transmission line maintenance robots," *Journal of Electrical Engineering and Technology*, vol. 11, no. 5, pp. 1412–1422, 2016.

[6] X. Ye, G. Wu, F. Fan, X. Peng, and K. Wang, "Overhead ground wire detection by fusion global and local features and supervised learning method for a cable inspection robot," *Sensor Review*, vol. 38, no. 3, pp. 376–386, 2018.

[7] A. B. Alhassan, X. Zhang, H. Shen, and H. Xu, "Power transmission line inspection robots: a review, trends and challenges for future research," *International Journal of Electrical Power & Energy Systems*, vol. 118, p. 105862, 2020.

[8] M. F. A. Jalal, K. S. M. Sahari, H. M. Fei, and J. C. T. Leong, "Design and development of three arms transmission line inspection robot," *Journal of Robotics, Networking and Artificial Life*, vol. 5, no. 3, pp. 157–160, 2018.

[9] H. Kalani, M. Malayjerdi, and M. Hasanpour Dehnavi, "H2M robot: a new prototype robot for insulation of high voltage transmission," *International Journal of Intelligent Robotics and Applications*, vol. 3, no. 1, pp. 87–98, 2019.

[10] W. Haitao, Y. Biwu, P. Ziheng et al., "Optimal design and stress analysis of the transmission line inspection robot along the ground line," *The Journal of Engineering*, vol. 2019, no. 16, pp. 3088–3091, 2019.

[11] C. M. Shruthi, A. P. Sudheer, and M. L. Joy, "Optimal crossing and control of mobile dual-arm robot through tension towers by using fuzzy and Newton barrier method," *Journal of the Brazilian Society of Mechanical Sciences and Engineering*, vol. 41, no. 6, pp. 245–270, 2019.

[12] A. B. Alhassan, X. Zhang, H. Shen et al., "Investigation of aerodynamic stability of a lightweight dual-arm power transmission line inspection robot under the influence of wind," *Mathematical Problems in Engineering*, vol. 2019, Article ID 2139462, , 2019.

[13] M. Z. Ayyildiz and K. Etinkaya, "Comparison of four different heuristic optimization algorithms for the inverse kinematics solution of a real 4-DOF serial robot manipulator," *Neural Computing & Applications*, vol. 27, no. 4, pp. 825–836, 2016.

[14] J. M. S. T. Motta, C. H. Llanos-Quintero, and R. C. Sampaio, "Inverse kinematics and model calibration optimization of a five-DOF robot for repairing the surface profiles of hydraulic turbine blades," *International Journal of Advanced Robotic Systems*, vol. 13, no. 114, 2016.

[15] C. Sun, W. He, and J. Hong, "Neural network control of a flexible robotic manipulator using the lumped spring-mass model," *IEEE Transactions on Systems, Man, and Cybernetics: Systems*, vol. 47, no. 8, pp. 1863–1874, 2017.

[16] K. Wang, M. Luo, T. Mei, X. Lin, and Y. Cao, "Posture error correction of a six-DOF serial manipulator based on genetic algorithms," *Lecture Notes in Electrical Engineering*, vol. 226, no. 5, pp. 203–211, 2013.

[17] M. Moness and A. M. Moustafa, "Tuning a digital multivariable controller for a lab-scale helicopter system via simulated annealing and evolutionary algorithms," *Transactions of the Institute of Measurement and Control*, vol. 37, no. 10, pp. 1254–1273, 2015.

[18] X. Wu, J. Lin, K. Zhang, and M. Cheng, "Optimal impulsive control for advertising strategy problems based on a gradient-based PSO algorithm," *Transactions of the Institute of Measurement and Control*, vol. 41, no. 8, pp. 2280–2292, 2019.

[19] H. J. Li, W. Jiang, Y. D. Yan, and W. Chen, "Robust motion control for multi-split transmission line four-wheel driven mobile operation robot in extreme power environment," *Industrial Robot: The International Journal of Robotics Research and Application*, vol. 47, no. 2, pp. 219–229, 2020.

[20] H. J. Zhang, W. Jiang, and A. Y. Zhang, "Operation motion planning and principle prototype design of four-wheel-driven mobile robot for high-voltage double-split transmission lines," *Mathematical Problems in Engineering*, vol. 2020, no. 2, 17 pages, Article ID 6195320, 2020.

[21] Z.-b. Zuo and R. Yi, "Obstacle-navigation control of inspection robot for power transmission lines based on knowledge base," *Computer Engineering and Applications*, vol. 44, no. 3, pp. 236–239, 2008.

[22] E. J. Lima, M. H. S. Bomfim, and M. A. d. M. Mourão, "POLIBOT-Power lines inspection RoBOT," *Industrial Robot: An International Journal*, vol. 45, no. 1, pp. 98–109, 2018.

[23] W.-bin Guo, H.-g. Wang, Y. Jiang et al., "Obstacle navigation planning for a power transmission line inspection robotJ," *Robot*, vol. 34, no. 4, pp. 505–512, 2012.

[24] G. Tao and L. Fang, "A multi-unit serial inspection robot for power transmission lines," *Industrial Robot: The International Journal of Robotics Research and Application*, vol. 46, no. 2, pp. 223–234, 2019.

[25] S. Yi-feng, H.-g. Wang, Li Zhen-hui et al., "Vision based transmission line broken strand detection and robot behavior planning," *Robot*, vol. 37, no. 2, pp. 204–211, 2015.
[26] Y. Jiang, H.-g. Wang, and F. Li-jin, "Gait control of micro wall-climbing robot based on initiative exploration," *Journal of Mechanical Engineering*, vol. 45, no. 07, pp. 56–62, 2009.
[27] W. Wang, G.-p. Wu, Y.-c. Bai et al., "Hand-eye-vision based control for an inspection robot's autonomous line grasping," *Journal of Central South University*, vol. 21, no. 6, pp. 2216–2227, 2014.
[28] W. Wang, Y. Bai, G. Wu et al., "An electromagnetic navigation method for line-following robot based on information fusionJ," *Automation of Electric Power Systems*, vol. 37, no. 16, pp. 73–79, 2013.
[29] Y. Yan, W. Jiang, A. Zhang et al., "Research on configuration design and operation effect evaluation for ultra high voltage (UHV) vertical insulator cleaning robot," *Industrial Robot: The International Journal of Robotics Research and Application*, vol. 47, no. 1, pp. 90–101, 2019.
[30] W. Jiang, A. Zhang, G. Wu et al., "Manipulator visual localization motion control for power cable mobile robot in dynamic-unstructured environment," *Industrial Robot: The International Journal of Robotics Research and Application*, vol. 46, no. 1, pp. 93–103, 2019.
[31] W. Jiang, G. Wu, F. Fan et al., "Structure singular value theory based robust motion control of live maintenance robot with reconfigurable terminal function for high voltage transmission line," *International Journal of Advanced Robotic Systems*, vol. 15, no. 2, pp. 1–13, 2018.

Hindawi
Complexity
Volume 2020, Article ID 5013871, 29 pages
https://doi.org/10.1155/2020/5013871

Research Article

Data-Driven Bearing Fault Diagnosis of Microgrid Network Power Device Based on a Stacked Denoising Autoencoder in Deep Learning and Clustering by Fast Search without Data Labels

Fan Xu,[1,2] **Xin Shu**,[3,4] **Xin Li**,[5] **and Xiaodi Zhang**[6]

[1]*School of Automation, China University of Geosciences, Wuhan 730072, China*
[2]*School of Data Science, City University of Hong Kong, Tat Chee Avenue, Kowloon 990777, Hong Kong, China*
[3]*China Railway Major Bridge Engineering Group Co., Ltd., Wuhan 730072, China*
[4]*State Key Laboratory for Health and Safety of Bridge Structures, Wuhan 730072, China*
[5]*School of Energy and Power Engineering, Wuhan University of Technology, Wuhan 730072, China*
[6]*State Grid Beijing Electric Power Company, Beijing 100080, China*

Correspondence should be addressed to Fan Xu; fanxu8@cityu.edu.hk

Received 18 May 2020; Revised 6 September 2020; Accepted 5 October 2020; Published 2 November 2020

Academic Editor: Atila Bueno

The traditional health indicator (HI) construction method of electric equipment devices in microgrid networks, such as bearings that require different time-frequency domain indicators, needs several models to combine. Therefore, it is necessary to manually select appropriate and sensitive models, such as time-frequency domain indicators and multimodel fusion, to build HIs in multiple steps, which is more complicated because sensitivity characteristics and suitable models are more representatives of bearing degradation trends. In this paper, we use the stacked denoising autoencoder (SDAE) model in deep learning to construct HI directly from the microgrid power equipment of raw signals in bearings. With this model, the HI can be constructed without multiple model combinations or the need for manual experience in selecting the sensitive indicators. The SDAE can extract the representative degradation information adaptively from the original data through several nonlinear hidden layers automatically and approximate complicated nonlinear functions with a small reconstruction error. After the SDAE extracts the preliminary HI, a model is needed to divide the wear state of the HI constructed by the SDAE. A cluster model is commonly used for this, and unlike most clustering methods such as k-means, k-medoids, and fuzzy c-means (FCM), in which the clustering center point must be preset, cluster by fast search (CFS) can automatically find available cluster center points automatically according to the distance and local density between each point and its clustering center point. Thus, the selected cluster center points are used to divide the wear state of the bearing. The root mean square (RMS), kurtosis, Shannon entropy (SHE), approximate entropy (AE), permutation entropy (PE), and principal component analysis (PCA) are also used to construct the HI. Finally, the results show that the performance of the method (SDAE-CFS) presented is superior to other combination HI models, such as EEMD-SVD-FCM/k-means/k-medoids, stacked autoencoder-CFS (SAE-CFS), RMS, kurtosis, SHE, AE, PE, and PCA.

1. Introduction

The microgrid power equipment (bearings) is a very commonly used mechanical device in the industrial field, but it wears down easily. Its status and reliable operation are of great significance in ensuring power system safety and reducing equipment operating costs. As bearing running time increases, performance will gradually degrade. The quality of bearings also affects the operation of adjacent entire power system [1]. An indicator is commonly used to assess the health status of the bearing, which can provide a sound foundation for bearing performance degradation assessment (PDA) [2]. The signals are often used as an indicator to monitor the status because the quality of the bearing vibration signal can indicate bearing health in the PDA [3, 4]. Many models, including various statistical parameters and

mechanical signal-processing methods, are often used to extract useful degradation features for constructing bearing health indicators. Root mean square (RMS) and kurtosis are the most commonly used time-domain statistical parameters and can be considered for monitoring the health status of bearings by using a vibration signal. Williams et al. used RMS and kurtosis and demonstrated that they could effectively reflect and extract the bearing fault features [5]. Tse and Wang developed a method based on RMS to construct a health indicator for bearing PDA models, after the original vibration signal has been filtered from a ranged frequency band [6]. In [6], RMS is used to track the degradation status at the point when the vibration energy has changed. Shen et al. used multiple time indicators, including the RMS, to extract the useful degradation characteristics of bearings. They used a multivariable support vector machine to predict the remaining useful life of microgrid power equipment (bearings) [7]. Lei et al. also considered RMS for extracting the degradation trend to evaluate the degradation status of bearings. They demonstrated that the RMS could provide useful status information in the degradation stage, but not under normal conditions [8]. In [9], RMS and kurtosis were used to monitor bearings with a low filter, to filter out the useless frequency band and retain the useful band, according to the bearing working frequency. Lei et al. used multidimensional time-frequency, including RMS and kurtosis, for bearing fault feature extraction and fault diagnosis [10]. Other statistical indicators such as entropy models, including Shannon entropy (SHE), approximate entropy (AE), and permutation entropy (PE), are useful ways to assess the gradation trend of a mechanical device. AE can represent the regularity of multidimensional time series and contains more time-related information by using a coarse-graining operation for a time series [11, 12]. Yan et al. presented a health indicator for bearing PDA based on AE. As the working condition of the bearing deteriorates, the degree of wear increases and the number of frequency components contained in the vibration signal will increase, eventually causing its regularity to decrease and its corresponding AE value to increase. A detailed analysis of the impact of parameters on the AE model is described in this study [13]. The computational efficiency of PE is higher than that of AE as it only uses the order of the values and it is robust under a nonlinear distortion of the signal [14]. Yan et al. used PE as a health indicator to track the degradation of bearings, as it can describe the complexity of a vibration signal measured in a physical system by using phase-space reconstruction and takes into account the nonlinear behavior of the vibration signal [15]. Many traditional mechanical signal-processing models, such as wavelet transfer, EMD [16], and ensemble empirical mode decomposition (EEMD) [17], are often used to construct health indicators for the bearing PDA model. Qiu et al. used wavelet transfer to filter the noise, which could mask the bearing vibration signal, and then SHE was used to optimize the Morlet wavelet shape to extract the weak fault feature [18]. Lou et al. used the wavelet and fuzzy inference to extract useful fault features for bearing fault diagnosis [19]. Compared with wavelet transfer, EMD can decompose the original vibration signal into intrinsic mode functions (IMFs) adaptively without wavelet bias function selection and decomposition level choices. Wang et al. [20] used the EMD to decompose the vibration signal into IMFs and then applied singular value decomposition (SVD) to calculate the singular values of the IMFs. After these two steps, the Mahalanobis distance was used to construct a health indicator for bearing PDA. Rai et al. [21] considered the EEMD for decomposing the bearing vibration signal into IMFs and then SVD was used to calculate the singular values (SVs). Finally, k-medoids were used to find the available cluster center points, which can reflect the bearing degradation status by using a health indicator, known as the confidence value (CV), to build the bearing PDA model.

These have achieved significant success in health indicator construction and are used for bearing PDA. However, there are some problems with these PDA models.

(1) Time-frequency domain indicators are commonly used methods and must select sensitive indicators to show the difference between different faults and to improve the accuracy of fault classification. Wei et al., for example, considered the self-weight to evaluate and judge the quality of the time-frequency domain indicators for fault diagnosis [22]. The optimized indicators can then be used to diagnose faults and to improve the identification accuracy. Tse et al. selected commonly used sensitivity time-frequency indicators to extract the oil sand pump degradation trend with principal component analysis (PCA) [23]. Thus, manual experience can be applied in filtering the sensitivity indexes selected, ensuring they can achieve and improve the performance of fault diagnosis and the PDA of a device in a complex mechanical system.

(2) The operating environment of complex mechanical systems is variable, and the commonly used time-frequency domain indicators will exhibit different advantages and disadvantages depending on the operating conditions. Therefore, relying on manual experience to select sensitive features applicable to complex and varied mechanical equipment operating environments is difficult.

(3) In addition, commonly used models should be combined to extract useful degradation information from the raw vibration, such as EEMD combined with SVD and a clustering model to construct the health indicator for evaluating the PDA of bearings. Thus, these combined models to some extent lack versatility.

Therefore, these fusion time-frequency indicators and combined models are complicated and are reliant on manual experience.

To overcome these drawbacks, in this study, the stacked denoising autoencoder (SDAE) [24, 25] from deep learning is used to extract the initial degradation level for bearing PDA directly from the raw vibration signal, without selecting various indicators and model combinations. The deep architectures of the SDAE enable it to extract the

representative information adaptively from the original data through several nonlinear hidden layers and approximate complicated nonlinear functions, with a small reconstruction error and without manual experience and data labels [26]. Thus, there is no need for manual experience or prior knowledge of the SDAE. The bearing degradation trend can be extracted by using encoder and decoder processes and reconstructing the input through several hidden layers. The SDAE is an unsupervised model, which is robust when there is noise in the original vibration signal. It is an improved model based on a stacked autoencoder (SAE), which is a basic deep learning model that is widely used in different domains, such as fault feature extraction and fault diagnosis.

Feng et al. [26] used the SAE to extract the bearing fault information from the frequency-domain signal directly after fast Fourier transform (FFT) without time-frequency indicator selection. Lv et al. used a weighted time series fault diagnosis method based on the SAE. The proposed model in this study not only captures the high-order correlations among monitoring variables but also uses the time correlations among samples [29]. To further explore more representative fault characteristics using the SAE network, Qi et al. combined EEMD and the autoregressive (AR) model to preprocess the collected nonstationary vibration signals and obtain AR parameters based on intrinsic extraction. The decomposed mode function components are selected as an input feature of the SAE network [27, 28].

The vibration data gathered from these various engineering devices contain noise, and the empty and destroyed data collected will make the analysis difficult. The SDAE is robust because it destroys the original data into zero according to the denoising probability and reconstructs the input data by using encoding and decoding. This denoising operation improves the SAE so that it can learn a more robust representation. Therefore, the SDAE is more robust and stable than the SAE. Xu et al. used the SDAE to train the bearing vibration signal after a fast Fourier transform (FFT) and extracted useful fault features under various conditions. The SDAE was found to reduce the feature dimension to 2 directly without PCA. The clustering model was then used for bearing fault diagnosis [29]. The authors also demonstrated that the SDAE is more robust than the SAE. Additionally, the SDAE has been used successfully in other domains, including multimodal video classification, physiological signal processing, and 3-D object identification [30–34]. However, few studies have focused on the PDA of bearings when using the SDAE, and most instead consider *r* bearing fault diagnosis. The SDAE has had many successful applications, so it is used in this study to extract the initial degradation trend for bearings directly from the original vibration signal.

After the SDAE has extracted the degradation trend to construct a health status without a data label, the clustering model is a common method of building a health indicator for bearing PDA and for determining the degradation status by calculating the distance between each sample point and its cluster center point. Pan et al. proposed a model based on wavelet transfer and fuzzy c-means (FCM) for bearing PDA [31] and developed a method based on EEMD, SVD, and k-medoids clustering models to construct a health indicator for bearing PDA. They demonstrated that the proposed model was better than other models such as EEMD-SVD-k-means [21], RMS, and kurtosis. However, clustering models such as FCM, k-means, and k-medoids require cluster number selection before calculation. Typically, the three degradation statuses of Normal, Slight, and Severe are suitable for bearing degradation division. These clustering models have successfully been used in the PDA of bearings.

However, these clustering models need to preset the number of clusters. Several states may sometimes exceed these predefined three statuses. Manually selecting the number of degraded trend states by using and selecting the number of cluster center points will lead to erroneous judgments. For example, a bearing may have only two degradation stages such as Normal and Severe at one time, and not the three statuses. This preset three-degradation status method cannot adaptively meet the requirements of dynamic changes in different situations of data acquisition under complex project operating conditions.

To solve this problem, in this paper, we use a clustering by fast search (CFS) model for bearing PDA. CFS can find the available cluster center number automatically according to the local density and the distance between any two samples [34]. CFS has been successfully used in other domains. To solve most current clustering techniques, only static data can be processed into clusters. Zhang et al. proposed a CFS model based on the peak of k-medoids to integrate the current model into the previous model to achieve final clustering and applied it to industrial dynamic acquisition data analysis. Effectively analyzing these data can help improve industrial services and ensure the system has no possibility of symptomatic failure [35]. Xu et al. used the EEMD with base-scale entropy to extract the useful fault information of bearings under different conditions. The base-scale entropy-based feature vector is then used as the input of CFS for fault diagnosis. CFS has been successfully applied in various areas, but few studies report that CFS has been used for the PDA of bearings [36]. Thus, in this study, CFS is used to find the available cluster center point and then construct a health indicator, as in [21], to evaluate the degradation status.

As mentioned above, an unsupervised method based on the SDAE and CFS is proposed to construct a health indicator for bearing PDA without data labels or prior knowledge.

The contribution of this paper is as follows:

(1) The SDAE extracts the bearing degradation from the original vibration signal directly without manual intervention, as is often used to select sensitive time-frequency indicator and combine several available models to construct HI. The SDAE and CFS are used in this paper with bearing PDA because another research has investigated bearing PDA using the SDAE and AP.

(2) To demonstrate that the model proposed is better than other combined models, including EEMD-SVD-FCM/k-means/k-medoids, SAE-CFS, PCA,

RMS, kurtosis, SHE, AE, and PE, a detailed comparative analysis is provided.

The rest of this paper is organized as follows. The basic theories of the SDAE and CFS are given in Section 2. Section 3 describes the procedures of the method proposed, the experiment comparison analysis is given in Section 4, and Section 5 concludes the paper.

2. Basic Theories of the SDAE and CFS

2.1. Basic Theory of the SDAE. In this section, the basic unit in the SDAE, DAE, which is based on AE, is used. Then, the basic structure of the SDAE is then described, which is stacked from DAE.

2.1.1. Autoencoder (AE). The main idea of AE [25] is to build constant functions between input X and output Z and to achieve dimensionality reduction and preserve data feature information. It can be divided into two parts: encoder and decoder.

(1) Encoder. Figure 1 illustrates how encoding is the process of implementing an input dataset X mapped into a low-dimensional space by an activation function. The encoder performs a mapping conversion from the input vector $X = \{x_1, x_2, \ldots, x_n\}$ to the output representation $Y = \{y_1, y_2, \ldots, y_n\}$ by using an active function. n is the total number of samples. The calculation expression is as follows:

$$Y = f_\delta(X) = s(Wx + b), \tag{1}$$

where f_δ and s are the sigmoid activation functions, where $f_\delta(X) = 1/1 + e^{-X}$, and $f_\delta(X)$ is the abbreviation of $s(Wx + b)$ for input X. W is the weight vector in the neural network between the former and latter layers, and b denotes the bias item.

(2) Decoder. Decoding is the procedure of mapping Y from a high-dimensional space into a high low-dimensional space $Z = \{z_1, z_2, \ldots, z_n\}$ and reconstructing the input sample X into Z. The calculation is as follows:

$$Z = g_\delta(Y) = s(Wy + b), \tag{2}$$

where g_δ and s are the sigmoid activation functions, where $g_\delta(Y) = 1/1 + e^{-y}$. $g_\delta(Y)$ is the abbreviation of $s(Wy + b)$. Therefore, the reconstructed error (lost function) between Z and X is defined as

$$J(X, Z) = \frac{1}{n}\|Z - X\|^2. \tag{3}$$

The backpropagation algorithm is used to adjust the weight vector W and bias item b and train the autoencoder network to reduce the reconstructed error. Hence, the restrictive error $J(X, Z)$ is converged and minimized until it meets the termination condition, i.e., it exceeds the maximum iteration.

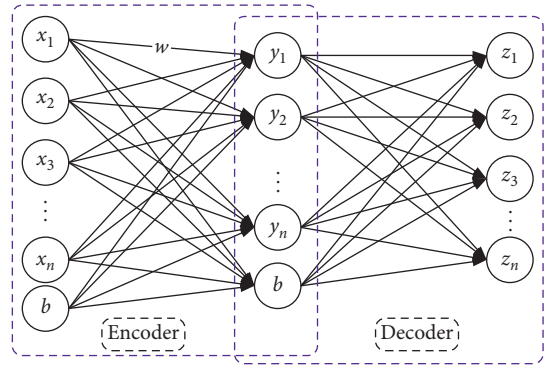

Figure 1: Structure of AE.

2.1.2. Denoising Autoencoder (DAE). The data collected in actual engineering often contain noise, and hence the characteristics obtained by the autoencoder will cause errors owing to the presence of noise. The denoising autoencoder (DAE) [37] solves this problem by destroying the noise-containing data into zero according to the denoising probability P and reconstructing the destroyed input X_1 into output Z by using the encoder and decoder in AE. The basic structure of DAE is shown in Figure 2.

The black round node in Figure 2 is the damaged data point in X_1, and P denotes the denoising probability. Some parts of the input data X are therefore set as zero and then X is changed to dataset X_1. f and g denote the sigmoid activation functions in formulas (1) and (2). The following calculation steps are the same as for AE when an encoder and a decoder are used to reconstruct the output Z into the original input data X.

2.1.3. Stacked Denoising Autoencoder (SDAE). The SDAE contains three layers: (1) an input layer; (2) several hidden layers; and (3) an output layer. It uses several hidden layers, which are stacked from several DAE units, to extract the useful information. Therefore, the output Z from the previous DAE hidden layer is regarded as the input of the next DAE hidden layer. The connection weight matrix W and bias vector b are then iteratively updated during the pretraining period. After the training has been completed, the entire network is fine-tuned, and after the above steps, the SDAE is formed. The basic structure of the SDAE is shown in Figure 3. Here, N is the number of DAE hidden layers in the SDAE.

2.2. Basic Theory of CFS. The CFS clustering algorithm is mainly based on the characterization of the cluster center.

(a) The cluster center point itself has a high density and is surrounded by data points whose densities are not more than those of its own neighbors.

(b) The distance between the cluster center point and other data points in another cluster is better.

The detailed computational procedures of CFS clustering are given in [32], and its calculation process is as follows:

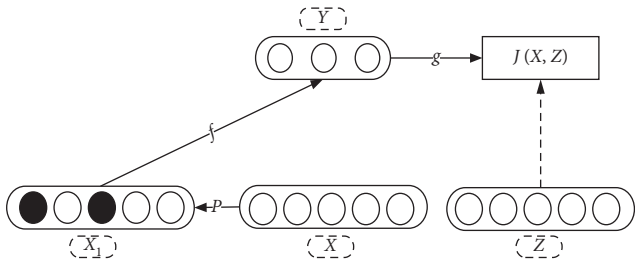

Figure 2: Basic structure of DAE.

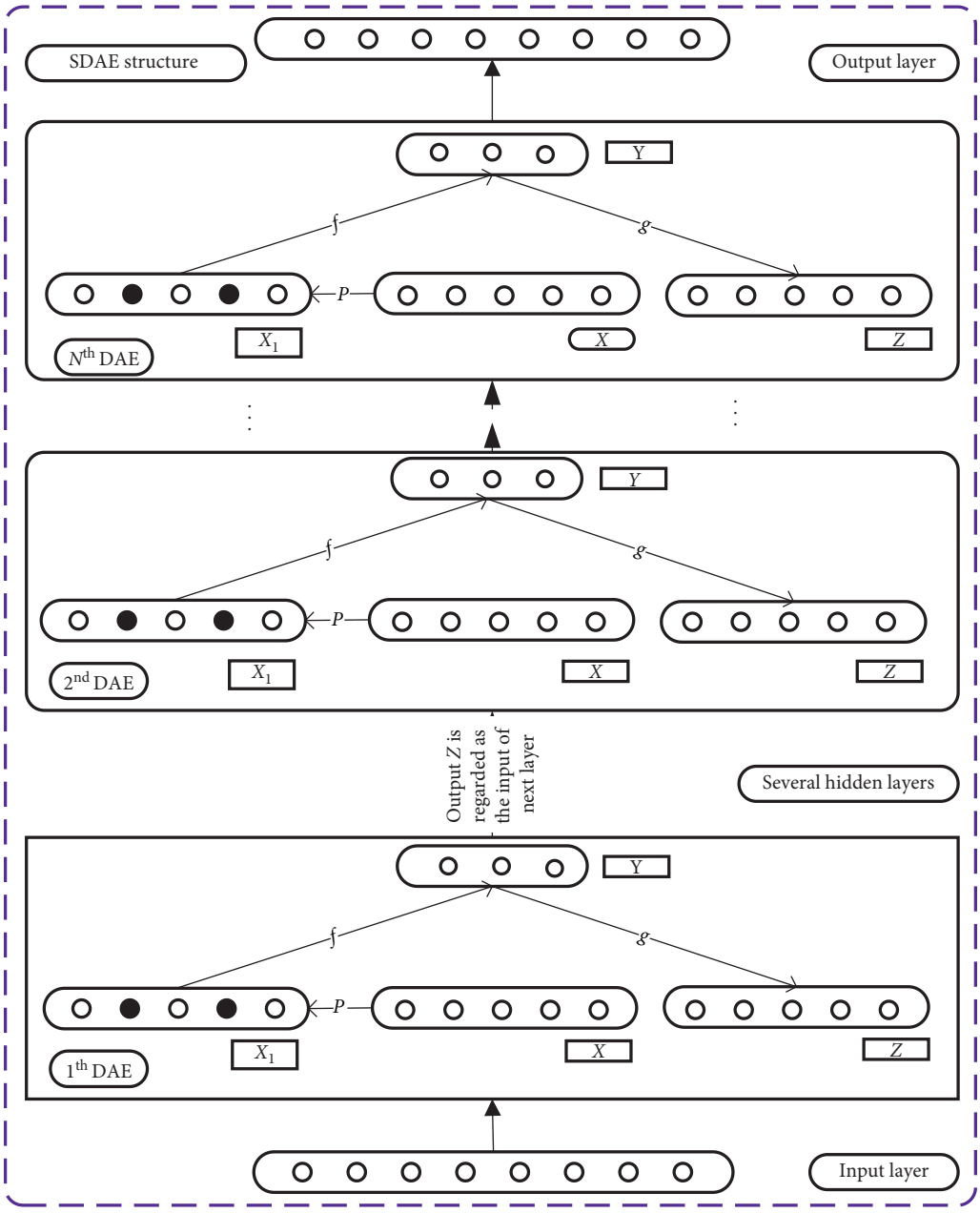

Figure 3: Basic structure of the SDAE.

(1) For a given dataset $X = \{x_1, x_2, \ldots, x_n\}$
The distance between any two points x_i and x_j can be calculated by

$$d_{ij} = \mathrm{dist}\left(x_i, x_j\right). \tag{4}$$

(2) The local density ρ_i for a data point x_i is calculated by

$$\rho_i = \sum_{j=1}^{N} e^{-\left(d_{ij}/d_c\right)^2}, \tag{5}$$

where ρ_i denotes the total number of distances that are less than the cutoff distance d_c between the data point x_i and other points and N is the total number of samples.

(3) Calculate the distance δ_i, assuming that the $\{q_i\}_{i=1}^{N}$ is the descending order of $\{\rho_i\}_{i=1}^{N}$, where $\{\rho_i\}_{i=1}^{N}$ meets the condition: $\rho_{q1} \geq \rho_{q2} \geq \cdots \geq \rho_{qN}$, and hence δ_i can be defined as

$$\delta_{q_i} = \begin{cases} \min\limits_{j<i}\left\{d_{q_i q_j}\right\}, & i \geq 2, \\ \max\limits_{j\geq 2}\left\{\delta_{q_j}\right\}, & i = 1, \end{cases} \tag{6}$$

where δ_i indicates the greatest distance between any one point and point x_i when x_i has the greatest local density. Otherwise, δ_i is the smallest distance between any one point and point x_i when x_i has the smallest local density.

(4) Compute γ according to the following equation:

$$\gamma_i = \rho_i * \delta_i. \tag{7}$$

(5) Use γ to determine the potential clustering center point when γ is in descending order. The authors suggest that the greater the γ_i, the greater the possibility of point x being a cluster center point. The stepped data points with the greater γ values are sequentially selected as the cluster center points, that is, the γ value shows a significant jump when the cluster center point transitions to the noncluster center point. These points with skipping are thus selected as cluster center points, according to this characteristic. Finally, the number of distances between each data point and the cluster center is less than the number of cutoff distances required to achieve classification.

3. Procedure of the Presented Model

The procedure of the method comprises four steps: (1) data preprocessing; (2) preliminary degradation trend generation; (3) degradation trend dimension reduction; and (4) bearing degradation assessment and confrontation analysis. The details of these steps are as follows.

(1) Data preprocessing: to extract the useful bearing degradation trend and preprocess the data more easily, the absolute amplitude values of all original vibration signals are regarded as the input of the SAE and SDAE for training, after standardizing into [0, 1].

(2) Preliminary degradation trend generation: for the SAE and SDAE, there are nine hidden layers from which the useful initial degradation trend of the bearing can be extracted. The dimension of the extracted bearing degradation trend by each hidden layer, except the last, is not 2. To demonstrate that the SDAE is more robust and stable than the SAE, PCA is used to reduce the dimension of the extracted degradation for the first eight hidden layers. After EEMD is decomposed using the original vibration signal, SVD is used to calculate the SVs to identify the degradation trend. In addition, to show that the model presented is superior to others, RMS, kurtosis, SHE, AE, PE, and PCA are also used for extraction of the degradation feature.

(3) Degradation trend dimension reduction: for data visualization, the number of neural nodes at the last hidden layer in the SAE and SDAE is set directly to 2. For EEMD, the two IMF components are selected according to the two largest correlation coefficients, which are calculated from each IMF and the original vibration signal. The greater the correlation coefficient value, the greater the amount of useful vibration information it contains. Then, SVD is used to compute the SVs for dimension reduction. For PCA, the first two principal components (PCs) are selected as the extracted features.

(4) Bearing degradation severity assessment and confrontation analysis:

(a) Bearing degradation severity assessment: the two-dimensional degradation features extracted using the SAE and SDAE are selected as the input of CFS to find the available cluster center point. The health indicator, or confidence value (CV), is then used to build a PDA model. The details of the CV calculation are as follows:

$$\mathrm{CV} = \exp\left(\frac{-\mathrm{DI}}{c}\right), \tag{8}$$

where DI is the Euclidean distance, which is often used to compute the distance between each point A (x_1, y_1) and its cluster center point B (x_2, y_2). DI is then calculated by

$$\mathrm{DI} = \sqrt{\left(x_1 - x_2\right)^2 + \left(y_1 - y_2\right)^2}. \tag{9}$$

The main purpose of DI is to transfer all of the CVs to [0, 1] by using one cluster center point. c denotes the scale factor. The CV is close to 1 when the "Normal" clustering center point is used, which indicates that

the sample belongs to "Normal" [21]. For the ease of the comparison analysis, all CVs are normalized to [0, 1], and then the CV degradation trend curve is smoothed by using a smoothing function through the four-time window.

(b) Confrontation analysis: the method proposed is demonstrated to be superior to other models such as the SAE-CFS, EEMD-SVD-FCM/k-means/k-medoids in [21], PCA, RMS, kurtosis, SHE, AE, and PE, through the detailed analysis given in the following section. The SVs in SVD obtained from EEMD and SVD are regarded as the input of FCM, k-means, and k-medoids to find the available cluster center points. Then, the CVs are calculated according to equation (8).

Through the above steps, all CVs are obtained from the proposed method, SAE-CFS, EEMD-SVD-FCM, k-means, and k-medoids. The steps of the method are shown in Figure 4.

4. PDA Building and Comparison Analysis

In this section, the experimental data and the data collected platform are first introduced, and in the following step, the SAE and SDAE are used to extract the degradation; hence, the last step is the smoothness comparison. The extracted features are then used to find the clustering center points with CFS. Finally, a comparison analysis is given.

4.1. Original Vibration Signals. The experimental data acquisition platform is shown in Figure 5. The operating conditions of the bearing depend on the instantaneous measurement of the radial force exerted on the bearing, the rotation speed of the shaft that manipulates the bearing, and the magnitude of the torque exerted on the bearing. The bearing degradation feature is based on two sensors, vibration and temperature. The vibration sensor consists of two micro accelerometers that are perpendicular to each other. The first is in the vertical position, and the other is in the horizontal position. In addition, the vibration sensor is fixed on the outer ring of the bearing. The data sampling frequency is 25.6kHz. The temperature sensor is not described in detail here. The vibration data in the horizontal position are used in the experiment.

For more information on the experimental platform, refer to the literature [38].

The experimental dataset is an accelerated degradation test of the bearing under various operating conditions to obtain the measured data in the bearing life cycle for fault detection and prediction of the bearing's remaining life [38]. The three load conditions are 4000 N, 4200 N, and 5000 N. The corresponding speeds are approximately 1800 rpm, 1650 rpm, and 1500 rpm. The experimental device samples the data every 0.1 seconds. The data length of each sample is 2560. The details of the experimental data for bearing 1 are given in Table 1. The original vibration time-wave for bearings 11–15 is shown in Figure 6. Bearings 11–14 have 2 or 3 degradation statuses. For bearings 11 and 13, the amplitude of the vibration signal is gradually increased. The marked red rectangle denotes the Severe status in Figure 6. Bearing 12 clearly shows a jump and some noise under the Normal condition. Hence, it has only two degradation statuses (Normal and Severe). Compared with bearing 12, bearing 14 has two obvious jumping points; hence, bearing contains three statuses. The vibration signal in the blue rectangle denotes the Slight condition, and the Severe condition is shown in the red rectangle. It is difficult to identify the status at first glance without extensive manual experience. The degradation status of bearing 15 is even more problematic as it cannot be seen clearly when extracted manually because there is massive noise. We also take one sample to show the frequency result. The FFT results are shown in Figure 7. The signal is more prominent at the frequency of the range [350, 450] except bearing 15, which are not the approximate integer times the working frequency (25.6 Hz). Therefore, this result indicates that the frequency-domain signal contains no more useful degradation trend information. Moreover, there is no useful information from frequency domain for bearing 15 because the massive noise result makes the degradation trend in the frequency domain not good. Therefore, we use the absolute amplitude from original signal to extract the degradation of bearing and reduce the manual experience.

In the following section, the SDAE and SAE are used to extract the preliminary degradation trend and CFS is then used to find some available clustering center points, which are in turn used to determine the degradation trends and construct the health indicator CV for assessing the bearing's PDA.

4.2. Degradation Trend Extracted by the SAE and SDAE. In this part, the SAE and SDAE are used to extract the preliminary degradation trend through several hidden layers. Before preliminary degradation extraction, the absolute values of the vibration amplitudes for all bearings are considered as the input of the SAE and SDAE to reduce the data dimension for convenient data visualization. The hidden layers in the SAE and SDAE have a triangular structure, that is, the number of hidden layer nodes is half of the former adjacent hidden layer. In [29], the authors use a triangular hidden layer structure to extract the potential fault feature and confirm the validity of the proposed model. Note that the triangular structure often results in the number of latter hidden layer nodes being half of the number of former adjacent hidden layer nodes.

Therefore, the number of the first nine hidden layers' neural nodes is set at [1280, 640, 320, 160, 80, 40, 20, 10, and 2] in the SAE and SDAE. The maximum iteration number for each layer is 50. With regard to the learning rates in the SAE and SDAE, the lower the learning rate is, the more slowly the update speed changes for the cost function. A small value will result in a local minimum [37, 39]; hence, we use 0.1 in this study. In SDAE, if the value of the denoising probability P is too great, more information will be lost from the original data. The authors suggest that the parameter P is typically fixed below 0.5 [37, 39]. Therefore, in this study, a low value of 0.1 is used for denoising probability P.

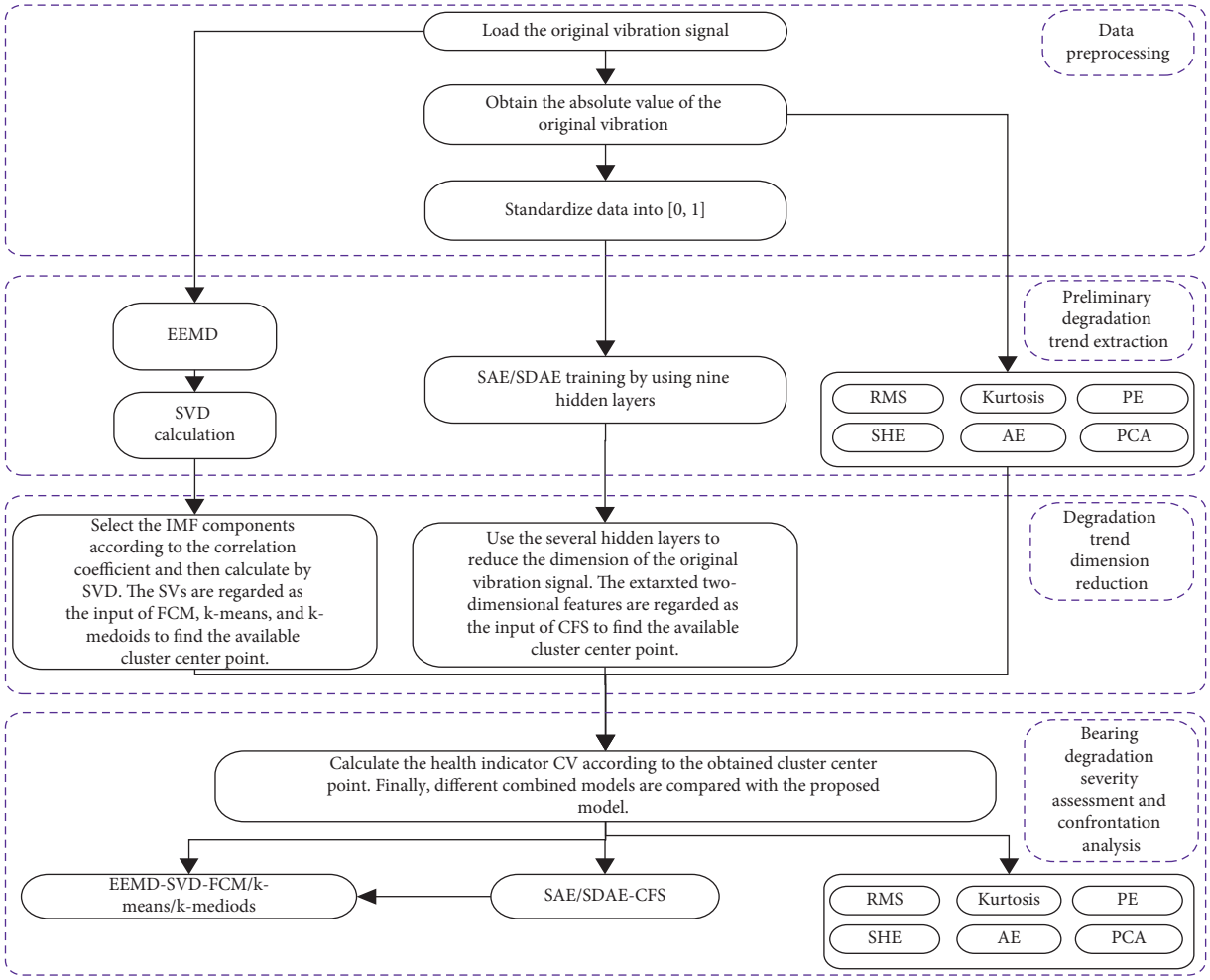

Figure 4: Flowchart of the method presented.

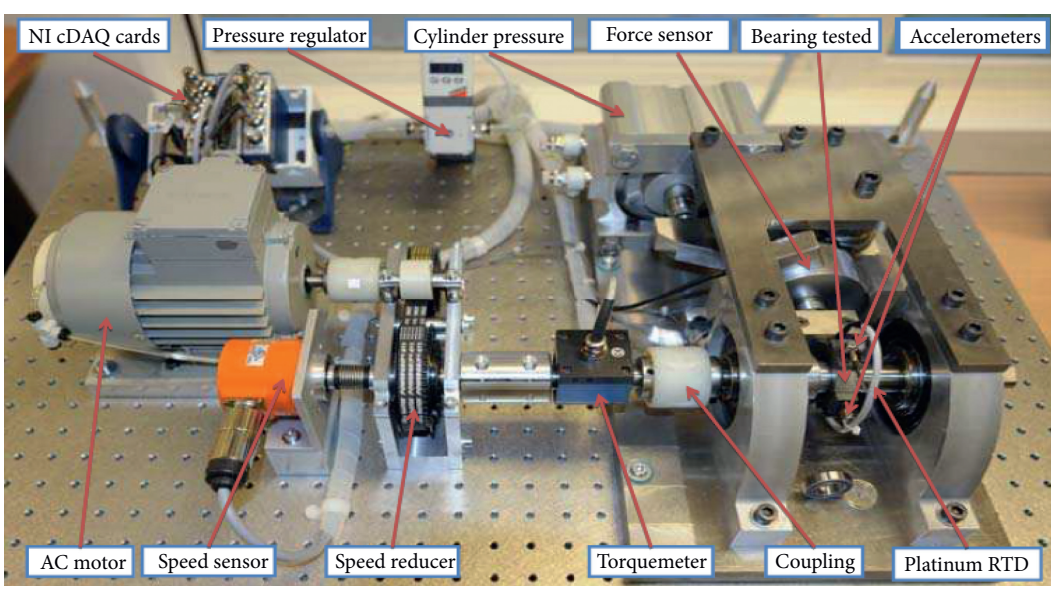

Figure 5: The experimental data acquisition platform.

To demonstrate that the robustness and feature extraction performance of the SDAE are superior to those of the SAE, the degradation trends of all bearings from the first eight hidden layers are used for comparison. For easy visualization of the data, PCA is used to reduce the dimensions of the extracted degradation vectors to two for the first eight

Table 1: Detailed information on the experimental data.

Working conditions	Bearings				
	Bearing 11	Bearing 12	Bearing 13	Bearing 14	Bearing 15
Load (N)	4200	4200	4200	4200	4200
Speed (rpm)	1800	1800	1800	1800	1800
Length	2560	2560	2560	2560	2560
Sample numbers	2803	873	1802	1139	2302

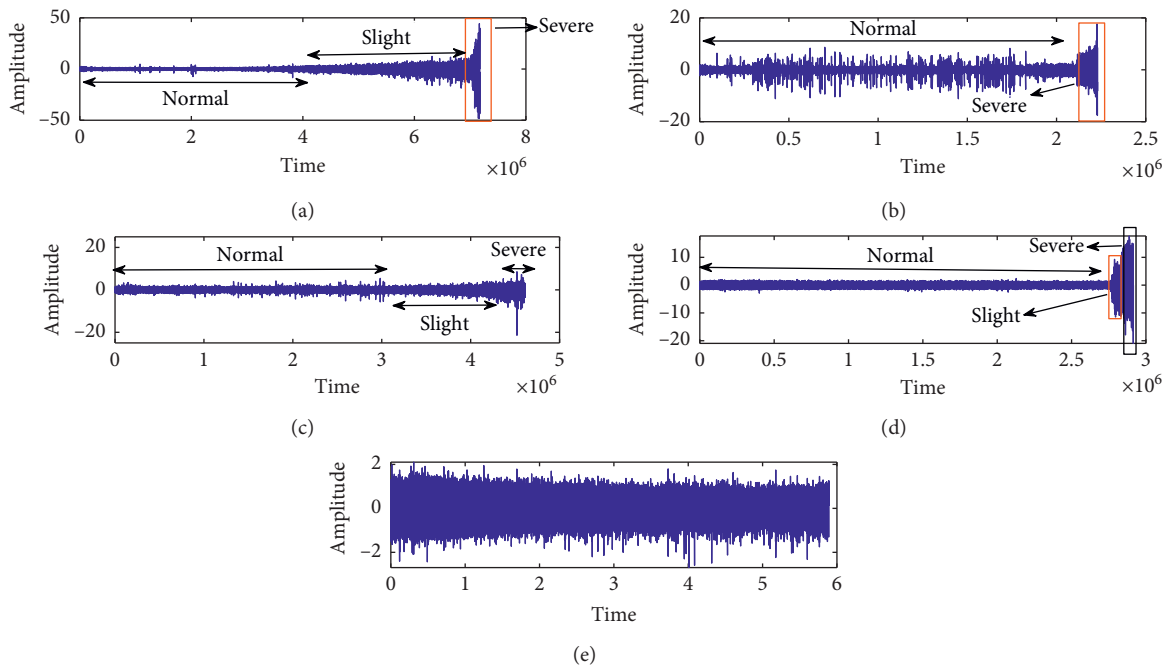

Figure 6: Time-wave figure of the original vibration for bearings 11–15. (a) Bearing 11. (b) Bearing 12. (c) Bearing 13. (d) Bearing 14. (e) Bearing 15.

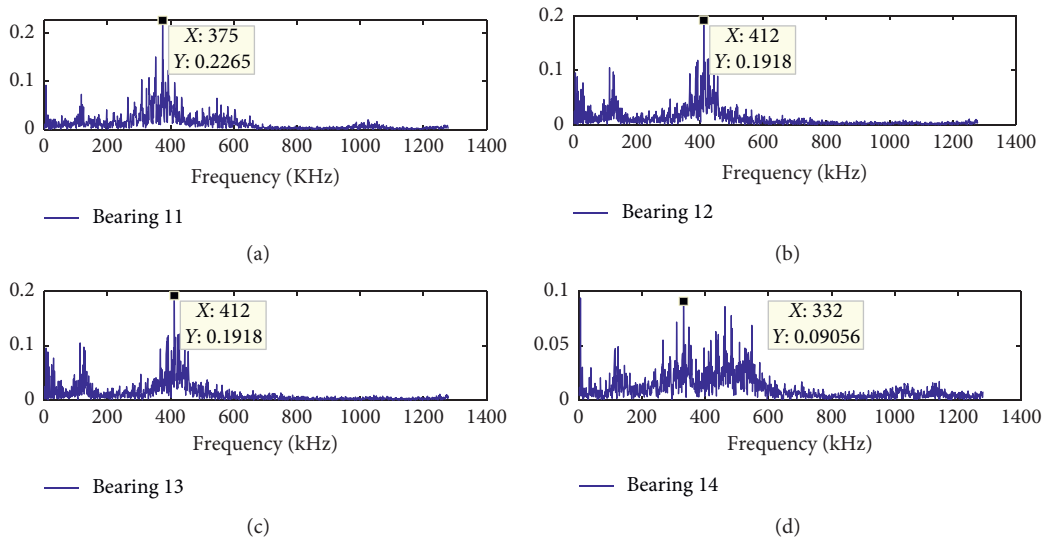

Figure 7: Continued.

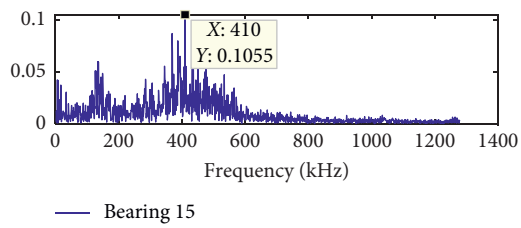

(e)

Figure 7: The frequency-domain signal through FFT for bearings 11–bearing 15. (a) Bearing 11. (b) Bearing 12. (c) Bearing 13. (d) Bearing 14. (e) Bearing 15.

hidden layers. The results of the first two principal components (PC1-PC2) are shown in Figures 8 and 9 (due to limited space, only bearing 11 is given as an example in this study).

Figures 8 and 9 show that the degradation trend can be extracted successfully from the original vibration signal after the original vibration data have been trained by the SAE and SDAE. All curves show monotonic growth or reduction at each hidden layer, and compared with the SAE, they are more stable and less noisy in the SDAE at each layer, and there is little or no noise before the first 1500 points. In Figure 9, they look like a straight line without fluctuation when the SDAE is used, but there is a small amount of curve fluctuation at the seventh hidden layer in the SAE. Take the 391st data point as an example. In Figure 8, as the number of hidden layers increases, the 391st data contains obvious noise, even though the 391st data point in the trend is extracted from the last hidden layer. But Figure 9 shows that with the increase of number of hidden layers, the noise contained in the 391st data point gradually weakens, for example, starting from the sixth hidden layer, the noise of the 391st data point is obviously weakened. SDAE sets part of the input data to 0 and reconstructs it through the denoising rate; this can reduce the noise, and hence the denoising effect of SDAE is better than SAE.

The SAE and SDAE are also used to extract the degradation trend for different bearings (11–15), and the corresponding results through the ninth hidden layer are shown in Figures 10 and 11, respectively. Similar to bearing 11, as the number of hidden layers increases, the noise of the HI curve extracted through the final hidden layer by SDAE is not obvious, while the noise of the HI curve extracted by SAE is still obvious, such as bearing 14 in Figures 10 and 11.

In Figures 10 and 11, all curves show a monotonous increase and decrease, except for bearing 15. Compared with the SAE, there is an obvious monotonous increase or decrease curve for bearings 11–14 when the SDAE is used in Figure 11. Starting from around the 1000th point, the curve shows a stable status for bearing 15 in Figure 11. Before the 1000th data point, there is an evident rising and falling trend when SDAE is used. There is no conspicuous trend at the ninth hidden layer when the SAE is used in Figure 8, as it is submerged in massive noise. The SDAE destroys and reconstructs the input to improve its robustness, confirming that the SDAE has a denoising ability. The trend for bearings 12 and 14 looks like a straight line and is not rising and falling because the vibration amplitude is very smooth at each stage. This is in accordance with Figure 6. In Figure 10, particularly for bearing 14, there is some noise in the SAE under the Normal condition, while there is a stable line in Figure 11 when the SDAE is used. The line pattern for bearing 13 is similar. These results demonstrate that the robustness and stability of the SDAE are superior to those of the SAE. In addition, the SAE and SDAE can extract the preliminary degradation characteristics well without extensive manual experience and tagged data labels.

However, at first glance, bearings 12 and 14 have only two states in the manual process. However, there are two degradation statuses: Normal and Severe, and perhaps three: Normal, Slight, and Severe, for bearing 14. Identifying how many degradation statuses there are for bearing 15 is difficult with the naked eye, and determining the number of degradation statuses a bearing should have using manual experience and the naked eye can in general be erroneous. Therefore, CFS is used to find the cluster center point under different degradation statuses and can be an option an engineer can use to determine the degradation status of a bearing.

4.3. Constructing a Health Indicator CV and Judging Degradation by Using CFS. Before CFS calculation, some parameters need to be preset, such as the cutoff d_c. In [32], the authors advise that the average number of a neighbor data point for other points should not exceed d_c. In general, the average neighbor data point accounts for about 1–2% of the total number of data points. Hence, the average number of a neighbor data point is often set at about 1–2% of the total sample size. If the local density ρ_i of point x_i is too great, it will result in low discrimination; if d_c is too small, the same cluster class will be split into multiple parts [32]. The results of local density ρ_i and the distance δ_i when the SAE/SDAE-CFS is used for bearings 11–15 are shown in Figure 12. The corresponding two-dimensional clustering results when the SAE/SDAE-CFS is used are also shown in Figures 12 and 13.

(1) As shown in Figures 14(a) and 14(c) and Figures 15(a) and 15(c), three points (A, B, and C) are filtered by using the cutoff distance d_c and the local density ρ_i. The greater the value of the cutoff distance

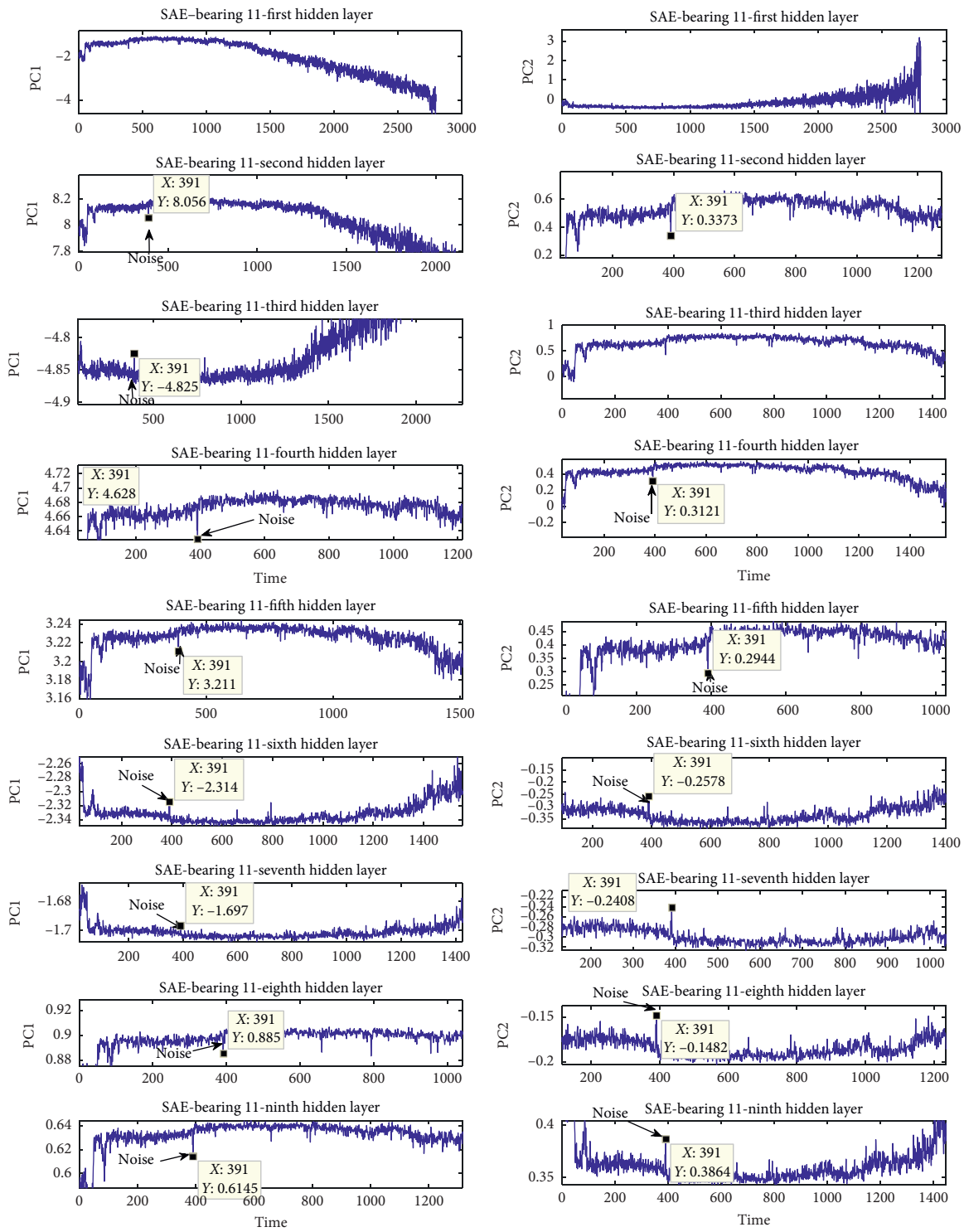

Figure 8: Extracted degradation through every hidden layer for bearing 11 by using the SAE.

d_c and the local densityρ_i, the more likely it is to become the cluster center point. Hence, these three points with obvious jumping are selected as the clustering center points, and there are only two points with obvious jumping.

(2) Compared with the SAE, the selected clustering center points with jumping for bearings 13 and 15 in Figures 16(c) and 16(e) are more obvious when the SDAE is used. For example, in Figure 14(c), bearing 13 contains three clustering center points, but the

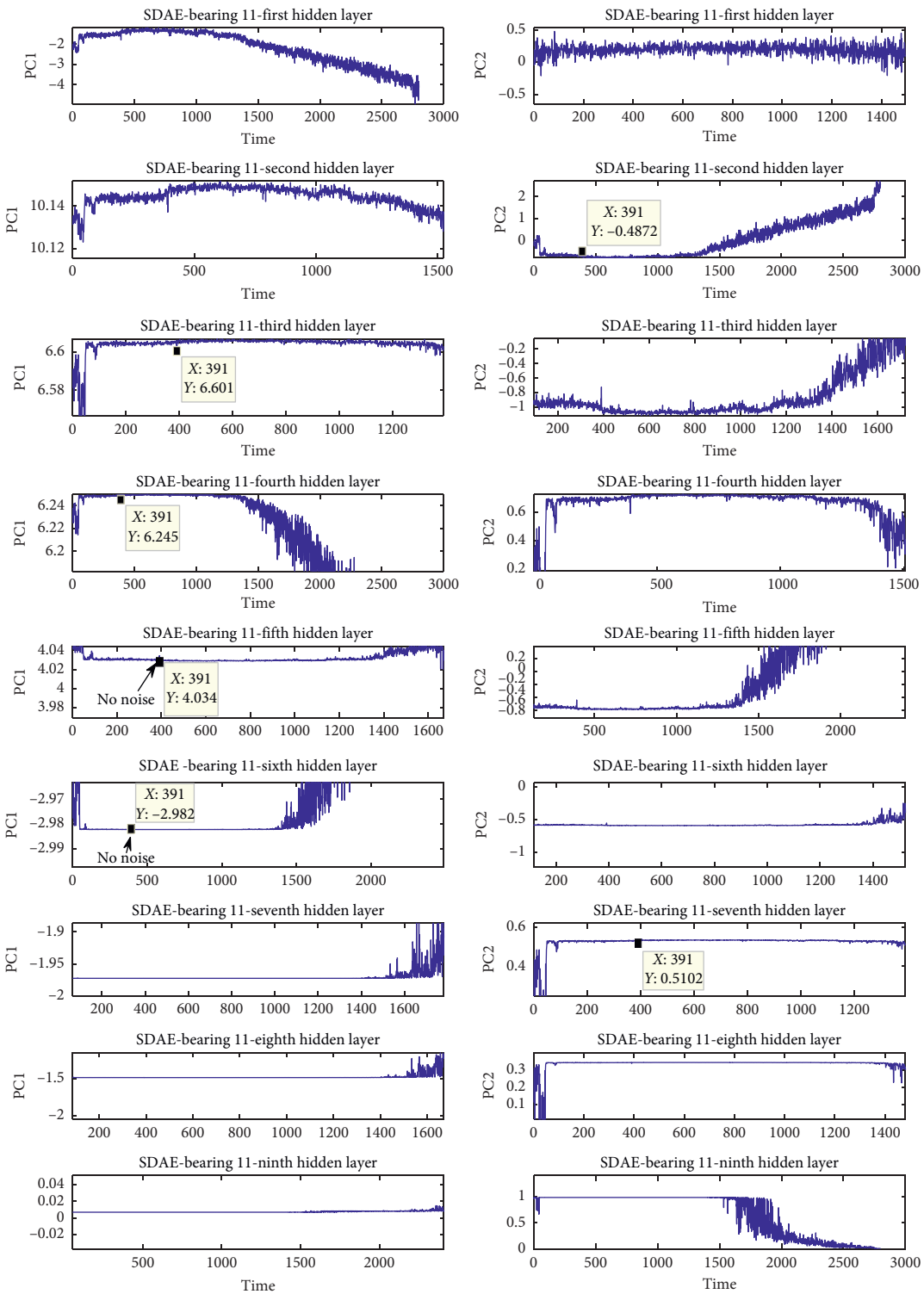

Figure 9: Extracted degradation through every hidden layer for bearing 11 by using the SDAE.

third clustering center candidate point (C) is close to the fourth (D). The third clustering center candidate point (C) is separated and filtered far away from the fourth in Figure 16(c). It is easier to choose and determine the clustering center points by using the SDAE. This is also shown in Figure 16(e), where four selected clustering center points are very clearly filtered far away from other points that are close to

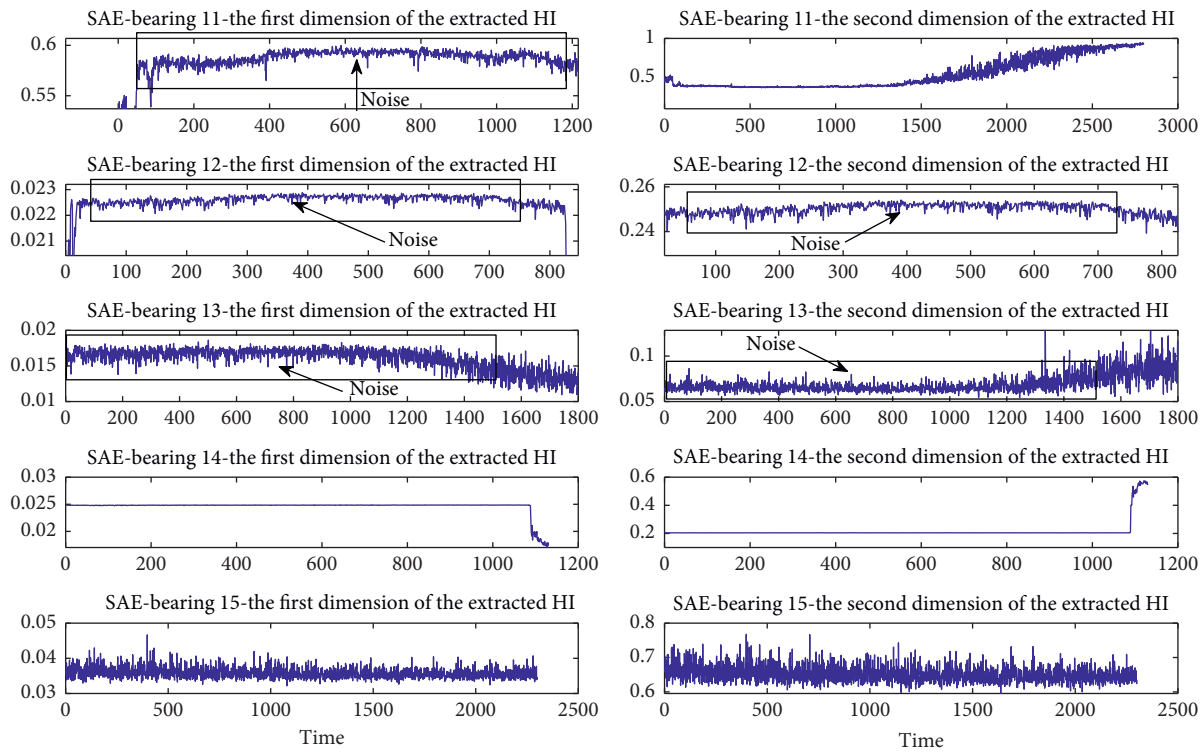

Figure 10: The extracted two-dimensional degradation features for bearings 11–15 through the final hidden layer by using the SAE.

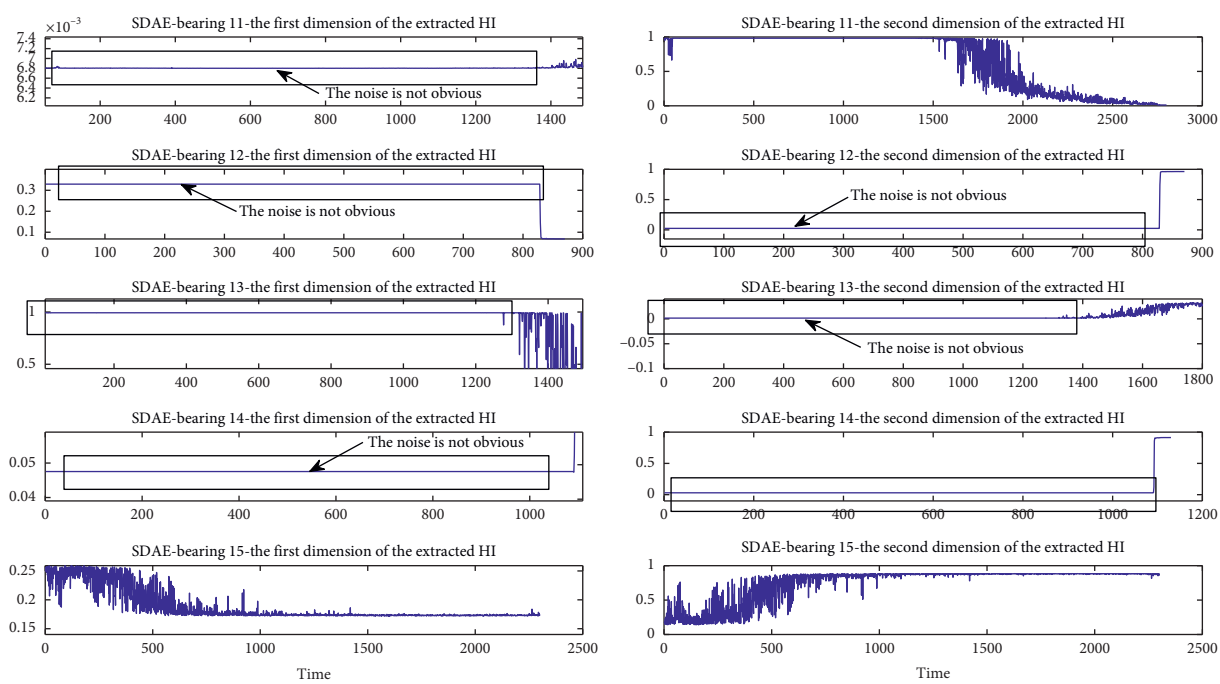

Figure 11: Extracted two-dimensional degradation features for bearings 11–15 through the final hidden layer by using the SDAE.

the horizontal axis. However, in Figure 14(c), many data points are scattered because there is massive noise in Figure 8 when the SAE is used. Thus, the feature extraction of the SDAE is superior to that of the SAE.

(3) Figures 12 and 13 show that compared with the SAE-CFS, the SDAE-CFS performs better at clustering. In Figures 13(b) and 13(d), all samples are separated well by using the SDAE, as few points are scattered around its clustering center point in Figure 12(d),

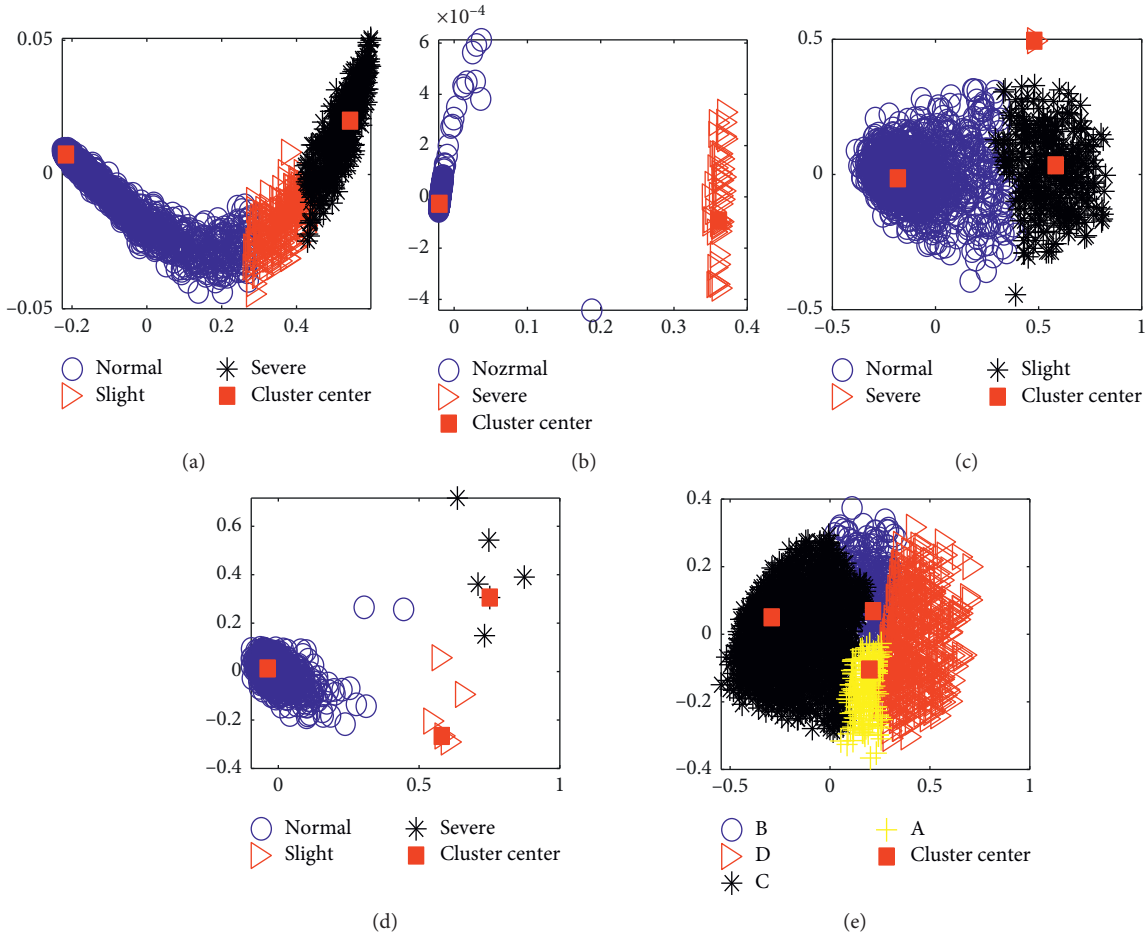

Figure 12: Two-dimensional clustering result by using the SAE and CFS for bearings 11–15. A: Normal1; B: Normal2; C: Slight; D: Severe. (a) CFS-bearing 11. (b) CFS-bearing 12. (c) CFS-bearing 13. (d) CFS-bearing 14. (e) CFS-bearing 15.

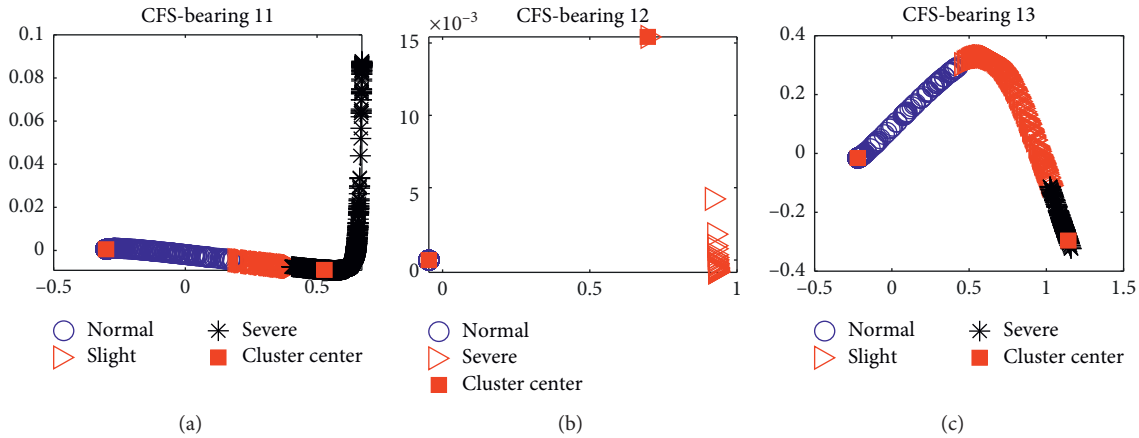

Figure 13: Continued.

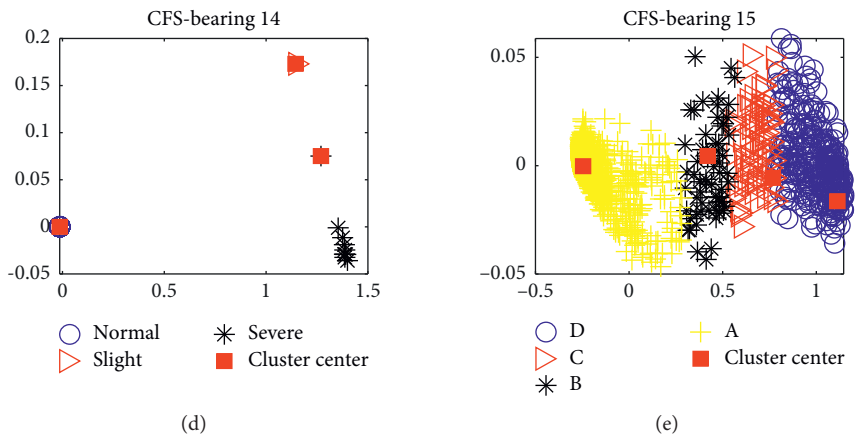

Figure 13: Two-dimensional clustering result by using the SDAE and CFS for bearings 11–15. A: Normal1; B: Normal2; C: Slight; D: Severe. (a) CFS-bearing 11. (b) CFS-bearing 12. (c) CFS-bearing 13. (d) CFS-bearing 14. (e) CFS-bearing 15.

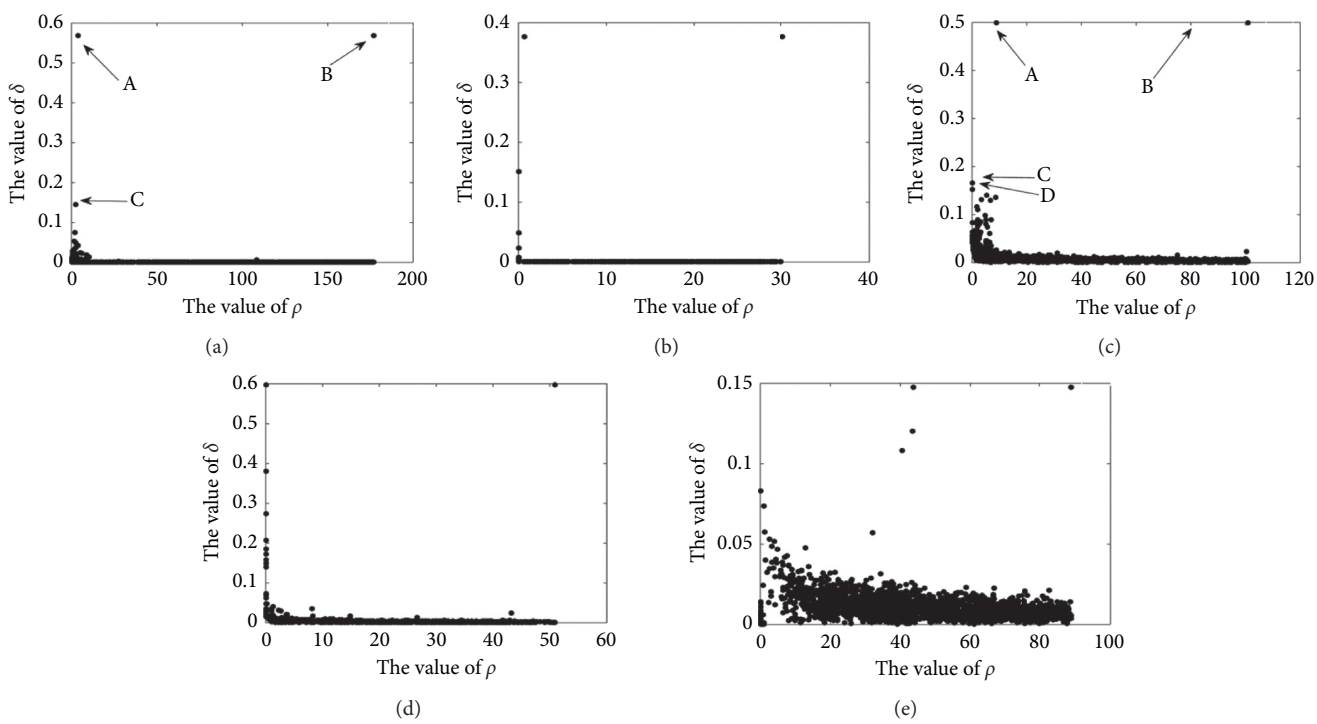

Figure 14: Result of local density ρ_i and the distance δ_i by using the SAE-CFS for bearings 11–15. (a) SAE-CFS-bearing 11. (b) SAE-CFS-bearing 12. (c) SAE-CFS-bearing 13. (d) SAE-CFS-bearing 14. (e) SAE-CFS-bearing 15.

but there is only one point identifiable under the Normal condition in Figure 13(d) using the naked eye. This is consistent with the situation in Figure 10 because when the SAE is used, the extracted degradation curve contains some noise under the Normal condition throughout the entire life.

(4) It should be noted that bearing 15 clearly contains four clustering center points when the SDAE is used in Figures 12(e) and 13(e). Thus, bearing 15 has four degradation statuses. Identifying the degradation trend of bearing 15 from Figure 5 is difficult using the naked eye or manual experience, but CFS can enable us to determine the number of degradation statuses for bearing 15 without prior knowledge.

(5) In Figures 12(e) and 13(e), four symbols, A to D, denote the different degradation statuses for bearing 15: A—Normal1, B—Normal2, C—Slight, and D—Severe. We use RMS as a reference to determine the degradation trend and demonstrate that CFS can find the available and suitable cluster center point number that is the same as RMS. The RMS obtained from bearing 15 is shown in Figure 17, and it is evident that starting from the 66th point, the RMS curve increased sharply until the 141st point. After

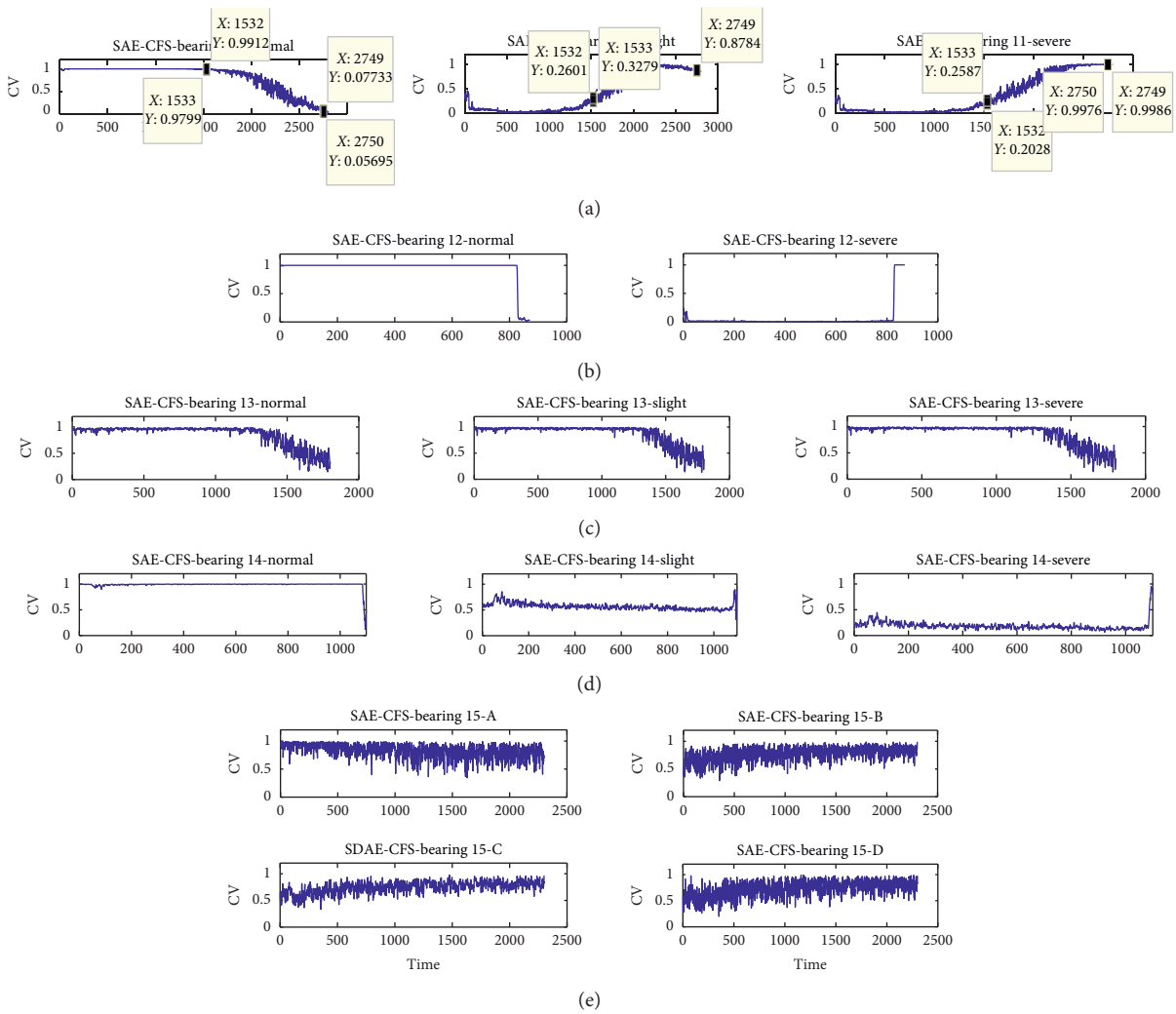

Figure 15: CVs for bearings 11–15 by using the SAE-CFS under various conditions such as "Normal," "Slight," and "Severe."

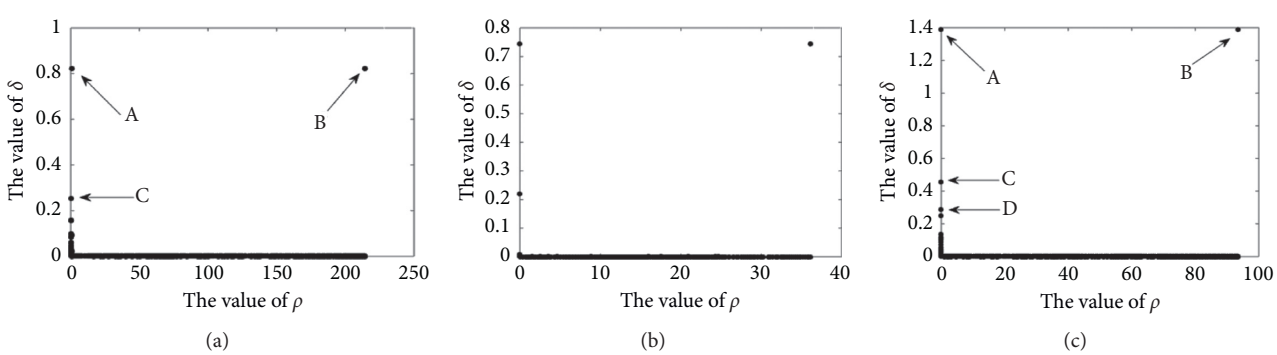

Figure 16: Continued.

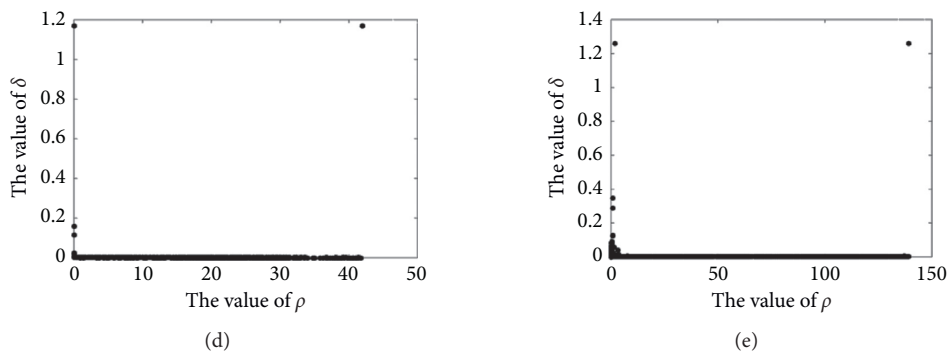

Figure 16: Result of local density ρ_i and the distance δ_i by using the SDAE-CFS for bearings 11–15. (a) SDAE-CFS-bearing 11. (b) SDAE-CFS-bearing 12. (c) SDAE-CFS-bearing 13. (d) SDAE-CFS-bearing 14. (e) SDAE-CFS-bearing 15.

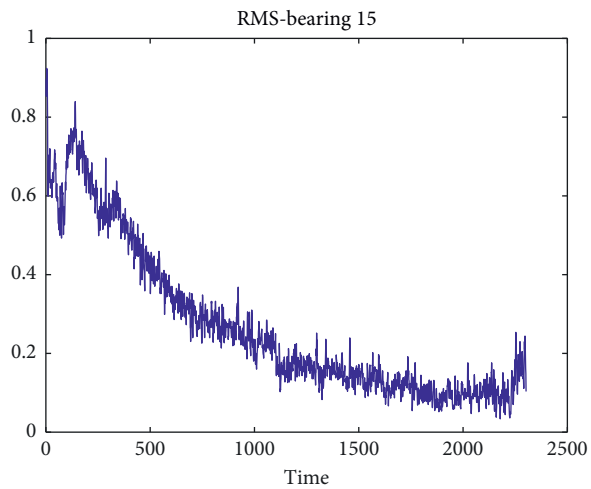

Figure 17: RMS for bearing 15 under various conditions such as "Normal," "Slight," and "Severe."

the 141st point, there is another increase until the 359th point. The curve decreased sharply from the 359th point to the 1104th point, while it became stable from the 1104th point to the endpoint. Hence, there are four degradation statuses for bearing 15: A—Normal1 (from 1 to 66), B—Normal2 (from 66 to 141), C—Slight, and D—Severe. Finally, the CVs calculated by using different clustering center points are shown in Figures 15 and 18. These results demonstrate that CFS can give us an option to determine the number of degradation statuses for bearing 15 without prior knowledge.

(6) In Figure 18(e), the degradation trend is similar to that of RMS, and several turning points, such as the 66th point, the 359th point, and the 1104th point, can reflect the degradation trend of bearing 15 well by using our presented model. Each subfigure in Figure 18(e) can be regarded as a reference to determine the degradation trend together with other curves. The first three subfigures in Figure 18 show that starting from the 359th point, these three curves clearly become stable, so it is easier to judge the Severe status for bearing 15 after the 1104th point. Furthermore, from the 1104th point, all CV curves are more stable than the RMS curve. Before the 359th point, most CVs are close to 1 and clustering center points (A and B) are used under the Normal condition. After the 359th point, there is an obvious increase when clustering center point C is used, so some points under the Slight condition are close to 1. These results indicate that our proposed model can reflect the degradation trend well and more precisely than RMS without prior knowledge.

(7) In Figure 18, starting from the 1532nd point until the 2750th point, bearing 11 changes status from Normal to Slight. After the 2750th point until the endpoint, the status for bearing 11 changes from Normal to Severe. These state turning points for bearings 13 and 14 are [1275, 1720] and [1088, 1093], respectively. For bearing 12, they are [827, 830].

The above results show that the SDAE is more robust than the SAE and that CFS has a good ability to choose the clustering center point well under different conditions without prior knowledge. In the following sections, other

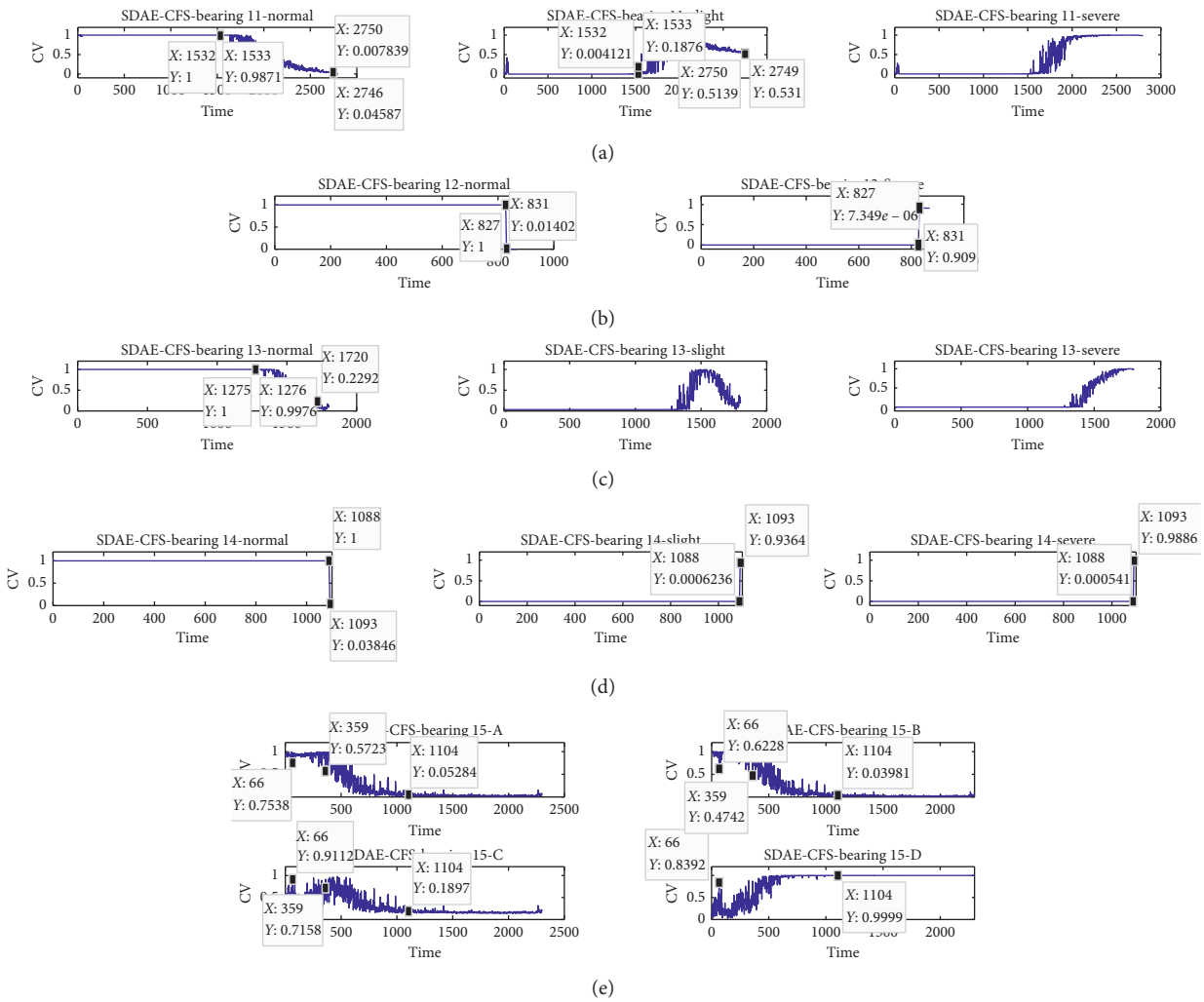

Figure 18: CVs for bearings 11–15 resulting from using the SDAE-CFS under various conditions such as "Normal," "Slight," and "Severe."

models presented in [21], such as the time-frequency indicators RMS and kurtosis and PCA, are considered and compared with our proposed model.

4.4. The Presented Method Compared with RMS, Kurtosis, and PCA. In this section, time-frequency indicators, including RMS and kurtosis, and PCA are compared with the SDAE-CFS.

4.4.1. RMS and Kurtosis. The results of RMS and kurtosis calculated from bearings 11–15 are shown in Figures 19 and 20.

(1) In Figure 20, the degradation trend is obviously obscured by noise, which will easily result in the degradation status being misjudged, particularly for bearings 11 and 12. Unlike kurtosis and RMS, the SDAE-CFS, shown in Figure 18, can reflect the degradation well.

(2) Some RMS curves have small fluctuations and few noises. Thus, all of the stable and smooth curves of RMS are inferior to those of the SDAE-CFS. In Figure 18, most of the CV curves under different conditions look like straight lines at first glance, especially under the Normal condition; these CV curves can be used to identify the degradation status more easily than those of RMS when the degradation status has changed. For example, the status change from Normal to Severe in bearing 12 is very clear, starting from the 827th point; there is an obvious jump in Figure 18, while the RMS curves in Figure 19 show a gradual change, not a jump.

(3) For bearing 15, the degradation trend must be judged manually, while CFS can find the available number of the degradation status automatically. Therefore, these results demonstrate that the proposed model is better than RMS and kurtosis. In addition, CFS can provide the available clustering center point to assess the number of the degradation statuses.

4.4.2. PCA. In this section, PCA is used to extract the bearings' degradation trend. The first two components (PC1-PC2) are used to show the results of the

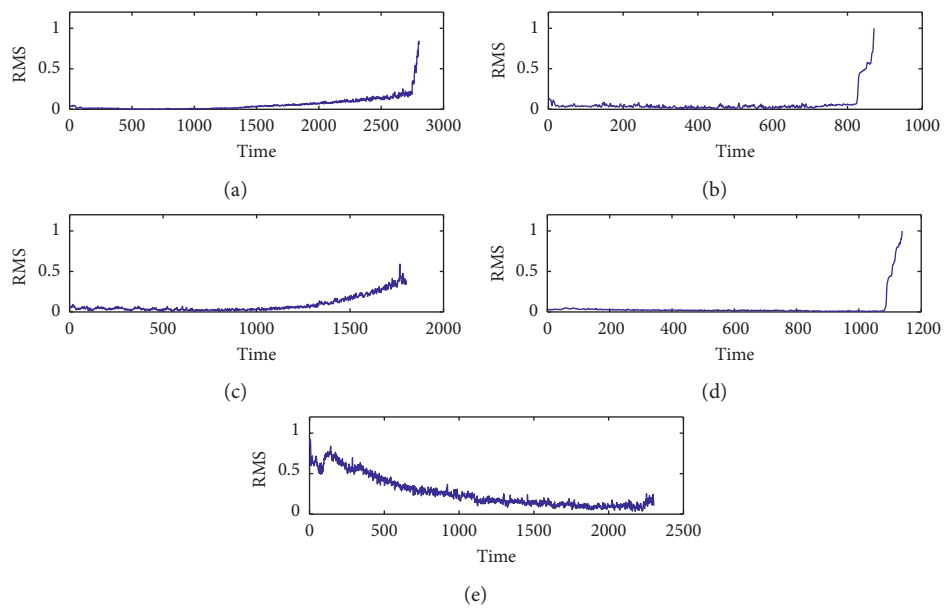

Figure 19: CVs for bearings 11–15 by using RMS under various conditions such as "Normal," "Slight," and "Severe." (a) RMS-bearing 11. (b) RMS-bearing 12. (c) RMS-bearing 13. (d) RMS-bearing 14. (e) RMS-bearing 15.

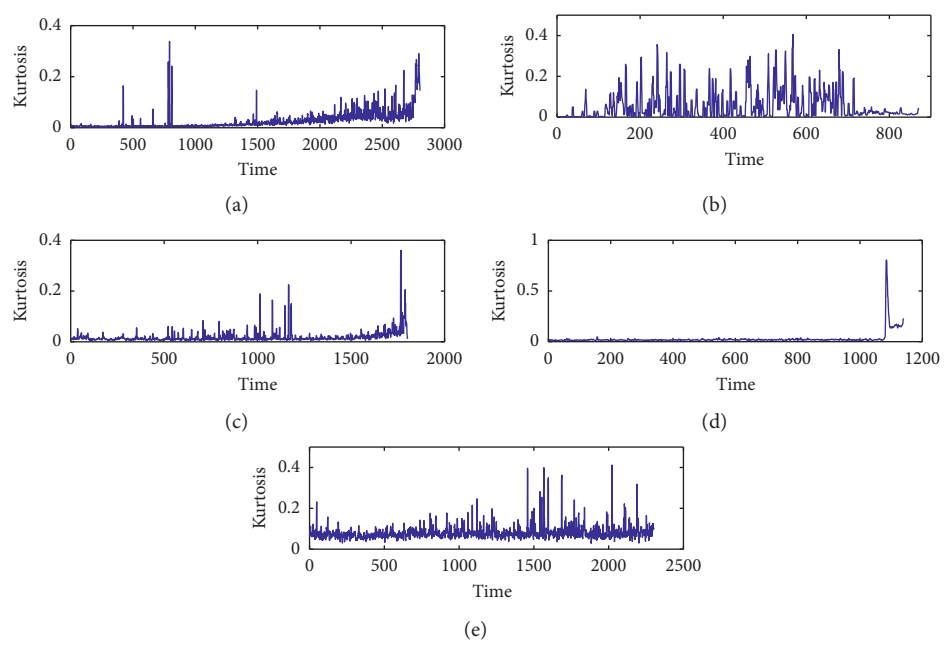

Figure 20: CVs for bearings 11–15 by using kurtosis under various conditions such as "Normal," "Slight," and "Severe." (a) Kurtosis-bearing 11. (b) Kurtosis-bearing 12. (c) Kurtosis-bearing 13. (d) Kurtosis-bearing 14. (e) Kurtosis-bearing 15.

degradation. In Figure 21, there is no obvious degradation for bearing 15 because much noise masks the trend of the degradation. The SDAE used the DAE to destroy the data to zero and then reconstruct it. Therefore, the SDAE is more robust and stable than PCA and CFS in finding suitable clustering center points to determine the degradation status. In addition, most of the CV curves obtained from PCA are not as stable and smooth as those of the SDAE-CFS.

4.5. The Presented Method Compared with EEMD-SVD-k-Means/k-Medoids/FCM. In this section, the proposed model is compared with other models in [21], such as EEMD-SVD-k-medoids/k-means/FCM. Some parameters should be set before calculating EEMD and k-medoids/k-means/FCM.

(1) EEMD: two parameters must be selected before the EEMD calculation; m is the ensemble number and

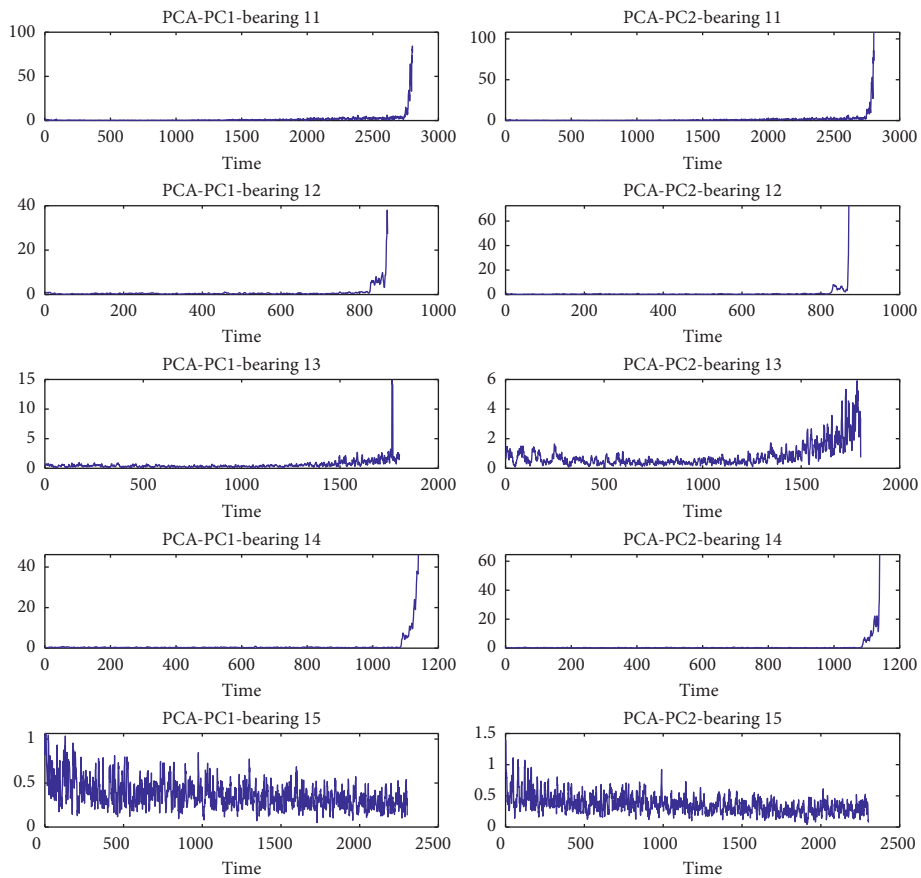

Figure 21: CVs for bearings 11–15 by using PCA under various conditions such as "Normal," "Slight," and "Severe."

the amplitude of the added white noise $n_i(t)$ [17]. The added white noise is calculated from the standard deviation (SD) of the original vibration signal. In [17], the authors advise that the white noise should be set at 20% of the standard deviation from the original data [17]. For parameter m, a few hundred numbers will result in greater accuracy. Hence, the parameter $m = 100$ is selected in this study.

(2) k-Medoids/k-means/FCM: in FCM, the iteration convergence termination tolerance $\varepsilon = 1e - 6$. Euclidean distance is used to calculate the similarity between any two samples in FCM/k-means/k-medoids. The parameter c is the number of clustering center points. For bearings 11, 13, and 15, $c = 3$, for bearing 12, $c = 2$, and for bearing 15, $c = 4$.

First, EEMD is used to decompose the original signals to IMFs. As space is limited, here we only use bearings 11 and 12 as examples. IMFs obtained from EEMD are shown in Figure 22. The amplitude of the first two IMFS is greater than that of the others because all IMFs are decomposed in order of frequency from high to low. In addition, the correlation coefficient is used to calculate the degree of relevance between each IMF and the original signal. The values of the corresponding correlation coefficients are shown in Figure 23. The two highest values are for IMF1 and IMF2. This indicates that these first two IMFs contain useful information about the original signal. Therefore, IMF1 and IMF2 are used to calculate the SVs (SV1 and SV2) through SVD. The results for SV1 and SV2 are shown in Figure 24. In this figure, bearing 11 has 3 statuses while bearing 12 has 2. The black rectangle denotes the Severe status. Therefore, these two extracted feature vectors [SV1, SV2] are regarded as the input of k-medoids/k-means/FCM for finding the available clustering center points. The two-dimensional clustering figure of the bearings when EEMD-SVD-k-medoids/k-means/FCM is used for bearings 11–15 is shown in Figure 25. The corresponding CVs for bearings 11–15 obtained from EEMD-SVD-k-medoids/k-means/FCM under various conditions are shown in Figure 26.

(1) Figures 12 and 13 show that the SAE/SDAE-CFS performs better at clustering when compared with EEMD-SVD-k-medoids/k-means/FCM. In Figure 13(b), all samples are separated well when CFS is used, for example, bearing 12. At first glance, the points simply look like a point overlapping with its clustering center point under the Normal condition. However, some points are scattered around their clustering center points in Figures 25(b), 25(g), and 25(l). The same holds in Figures 25(d), 25(i), and 25(n) for bearing 14.

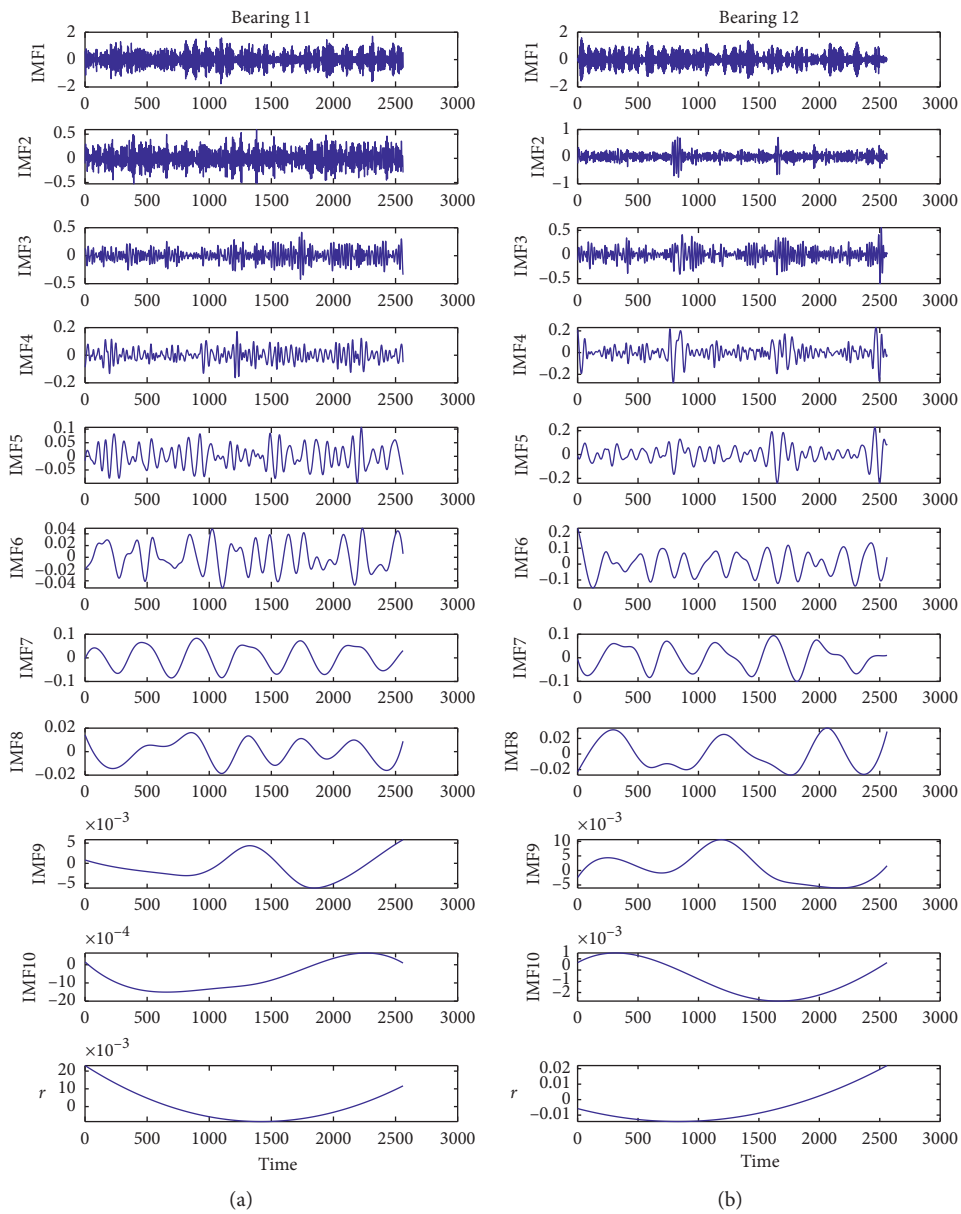

Figure 22: Results of IMFs when using EEMD for bearings (a) 11 and (b) 12.

(2) For bearing 15, the number of clustering center points is set at 4 according to the CFS clustering result referred to above. Thus, CFS can provide us with an available option to determine the number of degradation statuses for bearing 15 without prior knowledge, but k-medoids/k-means/FCM cannot do this.

(3) In Figures 26(b), 26(g), and 26(l), there is some noise under the Severe status for bearing 12. This noise may be mistakenly assessed when judging the state of degradation. In Figure 18(b), there are only two straight lines to divide the trend statuses.

(4) In Figure 18(a), the CV line shows an obvious increase between the Normal and Slight statuses for bearing 11, and it is easy to identify these statuses. However, in Figure 26, they are similar under the Normal and Slight conditions when EEMD-SVD-k-medoids/k-means/FCM is used.

(5) All CV lines in Figure 18 are more stable than those in Figure 26, particularly under the Normal status. In addition, there is some noise in Figure 26 when different models are used.

As mentioned, the proposed method (SDAE-CFS) exceeds the good results of EEMD-SVD-k-medoids/k-means/FCM, RMS, kurtosis, and PCA.

4.6. The Presented Method Compared with SHE, AE, and PE. In this section, typical health indicators such as SHE, AE, and PE are used to assess the bearing degradation trend.

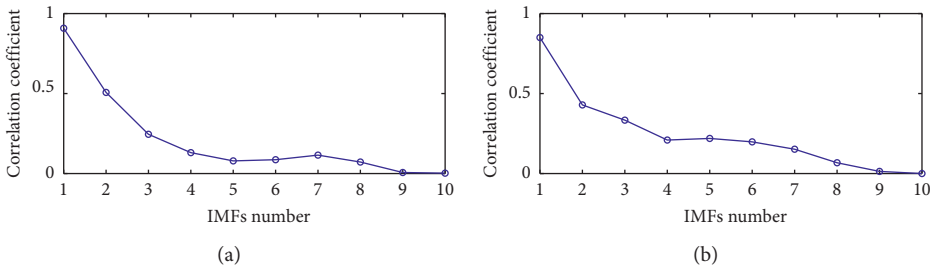

Figure 23: Correlation coefficients between each IMF and the original vibration signal. (a) Bearing 11. (b) Bearing 12.

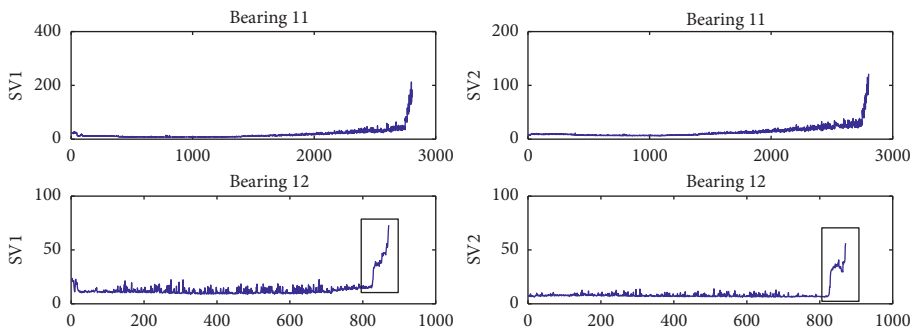

Figure 24: SV features extracted for bearings 11 and 12 from the first two IMFs by using SVD.

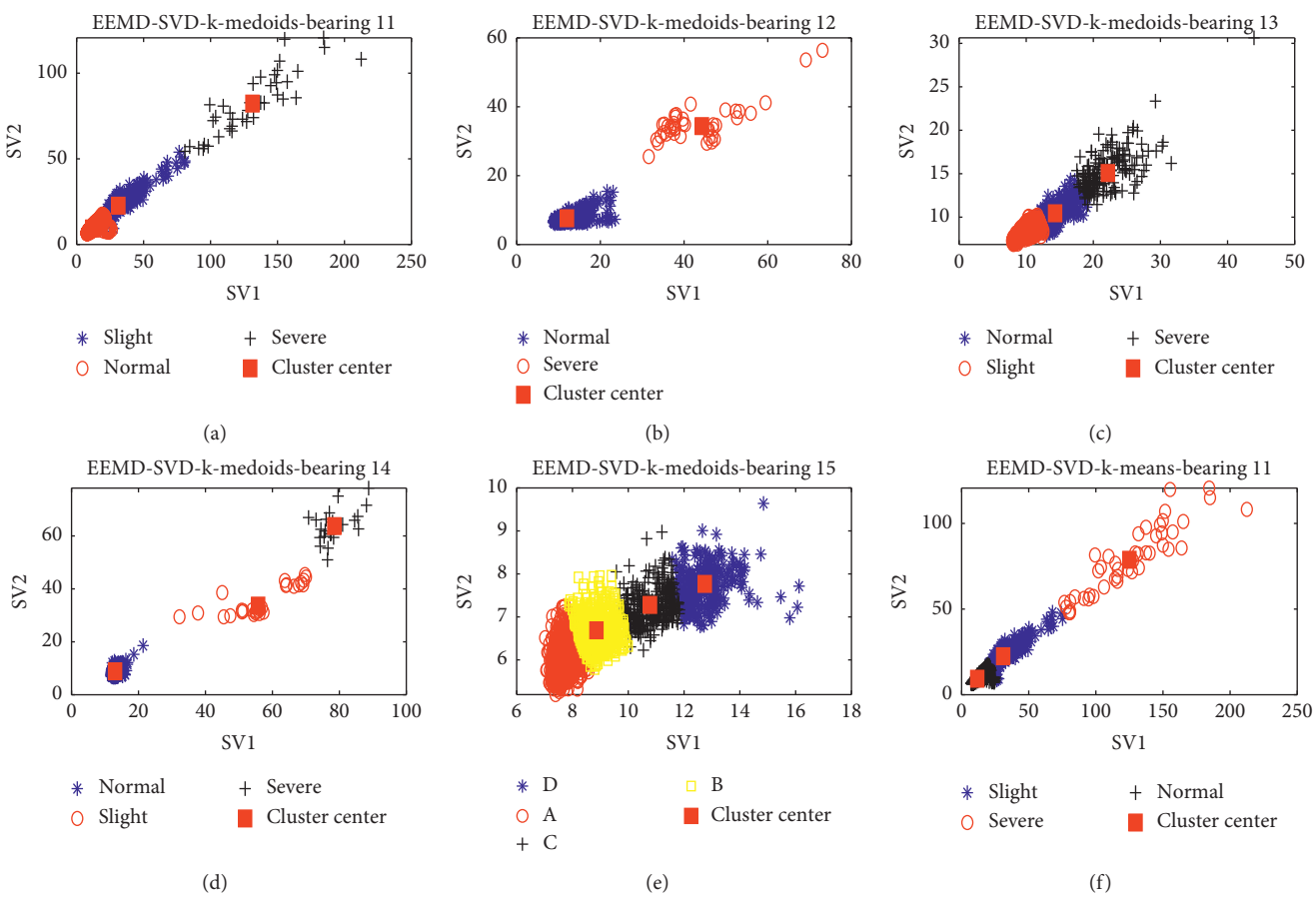

Figure 25: Continued.

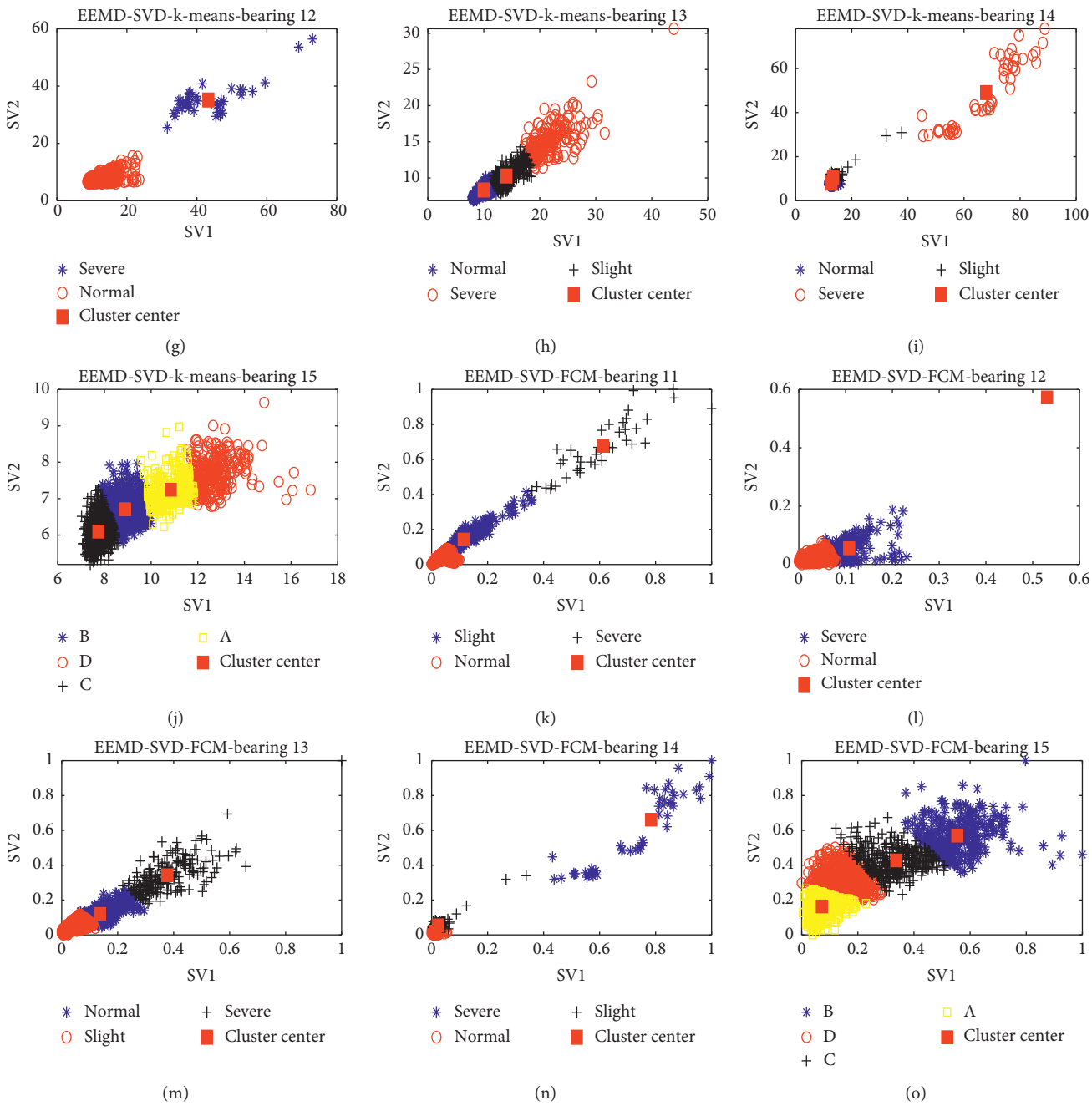

Figure 25: Two-dimensional clustering figure of bearings using EEMD-SVD-k-medoids/k-means/FCM. (a) Bearing 11. (b) Bearing 12. (c) Bearing 13. (d) Bearing 14. (e) Bearing 15. A: Normal1; B: Normal2; C: Slight; D: Severe.

Some parameters should be preconfigured before AE and PE calculation.

AE: the two parameters that should be set before calculation are embedded dimension and tolerance. Increasing the embedded dimension will cause the AE to include more useful information in the calculation, but it will also increase the computational cost. The authors suggest that the embedded dimension is often fixed at 2 [13]. Tolerance is often set at (0.1~0.25) ∗ SD, where SD is the standard deviation from the original data [13].

PE: in references [15, 40], the authors demonstrate that the embedded dimension should be in the range of 3~7. If the embedded dimension is more than 8, the corresponding calculation efficiency is poor because the reconstruction of phase space will homogenize the vibration signals. If the time delay is more than 5 and the embedded dimension is less than 4, the calculation cannot accurately detect small changes in the vibration signal. In addition, the experiment result demonstrates and the authors suggest that fixing the embedded dimension at 6 and the time delay at 3 could provide a suitable PE

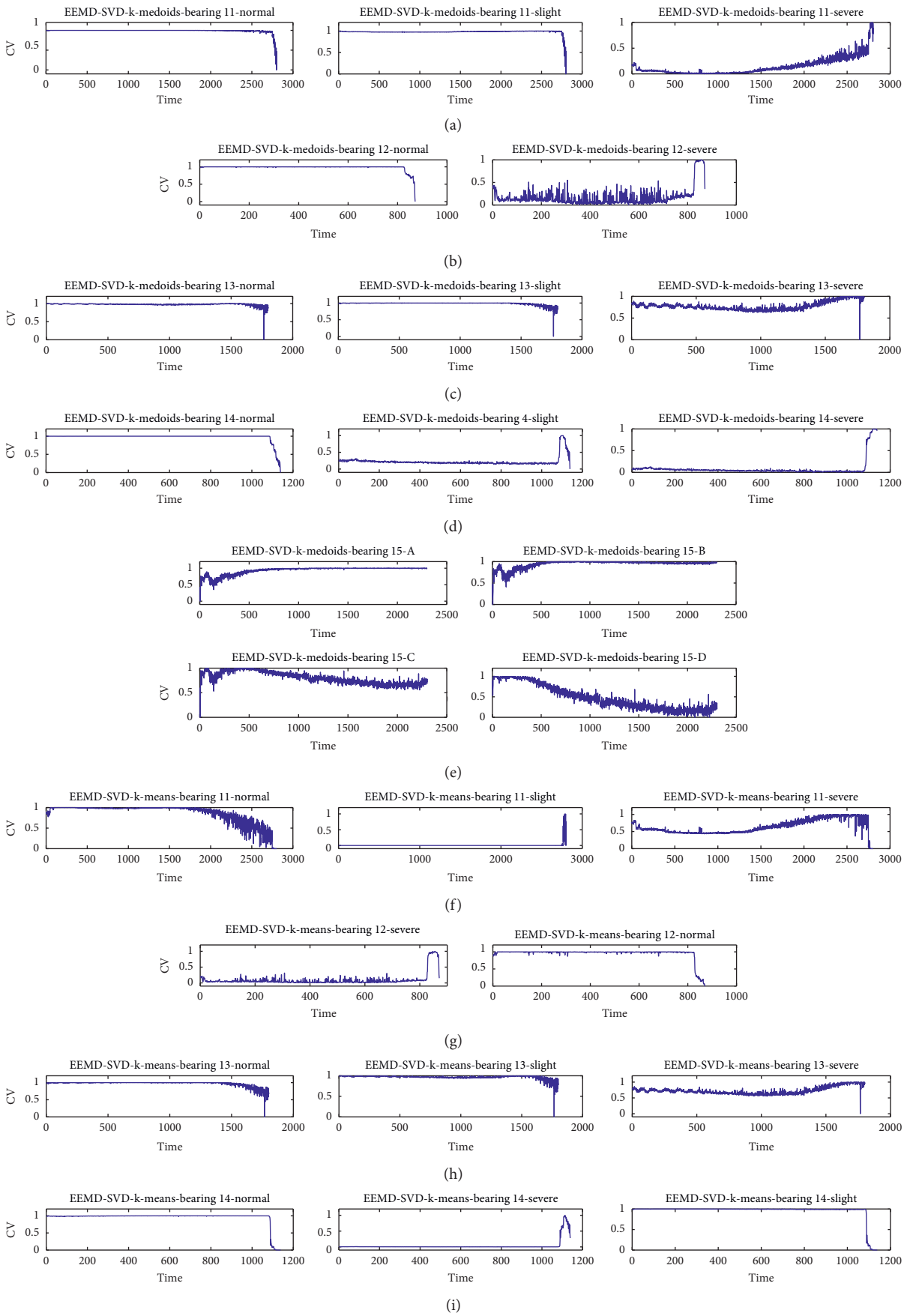

Figure 26: Continued.

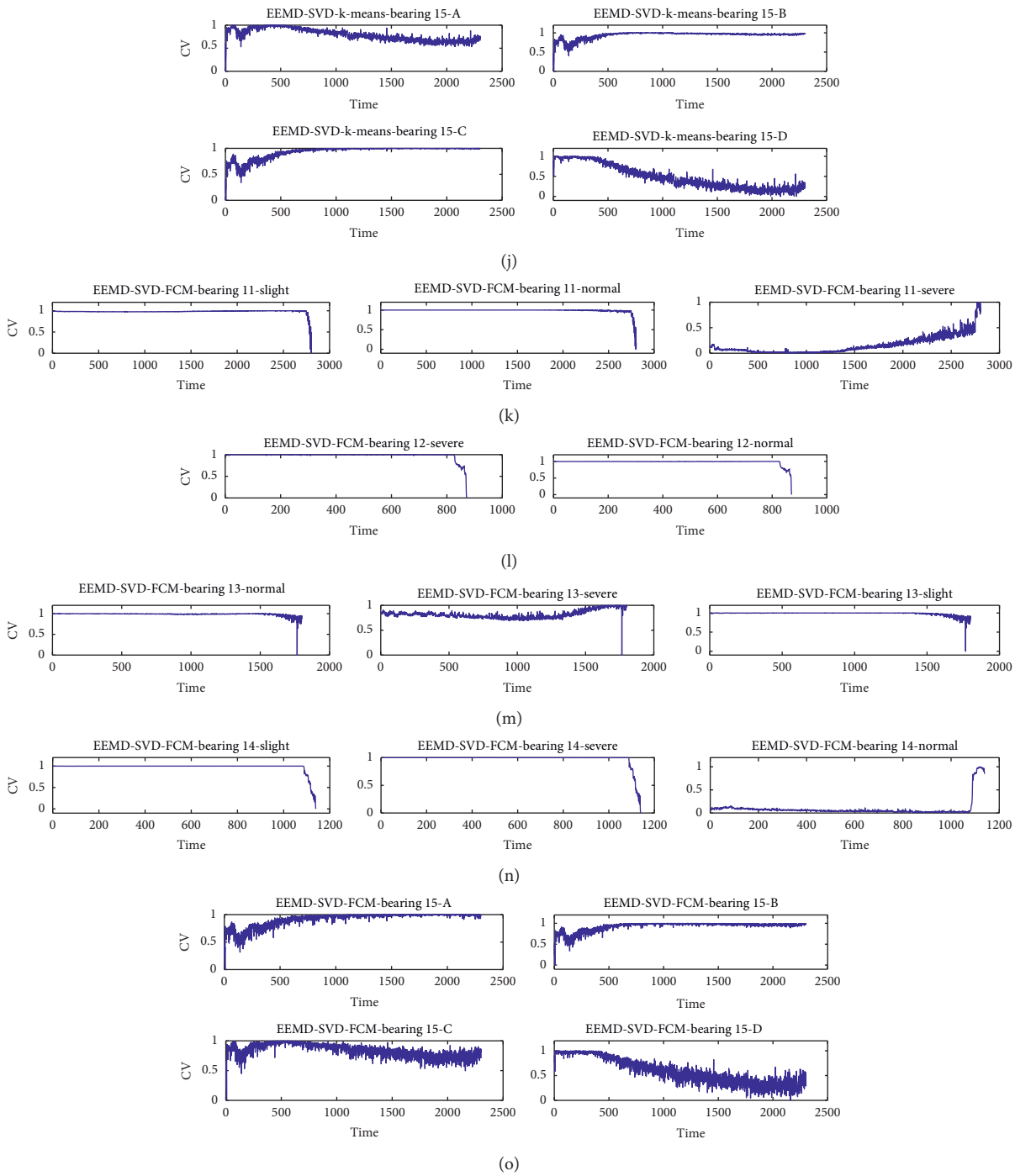

Figure 26: CVs for bearings 11–15 obtained from EEMD-SVD-k-medoids/k-Mean/FCM under various conditions such as "Normal," "Slight," and "Severe."

calculation [16]. Therefore, we also use an embedded dimension fixed at 6 and a time delay fixed at 3. The results of the degradation curve when SHE, AE, and PE are used are shown in Figures 25–27.

(1) In Figures 27 and 28, there is no clear degradation for bearing 15, so it is difficult to identify the degradation status. Although the SHE values for bearing 15 are close to a gentle straight line, there are some jump points where it is easier to misjudge different degradation statuses, and there is a lot of noise in Figure 28. Compared with SHE and PE, when AE is used, the curve line in Figure 29 has a blurred degradation trend for bearing 15, and AE cannot provide a suggestion for the number of degradation statuses with which to identify the degradation trend, while CFS can. In Figure 18, the four different CV curves can be used to

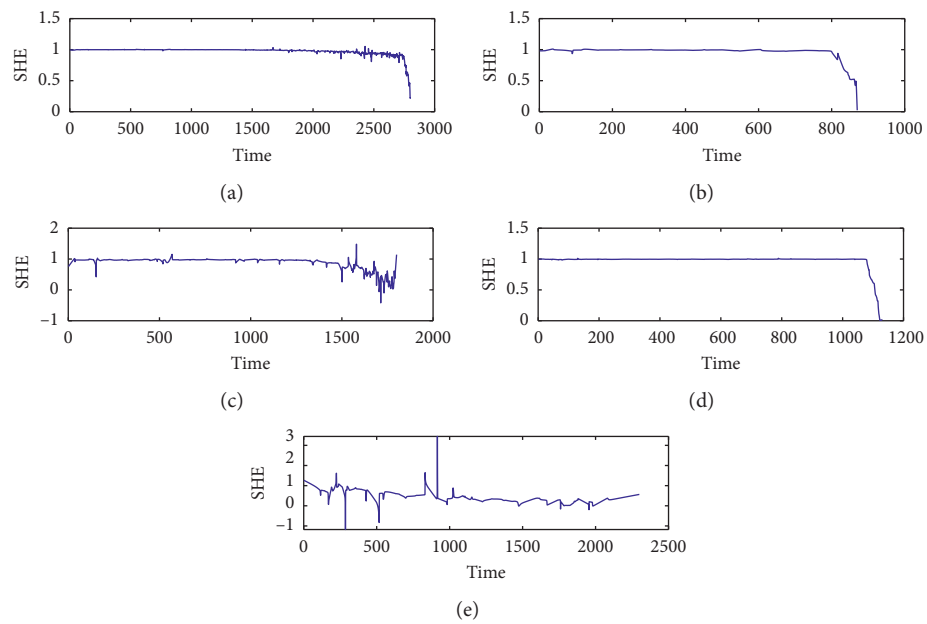

Figure 27: CVs for bearings 11–15 by using SHE. (a) Bearing 11. (b) Bearing 12. (c) Bearing 13. (d) Bearing 14. (e) Bearing 15.

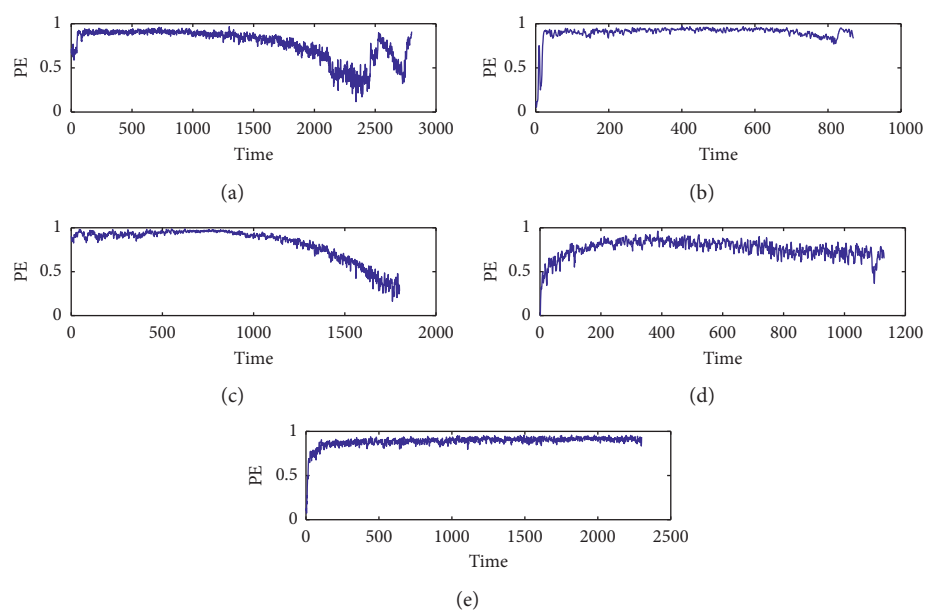

Figure 28: CVs for bearings 11–15 by using PE. (a) Bearing 11. (b) Bearing 12. (c) Bearing 13. (d) Bearing 14. (e) Bearing 15.

identify the differences and can be combined to divide the state by using different clustering center points.

(2) In Figure 27, not all curves show a monotonous increasing and decreasing trend, such as the SHE curves for bearings 11, 13, and 15. The PE values for bearing 11 are similar to those of SHE, while all CV curves in Figure 18 are monotonous increases and decreases. The noise in Figures 28 and 29 is obvious, for example, in Figure 29(b).

(3) For PE, starting from the 200th point, the curves for bearings 12 and 14 are close to stable in Figure 28, but the degradation trend for bearing 12 is from Normal to Severe around the 820th point, not around the 200th point. In addition, bearing 14 has three degradation statuses, but after the 200th point, the curve is stable until the end, as in Figure 28. The status of bearing 15 is similar to that of bearings 12 and 14.

To further demonstrate that the denoising effect of SDAE is good, we also use monotonicity (*Mon*) index. *Mon* uses the difference of any two adjacent HI points to calculate and assess the monotonicity of extracted HI [41]. If the difference

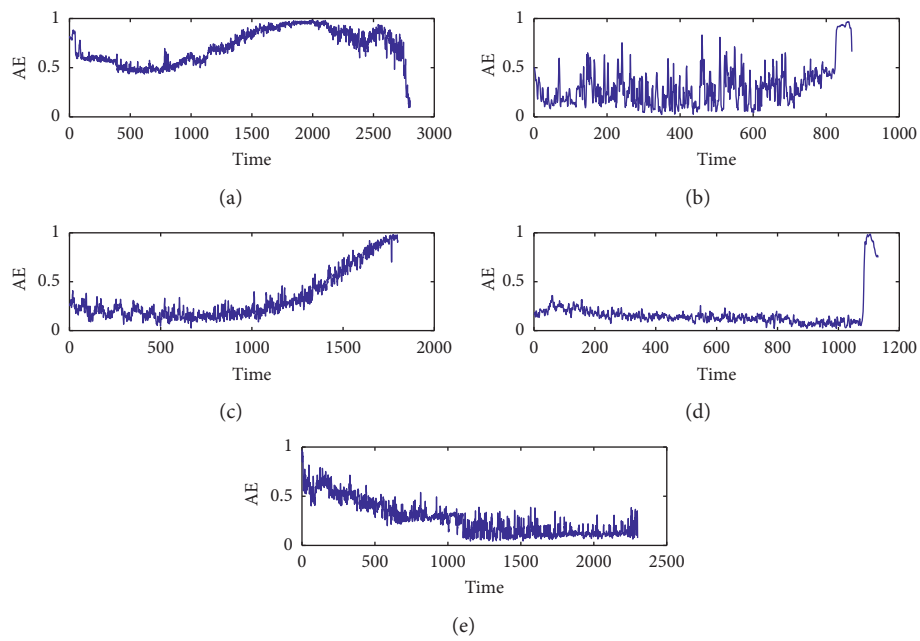

Figure 29: CVs for bearings 11–15 by using AE. (a) Bearing 11. (b) Bearing 12. (c) Bearing 13. (d) Bearing 14. (e) Bearing 15.

Table 2: *Mon* result of different models by using bearing 12 dataset.

Model	*Mon*
SDAE-CFS	0.9310
SAE-CFS	0.0288
EEMD-SVD-k-medoids	0.0161
EEMD-SVD-k-means	0.0092
EEMD-SVD-FCM	0.0230
RMS	0.0253
Kurtosis	0.0207
AE	0.0196
PE	0.0081
SHE	0.0334

value by using two adjacent HI data points is greater than 0, then the HI curve rises monotonically and vice versa. If the curve rises and falls monotonically within short spans, then the HI curve has significant noise and oscillations. The calculation of *Mon* is as follows:

$$\begin{aligned} Mon &= \left|\frac{\mathrm{DFA}}{t-1} - \frac{\mathrm{DFB}}{t-1}\right| = \left|\frac{\mathrm{DFA}-\mathrm{DFB}}{t-1}\right|, \\ \mathrm{DFA} &= \text{number of } \mathrm{dF} > 0, \\ \mathrm{DFB} &= \text{number of } \mathrm{dF} < 0, \\ \mathrm{dF} &= \frac{\mathrm{HI}_t - \mathrm{HI}_{t-1}}{\Delta t}, \quad 2 \le t \le N, \end{aligned} \tag{10}$$

where dF is the difference between any two adjacent HI points. The closer *Mon* is to 1, the better the performance is [41–53]. We take bearing 12 as an example; the *Mon* result of different models is shown in Table 2.

Table 2 shows that the *Mon* of SDAE-CFS is higher than that of other models. The SDAE sets the input data of each hidden layer according to the denoising rate and then reconstructs the input data. Therefore, the SDAE can denoise the extracted HI curve well.

5. Conclusions

The original vibrations over the entire life of the bearings under different conditions were used as the input for the SAE and SDAE to extract the degradation trend and directly reduce the dimension of the extracted feature to two without PCA. The results demonstrate that the SDAE was more robust and had better feature extraction performance than the SAE. CFS was then implemented to find the available clustering center point, which was used to assess the health status through the CV index without data labeling or prior knowledge. To verify the performance of the proposed method, it was compared with other combination models, such as EEMD-SVD-k-medoids/k-means/FCM, RMS, kurtosis, SHE, AE, PE, and PCA. The experimental results confirmed that the SDAE-CFS was more robust and stable than the other models. Finally, we also use the *Mon* index to evaluate the denoising effect of different models. The larger the value of *Mon*, the smaller the noise of the extracted HI curve, and vice versa. The model proposed in the article can significantly increase the value of *Mon* by a quantitative level, as shown in Table 2. SDAE-CFS can improve the value of *Mon* from two decimal places to one decimal point.

Data Availability

Previously reported bearing data were used to support this study and are available at https://ti.arc.nasa.gov/tech/dash/groups/pcoe/prognostic-data-repository/.

Conflicts of Interest

The authors declare that they have no financial and personal relationships with other people or organizations that can inappropriately influence their work. There is no professional or other personal interest of any nature or kind in any product, service, and/or company that could be construed as influencing the position presented in, or the review of, the manuscript.

Acknowledgments

This research was partly supported by the Green Intelligent Inland Ship Innovation Programme amd the National Natural Science Foundation of China (grant no. 51909199).

References

[1] W. Huang, J. Cheng, and Y. Yang, "Rolling bearing fault diagnosis and performance degradation assessment under variable operation conditions based on nuisance attribute projection," *Mechanical Systems and Signal Processing*, vol. 114, no. 1, pp. 165–188, 2019.

[2] A. Heng, A. C. C. Tan, J. Mathew, N. Montgomery, D. Banjevic, and A. K. S. Jardine, "Intelligent condition-based prediction of machinery reliability," *Mechanical Systems and Signal Processing*, vol. 23, no. 5, pp. 1600–1614, 2009.

[3] I. El-Thalji and E. Jantunen, "A summary of fault modelling and predictive health monitoring of rolling element bearings," *Mechanical Systems and Signal Processing*, vol. 60, pp. 252–272, 2015.

[4] A. Rai and S. H. Upadhyay, "A review on signal processing techniques utilized in the fault diagnosis of rolling element bearings," *Tribology International*, vol. 96, pp. 289–306, 2016.

[5] T. Williams, X. Ribadeneira, S. Billington, and T. Kurfess, "Rolling element bearing diagnostics in run-to-failure lifetime testing," *Mechanical Systems and Signal Processing*, vol. 15, no. 5, pp. 979–993, 2001.

[6] P. W. Tse and D. Wang, "State space formulation of nonlinear vibration responses collected from a dynamic rotor-bearing system: an extension of bearing diagnostics to bearing prognostics," *Sensors*, vol. 17, no. 2, pp. 1–16, 2017.

[7] Z. Shen, X. F. Chen, Z. J. He et al., "Remaining life predictions of rolling bearing based on relative features and multivariable support vector machine," *Journal of Mechanical Engineering*, vol. 49, no. 2, pp. 183–189, 2013.

[8] Y. Lei, N. Li, and J. Lin, "A new method based on stochastic process models for machine remaining useful life prediction," *IEEE Transactions on Instrumentation and Measurement*, vol. 65, no. 12, pp. 2671–2684, 2016.

[9] B. Y. Kosasih, W. Caesarendra, K. Tieu, A. Widodo, C. A. S. Moodie, and A. K. Tieu, "Degradation trend estimation and prognosis of large low speed slewing bearing lifetime," *Applied Mechanics and Materials*, vol. 493, pp. 343–348, 2014.

[10] Y. Lei, M. J. Zuo, Z. He, and Y. Zi, "A multidimensional hybrid intelligent method for gear fault diagnosis," *Expert Systems with Applications*, vol. 37, no. 2, pp. 1419–1430, 2010.

[11] S. M. Pincus, "Approximate Entropy as a measure of system complexity," *Proceedings of the National Academy of Sciences*, vol. 88, no. 6, pp. 2297–2301, 1991.

[12] S. Pincus, "Approximate entropy (ApEn) as a complexity measure," *Chaos: An Interdisciplinary Journal of Nonlinear Science*, vol. 5, no. 1, pp. 110–117, 1995.

[13] R. Yan and R. X. Gao, "Approximate entropy as a diagnostic tool for machine health monitoring," *Mechanical Systems and Signal Processing*, vol. 21, no. 2, pp. 824–839, 2007.

[14] T. Ye, Z. L. Wang, and L. Chen, "Self-adaptive bearing fault diagnosis based on permutation entropy and manifold-based dynamic time warping," *Mechanical Systems and Signal Processing*, vol. 114, no. 1, pp. 658–673, 2019.

[15] R. Yan, Y. Liu, and R. X. Gao, "Permutation entropy: a nonlinear statistical measure for status characterization of rotary machines," *Mechanical Systems and Signal Processing*, vol. 29, pp. 474–484, 2012.

[16] N. E. Huang, Z. Shen, S. R. Long et al., "The empirical mode decomposition and the Hilbert spectrum for nonlinear and non-stationary time series analysis," *Proceedings of the Royal Society of London. Series A: Mathematical, Physical and Engineering Sciences*, vol. 454, no. 1971, pp. 903–995, 1998.

[17] Z. Wu and N. E. Huang, "Ensemble empirical mode decomposition: a noise-assisted data analysis method," *Advances in Adaptive Data Analysis*, vol. 1, no. 1, pp. 1–41, 2009.

[18] H. Qiu, J. Lee, J. Lin, and G. Yu, "Wavelet filter-based weak signature detection method and its application on rolling element bearing prognostics," *Journal of Sound and Vibration*, vol. 289, no. 4-5, pp. 1066–1090, 2006.

[19] X. S. Lou and K. A. Loparo, "Bearing fault diagnosis based on wavelet transform and fuzzy inference," *Mechanical Systems and Signal Processing*, vol. 18, pp. 1077–1095, 2014.

[20] Z. Wang, C. Lu, Z. Wang, H. Liu, and H. Fan, "Fault diagnosis and health assessment for bearings using the Mahalanobis-Taguchi system based on EMD-SVD," *Transactions of the Institute of Measurement and Control*, vol. 35, no. 6, pp. 798–807, 2013.

[21] A. Rai and S. H. Upadhyay, "Bearing performance degradation assessment based on a combination of empirical mode decomposition and K-medoids clustering," *Mechanical Systems and Signal Processing*, vol. 93, pp. 16–29, 2017.

[22] Z. Wei, Y. Wang, S. He, and J. Bao, "A novel intelligent method for bearing fault diagnosis based on affinity propagation clustering and adaptive feature selection," *Knowledge-Based Systems*, vol. 116, pp. 1–12, 2017.

[23] P. W. Tse and D. Wang, "Enhancing the abilities in assessing slurry pumps' performance degradation and estimating their remaining useful lives by using captured vibration signals," *Journal of Vibration and Control*, vol. 23, no. 12, pp. 1925–1937, 2017.

[24] P. Vincent, H. Larochelle, and I. Lajoie, "Stacked denoising autoencoders: learning useful representations in a deep network with a local denoising criterion," *Journal of Machine Learning Research*, vol. 11, pp. 3371–3408, 2010.

[25] P. Vincent, H. Larochelle, and Y. Bengio, "Extracting and composing robust features with denoising autoencoders," *International Conference*, pp. 1096–1103, 2008.

[26] J. Feng, Y. G. Lei, and L. Jing, "Deep neural networks: a promising tool for fault characteristic mining and intelligent diagnosis of rotating machinery with massive data," *Mechanical Systems and Signal Processing*, vol. 72-73, pp. 303–315, 2016.

[27] F. Y. Lv, C. L. Wen, and M. Q. Liu, "Weighted time series fault diagnosis based on a stacked sparse autoencoder," *Journal of Chemometrics*, vol. 31, no. 9, pp. 1–16, 2017.

[28] Y. Qi, C. Shen, D. Wang, J. Shi, X. Jiang, and Z. Zhu, "Stacked sparse autoencoder-based deep network for fault diagnosis of

rotating machinery," *IEEE Access*, vol. 5, pp. 15066–15079, 2017.

[29] F. Xu, W. t. P. Tse, and Y. L. Tse, "Roller bearing fault diagnosis using stacked denoising autoencoder in deep learning and Gath-Geva clustering algorithm without principal component analysis and data label," *Applied Soft Computing*, vol. 73, pp. 898–913, 2018.

[30] B. Leng, S. Guo, X. Zhang, and Z. Xiong, "3D object retrieval with stacked local convolutional autoencoder," *Signal Processing*, vol. 112, pp. 119–128, 2015.

[31] Y. Liu, X. Feng, and Z. Zhou, "Multimodal video classification with stacked contractive autoencoders," *Signal Process*, vol. 120, pp. 761–766, 2015.

[32] J. Li, Z. Struzik, L. Zhang et al., "Feature learning from incomplete EEG with denoising autoencoder," *Neurocomputing*, vol. 165, pp. 23–31, 2014.

[33] Y. Pan, J. Chen, and X. Li, "Bearing performance degradation assessment based on lifting wavelet packet decomposition and fuzzy c-means," *Mechanical Systems and Signal Processing*, vol. 24, no. 2, pp. 559–566, 2010.

[34] A. Rodriguez and A. Laio, "Clustering by fast search and find of density peaks," *Science*, vol. 344, no. 6191, pp. 1492–1496, 2014.

[35] Q. C. Zhang, C. S. Zhu, L. T. Yang, Z. K. Chen, L. Zhao, and P. Li, "An incremental CFS algorithm for clustering large data in industrial internet of things," *IEEE Transactions on Industrial Informatics*, vol. 13, no. 3, pp. 1193–1201, 2017.

[36] F. Xu, Y. J. Fang, R. Zhang, Z. M. Kong, and R. L. Tang, "A fault diagnosis method combined with ensemble empirical mode decomposition, base-scale entropy and clustering by fast search algorithm for roller bearings," *Journal of Vibroengineering*, vol. 18, no. 7, pp. 4472–4490, 2016.

[37] C. C. Tan and C. Eswaran, "Using autoencoders for mammogram compression," *Journal of Medical Systems*, vol. 35, no. 1, pp. 49–58, 2011.

[38] P. Nectoux, R. Gouriveau, and K. Medjaher, *PRONOSTIA: An Experimental Platform for Bearings Accelerated Life Test IEEE International Conference on Prognostics and Health Management*, Denver, CO, USA, 2012.

[39] J. Dolz, N. Betrouni, M. Quidet et al., "Stacking denoising auto-encoders in a deep network to segment the brainstem on MRI in brain cancer patients: a clinical study," *Computerized Medical Imaging and Graphics*, vol. 52, pp. 8–18, 2016.

[40] C. Bandt and B. Pompe, "Permutation entropy: a natural complexity measure for time series," *Physical Review Letters*, vol. 88, pp. 174102–174111, 2002.

[41] K. Javed, R. Gouriveau, N. Zerhouni, and P. Nectoux, "Enabling health monitoring approach based on vibration data for accurate prognostics," *IEEE Transactions on Industrial Electronics*, vol. 62, no. 1, pp. 647–656, 2015.

[42] Z. Wu, Q. Li, W. W. Wu, and M. B. Zhao, "Crowdsourcing model for energy efficiency retrofit and mixed-integer equilibrium analysis," *IEEE Transactions on Industrial Informatics*, vol. 16, no. 7, pp. 4512–4524, 2019.

[43] Z. Kong, S. Yang, D. Wang, L. Hanzo, and H. Z. Lajios, "Robust beamforming and jamming for enhancing the physical layer security of full duplex radios," *IEEE Transactions on Information Forensics and Security*, vol. 14, no. 12, pp. 3151–3159, 2019.

[44] J. Lai and X. Lu, "Nonlinear mean-square power sharing control for ac microgrids under distributed event detection," *IEEE Transactions on Industrial Informatics*, vol. 1, 2020.

[45] Z. C. Dong, M. Tian, R. L. Tang, X. Li, and J. G. Lai, "Improving the robustness of spatial networks by link addition: more and dispersed links perform better," *Nonlinear Dynamics*, vol. 100, pp. 2287–2298, 2020.

[46] Z. Dong, M. Tian, Y. Lu, J. Lai, R. Tang, and X. Li, "Impact of core-periphery structure on cascading failures in interdependent scale-free networks," *Physics Letters A*, vol. 383, no. 7, pp. 607–616, 2019.

[47] F. Xu, Z. L. Huang, F. F. Yang, D. Wang, and K. L. Tsui, "Constructing a health indicator for roller bearings by using a stacked auto-encoder with an exponential function to eliminate concussion," *Applied Soft Computing*, vol. 89, Article ID 106119, 2020.

[48] F. Xu, Y. J. Fang, and R. Zhang, "PCA-GG rolling bearing clustering fault diagnosis based on EEMD fuzzy entropy," *Computer Integrated Manufacturing System*, vol. 22, no. 11, pp. 2631–2642, 2016.

[49] R. Tang, X. Li, and J. Lai, "A novel optimal energy-management strategy for a maritime hybrid energy system based on large-scale global optimization," *Applied Energy*, vol. 228, pp. 254–264, 2018.

[50] J. Lai, X. Lu, X. Yu, and A. Monti, "Stochastic distributed secondary control for ac microgrids via event-triggered communication," *IEEE Transactions on Smart Grid*, vol. 11, no. 4, pp. 2746–2759, 2020.

[51] R. Tang, Z. Wu, and X. Li, "Optimal operation of photovoltaic/battery/diesel/cold-ironing hybrid energy system for maritime application," *Energy*, vol. 162, pp. 697–714, 2018.

[52] J. Lai, X. Lu, X. Yu, and A. Monti, "Cluster-oriented distributed cooperative control for multiple AC microgrids," *IEEE Transactions on Industrial Informatics*, vol. 15, no. 11, pp. 5906–5918, 2019.

[53] J. G. Lai, X. Q. Lu, A. Monti, and G. P. Liu, "Stochastic distributed pinning control for co-multi-inverter networks with a virtual leader," *IEEE Transactions on Circuits and Systems-II*, vol. 67, no. 10, pp. 2094–2098, 2019.

Hindawi
Complexity
Volume 2020, Article ID 8840421, 14 pages
https://doi.org/10.1155/2020/8840421

Research Article

RLS Impedance Intelligence Control Algorithm for Wire Peeler of Robot in Complex Power Networks

Xianjin Xu,[1] **Shichao Hu**,[1] **Yu Yan**,[2] **Yuhang Yang**,[1] **Zhiyong Yang**,[1] **and Haoda Chen**[1]

[1]*College of Mechanical Engineering, Hubei University of Technology, Wuhan 430068, China*
[2]*State Grid of Hunan Electric Power Company Maintenance Company, Changsha 410004, China*

Correspondence should be addressed to Xianjin Xu; xxjoyjn@126.com

Received 20 August 2020; Revised 20 September 2020; Accepted 13 October 2020; Published 29 October 2020

Academic Editor: Ruoli Tang

Considering the wire core which is easily damaged because of the instability of the power distribution robot during the process of peeling the insulation layer, we have proposed a cutting force tracking control algorithm based on impedance control that is suitable for the end peeling instrument. At present, the task requirement of sudden changes about environment stiffness cannot be accomplished by many impedance control approaches due to the complexity of working environment stiffness about power distribution robot; then, the Recursive Least Square (RLS) method was introduced into the impedance control algorithm to identify the cable insulation layer and cable core stiffness online to achieve accurate and stable tracking of the cutting force. Furthermore, the impedance control of peeling cable insulation layer and the proposed RLS method were simulated and tested contrastively, and the high-voltage cable peeling experiment was performed. The results of simulation and experiment showed that the force control algorithm based on RLS parameter identification still has good force tracking performance during the environment stiffness changes suddenly, and the steady-state error approaches zero, demonstrating the feasibility and effectiveness of the RLS impedance control algorithm, which has important practical significance for improving power distribution efficiency.

1. Introduction

The role of the power distribution robot is to peel the cable insulation layer of the transmission wire and guided current wire in the field of power networks in order to fulfill the parallel connection between the guided current wire and the main high-voltage transmission wire. But two situations usually occur when the end effector of the power distribution robot peels the cable insulation layer due to the complexity of the process, one of which is that the cutting force is so heavy that the wire core is damaged directly by the cutter and the other is that the wire insulation layer cannot be completely removed because of insufficient cutting force, both of which will affect the power distribution effect. It is necessary that the enough and accurate cutting force should be provided by the end effector to improve the power distribution work efficiency; some researchers have tried to design a novel peeler structure to overcome the problem of easy damage to the wire core in terms of structural design; however, the problem of easy damage to the wire core cannot be settled because the accurate cutting force cannot be grasped only through depending on the pure mechanical structure. Considering the fact that the problem cannot be solved purely depending on structural design in the working environment of power distribution robot, some control methods are applied to the wire peeling operation link by many later scholars. The embedded control technology was applied to this field in [1, 2]; it could appropriately reduce the wire core damage rate to a certain extent through combining with embedded control algorithm based on the experiment, but the embedded control algorithm was limited to its low stability and could not be effectively adapted to the working environment of the power distribution robot. The authors in [3, 4] have introduced the master-slave control combined with impedance control method into the operation process of power distribution robot to initially achieve compliant

contact between the end peeler and wire, but the stiffness between the wire core and insulation layer is different whose stiffness parameter cannot be identified by impedance control; especially, when the environment stiffness changes, the stability of impedance control is so poor that the cutting force error biases largely.

As we know, the impedance control was first proposed by the scholar Hogan in [5–8] in order to achieve the purpose of compliance control by adjusting the stiffness parameter of the end effector to obtain the ideal dynamic relationship between position and force, but the control accuracy closely relies on sufficient knowledge on the environment. In real engineering, the cognition of the environment is limited due to the collection of various practical factors, which results in force errors in impedance control; especially, the task requirements cannot be satisfied when the environment stiffness changes suddenly. This paper focuses on the inaccuracy problem of contact force between wire peeler and wire during the peeling process of power distribution robot to propose an impedance force tracking control algorithm based on the Recursive Least Squares (RLS) method of parameter identification, which can achieve stiffness parameter identification between wire core and wire insulation layer to make the cutting force quickly and accurately track the reference force and achieve the compliant peeling of wire insulation and mainly can provide important practical guiding significance for improving the efficiency of power robot.

2. Impedance Control Strategy on Wire Peeler

2.1. The Structure Design of End Peeler. Compared with the complicated and bulky structure of end peeler designed by scientific researchers over the past, the peeler designed in this paper is more flexible and compact, its structure is composed of a cable clamping motor, cable clamping block, and cutting blade, as shown in Figure 1, the inner surface of the clamping block is equipped with oblique thread, a cutting blade is mounted on one side, and the clamping motor rotates forward or backward to separate or close the clamping device. Before operation, the cable clamping motor rotates to separate the cable clamping block and align the thread hole with the cable, then, the clamping motor will rotate toward opposite direction to drive the cable clamping block to close when the cable is clamped, the cutting blade synchronously starts cutting in cable insulation layer, and the depth of the blade cutting in the insulation layer is controlled by force sensor. After the wire clamp block clamps the wire, the rotating motor is controlled to run the drive gear counterclockwise, one side of the drive gear is connected to the cable peeling device which is driven to rotate around the center of the gear, and the cable peeling device clamps the wire, making a circular motion around the central axis of the wire to cut the wire insulation layer, relying on the cutting force to realize the axial feed, and converting the output shaft's rotary motion into the perpendicular circumference motion of the peeling device, which can enhance the smoothness of the peeling device.

2.2. The Design of Cutting Force Impedance Controller. The process of contact between the end peeler of the robot and the cable can be regarded as a second-order dynamic relationship which can be described by the following dynamic equation:

$$M_t\left(X-\ddot{X}_r\right)+B_t\left(\dot{X}-\dot{X}_r\right)+K_t\left(X-X_r\right)=F-F_r, \quad (1)$$

where M_t, B_t, and K_t are the inertia matrix, damping matrix, and stiffness matrix, respectively, which commonly determine the dynamic characteristic, X_r and X are the reference position and actual position of the end peeler, respectively, $\dot{X}_r$ and $\dot{X}$ are the expected velocity and actual velocity, $\ddot{X}_r$ and $\ddot{X}$ are the expected acceleration and actual acceleration, respectively, and F_r and F are the reference contact force and the actual cutting force during the contact between the end peeler and cable. The contact force is zero before the end peeler contacts the wire; this process can achieve position tracking when the end peeler gradually contacts the wire; the impedance controller will generate the correction arguments of position control and combine the desired reference position values to form position control command, which can achieve the purpose of compliant and nondestructive contact between the end peeler and the wire; the entire process can be explained as shown in Figure 2, including the two-subsystem impedance of the end peeler and wire.

The process in which the end peeler is cut into the wire insulation layer can be regarded as a one-dimensional situation, and the force tracking impedance controller can be designed as follows:

$$m_t\left(\ddot{x}-\ddot{x}_r\right)+b_t\left(\dot{x}-\dot{x}_r\right)+k_t\left(x-x_r\right)=f-f_r. \quad (2)$$

We can obtain the transfer function of impedance control after taking Laplace transform to equation (2) in the frequency domain:

$$x_f=\frac{e_f(s)}{m_t s^2+b_t s+k_t}. \quad (3)$$

Equation (3) can be regarded as a low-pass filter; we combine the correction of the position obtained by filtering the force errors with the reference position value to form the position control command:

$$x_d=x_r+x_f. \quad (4)$$

Finally, the obtained position control command is converted into the drive voltage of the servo motor through the position controller. As we know, the proportional link can effectively suppress the system deviation and accelerate the system response in PID domain, and the integral link can eliminate the steady-state deviation in [9–12], so the incremental PI control was taken to use in position control and the incremental PI control algorithm is as follows:

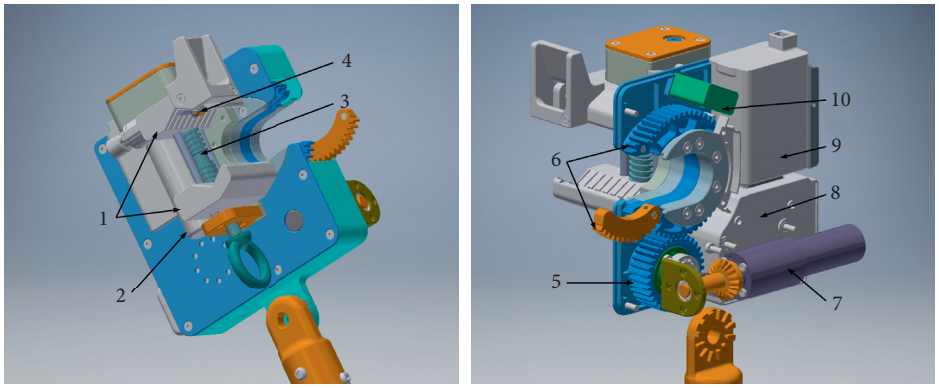

Figure 1: Schematic diagram of cable peeling structure. (1) Cable clamping block; (2) cable clamping motor; (3) bidirectional screw; (4) peeling cutter; (5) driving gear; (6) openable gear; (7) rotatory motor; (8) control system; (9) lithium battery; and (10) force sensor.

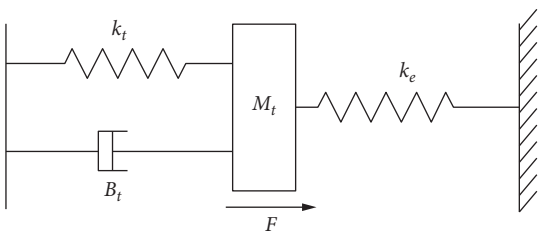

Figure 2: The contact impedance model between cable peeler and wire.

$$\begin{aligned} x(k+1) &= x(k) + \Delta x(k+1), \\ \Delta x(k+1) &= k_p(e(k+1) - e(k)) + k_i e(k+1), \\ e(k+1) &= x_d(k+1) - x(k+1), \\ x_d(k+1) &= x_r(k+1) + \Delta x_f(k+1). \end{aligned} \tag{5}$$

In the above formula, $x(k)$ and $x(k+1)$ represent the (k) th, $(k+1)$ th position output value, $x(n+1)$ represents the $(n+1)$ th increment, k_p and k_i are the proportional gain and integral gain, respectively, $x_r(k+1)$ is the reference position of the peeler during the $(k+1)$ th sampling, and $x_d(k+1)$ represents the desired input value of the position controller.

2.3. The Steady-State Analysis of Impedance System. It is necessary to analyze the stability of the system to improve the force control accuracy of the power distribution robot when the wire insulation layer is being peeled and simultaneously to strengthen the cutting force tracking performance; f is equal to zero in equation (2) before the wire peeler contacts the wire; when the time t approaches ∞, then x approaches x_r, which means that the position tracking is realized, and when the end peeler is in stable contact with the wire, something should be satisfied as follows:

$$x = x_e + \frac{f}{k_e}. \tag{6}$$

Here, x_e and k_e represent the initial contact position and the stiffness of wire, respectively, and x_r represents the reference position value, so

$$\ddot{x}_r = \dot{x}_r = 0. \tag{7}$$

Substituting equation (6) into equation (2), we can obtain the following equation:

$$\begin{aligned} m_t\ddot{e}_f + b_t\dot{e}_f + (k_t + k_e)e_f = m_t\ddot{f}_r + b_t\dot{f}_r + k_t f_r \\ - k_t k_e(x_r - x_e), \end{aligned} \tag{8}$$

where $e_f = f_r - f$, and when f_r is constant, the steady-state deviation can be obtained as

$$e_f(s) = \frac{k_t}{k_e + k_t}\left[f_r + k_e(x_e - x_r)\right] = k_{\text{eq}}\left(\frac{f_r}{k_e} + x_e - x_r\right), \tag{9}$$

where k_{eq} is the equivalent stiffness of end peeler and wire, which is similar to the series connection of two different stiffness springs, shown as follows:

$$k_{\text{eq}} = \left(k_t^{-1} + k_e^{-1}\right)^{-1} = \frac{k_t k_e}{k_t + k_e}. \tag{10}$$

Furthermore, we can obtain the steady-state contact force:

$$f_{st} = f_r - e_f(s) = k_{\text{eq}}\left(\frac{f_r}{k_t} + x_r - x_e\right). \tag{11}$$

Combining equation (9), we can see that when we know the initial contact position x_e and the wire stiffness value k_e, the force deviation can be made to be zero, in which k_e can be estimated by experiment or obtained through experience, and when $x_e = x_r$, according to equation (2), we can know the natural frequency and damping ratio of the second-order system during the contact between end peeler and wire:

$$\omega_n = \sqrt{\frac{(k_t + k_e)}{m_t}},$$
$$\xi = \frac{b_t}{\left(2\sqrt{(k_t + k_e)m_t}\right)}. \tag{12}$$

The stability during the contact between the peeler and the wire depends on the target impedance controller parameters, and the dynamic performance depends on the damping ratio and natural frequency. As we know, the greater the inertia is, the greater the impact of the system is, and the greater the damping is, the smaller the system overshoot is, but the system energy consumption will increase. The smaller the stiffness is, the smaller the steady state of force control will be and the system response will slow. The estimation error Δx_e of x_e satisfies the following formula:

$$-k_t^{-1} f_r < \Delta x_e \leq k_t^{-1} f_r. \tag{13}$$

At this time, the desired cutting force is not affected by the position control error, which has strong robustness to the uncertainty of the system model and the disturbance of the contact force.

3. The Impedance Control Based on RLS Method

3.1. The Deduction of Recursive Least Square Algorithm. When the end effector of the power distribution robot is in contact with the environment, to accurately measure the contact force, we must rely on full cognizance to the environmental stiffness which cannot be measured directly, so we need to obtain the environment stiffness through an indirect method. The Recursive Least Square (RLS) algorithm is more and more used by virtual of its simple principle, a small amount of calculation, and online parameter identification [13–15], which can be effectively integrated with other control algorithms to improve performance [16], so we can use the iterative characteristics of the RLS algorithm to get the stiffness information of environment and further to get the best control effect approaching to ideal situation. In this paper, the RLS algorithm is introduced into impedance control to perform online identification of wire insulation stiffness and core stiffness, which can effectively improve the force control accuracy of power distribution robots during peeling the insulation.

In Section 2.3, the stable contact force deviation e_f (equation (9)) is obtained, and we set the difference between the actual displacement and the assumed displacement to be Δx_e and the difference between the actual environmental stiffness and the assumed environmental stiffness to be Δk_e; then

$$\begin{cases} \Delta x_e = x_e - \hat{x}_e, \\ \Delta k_e = k_e - \hat{k}_e. \end{cases} \tag{14}$$

Further, we can obtain

$$e_s = \frac{k_t}{k_e + k_t}\left(k_e \Delta x_e - \frac{\Delta k_e}{\hat{k}_e} f_r\right). \tag{15}$$

Therefore, the main factors that cause force deviation are environment stiffness and position deviation; usually, the position error is not so large that the main factors causing the deviation are environment stiffness during the operation of the power distribution robot. So we can update the reference position x_r timely by using the method of online parameter identification based on the RLS algorithm to obtain the wire stiffness information and further to achieve accurate control of the cutting force. Let $\varphi(i), \phi(i)$ be the expected output signal and the actual output signal of the impedance controller, respectively; the signal error can be described as

$$e(i) = \phi(i) - \varphi(i). \tag{16}$$

The recursive calculation function can be shown as

$$\begin{cases} L(n) = \sum_{i=1}^{n} e^2(i) = \sum_{i=1}^{n} [\phi(i) - \varphi(i)]^2, \\ e(i) = \phi(i) - Z^T X(i), \end{cases} \tag{17}$$

where Z is the weight function, the forgetting factor $\lambda, \lambda \in (0, 1]$ is introduced when the control system is unstable, and the recursive calculation function is synchronously modified as

$$\begin{aligned} L(n) &= \sum_{i=1}^{n} \lambda^{n-1} e^2(i) = \sum_{i=1}^{n} \lambda^{n-1} [\phi(i) - \varphi(i)]^2 \\ &= \sum_{i=1}^{n} \lambda^{n-1} \left[\phi(i) - Z^T X(i)\right]^2. \end{aligned} \tag{18}$$

To deploy the above function into a power series,

$$L(n) = e^2(n) + \lambda e^2(n-1) + \lambda^2 e^2(n-2) + \cdots + \lambda^{n-1} e^2 + \lambda^n e^2. \tag{19}$$

From the above equation, we can find that the coefficient of the quadratic to error is 1; suppose that λ is so smaller that the energy signal approaches closely the latest quadratic to the error, and the proportion of errors in front of the equation become more and more small, meaning that the parameter identification effect is better. The function of the forgetting factor is to avoid data saturation in the process of obtaining the environmental stiffness parameters [13, 14], and simultaneously, the forgetting factor has been introduced to improve the convergence speed of the algorithm and update the stiffness parameters in time [17, 18], which is beneficial to the reliability of the data. The identified performance generally can be expressed through the minimum variance of the error during the process of parameter identification, and the average errors usually are chosen to be the threshold, when the errors are less than the threshold, meaning that the system gradually approaches stability during this period and the value of forgetting factor λ is finitely close to 1, which can reduce the identification error.

On the other hand, λ is greater than the error threshold, meaning that the system parameters have mutated and λ has approached $\lambda_{\min}$ along a curve. Considering that the value range of forgetting factor is $\lambda \in [0, 1)$ and in order to accelerate the identification speed, the correction principle of forgetting factor is shown in Figure 3 and can be expressed by the following equation:

$$\lambda(t) = 1 - \alpha_1 \left[\frac{\arctan(\alpha_2(|e(t)| - \alpha_3))}{\pi + 0.5} \right]. \tag{20}$$

Here, α_1, α_2, and α_3 have played different roles in the adjustment process of the forgetting factor according to the size of the error; when the error is greater than the threshold α_3, the value of the forgetting factor is $1 - \alpha_1$, which is smaller during the period and can accelerate the process of adjustment to reduce the error. When the error is so small that its value infinitely approaches 1 to make the system stable and the whole adjustment process makes the error stable around α_2 and changes smoothly, the problem of untimely cutting force tracking caused by the excessive variation of the error caused by the sudden change of input signal has been solved according to adjustment of the forgetting factor, and the defect that the ability of parameter correction in RLS becomes weak with the increase of the number of iterations has been settled, which has obvious advantages for the time-varying stiffness parameter identification.

In order to make the identification effect of stiffness parameters better, we need to get the best weight function

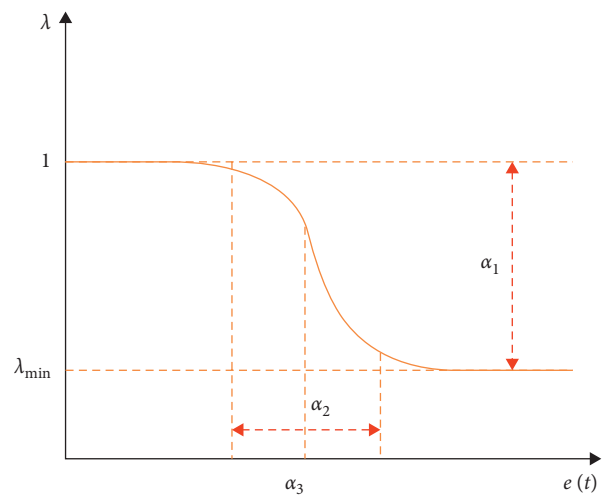

Figure 3: Correction schematic diagram to the forgetting factor.

from theoretical analysis, and if we want to get the best weight function Z, we should minimize the iteration function $Z_k(n)$, so differentiate equation (21) to obtain

$$\frac{\partial L(n)}{\partial Z_k(n)} = -2 \sum_{i=1}^{n} \lambda^{n-1} e(i) X(i) = 0. \tag{21}$$

Further, simplify equation (21) to get

$$\begin{cases} \sum_{i=1}^{n} \lambda^{n-1} \left[\left[\phi(i) - Z^T X(i) \right] X(i) = 0, \\ Z \sum_{i=1}^{n} \lambda^{n-1} X(i)^T X(i) = \sum_{i=1}^{n} \lambda^{n-1} X^T(i) \phi(i). \end{cases} \tag{22}$$

For calculating conveniently, let us define the following equation:

$$\begin{cases} Q(n) = \sum_{i=1}^{n} \lambda^{n-1} X^T(i) X(i), \\ P(n) = \sum_{i=1}^{n} \lambda^{n-1} XT(i) \phi(i). \end{cases} \tag{23}$$

Then equation (22) can be expressed as

$$ZQ(n) = P(n), \tag{24}$$

where $Q(n)$ and $P(n)$ are both functions of n; we can see that Z is a function of n, so there is

$$Z(n) = Q^{-1}(n) P(n) = R(n) P(n). \tag{25}$$

Here, $R(n) = Q^{-1}(n)$, and equation (23) can be denoted as the following iterative form:

$$\begin{cases} Q(n) = \lambda Q(n-1) + X(n) X^T(n), \\ P(n) = \lambda P(n-1) + \phi(n) X(n). \end{cases} \tag{26}$$

Substitute $R(n)$ into equation (26) to get

$$\begin{aligned} R(n) &= \left[\lambda R^{-1}(n-1) + X(n) X^T(n) \right]^{-1} \\ &= \frac{1}{\lambda} \left[R(n-1) - K(n) X^T(n) R(n-1) \right]. \end{aligned} \tag{27}$$

Define the gain $K(n)$ as follows:

$$K(n) = \frac{R(n-1) X(n)}{\lambda + X^T(n) R(n-1) X(n)}. \tag{28}$$

Substitute equations (28) and (26) into equation (25) to get the final expression of weight function:

$$Z(n) = Z(n-1) + K(n) e(n-1). \tag{29}$$

The entire RLS algorithm can be represented as Figure 4 according to the flowchart.

3.2. The Impedance Control Based on RLS Algorithm. The process of contact between the end peeler and the wire is

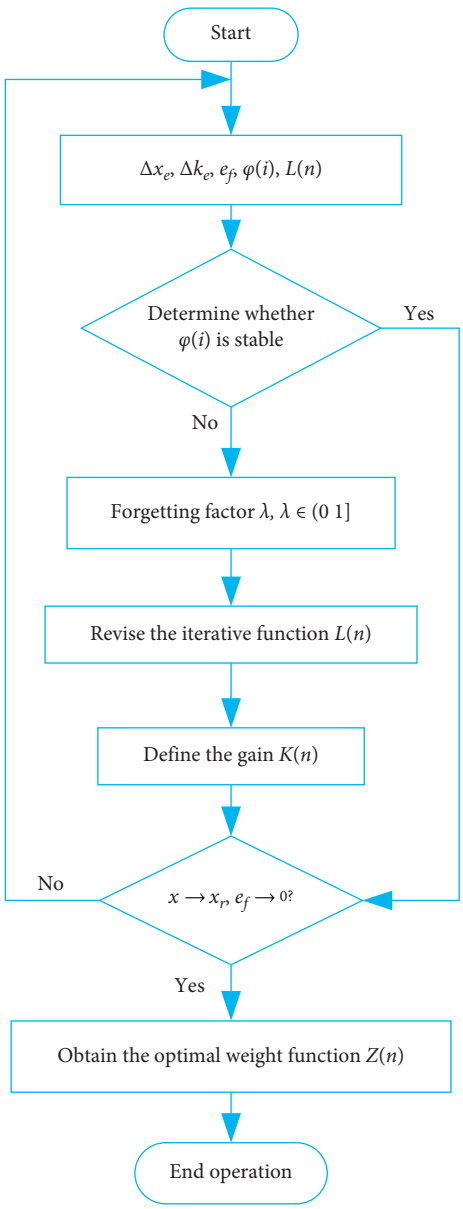

Figure 4: The flowchart of RLS algorithm.

regarded as the action borne force of the spring with stiffness k_e, which can be regarded as a one-dimensional situation where $f = k_e x$, and f is the actual cutting force applied to the wire by the end peeler and being collected by the force sensor, x is the displacement of the end peeler which can be measured by the motor encoder, any set of data (x_t, f_t) is obtained during the sampling process, and $\widehat{k}_e$ is estimated by the RLS algorithm.

So the following relation can be gained:

$$\begin{aligned} \widehat{k}_e(t) &= \left(x_t^T x_t\right)^{-1} x_t^T f_t, \quad (t \in N^*), \\ R_{t+1} &= \frac{R_t}{\left(\lambda_t + x_{t+1}^T x_{t+1}\right)}, \\ \widehat{K}_e(t+1) &= \widehat{K}_e(t) + K_e(t+1)\left(f_{t+1} - \widehat{k}_e(t) x_{t+1}\right), \\ k_e(t+1) &= R_{t+1} x_{t+1}. \end{aligned} \tag{30}$$

The RLS algorithm is applied to the wire peeling process of the power distribution robot; in order to reduce the data error, the average value obtained during the sampling period is used to be the actual value of the cutting force to the wire peeler. When the errors where the values are compared with expected reference force to get are less than 0.01, the RLS impedance system can be regarded as stable, the calculation based on the Recursive Least Square method is being stopped, and the updating algorithm of reference position to the cutting force based on RLS parameter identification can be obtained:

$$\begin{aligned} x_r(t+1) &= \frac{f_r}{k_e(t+1)} + x_e, \\ x_d(t+1) &= \frac{f_r}{k_e(t+1)} + x_e + x_f. \end{aligned} \tag{31}$$

The entire principle of impedance control process based on RLS algorithm can be described by the following impedance control system diagram frame shown in Figure 5.

4. Simulation Analysis

The power distribution robot is taken to be research object in this paper to consider the problem of the unstable cutting force which is produced by the end peeler and the wire during the peeling process, and we have proposed an impedance control algorithm based on Recursive Least Square (RLS) method of parameter identification to achieve a smooth contact between the peeler and wire. To verify whether the algorithm can achieve stable tracking of the cutting force in the case of sudden changes to environmental stiffness, the algorithm of each controller is written and sealed in the Simulink environment.

4.1. Simulation of Impedance Control. In order to make the response speed of each controller the best and the system overshoot and the steady-state error the lowest, we have run and debugged the simulation system many times, and the parameters are set to be $m_t = 1, b_t = 120\,\mathrm{N/(m/s)}, k_t = 800\,\mathrm{N/m}, k_p = 4.07$, and $k_i = 2.38$, respectively, which can refer to the effective literature [19, 20], the stiffness of wire to be $k_e = 1000\,\mathrm{N/m}$, and the equivalent stiffness of system to be $k_{\mathrm{eq}} = 444\,\mathrm{N/m}$. Considering that the wire insulation layer is generally plastic and the wire core is metal whose stiffness is different, when carrying out impedance simulation, we perform the tracking simulation including the constant force

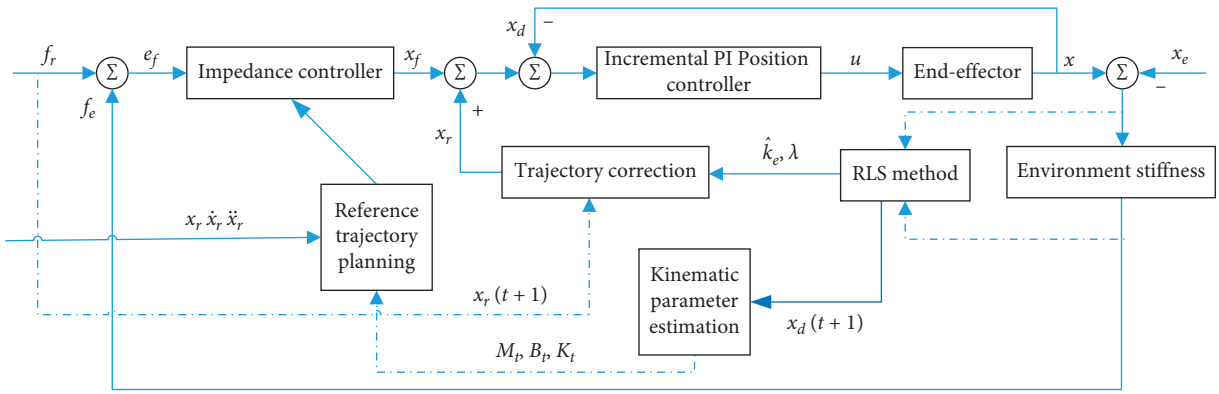

Figure 5: The block diagram of RLS impedance control system.

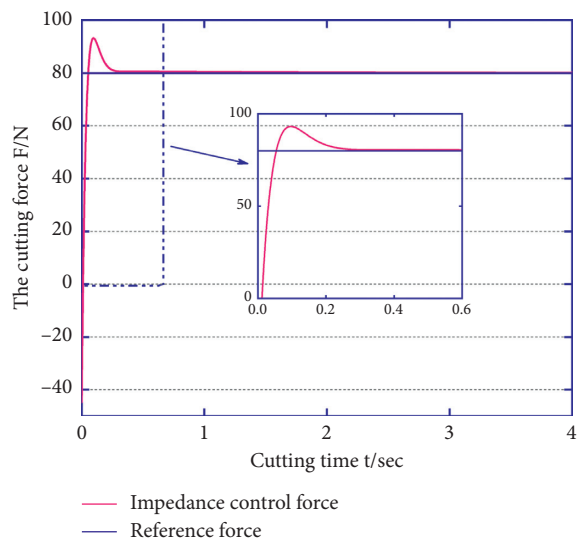

Figure 6: The response curve of constant force tracking.

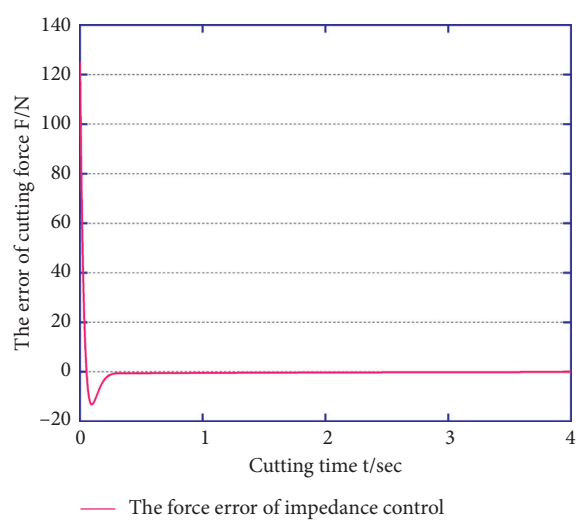

Figure 7: The error curve of constant force tracking.

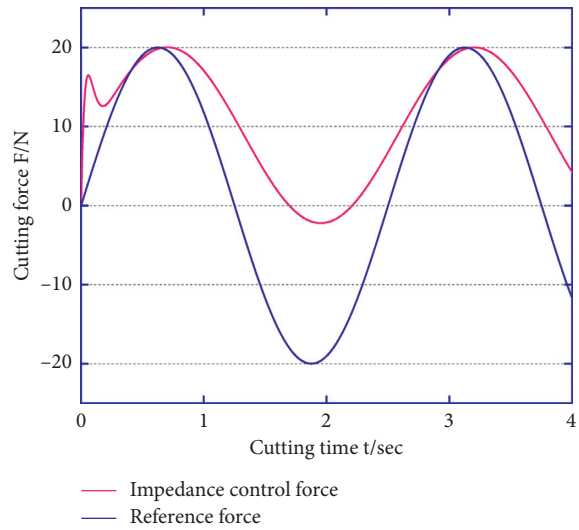

Figure 8: The response curve of sine force tracking.

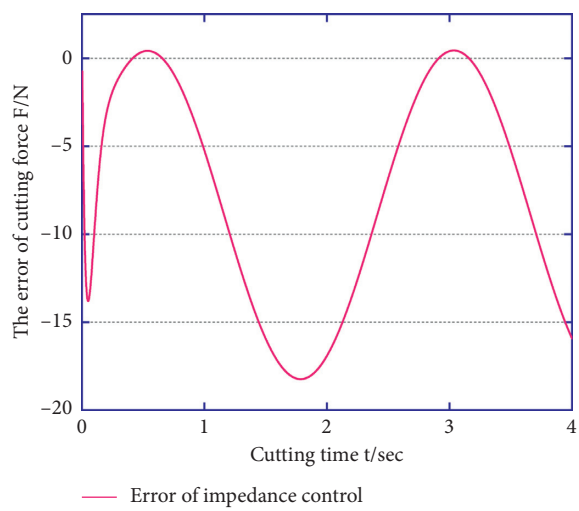

Figure 9: The error curve of sine force tracking.

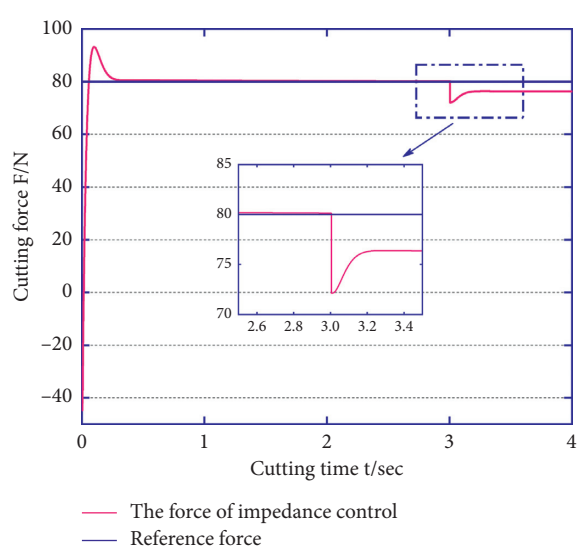

Figure 10: The constant force tracking curve on mutated stiffness.

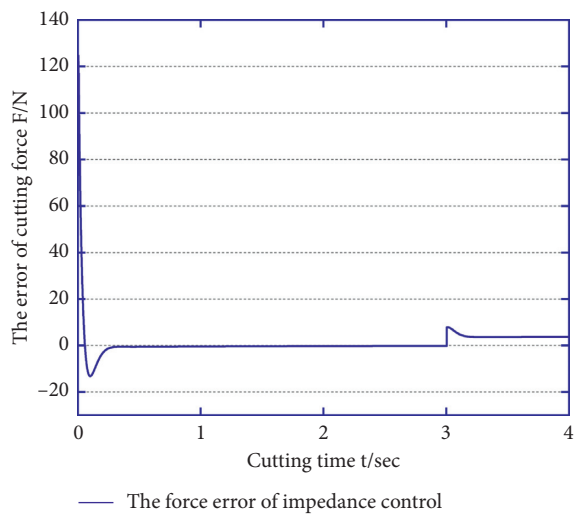

Figure 11: The curve of constant force tracking on mutated stiffness.

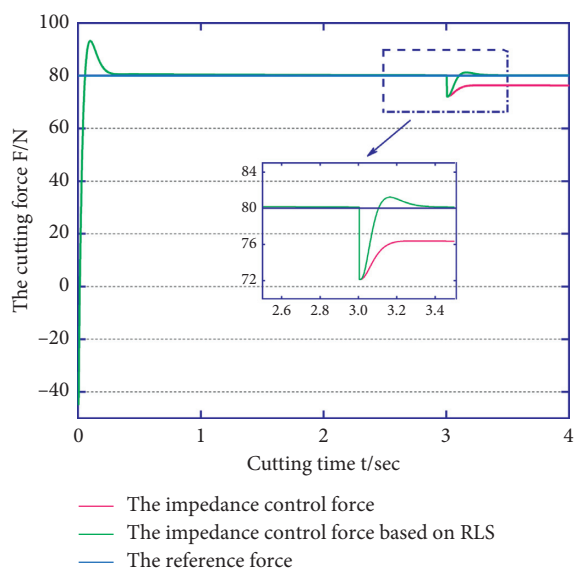

Figure 12: The constant force tracking response curve of RLS on mutated stiffness.

$F = 80\,\mathrm{N}$ and the sine force $F = 20\sin(0.8\pi)$ whose amplitude is 20 and frequency is 0.4 Hz, respectively, assuming that the environment stiffness mutates suddenly after simulating 3 s and the mutated environment stiffness is $k_e' = 900\,\mathrm{N/m}$, setting the total simulation time to be 4 s, the force sampling time to be 1 mm, and the initial position of the peeler to be 0.05 mm; the simulation results can be obtained and shown as in Figures 6–11.

4.2. The Impedance Control Based on RLS Algorithm. In order to verify that the RLS algorithm still has good force tracking performance when the environment stiffness changes suddenly, the impedance control algorithm of the power distribution robot is comparatively simulated under the same conditions, the parameters of each controller are set to be the same as in Section 3.1, the forgetting factor which belongs to Recursive Least Square method is set to be $\lambda = 0.975$, and the following simulation results are obtained as shown in Figures 12–17.

It can be seen from the simulation results that the impedance control based on RLS can respond quickly and stably in a relatively short period of time before and after the environmental stiffness mutates, and the error is always approaching zero whether it is a constant force tracking or a sine force tracking, which should attribute

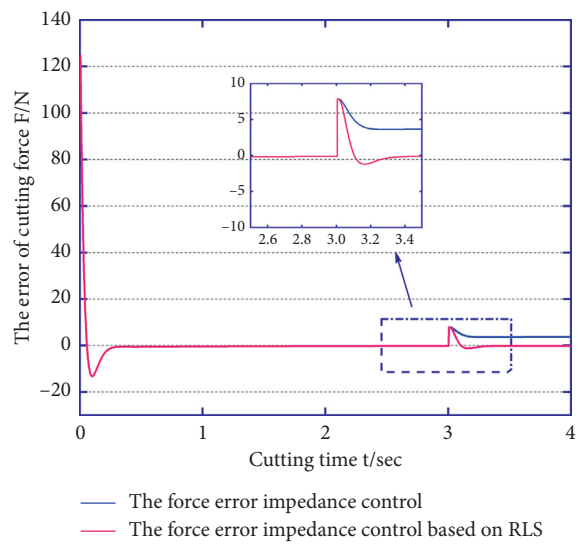

Figure 13: The constant force tracking error curve of RLS on mutated stiffness.

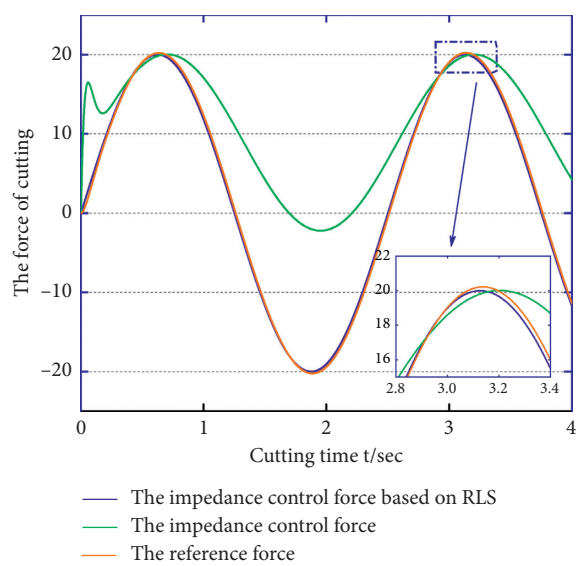

Figure 14: The response curve of sine force based on RLS.

to the superiority of the RLS impedance control algorithm to a certain extent; it can reflect the feasibility and effectiveness of the impedance control algorithm based on RLS, compared with the impedance control algorithm of the peeling link in the power distribution robot operation. On the contrary, compared with the simulation results of impedance control in Figures 10 and 11, we can know that impedance control can only complete certain tasks without any mutated environmental stiffness, but it is difficult to complete tasks when the environmental stiffness changes suddenly that is because ordinary impedance control cannot identify the environmental stiffness.

5. Experiment

When performing the peeling experiment of the robot's high-voltage wire, we firstly select the commonly used wire whose main core is steel and the subordinate material is an aluminum strand in the 10 kV distribution networks (GB/T1179-2008: round and overhead wire with concentric strand), and the performance parameters of the high-voltage are shown in Table 1.

The experimental site is shown in Figure 18, and the end peeler has been assembled with the end flange of the UR10e, which is a collaborative 6-axis robot to verify the

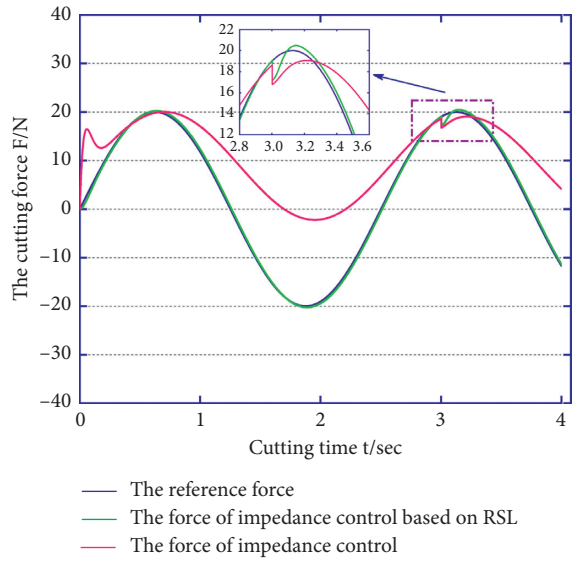

Figure 15: The sine force tracking response curve based on RLS of mutated stiffness.

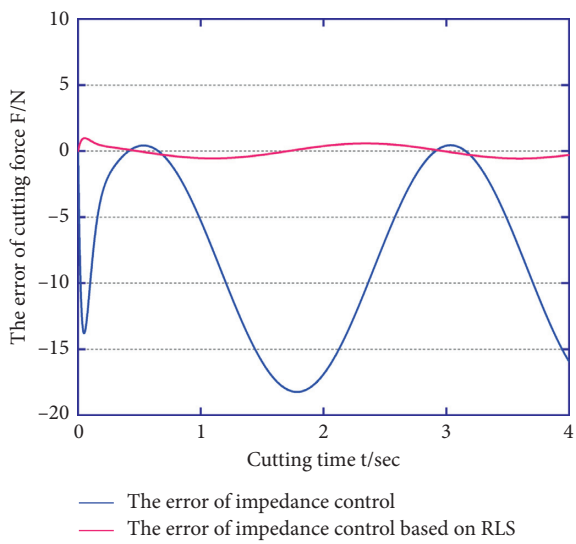

Figure 16: The sine force tracking error curve of RLS.

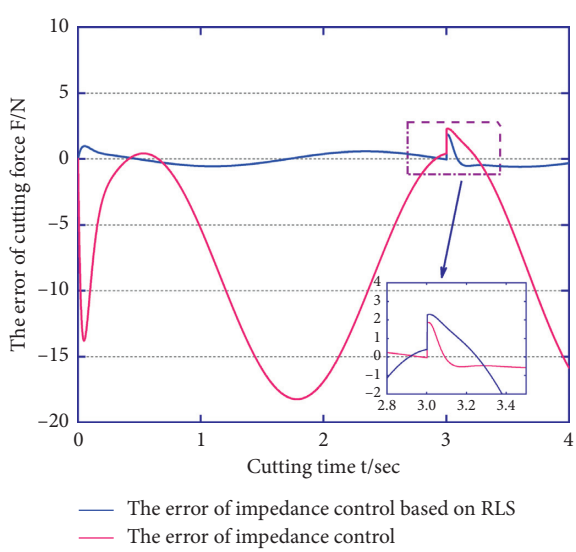

Figure 17: The sine force tracking error curve of RLS on mutated stiffness.

Table 1: The performance parameter of high-voltage wire.

Normal cross-section (aluminum/steel)		150/20	
Steel proportion		13%	
Number of single wires	Aluminum		24
	Steel		7
Standard thickness of insulation (mm)		3.4	
Diameter (mm)	Steel core		5.55
	Helix line		16.7
The insulation material		XLPE	
Density of XLPE (g/cm^3)		0.92	
Elastic modulus of XLPE (MPa)		12201	

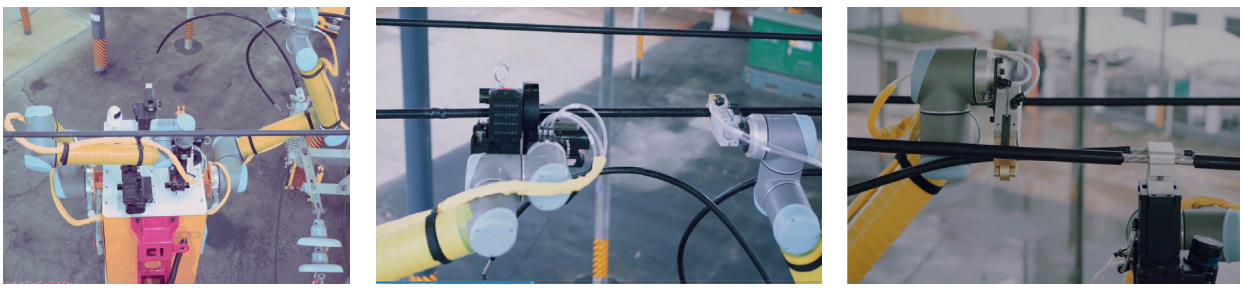

(a) (b) (c)

Figure 18: The RLS impedance control experiment to peeler of power robot. (a) Preparation process before peeling. (b) Process of peeling insulation. (c) Connect the lead current wire.

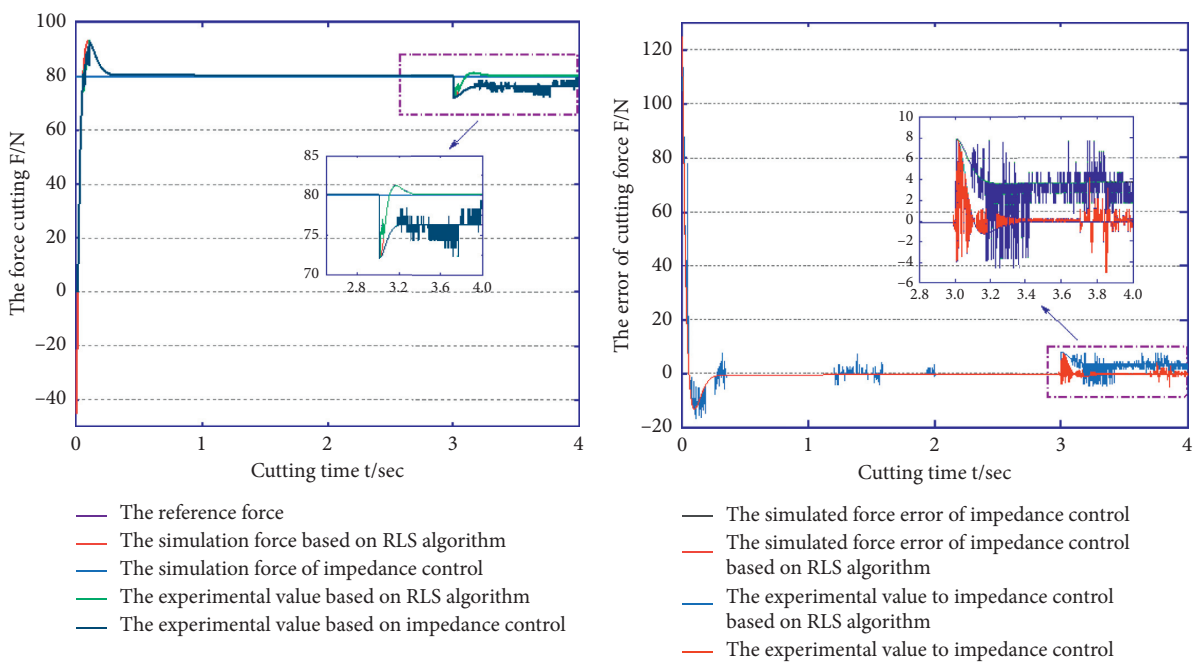

(a) (b)

Figure 19: Comparison of the simulated and experimental values.

peeling effect of the cutting force control algorithm to the peeler during the peeling process of the power distribution networks. In the process of setting the force controller parameters, the sampling interval of force control is set to be $T_s = 1$ ms, the time that is used to peel the wire insulation layer is set to be 4 s, the speed of the wire peeler which moves around the wire axial is 3.75 cm/s, the parameters to the target impedance

controller are set to be the same as the previous chapter during peeling the wire, and the test of impedance control and the test being improved RLS impedance control are carried out, respectively.

5.1. Analysis of Experiment. Comparing the experimental values with simulated values in Figure 19, it can be seen that they are basically identical, and what is most important is that the errors of cutting force, experimental and simulated, especially the force value to impedance control based on RLS algorithm, are so small, approaching zero, which proves that the proposed strategy to impedance control based on RLS algorithm is accurate and feasible; last but not least, the wire can be peeled clearly and not be damaged during the robot peeling experiment, which has important practical significance for improving power distribution efficiency and the development of power distribution networks.

6. Conclusion

Considering the wire core which is easily damaged due to the instability of the power distribution robot in the field of distribution networks operations, we have proposed an impedance force tracking control algorithm based on RLS algorithm, which can effectively identify the stiffness between the insulation layer of wire and wire core during the peeling process and can provide more accurate cutting force for the end peeler.

In order to verify the effectiveness and feasibility of the proposed algorithm, a simulation model based on the RLS impedance tracking control algorithm was built in the Simulink environment. At the same time, both the simulation and experiment on peeling link to the impedance control of the power distribution robot and the proposed impedance control algorithm based on RLS were implemented; comparing the results of simulation and experiment, which showed that the proposed RSL algorithm can still have better force tracking performance in the case of a sudden change to environment stiffness and the steady-state error approached zero, this algorithm based on RLS has high stability and feasibility compared with the traditional impedance control, which can provide theoretical guide and important practical significance for solving the problem that the wire core is easily damaged during the operation of power distribution robot. The impedance control algorithm based on RLS parameter identification will be further optimized and improved in the future; this is a difficult and long-term process.

Nomenclature

RLS: The Recursive Least Square method
$M_t\,(m_t)$: The inertia matrix of system
$B_t\,(b_t)$: The damping matrix of system
$K_t\,(k_t)$: The stiffness matrix of system
$\ddot{X}_r\,(\ddot{x}_r)$: The desired acceleration of peeler
$\dot{X}_r\,(\dot{x}_r)$: The desired velocity of peeler
$\ddot{X}_r\,(\ddot{x}_r)$: The desired displacement of peeler
$F\,(f)$: The contact force of end peeler
$F_{\mathrm{r}}\,(f_{\mathrm{r}})$: The reference force of controller
f_{st}: The steady-state contact force
x_{r}: The reference position
x_e: The initial position of peeler
x_d: The control command of position
k_e: The stiffness of wire
k_{eq}: The equivalent stiffness of system
ξ: The damping ratio of system
ω_n: The natural frequency of system
α: The threshold of parameter λ
λ: The forgetting factor
$L\,(n)$: The recursive calculation function
$Z_k\,(n)$: The optimal weight function.

Data Availability

The experiment data used to support the findings of this study are included within the article.

Conflicts of Interest

The authors declare that there are no conflicts of interest regarding the publication of this paper.

Acknowledgments

The authors state that the research and publication of this paper were supported absolutely by the National Natural Science Foundation of China (Grant no. 61375092).

References

[1] J. Li and D. M. Li, "Development of automatic wire stripper for high voltage live working robot," *Manufacturing Automation*, vol. 15, no. 4, pp. 111–114, 2011.
[2] Y. L. Zhao, H. Qi, F. M. Chen et al., "Development of a special remote wire stripper for high voltage live working robot," *Manufacturing Automation*, vol. 26, no. 2, pp. 117–119, 2010.
[3] X. L. Ma, *Design and Optimization of Working Manipulator of High Voltage Live Working Robot*, Shangdong Jianzhu University, Jinan, China, 2012.
[4] S. Y. Lu and M. C. Fu, "DWR-I remote operation high voltage live working robot," *Journal of Shanghai Jiaotong University*, vol. 6, no. 6, pp. 911–913, 2015.
[5] J. Li, Q. Wei, W. S. Chang et al., "Adaptive force impedance control algorithm based on impedance control," *Robot*, vol. 1, no. 1, pp. 911–913, 1991.
[6] N. Hogan, "Impedance control: an approach to manipulation: Part I-theory," *Journal of Dynamic Systems, Measurement, and Control*, vol. 107, no. 1, pp. 1–7, 1985.
[7] T. Lasky and T. Hsia, "On force-tracking impedance control of robot manipulator," in *Proceeding of the IEEE International*

Conference on Robotics and Automation, pp. 274–280, Sacramento, CA, USA, April 1991.

[8] A. Farhad, "Robust impedance control of manipulators carrying a heavy payload," *Journal of Dynamic Systems, Measurement, and Control*, vol. 11, no. 6, pp. 1–8, 2010.

[9] T. N. Yogyakarta, "Efficient PID controller based hexapod wall following robot," in *Proceedings of the International Conference on Electrical Engineering, Computer Science and Informatics*, Bandung, Indonesia, September 2019.

[10] C. Igncaio, D. P. Mariano, and G. A. Gerardo, "Double Q-PID algorithm for mobile robot control," *Expert System with Application*, vol. 137, no. 12, pp. 292–307, 2019.

[11] C. F. Juang and C. Hsu, "Reinforcement ant optimized fuzzy controller for mobile-robot wall-following control," in *Proceedings of the IEEE Trans. Ind. Electron*, Japan, December 2019.

[12] Y. L. Kiam, A. Heong, and C. Gregory, "PID control system Analysis," *IEEE Transactions on Control Systems Technology*, vol. 13, no. 4, pp. 141–148, 2007.

[13] H. Qian, C. Jiang, Y. K. Pan et al., "Online identification of voltage regulator model based on adaptive forgetting factor RLS algorithm," *Nuclear Power Engineering*, vol. 6, no. 12, pp. 77–80, 2019.

[14] H. Y. Wang, Y. S. Zhang, and G. Zhang, "Impedance on system identification and adaptive control system simulation algorithm," *Control Engineering of China*, vol. 15, no. 9, pp. 77–80, 2008.

[15] Q. Q. Luo, J. H. Su, Z. G. Lin et al., "Parameter identification method of virtual synchronous generator .based on recursive least square method," *Automation of Electric System*, vol. 43, no. 9, pp. 215–220, 2019.

[16] H. B. Li, P. Liu, Q. P. Ren et al., "A self-tuning controller of generalized minimum variance with improved Least-squares algorithm under ASM test," *Machinery Design & Manufacture*, vol. 6, no. 7, pp. 171–173, 2012.

[17] L. Li, Z. Chen, B. W. Wang et al., "Sensorless robot end-effect contact force estimation based on VFF-RLS," *Machinery Design & Manufacture*, vol. 15, no. 9, pp. 77–80, 2017.

[18] H. X. Shen and B. L. Jin, "Permanent magnet synchronous motor forgetting factor recursive least square parameter identification," *Journal of System Simulation*, vol. 9, no. 9, pp. 3404–3410, 2018.

[19] Z. Yang, "Research on parameter regulation of robot impedance control algorithm," *Journal of Zaozhuang University*, vol. 25, no. 2, pp. 89–93, 2008.

[20] M. Kushwah and P. A. Patra, "Tuning PID controller for speed control of DC motor using soft computing techniques–a review," *Advanced Electronic and Electrical Engineering*, vol. 4, no. 2, pp. 141–148, 2014.

Hindawi
Complexity
Volume 2020, Article ID 3102729, 15 pages
https://doi.org/10.1155/2020/3102729

Research Article

Joint Virtual Energy Storage Modeling with Electric Vehicle Participation in Energy Local Area Smart Grid

Rui-Cheng Dai,[1] Bi Zhao,[1] Xiao-Di Zhang,[1] Jun-Wei Yu,[2] Bo Fan,[3] and Biao Liu[2]

[1]*State Grid Beijing Electric Maintenance Company, Beijing 100080, China*
[2]*State Grid Xinjiang Urumchi Electric Power Supply Company, Urumchi 830011, China*
[3]*Office of Scientific Research and Development Wuhan University, Wuhan 430072, China*

Correspondence should be addressed to Xiao-Di Zhang; 534053362@qq.com

Received 4 July 2020; Revised 17 August 2020; Accepted 12 October 2020; Published 28 October 2020

Academic Editor: Jingang Lai

In this research, the joint virtual energy storage modeling with electric vehicle participation in energy local area Smart Grid is considered. This article first constructs a virtual energy storage model and a joint virtual energy storage model for air conditioning and electric vehicles. Therefore, for the optimization problem of virtual energy storage power, a continuous rolling optimization algorithm to determine the feasible solution of the high-dimensional complex constraint optimization problem is proposed to solve the optimization problem. Finally, the analysis, for example, illustrates the economics of joint virtual energy storage in the Smart Grid. The results prove that air conditioning and electric vehicles have the ability to jointly participate in virtual energy storage, and the comparison proves that joint virtual energy storage can effectively improve the economics of electricity consumption.

1. Introduction

Due to the access of large-scale distributed power equipment, especially the strong randomness of wind power and solar energy, energy storage capacity is of vital importance in the Smart Grid [1–5]. However, batteries are expensive and easily cause pollution [6]. In recent years, a large number of scholars have put forward the concept of virtual energy storage and thus have studied the virtual energy storage with air conditioning participation. The study in [7] analyzes the way of virtual energy storage in the Smart Grid from two aspects: electricity price control and direct control. The study in [8] used the building's heat storage capacity to establish a building-based virtual energy storage system model, by managing the charging (or discharging) power of the virtual energy storage system according to the user's indoor temperature limit and applying it to the microgrid; this literature successfully improved running economy. The study in [9] established a thermodynamic model of air conditioning load with the air conditioning set value as the dependent variable and used it to absorb the strong random distributed new energy power generation equipment output, which improved the energy utilization as well as the stability of the system operation. The study in [10] conducted an in-depth analysis of the direct controllability of some demand-side loads and thus dug into the potential of air conditioning load virtual energy storage. Based on the premise of satisfying the user's comfort requirements, relying on its virtual energy storage to suppress the output of distributed wind turbines with strong randomness, in order to reduce the configuration capacity of energy storage equipment and reduce the cost of energy Internet management regulation, for the controllable load equipment air conditioning, with consideration of its load-adjustable space, the study in [11] established an air conditioning load double-layer optimal scheduling and control model and maximized the interests for both parties through the coordination and optimization between the macrolevel power company and the microlevel direct load control agents. The study in [12–14] improves the economy of energy consumption through the demand response of air conditioning and refrigerator, respectively, on the premise that user comfort can be guaranteed. Although

the virtual energy storage is not explicitly proposed, describing control objects with controllable load and demand response instead, the control method is consistent with that in the research of virtual energy storage.

Furthermore, there are many optimization algorithms applied to multienergy optimization [15, 16] in Smart Grid. In literature [17], a hybrid constraint handling strategy (HCHS) based on nondominated sorting genetic algorithm II (NSGAII) is proposed to deal with the typical constraints, by which the constraint violations can be removed in several steps during the evolutionary process. The study in [1] proposed an artificial shark optimization (ASO) method to remove the limitation of existing algorithms for solving the economical operation problem of microgrid. The study in [18] presents a new metaheuristic optimization algorithm, the firefly algorithm, and an enhanced version of it, called chaos mutation firefly algorithm (CMFA), for solving power economic dispatch problems while considering various power constraints such as valve-point effects, ramp rate limits, prohibited operating zones, and multiple generator fuel options. In literature [19], an improved genetic algorithm is proposed to overcome the obstacle of infeasibility and exhibit better economic dispatch. The study in [20] proposes a new distributed method, namely, the neural-network-based Lagrange multiplier selection (NN-LMS), to prominently reduce the iterations and avoid an oscillation. A calibrated building simulation model was developed in literature [21] and used to assess the effectiveness of demand response strategies under different time-of-use electricity tariffs in conjunction with zone thermal control.

This article first constructs a virtual energy storage model and a joint virtual energy storage model for air conditioning and electric vehicles. Therefore, for the optimization problem of virtual energy storage power, a continuous rolling optimization algorithm to determine the feasible solution of the high-dimensional complex constraint optimization problem is proposed to solve the optimization problem. Finally, the analysis, for example, illustrates the economics of joint virtual energy storage in the Smart Grid.

2. Virtual Energy Storage Modeling with Air Conditioning and Electric Vehicles Participation

2.1. The Overall Structure of Virtual Energy Storage System with Air Conditioning Participation

2.1.1. Physical Model of Virtual Energy Storage with Air Conditioning Participation. For the air conditioning and building virtual energy storage system that relies on temperature for adjustment, the overall structure diagram is shown in Figure 1.

The virtual energy storage of air conditioning and building can be abstracted as a closed-loop system with feedback as shown in Figure 2.

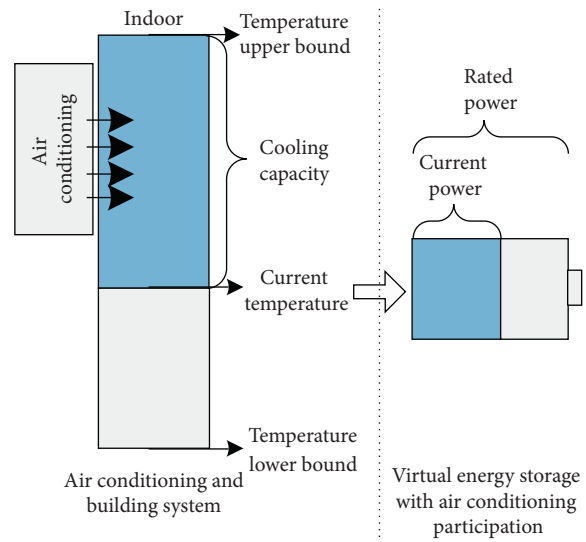

Figure 1: Schematic diagram for virtual energy storage with air conditioning participation.

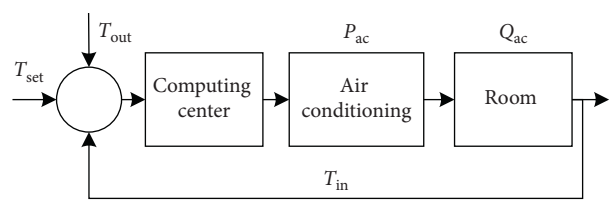

Figure 2: Schematic diagram of a closed-loop system in virtual energy storage with air conditioning participation.

2.1.2. Thermodynamic Model of Thermoelectric Conversion of Air Conditioning. The commonly used thermodynamic equivalent equations [22, 23] are expressed as follows:

$$\frac{\mathrm{d}T_{\mathrm{in}}(t)}{\mathrm{d}t} = \frac{Q_{\mathrm{ac}}(t)}{\mathrm{SC}} + \frac{\left(T_{\mathrm{out}}(t) - T_{\mathrm{in}}(t)\right)}{\mathrm{RSC}}. \tag{1}$$

In equation (1), $T_{\mathrm{in}}(t)$ and $T_{\mathrm{out}}(t)$ are the indoor and outdoor temperatures, respectively, in units of °C; $Q_{\mathrm{ac}}(t)$ is the air conditioning cooling capacity, in units of kW; R is the equivalent thermal resistance, in units of °C/kW; C is the building equivalent heat capacity, in units of kJ/°C; S is the building area. The above environmental parameters all have an impact on the virtual energy storage capacity of the air conditioning.

The relationship between the electric power of the air conditioning equipment and the cooling capacity is as follows:

$$P_{\mathrm{ac}}(t) = \frac{Q_{\mathrm{ac}}(t)}{\eta}. \tag{2}$$

$P_{\mathrm{ac}}(t)$ is the air conditioning power in kW; η is the air conditioning thermoelectric conversion coefficient.

2.2. Important Parameters of Virtual Energy Storage with Air Conditioning Participation

2.2.1. Air Conditioning Virtual Energy Storage Remaining Power and Rated Capacity. When the indoor temperature reaches the comfort zone boundary, if the virtual energy storage remaining power is set to 0, it can be determined that, at time t, the air conditioning virtual energy storage power $S_{\text{ac-virtual}}(t)$ is

$$S_{\text{ac-virtual}}(t) = \begin{cases} \dfrac{\text{SC}\left(T_{\max} - T_{\text{in}}(t)\right)}{\eta}, & \text{summer}, \\ \dfrac{\text{SC}\left(T_{\text{in}}(t) - T_{\min}\right)}{\eta}, & \text{winter}. \end{cases} \tag{3}$$

Besides, the expression of air conditioner virtual energy storage rated capacity $S_{\text{ac-virtual-}N}$ is

$$S_{\text{ac-virtual-}N} = \frac{\text{SC}\left|T_{\max} - T_{\min}\right|}{\eta}. \tag{4}$$

From the above derivation, the relationship among the remaining power of virtual energy storage, the rated capacity, and the equivalent heat capacity of the building as well as the comfortable temperature range of the human body can be clearly shown.

2.2.2. Natural Power Consumption in Virtual Energy Storage with Air Conditioning Participation. For the virtual energy storage with air conditioner participation, when the indoor and outdoor temperatures are different, there is always heat exchange in the air conditioning and building virtual energy storage system. At this time, the air conditioning needs a certain amount of power to maintain the indoor temperature equal to the set temperature, that is, natural power consumption for virtual energy storage of air conditioning:

$$P_{\text{ac}-o}(t) = \frac{Q_{\text{s}}(t)}{\eta} = -\frac{T_{\text{out}}(t) - T_{\text{in}}(t)}{\eta R}. \tag{5}$$

$P_{\text{ac}-o}(t)$ will change according to the change of indoor and outdoor temperatures. When the air conditioner power is $P_{\text{ac}-o}(t)$, the balance of indoor and outdoor temperature can be maintained.

2.2.3. Virtual Charge and Discharge Power of Virtual Energy Storage with Air Conditioning Participation. When the air conditioning is running, in the time period which contains time t, it can be known from equation (2) that its average operating power is $P_{\text{ac}}(t)$. Considering the natural loss of electric energy of the air conditioner virtual energy storage $P_{\text{ac}-o}(t)$, the virtual power of the air conditioning virtual energy storage is shown in the following equation:

$$P_{\text{ac-virtual}}(t) = P_{\text{ac}}(t) - P_{\text{ac}-o}(t). \tag{6}$$

In equation (6), $P_{\text{ac-virtual}}(t)$ is the virtual power of the virtual energy storage that the air conditioning participates in. For equation (1), within a period of time, the temperature in the room where the air conditioner works will change to the set temperature, where τ is the length of the time period. Then, equation (1) has

$$\Delta T_{\text{in}}(t) = T_{\text{set}}(t) - T_{\text{in}}(t), \tag{7}$$

$$\Delta t = \tau. \tag{8}$$

After organization,

$$T_{\text{set}}(t) - T_{\text{in}}(t) = \tau \times \left(\frac{Q_{\text{ac}}(t)}{\text{SC}} + \frac{\left(T_{\text{out}}(t) - T_{\text{in}}(t)\right)}{\text{RSC}}\right). \tag{9}$$

After calculation with respect to equation (2), the relationship between the air conditioning power and the indoor and outdoor temperature as well as the set temperature and the length of the time period in the tth time period is obtained as follows:

$$P_{\text{ac}}(t) = \frac{\text{RSCT}_{\text{set}}(t) - (\text{RSC} - \tau)T_{\text{in}}(t) - \tau T_{\text{out}}(t)}{\tau\eta R}. \tag{10}$$

Equations (2), (5)–(7), and (10) are combined to obtain the relationship between the virtual charging power and temperature of the virtual energy storage as follows:

$$P_{\text{ac-virtual}}(t) = \frac{\text{SC}\left(T_{\text{set}}(t) - T_{\text{in}}(t)\right)}{\tau\eta}. \tag{11}$$

2.3. The Overall Structure of the Virtual Energy Storage System with the Participation of Electric Vehicles. The schematic diagram of virtual energy storage with electric vehicle participation is shown in Figure 3.

The total capacity of the electric vehicle battery is fixed. The battery capacity of each electric vehicle can be used for energy storage in addition to the daily required power. Therefore, the amount of electricity that can be used for virtual energy storage of a single electric vehicle can be determined, and then the total virtual energy storage power of the electric vehicle cluster can be determined.

2.4. Important Parameters of Virtual Energy Storage for Electric Vehicle Participation

2.4.1. Rated Capacity of Virtual Energy Storage for Electric Vehicle Clusters. Let the number of electric vehicles in the ith region at time t be $\text{NE}_i(t)$, the electric vehicles arriving be $\text{NE}_{\text{arrive},i}(t)$, the electric vehicles leaving be $\text{NE}_{\text{leave},i}(t)$, and the number of distributed charging piles be P_i. Then in the period of time t, the maximum controllable number of electric vehicles in the entire area is shown in

$$\begin{aligned} \max \text{NE}_i(t) = {} & \max \text{NE}_i(t-1) + \max \text{NE}_{\text{arrive},i}(t) \\ & - \min \text{NE}_{\text{leave},i}(t). \end{aligned} \tag{12}$$

Then in the area i, the number of electric vehicles participating in the virtual energy storage in the time period t is shown in

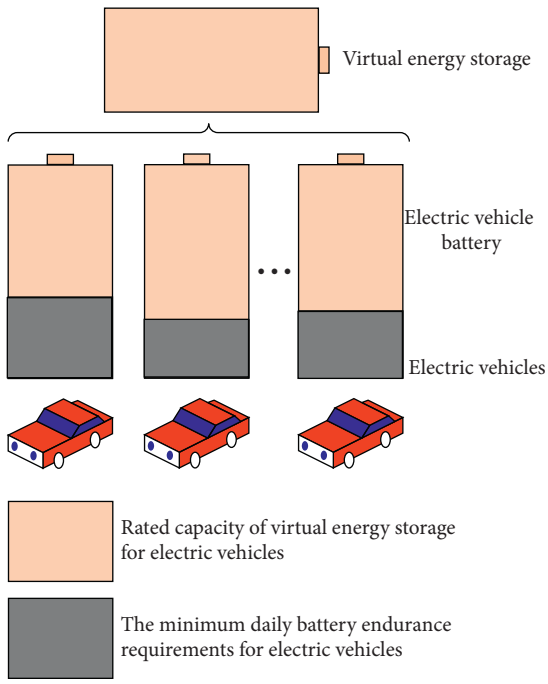

Figure 3: Schematic diagram of the virtual energy storage process of electric vehicles.

$$\mathrm{NE}_i(t) = \min\left(P_i, \max \mathrm{NE}_i(t)\right). \tag{13}$$

Then for the remaining energy in the virtual energy storage at different times in the area i, equation (14) is as follows:

$$S_{\mathrm{EV-virtual},i}(t) = \sum_{j=1}^{\mathrm{NE}_i(t)} \left(W_{j,i}(t) - W_{j,i}^0\right). \tag{14}$$

In equation (14), $S_{\mathrm{EV-virtual},i}(t)$ is the virtual energy storage capacity of electric vehicles in the period of t in the ith region; $W_{j,i}(t)$ is the remaining power of the jth electric vehicle in the ith region in the time period t; $W_{j,i}^0$ is the minimum electric power required for the jth electric car in the ith area, which does not change with time.

Then, the rated energy storage of electric vehicles in the ith area is

$$S_{\mathrm{EV-virtual},i,N}(t) = \sum_{j=1}^{\mathrm{NE}_i(t)} \left(W_{j,i,N}(t) - W_{j,i}^0\right), \tag{15}$$

where $S_{\mathrm{EV-virtual},i,N}(t)$ is the rated energy storage capacity of the virtual energy storage in the time period t and $W_{j,i,N}(t)$ is the rated battery capacity of the jth electric vehicle in the area i in the time period t.

2.4.2. Virtual Charging and Discharging Power for Virtual Energy Storage of Electric Vehicles. The charge and discharge power of the virtual energy storage of electric vehicles can be expressed by the following equation:

$$P_{\mathrm{EV-virtual},i}(t) = P_{\mathrm{EV}} \times \mathrm{NE}_i(t). \tag{16}$$

In equation (16), P_{EV} is the charging and discharging power of the electric vehicle charging and discharging piles, $P_{\mathrm{EV-virtual},i}(t)$ is the virtual charging power of the virtual energy storage of the electric vehicle in the area i with time period which includes time t, and $\mathrm{NE}_i(t)$ is the number of electric vehicles participating in the virtual energy storage in the area i with time period which includes time t.

From the perspective of the electric vehicle's virtual energy storage capacity, its charging power meets

$$P_{\mathrm{EV-virtual},i,\mathrm{in}}(t) = \frac{S_{\mathrm{EV-virtual},i,N}(t) - S_{\mathrm{EV-virtual},i}(t)}{\tau}. \tag{17}$$

From the perspective of the virtual energy storage capacity of electric vehicles, the discharge power meets

$$P_{\mathrm{EV-virtual},i,\mathrm{out}}(t) \frac{S_{\mathrm{EV}v,i}}{\tau}. \tag{18}$$

In equations (17) and (18), τ is the length of the discharge time period.

3. Construction of the Mathematical Model of Joint Virtual Energy Storage Optimization Based on the Rolling Optimization Method

Aiming at the problem of determination of high-dimensional complex constraint decision variables in global optimization of electric vehicle virtual energy storage model, this paper proposes a feasible solution continuous rolling correction algorithm.

Aiming at the global optimization problem of electric vehicle virtual energy storage output power, during the initialization process, due to the complexity of mutual coupling of local constraints and global constraints, the probability of obtaining a feasible solution is low, and initialization cannot be completed. In order to solve the above problems, this paper proposes constructing a standard function to measure the global constraint error that satisfies the local constraint decision variables during initialization and thus continuously revising the decision variables through continuous rolling optimization. Experiments show that this method can effectively improve the initialization efficiency of complex constrained optimization problems with high-dimensional decision variables and then obtain the global optimized output power of electric vehicle virtual energy storage, which verifies the economics of electric vehicle with the combination of virtual energy storage.

3.1. Rolling Optimization Process. For the value of the virtual energy storage power in different time periods, the optimization result of the previous period will affect the virtual energy storage power range in the next period. Drawing on the idea of rolling optimization, the value of virtual energy storage power can be adjusted continuously with the advancement of the sampling time to determine the power of virtual energy storage in each period. The process is shown in Figure 4.

The state in the time period t mainly includes the outdoor temperature and the number of arriving and leaving

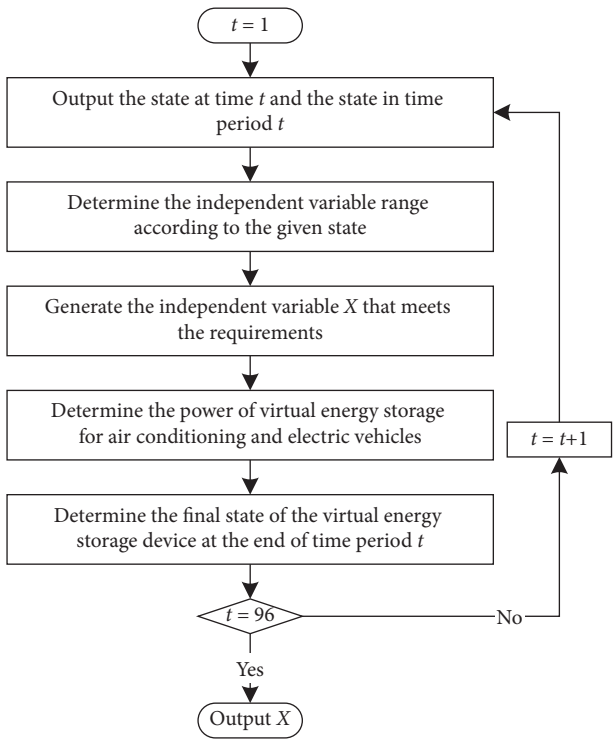

Figure 4: Flowchart of virtual energy storage capacity and output power rolling optimization.

electric vehicles as well as the remaining power of the power battery. The state at time t refers to the indoor temperature at time t and the total remaining capacity of the electric vehicle's virtual energy storage at time t.

For the virtual energy storage in which air conditioning participate,

$$T_{\text{in}}(t+1) = T_{\text{set}}(t) = \frac{\text{SCT}_{\text{in}}(t) + \tau\eta P_{\text{acv}}(t)}{\text{SC}}. \tag{19}$$

For electric vehicles, for the virtual energy storage state at time $t+1$ during the rolling optimization process in the region i, when the virtual energy storage state $S_{\text{EV-virtual},i}(t)$, the input power $P_{\text{EV-virtual-}in}(t)$, and the output power $P_{\text{EV-virtual-out}}(t)$ at the previous time are known, the status of the virtual energy storage capacity of electric vehicles at the beginning of the next time period can be determined:

$$\begin{aligned} S_{\text{EV-virtual},i}(t+1) = S_{\text{EV-virtual},i}(t) - P_{\text{EV-virtual-out}}(t) \\ \times \tau + P_{\text{EV-virtual-in}}(t) \times \tau. \end{aligned} \tag{20}$$

3.2. Objective Function. In the case where other conditions are certain and uncontrollable, for the virtual energy storage optimization scheduling in which air conditioning and electric vehicles jointly participate, the optimization objective function has the lowest total cost of electricity consumption throughout the day:

$$\begin{aligned} \min C = \min \sum_{t=1}^{T}\sum_{i=1}^{M}\left(C_{\text{WT},i}(t) + C_{\text{PV},i}(t) + C_{\text{grid},i}(t)\right) \\ + \sum_{i=1}^{M}\left(C_{\text{EV},i} + C_{\text{AC},i}\right). \end{aligned} \tag{21}$$

In equation (21), M is the total number of residential area and units in the area; in the area i at the time t, $C_{\text{WT},i}(t)$ and $C_{\text{PV},i}(t)$ are the total cost of wind power and photovoltaic power, respectively; $C_{\text{grid},i}(t)$ is the cost of purchasing electricity from the power grid; $C_{\text{EV},i}$ is the cost of virtual energy storage with electric vehicles participation in the area i throughout the day; $C_{\text{AC},i}$ is the cost of air conditioning virtual energy storage throughout the day in the area i.

In addition,

$$\begin{aligned} C_{\text{WT},i}(t) &= p_{\text{WT},i,\text{repare}} \times E_{\text{WT},i}(t), \\ C_{\text{PV},i}(t) &= p_{\text{PV},i,\text{repare}} \times E_{\text{PV},i}(t). \end{aligned} \tag{22}$$

In equation (22), $p_{\text{WT},i,\text{repare}}$ and $p_{\text{PV},i,\text{repare}}$ are the power generation maintenance costs of wind turbines and photovoltaic power generation, respectively. And their units are CNY/kWh; $E_{\text{WT},i}(t)$ and $E_{\text{PV},i}(t)$ are the power generation capacity of wind turbines and photovoltaic power generation during the time period which contains time t:

$$C_{\text{grid},i}(t) = p_{\text{grid}}(t) \times E_{\text{grid},i}(t). \tag{23}$$

In equation (23), $p_{\text{grid}}(t)$ is the price of electric energy in the time period which contains time t, which can be step price, peak-valley price, time-sharing price, or real-time price, and $E_{\text{grid},i}(t)$ represents time t:

$$C_{\text{EV},i} = p_{\text{EV}} \times E_{\text{EV},i}. \tag{24}$$

In equation (24), p_{EV} is the cost of virtual energy storage with electric vehicles participation; the unit is CNY/kWh; $E_{\text{EV},i}$ is the total amount of virtual energy storage with electric vehicles participation in the ith area in the whole day:

$$C_{\text{AC},i} = p_{\text{AC}} \times E_{\text{AC},i}. \tag{25}$$

In equation (25), p_{AC} is the cost of in virtual energy storage with air conditioning participation; the unit is CNY/kWh; $E_{\text{AC},i}$ is the total amount of virtual energy storage with air conditioning participation in the ith area throughout the day.

3.3. Restrictions

3.3.1. Energy Balance Constraint. The output power of all power sources and energy storage devices at time t should be

equal to the electricity consumption at that time, as shown in equation (26):

$$P_{ac-o} + P_{EV-o} + \text{demand} = P_{WT} + P_{PV} + P_{ac-virtual} + P_{grid} + P_{EV-virtual}. \quad (26)$$

P_{ac-o} is the natural power consumption load curve of the virtual energy storage of the air conditioning, P_{EV-o} is the charging power load curve of the electric vehicle, demand is the daily load demand, P_{WT} is the wind power, P_{PV} is the photovoltaic power, $P_{ac-virtual}$ is the input (or output) power of the virtual energy storage with air conditioning participation, P_{grid} is the power of the power grid, and $P_{EV-virtual}$ is the input (or output) power of the virtual energy storage involved in electric vehicles.

3.3.2. Output Power Constraints. Any distributed power supply and virtual energy storage device have a limitation for power rating, as shown in equation (27):

$$P_{i,\min}(t) < P_i(t) < P_{i,\max}(t). \quad (27)$$

In this equation, $P_{i,\min}(t)$ and $P_{i,\max}(t)$ are the minimum and maximum values of the average output power of the ith device in the period of time t, respectively.

3.3.3. Restrictions on the Basic Driving Power Demand of the Next Day after the Electric Vehicle Participates in the Virtual Energy Storage. The remaining power of any electric vehicle can at least meet the needs of traveling the next day, as shown in equation (28):

$$W_{j,i} - W_{j,i}^0 > 0. \quad (28)$$

$W_{j,i}$ is the remaining power of the jth electric car in the ith area, and $W_{j,i}^0$ is the minimum power required for the jth electric vehicle in the ith area.

The remaining power constraint for electric vehicles is participating in virtual energy storage.

The remaining power of virtual energy storage cannot be negative:

$$S_{EV-virtual,i} > 0. \quad (29)$$

$S_{EV-virtual,i}$ is the remaining power of the ith electric vehicle.

4. Continuous Rolling Optimization of Feasible Solution Initialization for High-Dimensional Complex Constrained Optimization Problem

By analyzing the rolling optimization model proposed above, we can find that the model built in this chapter has the following characteristics:

(1) The dimension of decision variables is high
(2) There are local constraints described by the rolling optimization model among decision variables
(3) There are global constraints on decision variables

This section proposes a continuous rolling optimization algorithm for initializing feasible solutions for high-dimensional complex constrained optimization problems for rolling optimization models and complex constraints, so as to obtain decision variables that simultaneously satisfy multiple types of constraints.

4.1. Treatment Strategy for Multiconstraint Problems. A large number of inequality constraints will result in multiple feasible regions with irregular shapes in the feasible solution space, and the decision variables must satisfy all the constraints, which requires the determination of the range of feasible regions. Take the feasible region of a two-dimensional optimization problem as an example, as shown in Figure 5.

In the figure shown above, A_1 and A_2 are, respectively, feasible regions of decision variables for two different constraints. Since the area of A_2 is small, processing the constraints in parallel will greatly reduce the probability of the decision variable falling in A_2. This will make it difficult for a large number of decision variables to meet the A_2 constraint conditions, resulting in inefficient decision variable selection. However, when the problem to be solved is a high-dimensional optimization problem, the shape of the feasible region corresponding to the constraint conditions is more difficult to determine, and the intersection between the feasible regions is also more difficult to obtain. For the optimization problems shown in this chapter, the dimension of its solution space is shown in equation (30) as follows:

$$D = D_1 + D_2 = N_1 \times T_1 + N_2 \times T_2. \quad (30)$$

In equation (30), N_1 and N_2 are the number of time periods divided per hour, which are both 4 in the questions in this chapter. Besides, T_1 and T_2 are the total time of the optimization cycle, which are both 24 in this paper, so for the optimization problem given in this chapter, its dimension is 192. In practical problems, as the influence factors considered increase, its dimensions may become larger.

4.2. Solution Feasible Probability. For the determination of the feasible solution with multiple constraints, this section uses the solution feasible probability to evaluate its efficiency, as shown in equation (31):

$$P_{(A_1 \cap A_2)/(A_1)} = \frac{P_{A_1 \cap A_2}}{P_{A_1}}. \quad (31)$$

The following is an analysis of its value, first of all for the one-dimensional optimization problem. The feasible solution selection process is shown in Figure 6.

In the two one-dimensional constraints given in the above figure, if N feasible solutions are determined in parallel, the process is to first generate N feasible solutions for A_1 constraint in the $[x_1, x_2]$ interval and then judge whether it meets A_2. According to the range covered by A_1 and A_2, we can know the solution feasible probability when the feasible solutions are evenly distributed:

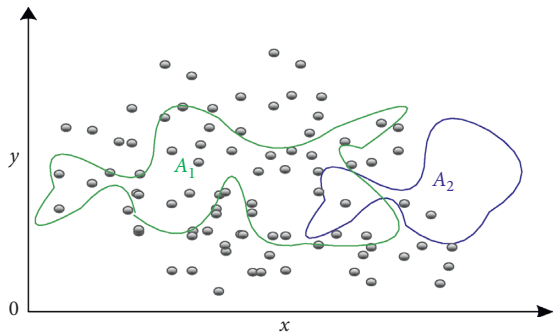

Figure 5: Schematic diagram of the feasible domain for the solution of a two-dimensional optimization problem.

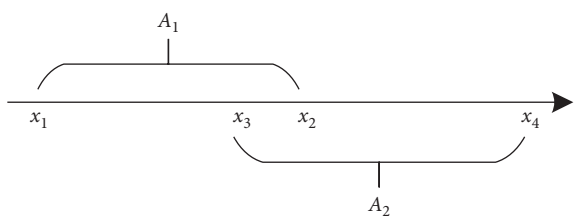

Figure 6: Schematic diagram of feasible solutions for one-dimensional optimization problems.

$$P_{(A_1 \cap A_2)/(A_1)} = \frac{P_{A_1 \cap A_2}}{P_{A_1}} = \frac{x_2 - x_3}{x_2 - x_1}. \tag{32}$$

Claim: after choosing a feasible solution with A_1 constraint, the probability of satisfying A_2 constraint is $P_{(A_1 \cap A_2)/(A_1)}$.

The following dimension of the optimization problem is increased. In the two-dimensional optimization problem, the solution feasible probability is discussed. The simpler inequality constraint is selected; thus, the selection process of a feasible solution is shown in Figure 7.

The feasible probability is shown in

$$P_{(A_1 \cap A_2)/(A_1)} = \frac{P_{A_1 \cap A_2}}{P_{A_1}} = \frac{x_2 - x_3}{x_2 - x_1} \times \frac{y_2 - y_3}{y_2 - y_1}. \tag{33}$$

According to the solution feasible probability of the low-dimensional complex constrained optimization problem, if its $P_{(A_1 \cap A_2)/(A_1)}$ in each dimension is P, then the solution feasible probability of the N-dimensional multiconstrained optimization problem should be P^N. When N is too large, the probability of its feasible solution selection probability will be very small, and it is easy to make the optimization process fall into an infinite loop. The following experiment determines the feasible probability of the solution of the optimization problem in different dimensions and sets P to 0.5. The results are shown in Table 1.

In view of the dimensional disaster in this paper, the undeterminable problem of feasible solutions in this chapter could be analyzed and solved. Therefore, this section proposes a continuous rolling optimization algorithm to solve the inefficiency problem of multiconstrained feasible solutions.

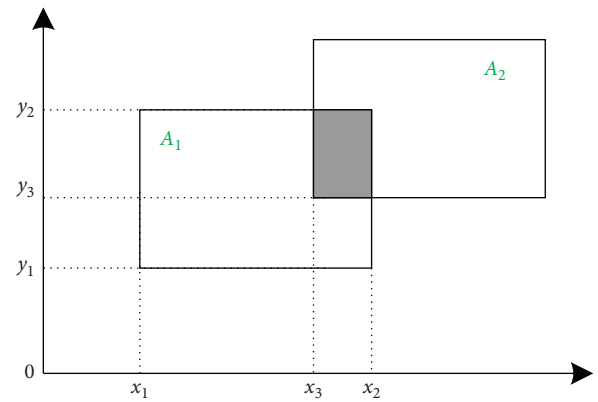

Figure 7: Schematic diagram of the feasible solution of the two-dimensional optimization problem.

Table 1: Probability comparison of random initialization solutions for optimization problems in different dimensions.

The dimension of optimization problem	Solution feasible probability with theoretical calculation (%)	The solution feasible probability error with experimental results (%)
1	50	50
2	25	25
3	12.5	12.5
5	3.125	3.125
10	0.09765625	0.09765625

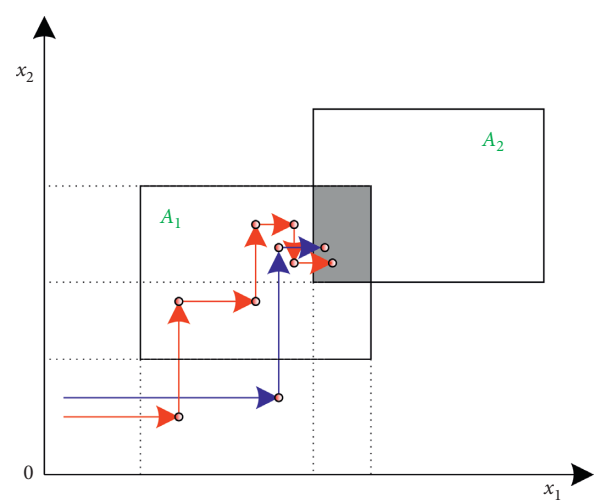

Figure 8: Continuous rolling revision selection process of feasible solutions for two-dimensional optimization problems.

4.3. Algorithm Flow. For the high-dimensional complex constrained optimization problem, the analysis is first based on the two-dimensional optimization problem. When the optimization problem is faced with global constraints and local constraints, the optimization process is shown in Figure 8, where A_1 represents the constraint condition 1 and A_2 represents the constraint condition 2.

In the figure shown above, the red and blue paths are the optimization paths of the results with two consecutive

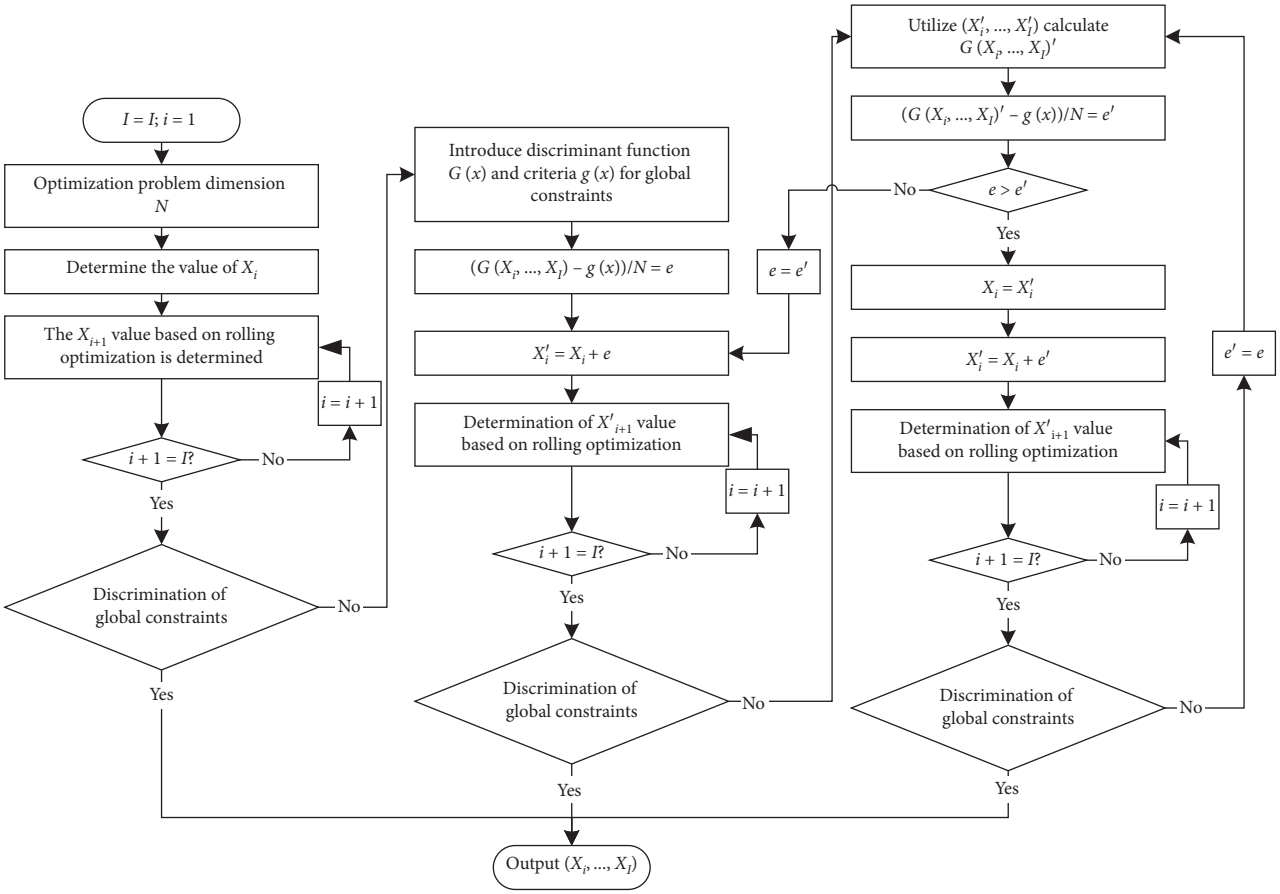

Figure 9: Flowchart of continuous rolling optimization algorithm.

optimizations. Since A_1 represents local constraints and x_1 has a mutual influence with x_2, combined with the rolling optimization model proposed in the previous section, the evolutionary process of the continuous rolling optimization algorithm determined by the local constraint and the global constraint common feasible region of the optimization problem can be determined as shown in Figure 9.

The specific steps are as follows:

(1) Determine the value of the N-dimensional decision variable $x_1, \ldots, x_i$.

(2) Determine whether the global optimization requirements are met; thus, directly output the N feasible domain decision variable $x_1, \ldots, x_i$ if the requirements are all met. Based on the feasible probability of the solution, the N-dimensional decision variable $x_1, \ldots, x_i$ at this time is difficult to meet the requirements; if not, go to step (3).

(3) Introduce the global constraint condition discriminant function $G(x)$, which is related to the constraint condition of the optimization problem, but not directly a constraint condition. It needs to be formulated according to different global constraints. The conditional discriminant function $G(x)$ selected in this chapter is the remaining power of virtual energy storage with electric vehicle participation. Under actual operating conditions, when all electric vehicles leave the residential area, the remaining power of virtual energy storage with electric vehicle participation should be 0, so its standard function $g(x) = 0$.

(4) Determine the average error according to the conditional discriminant function $G(x)$ and its standard function value $g(x)$.

(5) Obtain a new N-dimensional decision variable $x'_1, \ldots, x'_i$ based on $x'_i = x_i + e$, judge whether it meets the global optimization requirements, and directly output the N-dimensional feasible region decision variable $x'_1, \ldots, x'_i$ if it meets all requirements; if not, go to step (6).

(6) Determine the new average error e' based on the N-dimensional feasible region decision variable $x'_1, \ldots, x'_i$ and the global constraint discriminant function $G(x)$, as well as its standard function value $g(x)$.

(7) Compare e with e'; if the error becomes larger after the correlation for average error e (i.e., $e' > e$), then let $e = e'$ and go back to step (5). Recalculate the N-dimensional feasible domain decision variable $x'_1, \ldots, x'_i$; if the error is significantly reduced (i.e., $e' < e$), then update the N-dimensional feasible region decision variable $x_1, \ldots, x_i$, obtain the new N-dimensional decision variable $x'_1, \ldots, x'_i$ for the new

average error e', and then determine whether the global optimization requirements are met; thus, directly output the N-dimensional feasible domain decision variable $x_1', \ldots, x_i'$ if it meets all requirements; if not, go to step (8).

(8) Update the newly generated e' so that $e = e'$; therefore, determine the new average error e' based on the updated N-dimensional feasible domain decision variable $x_1', \ldots, x_i'$, and then go to step (7).

4.4. Optimization Effect Analysis. In the problem solved in this chapter, one of the decision variables is the input and output power of the virtual energy storage with electric vehicle participation in each time period, and the remaining power of the electric vehicle virtual energy storage is used as the standard to detect whether the global optimization is completed. The distribution diagram of the arrival and departure time of electric vehicles in this simulation is shown in Figure 10. The results of the comparison between the unoptimized and optimized global constraint detection standard function values are shown in Figure 11.

As can be seen from Figure 10, the last two vehicles in the area left within the time period of 10:00–10:15 and the total power 47.78 kWh can be determined by calculation.

As can be seen from Figure 11, at 10:00 before rolling optimization, when the last two electric vehicles have not left, the remaining power of virtual energy storage is 154.4 kWh. According to simulation calculations, the remaining power of the two electric vehicles is 47.78 kWh. That is, after the last two vehicles have left, the remaining energy of the virtual energy storage is still not 0, which obviously does not meet the global constraints, indicating that the decision variables fall outside the feasible domain of the global constraints, and the initialization fails. If the continuous rolling optimization algorithm is not adopted, the decision variables need to be initialized again.

After the continuous rolling optimization determined for the high-dimensional complex constraint optimization feasible solution, the results are consistent with the electric vehicle arrival and departure states, indicating that the continuous rolling optimization algorithm [5, 24] for the high-dimensional optimization of global constraints and local constraints that jointly govern the feasible domain can effectively limit the decision variables within the global constraints and local constraints that jointly govern the feasible domain for the problems in this chapter, which helps improve the optimization efficiency.

5. Analysis

This section first simulates the virtual energy storage capacity of air conditioning and electric vehicles and illustrates the feasibility of virtual energy storage. Then virtual energy storage is optimized for scheduling. In the example calculation process, the virtual energy storage power range of air conditioning and electric vehicles is first determined, and then the day is divided into 96 time periods to optimize the virtual energy storage power within the power range.

5.1. Analysis of Air Conditioning and Electric Vehicle Virtual Energy Storage Capacity

5.1.1. Output Power of the Virtual Energy Storage Model with EV Participation. In the virtual energy storage in which electric vehicles participate, the input and output power of the virtual energy storage and the arrival and departure of the electric vehicle will affect the remaining power of the virtual energy storage. Under rolling optimization, the relationship can be obtained by Figure 12.

As can be seen from Figure 12, the continuous energy optimization of the electric vehicle's virtual energy storage output meets the local constraints; the virtual energy storage remaining power becomes 0 after all the electric vehicles leave, indicating that the virtual energy storage output power meets the global constraint conditions.

5.1.2. Output Power of Virtual Energy Storage Model with Air Conditioning Participation. In the virtual energy storage with air conditioning participation, the input and output power of the virtual energy storage and the natural power loss of the virtual energy storage based on the indoor and outdoor temperature difference will affect the remaining power of the virtual energy storage and the change of room temperature. Under rolling optimization, the changes of the above four parameters are shown in Figures 13 and 14.

It can be seen from the comparison that, within the temperature constraint range, the virtual energy storage of the air conditioner can realize the virtual power change of the virtual energy storage through the change of the air conditioner power.

5.2. Determination of the Range of Virtual Energy Storage Power for Air Conditioning and Electric Vehicles

5.2.1. Virtual Energy Storage Charge and Discharge Power Range with EV Participation. For the virtual energy storage of electric vehicles, according to the spatial and temporal distribution of electric vehicles given in Figure 12 and the power demand for driving on the day according to equations (17) and (18), the input and output power range of virtual energy storage with electric vehicles participation can be determined. The results are shown in Figure 15.

5.2.2. Determination of the Range of Charge and Discharge Power at the Starting Time in the Virtual Energy Storage with Air Conditioning Participation. The daily temperature change curve in this area is shown in the red line in Figure 13. Considering the natural consumption rate of the virtual energy storage of the air conditioning, the output power of the virtual energy storage reaches the maximum when the air conditioner is not running, which is $P_{\mathrm{ac-O}}(t)$; when the air conditioner is running, its input and output power are shown in equation (11). The maximum value of the virtual energy storage discharge power changes according to the change of the set temperature. The temperatures are set to 19.5°C, 20.5°C, and 21.5°C, respectively;

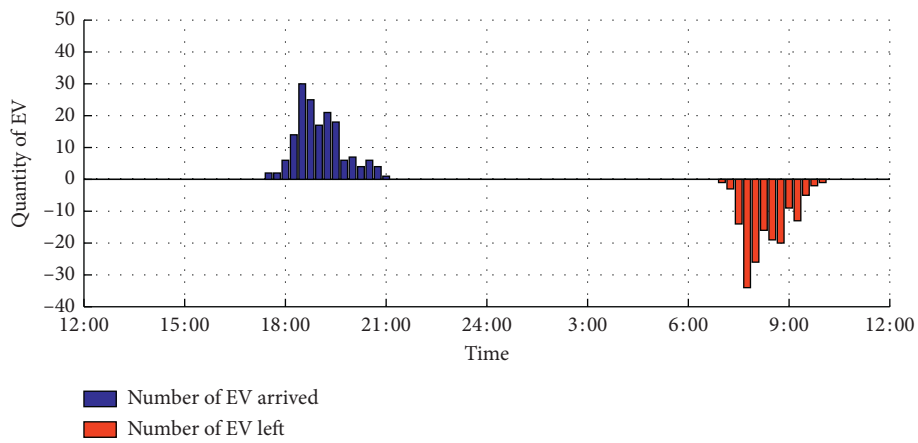

Figure 10: The distribution of vehicle arrival and departure times in this optimization.

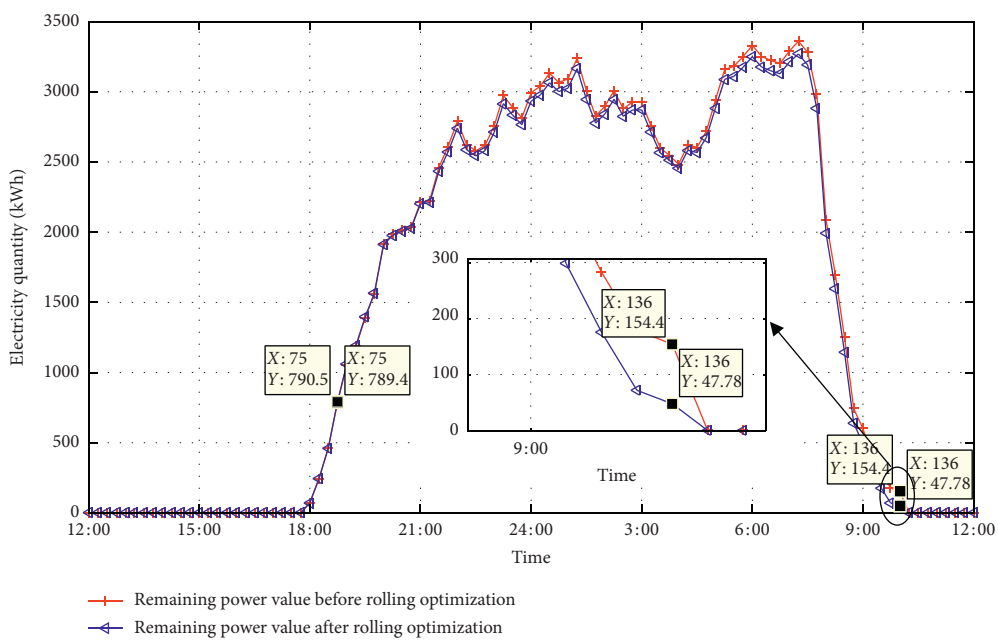

Figure 11: Comparison result of standard function value of global constraint detection.

in the following figure, the upper limit of the virtual energy storage output power changes as shown in Figure 16.

It can be seen from the above figure that the output power of the virtual energy storage decreases as temperature increases.

5.2.3. Economic Analysis of Optimization for Joint Virtual Energy Storage. Based on air conditioning, electric vehicles have the ability to adjust the operating power within a certain range to convert electrical energy into thermal energy storage or perform bidirectional energy exchange with the power grid to achieve the virtual energy storage capacity of energy transfer. The following is the simulation of the effect of virtual energy storage of air conditioning and electric vehicles in this example. Regarding the load of the resident users in the constant temperature community, consider a total of about 650 small high-rise (five-story) households with a total construction area of 65,000 square meters, a total air conditioning power of 1000 kW, and an average of about 1.5 kW per household; on the top floor, there is about 6500 square meters of photovoltaic panels installed, and 10 wind turbines equipped; the power of its distributed power generation equipment is shown in Figure 17.

Considering that virtual energy storage with electric vehicles participation only charges 0.4883 CNY/kWh, so when actually using electric vehicles for virtual energy storage, the discharge cost of electric vehicles is 0.6883 CNY/kWh, and the discharge efficiency is 80%. In addition, the maintenance cost for wind turbines and photovoltaic power generation is shown in Table 2 [8].

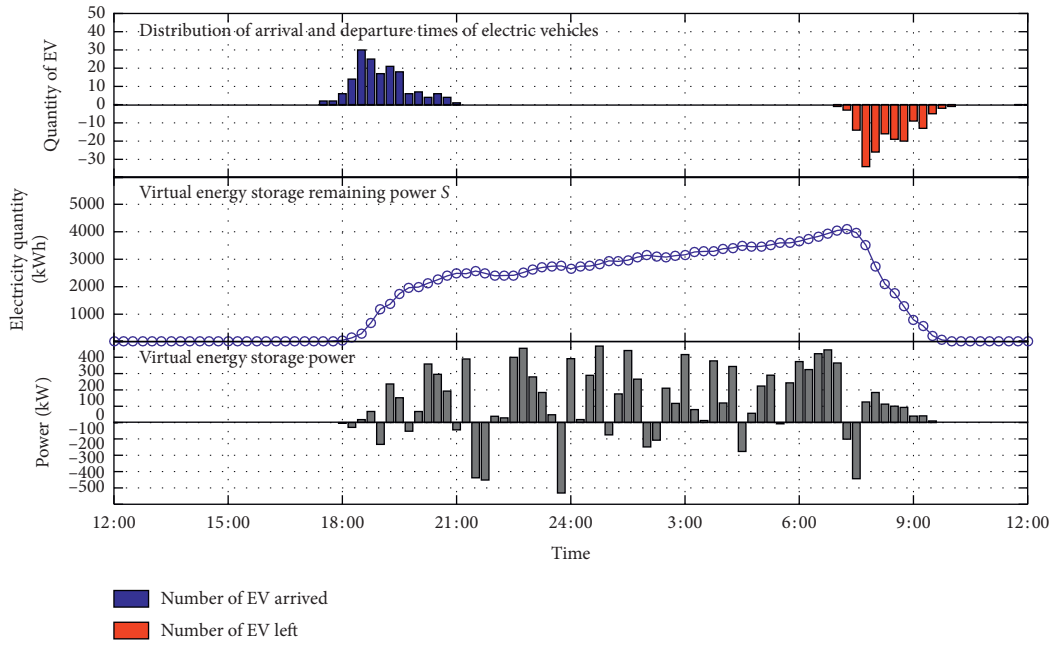

Figure 12: Comparison chart of electric vehicle's space-time distribution, remaining power, and power.

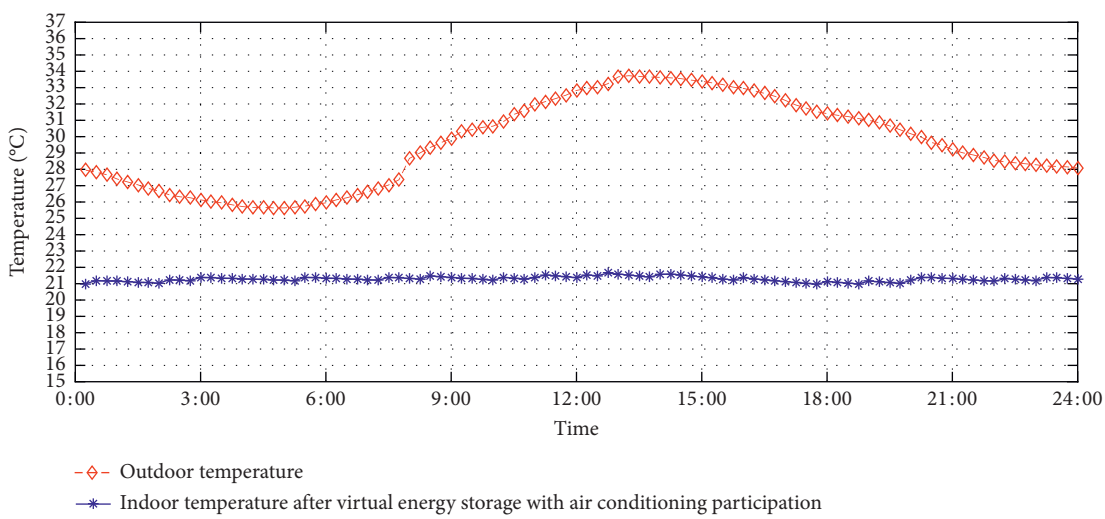

Figure 13: Comparison of indoor and outdoor temperature change curves.

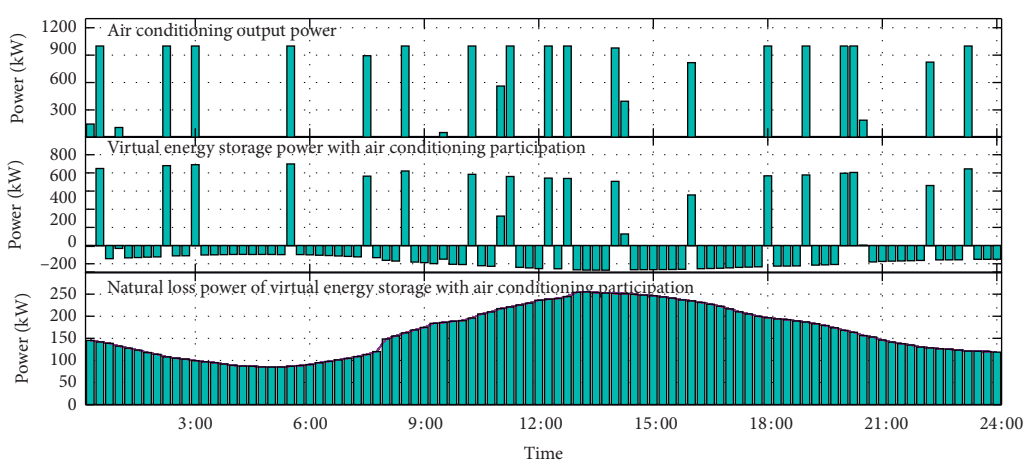

Figure 14: Comparison chart of the natural power consumption of the virtual energy storage with air conditioning participation, air conditioning power, and virtual power of virtual energy storage.

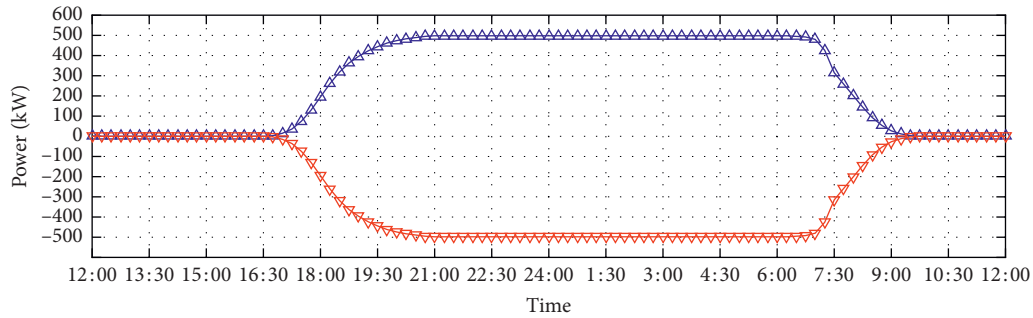

Figure 15: Chart of power range of virtual energy storage with electric vehicle participation.

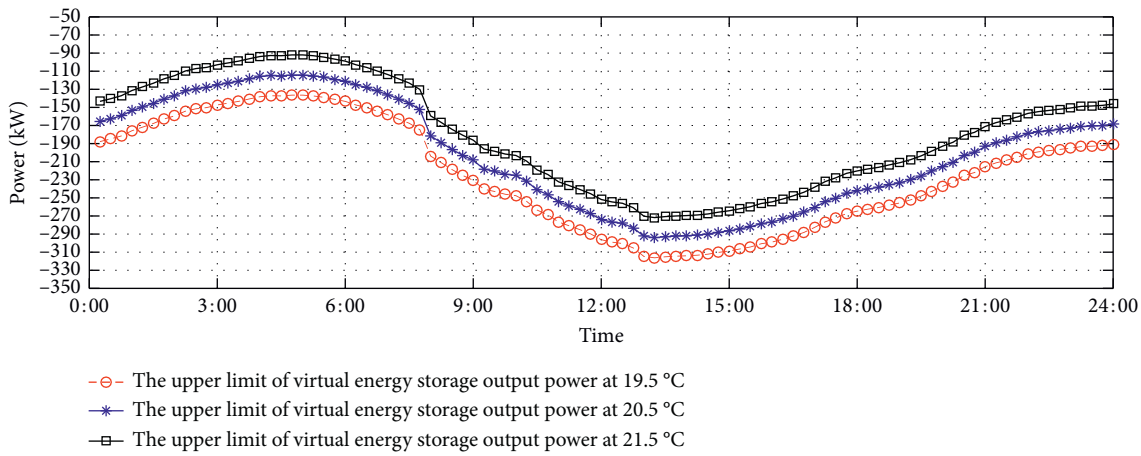

Figure 16: Comparison of the maximum output power of virtual energy storage at different set temperatures.

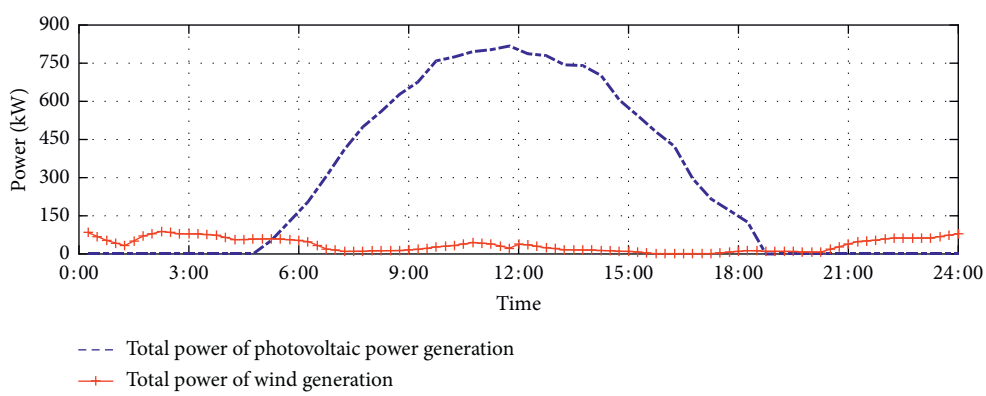

Figure 17: The total power of the wind turbine and photovoltaic power generation of the constant temperature small high-rise building in number 1 residential area.

Table 2: Maintenance cost table for wind turbine and photovoltaic power generation.

Parameter (CNY/kWh)	Value
Wind turbine maintenance cost	0.11
PV maintenance cost	0.08

The total load demand curve of the residents is shown in Figure 18.

This environment corresponds to four scenes, respectively.

Scenario 1. Electric vehicle and air conditioner jointly participate in virtual energy storage.

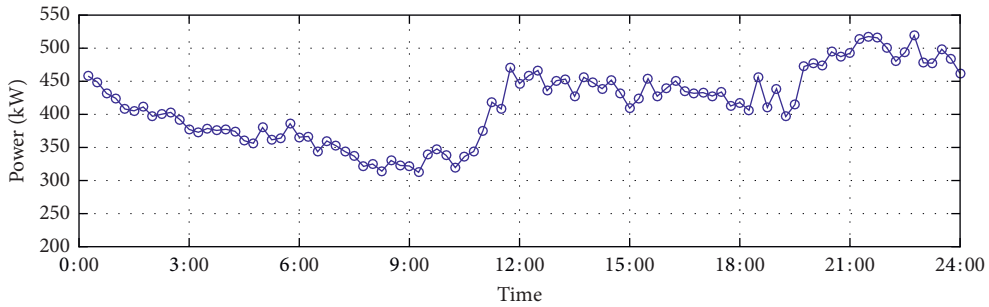

Figure 18: Daily load curve in residential area number 1.

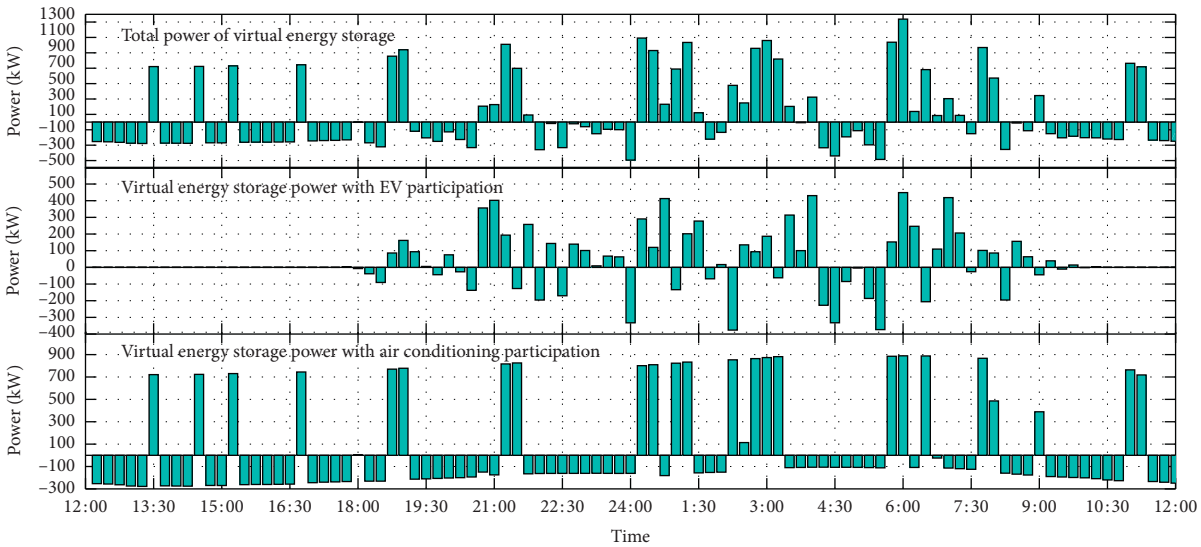

Figure 19: Optimized power of combined virtual energy storage in Scenario1.

Scenario 2. Electric vehicle participates in virtual energy storage.

Scenario 3. Air conditioner participates in virtual energy storage.

Scenario 4. Virtual energy storage is not called.

The economics of these four scenarios are compared as follows.

In Scenario1, the results obtained by air conditioning and electric vehicles participating in virtual energy storage optimization scheduling and the results of using electric vehicles or air conditioning alone to participate in virtual energy storage are shown in Figure 19.

In Scenario2, the results obtained by air conditioners independently participating in virtual energy storage optimization scheduling are shown in Figure 20.

In Scenario3, the results of electric vehicles independently participating in virtual energy storage optimization scheduling are shown in Figure 21.

In the above four scenarios, the comparison results of the total daily electricity charges in the residential area are shown in Table 3.

From the above comparative analysis, the following conclusions can be drawn:

(1) When the joint virtual energy storage of air conditioners and electric vehicles is adopted, the total cost of electricity charges in residential areas can be reduced by 10%.

(2) The photovoltaic power generation in residential areas is highly compatible with the operating time of air conditioners. Therefore, when participating in virtual energy storage alone, the effect of air conditioning participating in virtual energy storage is better than electric vehicles participating in virtual energy storage.

(3) Analyze the reasons for the different total electricity costs in residential areas under different scenarios on a certain day, mainly because air conditioning and electric vehicles can store the electrical energy generated by new energy power generation equipment, which reduces the phenomenon of wind and heat rejection, realizes the efficient utilization of new energy power generation equipment, and also reduces the cost of purchasing electricity from the power grid. Therefore, it has also proved that the joint

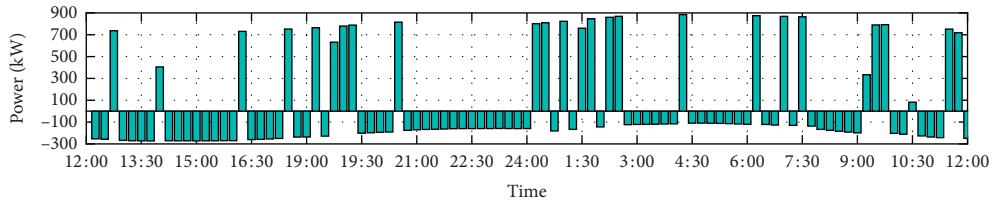

Figure 20: Output power of virtual energy storage with independent participation of air conditioning in Scenario2.

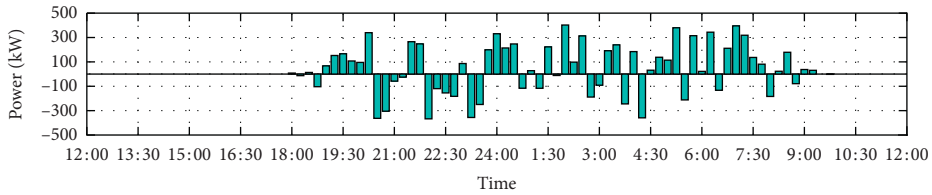

Figure 21: Output power of virtual energy storage with independent participation of electric vehicles in Scenario3.

Table 3: Comparison of the total electricity cost within one day for the constant temperature building in residential area number 1 under four scenarios.

Scenario	Total electricity cost	Electricity saving percentage
Joint virtual energy storage	6532.7	−9.6
Air conditioning virtual energy storage	6672.2	−7.6
Electric vehicles virtual energy storage	6718.7	−7
Without virtual energy storage scheduling	7227.6	—

participation of electric vehicles and air conditioning in virtual energy storage can improve the utilization rate of distributed new energy power generation equipment and improve the economics of electricity consumption.

6. Summary

This paper proposes the use of air conditioning and electric vehicles to jointly participate in virtual energy storage to realize the economic dispatch of energy local area Smart Grid in view of the current status of the controllable load of air conditioning and the load growth of electric vehicles.

Firstly, the virtual energy storage model of thermoelectric conversion with the participation of air conditioning load and the electric energy transfer virtual energy storage model with electric vehicle participation are established. Besides, the rolling optimization idea is introduced to restrict the input and output power of the virtual energy storage with air conditioning and electric vehicle participation.

Secondly, a joint virtual energy storage power optimization model is constructed, and for the solution of the model, in the initialization process of decision variables, due to the condition that dimensional disaster occurred and the initial feasible solution cannot be obtained, a continuous rolling optimization method is proposed for the feasible solution of the high-dimensional complex constraint optimization problem, so that the virtual energy storage power can simultaneously meet the local and global constraints under rolling optimization during the initialization process and thus improve the initialization efficiency.

Finally, the capacity and economy of joint virtual energy storage in residential areas are calculated. The results prove that air conditioning and electric vehicles have the ability to jointly participate in virtual energy storage, and the comparison proves that joint virtual energy storage can effectively improve the economics of electricity consumption. Therefore, the conclusion is that the joint virtual energy storage with the participation of electric vehicles and air conditioning helps improve the economics of consumer electricity consumption.

Data Availability

The data used in this paper comes from the statistics of urban travel data, which has not been published publicly. This paper only takes this data as an example to prove the effectiveness of the proposed method.

Conflicts of Interest

The authors declare that there are no conflicts of interest regarding the publication of this article.

Authors' Contributions

Rui-Cheng Dai and Xiao-di Zhang participated in the algorithm simulation and draft writing. Bi Zhao and Xiao-di Zhang participated in the concept, design, interpretation, and commenting on the manuscript, and the critical revision

of this paper. Jun-Wei Yu, Bo Fan, and Biao Liu participated in the data collection and analysis of the paper.

Acknowledgments

This work was supported by the National Natural Science Foundation of China (Grant nos. 51909199 and 51709215) and the Fundamental Research Funds for the Central Universities (WUT: 2020IVB012).

References

[1] S. Pawan and K. Baseem, "Smart microgrid energy management using a novel artificial shark optimization," *Complexity*, vol. 2017, Article ID 2158926, 22 pages, 2017.

[2] Y. Zou, Y. Chen, and Y. Zou, "Steady-state analysis and output voltage minimization based control strategy for electric springs in the smart grid with multiple renewable energy sources," *Complexity*, vol. 2019, Article ID 5376360, 12 pages, 2019.

[3] L. Xi, Y. Y. Li, and J. L. ChenLu, "A novel automatic generation control method based on the ecological population cooperative control for the islanded smart grid," *Complexity*, vol. 2018, Article ID 2456936, 17 pages, 2018.

[4] J. Lai, X. Lu, X. Yu, and A. Monti, "Stochastic distributed secondary control for ac microgrids via event-triggered communication," *IEEE Transactions on Smart Grid*, vol. 11, no. 4, pp. 2746–2759, 2020.

[5] J. Lai and X. Lu, "Nonlinear mean-square power sharing control for ac microgrids under distributed event detection," *IEEE Transactions on Industrial Informatics*, p. 1, 2020.

[6] D. Choi, A. J. Crawford, V. Viswanathan et al., "Lifecycle comparison and degradation mechanisms of Li-ion battery chemistries under grid and electric vehicle duty cycle combinations," *The Electrochemical Society*, vol. 1, p. 26, 2018.

[7] K. Mai, L. Yin, and Z. Li, "Energy optimization management of grid-connected wind-solar-battery domestic micro-grid based on virtual energy storage," *Distribution & Utilization*, vol. 34, no. 4, pp. 12–18, 2017.

[8] X. Jin, Y. Mu, H. Jia, J. Wu, T. Jiang, and X. Yu, "Dynamic economic dispatch of a hybrid energy microgrid considering building based virtual energy storage system," *Applied Energy*, vol. 194, pp. 386–398, 2017.

[9] X. Zhan, Y. Mu, and H. Jia, "Optimal scheduling method for a combined cooling, heating and power building microgrid considering virtual storage system at demand side," in *Proceedings of the CSEE*, vol. 37, no. 2, pp. 581–590, Barcelona, Spain, April 2017.

[10] X. Ai, Y. Zhao, and S. Zhou, "Study on virtual energy storage features of air conditioning load direct load control," *Proceedings of the CSEE*, vol. 36, no. 6, pp. 1596–1603, 2016.

[11] C. Gao, Q. Li, and Y. Li, "Bi-level optimal dispatch and control strategy for air-conditioning load based on direct load control," *Proceedings of the Chinese Society of Electrical Engineering*, vol. 34, no. 10, pp. 1546–1555, 2014.

[12] O. Erdinç, A. Tascikaraoglu, N. G. Paterakis, Y. Eren, and J. P. S. Catalao, "End-user comfort oriented day-ahead planning for responsive residential HVAC demand aggregation considering weather forecasts," *IEEE Transactions on Smart Grid*, vol. 8, no. 1, pp. 362–372, 2017.

[13] C. H. Wai, M. Beaudin, H. Zareipour, A. Schellenberg, and N. Lu, "Cooling devices in demand response: a comparison of control methods," *IEEE Transactions on Smart Grid*, vol. 6, no. 1, pp. 249–260, 2015.

[14] J. Peppanen, M. J. Reno, and S. Grijalva, "Thermal energy storage for air conditioning as an enabler of residential demand response," in *Proceedings of the 2014 North American Power Symposium (NAPS)*, pp. 1–6, Pullman, WA, USA, September 2014.

[15] J. Lai, X. Lu, X. Yu, and A. Monti, "Cluster-oriented distributed cooperative control for multiple ac microgrids," *IEEE Transactions on Industrial Informatics*, vol. 15, no. 11, pp. 5906–5918, 2019.

[16] J. Lai, X. Lu, X. Yu, and A. Monti, "Stochastic distributed secondary control for ac microgrids via event-triggered communication," *IEEE Transactions on Smart Grid*, vol. 11, no. 4, pp. 2746–2759, 2020.

[17] L. Xin, L. Jingang, and T. Ruoli, "A hybrid constraints handling strategy for multiconstrained multiobjective optimization problem of microgrid economical/environmental dispatch," *Complexity*, vol. 2017, Article ID 6249432, 12 pages, 2017.

[18] G. Xiong, J. Zhang, X. Yuan et al., "A novel method for economic dispatch with across neighborhood search: a case study in a provincial power grid, China," *Complexity*, vol. 2018, Article ID 2591341, 18 pages, 2018.

[19] W.-C. Yeh, M.-F. He, C.-L. Huang et al., "New genetic algorithm for economic dispatch of stand-alone three-modular microgrid in DongAo Island," *Applied Energy*, vol. 263, 2020.

[20] G. Ruan, H. Zhong, J. Wang, Q. Xia, and C. Kang, "Neural-network-based Lagrange multiplier selection for distributed demand response in smart grid," *Applied Energy*, vol. 264, Article ID 114636, 2020.

[21] F. Pallonetto, M. De Rosa, F. Milano, and D. P. Finn, "Demand response algorithms for smart-grid ready residential buildings using machine learning models," *Applied Energy*, vol. 239, pp. 1265–1282, 2019.

[22] W. Zhang, J. Lian, C.-Y. Chang, and K. Kalsi, "Aggregated modeling and control of air conditioning loads for demand response," *IEEE Transactions on Power Systems*, vol. 28, no. 4, pp. 4655–4664, 2013.

[23] N. Ruiz, I. Cobelo, and J. Oyarzabal, "A direct load control model for virtual power plant management," *IEEE Transactions on Power Systems*, vol. 24, no. 2, pp. 959–966, 2009.

[24] J. Lai, H. Zhou, and W. Hu, "Synchronization of hybrid microgrids with communication latency," *Mathematical Problems in Engineering*, vol. 2015, Article ID 586260, 10 pages, 2015.

Hindawi
Complexity
Volume 2020, Article ID 5641596, 10 pages
https://doi.org/10.1155/2020/5641596

Research Article

Cyber-Enabled Intelligence Control and Security Optimization for Complex Microgrid Networks Transient Frequency Stability Analysis of Power Systems considering Photovoltaic Grid Connection

Jun Wu,[1] Xiangyu Xing,[1] Chen Wu,[2] Baolin Li,[1] Wei Huang,[2] Peiying Gan,[1] and Hui Zhou[1]

[1]*School of Electrical Engineering & Automation, Wuhan University, Wuhan 430072, China*
[2]*Yunnan Power Grid Co., Ltd., Kunming 650000, China*

Correspondence should be addressed to Xiangyu Xing; 2015302540146@whu.edu.cn

Received 26 May 2020; Revised 28 August 2020; Accepted 16 September 2020; Published 12 October 2020

Academic Editor: Jingang Lai

In view of the photovoltaic grid-connected power system, the transient frequency stability of the system is analyzed in this paper. First, the photovoltaic grid-connected power system was modeled and analyzed. On this basis, the maximum frequency deviation is used as the index to determine the interval in which the system accommodates the maximum photovoltaic capacity, and the influence of frequency stability of the high-permeability photovoltaic high disturbance system is studied. Second, the evaluation and prediction methods of frequency dynamic characteristics of photovoltaic access nodes based on surface fitting are proposed, and the critical values of high penetration photovoltaic access for different grid points are given. Finally, an improvement measure based on the optimization of the frequency modulation parameters of large-capacity units is proposed, and the effectiveness of the proposed method in improving the transient frequency stability of the system after photovoltaic access is verified by the IEEE 39-standard system.

1. Introduction

Solar photovoltaic technology, as a universal and endless clean energy power generation method with the largest utilization potential, has attracted the attention of power practitioners and researchers. However, photovoltaic output is characterized by randomness, intermittence, no mechanical rotational inertia, and no participation in system frequency modulation, which brings new challenges to power grid control, making it difficult for the existing control mode to ensure the safety of power system. Therefore, at the level of mechanism analysis, there is necessity of (a) in-depth study of the mechanism of photovoltaic access on the frequency stability of power systems and (b) simulation verification based on the model of photovoltaic power generation units, with theoretical guidance on how to improve the system's transient stability after grid connection. Stability evaluation involves (a) study of the frequency characteristics of system nodes after photovoltaic grid connection and (b) proposing the evaluation method of system frequency support capability, which has reference value to engineering practice. Stability improvement measures are concerned with feasible measures for frequency modulation after photovoltaic grid connection, which has practical significance for the safe and stable operation of power systems.

A lot of relevant research has been carried out at home and abroad. With the promotion of microgrid technology, research on its control [1, 2] and other aspects is aimed at achieving flexible and efficient applications of distributed energy in various forms and huge quantities. Jingang Lai and his colleagues [3] proposed a cluster-oriented cooperative control strategy for multiple AC microgrids clusters, which enables maximum utilization of distributed energy resources.

In addition, a distributed cooperative control scheme is also proposed in order to implement a distributed secondary control for hybrid lossy microgrids, and sufficient conditions on the requirements for the network connectivity and the delays boundedness are presented, which guarantees the stability and synchronization of the controlled hybrid lossy microgrid power systems [4].

Connecting distributed photovoltaic to the distribution network in the form of microgrids is an effective way to solve grid frequency stability and other issues after photovoltaic grid connection. For the research on the transient model of photovoltaic power generation systems, the studies in [5–7] modeled modules such as photovoltaic arrays, power electronic converters, and their control systems, reviewed the research status of the entire photovoltaic power generation system model, and then summarized the method of using the above basic component model to build an overall model of a photovoltaic power generation system. Zhang et al. [8] adopted the Simulink simulation software to construct a MATLAB experimental simulation model of the photovoltaic power generation system, using the classic control algorithm-maximum power point tracking control and a subunit of relay protection logic control. Wang et al. [9] adopted the method of indirect combination modeling, in which the device-level electromechanical transient model was first established in the PSD-BPA environment, including the electromechanical transient model of typical doubly fed fans, energy storage units, and the photovoltaic power generation unit. Based on the device-level modeling, a power plant-level model was established, and the equivalent method was specifically used to realize the combination of the electromechanical transient models of the three combined power generation systems. Then, the correctness of the model was constructed and verified by numerical simulation under BPA environment.

In addition to focusing on the modeling of photovoltaic grid-connected systems to improve their performance, domestic and foreign scholars have also carried out studies on the frequency stability of photovoltaic grid-connected systems [10–15]. Kakimoto et al. and Zhou et al. [16, 17] believed that the key factor affecting the frequency stability of the system was the primary frequency regulation of the unit, so that the stability of the power system was likely to be significantly improved by setting reasonable adjustment coefficients and governor parameters. Du [18] studied the high-frequency problems caused by the system splitting after the new energy grid connection and analyzed the different impacts of the different settings of the protection definite value for the over-speed protection control of thermal power units. Du also studied the low-frequency problem and proposed an optimization strategy for low-frequency load shedding to solve the problem of increasing frequency of low-frequency load shedding. For Chen et al. [19], in order to improve the frequency stability of the grid-connected photovoltaic system, the control strategy of the optical storage grid-connected inverter based on virtual synchronous generators was studied, and the inertia and damping were introduced into the power control link to simulate a synchronous generator to achieve a frequency modulation and voltage regulation. Zheng et al. [20] studied the dynamic frequency characteristics of the power system under the impact of unbalanced power in the scenario of high-permeability photovoltaic and proposed countermeasures to improve the frequency characteristics from three aspects: changing inertia constant, changing mechanical power regulation performance, and changing generator electromagnetic power.

Based on the above analysis, this paper proposes a method to achieve system transient frequency stability caused by photovoltaic grid connection. Firstly, based on the modeling of photovoltaic grid-connected networks, the influence of large grid disturbances on frequency stability under the condition of high photovoltaic penetration is analyzed, and the maximum frequency deviation is used as an indicator to determine the maximum photovoltaic capacity of the system. Secondly, a method for evaluation and prediction of the frequency dynamic characteristics of photovoltaic access nodes based on surface fitting is proposed, and the critical values of high-permeability photovoltaic access at different grid-connected points can be calculated through the above method. Then, improvement measures based on optimization of frequency modulation parameters of large-capacity units are proposed to improve the transient frequency stability of the system after photovoltaic access. Finally, the validity of the proposed method is verified with an IEEE 39-node example.

2. Modeling of Photovoltaic Grid-Connected Systems

The power system simulation software PSD-BPA is used to build a transient model of each link of the photovoltaic grid-connected system in this paper. The photovoltaic power generation unit consists of three parts, namely, photovoltaic cell arrays, low-voltage box-type transformers, and voltage-type inverters. The topology of photovoltaic power generation unit is shown in Figure 1.

The photovoltaic grid-connected system model is composed of multiple photovoltaic power generation units and grid-connected system models. After the photovoltaic power generation units are connected in parallel, they are first boosted by a step-up transformer, and then the photovoltaic power generation system transmits the active power to the collection station via the 110 kV collection line. The photovoltaic grid-connected system includes parallel transmission of several photovoltaic power generation collection branches, and its topology is shown in Figure 2.

3. System Frequency Stability Impact of Large Disturbances in Photovoltaic High-Permeability Grids

3.1. Analysis of Mechanism. Based on the analysis of the frequency response characteristics of conventional units, this section studies the effect mechanism of the frequency stability of large disturbances in photovoltaic high-permeability grids. When the power system is disturbed, the electromagnetic power variation of the generator is affected

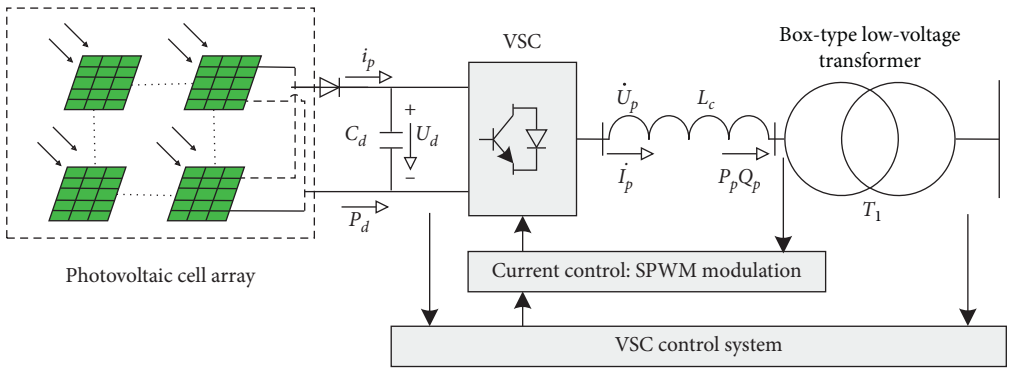

Figure 1: Topology of photovoltaic power generation unit.

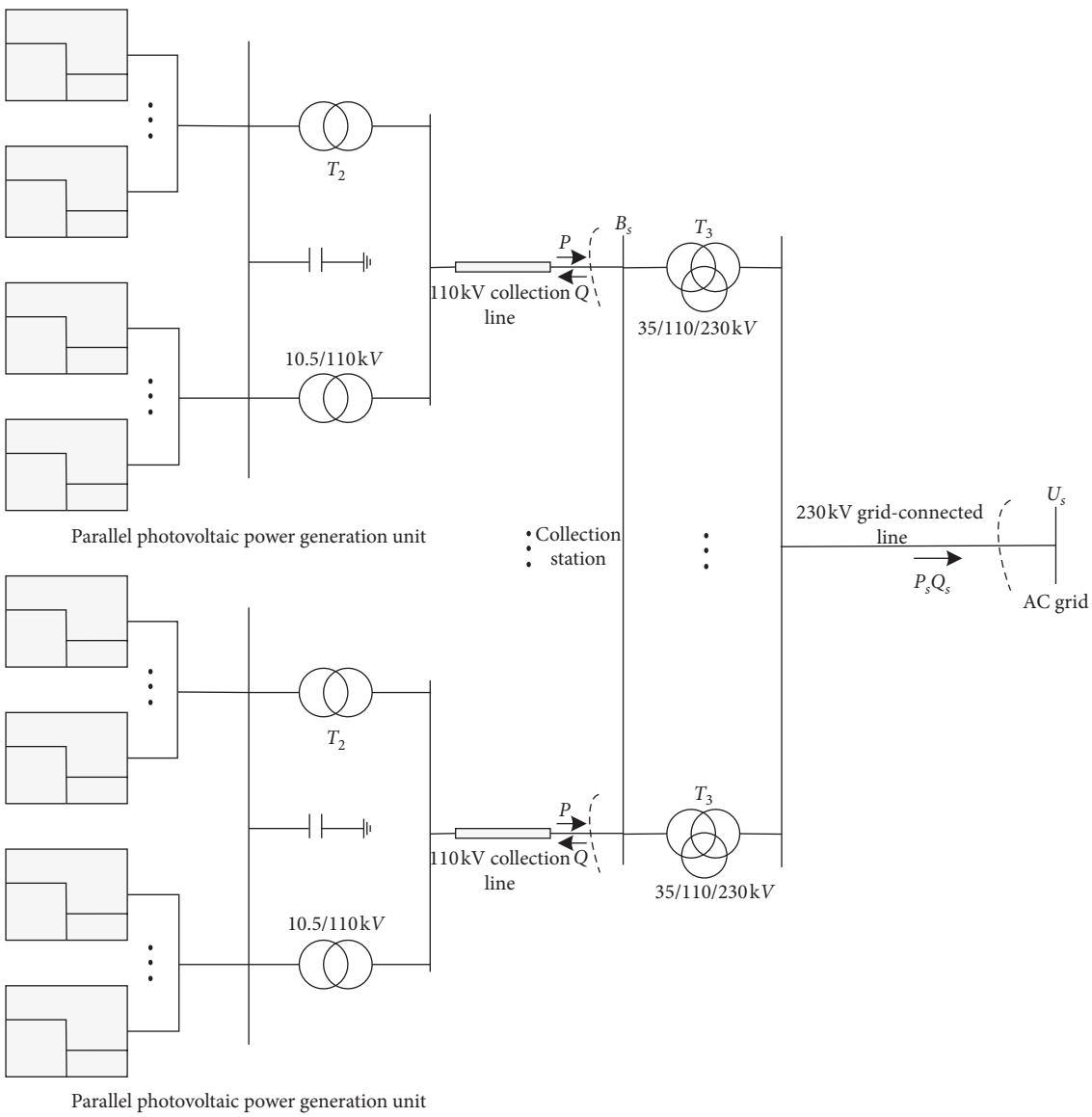

Figure 2: Photovoltaic grid-connected system model.

by factors such as power grid conditions and the primary frequency modulation of the unit, and the variation is complicated. In order to simplify the analysis, the method of using the inertia coefficient to calculate the constant distribution ratio is used in this paper to describe the change of the electromagnetic power.

When a system with n conventional generator sets has a multiple fault at node k, equation (1) is obtained, wherein ΔP_{ei} and ΔP represent the change of the electromagnetic power and disturbance power of the ith generator set; P_{sik} is the full-step power coefficient between nodes i and k; T_{ji} and R_i represent the inertia time constant and adjustment coefficient of the ith generator:

$$\begin{cases} \Delta P_{ei}(0^+) = -\left(\dfrac{P_{sik}}{\sum_{i=1}^{n} P_{sik}}\right)\Delta P, \\ \Delta P_{ei}(t) = -\left(\dfrac{T_{Ji}}{\sum_{i=1}^{n} T_{Ji}}\right)\Delta P, \\ \Delta P_{ei}(\infty) = -\dfrac{1}{R_i}\dfrac{\Delta P}{\sum_{i=1}^{n}(1/R_i)}. \end{cases} \tag{1}$$

After photovoltaic is connected to the power grid, m of the n conventional units in the system are replaced with photovoltaic generators. As m increases continuously, the system's moment of inertia decreases. At this time, the full-step coefficients, moments of inertia, and reactive power compensation coefficients of all conventional units are assumed to be identical. If the disturbance of multiple fault occurs in the photovoltaic grid-connected system, equation (2) is obtained:

$$\begin{cases} \Delta P_{ei}(0^+) = \left(\dfrac{P_{sik}}{\sum_{i=1}^{n'} P_{sik}}\right)\Delta P = \dfrac{1}{n'}\Delta P, \\ \Delta P_{ei}(t) = \dfrac{T_{Ji}\Delta P}{\sum_{a=1}^{m} T_{Ja} + \sum_{i=1}^{n'} T_{Ji}} = \dfrac{1}{n'}\Delta P, \\ \Delta P_{ei}(\infty) = -\dfrac{1}{R_i}\dfrac{\Delta P}{\sum_{a=1}^{m} 1/R_a + \sum_{i=1}^{n'} 1/R_i} = -\dfrac{1}{n'}\Delta P. \end{cases} \tag{2}$$

In equation (2), n is the number of remaining conventional units.

From equation (2), it can be seen that, under large disturbances, as the photovoltaic permeability of the system increases, the remaining conventional units bear more power shortage, and the instantaneous changes in electromagnetic power and steady-state deviations are more obvious; that is, the problem of transient frequency stability in the system is easier to detect.

3.2. Effect of Photovoltaic Output with Different Permeability on System Frequency Fluctuation. Based on IEEE 39-node standard calculation examples, this section uses PSD-BPA software simulation to verify and analyze the impact of photovoltaic power generation systems on the dynamic frequency characteristics of the system caused by factors such as output characteristics when large disturbances occur at different permeability. Figure 3 shows the geographical wiring diagram of the IEEE 39-node standard calculation system. The parameters are as follows: the reference capacity is 100 MW, the reference voltage is 100 kV, and the total generator installed capacity is 5,620 MW, of which the generator at node 31 is a balancing machine.

As the installed capacity of conventional units at bus 39 is the largest, which is 1000 MW, we may integrate the photovoltaic power station into the power grid through bus 2, and set the photovoltaic permeability at 0~100% of the installed capacity of conventional units at bus 39. With the help of PSD-BPA software simulation, the frequency dynamic characteristics of the system when large disturbances occur at different permeabilities are obtained, including the minimum and highest frequency dynamic processes of the system and the dynamic processes of the node frequency of the public access point bus 1 and the node bus 39, which is the largest load and is close to the grid connection point. Among them, the two major disturbance faults sets are as follows:

(1) Three-phase short circuit fault occurred on the branch bus 6–bus 11 at the fifth cycle and was cleared at the tenth cycle

(2) When increasing the photovoltaic active power output, the active power output of a conventional unit is cut off in the same proportion

The simulation results are shown in Figures 4 and 5, where Figure 4 is the dynamic curve of the minimum and highest frequency of the system, Figure 5(a) shows the dynamic curve of the frequency of node 1, and Figure 5(b) shows the dynamic curve of the frequency of node 39.

From Figures 4 and 5, it is known that the minimum and maximum frequency of the system and the dynamic frequency of bus 1 and bus 39 nodes change with the different photovoltaic permeability. Figure 4 indicates that the minimum and maximum dynamic frequency of the system have the same change trend, and under the disturbance condition, the photovoltaic high-permeability system may exceed the upper or the lower limit of the frequency; that is, there will be high- and low-frequency problems. Therefore, when evaluating the frequency stability of the system, the absolute value of the frequency deviation should be used as a reference index. The main reason is that as the photovoltaic permeability increases, the system inertia decreases, the remaining conventional units bear more power shortage, and the instantaneous changes in electromagnetic power and steady-state deviations are more obvious, so that the power angle is more likely to destabilize.

For example, in Figure 5, the difference of frequency dynamic between the permeability of 50% and 100% may be caused by factors such as voltage instability. With the increase of photovoltaic penetration, the dynamic frequency change process of the system is shown in Table 1 (unit: Hz).

Since the maximum frequency fluctuation allowed by the grid under the condition of a small system capacity is ±0.5 Hz, it is clear from Table 1 that the maximum acceptable photovoltaic penetration rate of this system is 20%~

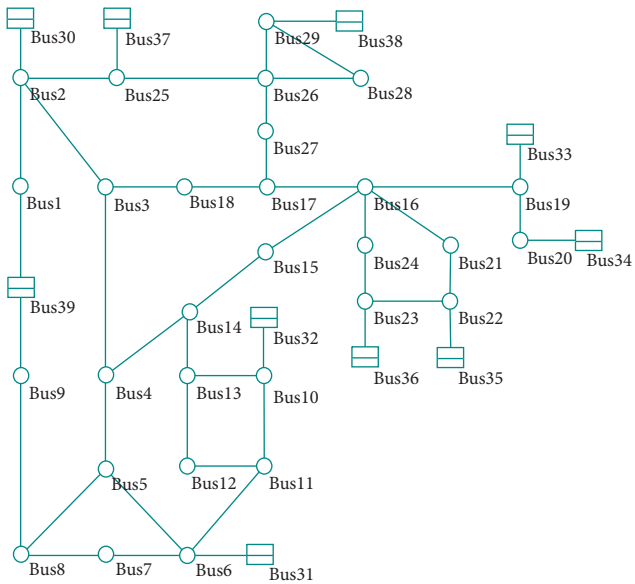

Figure 3: IEEE 39-node standard example geographic wiring diagram.

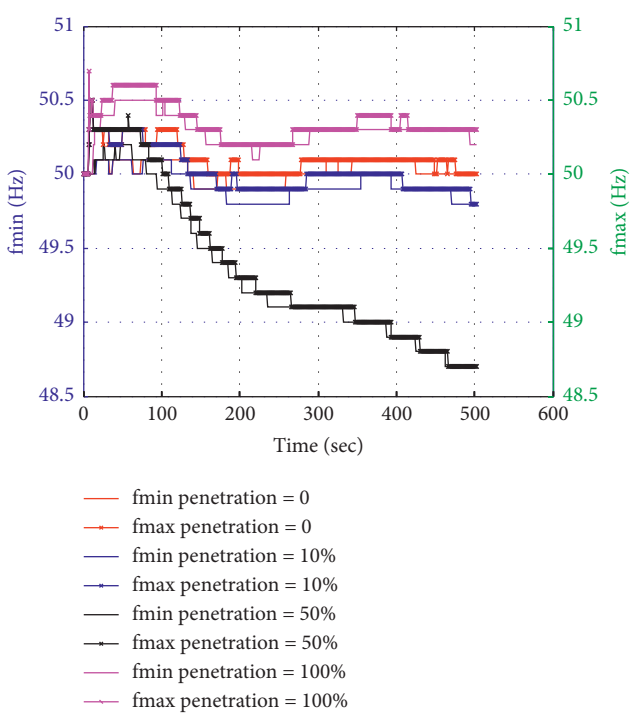

Figure 4: Minimum and maximum frequency dynamics of the system when different permeability fails.

30%; that is, the maximum installed capacity of photovoltaic falls in the range of 200 MW~ 00 MW. However, the critical photovoltaic installed capacity is difficult to give by the method of ergodic simulation test adopted in this section. The above analysis shows that the photovoltaic grid-connected frequency prediction and evaluation method proposed has great application reference value for determining the photovoltaic grid-connected points and its installed capacity in engineering practice. In fact, as long as any two of the three indicators are given in the method proposed in this article, the remaining one can be determined. Therefore, it is completely feasible to use this method to analyze the frequency characteristics after photovoltaic grid connection.

4. Evaluation Analysis and Prediction Method of the Frequency Dynamic Characteristics of Photovoltaic Access Nodes

4.1. Method and Data Acquisition of Node Frequency Dynamic Characteristics. When the system is subject to a power disturbance ΔP, the power system frequency changes. The dynamic frequency characteristic of a system is the time process when the system transitions from a normal state to another stable value. In this paper, the absolute value of the maximum node frequency deviation of all node frequencies in this dynamic process is used as a frequency index to characterize this process, as shown in

$$\Delta f = \left|\Delta f_{\max}\right| = \max\left(\left|f_{\max} - f_N\right|, \left|f_{\min} - f_N\right|\right). \quad (3)$$

At the same time, the electrical distance is used as an important index to measure the spatiotemporal distribution characteristics when the disturbance occurs at different locations. The length of the electrical distance is generally described by the size of the transfer reactance between the two points. When a large disturbance produces an active power shortage, the instantaneous unbalanced power at the initial stage of the disturbance is distributed among the units through an inverse proportional to the electrical distance.

This section is based on the IEEE 39 node standard calculation example. With the help of the PSD-BPA simulation software, a series of experimental data of $(\Delta P, S, \Delta f)$ were obtained by the ergodic simulation to change the position of the disturbance point and the amount of disturbance in the power flow file and the steady-state file multiple times.

4.2. Surface Generation and Analysis Method of Node Frequency Characteristic Based on Surface Fitting. Adopting the methods in the previous sections, we perform cubic spline interpolation on the obtained experimental data. By writing MATLAB program, the surface fitting of "frequency deviation-electrical distance-photovoltaic permeability" was realized. That is, the surface fitting of node frequency characteristics is studied based on the given discrete data.

In order to accurately calculate the frequency deviation value under different disturbances and electrical distances, interpolation and fitting methods were used for accurate data processing, and the modified B-spline method was used to correct the nonsmooth surface fitted by the finite data points obtained from BPA simulation. Generally, the more control points to fit the surface are followed by higher accuracy, but the calculation is more complicated, and there is also more occurrence of singular phenomenon. Therefore, the number of initial control points should be minimized to satisfy accuracy.

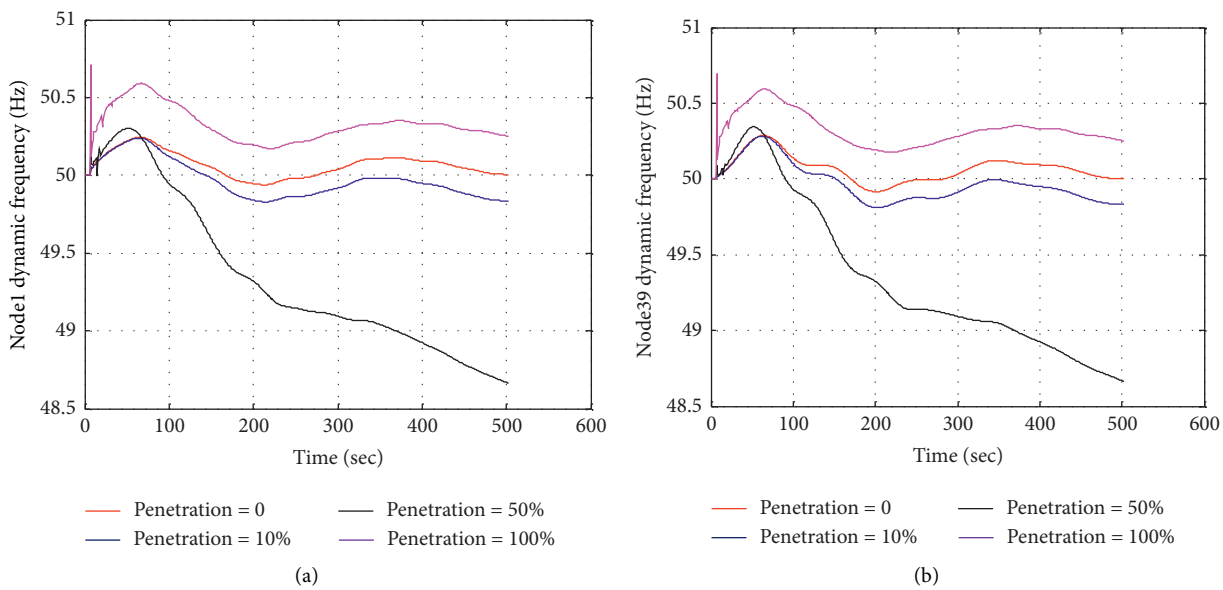

Figure 5: Frequency dynamics of node 1 and node 39 when different permeability fails.

Table 1: Frequency dynamic response of the system when different PV permeability fails.

Photovoltaic penetration (%)	Minimum bus frequency (Hz)	Maximum bus frequency (Hz)	Absolute maximum frequency deviation (Hz)
0	49.994602	50.011600	0.011600
10	49.830513	49.844547	0.169487
20	49.657547	49.669304	0.342453
30	49.441223	49.452263	0.558777
40	49.141018	49.149567	0.858982
50	48.660889	48.671333	1.339111

Finally, the accuracy of the fitted surface is verified according to

$$G = \frac{\Delta f - \Delta f'}{\Delta f'} \times 100\%. \quad (4)$$

In equation (4), Δf and $\Delta f'$ are the fitted and simulated values of the frequency index.

4.3. Analysis of Examples. In the IEEE 39-node system, the photovoltaic access node bus 2 is selected as the observation point, and the cutoff points are sequentially selected as bus 32, bus 35, bus 38 and bus 39, and the disturbance amount is sequentially set to 0.1, 0.2, 0.3, 0.4, 0.5, and 0.6. That is, the installed photovoltaic capacity is 100 MW, 200 MW, 300 MW, 400 MW, 500 MW, and 600 MW. The simulation was performed with the help of power system simulation software PSD-BPA, and 6 groups of experimental data were calculated according to equation (3).

By using the B-spline surface fitting method, the above experimental data were interpolated and then fitted to obtain the node frequency characteristic surface under disturbance, as shown in Figure 6.

The accuracy of the fitting results of the node frequency characteristics of the curved surface obtained by cubic interpolation of B-spline is calculated according to equation (4). The specific method is as follows: first, an electrical distance is determined to verify the accuracy of the absolute value of the frequency deviation under different disturbance amounts. Then, a disturbance quantity is determined in the same way to verify the accuracy of the absolute value of the frequency deviation under different disturbance amounts. Among them, the predicted value is read from the drawn surface according to the handle function in MATLAB. The specific accuracy verification results are shown in Table 2.

The accuracy verification shows that the node frequency and voltage characteristics prediction based on surface fitting proposed in this paper meets sufficient accuracy, and the error is less than 2%. Therefore, we can process the prediction results: let S take 0.0012, 0.0080, 0.0103, 0.0331, and other electrical distances, respectively, and use the MATLAB to handle function to take points on the drawn surface to get the corresponding ΔP, which is approximated as the critical value of photovoltaic permeability. For example, when S is 0.0012, the critical photovoltaic permeability corresponding to the frequency index is 272.4 MW, which has great application reference value in determining the photovoltaic

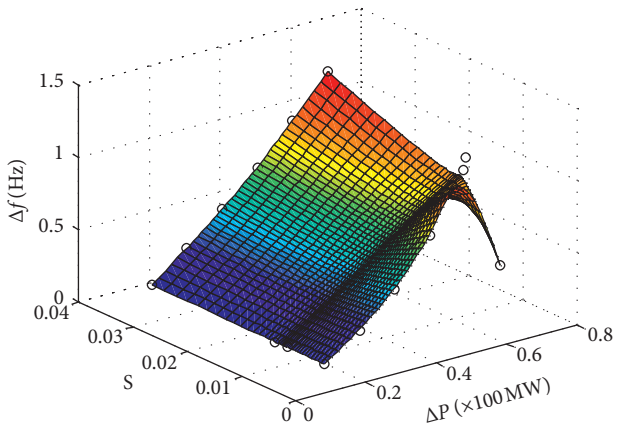

Figure 6: Node frequency characteristic surface under disturbance.

Table 2: Verification of the frequency index value when the disturbance amount and the electrical distance are, respectively, fixed.

ΔP	S	Δf	$\Delta f'$	G (%)
0.25	0.0148	0.408958	0.4158	1.6730
0.35	0.0148	0.591370	0.5946	0.5462
0.35	0.0295	0.59206	0.5964	0.7330

grid-connected point and its installed capacity in engineering practice.

5. Improvement Measures of Frequency Stability Based on Optimization of Frequency Regulation Parameters of Large-Capacity Units

5.1. Evaluation Index and Evaluation Method of Node Frequency Support Capability. In order to simplify the problem, in consideration of the transient frequency instability accident, the system frequency must first reach the trip conditions of triggering the generator set, and the transient frequency boundary condition of the unit trip is used as an index to evaluate the system frequency stability [21]. The definition of the frequency margin index of the node transient frequency offset safety is shown in

$$\eta = \frac{f'_{cr} - f_{cr}}{f_N - f_{cr}}. \tag{5}$$

In (5), f_N, f_{cr}, and f'_{cr} represent rated frequency value, generator high- and low-frequency protection value, and critical safety threshold, respectively. Node transient frequency offset safety is shown in Figure 7. Figure 7(a) reflects the relationship between the system frequency and time after the disturbance occurs. It can be seen that the system frequency finally stabilizes after a short and large fluctuation, and the frequency drops compared to before the disturbance. Figure 7(b) reflects the relationship between the system safety frequency margin index and the disturbance power. It can be seen from Figure 7(b) that when the disturbance reaches the critical value, the system frequency safety will be threatened.

Equation (5) shows that, in case of $\eta > 0$, the node transient frequency is safe; otherwise it is not safe; hence, $\eta = 0$ is critical safety. Similarly, the critical disturbance amount in Figure 7(b) can also be used as a determination condition whose value is calculated by interpolation according to

$$\Delta P_3 = \frac{\eta_2 \Delta P_1 - \eta_1 \Delta P_2}{\eta_2 - \eta_1}. \tag{6}$$

5.2. Analysis of Primary Frequency Regulation Parameters of Conventional Units. In this paper, the speed regulation system of a hydroturbine unit is taken as an example to analyze the influence of the optimization of one frequency regulation parameter on improving the frequency stability of the system. The model of the turbine governor and prime mover is shown in Figure 8.

Figure 8 indicates that the closed-loop transfer function of the governor is described as

$$\frac{P_M}{P_0 R - K' \Delta\omega} = \frac{\left(1/T_G\left(1 + sT_P\right)\right)(1/s)\left(1 - sT_W/1 + s\left(T_W/2\right)\right)}{1 + \left(R + \left(sD_d T_d/1 + sT_d\right)\right)\left[\left(1/T_G\left(1 + sT_P\right)\right)(1/s)\right]}. \tag{7}$$

According to the criterion of the generator dynamic stability characteristic equation, we can obtain

$$T_d^{\,2}\left(R + D_d\right) + T_d\left(T_G + D_d T_P\right) + T_G T_P > 0. \tag{8}$$

In equation (8), the soft feedback coefficient is related to the water hammer effect time constant. Therefore, the main factors affecting the dynamic characteristics of the unit are the adjustment coefficient, the governor response time, and the time constant of the pilot valve.

The dead zone of the governor is also an important parameter that affects the system frequency. If set properly, the dead zone plays a role in filtering out disturbance signals with lower speeds and making the unit power stable. Conversely, if the dead zone set is too small, the unit is likely to be damaged because the valve is adjusted too frequently; if the dead zone set is too large, the frequency regulation ability is affected because the governor does not operate.

5.3. Effect of Frequency Modulation Parameter Optimization on Transient Frequency. Since the space for governor response time to be optimized is very limited, it is not feasible to operate the governor in actual engineering. Therefore, this article mainly studies the two aspects of optimizing the governing coefficient and the dead zone of the governor. Taking bus 32 as an example, the idea of simulation setup is as follows: (1) control the dead zone of the governor, set the adjustment coefficients to 0.02, 0.03, 0.04, 0.05, and 0.06, respectively, and calculate the critical disturbance of the system according to the above method; (2) the control adjustment coefficient remains unchanged, and the dead zone of the governor is set as 2r/min, 3r/min, 4r/min,

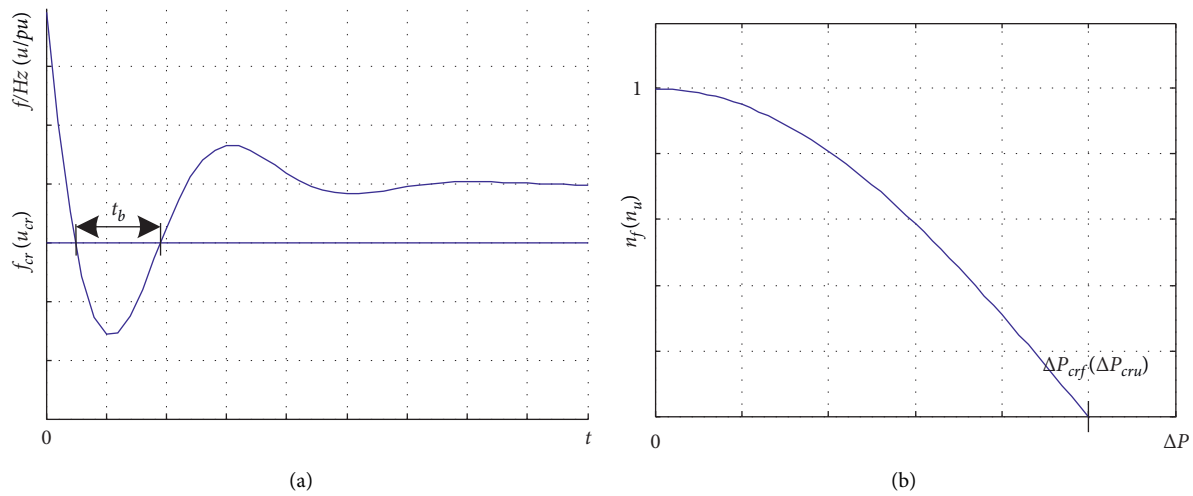

Figure 7: Node transient frequency offset security diagram.

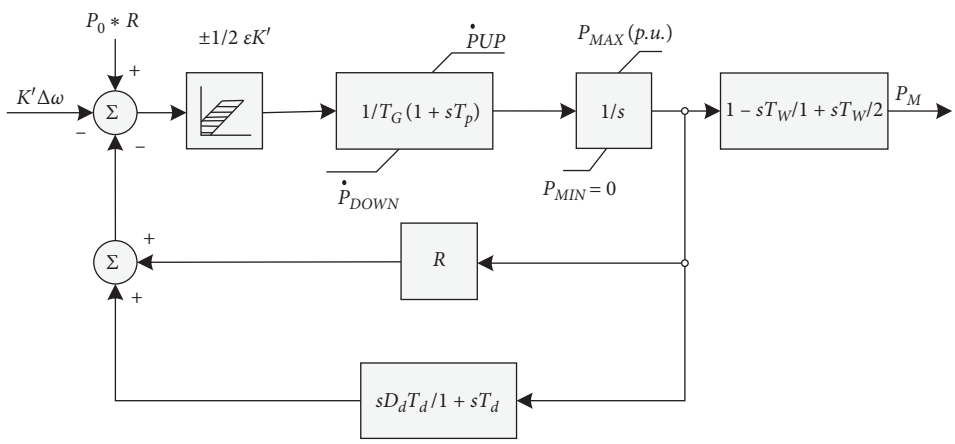

Figure 8: Typical structure of the turbine governor and prime mover model.

5r/min, and 6r/min. The critical disturbances of the system are calculated according to the above methods.

After simulation calculations, the results after optimized settings are shown in Figures 9 and 10.

From Figures 9 and 10, it can be seen that the critical disturbance amount that satisfies the frequency transient stability margin index seems to increase first and then decrease with the increase of the adjustment coefficient; as the dead zone of the governor increases, there is a tendency of monotonic decrease. Therefore, if the adjustment coefficient is too large or too small, the value of the frequency stability margin index decreases, and the corresponding critical disturbance amount also decreases accordingly. The size of the governor's dead zone determines the maximum frequency transient process and its maximum offset. The smaller governor dead zone set is followed by smaller maximum value of the frequency offset during the transient process, and the fluctuation process is smaller too.

Combining the above simulation experiments and analysis results, we can conclude that when the frequency stability margin index is considered to be satisfied in the IEEE 39-node example, setting the frequency adjustment parameter of the large-capacity unit to the adjustment coefficient $R = 0.04$ and $\varepsilon = 2$r/min is optimal. At this time,

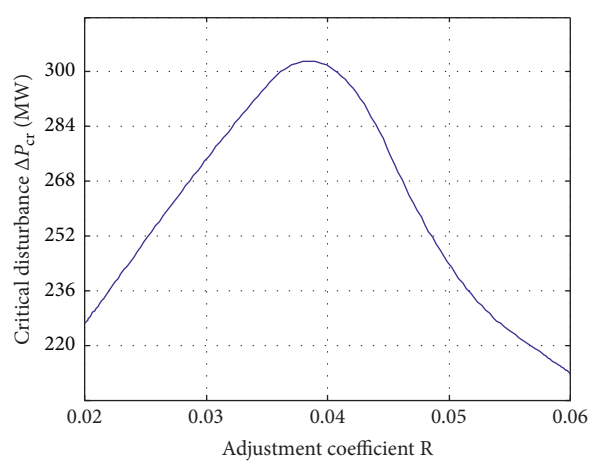

Figure 9: Critical disturbance amount curve after optimization of adjustment coefficient.

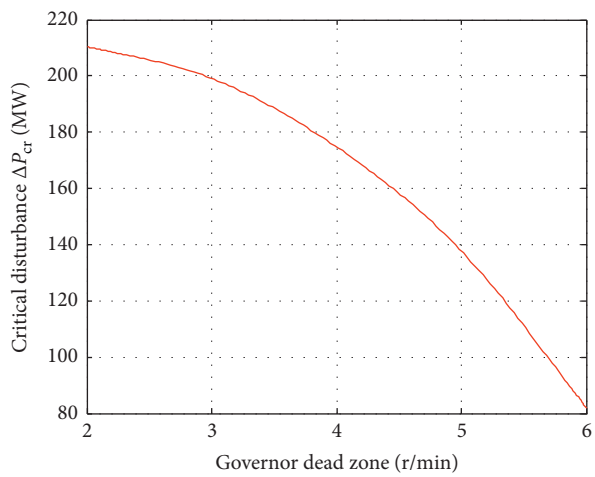

Figure 10: Critical disturbance amount curve after optimization of governor dead zone.

ΔP_{cr} = 304.5 MW, while the critical disturbance amount based on the nodal frequency characteristic surface before optimization is $\Delta P'_{cr}$ = 288.8 MW, which indicates that the frequency stability is significantly improved.

6. Conclusions

With the increasing proportion of photovoltaic power generation capacity in the total installed capacity of power systems, photovoltaic output is featured by randomness, intermittentness, no mechanical inertia, and "electric power electronics", which makes the control of power grids more complex and also profoundly changes the transient frequency stability characteristics of the system. In this paper, the influence mechanism of photovoltaic grid-connected power system frequency was analyzed, and the analysis method of frequency transient stability of photovoltaic grid-connected power system was proposed. The main conclusions are as follows:

(1) Based on the establishment of a BPA transient model of a photovoltaic grid-connected system, this paper explores the high- and low-frequency effects of the transient frequency of the system under the high permeability of photovoltaic under large disturbance. The mechanism analysis shows that as the photovoltaic permeability of the system increases, the problem of transient frequency stability in the system is easier to detect.

(2) A method for evaluating and analyzing the frequency characteristics of photovoltaic access nodes based on surface fitting is proposed. The IEEE 39-node standard system is used as an example to verify the effectiveness and correctness of the proposed method. Through the above method, the critical photovoltaic penetration rate of a certain node of the power grid can be determined, and the frequency dynamic characteristics of photovoltaic grid-connected nodes can be predicted and evaluated, which has great application reference value for determining the photovoltaic grid-connected points and its installed capacity in engineering practice. According to the simulation experiments and the accuracy check of the prediction results, it is verified that the prediction results have high accuracy.

(3) The measures for improving transient frequency stability based on optimization of frequency modulation parameters of large-capacity units are also proposed. The simulation results of IEEE 39-node standard system show that, by optimizing the adjustment coefficient of the large-capacity unit, the critical disturbance based on the nodal frequency characteristic surface can be increased, thereby significantly improving the frequency stability after photovoltaic grid connection.

Data Availability

No data were used to support this study.

Conflicts of Interest

The authors declare that there are no conflicts of interest regarding the publication of this paper.

Acknowledgments

This work was supported by the Technology Project of Yunnan Power Grid Co., Ltd. (0560002018030301XT00120).

References

[1] J. Lai, X. Lu, X. Yu, and A. Monti, "Stochastic distributed secondary control for ac microgrids via event-triggered communication," *IEEE Transactions on Smart Grid*, vol. 11, no. 4, pp. 2746–2759, 2020.

[2] J. Lai and X. Lu, "Nonlinear mean-square power sharing control for AC microgrids under distributed event detection," *IEEE Transactions on Industrial Informatics*, p. 1, 2020.

[3] J. Lai, X. Lu, X. Yu, and A. Monti, "Cluster-oriented distributed cooperative control for multiple AC microgrids," *IEEE Transactions on Industrial Informatics*, vol. 15, no. 11, pp. 5906–5918, 2019.

[4] J. Lai, H. Zhou, W. Hu, X. Lu, and L. Zhong, "Synchronization of hybrid microgrids with communication latency," *Mathematical Problems in Engineering*, vol. 2015, pp. 1–10, Article ID 586260, 2015.

[5] D. W. Liu, S. Y. Chen, and M. Ma, "A review of photovoltaic power generation system models," *Power System Technology*, vol. 35, no. 8, pp. 47–52, 2011.

[6] L. H. Stember, W. R. Huss, and M. S. Bridgman, "A methodology for photovoltaic system reliability & economic analysis," *IEEE Transactions on Reliability*, vol. R-31, no. 3, pp. 296–303, 1982.

[7] M. Ding, W. S. Wang, X. L. Wang et al., "Summary of the influence of large scale photovoltaic power generation on power system," *Proceedings of Chinese Society for Electrical Engineering*, vol. 34, no. 1, pp. 1–14, 2014.

[8] W. Zhang, T. Y. Xiang, A. Li et al., "Photovoltaic grid-connected transient stability calculation model based on MATLAB-PSASP," *Electrical Power Automation Equation*, vol. 32, no. 6, pp. 80–85, 2012.

[9] H. H. Wang, Y. Tang, C. Jing, J. Hou et al., "Combined modeling and equivalence of wind and light storage combined power generation system," *Proceedings of Chinese Society for Electrical Engineering*, vol. 31, no. 34, pp. 1–11, 2011.

[10] Y. Guan, J. C. Vasquez, J. M. Guerrero, Y. Wang, and W. Feng, "Frequency stability of hierarchically controlled hybrid photovoltaic-battery-hydropower microgrids," *IEEE Transactions on Industry Applications*, vol. 51, no. 6, pp. 4729–4742, 2015.

[11] F. Chan and H. Calleja, "Design strategy to optimize the reliability of grid-connected PV systems," *IEEE Transactions on Industrial Electronics*, vol. 56, no. 11, pp. 4465–4472, 2009.

[12] M. Liserre, R. Teodorescu, and F. Blaabjerg, "Stability of photovoltaic and wind turbine grid-connected inverters for a large set of grid impedance values," *IEEE Transactions on Power Electronics*, vol. 21, no. 1, pp. 263–272, 2006.

[13] H. Suyono and M. Zainuddin, "Injection impact of photovoltaic distributed generations (PVDG) on power distribution system stability," *Applied Mechanics and Materials*, vol. 785, pp. 403–408, 2015.

[14] J. Bank, B. Mather, J. Keller, and M. Coddington, "High penetration photovoltaic case study report," Office of Scientific & Technical Information, Technical Report, National Renewable Energy Laboratory (NREL), Denver, CO, USA, 2013.

[15] M. S. Widyan, "Operational performance stability of grid-connected photovoltaic generator via DC–DC converter and 48-pulse voltage source inverter," *International Journal of Modelling and Simulation*, vol. 37, no. 2, pp. 96–107, 2016.

[16] N. Kakimoto, S. Takayama, H. Satoh, and K. Nakamura, "Power modulation of photovoltaic generator for frequency control of power system," *IEEE Transactions on Energy Conversion*, vol. 24, no. 4, pp. 943–949, 2009.

[17] H. F. Zhou, L. Q. Ni, and T. S. Xu, "Study on dynamic characteristics of power system power frequency," *Power System Technology*, vol. 33, no. 16, pp. 58–62, 2009.

[18] Y. W. Du, "Research on frequency safety and stability characteristics and control of power grid under new energy access conditions," M. S. thesis, North China Electric Power University, Beijing, China, 2017.

[19] W. Q. Chen, X. N. Xin, and Z. P. Cheng, "Control technology of optical storage grid-connected power generation based on virtual synchronous generator," *Transactions of Nonferrous Metals Society of China*, vol. 33, no. 2, pp. 538–545, 2018.

[20] C. Zheng, S. Y. Wang, B. Q Zhang et al., "Dynamic frequency characteristics and countermeasures of photovoltaic high-permeability grid," *Power System Technology*, vol. 43, no. 11, pp. 4064–4073, 2019.

[21] C. G. Li, "Research on transient frequency stability assessment and control of power system," Ph. D. thesis, Shandong University, Jinan, China, 2012.

Hindawi
Complexity
Volume 2020, Article ID 4725808, 19 pages
https://doi.org/10.1155/2020/4725808

Research Article

Hierarchical Multiobjective Dispatching Strategy for the Microgrid System Using Modified MOEA/D

Xiaofeng Wan, Hai Lian, Xiaohua Ding, Jin Peng, and Yining Wu

School of Information Engineering, Nanchang University, Nanchang 330031, China

Correspondence should be addressed to Xiaofeng Wan; xfwan@ncu.edu.cn

Received 29 July 2020; Revised 26 August 2020; Accepted 13 September 2020; Published 28 September 2020

Academic Editor: Xin Li

The large-scale electric vehicles connected to the microgrid have brought various challenges to the safe and economic operation of the microgrid. In this paper, a hierarchical microgrid dispatching strategy considering the user-side demand is proposed. According to the operation characteristics of each dispatch unit, the strategy divides the microgrid system into two levels: source-load level and source-grid-load level. At the source-load level, priority should be given to the use of the renewable energy output. On the basis of considering the user demand, energy storage, electric vehicles, and dispatchable loads should be utilized to maximize the consumption of the renewable energy and minimize the user's electricity cost. The source-grid-load level can smooth the tie-line power fluctuation through dispatching of the power grid and diesel generators. Furthermore, the study presents a modified MOEA/D algorithm to solve the hierarchical scheduling problem. In the proposed algorithm, a modified Tchebycheff decomposition method is introduced to obtain uniformly distributed solutions. In addition, initialization and replacement strategies are introduced to enhance the convergence and diversity. A wind-photovoltaic-diesel-storage hybrid power system is considered to verify the performance of the proposed dispatching strategy and the modified algorithm. The obtained results are compared with other dispatching approaches, and the comparisons confirm the effectiveness and scientificity of the proposed strategy and algorithm.

1. Introduction

With the shortage of global resources and the aggravation of ecological pollution, countries all over the world begin to take the microgrid as an important supplement for the operation of the main network [1]. As the basis and core problem of the optimal operation of the microgrid system, economic environment dispatching of the microgrid has been concerned by scholars all over the world. On the premise of meeting the power system security constraints, the economic/environmental dispatching (EED) problem needs to make use of the existing technology to reasonably schedule the microsource operation mode and unit output. On the contrary, the core of the EED problem is to minimize environmental pollution and maximize economic benefits in the whole scheduling period [2].

However, reducing the pollution of the environment and improving the economic benefits of the microgrid are two goals that influence and restrict each other. There is no absolute optimal solution to make both optimal at the same time. Therefore, in order to find the optimal solution to the scheduling problem, scholars from various countries have proposed various schemes. Hernandez-Aramburo et al. [3] established a microgrid model with two reciprocating natural gas generators, cogeneration systems, wind turbines, and photovoltaic arrays. Moreover, the system was optimized with minimum fuel consumption as the objective function. Mohamed and Koivo [4] also considered the model with the lowest operation and maintenance cost and the lowest environmental cost. The multiobjective economic environment scheduling problem is transformed into a single-objective optimization problem by using the maximum fuzzy satisfaction degree in [4], which significantly reduces the calculation difficulty. However, because the membership function is mainly based on the practical experience, the reliability of the optimization result may be

somewhat reduced. Farzin et al. [5] used the nondominant sorting genetic algorithm with elite strategy (NSGA-II) to solve the microgrid scheduling problem, where the objective functions are the minimum operation cost and the minimum load reduction index of the microgrid. In [6], an artificial shark optimization (ASO) was proposed to solve the economical operation problem of the MG. By comparing with other heuristic algorithms, the ASO performs relatively better than the existing techniques.

Farzin et al. and Singh and Khan [5, 6] used classic bionic algorithms to solve the dynamic economic environment dispatching problem in the microgrid and achieved better results. However, as a classic bionic algorithm, its related research and application have been more in-depth and extensive, but it also exposes its integrated evolutionary solution strategy, poor optimization ability for complex optimization problems, and weak ability to cover the optimal frontier [7]. In contrast, the MOEA/D algorithm adopts the method of decomposing multiobjective problems into a certain number of single-objective problems [8]. This algorithm represents a new development direction of multiobjective optimization problems. In recent years, it has gradually attracted extensive attention from scholars. Ross et al. [9] proposed a novel multiobjective dynamic economic emission dispatch (DEED) model considering the EVs and uncertainties of wind power. Also, it proposes a two-step dynamic constraint processing strategy for decision variables based on the penalty function, and on this basis, the multiobjective evolutionary algorithm based on decomposition (MOEA/D) algorithm is improved to solve the problem. The MOEA/Dusing the localized penalty-based boundary intersection (LPBI) method was proposed in [10]. The algorithm is demonstrated to outperform its competitors on the hybrid renewable energy system (HRES) model as well as a set of benchmarks.

EVs have the potential for low-carbon development and sustainable development. EVs with renewables to participate in the scheduling can improve the utilization of energy. Therefore, it is necessary to study how to arrange them to participate in grid dispatching. Based on the randomness of the wind energy and electric vehicles, the probability density function of wind speed and the energy storage and travel characteristic model of EVs are established in [11]. The improved MOEA/D problem is used to solve the DEED problem, but the effect of the load demand on the DEED problem is not considered in [11]. Lu et al. [12] established a multiobjective optimization model of the microgrid including EVs, but only small-scale EVs were considered to connect to the grid. Zhao et al. [13] proposed a distribution network with the inn for electric vehicles and photovoltaic arrays, which verified that fragmented energy management could effectively reduce the fluctuation of renewables. However, only one charging pile was considered, and the grid with a large number of electric vehicles was not considered. Li et al. [14] introduced the double-chain structure and dynamic rotation angle adjustment strategy. It proposed an improved quantum genetic algorithm, optimized the EED problem of EVs connected to the microgrid system, and verified the superiority of this improved algorithm compared with other algorithms. Whether it is a single-objective or multiobjective optimization, the objective function of microgrid scheduling is relatively limited. More importantly, the operation characteristics of distributed energy generation and the interests of users are not adequately considered in those dispatching models.

In addition, in order to fully consider the interests of the user side, some scholars have begun to study the dispatchable load in the microgrid system. The model established in [15], based on the time-of-use power price mechanism, considered the overall economic optimization of multiobjective and multi-interest groups within the microgrid. The model provided effective help for the operation of the microgrid system and realized electric power marketing for the demand side by using a variant of the NSGA-II algorithm. Zheng et al. [16] considered a microgrid composed of distributed energy, energy storage, and transferable loads. And it changed users' electricity consumption habits through dispatchable loads. Strbac et al. [17] reported the electricity price of interruptible loads based on the economic dispatching model's existing price. Qiu et al. [18] considered the cost of the interruptible load and proposed a scheduling model with the objective function of power grid economic optimization. The results showed that the model could improve the flexibility of scheduling in [18].

At the same time, there are many studies on hierarchical scheduling of microgrids and electric vehicles, and many scholars begin to consider the generation-side and the user-side demand comprehensively [19]. Liu et al. [20] proposed the hierarchical energy system management strategy, considering the diversity of the load and the demand-side response. In [20], the microgrid system was divided into the user layer and microsource layer and used the NSGA-II to realize coordinated control between distributed energy resources (DER), controllable loads, and energy storages (ES). Wang et al. [21] proposed a two-stage scheduling strategy, combining day-ahead scheduling with real-time scheduling. Thus, the load management center could conduct rolling optimization by tracking the load curve and then giving a clear charge and discharge plan for EVs. Ye et al. [22] presented a hierarchical multistage scheduling scheme for the AC/DC hybrid active distribution network. This two-level model avoids the difficulty of solving multiobjective optimization and can clarify the role of various stakeholders in the system scheduling. However, few studies comprehensively consider the operating characteristics of DER and generation and load integrated optimal dispatching.

Based on the above background and research results, this paper proposes a microgrid hierarchical dispatching strategy containing wind turbines (WTs), photovoltaic arrays (PVs), diesel generators (DGs), schedulable loads, and EVs. In the microgrid system, the hierarchical strategy gives full consideration to the influence of the user demands on the economic operation. It uses the modified MOEA/D algorithm to solve the problem. In the proposed strategy, according to the operation characteristics of each dispatch unit, the system is divided into the source-load level and the source-gird-load level. At the source-load level, the dispatchable load and the vehicle-to-grid (V2G) model of

electric vehicles are established to maximize the consumption of the renewable energy. Thus, it can achieve peak load cutting of the system load curve and maximize the user's interests. In dispatching of the source-gird-load level, the output of the DGs and the power of connection lines of the main grid are taken as the decision variables. The objectives of the level are to reduce the overall operation cost and power fluctuation between the microgrid and the main grid. On the premise of meeting the grid energy constraint, the overall optimization of the system side and the user side is realized.

The main result of this paper has the following three points: first, it adopts a hierarchical scheduling strategy. Based on the operation characteristics of each dispatch unit, the strategy divides the microgrid system into two levels: source-load level and source-grid-load level. Furthermore, it proves the scientific nature and effectiveness of the dispatching strategy in the simulation. Second, this paper improves the MOEA/D algorithm for solving the multiobjective problem. A modified Tchebycheff decomposition method is introduced as the decomposition approach in order to obtain uniformly distributed Pareto solutions. And this paper proposes a strategy of initializing the primary population based on the constraint violation value. In addition, a replacement strategy based on the maximum fitness value improvement is also integrated. In the end, it proves that hierarchical scheduling is more capable of coordinating the interests of all stakeholders than conventional scheduling strategies. And through the final comparison experiment, it can be indicated that the participation of schedulable load can effectively improve user satisfaction and reduce load variance.

The rest of this paper is organized as follows. Section 2 introduces the hierarchical dispatching strategy and details of the dispatching processes of the source-load level and the source-grid-load level, respectively. In Section 3, it outlines the mathematical models of EVs and dispatchable load, and on this basis, the microgrid hierarchical dispatching model is established. Section 4 describes the modified MOEA/D algorithm in detail and gives the pseudo-code of the improved part. Section 5 realizes the simulation of the scheduling model in Matlab and compares it with other scheduling strategies and the original algorithm, respectively. The conclusion is drawn in Section 6.

2. The Hierarchical Dispatching Strategy of the Microgrid

The microgrid system with controllable loads, EVs, WTs, PVs, DGs, and ES is shown in Figure 1. In order to solve the economic optimization problem of this complex microgrid system, this section proposes a hierarchical scheduling strategy considering the interests of multiple stakeholders and the characteristics of distributed power supply. According to the operation characteristics of each dispatch unit, the strategy divides the microgrid system into two levels, source-load level and source-grid-load level, based on the coordinated and optimized operation of the source-grid-load system.

2.1. Source-Load Level. The purpose of source-load level dispatching is to reduce the peak-valley difference of the total loads. The strategy of the level takes into account the demand response of the user side and guides users to change the way of electricity consumption from the perspective of the electricity market such as electricity price. The consumption of renewable energy can be realized through source-load level dispatching, which makes the load curve closer to the renewable output curve. More importantly, it can well mobilize the enthusiasm of users to participate in grid dispatching, thus improving the reliability and stability of the grid. The dispatching objects of the source-load stage are EVs, ES, and controllable loads.

EVs have dual characteristics of load and onboard energy storage. Reasonable charging and discharging of electric vehicles can effectively achieve peak-load shifting. Since electric vehicles not only need to satisfy users' travel needs but also need to participate in grid dispatching, this paper divides electric vehicles into two categories: one is subjected to users' driving habits, and the other is entirely subjected to the microgrid management, which is fully dispatchable [23]. The probabilistic travel model of EVs, managed by orderly charging and discharging, is subjected to users' driving habits. Its output curve is obtained by the Monte Carlo simulation algorithm [24]. The fully dispatchable EVs can reduce the peak and valley differences of the load, and energy storage cooperates with dispatchable EVs to smooth the load's peak-valley difference.

On the user side, the load can be divided into dispatchable load and undispatchable load [20], in which the dispatchable load can be divided into transferable load and interruptible load. Undispatchable load cannot be interrupted in the optimization process; otherwise, it will cause severe economic loss and social harm. The interruptible load is the lowest among all loads. When the power supply of the system cannot meet all load demands, the load can be interrupted for a short period of time. At this time, corresponding power failure compensation will be provided to the user side [18]. The total electric quantity of the transferable load in the dispatching period is a certain amount. On the premise of not exceeding the maximum allowable transfer electric quantity, the start-up time of the transferable load can be delayed or advanced, such as washing machines and charging equipment in the household load. Therefore, scheduling of the transferable load is an important measure in the microgrid optimal scheduling. It can not only cut the peak and fill the valley and absorb extra renewable energy but also realize the economic operation of the microgrid [16]. The dispatchable load studied in this paper is the transferable load.

The multiobjective optimization algorithm obtains the Pareto optimal solution set with minimum user cost and minimum system net load variance. Using the method of fuzzy membership degree [7], the compromise solution is selected in the Pareto solution set for analysis, and the output curve of each scheduling unit of the solution is substituted into the next step.

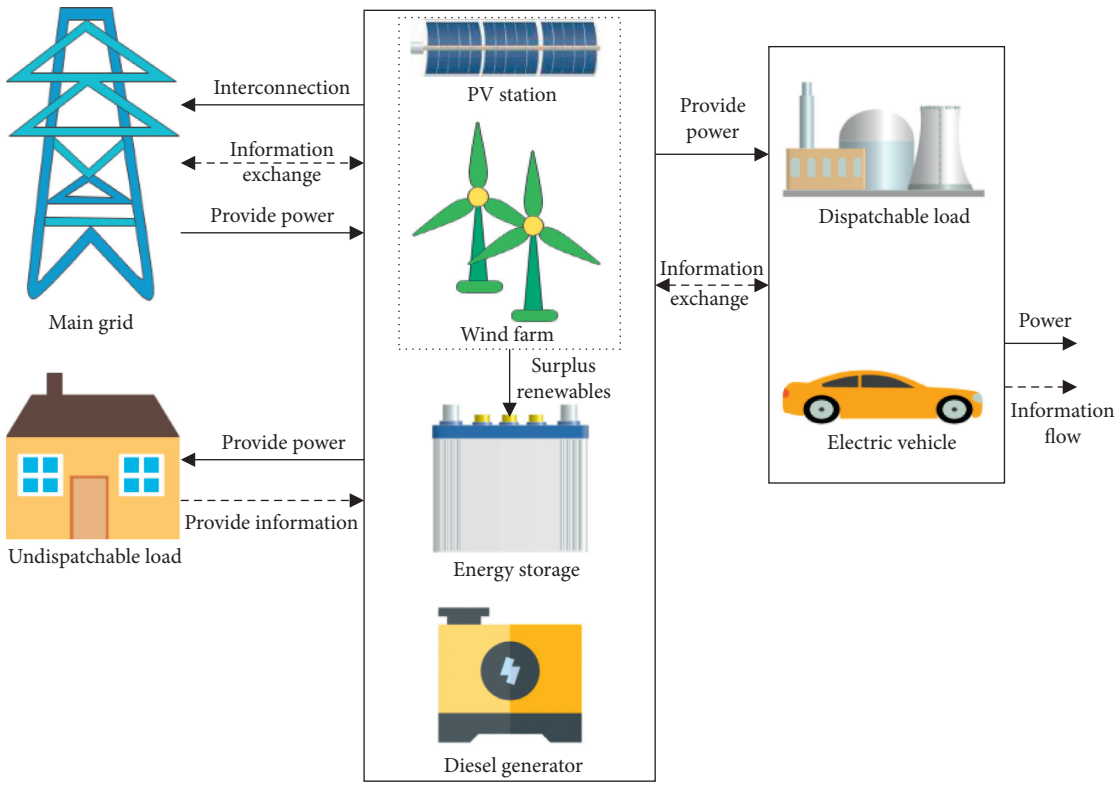

Figure 1: WT-PV-ES-DG-EV hybrid power system with the dispatchable load.

2.2. Source-Grid-Load Level. The net load from the first level is absorbed at the source-grid-load level by the diesel generators and connection lines of the main grid, while the surplus renewable energy is sold to the main grid to gain benefits. The dispatching object of this level is the output of a large power grid and diesel generators. The second dispatching stage's main purpose is to reduce the overall operation cost of the microgrid, as well as the power fluctuation of the connection lines of the grid. The objective function is to minimize the operation cost and the power fluctuation between the microgrid and the main grid. The ramp-rate constraint is adopted for the DGs. And the output upper and lower limits and power balance constraints of the generators should be satisfied at the same time. The net load of the microgrid obtained in the first step is substituted at this level, and the MOEA/D algorithm is used again to obtain the optimal Pareto frontier distribution of the system. After calculation, the compromise optimal solution is selected to discuss the results.

3. Mathematical Model and Characteristic Analysis of the Microgrid

According to the scheduling policy's description, scheduling of the microgrid system is divided into two levels: source-load level and source-grid-load level. This section will carry out mathematical modeling to the EVs and the dispatchable load and establish the corresponding objective function at each level of the system. In order to ensure safe and reliable operation of the system, the last part of this section will systematically introduce the constraints of microgrid scheduling.

3.1. Electric Vehicle Modeling

3.1.1. Probabilistic Model of Electric Vehicle Travel. The probability density functions (PDFs) of the EV's departure and return journey were obtained by fitting the statistical data in [25]. The return trip time of the last trip of electric vehicles satisfies the normal distribution $t_0 \sim N(\mu_t, \sigma_t^2)$, and the PDF is as follows:

$$f_t(x) = \begin{cases} \dfrac{1}{\sigma_t\sqrt{2\pi}}\exp\left(-\dfrac{(x-\mu_t)^2}{2\sigma_t^2}\right), & \mu_t - 12 < x < 24, \\ \dfrac{1}{\sigma_t\sqrt{2\pi}}\exp\left(-\dfrac{(x-(\mu_t-24))^2}{2\sigma_t^2}\right), & 0 < x < \mu_t - 12, \end{cases} \tag{1}$$

where the expectation μ_t is 17.6 and variance σ_t is 3.4.

Driving distance S approximately obeys lognormal distribution $S \sim \log N(\mu_s, \sigma_s^2)$. The PDF is as follows:

$$f_s(x) = \left(\frac{1}{x}\right)\left(\frac{1}{\sigma_s\sqrt{2\pi}}\right)\exp\left(-\frac{(\ln x - \mu_s)^2}{2\sigma_s^2}\right), \tag{2}$$

where the expectation μ_s is 3.2 and the standard deviation σ_s is 0.88.

The daily energy consumption of the electric vehicle can be obtained from the daily driving distance, so as to obtain

the charged state when the battery of the electric vehicle enters the network:

$$S_{\mathrm{OC,EC}} = \left(1 - \frac{\mathrm{SW}_{100}}{100C}\right) \times 100\%, \tag{3}$$

where $S_{\mathrm{OC,EC}}$ is the state of charge (SOC) when entering the network, W_{100} is the power consumption of 100 kilometers, and C is the total capacity of the battery.

$T_{\mathrm{all-disc}}$ is the total discharge duration required to discharge the electric vehicle to the lower limit of the state of charge when it is fully charged:

$$T_{\mathrm{all-disc}} = \frac{\left(S_{\mathrm{OC,max}} - S_{\mathrm{OC,min}}\right)\mathrm{C}}{P_{\mathrm{disc}}}, \tag{4}$$

where $S_{\mathrm{OC,max}}$ and $S_{\mathrm{OC,min}}$ are the upper and lower limits of the charged state of the battery, respectively, and P_{disc} is the discharge power of the EV.

The actual discharge duration T_{disc} is

$$T_{\mathrm{disc}} = T_{\mathrm{all-disc}} - \left(\frac{SW_{100}}{100P_{\mathrm{disc}}}\right). \tag{5}$$

The discharge time $T_{\mathrm{start-disc}}$ is obtained from the comparison between the last return time and the starting time of the morning and evening peak of the original load in the microgrid. The end time of discharge $T_{\mathrm{end-disc}}$ is determined by the beginning time of discharge $T_{\mathrm{start-disc}}$ and the duration of discharge T_{disc}. The upper limit of $T_{\mathrm{end-disc}}$ is 12:00 p.m. Due to the limitation of the discharge time, some EVs have not completely discharged their electricity. Therefore, the initial state of charge at the beginning of charging varies with the discharge condition, and the initial state of charge is only determined by the above discharge condition.

The charging load P_{EV} required by a single electric vehicle is the total energy consumed in a day:

$$P_{\mathrm{EV}} = \left(\frac{\mathrm{SW}_{100}}{100}\right) + P_{\mathrm{disc}}\left(T_{\mathrm{end-disc}} - T_{\mathrm{start-disc}}\right). \tag{6}$$

Since the charging time of each EV is independent, the corresponding parameters of each EV can be obtained by random tests. According to the obtained charging and discharging initial time and the maximum discharge power by the Monte Carlo method, the charging time $T_{\mathrm{char}}(i)$ and discharging time $T_{\mathrm{dischar}}(i)$ of the i-th EV and the daily charging and discharging load $E_{\mathrm{ev}}(t)$ of each EV at time t are decided.

3.1.2. Dispatchable Electric Vehicle Modeling. Large-scale EV which are dispatched directly in the microgrid system will produce "dimension disaster." The area of electric cars is gathered by agents in this paper, equivalent to large aggregate "virtual electric vehicles." Then, through the system scheduling mechanism, all the aggregates are dispatched to alleviate the pressure on the system side [26]. The following part mainly focuses on the scheduling problem of system-side aggregates.

In order to meet the travel characteristics and energy storage characteristics of electric vehicles, this paper makes the following assumptions about dispatchable EVs:

(1) The SOC of electric vehicles is 100% when they leave home every morning

(2) Electric vehicles can drive to and from work within an hour starting at 7 o'clock and 17 o'clock and can flexibly participate in grid dispatching during the rest of the time

The minimum SOC limit and rated charge and discharge power of the vehicle battery in the dispatching cycle are set at 20% of the rated value. And the charging and discharge efficiency is set at 0.85. The total driving distance of each EV in one dispatching period is 50 km. Taking into account the V2G behavior of electric vehicles and considering the energy consumption to meet users' driving needs, the remaining electric quantity S_t of electric vehicles in time t can be obtained [27]:

$$S_t = S_{t-1} + \eta_C P_{\mathrm{Ch},t}\Delta T - \left(\frac{1}{\eta_D}\right)P_{\mathrm{Dch},t}\Delta T - S_{\mathrm{Trip},t}, \tag{7}$$

where η_C and η_D are the charging and discharging efficiency, ΔT is the scheduling interval, and $S_{\mathrm{Trip},t}$ is the energy consumed by the electric vehicle in the process of driving in time period t:

$$S_{\mathrm{Trip},t} = \Delta S \times L, \tag{8}$$

where ΔS presents the average power consumption per unit distance and L is the driving distance.

In order to ensure battery's life and operation safety, its remaining capacity S_t must be limited within a certain range, that is,

$$S_{\min} \le S_t \le S_{\max}, \tag{9}$$

where $S_{\max}$ and $S_{\min}$ are the upper and lower limits of battery power.

The charging and discharging power of an electric vehicle have a certain safety constraint and cannot exceed its rated charging and discharging power as follows:

$$\begin{cases} P_{\mathrm{Ch},t} \le P_{\mathrm{NCh}}, \\ P_{\mathrm{Dch},t} \le P_{\mathrm{NDch}}, \end{cases} \tag{10}$$

where P_{NCh} and P_{NDch} present the rated charging and discharging power of an electric vehicle.

The most important function of electric vehicles is to meet the vehicle owners' travel needs. Since too many charge and discharge cycles will damage the battery life, this paper sets that only one charge and discharge cycle is completed in each scheduling cycle. The vehicle owners' travel needs are constrained as follows:

$$\sum_{t=1}^{T} S_{\mathrm{Trip},t} = \sum_{t=1}^{T} \eta_C P_{\mathrm{Ch},t}\Delta T - \sum_{t=1}^{T} \frac{1}{\eta_D} P_{\mathrm{DCh},t}\Delta T. \tag{11}$$

3.2. Schedulable Load Modeling. Dispatching of the transferable load is an important measure in optimal dispatching of the microgrid. It can also realize peak-load shifting optimization and the absorption of renewable energy, as well as the optimal economic operation of the microgrid. In this paper, the load of the microgrid system is composed of the undispatchable load and transferable load. The load model is as follows [28]:

$$P_L = P_{L,\mathrm{im}} + P_{L,\mathrm{tr}}, \tag{12}$$

where P_L, $P_{L,\mathrm{im}}$, and $P_{L,\mathrm{tr}}$ are, respectively, the total load power of the system, the undispatchable load power, and the transferable load power.

Transferable loads can be transferred from one time period to another, but the total power of transferable loads remains the same in one scheduling period T:

$$P_{L,\mathrm{tr}} = \sum_{t=1}^{T} P_{L,\mathrm{tr}}(t), \tag{13}$$

where $P_{L,\mathrm{tr}}(t)$ is the demand of the transferable load in time period t.

In addition, transferable load shall be transferred within the load power range:

$$P_{L,\mathrm{tr}}^{\min}(t) \le P_{L,\mathrm{tr}}(t) \le P_{L,\mathrm{tr}}^{\max}(t), \tag{14}$$

where $P_{L,\mathrm{tr}}^{\max}(t)$ and $P_{L,\mathrm{tr}}^{\min}(t)$, respectively, represent the upper and lower limits of the power consumption of the transferable load in time t.

3.3. Objective Functions. In this paper, we study the economic scheduling problem of the WT-PV-DG-ES microgrid system, which takes into account V2G and the dispatchable load. Economic scheduling, as a complex multiobjective optimization problem, is worth considering not only the operation cost but also the environmental protection, user satisfaction, and load peak-valley difference. On the one hand, dispatching of the source-load level is to improve the satisfaction of the user's electricity expenditure; on the other hand, it is to realize the absorption of renewable energy and make the load curve fit the renewable energy output as much as possible [21]. The objective functions of the source-grid-load level are the power fluctuation of the tie line between the main grid and the microgrid and the comprehensive operation cost of the system. The objective functions of the optimization model will be established in the following.

3.3.1. User-Side Cost and Load Variance. In the first stage of dispatching, the user cost mainly refers to the user electricity charge C_{load} and the discharge subsidy C_{dis} of V2G:

$$\begin{aligned} f_{\mathrm{user}} &= C_{\mathrm{load}} - C_{\mathrm{dis}}, \\ C_{\mathrm{load}} &= \sum_{t=1}^{T}\left(P_{L,\mathrm{im}}(t) + P_{L,tr}(t) + P_{\mathrm{ev,ch}}(t)\right)p_L(t), \\ C_{\mathrm{dis}} &= \sum_{t=1}^{T} P_{\mathrm{ev,dis}}(t)p_{\mathrm{ev}}, \end{aligned} \tag{15}$$

where T is the number of scheduling time periods. Scheduling of the day studied in this paper is 24 hours; $P_{\mathrm{ev,ch}}(t)$ and $P_{\mathrm{ev,dis}}(t)$ are the charging power and discharging power of the EV in time period t, both of which are positive; p_{ev} is the uniform discharge subsidy of the microgrid system to the electric vehicle; and $p_L(t)$ is the TOU (time-of-use) price in t period.

In order to alleviate the impact of the wind turbine and photovoltaic grid connection on the power grid and reduce the fluctuation of the load, the objective function was established by taking the minimum load variance f_{var} of grid connection as the optimization objective [29]:

$$\begin{aligned} f_{\mathrm{var}} &= \left(\frac{1}{T}\right)\sum_{t=1}^{T}\left(P_L(t) + P_{ES}(t) + P_{ev,ch}(t) - P_{ev,dis}(t) - P_{new} - P_{av}\right)^2, \\ P_{\mathrm{av}} &= \sum_{t=1}^{T}\frac{\left(P_L(t) + P_{ES}(t) + P_{ev,ch}(t) - P_{ev,dis}(t) - P_{new}\right)}{24}, \end{aligned} \tag{16}$$

where $P_{\mathrm{ES}}(t)$, P_{new}, and P_{av}, respectively, represent the output of the ES in time period t, the predicted renewable energy output power, and the average load in the dispatching period.

3.3.2. Integrated Operation Cost and Power Fluctuation. At the second-level dispatching, the scheduling objects are the power grid and DGs. It aims to reduce the comprehensive operation cost on the system side and improve the safety and reliability of the microgrid system, which is reflected by the power fluctuation of connection lines of the main grid. Therefore, the objective function is the minimum integrated operation cost $f_{\cos t}$ of diesel generators and the power grid [30] and the power fluctuation f_{flu} of the tie lines.

As the problem of air pollution becomes more and more serious, more and more countries and regions begin to consider environmental protection. However, conventional thermal power units will produce greenhouse gases and air pollutants in the process of power generation, such as SO_x and NO_x [6]. Therefore, it is very necessary to reduce the emission of air pollutants caused by thermal power units. The comprehensive operation cost $f_{\cos t}$ refers to the comprehensive operation cost of DGs $C_{\mathrm{de},\cos t}$ and the power grid $C_{\mathrm{grid,cost}}$. The operating cost of DGs includes operating and maintenance cost $C_{\mathrm{de,om}}$, fuel cost $C_{\mathrm{de,fuel}}$, and environmental governance cost $C_{\mathrm{de,en}}$ [7]:

$$\begin{aligned} f_{\cos t} &= C_{\mathrm{de},\cos t} + C_{\mathrm{grid},\cos t}, \\ C_{\mathrm{de},\cos t} &= C_{\mathrm{de,om}} + C_{\mathrm{de,fuel}} + C_{\mathrm{de,en}}, \\ C_{\mathrm{de,om}} &= \sum_{t=1}^{T} K_{\mathrm{om,de}}P_{\mathrm{de}}(t), \\ C_{\mathrm{de,fuel}} &= \sum_{t=1}^{T}\left(a + bP_{\mathrm{de}}(t) + c\left(P_{\mathrm{de}}(t)\right)^2\right), \\ C_{\mathrm{de,en}} &= \sum_{t=1}^{T}\sum_{k=1}^{K}\left(C_k\gamma_{\mathrm{de},k}\right)P_{\mathrm{de}}(t), \end{aligned} \tag{17}$$

where $K_{\mathrm{om,de}}$ is the running maintenance coefficient of the diesel engine; a, b, and c are the fuel coefficients of the diesel engine; C_k is the treatment of category k pollutants; and $\gamma_{\mathrm{de},k}$ is the emission of class k pollutants generated by DG operation.

The operating cost $C_{\mathrm{grid,cost}}$ of the main grid connection lines includes the electricity transaction cost $C_{\mathrm{grid,price}}$ between the main grid and the microgrid and the environmental governance cost $C_{\mathrm{grid,en}}$ generated during operation:

$$\begin{aligned} C_{\mathrm{grid,cost}} &= C_{\mathrm{grid,price}} + C_{\mathrm{grid,en}}, \\ C_{\mathrm{grid,price}} &= \sum_{t=1}^{T} p_L(t) P_{\mathrm{grid}}(t), \\ C_{\mathrm{grid,en}} &= \sum_{t=1}^{T}\sum_{k=1}^{K}\left(C_k \gamma_{\mathrm{grid},k}\right)\left|P_{\mathrm{grid}}(t)\right|, \end{aligned} \tag{18}$$

where C_k presents the treatment of category k pollutants; $\gamma_{\mathrm{grid},k}$ is the emission of class k pollutants generated by the grid; and $P_{\mathrm{grid}}(t)$ is the tie-line power of the main network at time t, whose value is positive, which means that the microgrid buys electricity from the main grid, and negative means that the microgrid sells electricity to the main grid. The expression of power fluctuation f_{flu} of the connection lines is as follows [31]:

$$f_{\mathrm{flu}} = \sum_{t=1}^{T-1}\left|P_{\mathrm{grid}}(t+1) - P_{\mathrm{grid}}(t)\right|. \tag{19}$$

3.4. System Constraints. In order to ensure normal and safe operation of the system, the following general constraints are required [27].

3.4.1. System Equality Constraint. The power balance constraint is expressed in the form of equality constraint, which represents the unit output's satisfaction with the load in each dispatching period:

$$P_{\mathrm{grid}}(t) + P_{\mathrm{new}}(t) + P_{\mathrm{de}}(t) = P_L(t) + P_{\mathrm{ES}}(t) + P_{\mathrm{EV}}(t). \tag{20}$$

Interpretation of the equation: $P_{\mathrm{grid}}(t)$ represents the power of the main grid connection lines at time t; $P_{\mathrm{new}}(t)$ represents the power of the WT and PV predicted at time t; $P_{\mathrm{de}}(t)$ is the output of the DGs at time t; $P_L(t)$ is to the net load power of the microgrid system at time t; and $P_{\mathrm{EV}}(t)$ and $P_{\mathrm{ES}}(t)$, respectively, represent the output state of the EV and ES unit at time t; the positive value represents charging, and the negative value represents discharge. The units of the above parameters are kw·h.

3.4.2. Upper and Lower Bound Constraints.

$$P_{\mathrm{Gi}}^{\min} \le P_i(t) \le P_{\mathrm{Gi}}^{\max}, \tag{21}$$

where $P_{\mathrm{Gi}}^{\min}$ and $P_{\mathrm{Gi}}^{\max}$ represent the lower and upper limits of power per unit time of generator i, respectively.

3.4.3. Ramp-Rate Constraints. The ramp-rate constraints are the unit lift (drop) power capacity within the unit scheduling period:

$$\begin{aligned} P_i(t) - P_i(t-1) - U_{\mathrm{Ri}}\Delta T \le 0, \\ P_i(t-1) - P_i(t) - D_{\mathrm{Ri}}\Delta T \le 0, \end{aligned} \tag{22}$$

where U_{Ri} and D_{Ri} are the lift and drop ramp rate of generator i, respectively. The object of the ramp-rate constraint is diesel generator.

3.4.4. Energy Storage Constraints. Constraint of the state of charge is given by

$$S_{\min} \le S(t) \le S_{\max}. \tag{23}$$

Energy storage output limits:

$$P_{\mathrm{ES}}^{\min} \le P_{\mathrm{ES}}(t) \le P_{\mathrm{ES}}^{\max}, \tag{24}$$

where $S_{\max}$, $S_{\min}$, $P_{\mathrm{ES}}^{\min}$, and $P_{\mathrm{ES}}^{\max}$ represent the upper and lower limits of the charged state and output of the energy storage unit, respectively.

3.4.5. Spinning Reserve Constraint. The configuration of spinning reserve capacity has played a positive role in the actual operation of the power system. Due to the uncertainty and intermittency of the renewable output, it is necessary to have a certain reserve capacity to ensure the safety and reliability of the grid connection [32].

$$\sum_{i=1}^{N} P_{i,\max} + P_{\mathrm{wt}} + P_{\mathrm{pt}} \ge P_{\mathrm{ev},t} + P_{L,t} + S_{R,t}, \tag{25}$$

where $S_{R,t}$ is the spinning reserve capacity requirement of the system at time t.

4. Modified MOEA/D Algorithm

As described in the previous section, the economic scheduling problem of the microgrid is a multiobjective optimization problem. The optimization problem needs to consider complex unit operation and system constraints, some of which are nonlinear and time-coupled equality and inequality constraints. This section will introduce the general framework of the multiobjective optimization problem. In order to solve this problem, this paper adopts the MOEA/D algorithm and improves some shortcomings of the algorithm. The last part gives detailed steps for the modified MOEA/D algorithm.

4.1. Multiobjective Optimization Problem. In general, a multiobjective optimization problem consists of two or more mutually restrictive objectives to be optimized and a series of equality and inequality constraints to be satisfied.

Multiobjective optimization problems are usually expressed in the following forms [30]:

$$\begin{aligned} &\min F = \{f_1(x), f_2(x), f_3(x), \ldots, f_M(x)\}, \\ &\quad x = [x_1, x_2, x_3, \ldots, x_n], \\ &\text{subject to } g_j(x) \geq 0, \quad j = 1, 2, \ldots, G, \\ &h_k(x) = 0, \quad k = 1, 2, \ldots, H, \\ &x_i^{\min} \leq x_i \leq x_i^{\max}, \quad i = 1, 2, \ldots, n. \end{aligned} \tag{26}$$

In this paper, the i-th objective function of the multiobjective optimization problem is represented by $f_i(x)$; x is an n-dimensional decision vector. And G and H represent the number of inequality constraints and equality constraints, respectively. In single-objective optimization problems, the optimal solution is usually unique. However, due to the mutual restriction between different objective functions in multiobjective problems, the optimal solutions of multiobjective optimization usually consist of a solution set. Therefore, in order to solve the multiobjective optimization problem, it is necessary to understand the concepts of Pareto dominance, Pareto optimal, Pareto-optimal set, and Pareto-optimal front [33]. According to these definitions, a multiobjective optimization problem can be treated as finding Pareto-optimal solutions or approaching the Pareto-optimal front [34].

4.2. The Main Framework for the MOEA/D Algorithm. As described in [35], the objective functions of a multiobjective problem are usually contradictory, and generally, there is no one solution in the feasible region that can minimize all the objective functions at the same time. Therefore, the purpose of the multiobjective optimization problem is to find all the nondominant or noninferior solutions. In order to find all nondominant solutions, the MOEA/D algorithm decomposes a multiobjective problem into a series of single-objective subproblems by using the weighted sum approach, the Tchebycheff approach, and the boundary intersection approach [36]. These subproblems then produce offspring through collaborative optimization using an evolutionary algorithm [8]. These subproblems are optimized by referring to information about their neighborhood problems. The neighborhood relation of subproblems refers to the Euclidean distance based on their aggregation coefficient vectors [8]. Pareto-optimal front of a multiobjective problem can be decomposed into N scalar optimization subproblems in MOEA/D. As described in [34], the above decomposition method transforms the approximate frontier of the multiobjective optimization problem into a series of single-objective optimization problems. Here, we use the Tchebycheff approach to explain the main framework of the MOEA/D algorithm. The j-th single-objective optimization subproblem is expressed as

$$\begin{aligned} g^{\text{te}}\left(x \mid \lambda^j, z\right) &= \max_{1 \leq i \leq m} \left\{\lambda_i^j \left| f_i(x) - z_i^* \right|\right\}. \\ \lambda^j &= \left(\lambda_1^j, \lambda_2^j, \ldots, \lambda_m^j\right)^T. \end{aligned} \tag{27}$$

The MOEA/D algorithm is designed to optimize N problems at the same time rather than to solve multiple problems in one run. In [36], the neighborhood of λ^j is composed of T weight vectors, which are in $\{\lambda^1, \lambda^2, \ldots, \lambda^N\}$, closest to it. Neighborhood weight vectors of λ^j are the neighborhoods of the j-th subproblem. The population is composed of the optimal solution for each subproblem at the moment.

4.3. Improved Tchebycheff Decomposition Method. According to Section 3, the value range and measurement unit of each objective function are different. As a result, each objective function will have a certain weight before being weighted, which may lead to local convergence or failure, to obtain the uniformly distributed Pareto front. For example, the value range of objective 1 is [1500, 1800], and the value range of objective 2 is [30, 50], so the algorithm will focus on the optimization of objective 1 in the process of optimization. Although some articles proposed an improved Tchebycheff approach to reduce the impact of different units and value ranges, a single-target optimization subproblem is as follows [37]:

$$\min g^{\text{tch}}\left(F(x) \mid \omega, z^*\right) = \max_{1 \leq i \leq m} \left\{\frac{f_i(x) - z_i}{\omega_i}\right\}, \tag{28}$$

where m represents m objective functions; $f_i(x)$ and z_i, respectively, represent the i-th objective function value and the ideal value of the objective; and $\omega = (\omega_1, \omega_2, \ldots, \omega_m)^T$ is the weight vector, which satisfies

$$\|\omega\|_1 = \sum_{i=1}^{m} \omega_i = 1. \tag{29}$$

However, when confronted with a complex multiobjective optimization problem, the obtained Pareto front is still not uniform [8]. So here, we propose the modified Tchebycheff approach to overcome the above shortcomings. In the modified Tchebycheff approach, the decomposition of Tchebycheff mentioned above is extended, and a new Tchebycheff decomposition method with a norm constraint on the direction vector is proposed [38]. In this decomposition, each subproblem is constructed based on a direction vector λ, such as (30), which satisfies $\|\lambda^i\|_2 = 1$, rather than the weight vector ω mentioned above. At this point, the representation of each subproblem is shown in (31):

$$\begin{aligned} \lambda^i &= \frac{\omega^i}{\left\|\omega^i\right\|_2}, \quad i = 1, 2, \ldots, N, \\ \lambda^i &= \left(\lambda_1^i, \lambda_2^i, \ldots, \lambda_m^i\right), \quad \left\|\lambda^i\right\|_2 = 1, \end{aligned} \tag{30}$$

$$\min g^{\text{tch}}\left(F(x) \mid \lambda, z^*\right) = \max_{1 \leq i \leq m} \left\{\frac{f_i(x) - z_i}{\lambda_i}\right\}. \tag{31}$$

Based on the modified Tchebycheff decomposition, the particle is in the direction vector corresponding to its subproblem, so the particle distribution is also uniform [38]. Therefore, the improved decomposition method can obtain

a more uniform frontier solution than the original decomposition.

4.4. Initialization Strategy. Obviously, in the microgrid hierarchical dispatching model, there are various high-dimensional nonlinear and time-coupled constraints, which make the feasible solution domain relatively narrow and topologically complex [38]. Therefore, the basic algorithm must be improved according to the characteristics of the problem. And in order to obtain the optimal feasible solution, the effective treatment of the complex constraints of the model is proposed.

Since the process of optimization starts from the initialization of particles, the selection of primary particles is crucial. If the primary particles can be uniformly distributed in the whole space and most of them meet the constraints, the offspring can maintain better diversity in the subsequent process. On the contrary, if all constraints are hard constraints at the beginning of algorithm optimization, such as they are forced to return to the constraint range or constraint boundary when particles do not meet the constraints, it will greatly reduce the diversity of optimization results [38].

Therefore, this paper proposes a strategy of initializing the primary population based on the constraint violation value as outlined in Algorithm 1. First, an initial population P containing N particles is generated according to the given data. And the initial population may not satisfy all the constraint conditions. Secondly, differential evolution is used to generate N offspring, and $2N$ particles are arranged from small to large according to the constraint violations. Then, the first N particles with fewer constraint violations are added to the external file. When comparing the constraint violations of the N-th particle with ξ and the two are equal, it means that the first N particles satisfy all constraints. In order to ensure diversity, ξ is set as a constant close to zero. If the N-th particle constraint violation is lower than ξ, the particles in the external archives are the first-generation population meeting most of the constraints, otherwise back to the second step. Through this optimization, the first-generation particles can enter into the optimization process of the algorithm under the condition that most of the constraints are satisfied. Since the particles are not forced to satisfy all constraints, the diversity is not lost. On the contrary, in the optimization process, the offspring particles just need to make small adjustments to meet the constraints, so the convergence can be achieved at a faster speed.

$$\begin{aligned} &g_j(x) \geq 0, \quad j = 1, 2, \ldots, G, \\ &h_k(x) = 0, \quad k = 1, 2, \ldots, H, \\ &\text{violation}(x) = \sum_{1 \leq j \leq G} \max\left(g_j(x), 0\right) + \sum_{1 \leq k \leq H} \left(h_k(x)\right)^2. \end{aligned} \tag{32}$$

4.5. Replacement Strategy. Population replacement strategy is a key part of MOEAs, which has been studied by many people in recent years [39]. Although most improved population renewal strategies can successfully improve MOEA/D performance, only a part of the subproblem performance can be optimized [40].

This paper adopts a replacement strategy based on the maximum fitness value improvement as outlined in Algorithm 2. Firstly, parameters are initialized that $l = -1$ and MaxFitImp $= -\infty$. Secondly, the difference between the fitness value of offspring particle y and parent particle x^i in each subproblem is obtained. $V_{\text{improvement}}$ represents the value of the improvement of offspring particle y over parent particle x^i in subproblem i. l represents the subproblem of the maximum fitness increase obtained by particle y. Then, if MaxFitImp is greater than zero, the existence of subproblem l is proved. In this subproblem, the fitness value of the parent generation is larger than that of the offspring. It means that offspring y is superior to the parent generation particle, and the corresponding parent particle x^i is replaced by y. Finally, in order to improve the robustness of the algorithm, y is randomly selected to replace a certain number of parent solutions. The pseudo-code of the replacement strategy based on the maximum fitness value improvement is shown as follows:

$$\begin{aligned} V_{\text{improvement}} &= g^{\text{tch}}\left(F\left(x^i\right) \middle| \lambda^i, z\right) - g^{\text{tch}}\left(F\left(y^i\right) \middle| \lambda^i, z\right), \quad i = 1, 2, \ldots, N, \\ l &= \arg\max_{1 \leq i \leq N} \left[g^{\text{tch}}\left(F\left(x^i\right) \middle| \lambda^i, z^*\right) - g^{\text{tch}}\left(F\left(y^i\right) \middle| \lambda^i, z^*\right)\right], \quad i = 1, 2, \ldots, N. \end{aligned} \tag{33}$$

4.6. Best Compromise Solution Based on Fuzzy Decision. After obtaining the Pareto optimal solution set, it is necessary to find the best compromise solution in the final nondominant solution set by decision. In this paper, we use the fuzzy decision function to get a relatively satisfactory final solution in the Pareto front. In order to obtain the most precise judgment for the decision maker, the satisfaction degree of each objective function of the i-th solution can be defined as follows [7]:

$$\mu_{\text{ij}} = \begin{cases} 1, & F_{\text{ij}} \leq \min\left(F_j\right), \\ \dfrac{\max\left(F_j\right) - F_{\text{ij}}}{\max\left(F_j\right) - \min\left(F_j\right)}, & \min\left(F_j\right) \leq F_{ij} \leq \max\left(F_j\right), \\ 0, & \max\left(F_j\right) \leq F_{ij}, \end{cases} \tag{34}$$

Require:
N: population size
EP: external archive, and EP = Ø
V_i: summing all the constraint violations of the i-th solution
Output: population: EP = $\{x^1,\ldots,x^N\}$
Step 1: N particles are generated randomly according to the boundary constraints
Step 2: producing N solutions using the DE operations
Step 3: calculating the overall constraint violations V_i, $i = 1, 2, ..., 2N$
Step 4: sorting the solutions according to the overall constraint violations in the increasing order and selecting the first N number of solutions
Step 5: **If** $V^N > \xi$, **then** set EP = $\{x^1,\ldots,x^N\}$, and return to Step 2
Step 6: output EP = $\{x^1,\ldots,x^N\}$

Algorithm 1: Initialization of the population.

Require:
j: index of the selected subproblem for reproduction.
Neigh_j: indices of the neighbor subproblems of the j-th subproblem, $\text{Neigh}_j = B_j = \{j_1, \ldots, j_T\}$
N: size of the evolutionary population y: newly generated offspring
z: reference point
λ^i: direction vector x^i: decision vector
F^i: objective function of i-th sub-problem
n_r: maximum number of the replaced parent solutions by one offspring solutions
Output: Population: $\{x^1, \ldots, x^N\}$ objective function values: $\{F^1, \ldots, F^m\}$
Step 1 Initialization:$c = 0$ MaxFitImp $= -\infty l = -1$
Step 2 Find the sub-problem of maximal fitness improvement
For $i = 1$ to N do
$V_{\text{improvement}} = g^{\text{tch}}(F(x^i) \mid \lambda^i, z) - g^{\text{tch}}(F(y) \mid \lambda^i, z)$
If $V_{\text{improvement}} \geq$ MaxFitImp, **then** MaxFitImp $= V_{\text{improvement}}$ and $c = c + 1$
Step 3 Replace a parent solution:
If MaxFitImp > 0, **then** set $x^i = y$, $F(x^i) = \text{F}(y)$ and $c = c + 1$
Step 4 Replace improvable parent solutions randomly:
While $c < n_r$ and $\text{Neigh}_j \neq \varnothing$ do
(1) Randomly select an index i from $Neigh_j$
(2) **If** $g^{\text{tch}}(F(x^i) \mid \lambda^i, z) - g^{\text{tch}}(F(x^i) \mid \lambda^i, z) > 0$ then set $x^i = y$, $F^i = F(y)$ and $c = c + 1$
(3) Delete i from Neigh_j
End of While

Algorithm 2: Replacing the parent solution.

where μ_{ij} represents the satisfaction degree of the j-th objective function of the i-th solution. The higher the value of μ_{ij} is, the more satisfied the value of the objective function will be; $\min(F_j)$ and $\max(F_j)$ are the minimum and maximum bounds of the j-th objective function, respectively.

For each nondominant solution, the normalized membership function can be expressed as

$$\mu_i = \frac{\sum_{j=1}^{N_{\text{obj}}} \mu_{\text{ij}}}{\sum_{i=1}^{M} \sum_{j=1}^{N_{\text{obj}}} \mu_{\text{ij}}}, \tag{35}$$

where M is the number of nondominant solutions and N_{obj} is the number of objective functions. The larger the value of μ_i, the better the solution, so the maximum value of μ_i is the best compromise.

4.7. Detailed Steps of the Modified MOEA/D Algorithm. The microgrid optimization dispatching problem involves solving control variables and calculating state variables. The control variables of the problem are generator active power outputs. And the state variables are composed of renewable power output and load demand. All the control variables constitute an individual which represents one solution to the microgrid dispatching problem. When using the modified MOEA/D algorithm to solve the multiobjective optimization problem, the detailed steps are shown in Figure 2.

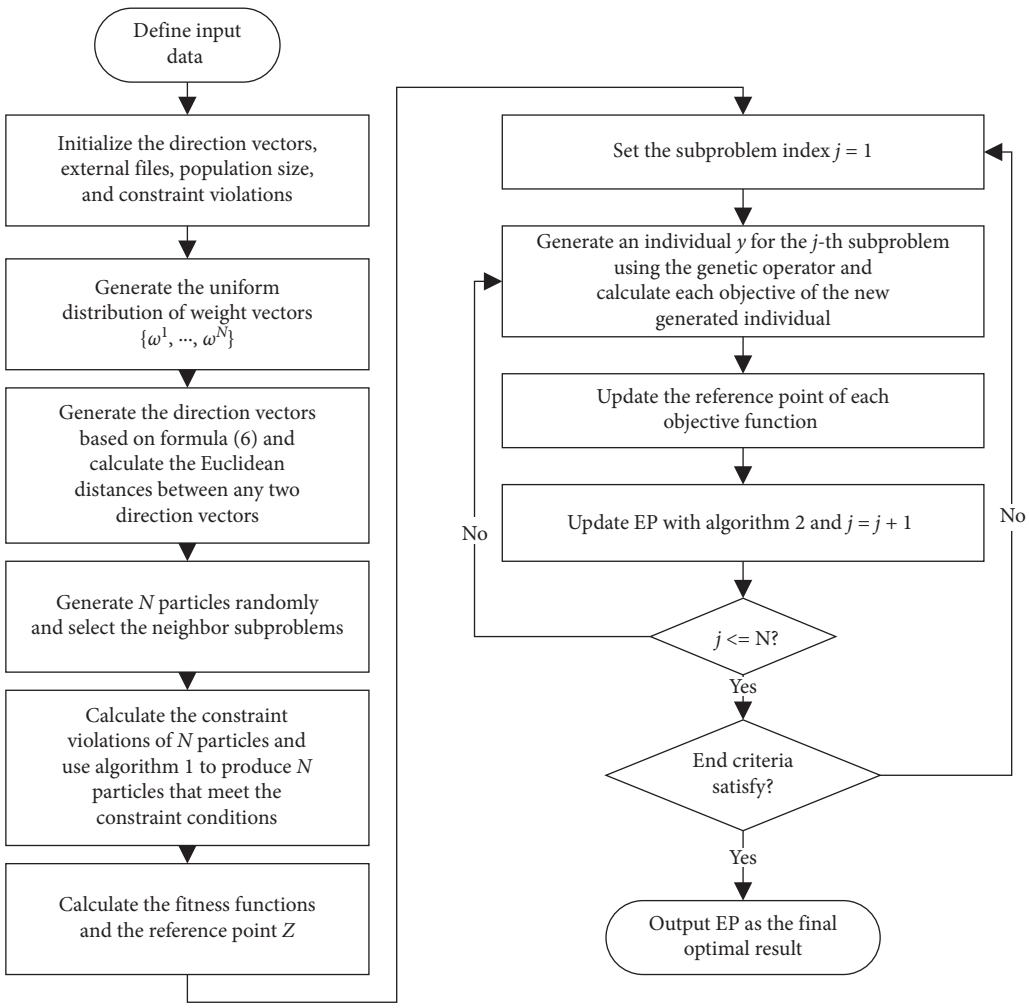

Figure 2: The general main framework of the modified MOEA/D.

5. Simulation Results and Analysis

5.1. Example Parameters. According to the relevant historical data and models, the curve of the renewable energy output and the daily load curve were simulated by the Monte Carlo method [41]. Referring to a real microgrid system in the central region of China, the output of the wind turbine and photovoltaic arrays and the total load are shown in Figure 3, in which the dispatchable load is 10% of the total load. The system contains two diesel generators with a capacity of 0.6 MW and 0.8 MW, respectively, 1 MW lead-acid batteries for energy storage, and 700 EVs with a battery capacity of 24 kw·h. Among them, 400 EVs are subject to user habits, and 300 are fully dispatchable.

In this paper, day-ahead economic dispatching is adopted for the microgrid system, the total dispatching cycle is 24 hours a day, the unit time interval is 1 h, and the electricity price of the main grid adopts TOU price [42]. The electricity price data are shown in Figure 4.

The operating parameters of EVs, ES, DGs, and the power grid are shown in Table 1. And the types of pollutants and the disposing cost are shown in Table 2.

5.2. Obtained Optimal Results

5.2.1. Source-Load Level Dispatching. The Monte Carlo algorithm is used to simulate the travel of 400 EVs. The results and the daily load curve of the system are shown in Figure 5.

As can be seen from the figure, the morning peak load begins to appear in the system at 8:00 a.m., and almost all the EVs finish charging and leave the microgrid system before the morning peak. During the period from 9:00 a.m. to 16:00 p.m., the EVs neither charge nor discharge, that is, they are off the grid. After 17:00 p.m., the EVs return to discharge and participate in system dispatching. And the travel curve is more in line with the user's travel habits. On the contrary, the charging time of EVs is basically from 23:00 p.m. to 8:00 a.m., when the total load is in a low state, and the electricity price is low. Obviously, charging in this period can save charging cost for users. Electric vehicles return to the system after 17:00 p.m. to support peak load demand by discharging. It can alleviate the power shortage in the evening peak and obtain the discharge subsidy. WT, PV, ES, transferable loads, and EVs participate in level dispatching. The simulated traffic data of 400 electric vehicles and the microgrid load are substituted into the mathematical model established above. The objective functions

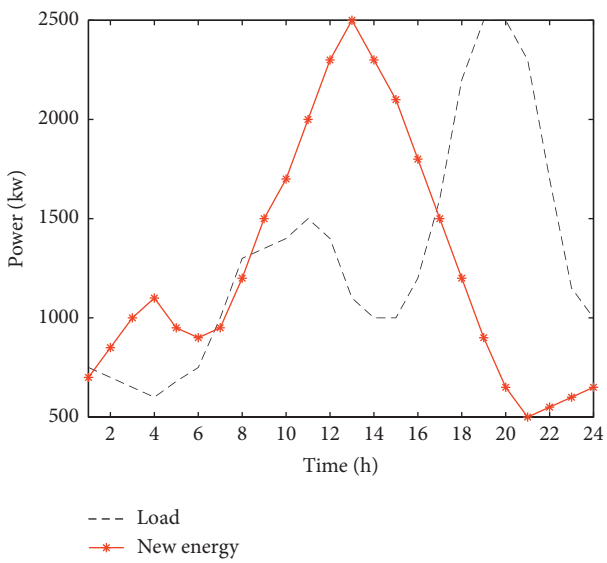

Figure 3: Load curve and renewable energy output curve.

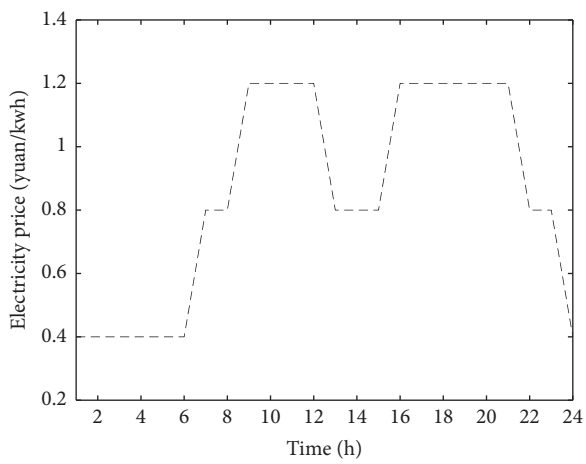

Figure 4: Electric TOU price.

are user cost and load variance in level dispatching. The Pareto front is obtained by using the modified MOEA/D algorithm, as shown in Figure 6.

The fuzzy decision method is used to select (13,732 kw, 25,437 yuan) as the final compromise solution for further analysis. As shown in Figure 7, afterLoad and Load represent the load curves of the transferable load participating in scheduling and not participating in scheduling. And trLoad represents the outpower of the transferable load. It can be seen from the figure that, between 11:00 and 16:00, the electricity price is low, and the power of renewables is large. Thus, most of the transferable loads participate in dispatching in this time period, and the load value of afterLoad is higher than the original load value in this time period. It can be indicated that the original load curve's peak value is greatly reduced when the schedulable load is added.

The curve of netLoad represents the net load of the user side in Figure 8. The netLoad value consists of undispatchable loads, transferable loads, energy storage, and two types of EVs. And the curve of EV is the charging and discharging power of dispatchable EVs. As can be seen from Figure 8, the trend of the EV curve basically follows the output power curve of the renewables. The EVs are driven off-grid from 7:00 a.m. to 8:00 a.m. and from 17:00 p.m. to 18:00 p.m. Then, EVs participate in microgrid scheduling with energy storage in the rest of the time. The output of the energy storage unit also follows the total output of the renewables and the load curve, but the output is not very obvious due to the limitation of its SOC. During the evening peak, EVs discharge along with the energy storage to provide power to the load. When the output of renewable energy is enough to meet the load demand, the energy storage battery and electric vehicle are charged to absorb the redundant renewable energy. At the same time, it can be seen from the figure that the net load curve has been as close to the renewable energy output curve as possible. Thus, it demonstrates that the purpose of maximizing the consumption of renewable energy is achieved. Due to the limitation of the SOC of the energy storage unit, all the surplus renewables have not been absorbed in some periods. The surplus power will be sold to the main grid in the next step.

5.2.2. Source-Grid-Load Level Dispatching. In this stage, the modified MOEA/D algorithm is still used to solve the problem. The objective functions are the minimization of the total operating cost of the system and the power fluctuation of the tie lines. The Pareto front obtained by MOEA/D has been illustrated in Figure 9. It can be seen from the figure that the Pareto front is uniformly distributed. According to the fuzzy decision degree, the compromise optimal solution of the curve is selected, and the results are discussed.

The power outputs of the connection lines and two DGs are shown in Figure 10. If the curve of the grid is negative, it means that the surplus renewables are sold to the main network. The curve of netLoad in the figure consists of the original undispatchable load, the transferable load, the EVs, the ES, and the renewable output. From 7:00 a.m. to 22:00 p.m., renewable energy power is still not consumed after the first step of optimization. Thus, the value of netLoad at this time is less than zero. The redundant renewables are sold to the main network through the connection lines to obtain income for the microgrid side. At this time, the diesel generator stops working, and the power of the connection lines is the same as the netLoad value. When netLoad is positive, the needed power is mainly provided by the main grid due to the low electricity price and the expensive generation cost of the DGs. It can be seen from the figure that the power of tie lines basically fluctuates with the netLoad curve. Two diesel generators are used as the backup supplementary power supply to provide partial power support for the load of the microgrid.

5.3. Comparison of Algorithms. In order to prove the effectiveness of the improved algorithm, this part uses the initial MOEA/D algorithm to solve the hierarchical scheduling problem. We take source-load level scheduling as an example and compare the Pareto solution sets that the two algorithms obtained as follows.

Table 1: Operating parameters.

Operating parameter	Type				
	EV	ES	DG1	DG2	Grid
P_min (kw)	4	200	600	800	1500
P_max (kw)	−4	−200	0	0	−1000
C_min (kw)	—	—	100	150	—
C_max (kw)	—	—	−100	−150	—
Discharge efficiency	0.9	0.9	—	—	—
Charge efficiency	0.9	0.9	—	—	—
S_min (kw)	0.3	0.25	—	—	—
S_max (kw)	0.9	0.95	—	—	—
Operation and maintenance coefficient (yuan/kw)	—	0.104	0.236	0.236	—

Table 2: Pollutant emission factor and disposing cost.

Emission type		CO_2	SO_2	NO_x
Cost (yuan/kg)		0.21	14.824	62.964
Emission	DG	649	0.206	9.89
Coefficient (g/kw·h)	Grid	889	1.8	1.6

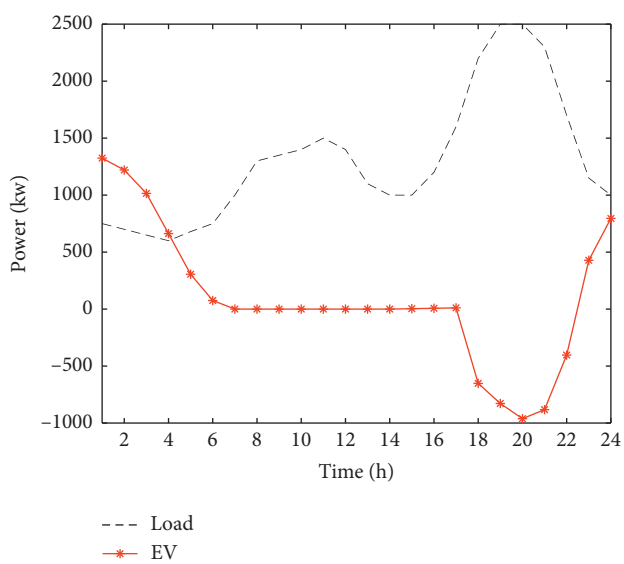

Figure 5: Daily load curve and output of EVs following users' driving habits.

As can be seen in Figure 11, the improved MOEA/D algorithm is closer to the real Pareto frontier than the original algorithm. In order to further explain the performance of the improved algorithm better than the original algorithm, the relationship between the objective functions and the number of iterations is shown in Figure 12.

It can be seen from the figure that although both algorithms eventually converge to the approximate position in the same objective functions, the improved MOEA/D algorithm converges faster than the original algorithm. More importantly, the improved MOEA/D algorithm can eventually reach a smaller value of objective functions. It indicates that the modified MOEA/D algorithm is more effective in this problem.

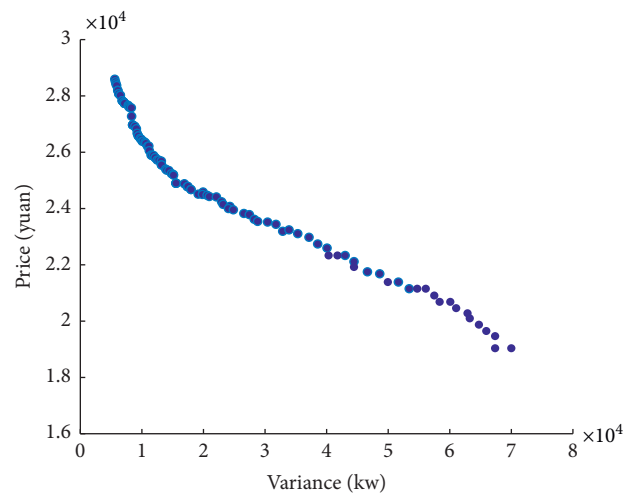

Figure 6: Pareto front of the source-load level.

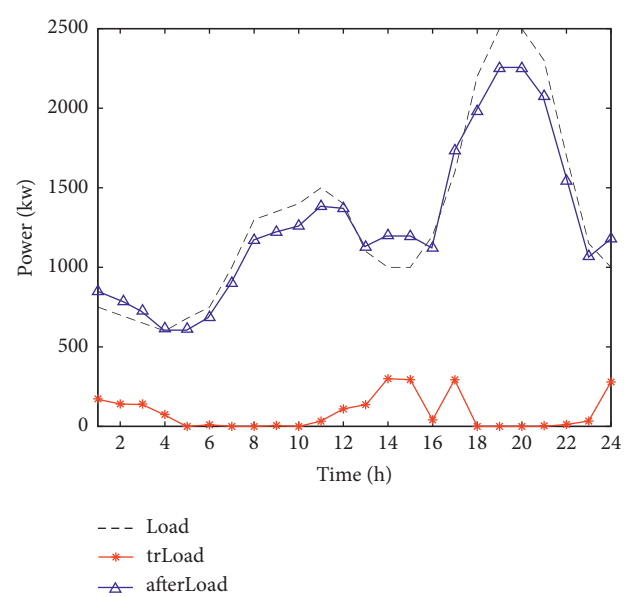

Figure 7: Load curves after dispatching.

5.4. Analysis of Dispatchable Loads. According to Qiu et al. [18], this section establishes the source-load level scheduling strategy excluding the dispatchable load and compares it with

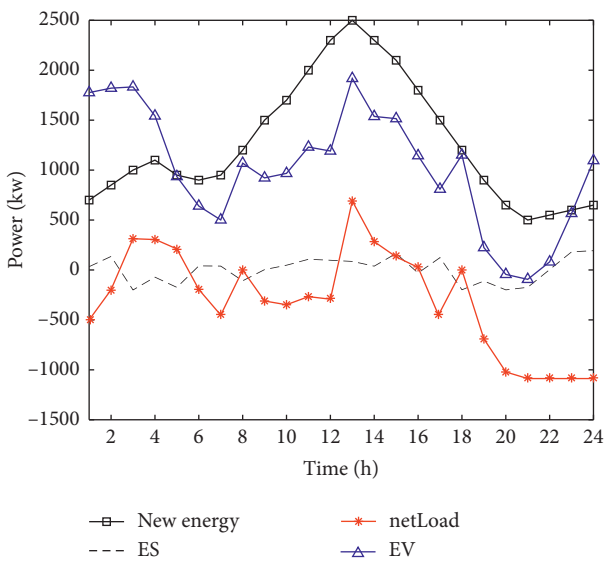

Figure 8: Power output of each unit at the source-load level.

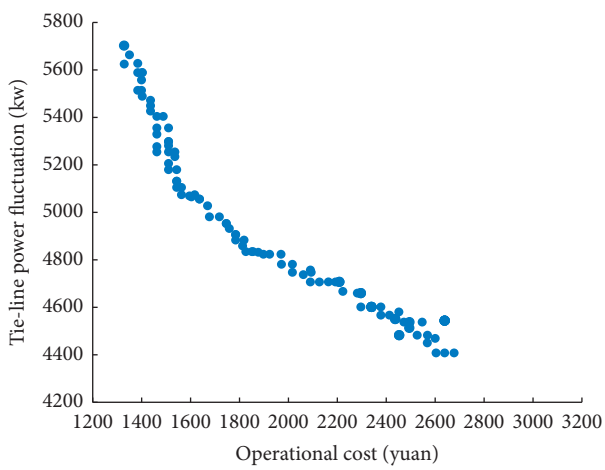

Figure 9: Pareto front of the source-grid-load level.

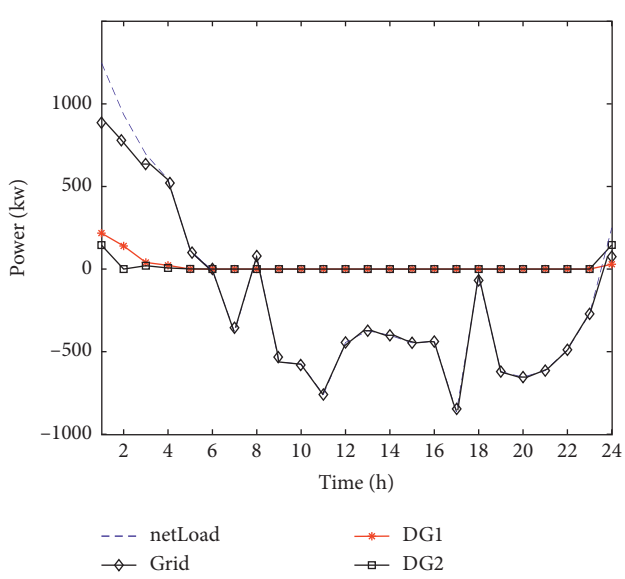

Figure 10: Power output of each unit at the source-grid-load level.

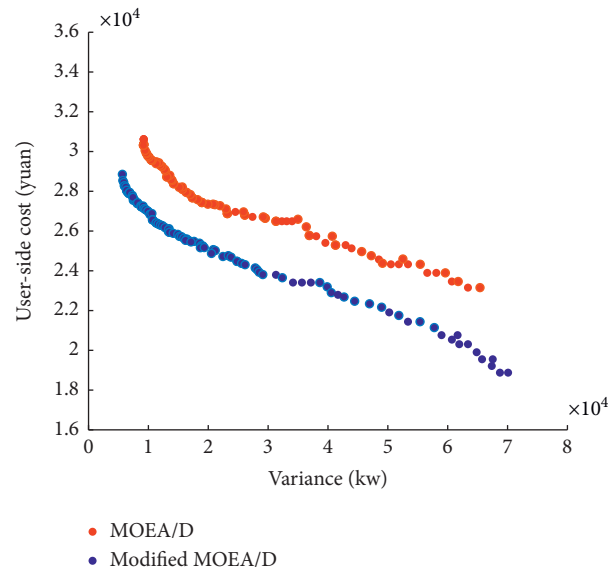

Figure 11: Algorithmic comparison.

the scheduling model proposed in this paper. The strategy of nonconsidering dispatchable loads is adopted in the source-load level, and the curve of netLoad is shown in Figure 13. By comparison with Figure 6, it can be seen that the netLoad curve still follows the output of renewables in Figure 13. However, after considering the schedulable load, the netLoad curve is more consistent with the renewable energy curve in Figure 6, especially in the period from 1:00 to 4:00.

In order to better illustrate the satisfaction of the user side after joining the demand-side response, this section divides user satisfaction into two aspects of comfort and economy:

$$\begin{aligned} U_{\text{com}} &= 1 - \frac{\sum_{t=1}^{24} |\Delta P_t|}{\sum_{t=1}^{24} P_L^{\text{before}}(t)}, \\ U_{\text{eco}} &= 1 - \frac{\sum_{t=1}^{24} p_L(t)\left(P_L^{\text{after}}(t) - P_L^{\text{before}}(t)\right)}{\sum_{t=1}^{24} p_L(t) P_L^{\text{before}}(t)}, \\ U &= U_{\text{com}} U_{\text{eco}}, \end{aligned} \tag{36}$$

where U_{com}, U_{eco}, and U represent the degree of comfort, economy, and comprehensive satisfaction of users, respectively. And $|\Delta P_t|$ is the sum of the absolute value of the electric quantity change in each period before and after the optimization; it is equal to the dispatching load in this paper. $P_L^{\text{before}}(t)$ and $P_L^{\text{after}}(t)$ represent the total load value of t period before and after optimization. The comprehensive satisfaction degree of users is introduced to quantify the satisfaction degree of the scheduling strategy. When the schedulable load is not considered, the user's comfort degree is the largest. At the same time, U_{com} and U_{eco} are all equal to one. The load variance value, user-side cost, and user satisfaction rate of the two strategies are shown in Table 3.

From Table 3, it can be indicated that, due to considering the transferable loads, some of the loads will be shifted to the period with a low price in the proposed strategy. Thus, the user-side cost is smaller than the strategy of nonconsidering

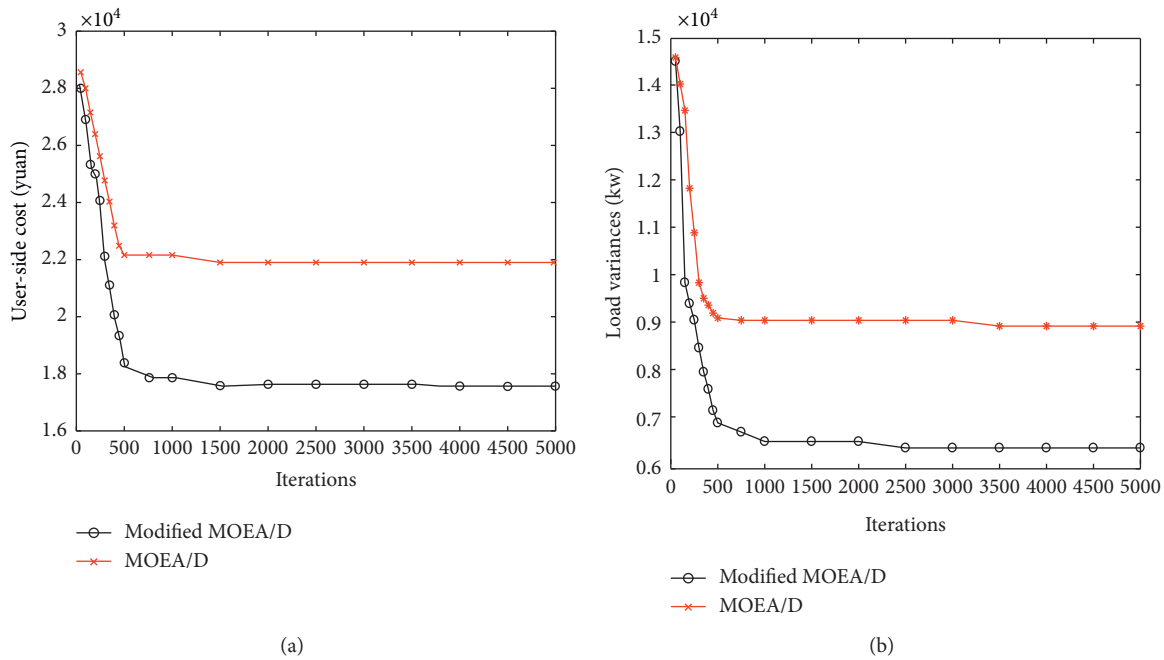

Figure 12: Comparison of convergence. (a) The curve of the value of the user-side cost. (b) The curve of the value of load variances.

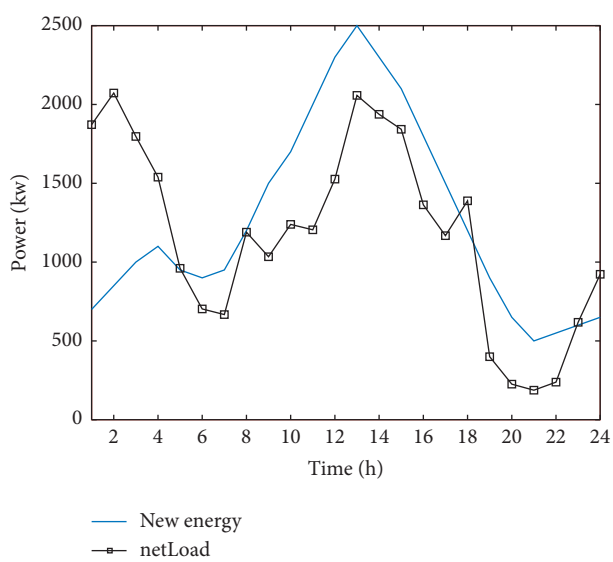

Figure 13: The curve of netLoad and renewables in the strategy without considering the dispatchable load.

dispatchable loads. At the same time, the dispatchable load can improve renewable energy utilization and reduce the load variance. By comparing the user satisfaction degrees, it can be seen that the comfort degree decreased by 11%, but the electricity cost decreased by 16%, and the overall satisfaction increased by 4%.

It can be indicated that the proposed strategy can reduce the impact on users' comfort as much as possible and maximize the economic benefits of users. Therefore, the strategy with dispatchable loads can maximize users' satisfaction, and the transferable loads can greatly optimize the scheduling results in the dispatching process.

5.5. Comparison with the Nonhierarchical Dispatching Strategy. In the microgrid system mentioned above, the dispatching strategy without considering hierarchy is used to solve the optimization problem. For a comprehensive comparison, the nonhierarchical scheduling strategy is divided into nonhierarchical scheduling 1 and nonhierarchical scheduling 2. The objective functions of nonhierarchical scheduling 1 are the lowest user cost and operating cost of the microgrid, while the objective functions of nonhierarchical scheduling 2 are the minimum load variance and the minimum power fluctuation of the connection lines. These two scheduling problems are still multiobjective optimization problems, so the modified MOEA/D algorithm is adjustable to solve them. The operation results of the three scheduling policies are compared, as shown in Table 4.

As can be seen from Table 4, compared with the result of the hierarchical scheduling strategy, the user-side cost and microgrid cost increased by 40% and 10%, respectively, in nonhierarchical strategy 1. In a dispatching period, the load variances of nonhierarchical strategy 2 increased by 21%, and the power fluctuation of the tie lines increased by 32%. It can be drawn that the hierarchical strategy can obtain better optimization results than nonhierarchical strategies in the same objective functions. Besides, the optimization of the other two objectives can be realized in the hierarchical strategy. It can be seen that, in the microgrid system proposed in this paper, the indexes of the hierarchical strategy are better than those of the nonhierarchical strategy. And the result of this comparative experiment proves the comprehensiveness of hierarchical scheduling.

Table 3: Comparison of simulation results of dispatching strategies.

Dispatching strategy	Load variance	User-side cost	U_{com}	U_{eco}	U
Considering dispatchable load	13732	25437	0.89	1.16	1.04
Nonconsidering dispatchable load	19969	27957	1	1	1

Table 4: Comparison of operation results of three dispatching models.

Dispatching strategy	Load variance	User-side cost	Operating cost of the microgrid	Tie-line power fluctuation
Hierarchical strategy	13732	25437	1675	5073
Nonhierarchical strategy 1	30622	27980	2345	9131
Nonhierarchical strategy 2	16616	43752	3786	6696

6. Conclusion

In this paper, a microgrid hierarchical dispatching strategy is proposed. The source-load level strategy considers user-side fees, and load variance, the operation cost of the microgrid, and the power fluctuation of the connection lines are minimized at the source-grid-load level of the system. The modified MOEA/D algorithm is used to solve the optimal dispatching problem. Through analysis and comparison with the result of the final scheduling, the following conclusions can be drawn:

(1) The participation of schedulable load and EVs in microgrid dispatching has a significant effect on peak load clipping and valley filling of the load curve. Moreover, it also improves the utilization rate of renewable generation and the microgrid's income to a certain extent.

(2) By comparing the modified MOEA/D with the original algorithm, it can be found that the replacement strategy based on the maximum value and the initialization strategy based on the constraint violations can effectively improve the convergence speed of the algorithm.

(3) The hierarchical scheduling strategy can fully consider the operation characteristics of the generation units at each level of scheduling. It can not only improve the overall satisfaction of users but also reduce the economic operation cost of the microgrid. Thus, the proposed strategy can realize the win-win situation of user satisfaction, good economy, and high system security.

Abbreviations

Parameters

μ_t: Expectation of t_0
σ_t: Variance of t_0
μ_s: Expectation of S
σ_s: Standard deviation of S
W_{100}: Power consumption of 100 kilometers
C: Total capacity of the EV battery
$S_{\mathrm{OC,max}}(S_{\mathrm{OC,min}})$: Upper (lower) limit of the SOC
η_C, η_D: Charging and discharging efficiency
ΔT: Scheduling interval
ΔS: Average power consumption per unit distance
$S_{\max}(S_{\min})$: Upper (lower) limits of battery power
$P_{\mathrm{NCh}}(P_{\mathrm{NDch}})$: Rated charging (discharging) power of an EV
P_L: Total load power of the system
$P_{L,\mathrm{tr}}$: Transferable load power
C_{dis}: Discharge subsidy
T: Number of scheduling time periods
p_{ev}: Uniform discharge subsidy of the microgrid system to the electric vehicle
$K_{\mathrm{om,de}}$: Running maintenance coefficient
$U_{\mathrm{Ri}}(D_{Ri})$: Lift (drop) ramp rate of generator i
$S_{\max}(S_{\min})$: Upper (lower) limits of the SOC
$P_{\mathrm{ES}}^{\min}(P_{\mathrm{ES}}^{\max})$: Upper (lower) output limits of ES
x: Decision vector
λ: Direction vector
G: Number of inequality constraints
H: Number of equality constraints
m: Objective functions
ω: Weight vector
ξ: A constant close to zero
N: Population size
EP: External archive
y: Offspring particle
z: Reference point
N_{obj}: Number of objective functions
M: Number of nondominant solutions
a, b, c: Fuel coefficients of the diesel engine

Variables

t_0: Return trip time of the last trip of electric vehicles
S: Driving distance
$S_{\mathrm{OC,EC}}$: SOC of the EV battery
P_{disc}: Discharge power of the EV
$T_{\mathrm{start-disc}}(T_{\mathrm{end-disc}})$: Beginning (end) time of EV discharge
T_{disc}: Duration of discharging
P_{EV}: Charging load of the EV
$T_{\mathrm{char}}(i)(T_{\mathrm{dischar}}(i))$: Charging (discharging) time of the i-th EV

$E_{ev}(t)$: Daily charging and discharging load of each EV at time t
S_t: Remaining electric quantity of an electric vehicle in time t
$S_{\mathrm{Trip},t}$: Energy consumed by the electric vehicle in the process of driving in time period t
L: Driving distance
$P_{L,\mathrm{tr}}^{\max}(t)(P_{L,\mathrm{tr}}^{\min}(t))$: Upper (lower) limits of the power consumption of the transferable load in time t
C_{load}: User electricity charge
$P_{\mathrm{ev,ch}}(t)(P_{\mathrm{ev,dis}}(t))$: Charging (discharging) power of the EV in time period t
p_L: TOU price
f_{var}: Load variance
P_{ES}: Output of the ES
P_{new}: Predicted renewable energy output power
P_{av}: Average load
$f_{\cos t}$: Integrated operation cost of DGs and the power grid
f_{flu}: Power fluctuation of the tie lines
$C_{\mathrm{de,\cos t}}$: Comprehensive operation cost of DGs
$C_{\mathrm{grid,\cos t}}$: Comprehensive operation cost of the power grid
$C_{\mathrm{de,om}}$: Operating and maintenance cost of DGs
$C_{\mathrm{de,fuel}}$: Fuel cost of DGs
$C_{\mathrm{de,en}}$: Environmental governance cost of DGs
C_k: Treatment of category k pollutants
γ_{de}: Emission of pollutants generated by DGs
$C_{\mathrm{grid,price}}$: Electricity transaction cost
$C_{\mathrm{grid,en}}$: Environmental governance cost
γ_{grid}: Emission of pollutants generated by the grid
P_{grid}: Tie-line power of the main network
P_{de}: Output of the DGs
P_{new}: Power of the WT and PV predicted
P_{ES}: Output state of ES
S_R: Spinning reserve capacity requirement of the system
$f_i(x)$: i-th objective function of the multiobjective optimization problem
z_i: Ideal value of the i-th objective function
V_i: Summing all the constraint violations of the i-th solution
$V_{\mathrm{improvement}}$: Value of the improvement of the offspring particle
l: Subproblem of the maximum fitness
Neigh_j: Indices of the neighbor subproblems of the j-th subproblem
F^j: Objective function of the j-th subproblem
n_r: Maximum number of the replaced parent solutions by one offspring solution
μ_{ij}: Satisfaction degree of the j-th objective function of the i-th solution
U_{com}: Degree of comfort satisfaction of users
U_{eco}: Degree of economy satisfaction of users
U: Degree of comprehensive satisfaction of users
$|\Delta P_t|$: Sum of the absolute value of the electric quantity change in each period
$P_L^{\mathrm{before}}(t)$: Total load value of t period before optimization
$P_L^{\mathrm{after}}(t)$: Total load value of t period after optimization

Acronyms

EED: Economic/environmental dispatching
NSGA-II: Nondominant sorting genetic algorithm with elite strategy
ASO: Artificial shark optimization
MG: Microgrid
DEED: Dynamic economic emission dispatch
MOEA/D: Multiobjective evolutionary algorithm based on decomposition
LPBI: Localized penalty-based boundary intersection
HRES: Hybrid renewable energy system
EV: Electric vehicle
DER: Distributed energy resources
ES: Energy storages
WT: Wind turbine
PV: Photovoltaic arrays
DG: Diesel generator
V2G: Vehicle-to-grid
SOC: State of charge
TOU: Time of use
PDF: Probability density function.

Data Availability

The data used to support the findings of this study are available from the corresponding author upon request.

Conflicts of Interest

The authors declare no conflicts of interest.

Authors' Contributions

X.W., H.L., and X.D. conceived and designed the study; X.W. and H.L. performed the study; X.W., J.P., and Y.W. reviewed and edited the manuscript; and X.W. and H.L. wrote the paper. All authors read and agreed to the published version of the manuscript.

Acknowledgments

This work was supported in part by the National Natural Science Foundation of China (NSFC: 61563034), the International S&T Cooperation Program of China (ISTCP: 2014DFG72240), and Higher School Science and Technology Floor Plan in Jiangxi Province (KJLD14006).

References

[1] R. Bayindir, E. Hossain, and S. Vadi, "The path of the smart grid-the new and improved power grid," in *Proceedings of the International Smart Grid Workshop And Certificate Program (ISGWCP)*, pp. 1–8, Istanbul, 2016.

[2] C. Wei, X. Bai, and T. Kim, "Advanced control and optimization for complex energy systems," *Complexity*, vol. 2020, p. 3, Article ID 5908102, 2020.

[3] C. A. Hernandez-Aramburo, T. C. Green, and N. Mugniot, "Fuel consumption minimization of a microgrid," *IEEE Transactions on Industry Applications*, vol. 41, no. 3, pp. 673–681, 2005.

[4] F. A. Mohamed and H. N. Koivo, "Online management of microgrid with battery storage using multiobjective optimization," in *Proceedings of the International Conference on Power Engineering, Energy and Electrical Drives (POWERENG)*, pp. 231–236, Setubal, Portugal, 2007.

[5] H. Farzin, M. Fotuhi-Firuzabad, and M. Moeini-Aghtaie, "A stochastic multi-objective framework for optimal scheduling of energy storage systems in microgrids," *IEEE Transactions on Smart Grid*, vol. 8, no. 1, pp. 117–127, 2017.

[6] P. Singh and B. Khan, "Smart microgrid energy management using a novel artificial shark optimization," *Complexity*, vol. 2017, Article ID 2158926, 2020.

[7] J. Zhang, Q. Tang, P. Li, D. Deng, and Y. Chen, "A modified MOEA/D approach to the solution of multi-objective optimal power flow problem," *Applied Soft Computing*, vol. 47, pp. 494–514, 2016.

[8] Q. Zhang and H. Li, "MOEA/D: a multiobjective evolutionary algorithm based on decomposition," *IEEE Transactions on Evolutionary Computation*, vol. 11, no. 6, pp. 712–731, 2007.

[9] M. Ross, C. Abbey, F. Bouffard, and G. Joos, "Multiobjective optimization dispatch for microgrids with a high penetration of renewable generation," *IEEE Transactions on Sustainable Energy*, vol. 6, no. 4, pp. 1306–1314, 2015.

[10] M. Ming, R. Wang, Y. Zha et al., "Multi-objective optimization of hybrid renewable energy system using an enhanced multi-objective evolutionary algorithm," *Energies*, vol. 6, 2017.

[11] Y. Zhu, H. Gao, J. Xiao, B. Qu, F. Zhu, and L. Yang, "Dynamic multi-objective dispatch considering wind power and electric vehicles with probabilistic characteristics," *IEEE Access*, vol. 7, pp. 185634–185653, 2019.

[12] X. Lu, K. Zhou, and S. Yang, "Multi-objective optimal dispatch of microgrid containing electric vehicles," *Journal of Cleaner Production*, vol. 165, pp. 1572–1581, 2017.

[13] Z. Zhao, K. Wang, X. Jiang, and X. Wang, "Economic dispatch of distribution network with inn for electric vehicles and photovoltaic," *The Journal of Engineering*, vol. 2019, no. 16, pp. 2864–2868, 2019.

[14] Q. Li, S. Huang, Y. Cheng et al., "Economic optimization of microgrid based on improved quantum genetic algorithm," *Gaoya Dianqi/High Voltage Apparatus*, vol. 54, no. 3, pp. 136–145, 2018.

[15] F. Zhao, J. Yuan, and N. Wang, "Dynamic economic dispatch model of microgrid containing energy storage components based on a variant of NSGA-II algorithm," *Energies*, vol. 12, 2019.

[16] Y. Zheng, S. Li, and R. Tan, "Distributed model predictive control for on-connected microgrid power management," *IEEE Transactions on Control Systems Technology*, vol. 26, no. 3, pp. 1028–1039, 2018.

[17] G. Strbac, E. D. Farmer, and B. J. Cory, "Framework for the incorporation of demand-side in a competitive electricity market," *IEE Proceedings-Generation, Transmission and Distribution*, vol. 143, no. 3, pp. 232–237, 1996.

[18] J. Qiu, J. Zhao, and D. Wang, "Multi-objective generation dispatch considering the trade-off between economy and security," *IET Generation, Transmission & Distribution*, vol. 12, no. 3, pp. 633–642, 2018.

[19] T. U. Solanke and V. K. Ramachandaramurthy, "A review of strategic charging discharging control of grid connected electric vehicles," *Journal of Energy Storage*, vol. 28, 2020.

[20] H. Liu, T. L. Pan, and Z. L. Hao, "Hierarchical optimal dispatching strategy for microgrid system considering user-side resources," in *Proceedings of the 13th IEEE Conference on Industrial Electronics and Applications (ICIEA)*, pp. 1637–1642, Wuhan, China, 2018.

[21] X. Wang, C. Sun, R. Wang, and T. Wei, "Two-stage optimal scheduling strategy for large-scale electric vehicles," *IEEE Access*, vol. 8, pp. 13821–13832, 2020.

[22] C. Ye, S. Miao, Y. Li et al., "Hierarchical scheduling scheme for AC/DC hybrid active distribution network based on multi-stakeholders," *Energies*, vol. 11, 2018.

[23] L. T. Al-Bahrani, B. Horan, and M. Seyedmahmoudian, "Dynamic economic emission dispatch with load demand management for the load demand of electric vehicles during crest shaving and valley filling in smart cities environment," *Energy*, vol. 195, 2020.

[24] Y. Zhou, Z. Li, and X. Wu, "The multiobjective based large-scale electric vehicle charging behaviours analysis," *Complexity*, vol. 2018, p. 16, Article ID 1968435, 2018.

[25] R. Ewing and O. Clemente, "Validation of measures," *Measuring Urban Design*, vol. 46, pp. 83–98, 2013.

[26] Z. A. Arfeen, A. B. Khairuddin, A. Munir et al., "En route of electric vehicles with the vehicle to grid technique in distribution networks Status and technological review," *Energy Storage*, vol. 2, no. 2, 2019.

[27] H. Jiang, S. Ning, and Q. Ge, "Multi-objective optimal dispatching of microgrid with large-scale electric vehicles," *IEEE Access*, vol. 7, pp. 145880–145888, 2019.

[28] P. Palensky and D. Dietrich, "Demand side management: demand response, intelligent energy systems, and smart loads," *IEEE Transactions on Industrial Informatics*, vol. 7, no. 3, pp. 381–388, 2011.

[29] M. Hashim and J. Yong, "Coordinated vehicle-to-grid scheduling to minimize grid load variance," in *Proceedings of the International Conference on Electrical, Electronics and Computer Engineering (UPCON)*, pp. 1–6, Singapore, 2019.

[30] B. Y. Qu, J. J. Liang, Y. S. Zhu, Z. Y. Wang, and P. N. Suganthan, "Economic emission dispatch problems with stochastic wind power using summation based multi-objective evolutionary algorithm," *Information Sciences*, vol. 351, pp. 48–66, 2016.

[31] C. Zhang, W. Lin, D. Ke, and Y. Sun, "Smoothing tie-line power fluctuations for industrial microgrids by demand side control: an output regulation approach," *IEEE Transactions on Power Systems*, vol. 34, no. 5, pp. 3716–3728, 2019.

[32] L. Yang, D. He, and B. Li, "A selection hyper-heuristic algorithm for multiobjective dynamic economic and

environmental load dispatch," *Complexity*, vol. 2020, Article ID 4939268, 2020.

[33] Y. Yang, J. Wu, X. Zhu, and J. Wu, "A hybrid evolutionary algorithm for finding pareto optimal set in multi-objective optimization," in *Proceedings of the Seventh International Conference on Natural Computation (ICNC)*, Shanghai, 2011.

[34] Q. Zhang, H. Li, D. Maringer, and E. Tsang, "MOEA/D with NBI-style tchebycheff approach for portfolio management," in *Proceedings of the IEEE Congress on Evolutionary Computation*, pp. 1–8, Barcelona, Spain, 2010.

[35] R. Shang, Y. Wang, J. Wang, L. Jiao, S. Wang, and L. Qi, "A multi-population cooperative coevolutionary algorithm for multi-objective capacitated arc routing problem," *Information Sciences*, vol. 277, pp. 609–642, 2014.

[36] H. Li and Q. Zhang, "Multi-objective optimization problems with complicated pareto sets, MOEA/D and NSGA-II," *IEEE Transactions on Evolutionary Computation*, vol. 13, no. 2, pp. 284–302, 2009.

[37] A. R. Bhowmik and A. K. Chakraborty, "Solution of optimal power flow using nondominated sorting multi objective gravitational search algorithm," *International Journal of Electrical Power & Energy Systems*, vol. 62, pp. 323–334, 2014.

[38] X. Ma, Q. Zhang, G. Tian, J. Yang, and Z. Zhu, "On tchebycheff decomposition approaches for multiobjective evolutionary optimization," *IEEE Transactions on Evolutionary Computation*, vol. 22, no. 2, pp. 226–244, 2018.

[39] Z. Zhang, Q. Zhang, A. Zhou, M. Gong, and L. Jiao, "Adaptive replacement strategies for MOEA/D," *IEEE Transactions on Cybernetics*, vol. 46, no. 2, pp. 474–486, 2016.

[40] L. Wang, A. Zhou, M. Gong, and L. Jiao, "Constrained subproblems in a decomposition-based multiobjective evolutionary algorithm," *IEEE Transactions on Evolutionary Computation*, vol. 20, no. 3, pp. 475–480, 2016.

[41] G. Yang, Y. Li, Q. Yao, and R. Yong, "Study of reliability of grid connected photovoltaic power based on Monte Carlo method," in *Proceedings of the IEEE Power Engineering and Automation Conference (PEAM)*, pp. 92–95, Wuhan, China, 2011.

[42] H. Hou, M. Xue, Y. Xu et al., "Multiobjective joint economic dispatching of a microgrid with multiple distributed generation," *Energies*, vol. 11, pp. 1–19, 2018.

Hindawi
Complexity
Volume 2020, Article ID 8509142, 24 pages
https://doi.org/10.1155/2020/8509142

Research Article

Automatic Diagnosis of Microgrid Networks' Power Device Faults Based on Stacked Denoising Autoencoders and Adaptive Affinity Propagation Clustering

Fan Xu,[1] **Xin Shu**,[2] **Xiaodi Zhang**,[3] **and Bo Fan**[4]

[1]*School of Data Science, City University of Hong Kong, Tat Chee Avenue, Kowloon, Hong Kong 990777, China*
[2]*Wuhan Bridge Special Technology Company Limited of China Railway Major Bridge Engineering Group, Wuhan 730072, China*
[3]*State Grid Beijing Electric Power Company, Beijing 100080, China*
[4]*Office of Scientific Research and Development, Wuhan University, Wuhan 430072, China*

Correspondence should be addressed to Bo Fan; fanbo@whu.edu.cn

Received 22 May 2020; Accepted 6 July 2020; Published 26 July 2020

Academic Editor: Ning Cai

This paper presents a model based on stacked denoising autoencoders (SDAEs) in deep learning and adaptive affinity propagation (adAP) for bearing fault diagnosis automatically. First, SDAEs are used to extract potential fault features and directly reduce their high dimension to 3. To prove that the feature extraction capability of SDAEs is better than stacked autoencoders (SAEs), principal component analysis (PCA) is employed to compare and reduce their dimension to 3, except for the final hidden layer. Hence, the extracted 3-dimensional features are chosen as the input for adAP cluster models. Compared with other traditional cluster methods, such as the Fuzzy C-mean (FCM), Gustafson–Kessel (GK), Gath–Geva (GG), and affinity propagation (AP), clustering algorithms can identify fault samples without cluster center number selection. However, AP needs to set two key parameters depending on manual experience—the damping factor and the bias parameter—before its calculation. To overcome this drawback, adAP is introduced in this paper. The adAP clustering algorithm can find the available parameters according to the fitness function automatic. Finally, the experimental results prove that SDAEs with adAP are better than other models, including SDAE-FCM/GK/GG according to the cluster assess index (Silhouette) and the classification error rate.

1. Introduction

As a key part of mechanical systems in the electric devices in microgrid networks, the operational health of bearings is related to the operation of the entire device [1–4]. Processing and analysis are an important basis for the evaluation of the health status of the electric devices in microgrid networks. Using vibration signals for fault diagnosis has become common in recent years.

For nonlinear and nonstationary signals, various feature extraction, and diagnosis methods are continuously developed; time and frequency indicators, wavelet transformation (WT), and empirical mode decomposition (EMD) are commonly used for fault feature extraction and have achieved significant results. However, various time-frequency domain indicators and wavelet transformation (WT) cannot adaptively decompose vibration signals because different vibration signals have different working frequency bands. Thus, EMD is proposed as a way to adaptively decompose the signal into intrinsic mode functions (IMFs) based on the current envelope mean of the signal [5]. To overcome the drawbacks, such as mode-mixing problems cause by noise in EMD, a model named "ensemble empirical mode decomposition" (EEMD) was first presented in [6]. Many scholars have already applied EEMD in fault diagnosis [7, 8]. However, these traditional methods depend highly on manual experience and prior knowledge, such as choosing the available time frequency indicators and wavelet basis function, and they also need to integrate several available models for fault feature extraction.

An increasing number of scholars have focused on deep learning in fault diagnosis due to its powerful automatic extracting features. For example, many studies have employed stacked autoencoders (SAEs) to extract features and fault diagnosis automatically and successfully [9–13]. However, most of these papers consider SAEs with a classifier and data labels to complete the fault diagnosis. However, the data obtained from different actual engineering platforms contain noise, such as voice data and vibration signals in practice engineering. To enhance the robustness of SAEs, stacked denoising autoencoders (SDAEs) were created [14, 15]. Compared with SAEs, SDAEs introduce artificial noise, and some of the input data are randomly zeroed to reconstruct the original input data. In addition, SDAEs have been widely applied in many domains [16–18]. Therefore, SDAEs are utilized to extract bearing fault characteristics directly from the frequency domain signal to reduce the manual experience dependence in this paper.

In addition, marking data labels requires a great deal of labor and richly experimental engineering when working with large amounts of data. Therefore, no manual experience or prior knowledge is required to mark the fault type and fault label by using SDAEs without an output layer.

To identify the different fault types automatically, cluster model is used to complete the fault diagnosis without data labels in this paper. Fuzzy C-mean (FCM) is a commonly used model in fault diagnosis [19]. In FCM, to compute the distance between samples, Euclidean distance is often employed; hence, it is only available for data with a spherical distribution. Actually, many datasets do not have such characteristics. To solve this problem, the Gustafson–Kessel (GK) clustering algorithm [20] features an objective function based on the covariance matrix and is suitable for the cluster analysis of datasets with the correlation between variables [21]. However, the FCM and GK methods are still aimed at datasets with spherical shapes, while the Gath–Geva (GG) clustering method computes the distance between any two adjacent data points by using the maximum likelihood distance and has been successfully applied to the diagnosis of rolling bearing faults [22, 23]. In [24, 25], the authors used EEMD and GG to complete the bearing fault diagnosis.

However, all of the clustering models mentioned above need to preset the cluster numbers through manual experience before calculation. The affinity propagation (AP) clustering algorithm can automatically find the appropriate number of clusters. AP continuously performs message passing and iterative looping to generate K high-quality clusters, and it uses energy functions to minimize clusters and assign each data point to the nearest cluster [26]. Actually, there are two key parameters—the bias parameter p and damping factor *lam*—in the AP cluster model. One researcher [26] recommended setting p to the median value of all p_m samples without prior knowledge at the beginning stage. However, sometimes p_m cannot induce the AP algorithm to generate available cluster numbers because p_m is not selected on the basis of the clustering structure of the dataset itself. When the AP algorithm oscillates (i.e., the number of clustering classes generated during the iteration is constantly oscillating) and cannot converge, increasing *lam* can eliminate the oscillation, but *lam* must be manually increased when oscillating, and the algorithm is run again until the algorithm converges. The approach is to set *lam* directly to close to 1 to avoid oscillation, but the reliability and availability updates are slow, and the algorithm runs slowly. Therefore, Wang et al. developed a model named adaptive affinity propagation (adAP) to find the best cluster according to the cluster assessment index (Silhouette) [27]. The adAP scan biases parameter space to look for the cluster number space to find the suitable clusters, and it adjusts the damping factor to weaken the oscillation and adaptive escape oscillating technique when the damping factor method fails.

Therefore, a method based on SDAEs and adAP for bearing fault diagnosis is presented in this study. The main attributes are presented in the following section:

(1) Different from traditional multistep fusion fault diagnosis methods and the basic SDAE model, which require data labels for fault classification, SDAEs without an output layer are utilized to extract fault features directly from the frequency domain and weaken the dependence on manual experience to mark the data labels in this paper.

(2) There are few reports in the literature in which the adAP model is applied to bearing fault diagnosis.

(3) To prove the extracting feature performance of the proposed model (SDAE-adAP), classification accuracy and Silhouette are used to demonstrate the performance of adAP in suppressing some other models, such as FCM/GK/GG.

The rest of this paper is organized as follows. Section 2 contains a review of SAE. Experiment data and detailed procedures are presented in Section 3. A comparison analysis of the experiments is described in Section 4, and Section 5 concludes the paper.

2. Review of the SDAEs and adAP

2.1. Stacked Denoising Autoencoders

2.1.1. Autoencoders. Autoencoders (AEs) include encoders and decoders [28]. The basic structure is shown in Figure 1.

Encoders are used to map the input to the following hidden layer and obtain a new nonlinear extracted hidden feature z by using the following equation:

$$z = f(x) = s\left(w^{(1)}x + b\right), \tag{1}$$

where $x^i = [x_1, x_2, x_3, \ldots, x_j, \ldots, x_n]$, $i = 1, 2, 3, \ldots, N$, $j = 1, 2, 3, \ldots, n$, N is the sample number, n denotes the length of each sample, $w^{(1)}$ represents the connection matrix used to connect the original input data and the Lth hidden layer, s signifies the sigmoid active function $s(x) = 1/1 + e^{-x}$, and b is the bias item.

The decoder is utilized to map and reconstruct the extracted hidden feature z close to the original input x. The procedure above is calculated by

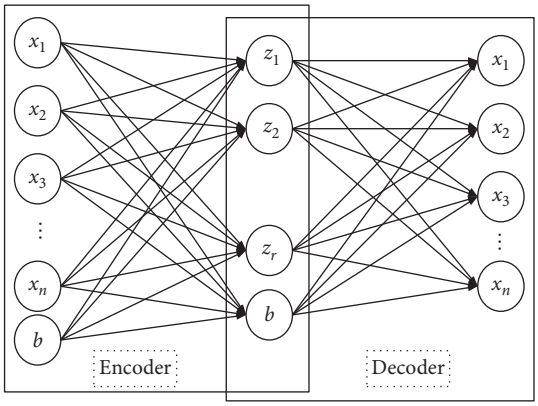

Figure 1: The network structure of AE.

$$x^{(i)} = g(z) = s\left(w^{(2)}z + b^{(2)}\right), \tag{2}$$

where g is the sigmoid function. The construction error is calculated by

$$J = \|x - g(f(x))\|^2, \tag{3}$$

and J can replace the following cost function:

$$\begin{aligned} J &= \|x - g(f(x))\|^2 = J(w,b) \\ &= \left[\frac{1}{N}\sum_{i=1}^{N}\left(\frac{1}{2}\left\|x^{(i)} - g\left(f\left(x^{(i)}\right)\right)\right\|^2\right)\right] + \frac{\lambda}{2}\sum_{L=1}^{2}\sum_{i=1}^{r_{1-1}}\sum_{j=1}^{r_L}\left(w_{ji}^{(i)}\right)^2, \end{aligned} \tag{4}$$

where r_L is the neural node number at the Lth hidden layer; λ is a regularization coefficient.

2.1.2. Denoising Autoencoders. Denoising autoencoders (DAEs) mix the training data into the noise (the data are randomly set to zero) and remove the noise to obtain the reconstructed output data. In the case of destroyed data, DAEs achieve a better description of the input data and enhance the robustness of the entire model. The structure of a DAE is shown in Figure 2.

In Figure 2, x indicates the raw input data and x_1 represents the destroyed input data according to the denoising rate P, y is the extracted feature obtained from x_1 by using the sigmoid function, and z denotes the output. The difference between DAEs and AEs is that DAEs destroy input data by denoising the rate P to $x \longrightarrow P(x_1/x)$. The reconstructed error between the output z and the original input x_1 is

$$J_D = \|x - z\|^2 = \left\|x - g(f(x_1))\right\|^2. \tag{5}$$

Hence, the cost function in equations (4) and (5) can be rewritten as

$$\begin{aligned} J_D &= \left\|x - g(f(x_1))\right\|^2 = J_D(w,b) \\ &= \left[\frac{1}{N}\sum_{i=1}^{N}\left(\frac{1}{2}\left\|x^{(i)} - g\left(f\left(x_1^{(i)}\right)\right)\right\|^2\right)\right] + \frac{\lambda}{2}\sum_{L=1}^{2}\sum_{i=1}^{r_{L-1}}\sum_{j=1}^{r_L}\left(w_{ji}^{(i)}\right)^2. \end{aligned} \tag{6}$$

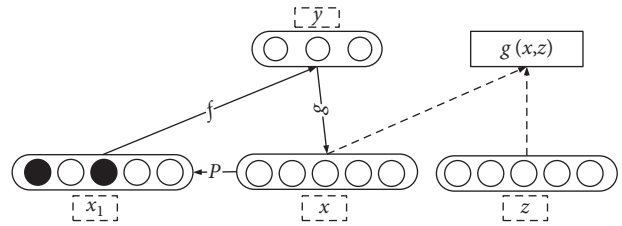

Figure 2: DAE structure.

2.1.3. Stacked Denoising Autoencoders. The SDAE concept was presented by Vincent [14, 15]. The core idea of SDAE is adding noise to the input data of each encoder. Therefore, a more robust feature expression can be learned. Figure 3 shows the structure of an SDAE. The learning process of SDAEs can be divided into two steps.

The first is the greedy layer-by-layer learning of SDAEs using unmarked samples. The specific process is as follows: assuming that the total number of hidden layers is L, input the original data into the first layer of the DAE, and perform unsupervised training to obtain the parameter $W(1)$ of the first hidden layer. After in each step, the trained $(L-1)^{\text{th}}$ layer is selected as input to train the Lth hidden layer to obtain $W(L)$, and the weights of each layer are trained. Second, the reconstructed error is reduced by the backpropagation method, which is also utilized to update the parameters and to make the network converge.

In the backpropagation error calculation process, it is necessary to calculate the residual δ of each hidden layer. For each output node i, δ is calculated as follows:

$$\delta_i^{L-1} = a_i^{L-1}\left(1 - a_i^{L-1}\right)\sum_{j=1}^{r_L} w_{ji}^{L-1}\delta_i^L, \tag{7}$$

where a_i^L denotes the output at the Lth hidden layer.

Use equations (8) and (9) for the SDAE network.

To adjust the parameters of each hidden layer, use the following equation:

$$w_{ji}^{L-1} = w_{ji}^{L-1} - \beta a_i^{L-1}\delta_i^L, \tag{8}$$

$$b_i^{L-1} = b_i^{L-1} - \beta\delta_i^L, \tag{9}$$

where β is the learning rate.

It should be mentioned that the input x is normalized before SAE and SDAE training; hence, the output range at each hidden layer should be [0, 1]. Moreover, the output range of the sigmoid function is [0, 1]. The sigmoid function's curve changes continuously between [0, 1]. Therefore, we chose the sigmoid function as the active function in this paper. In addition, the reconstruction error is not calculated for all training data; rather, in each iteration, the reconstruction error of certain training data is randomly optimized by the stochastic gradient descent model. Hence, the update speed for each round of parameters is greatly accelerated. Therefore, the gradient descent optimization model is used to update the weight parameter w and bias item b in this paper.

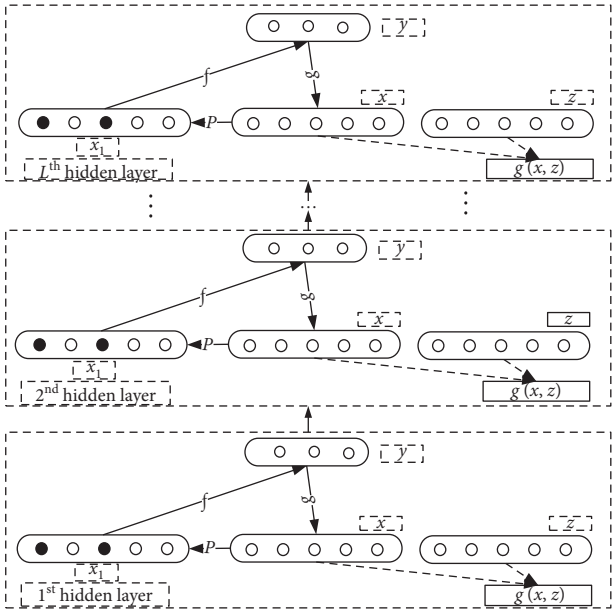

Figure 3: SDAE structure.

2.2. adAP Clustering Model. The AP algorithm works on the $N \times N$ similarity matrix S composed of N data points and regards all samples as cluster center point candidates at the beginning stage [26]. There are some tight clusters in the feature space, and the function $E(C)$ of one cluster represents the similarity sum between any one data point and the cluster centers. The calculation of $E(C)$ is as follows:

$$E(C) = -\sum_{j=1}^{K} S_j(i, C_i), \tag{10}$$

where K denotes the cluster number, C_i denotes the ith cluster center, and $S(i, C_i)$ represents the distance between each point and the corresponding cluster center point. The negative value of the distance between the two any adjacent points is assumed to be the degree of attraction or attribution, the kth point is more attractive to the closer data i^{th} point, and data point i agrees that the kth point has a greater sense of belonging to its cluster center. Therefore, the kth point of the cluster center is more attractive to other data points, and the possibility of becoming a cluster center will become greater.

The AP algorithm continuously collects relevant evidence from the data to select the available class representation: AP uses $R(i, k)$ to describe the degree to which the data point k is suitable as the cluster center point of data point i. $A(i, k)$ is called the degree of attribution and is used to describe the extent to which data point i selects data point k as its cluster center point. The literature [27] shows that the larger the R and A values of the data point k, the greater the probability will be that the data point k becomes the cluster center.

The AP algorithm generates k high-quality cluster classes through an iterative loop and minimizes the energy function of the cluster class. Finally, it assigns each data point to the nearest cluster class.

There are two key parameters (i.e., the bias parameter p and the damping factor *lam*) in AP. The deviation parameter $p(i)$ (usually a negative number) represents the degree to which the data point i becomes the cluster center.

As mentioned above, $R(i, k)$ and $A(i, k)$ can be calculated by

$$R(i,k) = S(i,k) - \max\{A(i,j) + S(i,j)\}, \quad (j = 1, 2, 3, \ldots, N, j \neq k, j \neq i), \tag{11}$$

$$A(i,k) = \min\left\{0, R(k,k) + \sum \{\max(0, R(j,k))\}\right\}, \quad (j = 1, 2, 3, \ldots, N, j \neq k, j \neq i). \tag{12}$$

From equations (11) and (12), when $p(k)$ is large, $R(k, k)$ and $A(i, k)$ also become larger; hence, the class represents k as the final cluster center. When $p(i)$ is larger, more cluster classes represent the final cluster center. Therefore, increasing or decreasing p affects the number of clustered classes. The authors recommend setting all p to p_m (which represents the median value of all elements in S) without prior knowledge at the beginning stage [26]. However, in many cases, p_m cannot make the AP algorithm produce optimal clustering results because the setting of p_m is not based on the clustering structure of the dataset itself. When the AP algorithm oscillates (i.e., the number of clustering classes generated during the iteration is constantly oscillating) and cannot converge, increasing *lam* can eliminate the oscillation. When oscillating, one must manually increase *lam* and rerun the algorithm until the algorithm converges. The approach is to set *lam* directly close to 1 to avoid oscillation, but the $R(i, k)$ and $A(i, k)$ updates are slow, and the algorithm runs slowly.

To overcome the drawbacks mentioned above, adAP searches the cluster number space by scanning the bias parameter space to find the optimal clustering result (called adaptive scanning) and adjusts the damping factor *lam* to eliminate the oscillation (called adaptive damping), thus lowering the p value to escape concussion (called adaptive escape).

The goal of adAP is to eliminate both oscillating and fast algorithms when oscillation occurs. Although it is more likely to increase *lam* to near 1 to eliminate oscillation, the larger *lam* is, the slower the R and A in equations (11) and (12) and the update become, and the more iterations the algorithm needs to achieve the update effect when *lam* starts from 0.6.

The adaptive adjustment damping factor technique is designed as follows:

(1) The AP algorithm performs a loop to detect whether oscillation is occurring.

(2) If there is oscillation, increase *lam* by one step (for example, 0.05); otherwise, proceed to step 1.

(3) Continue w cycles (to see the effect after w cycles).

(4) Repeat the steps above until the algorithm reaches the stop condition.

If increasing *lam* (e.g., *lam* is increased to 0.85 or higher) fails to depress oscillations, an adaptive escape technique should be designed to avoid oscillations. The fact that large *lam* has little effect suggests that oscillations are persistent under the given p, so the alternative is to decrease p away from the given value to escape from oscillations. This escape method is reasonable since it works together with the adaptive scanning of p discussed below, different from AP, which works under a fixed p. The adaptive escape technique is designed as follows: when oscillations occur and $lam \geq 0.85$ in the iterative process, p is decreased gradually until oscillations disappear. This technique is added in step 2 of the adaptive damping method: if oscillations occur, increase *lam* by a step (e.g., 0.05); if $lam \geq 0.85$, decrease p by step p_{step}. Otherwise, go to step 1 of the adaptive damping method. Both adaptive damping and adaptive escape techniques are used to eliminate oscillations at the same time. The monitoring window size $w = 40$ is appropriate as per our experiences (but occasionally, random vibrations and tolerant vibrations in initial iterations will be caught under too small w, and AP runs slowly under a w value that is too large). The pseudocodes of adaptive damping and adaptive escape are shown in the work of Kan et al. [28] (and *maxits* and *ps* will be set in the following step).

To keep the algorithm fast, the design of the bias parameter p is as follows.

The algorithm starts from the initial given p, and each iteration of the cyclic process updates the R and A (but the similarity matrix S is fixed); if the cyclic process converges to a certain cluster number K, in the stride p_{step} manner, gradually reduce p—that is, change $p(i)$ on the diagonal of S—and repeat the same cyclic process to obtain a different K. To avoid double counting, use the current R and A values after each reduction of p as a new starting point and continue to calculate R and A. The adaptive scanning technology for p is designed as explained in this section.

The acceleration technology of the p drop is designed as follows:

(1) The AP algorithm performs an iteration to check whether the number of cluster classes converges to K. If yes, go to step 2. Otherwise, $b = 0$; repeat step 1.

(2) Check if the number of clustering classes converges to K and $b < \text{iter}_{\max}$; if yes, count $b = b + 1$.

Otherwise, go to step 1.

If (3) $p = p + b * p_{\text{step}}$, go step 2.

The pseudocodes of adaptive p-scanning technology are shown in reference [28].

3. Experiment Setup

3.1. Experiment Data. The four basic faults—that is, normal (NR), ball fault (BF), inner race fault (IRF), and outer race fault (ORF)—were collected from a motor driving a power device [29]. The sampling frequency is 12 KHz. The fault diameters are 0.18 mm, 0.36 mm, and 0.54 mm. Detailed information about the data is displayed in Table 1. Each sample contains 2,048 points, and 50 samples are included under different conditions; thus, 500 samples were used for training and testing. Note that two datasets (A and B) were used for this study. Each dataset contains nine fault types under different working conditions. For each dataset, 300 samples under various conditions were chosen as the training dataset and the remaining 200 samples constitute the testing sample.

Table 1: The experiment data under various working conditions. Here, "1," "2," and "3" denote fault diameters of 0.18 mm, 0.36 mm, and 0.54 mm, respectively.

Datasets	Fault diameters (mm)	Fault type
A/B	0.18/0.36/0.54	NR
		BF1
		IRF1
		ORF1
		BF2
		IRF2
		ORF2
		BF3
		IRF3

3.2. Evaluation Index. By searching the class number space, adAP can output some clustering results with various cluster numbers. Therefore, the clustering validity method can be used to assess the performance of the clustering results. Among the many effectiveness indicators, the Silhouette index is widely used because of its evaluation ability for obvious cluster structures. The Silhouette index shows the interclass tightness of the cluster structure and the class separability [30]. Therefore, the Silhouette index is taken as an example to solve the optimal clustering result.

A dataset is divided into K clusters $C_i (i = 1, 2, \ldots, K)$,$a(t)$ is the mean distance between the sample t and other samples in the cluster C_j, and $d(t, C_i)$ represents the average distance between sample t and all of the samples in the cluster C_i. Then, $b(t) = \min\{d(t, C_i)\} i = 1, 2, 3, \ldots, K. i \neq j$. Therefore, the Silhouette index of a sample is calculated by

$$S_{\text{il}}(t) = \frac{b(t) - a(t)}{\max\{a(t), b(t)\}}. \tag{13}$$

It is easy to calculate the average $S_{\text{av}}(C_i)$ of all samples of a clusterC_i. It reflects the tightness of the cluster C_i (such as the average distance within the cluster) and the separability (such as the minimum interclass distance). The average value $S_{\text{av}}(C)$ for overall samples by using S_{il} can reflect the quality of the clustering results.

For a series of Silhouette index values of clustering results, the larger the value is, the better the clustering quality becomes. The cluster number corresponding to the largest value is the optimal cluster number, and the corresponding clustering result is also optimal [31]. The Silhouette value of the clustering result exceeding 0.5 denotes that each cluster can be separated well [31].

3.3. Procedures for the Proposed Model. The detailed procedures of the proposed method contain three sections: (1) data preprocessing, (2) feature extraction, and (3) fault diagnosis:

(1) Data preprocessing: the fast Fourier transformation (FFT) is utilized to transform the raw signal from the time domain to the frequency domain because the coefficient matrix is symmetrical after FFT operation. Hence, half of the coefficient matrix was used for SAE and SDAE training and testing. All input data are normalized into [0, 1].

(2) Feature extraction: since the dimension of the original data is high and cannot be visualized, PCA is used to reduce the feature dimension at each hidden layer to compare the feature extraction performance of the SAE and SDAE. Note that the extracted feature vector dimension is 3 at the final hidden layer without PCA operation.

(3) Fault diagnosis: after training the SAE and SDAE, 3-dimensional feature vectors are considered as the inputs of FCM, GK, GG, and adAP for fault identification. To verify that the clustering performance of the proposed SDAE-adAP is better than other models, such as SAE/SDAE-FCM/GK/GG, SAE-adAP, a clustering evaluation index (i.e., Silhouette) is used to assess the clustering performance results. In addition, the accuracy is also utilized to compare the identification performance of the different models. The detailed procedures are shown in Figure 4.

4. Fault Diagnosis and Comparison Analysis

4.1. Feature Extraction for Different Vibration Signals. First, the origin vibration signal is shown in Figure 5. As seen in Figure 5, distinguishing all signals is not easy. BF, IRF, and ORF signals have regularity, while all NR signals have no obvious periodic regularity because they are random vibrations, and their self-similarity is poor. Different from NR signals, BF, IRF, and ORF vibration signals contain a fixed vibration period in some unique frequency bands, and the self-similarity is higher than in NR signals. Particularly, when the inner ring is fixed, the outer ring rotates with the bearings, and the vibration regularity in BF signals becomes clearer. Therefore, the BF, IRF, and ORF vibration signals have strong periodic regularity, but it is still not easy to identify these fault vibration signals. To extract the useful fault feature effectively and identify these different signals easily, the FFT is utilized to transform the vibration signal because the frequency domain signal contains useful fault information [9]; here, take a BF2 signal as an example. The FFT result of the BF2 is shown in Figure 6. As illustrated in the two subfigures on the right in Figure 6, the working frequencies for BF primary highlight form 0 Hz to 150 Hz, as the BF signal working frequency is 58 Hz; thus, the fault frequency is a primary highlight on 58 Hz and the double frequency (117.2 Hz). Therefore, these results prove that the frequency domain signal subsequently contains useful fault information.

The coefficient matrixes are used for feature extraction through eight hidden layers. Some parameters in the SAE and SDAE should be set before training, such as the input size, the learning rate, the denoising rate, and the total number of the neural nodes at each hidden layer.

The length of each original sample is 2,048 points. The frequency domain coefficients of each sample after FFT transformation are symmetrical; hence, the length of each input sample in the SDAE is transformed to 1,024. In addition, the hidden layer adopts a triangular structure—that is, the number of nodes in the following adjacent hidden layer is half that of the previous hidden layer. Therefore, the number of nodes in the first hidden layer is 512. The neural node numbers at the first eight hidden layers are selected as 512, 256, 128, 64, 32, 16, 8, and 3. Then, the first three principal components (PCs) in PCA are chosen as the fault feature for data visualization and compared to the feature extraction ability of the SAE and SDAE.

Since much information is missing when the denoising probability p becomes too large, the SDAE will generate a high error rate. The authors suggest that parameter p is often set lower than 0.5 [32, 33]. p is set as 0.15 in this paper.

If the learning rate is too high, the convergence speed of reconstruction error will be fast, but it is easy to trap into the local optimal point. However, if the learning rate is too small, the SAE and SDAE models will exhibit slow convergence [34–41]. The learning rate β in equation (8) is 0.1, and the largest iteration number is 3,000 in this study.

The 3-dimensional results of different datasets for the training dataset through eight hidden layers by using SDAE/SAE with PCA dimension reduction under different conditions are shown in Figures 7 and 8. In Figure 7, "SAE-A-512-training data" means that 512 neural nodes exist at the first hidden layer through the SAE and dataset A. As shown in Figure 8, the various fault samples are separated well when the number of hidden layers increases.

In Figure 8, to the naked eye, the last two subfigures show only a shape, such as "BF3." However, in the former first seven hidden layers, compared with the SAE, when the number of hidden layers increases, the SDAE feature extraction ability becomes stronger. As with the SDAE-A-2 training data, all the BF2 samples look like only one sample at the naked-eye layer.

4.2. Fault Diagnosis by Using the adAP-Training Dataset. The results of adAP clustering are shown in Figure 9. The choice of descending stride p_{step} is the key to adAP. The smaller the p_{step} is, the more slowly the algorithm runs. Conversely, the larger the p_{step} is, the more likely it becomes that the number of clusters reflecting the intrinsic cluster structure of the dataset will be missed. The fixed stride is difficult to adapt to different cases of large and small clusters. Therefore, the adaptive adjustment technique of the descending stride p_{step} is as follows:

$$p_{\text{step}} = \frac{0.01 p_m}{q}, \tag{14}$$

where $q = 0.1\sqrt{K + 50}$. Hence, the algorithm can dynamically adjust q when generating K clusters to achieve a smaller step size when K is larger or a smaller step when K is smaller. When clustering N data points, it is generally considered

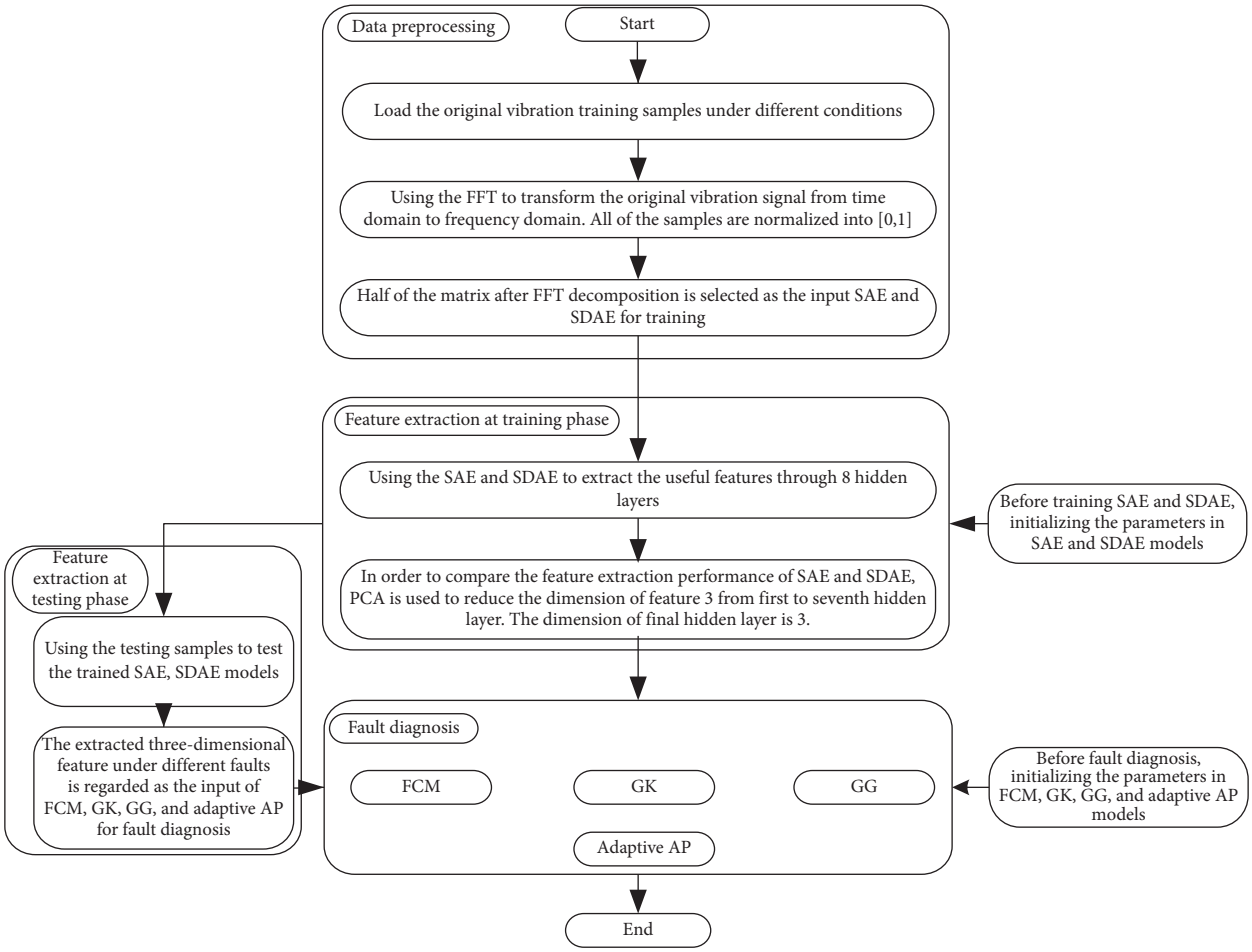

Figure 4: The procedure of the proposed model.

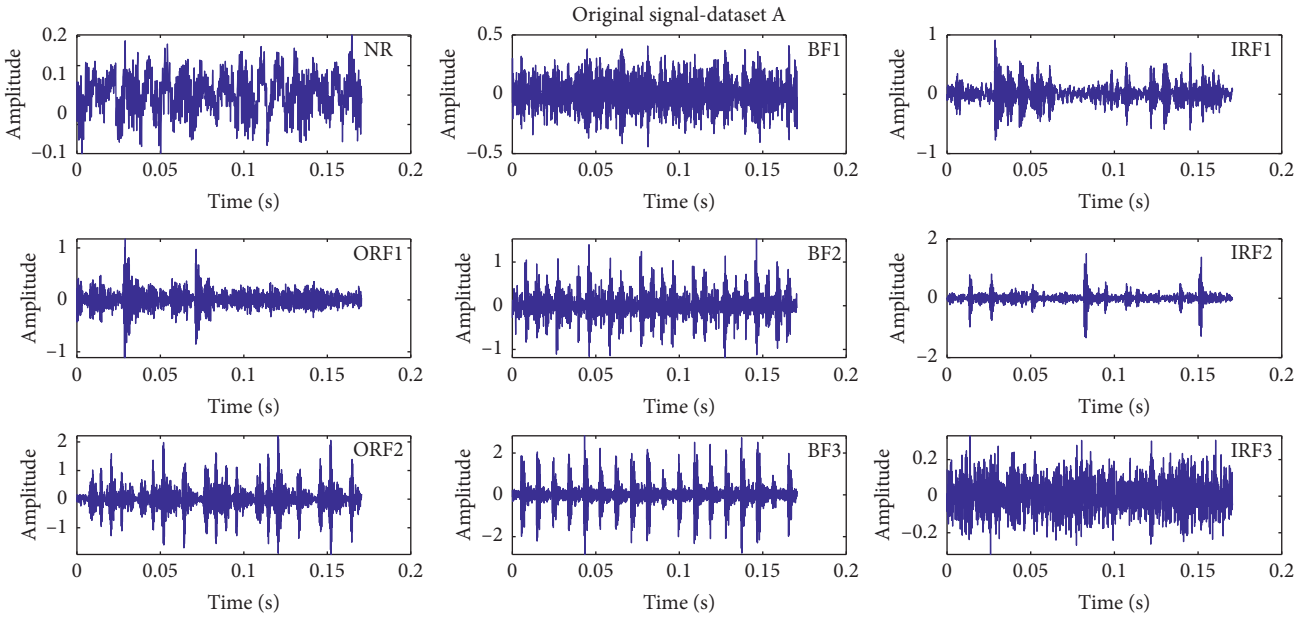

(a)

Figure 5: Continued.

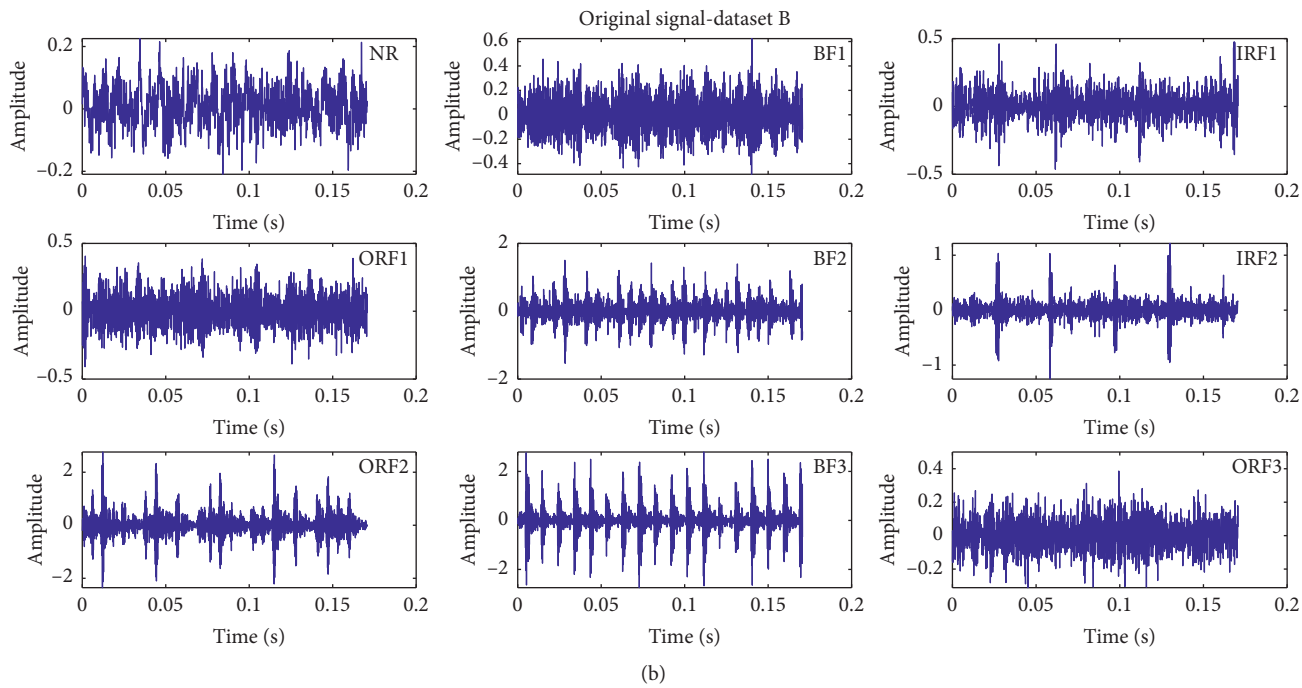

Figure 5: The original signal under various working conditions.

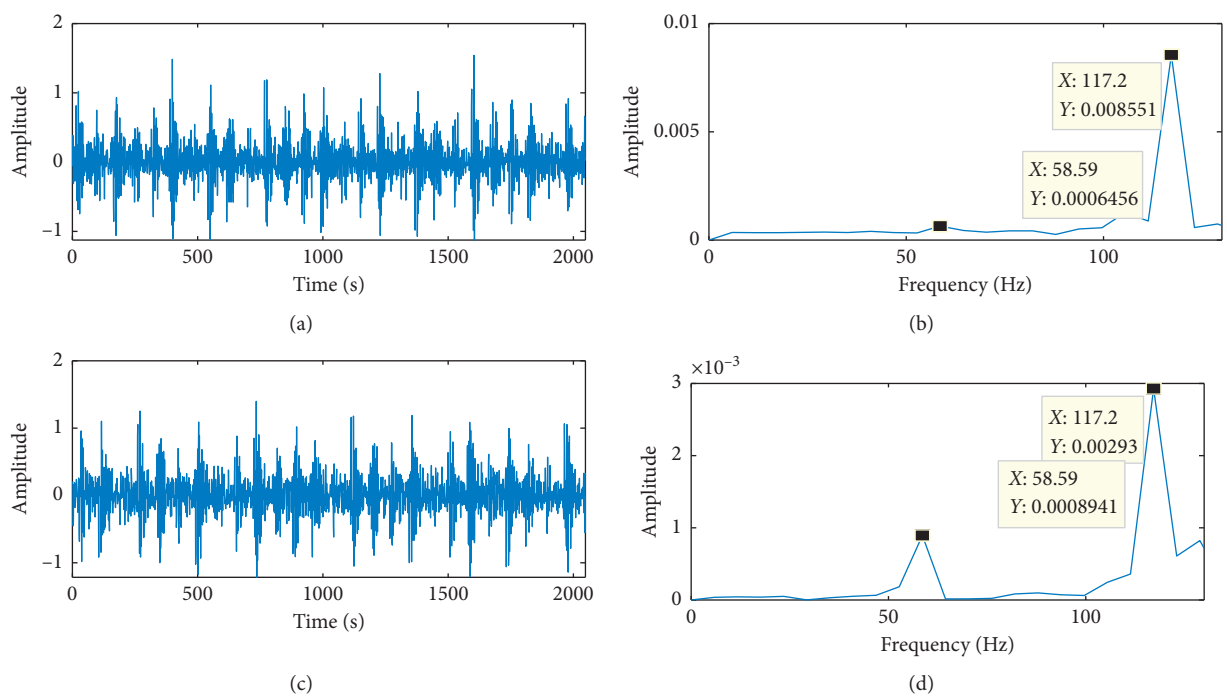

Figure 6: BF2 FFT results by using different datasets; here, the unit of the x-axis is second. (a) Original signal-dataset A-BF2. (b) Frequency domain-A-BF2. (c) Original signal-dataset B-BF2. (d) Frequency domain-B-BF2.

reasonable that the upper limit of the optimal number of clusters is the square root of N [35]. When the initial $p = p_m/2$, the number of cluster classes K that the algorithm converges at first can basically reach or exceed $\sqrt{N}$. However, the cluster number searched by the AP algorithm is more than $\sqrt{N}$ (because each data point is viewed at the beginning of the algorithm). For the cluster class, the starting value can be set to $p = p_m/2$. The minimum number of cluster 2 determines the lower bound of p, reducing p until the cluster number $K = 2$. To prevent the maximum number of

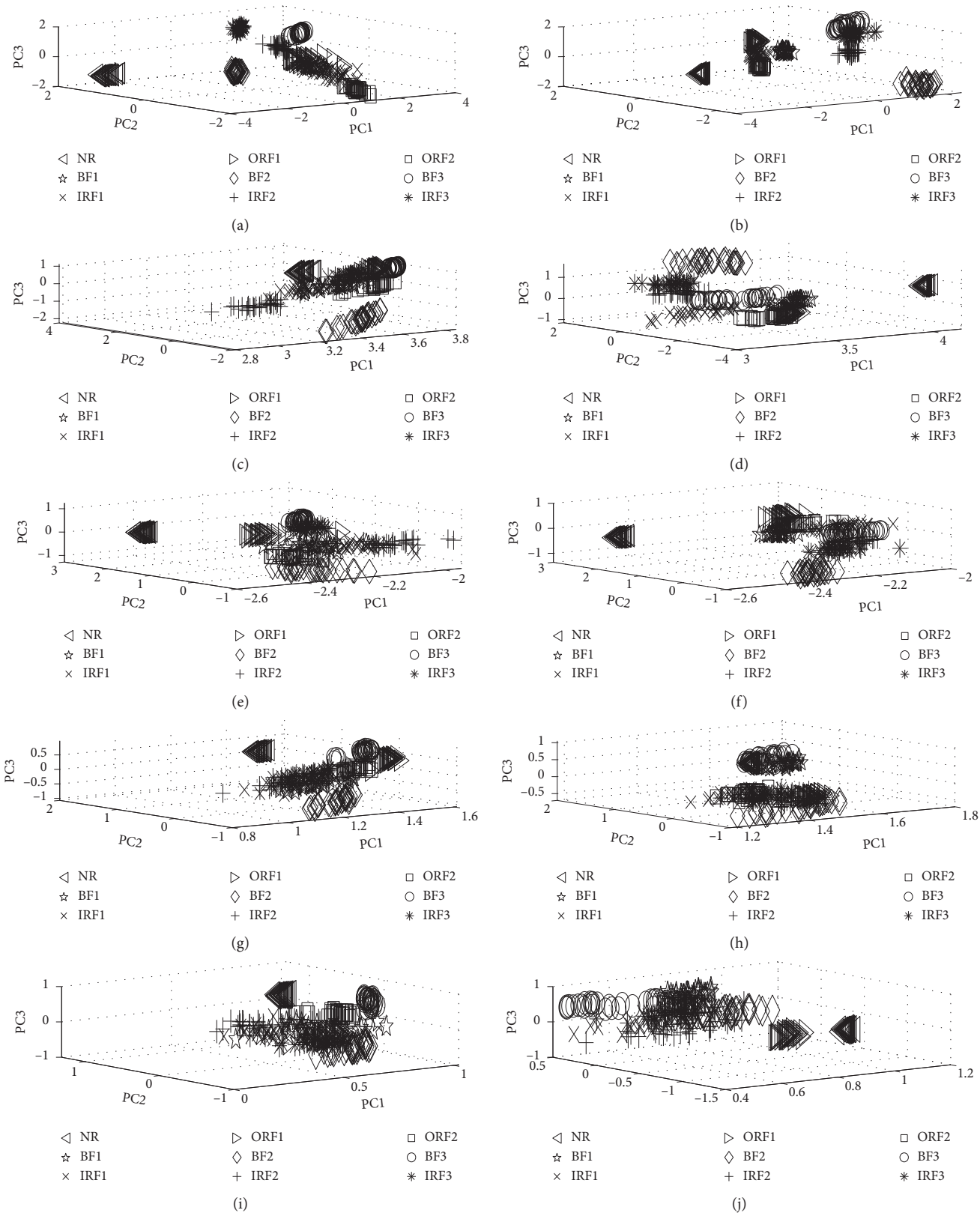

Figure 7: Continued.

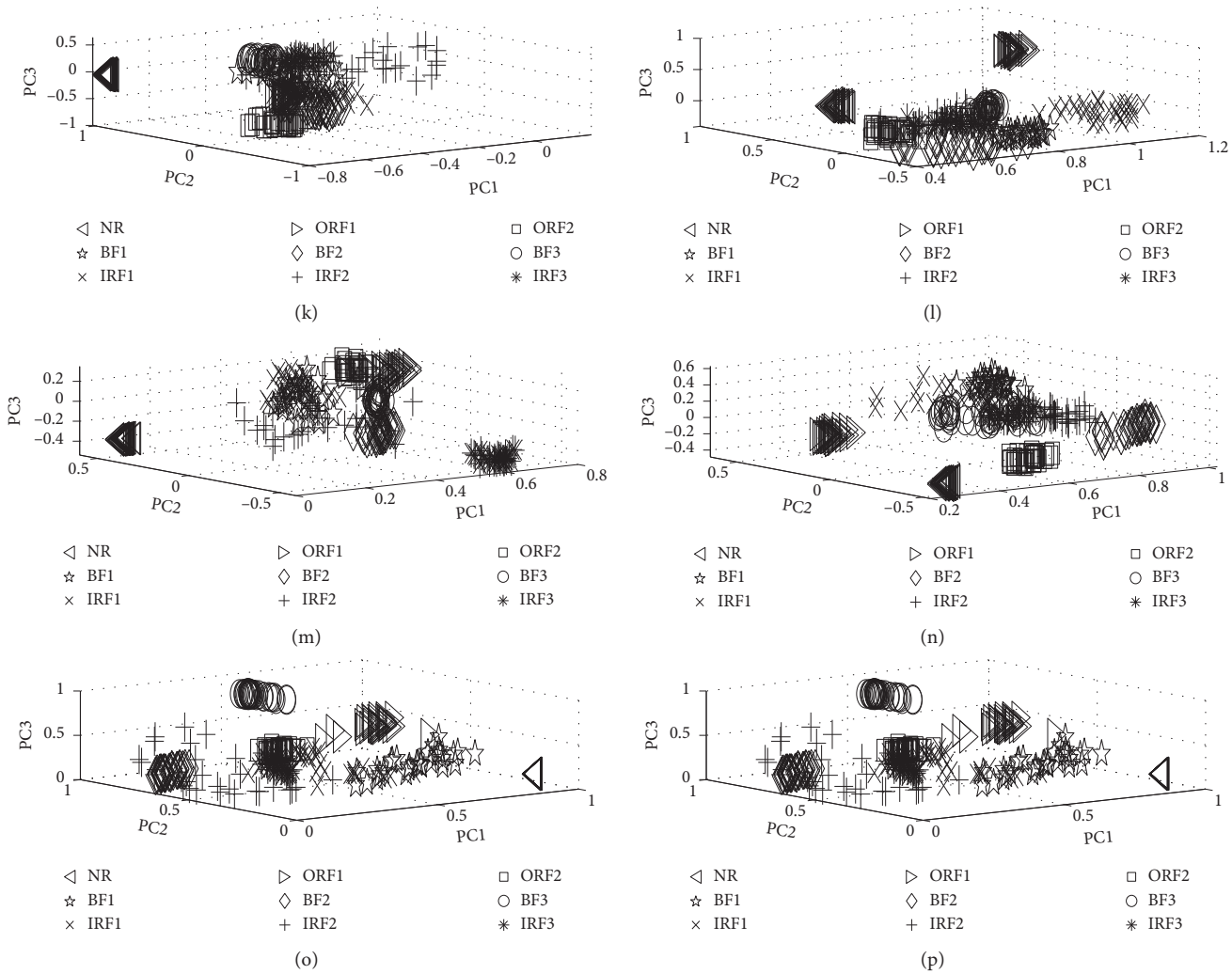

Figure 7: The 3-dimensional results of different datasets for the training dataset through eight hidden layers by using an SAE with PCA dimension reduction; 1–8 denote the hidden layer number. (a) SAE-A-512-training data. (b) SAE-B-512-training data. (c) SAE-A-256-training data. (d) SAE-B-256-training data. (e) SAE-A-128-training data. (f) SAE-B-128-training data. (g) SAE-A-64-training data. (h) SAE-B-64-training data. (i) SAE-A-32-training data. (j) SAE-B-32-training data. (k) SAE-A-16-training data. (l) SAE-B-16-training data. (m) SAE-A-8-training data. (n) SAE-B-8-training data. (o) SAE-A-3-training data. (p) SAE-B-3-training data.

iterations from affecting whether the algorithm reaches $K = 2$, the largest iteration number $\text{iter}_{\max}$ is fixed as 50,000 in this study.

After the parameters mentioned above are preconfigured, 3-dimensional features are chosen as the input of adAP for fault diagnosis. The 3-dimensional clustering results for training datasets A and B by using an SAE/SDAE with adAP are shown in Figure 9.

(1) In Figure 9, symbol "CC" denotes the cluster center points. There are two cluster points for BF2 samples, and the diamond symbol indicates the BF2 sample using dataset A. In the third subfigure, all BF2 samples have only one cluster center point.

(2) From Figure 9, all samples in the third and fourth subfigures are separated well, and they are very close to its cluster center point. The division between each cluster class is very clear. For example, BF3 and IRF3 samples are separated well by using an SDAE for dataset B in the fourth subfigure in Figure 9. Therefore, these scattered points easily lead to the generation of multiple or extra cluster center points.

These results demonstrate that the robustness and the feature extraction ability of SDAEs are better than those of SAEs. Moreover, adAP can find the cluster center point automatically.

The result of the energy function $E(C)$ by using an SDAE for training dataset A is shown in Figure 10. As seen in Figure 10, there are obvious oscillations in the curve during the first 130 iterations. Increasing the value of *lam* in the following steps gradually keeps the curve stable, as evidenced by the fact that the largest value of $E(C)$ occurs when the cluster number is 9. Actually, the parameter *lam* increases up to 0.7 when the number of iterations is 101, but the curve also has a random oscillation. Then, *lam* increases to 0.75

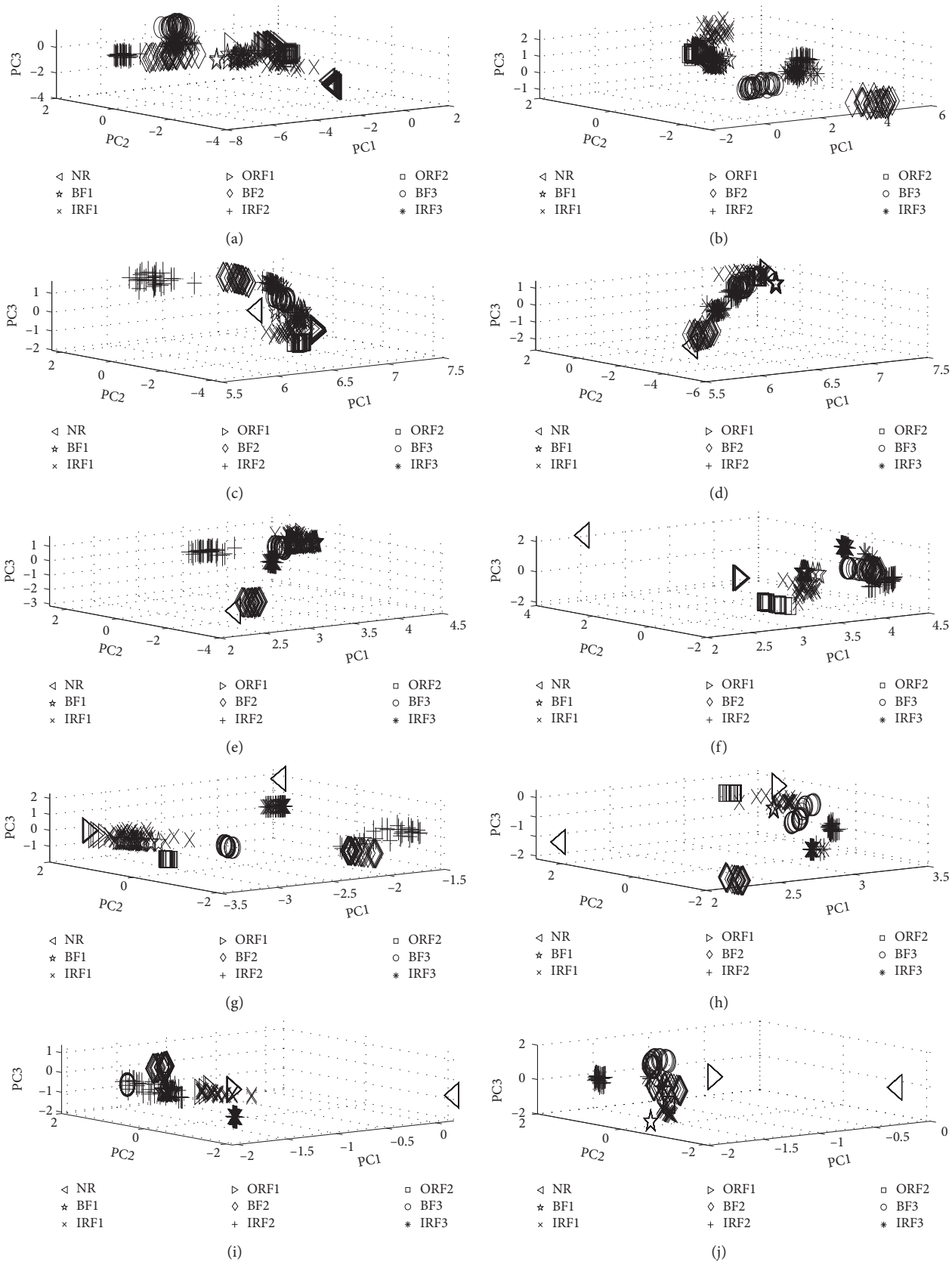

Figure 8: Continued.

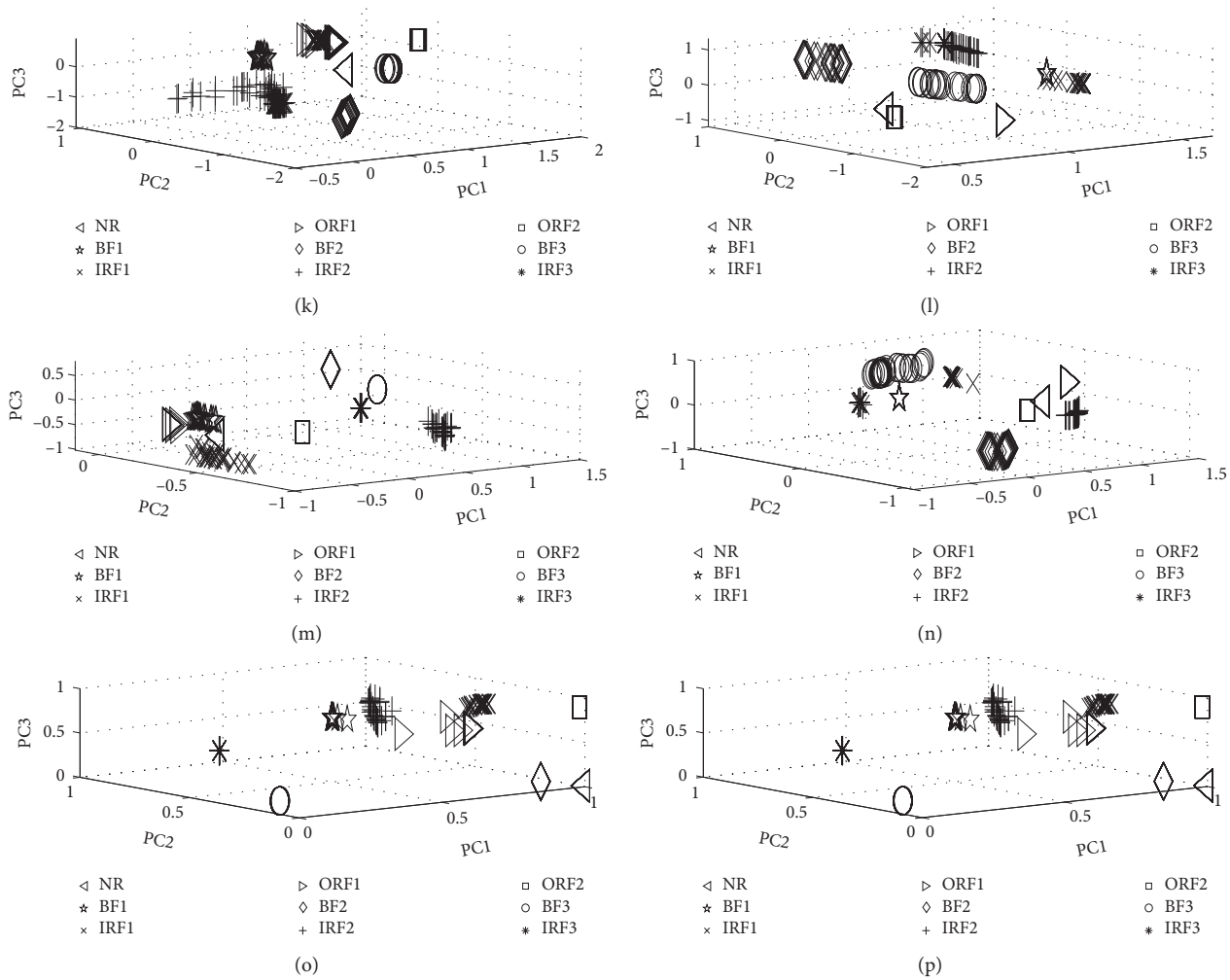

Figure 8: The 3-dimensional results of different datasets for the training dataset through eight hidden layers by using an SDAE with PCA dimension reduction; 1–8 denote the hidden layer number. (a) SDAE-A-512-training data. (b) SDAE-B-512-training data. (c) SDAE-A-256-training data. (d) SDAE-B-256-training data. (e) SDAE-A-128-training data. (f) SDAE-B-128-training data. (g) SDAE-A-64-training data. (h) SDAE-B-64-training data. (i) SDAE-A-32-training data. (j) SDAE-B-32-training data. (k) SDAE-A-16-training data. (l) SDAE-B-16-training data. (m) SDAE-A-8-training data. (n) SDAE-B-8-training data. (o) SDAE-A-3-training data. (p) SDAE-B-3-training data.

when the curve becomes stable starting from 131. With the increment of the iteration number, the value of *lam* becomes smaller than the former iteration.

Hence, the best cluster number is 9. The clustering index (Silhouette) in equation (13) is also used to assess the clustering result. The results of the Silhouette index with different cluster numbers by using an SAE/SDAE with adAP (the training dataset) are displayed in Table 2.

(1) From Table 2, the largest value is 0.954 by using an SDAE with dataset A when the cluster number is 9, but for the SAE used in dataset A, the largest value is 0.694, which is smaller than 0.954. It should be noted that the cluster number is 10, not 9, because the SAE generated some scatter points, such as BF3 in Figure 9. This result leads to the generation of extra cluster center points for the same fault samples.

(2) Although the best cluster number is 9 in the SAE, it is the same in the SDAE for dataset B, while the largest value of the Silhouette index is 0.889. Hence, the feature extraction ability of the SDAE exceeds that of the SAE, and adAP can find the available parameters automatically. The classification accuracy using the best cluster number is shown in Table 3. The lowest classification error rate is 0% for dataset A by using the SDAE, and the classification error rate of the SDAE is lower than that of the SAE on the whole.

4.3. Compared with FCM, GK, and GG. To further demonstrate that the proposed model (SDAE-adAP) is better than SAE/SDAE-FCM/GK/GG, the 3-dimensional clustering results for training dataset A and B by using the SAE/SDAE with FCM/GK/GG are shown in Figures 11 and 12.

Compared with the SAE, most of the samples are separated well and close to the center point in the SDAE. While some samples exhibit an overlap phenomenon—especially

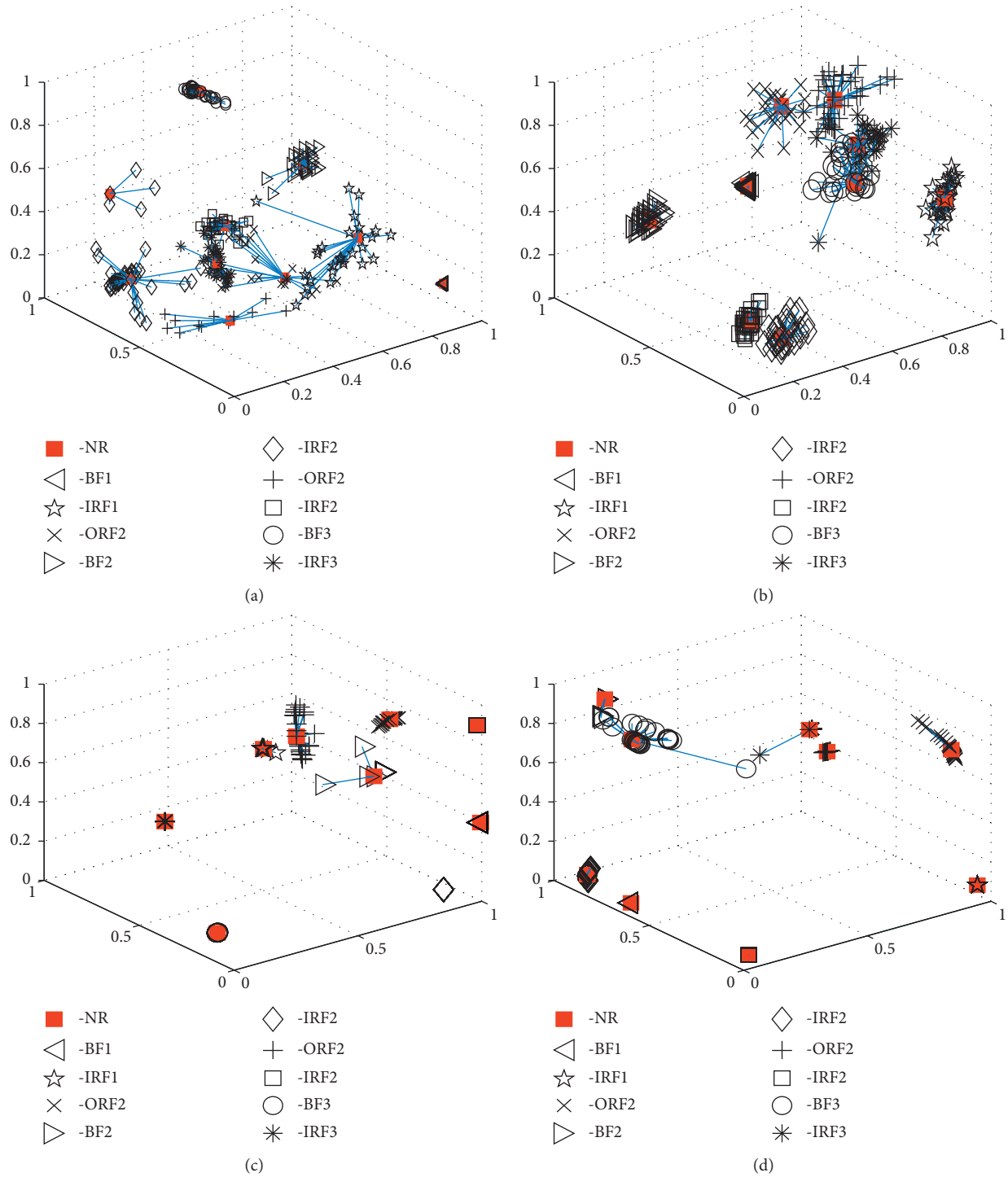

Figure 9: The 3-dimensional clustering results for the training dataset by using an SAE/SDAE with adAP. (a) SAE-A-training data-adaptive AP. (b) SAE-B-training data-adaptive AP. (c) SDAE-A-training data-adaptive AP. (d) SDAE-B-training data-adaptive AP.

IRF1 and BF1 in Figure 11(a)—these samples are separated well by using an SDAE. The classification accuracy achieved by using different combination models for training datasets A and B are displayed in Table 4. The lowest error rate is 0% in dataset A, and the lowest error rate of the proposed model SDAE-adAP is lower than other combination models, including SAE/SDAE-FCM/GK/GG and SAE-adAP.

4.4. Fault Diagnosis through the adAP-Testing Dataset. The testing datasets is used to test the performance model. As with the training dataset, the feature extraction procedure through several hidden layers in the SAE and SDAE is shown in Figures 13 and 14. As seen in Figures 13 and 14, all of the testing samples are separated well at the final hidden layer, such as the ORF2 samples. All of the ORF2 samples look like

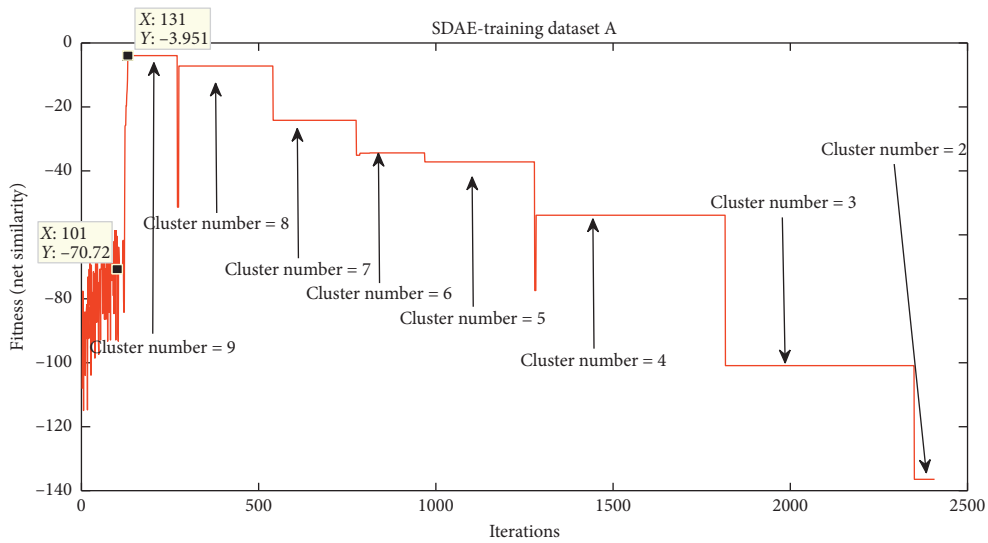

Figure 10: The results of the energy function (similarity) for all samples.

Table 2: The results of the Silhouette index with different cluster numbers by using an SAE/SDAE with adAP (the training dataset). Here, "—" means there is no cluster number equal to 10, 11, or 12.

Model	Dataset	Silhouette index										
		Cluster no.										
		2	3	4	5	6	7	8	9	10	11	12
SAE-adAP	A	0.330	0.391	0.484	0.538	0.592	0.635	0.664	0.683	0.694	0.672	0.662
	B	0.483	0.510	0.636	0.608	0.630	0.574	0.641	0.678	—	—	—
SDAE-adAP	A	0.413	0.549	0.695	0.738	0.808	0.839	0.935	0.954	—	—	—
	B	0.431	0.512	0.602	0.713	0.812	0.875	0.864	0.889	—	—	—

Table 3: The results of the best cluster number and classification error accuracy at the maximum Silhouette index value by using different models (the training dataset).

Dataset	Model	Best cluster no.	Silhouette index	Error rate (%)
A	SAE-adAP	10	0.6945	—
	SDAE-adAP	9	0.9545	0
B	SAE-adAP	9	0.6785	4.07
	SDAE-adAP	9	0.8898	2.22

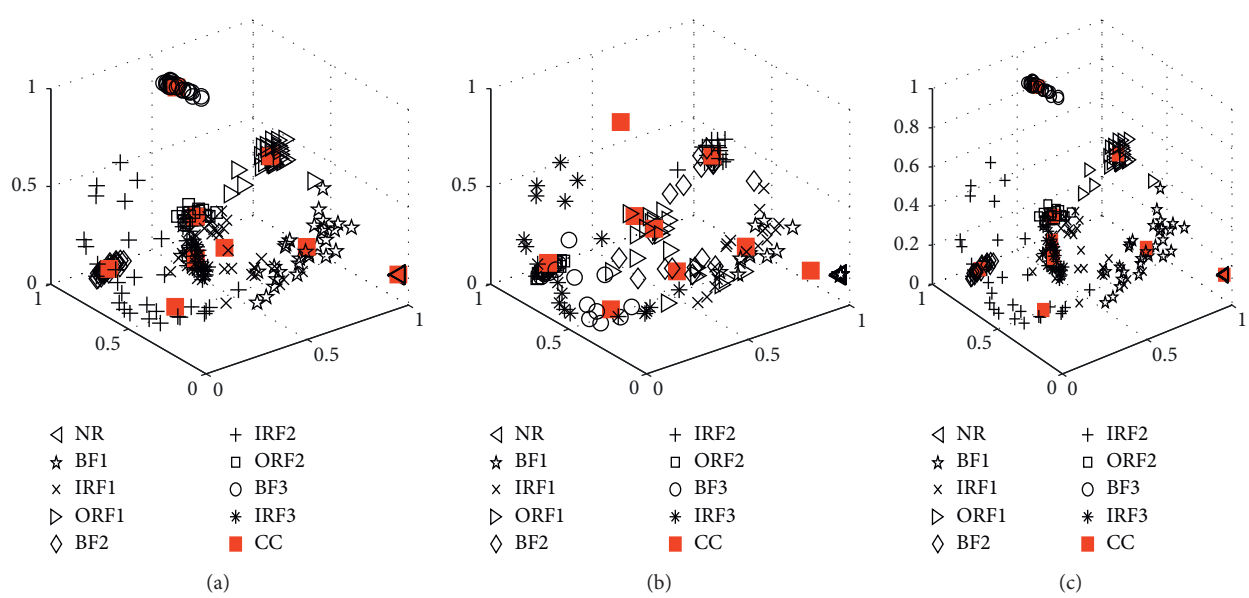

Figure 11: Continued.

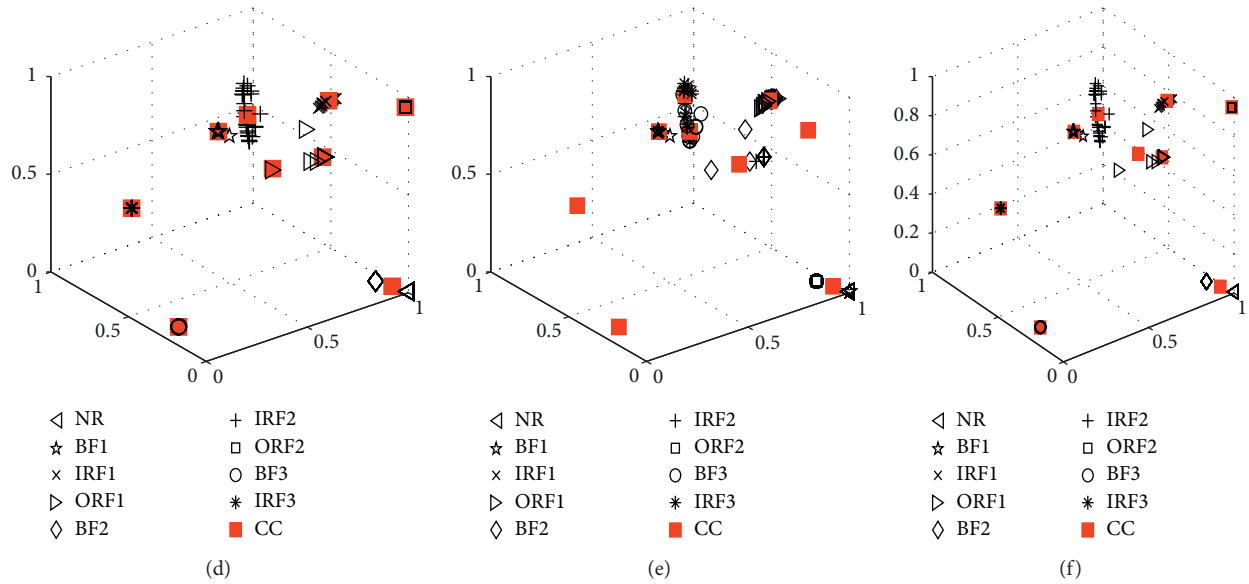

Figure 11: The 3-dimensional clustering results for training dataset A by using an SAE/SDAE with FCM/GK/GG. (a) SAE-FCM-A. (b) SAE-GK-A. (c) SAE-GG-A. (d) SDAE-FCM-A. (e) SDAE-GK-A. (f) SDAE-GG-A.

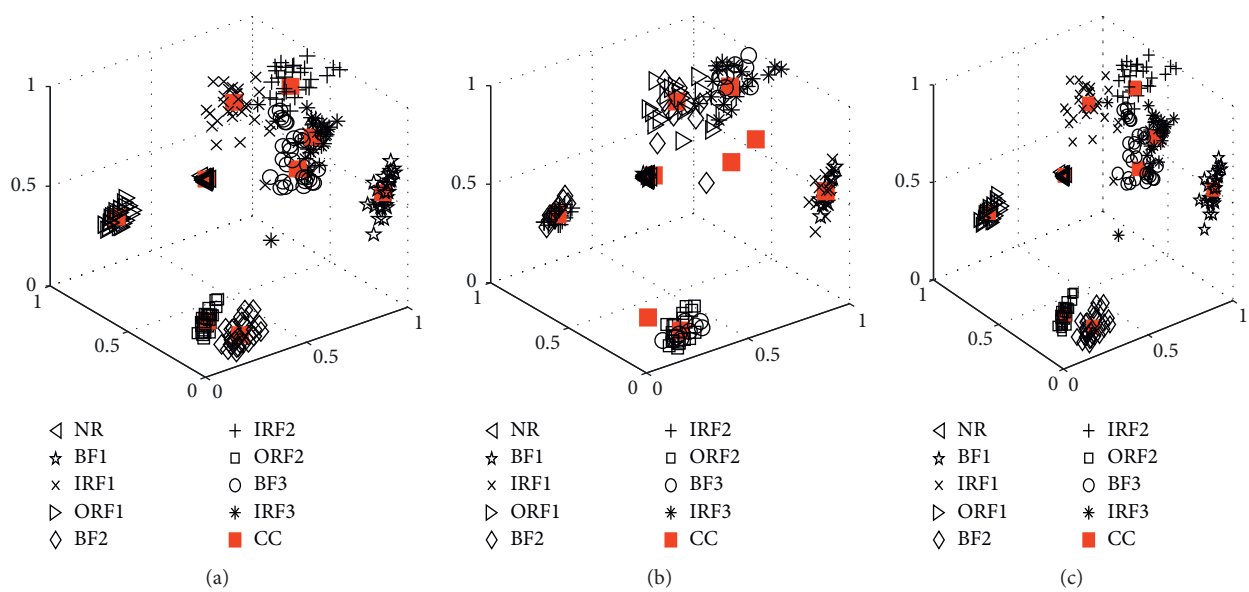

Figure 12: Continued.

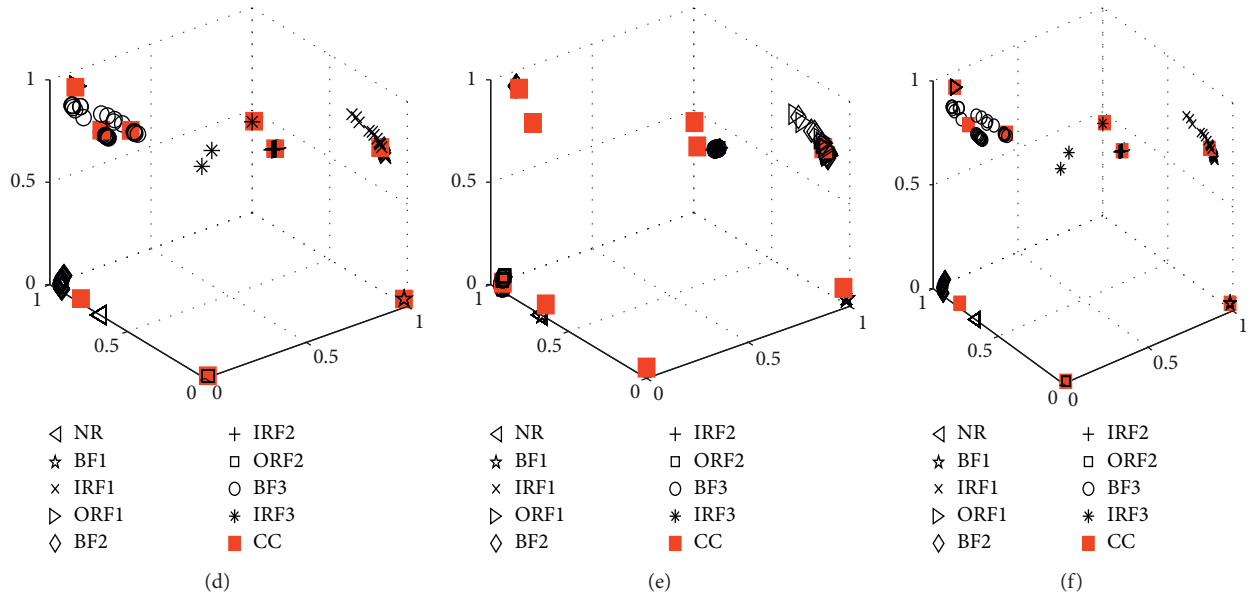

Figure 12: The 3-dimensional clustering results for training dataset B by using an SAE/SDAE with FCM/GK/GG. (a) SAE-FCM-B. (b) SAE-GK-B. (c) SAE-GG-B. (d) SDAE-FCM-B. (e) SDAE-GK-B. (f) SDAE-GG-B.

Table 4: The error classification accuracy obtained through various models (the training dataset).

Model	Dataset	Error rate (%)			
		FCM	GK	GG	adAP
SAE	A	8.15	16.3	6.03	—
	B	2.59	3.33	2.59	4.07
SDAE	A	11.1	21.1	11.1	0
	B	12.9	4.81	11.1	2.22

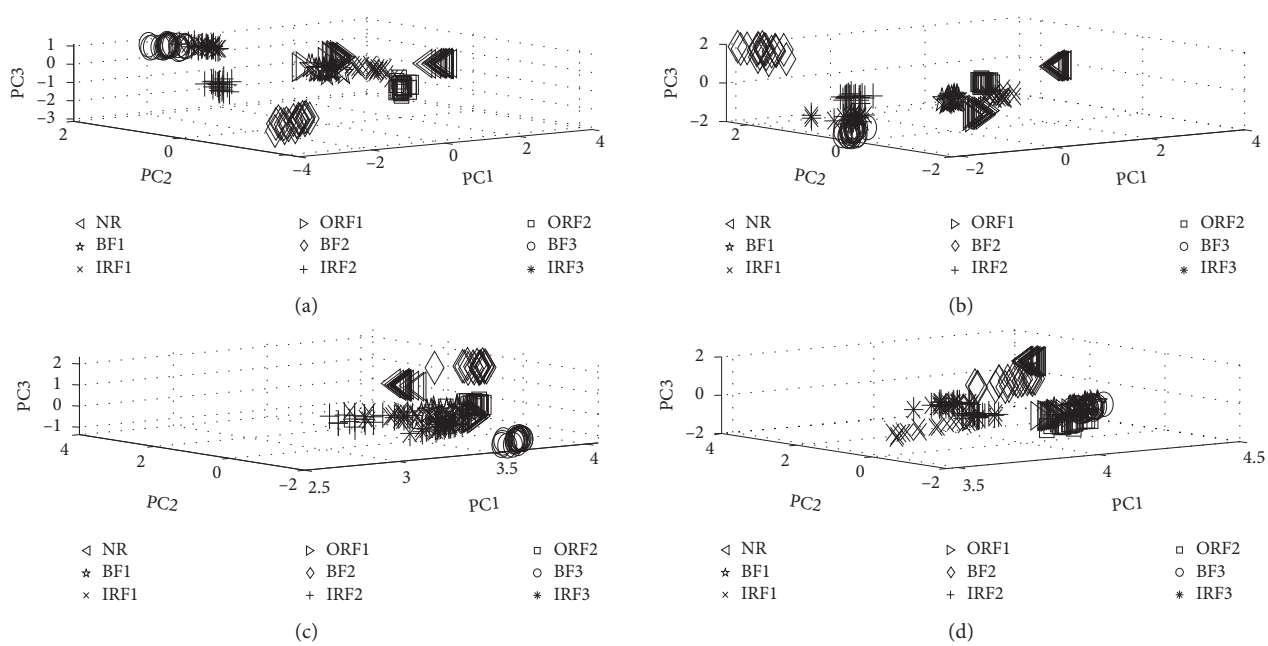

Figure 13: Continued.

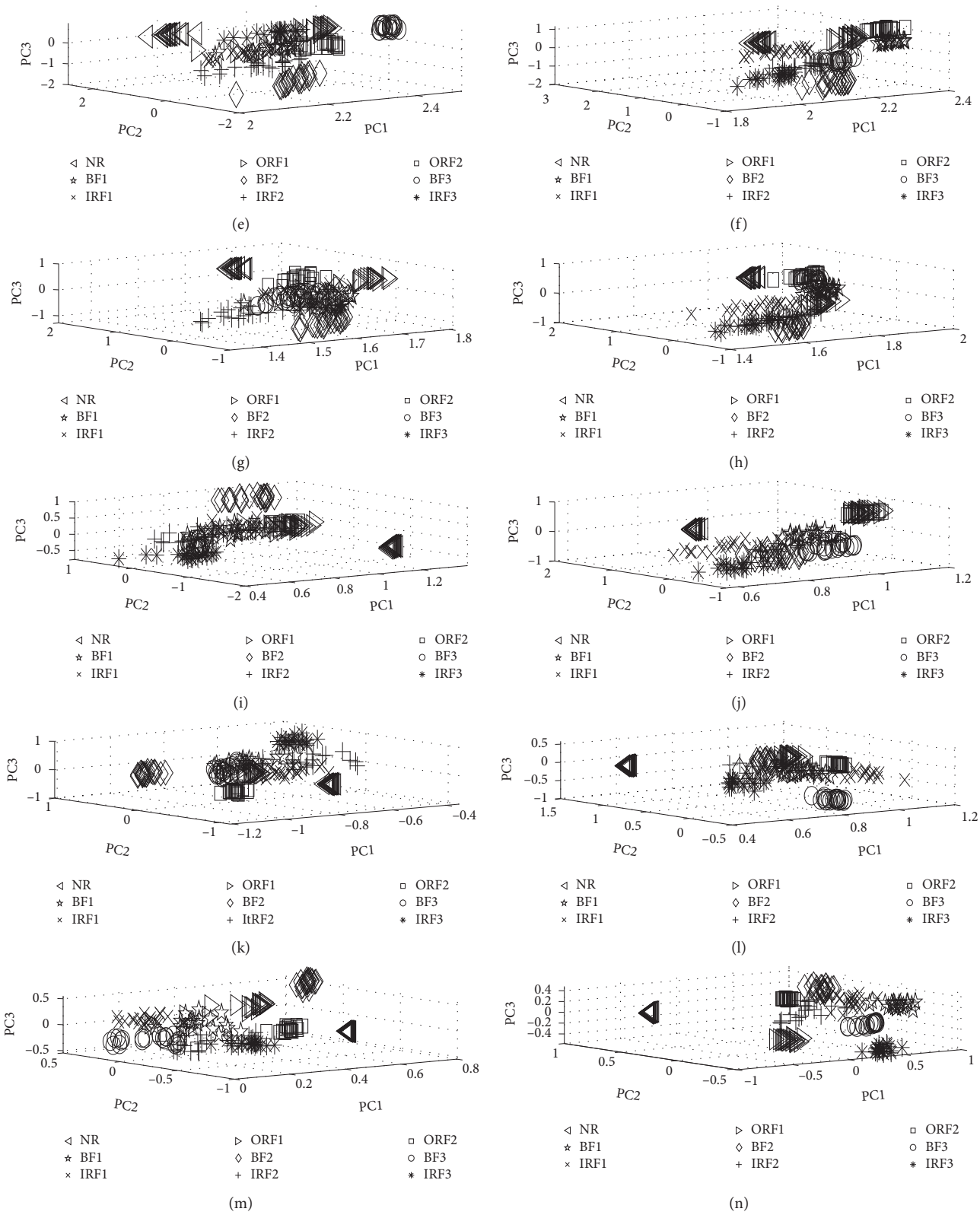

Figure 13: Continued.

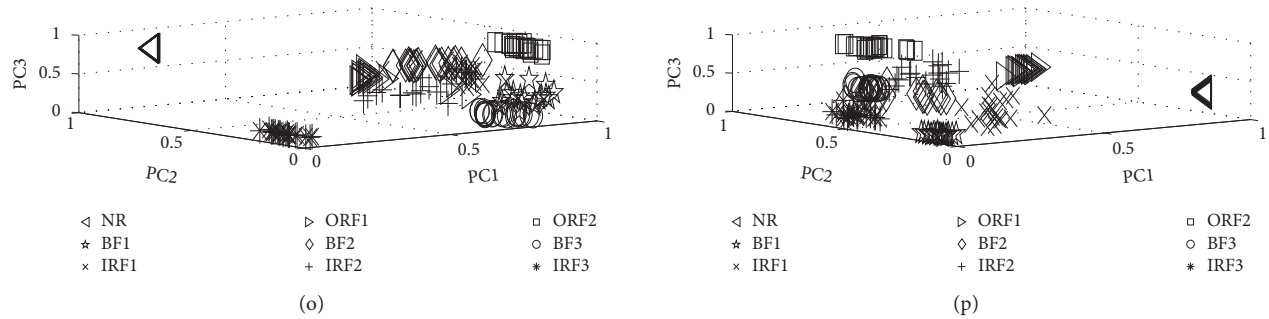

Figure 13: The 3-dimensional results of different datasets for the testing dataset through eight hidden layers by using an SAE with PCA dimension reduction; 1–8 denote the hidden layer number. (a) SAE-A-512-testing data. (b) SAE-B-512-testing data. (c) SAE-A-256-testing data. (d) SAE-B-256-testing data. (e) SAE-A-128-testing data. (f) SAE-B-128-testing data. (g) SAE-A-64-testing data. (h) SAE-B-64-testing data. (i) SAE-A-32-testing data. (j) SAE-B-32-testing data. (k) SAE-A-16-testing data. (l) SAE-B-16-testing data. (m) SAE-A-8-testing data. (n) SAE-B-8-testing data. (o) SAE-A-3-testing data. (p) SAE-B-3-testing data.

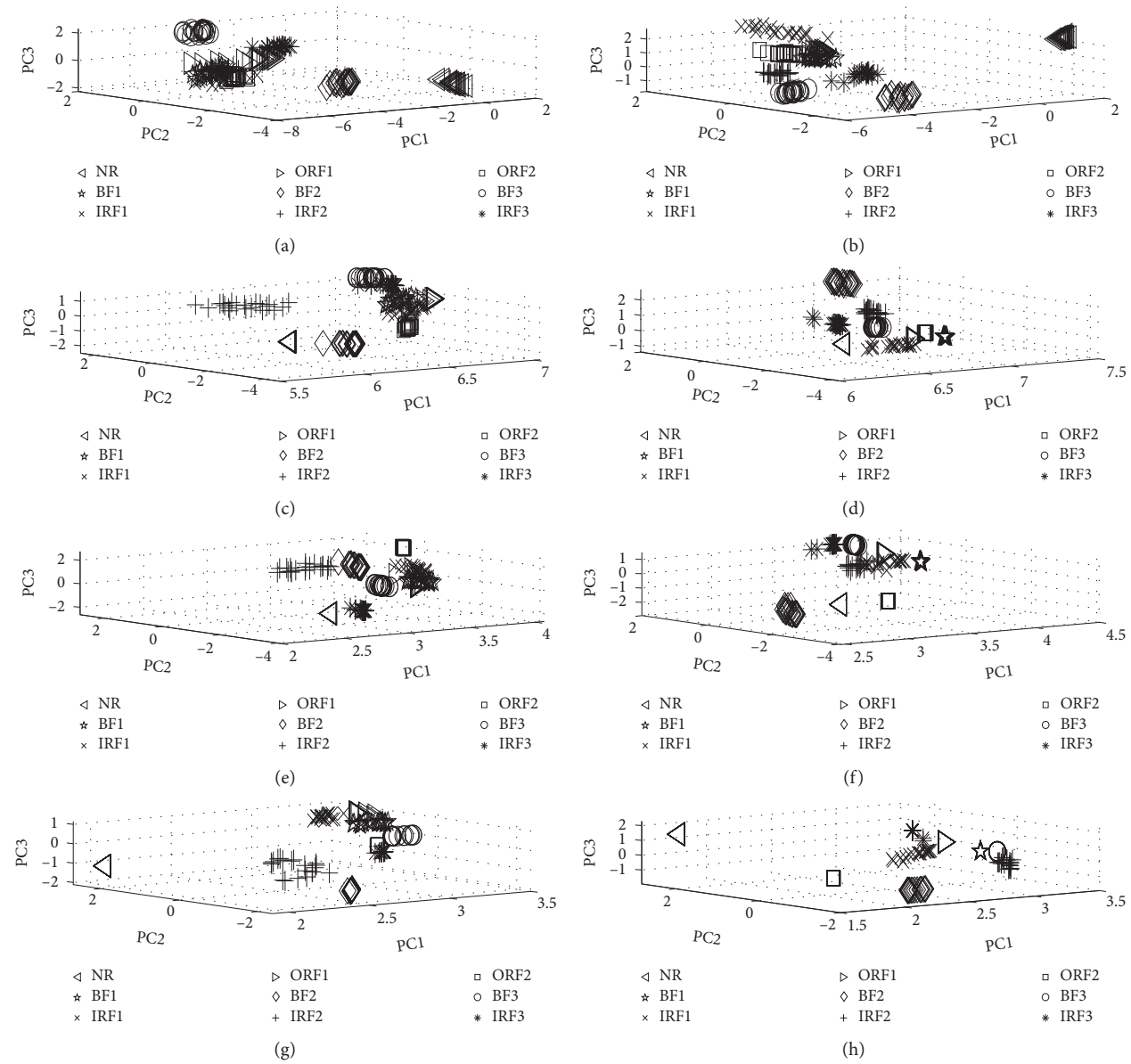

Figure 14: Continued.

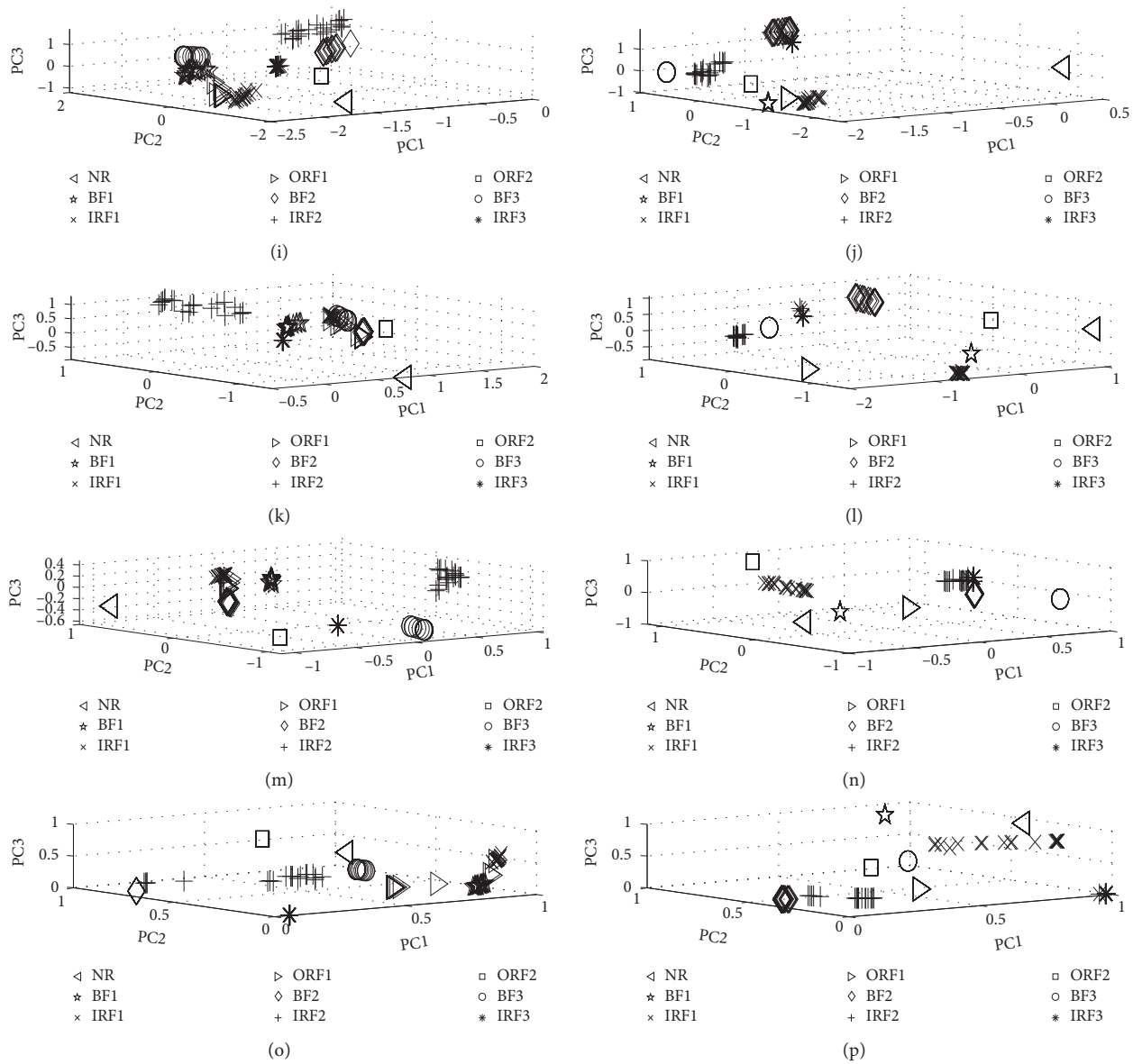

Figure 14: The 3-dimensional results of different datasets for the testing dataset through eight hidden layers by using an SDAE with PCA dimension reduction; 1–8 denote the hidden layer number. (a) SDAE-A-512-testing data. (b) SDAE-B-512-testing data. (c) SDAE-A-256-testing data. (d) SDAE-B-256-testing data. (e) SDAE-A-128-testing data. (f) SDAE-B-128-testing data. (g) SDAE-A-64-testing data. (h) SDAE-B-64-testing data. (i) SDAE-A-32-testing data. (j) SDAE-B-32-testing data. (k) SDAE-A-16-testing data. (l) SDAE-B-16-testing data. (m) SDAE-A-8-testing data. (n) SDAE-B-8-testing data. (o) SDAE-A-3-testing data. (p) SDAE-B-3-testing data.

a square at first glance by using the SDAE in Figure 14, while they are scattered in the SAE in Figure 13. Particularly in Figure 14, all samples, including the NR and other fault samples, are separated well when the number of hidden layers increases. The next step is to choose the extracted 3-dimensional features as inputs of adAP for fault diagnosis. The 3-dimensional clustering results for the testing dataset by using the SAE/SDAE with adAP are shown in Figure 15.

As seen in Figure 15, there are 10 cluster center points (red square points), but the actual number of clusters is 9, not 10. Moreover, all samples are separated well in the SDAE and scattered obviously around its cluster center point, as they were in Figures 13 and 14. The corresponding results of the Silhouette index with different cluster numbers by using the SAE/SDAE with adAP (the testing dataset) are listed in Table 5. In Table 5, the largest value of the Silhouette index values is 0.9167 and 0.9014 by using the SDAE with dataset B and dataset A, respectively, which are both higher than the largest value for the SAE (dataset A: 0.6815; dataset B: 0.7424). The value of the Silhouette index in the SDAE is larger than that of the SAE on the whole.

The results of the best cluster number and classification error accuracy at the maximum Silhouette index value by using different models (the testing dataset) are shown in Table 6. In Table 6, the lowest value is 2.22% in the SDAE model with dataset B. For dataset A, it is 4.44% when using

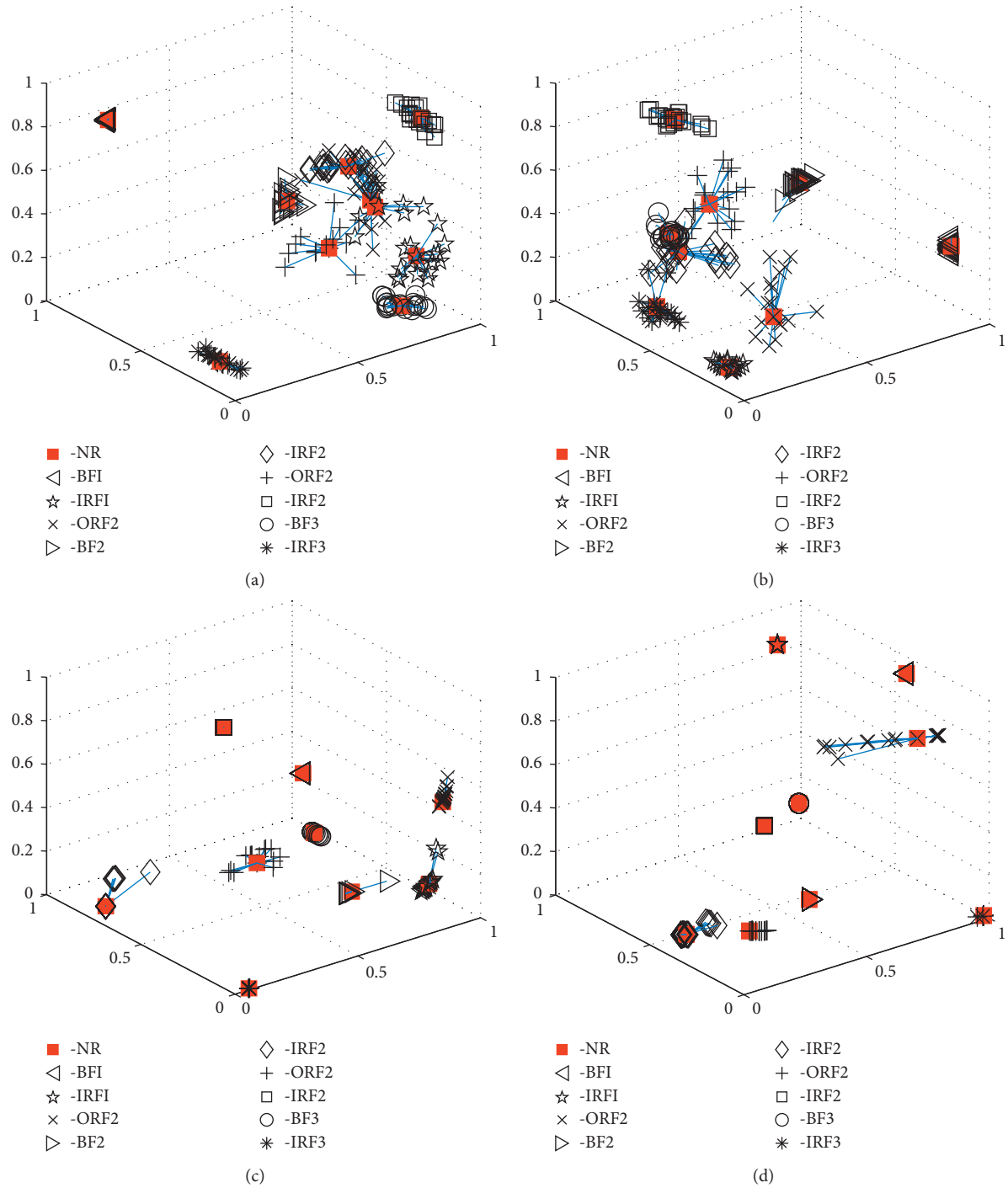

Figure 15: The 3-dimensional clustering results for the testing dataset by using an SAE/SDAE with adAP. (a) SAE-A-testing data-adaptive AP. (b) SAE-B-testing data-adaptive AP. (c) SDAE-A-testing data-adaptive AP. (d) SDAE-B-testing data-adaptive AP.

Table 5: The results of the Silhouette index with different cluster numbers by using an SAE/SDAE with adAP (the testing dataset).

Model	Dataset	Silhouette index										
		Cluster no.										
		2	3	4	5	6	7	8	9	10	11	12
SAE	A	0.3302	0.4377	0.5614	0.5892	0.6126	0.6416	0.6647	0.6791	0.6815	—	—
	B	0.3629	0.4259	0.4327	0.5173	0.6053	0.6367	0.7151	0.7424	0.7415	—	—
SDAE	A	0.4920	0.5050	0.5487	0.6660	0.7780	0.8214	0.8936	0.9014	—	—	—
	B	0.4370	0.5156	0.6237	0.6880	0.7510	0.8061	0.8969	0.9167	—	—	—

Table 6: The results of the best cluster number and classification error accuracy at the maximum Silhouette index value by using different models (the testing dataset).

Dataset	Model	Best clusters no.	Silhouette index	Error rate (%)
A	SAE-adAP	10	0.6815	—
	SDAE-adAP	9	0.9014	4.44
B	SAE-adAP	9	0.7425	5
	SDAE-adAP	9	0.9167	2.78

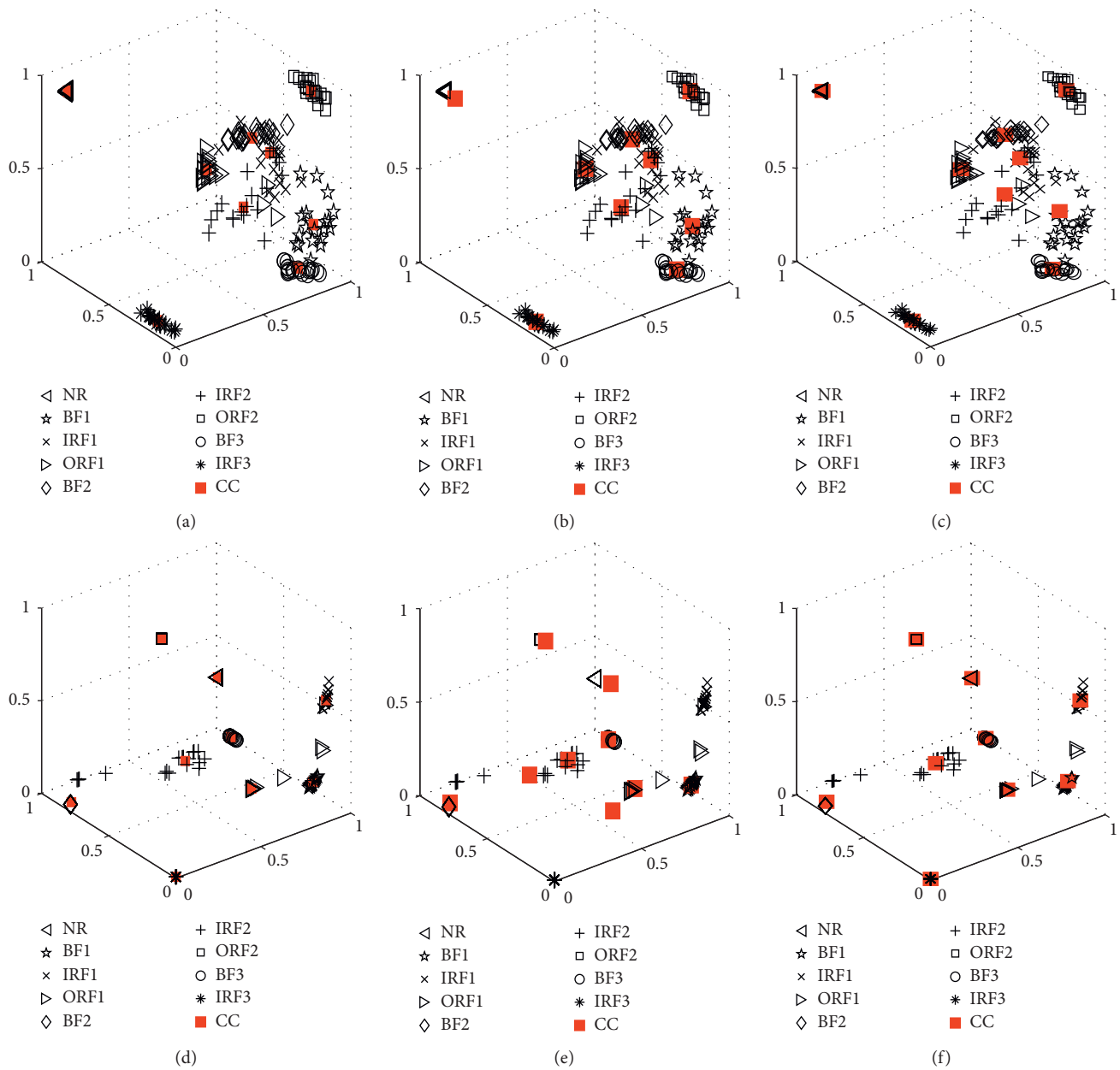

Figure 16: The 3-dimensional clustering results for the testing dataset A by using an SAE/SDAE with FCM/GK/GG. (a) SAE-FCM-A. (b) SAE-GK-A. (c) SAE-GG-A. (d) SDAE-FCM-A. (e) SDAE-GK-A. (f) SDAE-GG-A.

the SDAE. Therefore, these results prove that the robustness and feature extraction ability of the SDAE suppress the SAE. In addition, adAP can find the available cluster number by itself automatically. The 3-dimensional clustering results for training datasets A and B when using the SAE/SDAE with FCM/GK/GG are shown in Figures 16 and 17. Compared with the SAE, most of the samples are separated well and close to the center point in the SDAE. While some samples

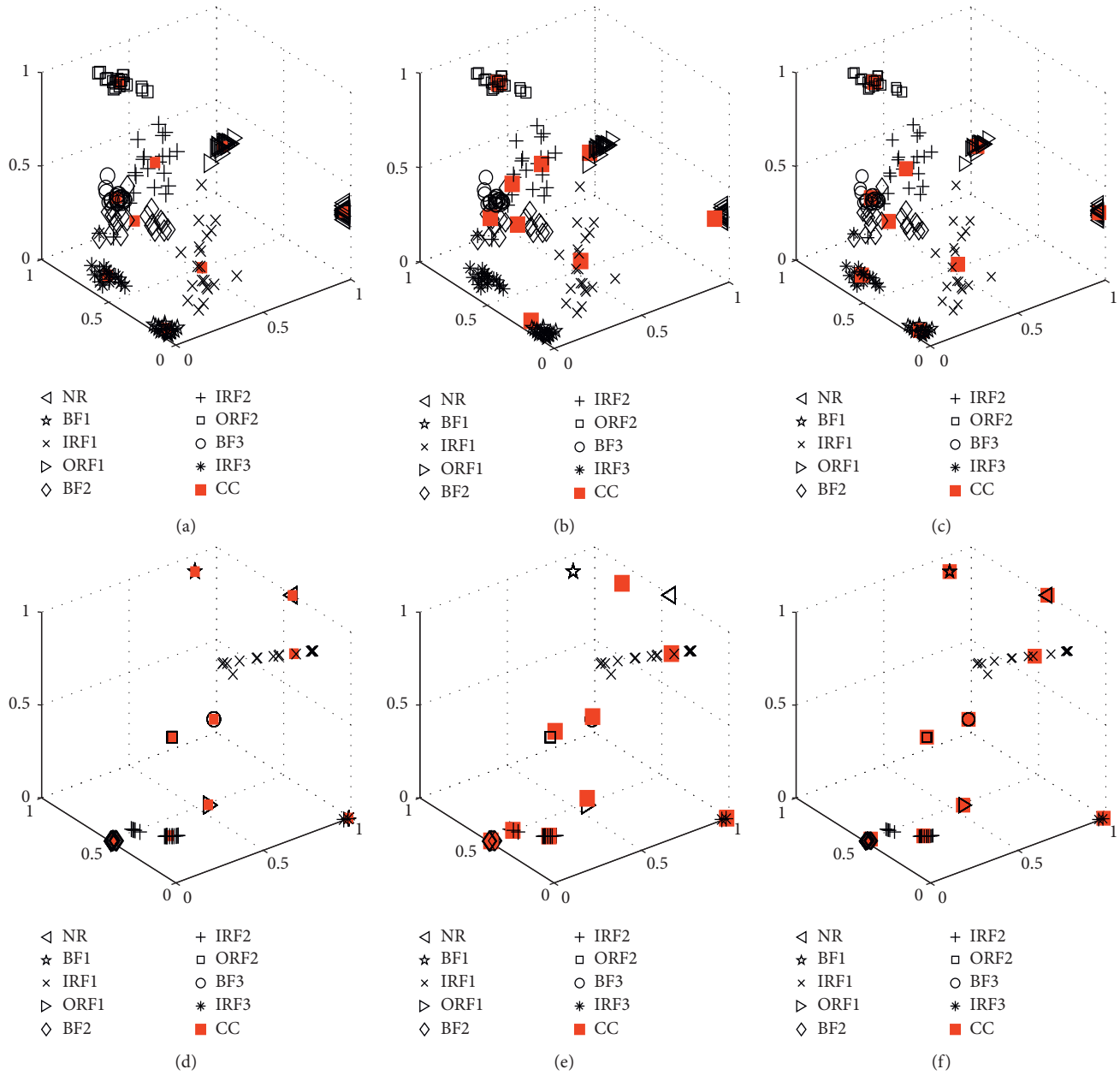

Figure 17: The 3-dimensional clustering for the testing dataset B by using an SAE/SDAE with FCM/GK/GG. (a) SAE-FCM-B. (b) SAE-GK-B. (c) SAE-GG-B. (d) SDAE-FCM-B. (e) SDAE-GK-B. (f) SDAE-GG-B.

Table 7: The error classification accuracy through various models (the testing dataset).

Model	Dataset	Error rate (%)			
		FCM	GK	GG	adAP
SAE	A	3.89	6.67	3.89	—
	B	1.67	11.1	0	5
SDAE	A	4.44	15	3.89	4.44
	B	2.78	13.3	2.22	2.78

exhibit an overlap phenomenon, especially IRF1 and BF1 in Figure 11(a), these samples are separated well by using the SDAE. The classification accuracy by using different combination models for training datasets A and B is shown in Table 7. The lowest error rate is 2.78% with dataset B in the SDAE, which is the same as other combination models, including SAE/SDAE-FCM/GK/GG and SAE-adAP. SAE-adAP is little higher than SAE-GG with dataset B, but adAP can find the available clustering center point automatically.

5. Conclusion

A method based on an SDAE and adAP for bearing fault diagnosis was presented in this study. To reduce the dependence on manual experiments to label data, we used an SDAE without an output layer to extract useful fault features from the frequency domain directly by using FFT decomposition. Additionally, to find the available parameters in

AP, we introduced adAP for bearing fault diagnosis in this paper. The results show that the performance of the proposed model suppresses other models, such as SAE/SDAE-FCM/GK/GG and SAE-adAP.

The advantages and disadvantages of this paper are as follows.

(1) Using the model proposed in this article can serve to mark different bearing fault signals. For example, the clustering result is used to label the different fault signals, and then an SAE with an output layer can be used to realize online automatic fault diagnosis.

(2) However, the data collected in the actual project contain noise, resulting in the misclassification and mislabeling of the clustering results. Therefore, the classification effect for the subsequent use of an SAE with an output layer is even worse. In order to solve this problem, for future research, we propose an improved SAE model, for example, by adding a data-smoothing model at each hidden layer to eliminate noise layer by layer on the signal, thus improving the accuracy of clustering and classification.

Abbreviations

WT: wavelet transformation
EMD: empirical mode decomposition
IMFs: intrinsic mode functions
EEMD: ensemble empirical mode decomposition
SAE: stacked autoencoder
SDAE: stacked denoising autoencoder
FCM: Fuzzy C-mean
GK: Gustafson–Kessel
GG: Gath–Geva
AP: affinity propagation
adAP: adaptive affinity propagation
PCA: principal component analysis
NR: normal
BF: ball fault
IRF: inner race fault
ORF: outer race fault
CC: cluster center
AE: autoencoder
FFT: Fast Fourier transformation.

Data Availability

Previously reported bearing data were used to support this study and are available at (data link: http://csegroups.case.edu/bearingdatacenter/pages/download-data-file). These prior studies (and datasets) are cited at relevant places within the text as references [29].

Conflicts of Interest

The authors declare that there are no conflicts of interest regarding the publication of this paper.

References

[1] A. Heng, S. Zhang, A. C. C. Tan, and J. Mathew, "Rotating machinery prognostics: state of the art, challenges and opportunities," *Mechanical Systems and Signal Processing*, vol. 23, no. 3, pp. 724–739, 2009.

[2] J. G. Lai, X. Q. Lu, A. Monti, and G. P. Liu, "Stochastic distributed pinning control for co-multi-inverter networks with a virtual leader," *IEEE Transactions on Circuits and Systems-II*, 2019.

[3] F. Resta, F. Ripamonti, and G. Cazzluani, "Independent modal control for nonlinear flexible structures: an experimental test rig," *Journal of Sound and Vibration*, vol. 329, no. 8, pp. 961–972, 2011.

[4] G. Bagordo, G. Cazzulani, F. Resta, and F. Ripamonti, "A modal disturbance estimator for vibration suppression in nonlinear flexible structures," *Journal of Sound and Vibration*, vol. 330, no. 25, pp. 6061–6069, 2011.

[5] N. E. Huang, Z. Shen, S. R. Long et al., "The empirical mode decomposition and the Hilbert spectrum for nonlinear and non-stationary time series analysis," *Proceedings of the Royal Society of London. Series A: Mathematical, Physical and Engineering Sciences*, vol. 454, no. 1791, pp. 903–995, 1998.

[6] Z. Wu and N. E. Huang, "Ensemble empirical mode decomposition: a noise-assisted data analysis method," *Advances in Adaptive Data Analysis*, vol. 1, no. 1, pp. 1–41, 2009.

[7] C. Yi, D. Wang, W. Fan, K. L. Tsui, and J. Lin, "EEMD based steady-state indexes and their applications to condition monitoring and fault diagnosis of railway axle bearings," *Sensors*, vol. 18, no. 3, pp. 1–21, 2018.

[8] D. Wang, W. Guo, and P. W. Tse, "An enhanced empirical mode decomposition method for blind component separation of a single-channel vibration signal mixture," *Journal of Vibration and Control*, vol. 22, no. 11, pp. 2603–2618, 2014.

[9] J. Lai, X. Lu, X. Yu, and A. Monti, "Cluster-oriented distributed cooperative control for multiple AC microgrids," *IEEE Transactions on Industrial Informatics*, vol. 15, no. 11, pp. 5906–5918, 2019.

[10] F. Y. Lv, C. L. Wen, and M. Q. Liu, "Weighted time series fault diagnosis based on a stacked sparse autoencoder," *Journal of Chemometrics*, vol. 31, no. 9, pp. 1–16, 2017.

[11] Y. Qi, C. Shen, D. Wang, J. Shi, X. Jiang, and Z. Zhu, "Stacked sparse autoencoder-based deep network for fault diagnosis of rotating machinery," *IEEE Access*, vol. 5, pp. 15066–15079, 2017.

[12] R. Tang, Z. Wu, and X. Li, "Optimal operation of photovoltaic/battery/diesel/cold-ironing hybrid energy system for maritime application," *Energy*, vol. 162, pp. 697–714, 2018.

[13] L. K. Wang, X. Y. Zhao, and J. G. Pei, "Transformer fault diagnosis using continuous sparse autoencoder," *SpringerPlus*, vol. 5, pp. 1–13, 2016.

[14] P. Vincent, H. Larochelle, and I. Lajoie, "Stacked denoising autoencoders: learning useful representations in a deep network with a local denoising criterion," *Journal of Machine Learning Research*, vol. 11, pp. 3371–3408, 2010.

[15] P. Vincent, H. Larochelle, and Y. Bengio, "Extracting and composing robust features with denoising autoencoders," in *Proceedings of the 25th International Conference on Machine Learning*, pp. 1096–1103, Helsinki, Finland, 2008.

[16] J. Lai, X. Lu, X. Yu, and A. Monti, "Stochastic distributed secondary control for ac microgrids via event-triggered communication," *IEEE Transactions on Smart Grid*, vol. 11, no. 4, pp. 2746–2759, 2020.

[17] J. Li, Z. Struzik, L. Zhang, and A. Cichocki, "Feature learning from incomplete EEG with denoising autoencoder," *Neurocomputing*, vol. 165, pp. 23–31, 2014.

[18] R. Tang, X. Li, and J. Lai, "A novel optimal energy-management strategy for a maritime hybrid energy system based on large-scale global optimization," *Applied Energy*, vol. 228, pp. 254–264, 2018.

[19] S. Q. Zhang, G. X. Sun, and L. Li, "Study on mechanical fault diagnosis method based on LMD approximate entropy and fuzzy C-means clustering," *Chinese Journal of Scientific Instrument*, vol. 34, no. 3, pp. 714–720, 2013.

[20] D. E. Gustafson and W. C. Kessel, "Fuzzy clustering with fuzzy covariance matrix," in *Proceedings of the IEEE Conference on Decision and Control Including the 17th Symposium on Adaptive Processes*, pp. 761–766, Lauderdale, FL, USA, 1979.

[21] S. T. Wang, L. Li, and S. Q. Zhang, "Mechanical fault diagnosis method based on EEMD sample entropy and GK fuzzy clustering," *Chinese Journal of Scientific Instrument*, vol. 24, no. 22, pp. 3036–3044, 2013.

[22] I. Gath and A. B. Geva, "Unsupervised optimal fuzzy clustering," *IEEE Transactions on Pattern Analysis and Machine Intelligence*, vol. 11, no. 7, pp. 773–780, 1989.

[23] J. C. Bezdek and J. C. Dunn, "Optimal fuzzy partitions: a heuristic for estimating the parameters in a mixture of normal distributions," *IEEE Transactions on Computers*, vol. C-24, no. 8, pp. 835–838, 1975.

[24] F. Xu, Y. J. Fang, and R. Zhang, "PCA-GG rolling bearing clustering fault diagnosis based on EEMD fuzzy entropy," *Computer Integrated Manufacturing System*, vol. 22, no. 11, pp. 2631–2642, 2016.

[25] K. Yu, T. R. Lin, and J. W. Tan, "A bearing fault diagnosis technique based on singular values of EEMD spatial condition matrix and gath-geva clustering," *Applied Acoustics*, vol. 121, pp. 33–45, 2017.

[26] B. J. Frey and D. Dueck, "Clustering by passing messages between data points," *Science*, vol. 315, no. 5814, pp. 972–976, 2007.

[27] K. J. Wang, J. Y. Zhang, D. Li et al., "Adaptive affinity propagation clustering," *Acta Automatica Sinica*, vol. 33, no. 12, pp. 1242–1246, 2007.

[28] M. Kan, S. Shan, and H. Chang, "Stacked progressive auto-encoders for face recognition across poses," in *Proceedings of the 2014 IEEE Conference on Computer Vision and Pattern Recognition*, IEEE Computer Society, Washington, DC, USA, pp. 1883–1890, 2014.

[29] Case Western Reserve University, *Bearing Data Center Test Seeded Fault Test Data*, Case Western Reserve University, Cleveland, OH, USA, 2013, http://csegroups.case.edu/bearingdatacenter/pages/download-data-file.

[30] S. Dudoit and J. Fridly, "A prediction-based resampling method for estimating the number of clusters in a dataset," *Genome Biology*, vol. 3, no. 7, pp. 1–21, 2002.

[31] P. K. Velamuru, R. A. Renaut, H. B. Guo et al., "Robust clustering of positron emission tomography data," in *Proceedings of the Joint Interface CSNA*, pp. 1–7, Amherst, MA, USA, 2005.

[32] J. Dolz, N. Betrouni, M. Quidet et al., "Stacking denoising auto-encoders in a deep network to segment the brainstem on MRI in brain cancer patients: a clinical study," *Computerized Medical Imaging and Graphics*, vol. 52, pp. 8–18, 2016.

[33] J. Yu and Q. S. Cheng, "The upper bound of the optimal number of clusters in fuzzy clustering," *Science in China*, vol. 32, no. 2, pp. 119–125, 2002.

[34] F. Xu, Z. L. Huang, F. F. Yang, D. Wang, and K. L. Tsui, "Constructing a health indicator for roller bearings by using a stacked auto-encoder with an exponential function to eliminate concussion," *Applied Soft Computing*, vol. 89, Article ID 106119, 2020.

[35] Z. Wu, Q. Li, W. W. Wu, and M. B. Zhao, "Crowdsourcing model for energy efficiencyretrofit and mixed-integer equilibrium analysis," *IEEE Transactions onIndustrial Informatics*, vol. 16, no. 7, pp. 4512–4524, 2019.

[36] Z. Kong, S. Yang, D. Wang, L. Hanzo, and H. Z. Lajios, "Robust beamforming and jamming for enhancing the physical layer security of full duplex radios," *IEEE Transactions on Information Forensics and Security*, vol. 14, no. 12, pp. 3151–3159, 2019.

[37] J. Lai and X. Lu, "Nonlinear mean-square power sharing control for ac microgrids under distributed event detection," *IEEE Transactions on Industrial Informatics*, 2020.

[38] Z. C. Dong, M. Tian, R. L. Tang, X. Li, and J. G. Lai, "Improving the robustness of spatial networks by link addition: more and dispersed links perform better," *Nonlinear Dynamics*, vol. 100, no. 3, pp. 2287–2298, 2020.

[39] F. Xu, W. t. P. Tse, and Y. L. Tse, "Roller bearing fault diagnosis using stacked denoising autoencoder in deep learning and gath-geva clustering algorithm without principal component analysis and data label," *Applied Soft Computing*, vol. 73, pp. 898–913, 2018.

[40] Z. Dong, M. Tian, Y. Lu, J. Lai, R. Tang, and X. Li, "Impact of core-periphery structure on cascading failures in interdependent scale-free networks," *Physics Letters A*, vol. 383, no. 7, pp. 607–616, 2019.

[41] R. L. Tang, Q. Lin, J. X. Zhou et al., "Suppressionstrategy of short-term and long-term environmental disturbances formaritime photovoltaic system," *Applied Energy*, vol. 259, Article ID 114183, 2019.